III-Nitride Devices and Nanoengineering

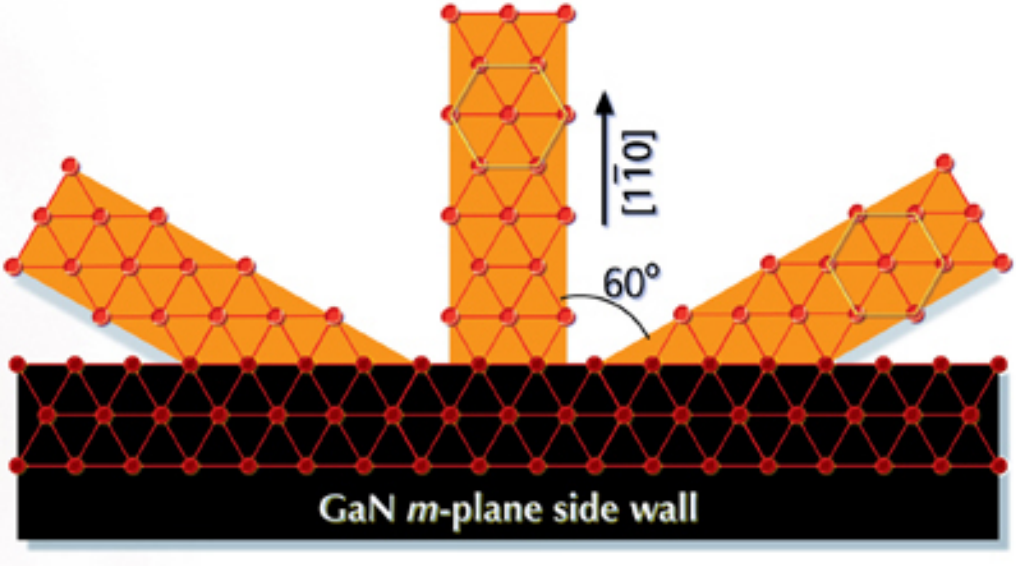

Imperial College Press

III-Nitride Devices and Nanoengineering

This page intentionally left blank

III-Nitride Devices and Nanoengineering

Zhe Chuan Feng
National Taiwan University, Taiwan

editor

ICP
Imperial College Press

Published by

Imperial College Press
57 Shelton Street
Covent Garden
London WC2H 9HE

Distributed by

World Scientific Publishing Co. Pte. Ltd.
5 Toh Tuck Link, Singapore 596224
USA office: 27 Warren Street, Suite 401-402, Hackensack, NJ 07601
UK office: 57 Shelton Street, Covent Garden, London WC2H 9HE

British Library Cataloguing-in-Publication Data
A catalogue record for this book is available from the British Library.

III-NITRIDE DEVICES AND NANOENGINEERING

ISBN-13 978-1-84816-223-5
ISBN-10 1-84816-223-5

Printed in Singapore.

PREFACE

Group III-Nitrides semiconductor materials, including GaN, InN, AlN, InGaN, AlGaN and AlInGaN, i.e. (Al,In,Ga)N, are excellent semiconductors, covering the spectral range from UV to visible and to infrared, with unique properties very suitable for modern electronic and optoelectronic applications. Remarkable breakthroughs have been achieved in recent years for research and development (R&D) in these materials and devices, such as high-power and high brightness blue-green-white light emitting diodes (LEDs) and blue laser diodes (LDs) as well as other optoelectronics and electronics devices and applications. III-Nitrides-based industry is forming up and new economic developments from these materials are promising. It is expected that III-Nitrides-based LEDs might replace the traditional light bulbs to realize a revolution in lightings and change entire human life in this century, similar to Edison's invention of the electric light bulb more than one-hundred year ago.

Recently, I have edited a book, **III-Nitride Semiconductor Materials**, and also published by Imperial College Press, which focused on III-Nitride semiconductor materials. The current is a sister complementary book of above one, focusing more on III-Nitride devices and nanoengineering but containing some materials not covered in the 1st book, such as AlGaN in Chapter 2.

The developments on these materials and devices are so quickly moving. Many data or knowledge, even just published quite recently, have been modified and needed to upgrade. This new book will cover the rapidly new developments and achievements in the field, in particular those made after entering the 21st century. It will face more to the engineering and materials side, not pure science.

The book is organized for a wide range of audiences and covers each of the basic and critical aspects of III-Nitrides science and technology. Each chapter, written by experts in the field, reviews the

important topics and achievements in recent years, discusses progresses made by different groups, and suggests further works needed. This book provides useful information to the device and nano-scale process, fabrication of LEDs, LDs, photodetectors and nano-devices, characterization, application and development on the III-Nitrides semiconductor devices and nanoengineering.

This book consists of 15 well-written review chapters and the topics of the book include: (1) An overview of the development of major light sources: From light bulbs to solid state lighting, (2) High pressure bulk crystal growth of (Ga,Al)N, (3) Structural and optical investigation of InGaN/GaN multiple quantum well light emitting diodes grown by metalorganic chemical vapor deposition, (4) MOCVD growth and efficiency improvement for ultraviolet light emitting diodes, (5) Fabrication of GaN light emitting diodes by laser-off technique, (6) High-resolution electron microscopy observations of GaN-based laser diodes, (7) Growth and development of III-nitride photodetectors, (8) Laser diodes grown on bulk GaN substrate, (9) III-Nitride lighting emitting diodes on Si, (10) Nitride Microdisplay and Micro-scale Light Emitting Diode Arrays, (11) III-nitride films and devices on Lithium metal oxides by molecular beam epitaxy, (12) III-Nitride light-emitting devices on patterned sapphire substrates, (13) Bandgap engineering of III-nitride devices on low-defect substrates, (14) III-Nitride nano-materials: growth and properties and (15) Recent trends in Indium Nitride nano-materials.

As seen, the current book presents the key properties of III-Nitrides devices and nanoengineering, describes key technologies and demonstrates the remaining challenging issues in nano-material preparation and device fabrication for future R&D in the 21st century. This book can serve well to material growers and evaluators, device design and processing engineers as well as potential users of III-Nitrides technologies, including new comers, postgraduate students, engineers and scientists in the III-Nitrides field**.**

Zhe Chuan Feng
(Professor in Photonics & Optoelectronics, and Electrical Engineering,
National Taiwan University, and MingDao University)

CONTENTS

Preface v

Chapter 1 An Overview of the Development of Major Light Sources: From Light Bulbs to Solid State Lighting
Y. S. Liu

1. Introduction 1
   1.1 Major milestones in the development of light sources 2
2. Incandescence light bulbs 4
3. Fluorescence light 6
4. Coherent light sources: semiconductor lasers 7
5. GaN–based blue and white LED 8
6. DOE ALITE 1995 10
7. Japan MITI's "21st Century Solid State Lighting Project" 1998 12
8. USA Next Generation Lighting Initiative Alliance (NGLIA) 14
9. China's National SSL Program 2006 15
10. Taiwan's solid state lighting program 16
    10.1 GaN-based solid state lighting research 16
    10.2 Next Generation Semiconductor Lighting Research and Development Consortium (2002-2005) 17
11. Conclusion 18

Chapter 2 High Pressure Bulk Crystal Growth of (Ga,Al)N
P. Geiser, J. Jun, B. Batlogg and J. Karpinski

1. Introduction 21
2. The group-III nitrides AlN, GaN and InN 23
   2.1 Crystal structure 23
   2.2 Material properties, defects and dopants 24
   2.3 Direct synthesis of group-III nitrides 30
3. Growth of group-III nitride bulk single crystals 33
   3.1 High nitrogen pressure apparatus for crystal growth (HNPSG) 34
   3.2 Cubic anvil cell for $Al_xGa_{1-x}N$ crystal growth (CAC) 37
4. Results and discussion 39
   4.1 $Al_xGa_{1-x}N$ bulk single crystals, growth results 39

4.2 Material characterization 41
4.3 Parameters influencing the Al content in $Al_xGa_{1-x}N$ 45
4.4 Suppression of crystal growth in $Ga_{1-y}Al_y$ alloys with $y > 0.01$ 48
4.5 GaN bulk single crystals 50
5. Conclusions and outlook 51

Chapter 3 Structural and Optical Investigation of InGaN/GaN Multiple Quantum Well Light Emitting Diodes Grown by Metalorganic Chemical Vapor Deposition
Z. C. Feng, J. R. Yang, A. G. Li and I. T. Ferguson

1. Introduction 58
2. Experimental 59
3. Structural properties of InGaN/GaN MQWs 60
3.1 High resolution X-ray diffraction (HRXRD) 60
3.2 High resolution transmission electron microscopy (HRTEM) 62
3.3 High-angle annular dark field (HAADF) images 63
4. Optical properties of InGaN/GaN MQW LEDs 64
4.1 Temperature dependent photoluminescence 64
4.2 PL band shifts and quantum efficiency 65
4.3 Excitation-power-dependent photoluminescence of InGaN/GaN green LED wafer 66
4.4 Different T-behavior of photoluminescence from InGaN/GaN green and blue LED wafers 69
5. Special electron microscopy of InGaN/GaN MQWs 72
5.1 V-shape defects 72
5.2 TEM digital analysis of lattice images (DALI) 73
5.3 Different TEM Studies on InGaN-based LEDs 74
6. Special luminescence spectroscopy of InGaN/GaN MQWs 75
6.1 Photoluminescence excitation (PLE) spectroscopy 75
6.2 PLE fitting and quantum confined Stokes effect 77
6.3 Temperature dependent time resolved photo-luminescence 78
6.4 Decay time versus temperature 81
6.5 Detection energy dependent time resolved Photoluminescence 82
7. Summary 83

Chapter 4 MOCVD Growth and Efficiency Improvement for Ultraviolet Light Emitting Diodes
S. J. Park and M. K. Kwon

1. Introduction 89
2. Issue of InGaN, AlInGaN, AlGaN material system 90
   2.1 InGaN 90
   2.2 AlInGaN 91
   2.3 AlGaN layer 92
3. Substrate issue 93
   3.1 Homoepitaxy on GaN substrate 93
   3.2 AlN substrate 97
4. Defect control of epi-layer 98
   4.1 Epitaxial lateral over-growth (ELOG) 98
   4.2 Delta doping 99
   4.3 Facet control technique 100
   4.4 Superlattice buffer 103
5. Internal quantum efficiency 104
   5.1 Band offset between well and barrier layer 105
   5.2 Pulsed atomic layer epitaxy (PALE) 107
   5.3 Ga droplet layer 109
   5.4 Si delta doped barrier layer 111
6. External quantum efficiency 112
   6.1 Patterned sapphire substrate (PSS) 113
   6.2 Mesh electrode 114
   6.3 DBR 114
   6.4 Photonic crystal (PC) 115
   6.5 PEC etching (phtoelectrochemical etching) 118
7. Summary 121

Chapter 5 Fabrication of GaN Light Emitting Diodes by Laser-off Technique
C. F. Chu, J. T. Chu, H. C. Kuo and S. C. Wang

1. Introduction 127
2. Current issues of conventional LED 129
   2.1 Thermal stable metallization of P-type ohmic contact 129
   2.2 Growth substrate 130
   2.3 Light output power 131
      2.3.1 Emitting area of GaN LEDs 131
      2.3.2 The reflectivity of GaN/material interface 134

2.4 Laser lift-off setup and process conditions 134
2.4.1 Laser system 134
2.4.2 Laser interaction on GaN material 136
2.4.3 Thermal model of laser interactions 139
2.4.4 LLO process 141
3. Major considerations and approaches for LLO of GaN LEDs 144
3.1 Laser energy requirements and modification 144
3.2 Selection of substrate and bonding metal 145
3.3 Two types of LLO-LEDs configurations 148
3.3.1 P-side up GaN LLO-LEDs 148
3.3.2 P-side down GaN LLO-LEDs 148
4. Fabrication of LLO-LEDs 149
4.1 Fabrication of freestanding P-side up GaN LLO-LEDs on conductive substrate 149
4.2 Fabrication steps of P-side down LLO-LEDs on Cu 151
4.3 Performance of P-side down LLO-LEDs on Cu 152

Chapter 6 High-Resolution Electron Microscopy Observations of GaN-Based Laser Diodes
M. Shiojiri

1. Introduction 159
2. HAADF-STEM imaging 161
3. Structural and compositional analysis of MQW InGaN/GaN layers and strained AlGaN/GaN superlattices 168
3.1 MQW InGaN/GaN layers 170
3.2 Strained AlGaN/GaN superlattices 178

Chapter 7 Growth and Development of III-Nitride Photodetectors
U. Chowdhury, C. J. Collins and P. Li

1. Introduction 190
1.1 Applications 190
1.2 Suitability 191
1.3 Types of photodetectors 192
1.4 Performance criteria 195
2. Visible-blind photodetectors 197
2.1 Early work 197
2.2 AlGaN based devices – towards solar-blindness 202
2.3 Devices grown on Si substrates 203
2.4 Avalanche detectors and phototransistors 204

2.5 Vacuum UV performance 206
2.6 Other miscellaneous works 207
3. Solar-blind photodetectors 209
3.1 Schottky devices and top-illuminated p-i-n devices 209
3.2 Back-illuminated p-i-n devices and focal-plane array 211
4. Conclusion 215

Chapter 8 Laser Diodes Grown on Bulk GaN Substrate
P. Perlin, M. Leszczynski, P. Prystawko, M. Boćkowski, I. Grzegory, C. Skierbiszewski and T. Suski

1. Introduction 223
2. GaN substrates for laser diodes applications 226
2.1 High nitrogen pressure solution growth method and its experimental set up 228
2.2 Habit and morphology of HNP-GaN crystals grown without seeding 230
2.3 Seeded growth by HNPS method 231
2.4 HVPE growth on HNP-GaN crystals 232
3. Homoepitaxial MOVPE growth of laser structures on bulk GaN substrates 232
4. Laser diodes grown on bulk GaN by molecular beam epitaxy 235
5. Performance of nitride laser diodes grown on bulk gallium nitride substrates 239
5.1 Overview 239
5.2 High-pressure grown GaN substrates for the future generation of high power laser diodes 240
6. Crystallographic defects in laser diode structures 243
6.1 Mismatch problem of AlGaN layers 243
6.2 Mg-related defects 245
6.3 In-related defects 246
7. Reliability of nitride laser diodes 246

Chapter 9 III-Nitride Lighting Emitting Diodes on Si
N. C. Chen and C. F. Shih

1. Introduction 253
2. Growth 254
2.1 Challenge of growing GaN on Si 254
2.2 Nucleation layers 256
2.3 Control of stress and reduction of dislocations 259

3. Recent development of the LEDs on Si 264
4. Conclusion 276

Chapter 10 Nitride Microdisplay and Micro-Scale Light Emitting Diode Arrays
H. W. Choi

1. Introduction 280
2. Light extraction in nitride materials 281
3. Micron-scale light emitting diodes 282
4. Micro-LED processing 285
5. Micro-displays 287
6. Interconnected micro-LEDs 288
7. Micro-optics and its integration to micro-LEDs 293
8. Novel geometry and configuration of micro-LEDs 295
9. Applications of micro-LED arrays 298
10. The future of micro-LEDs 300

Chapter 11 III-Nitride Films and Devices on Lithium Metal Oxides by Molecular Beam Epitaxy
G. Namkoong, S. Huang and A. Doolittle

1. Introduction 305
2. III-Nitride optoelectronic devices on $LiGaO_2$ 306
   2.1 Lithium gallate ($LiGaO_2$) substrates 306
   2.2 Polarity 308
   2.3 Strain in III-nitrides on $LiGaO_2$ 309
   2.4 III-nitrides on $LiGaO_2$ 315
   2.5 State of art MSM devices on $LiGaO_2$ 316
3. III-Nitride power transistor integration onto ferroelectric materials 320
   3.1 Integration of III-nitride based amplifiers/drivers on optical modulators 320
   3.2 Crystalline relationship between III-nitrides and $LiNbO_3$/$LiTaO_3$ 321
   3.3 Surface preparation 325
   3.4 Surface stability of $LiNbO_3$ and $LiTaO_3$ 327
   3.5 Polarity 328
   3.6 AlGaN/GaN power transistor integration on $LiNbO_3$ 331
4. Conclusions and outlook 333

Chapter 12 III-Nitride Light-Emitting Devices on Patterned Sapphire Substrates

D. S. Wuu, W. K. Wang and R. H. Horng

1. Introduction 337
2. Experimental details 339
   - 2.1 Fabrication of dry-etched patterned sapphire substrates 339
   - 2.2 Fabrication of wet-etched patterned sapphire substrates 340
3. Results and discussion 343
   - 3.1 Characterization of nitride-based LEDs grown on dry-etched patterned sapphire substrates 343
   - 3.2 Characterization of nitride-based LEDs grown on wet-etched patterned sapphire substrates 349
   - 3.3 Characteristics of flip-chip InGaN-based LEDs on patterned sapphire substrates 353
   - 3.4 Defect reduction and efficiency improvement of near-UV emitters via laterally overgrowth on GaN/patterned sapphire templates 357
4. Conclusions and outlook 362

Chapter 13 Bandgap Engineering of III-Nitride Devices on Low-Defect Substrates

S. Yu. Karpov

1. Introduction 367
2. Low-defect GaN and AlN substrates 371
3. Light-emitting diodes and laser diodes 374
   - 3.1 Factors controlling non-radiative carrier recombination in III-nitride heterostructures 374
   - 3.2 Indium-free light-emitting diodes with a thick active region 375
   - 3.3 Effect of crystal polarity on light-emitting diode operation 378
   - 3.4 Carrier confinement in the laser diodes 381
4. Field-effect transistors 385
   - 4.1 Threading dislocation effect on two-dimensional electron mobility 385
   - 4.2 Polarization dipoles in transistor heterostructures 386
   - 4.3 Transistors on AlN substrate and double-heterostructures 388
   - 4.4 A prototype of an N-polar transistor on AlN 389
5. Summary 391

Chapter 14 III-Nitride Nano-Materials: Growth and Properties
A. B. Djurišić, X. M. Cai and M. H. Xie

1. Introduction 399
2. Boron nitride nanostructures 401
3. Gallium nitride nanostructures 404
4. Aluminum nitride nanostructures 412
5. Indium nitride nanostructures 414
6. Ternary nitride alloy nanostructures and III-nitride nano-heterostructures 417
7. Conclusions and outlook 418

Chapter 15 Recent Trends in Indium Nitride Nanomaterials
A. Ganguly, K. H. Chen, L. C. Chen and S. Chattopadhyay

1. Introduction 431
2. Synthesis of Indium Nitride nanomaterials 432
   - 2.1 Thermal chemical vapour deposition (CVD) 433
     - 2.1.1 Catalyst-assisted growth 434
     - 2.1.2 Catalyst-free growth 438
   - 2.2 Molecular beam epitaxy (MBE) and plasma-assisted MBE 441
   - 2.3 Hydride vapour phase epitaxy (HVPE) 443
   - 2.4 Metalorganic vapour phase epitaxy (MOVPE) 444
   - 2.5 Chemical beam epitaxy (CBE) 445
   - 2.6 Metalorganic chemical vapour deposition (MOCVD) 445
   - 2.7 Solvothermal methods 448
3. Optical properties 449
   - 3.1 Photoluminescence 449
   - 3.2 Raman spectroscopy 451
4. Electrical properties 453
5. Applications 455
   - 5.1 Sensors 455
6. Concluding remarks 457

CHAPTER 1

AN OVERVIEW OF THE DEVELOPMENT OF MAJOR LIGHT SOURCES: FROM LIGHT BULBS TO SOLID STATE LIGHTING

Yung S. Liu

Institute of Photonics Technologies & Center for Photonics Research
National Tsing Hua University, Hsinchu 300, Taiwan
Email: liuys@mx.htnu.edu.tw

This chapter reviews briefly the major development of light sources including incandescence light, fluorescence light, lasers, particularly, the semiconductor laser and high-brightness blue/white GaN-based LED. It shows that the nano-science, in a broader sense, has played a critical role in the subsequent commercialization of these great inventions by making them become commercially viable products. It also reviews some major events and national initiatives that took place worldwide in the last decade, particularly, in USA, Japan, China and Taiwan, in the development of this emerging solid state lighting technology. These historically significant events have contributed to the development of a much desired and more efficient lighting source which could address some of the major challenges facing us today, namely, energy, environment and protection of our earth.

1. Introduction

After over a century since the introduction of electric light sources, two traditional lighting sources which are still commonly used today- the incandescence light and fluorescence light, have failed to achieve an electrical power efficiency over 25%. As the energy becomes scared, and our environment becomes endangered, a new and more efficient lighting source is critically needed.[1]

In the meantime, it is estimated there are about 2 billion population on the earth still do not have electricity, and therefore, do no have electrically generated light in their daily life.[2]

These two major challenges that the traditional lighting sources have failed to meet after they have been employed for over a century, namely, the low efficiency and low coverage of lighting on the earth. The emerging of GaN-based semiconductor lighting sources in the past decade promises to fulfill both of these challenges.[3,4]

In 1909, when the tungsten incandescence light bulb was first introduced commercially by GE, it had an efficacy of 10 lm/W. It look 30 years to reach this critical level of efficacy since the carbon filament light bulb was developed by Edison in 1879. For over a century, the incandescence light has been one of the major lighting sources. To date, the efficacy of the incandescence light bulbs is less than 20 lumen/W; only twice as much as what was achieved 100 years ago. There has been little progress made over the entire century.

Coincidentally, it took also about thirty years for LED to reach a level of brightness of 10 lm/W since the first LED was invented in early 1960. However, it is the high brightness GaN-based semiconductor blue and white LED light sources developed by Shuji Nakamura at Nichia in 1995 that opened a totally new chapter in the history of the development of lighting sources. These achievements have stimulated significant research interest and efforts in bringing this technology to commercially viable lighting products and this technology has been progressing in a truly amazing pace.

Today, an efficacy about 200 lm/W has been demonstrated[5]; an almost 20-fold improvement over what was first introduced a decade ago. At this level of efficiency, we could address those two most critical challenges that traditional lighting sources have failed to resolve, namely, to develop a highly efficient lighting source and to bring light to every corner of the world.

1.1. *Major milestones in the development of light sources*

If we list the major milestones in the development of light sources chronically, they are

- The incandescence light bulb developed by Thomas Edison in the late 19th century. This was the first time that electric lighting was introduced in the first 200 millennia of the human history;
- The invention of coherent light sources, particularly semiconductor lasers in the mid-20th century, This was the first time a light source with coherent properties was developed; and,
- The development of high-brightness blue/green GaN LED in the late 20th century, and later the high-brightness semiconductor-based solid state white light sources. This was the first time opening a new era of highly efficient and all solid state lighting sources.

All these breakthroughs have led to significant advancements of modern electronics, optoelectronics and material sciences and technologies, and made profound impacts upon how we live, work and communicate.

For example, the invention of incandescence light bulbs not only lit the world for the first time in the entire human history, but also created a major market for the electricity. It accelerated the development of electricity generation, transmission, and conditioning, and thus brought forth the infrastructure of a modern society that relies heavily on electricity.

The invention of lasers, particularly semiconductor lasers was the key component used in the modern fiber optical communication (the backbone of Internet), digital optoelectronics systems such as CD, DVD and laser printers. The development in these technologies has brought us the Internet and digital electronics that have made profound impacts upon our life.

The invention of high-brightness white LED, still in the early stage of development, has already made significant inroad from back light modules used in LCD displays, automobile lights and head lamps, to architecture lighting with a flurry of new applications coming out everyday.

These efficient light sources are going to save enormous amount of energy, reduce greenhouse gases generation, and make our environment cleaner. In addition, a high efficient solid state light source offers the

possibility of bringing light to billions of population on earth living in the darkness without electric light in the entire human history.

In the following sections, we discuss the critical role that the nano-science, in a broader scope, has played in improving the efficiency of these light sources and making these inventions commercially viable lighting sources.[6,7,8]

2. Incandescence light bulbs

When Edison was trying to make an incandescence light bulb work, there were several other similar attempts by other inventors, however, none of them could succeed in making the incandescence light bulb last long enough. Edison persisted and invented a carbon filament placed inside an oxygen-free bulb which could burn for forty hours by 1879. Nevertheless, the incandescence light bulbs at the time had two critical problems for being useful as a consumer product, namely, the efficiency was too low and the life was too short.

Fig. 1. The Edison's incandescence light bulb in 1882. (Courtesy of GE Company).

If Edison's effort were to end here, the incandescence light might not become as widely used as it is today and Edison might not be credited as

the great inventor of the incandescence light bulb. (This story sounds similar to the development of GaN-based LED a century later.)

Two technical breakthroughs were critical to making this light source technology useful and become a commercial successful product:[6,7,8]

First, there was a young chemist, Irving Langmuir, who was recruited by Edison to work on improvement of the life and efficiency of the incandescence light bulb. Langmuir discovered the bulb life and efficiency could be significantly improved when he introduced an inert gas into the light bulbs,

In the course of his investigations, Langmuir realized the importance of the adsorbed layer on the surface chemistry and developed the vacuum system for his experiments. He performed fundamental studies of surface chemistry and invented the apparatus for making mono-layers adsorbed films that bears his name, Langmuir-Blodgett films. He pioneered the science of monolayer adsorbed films and invented the first gas-filled incandescence light bulb that is used today.

Langmuir's pioneering work on the surface chemistry of monolayer became the foundation of surface sciences, today, generally called nano-sciences. He was awarded a Nobel Prize in chemistry in 1932 for his discoveries and investigation in surface chemistry. In fact, he was the first industrial scientist ever to receive a Nobel Prize for the work that was motivated to improve the light bulb's life and efficiency.

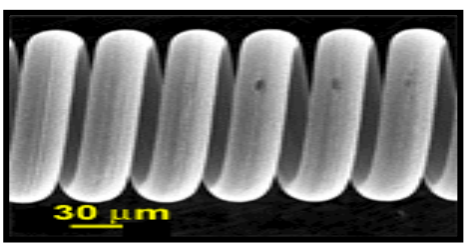

Fig. 2. The coiled tungsten filament used in the incandescence light bulb developed in 1909 by William Coolidge. (Courtesy of GE Company).

In the meantime, the effort seeking for a new filament material to improve the efficiency and life of the incandescence light bulbs led to the development of coiled tungsten filaments by Coolidge (Fig. 2). In 1909,

almost thirty years after the invention of light bulbs by Edison, the tungsten light bulb became a commercial product with an efficacy reaching 10 lumen/W which was about an order of magnitude improvement over that of the original Edison's light bulb.

As the incandescence light based on the principle of blackbody radiation, it was recognized that the efficacy of incandescence light could be improved by increasing the filament temperature at the expense of the operating life. Halogen lamps overcome this problem by introducing a small amount of halogen gas inside a quartz envelop to allow the lamp operated at a higher temperature, in the meantime, the tungsten evaporated from the surface will recombine with halogen gas and then redeposit onto the filament. This regenerative process employs a subtle surface chemistry to allow the lamp operated at a much higher temperature, thus improve the lamp efficacy while maintain a good life time; another wonder of nano-science!

The Halogen light has an efficiency of about 15-20 lumen/W. The efficacy of the incandescence lamp, however, has made little improvement in the last century in spite of intensive research effort. The incandescence light remains as a dominant light source used in the residential building in USA. The overall power conversion efficiencies of these incandescence lights are about 5%.

3. Fluorescence light

Perhaps few people realize that Edison was also an inventor of a fluorescence lamp and he even had a patent filed in 1896 for a x-ray fluorescent lamp and granted in 1907. This Edison's invention however never became a successful commercial product because X-ray is not economically feasible as a light source. It wasn't until 1938, a practical fluorescent lamp was successfully designed by GE and was subsequently marketed that year.[9]

A fluorescent lamp contains a small amount of mercury inside a tube filled with a low pressure inert gas like argon. The inside of the glass tube was coated with a phosphor layer. When the lamp is turned on, the discharge current induces electrons to collide and excite the mercury atoms. The UV emission from Hg atoms converts to visible light through

phosphors. The fluorescence lamps have efficacies ranging from 60-100 lumen/w and are the work horse in commercial indoor lighting. The overall power conversion efficiencies of various fluorescence lamps, however, are about 25%.

The incandescence and fluorescence lights are the dominant lighting sources used in residential and commercial indoor buildings and account for almost 90% electricity energy consumed for lighting. Non-building lighting such as street light and commercial outdoor lighting account for the rest of total electricity used for lighting. In general, the total electricity consumed for lighting is about 20% of the total amount of the electricity generated worldwide.[10]

4. Coherent light sources: semiconductor lasers

The invention of coherent light sources via the stimulated emission is a remarkable scientific and technical achievement. Among all the coherent light sources developed to date, the semiconductor laser represents one of the most important coherent light sources ever developed.

When the first GaAs semiconductor laser was operated at GE Research Labs by R.N. Hall and his co-workers in the mid-20 century, it was a rudimentary device (Fig. 3) operated at the liquid nitrogen temperature with a high threshold current density.[11] This device didn't become a commercially viable device until the invention of hetero-junction structures which allows the carrier confinement, and thus greatly reduces the laser threshold current.

More importantly, in the decades that followed, the development of molecular beam epitaxial (MBE) process and molecular engineering that provided a powerful instrument to allow the precise material growth atomic layer by layer in the nano-meter scale contributed significantly to the successful deployment of semiconductor lasers used today; another wonder of nano-science!

To date, GaAs-based laser devices are used in the fiber communication, digital devices such as CD/DVD and laser printers. It has made profound impacts to our life and to the way we communicate. Today, the most efficient semiconductor light emitting devices are semiconductor lasers in the infrared. This type of semiconductor light

emitting devices produces high power output on the order of hundred of watts in infrared. They are the preferred light sources which have replaced discharged flash-lamps for pumping solid state lasers. They are also used as the pump sources for the fiber amplifier; a critical component used commonly in the optical communication.

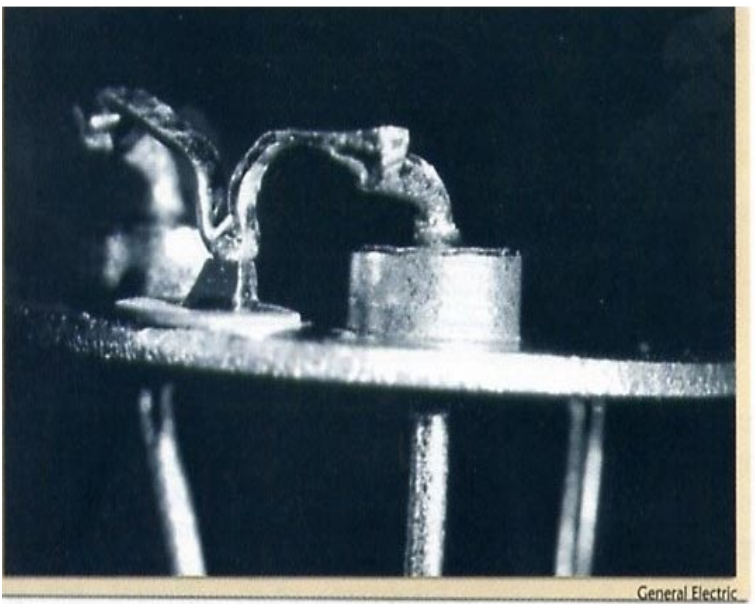

Fig. 3. The first semiconductor laser developed at GE. (Courtesy of GE Company).

5. GaN-based blue and white LED

When LEDs were invented in the late 60's, the output power was so low that they were used only as indicator lights in display panels. After nearly thirty year intensive development till mid-1990's, the efficiency of most LED devices were still very low, for example, GaP LED at 555 nm had an external quantum efficiency of 0.07%, and SiC LED at 470 nm 0.02% with the exception of GaAlAs red LED at 660 nm which had an external quantum efficiency of 12%.[12] Due to the lack of high power and high efficiency, major applications for LEDs till then were limited to the indicator light. In addition, lack of a high power LED in the blue and

green color has restricted the use of LED to less than full color applications.

In 1993, when the first high brightness blue GaN LED was commercialized by Nichia,[13] and two years later, the green GaN LED.[14] In the years that followed, Nichia further developed the high brightness white LED by mixing of blue LED with yellow phosphors. Since then, the field was revitalized and the outlook was totally changed. (Fig. 4)

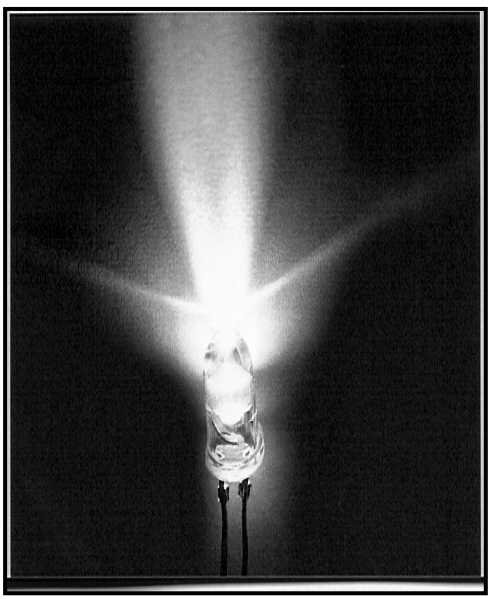

Fig. 4. The first GaN-based white LED developed by S. Nakamura at Nichia. (Courtesy of Nichia Company).

The applications of GaN LED have been rapidly expanded by the advancement made in the high power LED epi, device and packaging; all of these employ various advanced nano-technologies such as quantum-dots, quantum-rod, and photonic crystals. These sophisticated nano-technologies are found in the high power LED devices used in LCD backlights, automobile illumination, and the RGB white light sources in the projection display. In the future, we expect that nano-science and

technology will continue to play a critical role in realizing the ultimate goal of making a 200 lm/W device or beyond.[5]

6. DOE ALITE 1995

In 1995, US Department of Energy (DOE) organized a workshop, ALITE (Advanced Lighting Technologies) held in Washington DC that involved major lighting companies such as GE, Phillips and Osram to identify promising areas for pre-competitive research in the basic science of commercial light sources that might lead to major breakthroughs in the performance and efficiency. It was recognized at the time, that lighting consumes about 20% of the total electric energy generated in USA and the efficiencies of major light sources used over the century were merely 5-25%.

After intensive presentation and discussion among about 80 experts coming from world leading academic, industrial and research institutions, the ALITE Workshop reviewed all types of traditional light sources including incandescence lights, fluorescence lights, halogen and HID and other conventional light sources, the group concluded that in spite of the intensive R&D efforts, the technologies of three major conventional lighting sources, namely, incandescence, fluorescence and halogen, have not shown any significant improvements in the past thirty years.

In addition, the workshop further concluded at the time that the semiconductor light source is the only promising technology that mostly likely to make breakthroughs for achieving a much higher efficiencies. In the conclusion of the workshop, it was predicted that LED lighting would reach 10 lumen/watt by year 2000 and >100 lumen/watt by year 2005 with up to 100,000 hours of life. The output of the ALITE Workshop was published in a report (EPRI Report, TR-106022), called, "Vision 2000 Lighting Technology Roadmap" which could be seen as a white paper for the national solid state lighting project launched later.[15]

I left the workshop convinced that LED lighting is going to be an important technology for the GE lighting business and initiated a program at GE funded by the GE Lighting Business to look into the feasibility of using LED for general lighting applications in 1997. This was the very first funded project at GE on this emerging solid state

lighting technology after GE invented the LED in early 60s and then dropped the LED research program in early 70s. The reason for dropping the LED research program was "it will never be useful for general lighting applications" as concluded by the GE management.

At ALITE workshop, I also met Dr. George Craford who was heading the LED research program at HP. We had good exchange at the workshop discussing the possibility of using LED for lighting applications. After ALITE workshop, I made a special trip to visit him. We spent an afternoon together in his office at the HP Research Center in Palo Alto, CA, and continued the discussion in the following February 1996.

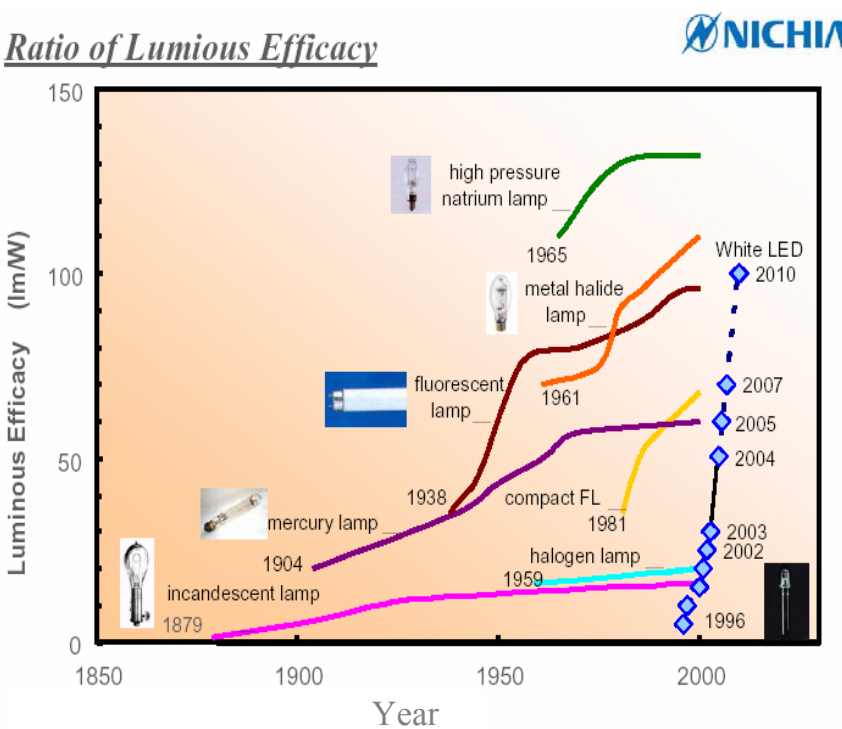

Fig. 5. The efficacies of major light sources evolved over the entire centuries. (Courtesy of Nichia Company).

In November 1996, HP and Philips announced in the news the formation of a joint venture called, LumiLEDs, to develop LED-based

lighting products and business. That was the very first business venture formed by a major international company devoted solely to the development of LED-based lighting sources. Personally, however, I was a bit disappointed for not having HP team up with GE to work together on this emerging lighting technology with a tremendous potential.

Almost at the same time, there were major technical breakthroughs taking place in Japan. Nakamura and his coworkers at Nichia published a paper, entitled, "High-brightness InGaN/AlGaN double-hetero-structure blue-green-light-emitting-diodes".[13,14] The research results were quickly commercialized as Nichia started to sell blue LED products. Nakamura and his coworkers further combined the blue GaN LED with YAG phosphors to generate white LED with an efficacy reaching over 10 lumen/W. This marked a new generation of high brightness LED and quickly transformed the LED into a new kind of light sources and opened a new era of solid state lighting! The evolution of various major light sources is shown in Fig. 5 in which the commercially available white LEDs sold by Nichia are used for comparison.

7. Japan MITI's "21st Century Solid State Lighting Project" 1998

In 1997, trying to capitalize the leadership role after having invented this new lighting sources, Japan's MITI (Ministry of International Trade and Industry) announced the plan for a 5-year, 5B Yuen (US$40M) national project, "The 21st Century Solid State Lighting" to develop GaN-based LED white light for general lighting applications with a goal of 120 lumen/W by 2010 (Fig. 6). At the time, this goal seemed to be too aggressive to be realistic when the commercial product announced at the time by Nichia was only about 10 lumen/W.

In October 1997, I represented GE to visit Dr. Yoshi Tabata, then MITI's Program Director, to understand the purpose and background of this national project. I was told that the targeted goal of 120 lumen/W was not an extrapolation from the technical roadmap, rather it was dictated by the Kyoto Protocal declared by the Japanese government to cut the total greenhouse gas emission at least 5% from the 1990 level in the commitment period from 2008-2012. MITI's 21st Century Lighting

Fig. 6. The poster for the national project on "21st Century Solid State lighting Project" initiated by MITI, Japan in 1998; the first national project ever on this technology in the world.

Project was formally launched in the following year in 1998 with participation of most companies from the LED industry in Japan except Nichia.

The MITI's solid state lighting project represented the first national effort in the world launched to develop efficient solid state light sources for general lighting purpose and was driven by the concern of environmental conservation by the Japanese government.

Prof. Tsunemasa Taguchi of Yamaguchi University was the PI leading this project and the project was jointly carried out by the New Energy and Industrial Technology Development Organization (NEDO) and the Japan Research and Development Center for Metals (JRCM) through a subsidy provided to NEDO by the Ministry of Economy, Trade and

Industry (METI). The Government provided a total funding of 6.2 Billion Yen between 1998 to 2004, and 2.5 Billion Yen, from 2004 to 2009.

The research topics in the 21st Century Lighting Project covered the following areas:

- Fundamental studies on emission mechanism in GaN-based compound semiconductors,
- Improvement of epitaxial growth methods for near ultraviolet (UV) LEDs.
- Large substrates for homo-epitaxial growth.
- Development of phosphors which generates white light excited by blue and near UV LEDs, and
- Realization of illumination source using white LEDs.

Japanese government's SSL initiative, not only focused on general lighting as the main target, it also focused on applications such as medical. One such project administrated by Ministry of Education, Culture, Sports, Science and Technology (MEXT) was "white LED to medical applications" which was to investigate high power white LED lighting systems for medical applications funded at 2.5B Yuen for five years from 2004 to 2009.

In retrospect, MITI's 21st Century Lighting Project is to be considered as one of the most significant national projects ever launched by any nations in the world.

8. USA Next Generation Lighting Initiative Alliance (NGLIA)

In USA, the Office of Naval Research (ONR) organized a workshop chaired by Dr. Y.S. Park in 1998 in Washington on the GaN LED technology. The workshop invited experts from GE, HP, Sandia Lab., Cree Research and UCSB among others. This workshop was conducted to assess its potential for general lighting applications.

The US Department of Energy (DOE) initiated programs on solid state lighting research and development since 2000. In partnership with the private industry, the Next Generation Lighting Initiative Alliance (NGLIA) was established. The DOE initiative has made significant

progress since then. The NGLIA includes both organic and organic LEDs as the viable technical approaches in the program. The members includes GELcore, Lumileds, Color Kinetics, Cree Inc., Dow Corning Corp., Osram Sylvania, Eastman Kodak and Air Products and Chemicals.

In the course of these initiatives, some significant accomplishments were made including: Lumileds Lighting in partnership with Sandia National Laboratories developed nano-photonics devices using quantum dots and demonstrated a quantum efficiency of 76%. Cree Inc. achieved 70 lumen/W with their commercial packaged LED operated at 350 mA in 2005; an increase of 43% in brightness compared with the current devices then.[15]

In 2006, President Bush signed National Energy Policy (NEP) called for "reliable, affordable and environmentally sound energy for America's future." The US Government allocated a budget of USD$50M to fund the SSL program in the next seven years. In particular, DOE has set the following mission statement for the SSL research and development effort:

> *"Guided by a Government-industry partnership, the mission is to create a new, U.S.-led market for high-efficiency, general illumination products through the advancement of semiconductor technologies to save energy, reduce costs and enhance the quality of the lighted environment."*

9. China's National SSL Program 2006

In 2003, the Ministry of Science and Technology of China (MOST) together with the Ministry of Information Industry, and the Chinese Academy of Sciences and other government bodies plus eleven local government initiated a government committee for China's SSL and formally launched the national SSL program.[16]

In February 2006, as part of government 11th five-year plan (2006-2010), MOST allocated RMB350M (USD$44M) to support the national solid-state lighting program. The growth of the high technology sector is key to China's future development, and LEDs are seen as an indispensable part.

One goal of the national SSL program is to stimulate domestic production through the use of public-private partnerships. Participation to the national program will include more than 15 research institutions and university research labs, as well as more than 2500 companies involved in LED wafers, chips, packaging and applications.

Another key goal of China's SSL program is energy savings. China is the second largest energy-consuming country after the US, and its energy consumption per dollar of GDP however is much higher than Japan, Europe or the US. The country has set an ambitious plan to quadruple its total GDP by 2015, but hold the increase of her energy consumption only by a factor of two.

Lighting is seen a key element for the increase of energy demand, especially as 14 million rural Chinese move to cities each year. The adoption of SSL will be an important element in reducing the growth of energy demand. China expects to be the largest market for LEDs and solid-state lighting in the world." From reports, it is apparent solid state lighting will become a rapid growing industry in Asia in general, and in China in particular.

10. Taiwan's solid state lighting program

Taiwan has become a leading producer of GaN LED with a production capacity of about 1.1B per month GaN chips and 1.25B per month of InGaAlP chips. Taiwan is now ranked as the world leading producer of both GaN and InGaAlP chips.[17] The MOCVD industry in Taiwan grew rapidly since 1998 with commercial MOCVD reactors installed in production estimated exceeding 300 units.

10.1. *GaN-based solid state lighting research*

From 1997 to 2000, the GaN program at ITRI (Industrial Technology Research Institute) funded by the government focussed on the epi-technology for growing InGaN LED UV and blue LED, and LED chip processes, such as contacts, dry etching and chipping processes for high power and high efficiency GaN-based LED devices for display and lighting applications.

Since 2001, the ITRI research program started to address packaging technologies as well as lighting applications critical to energy conservation. Technologies on special package designs for lighting application as well as packaging technologies using flip-chip for high power devices were developed. The program has been coupled closely to the lighting industry and LED-based lighting equipment. Demonstrations using solid state lighting for replacement of conventional lighting sources for energy saving and environmental conservation have also begun in this phase.

ITRI played in key role in technology development and personnel trainging for the industry. The close interactions between ITRI and local industry had contributed to the rapid growth of the MOCVD industry during this period.[18,19]

10.2. *Next Generation Semiconductor Lighting Research and Development Consortium* (*2002-2005*)

One of the major industrial projects funded by the Ministry of Economic Affairs was the "Next Generation Semiconductor Lighting Research and Development Consortium," formed in 2002 with participation of ten LED companies to develop advanced solid state lighting technologies with goals to achieve: (a) 100 lumen/W lab devices, and (b) 50 lumen/W proto-type commercial devices by 2005.

The consortium members were Epistar, Forepi, Ledtech, LiteOn, Opto-tech, Everbright, Kingbright, Tyntek, ParaLight, and Unity. Dr. Frank Chien of Forepi served as PI for this R&DC project.

This research and development consortium was successfully completed in 2005 by meeting its original technical goals. For the LED industry, this project was significant in that it was the first time, multiple companies worked together in a research project performing various tasks to achieve a common goal. It was a novelty to both the business culture and practice in Taiwan where most companies tend to work on research alone. Throughout the project, ITRI played a key role working with member companies in planning, organizing, facilitating and performing some of the technical tasks from the beginning till its completion.

The funding supports for solid state lighting programs come from Department of Industrial Technology, Ministry of Economics Affair (DOIT/MOEA) for research and engineering, and from Commission of Energy, Ministry of Economics Affairs for solid state lighting demonstration, and lighting-based module technologies.[20,21]

11. Conclusion

As the world energy becomes scared, and our environment becomes endangered, a new and efficient lighting source is critically needed to replace the traditional lighting sources which have electrical power efficiencies less than 25%. In the meantime, it is estimated there are about 2 billion population on earth still do not have the electricity, and therefore, do no have electrically generated light in their daily life. The traditional lighting sources have failed to meet these two challenges for over a century since they were introduced. The GaN-based semiconductor lighting source developed in the past decade promises to overcome both of these challenges.

In this chapter, we discussed major technological advancements in the history of the light source development including the invention of light bulbs in the late 19th century, the invention of coherent light lasers, particularly semiconductor lasers in mid-20th century, and the high-brightness blue/white GaN-based LED in the late 20th century. We showed that In each of these scientific breakthroughs, the nano-science and technology, in a broader sense, have played a key role in the subsequent commercialization of these inventions and made them into successful products.

We further reviewed several major events and national initiatives in USA, Japan, China and Taiwan for the development of viable solid state lighting sources to save energy, reduce green house gases and protect our environment and the earth..

Looking into the future, it is just as Edison proclaimed when he invented the incandescence light bulb that,

"... Where this thing's going to stop, Lord only knows…"

References

1. Jeff Y. Tsao, "Solid State lighting: lamps, chips and materials for tomorrow," *IEEE Circuits and Devices,* **3,** 28 (2004).
2. Dave Irvine-Holiday *et al.*, "Renewable energy based SSL – a key to economic development for the base of the pyramid and a must for millennium development goals," *Proc. The First International conference on White LED and Solid State Lighting*, p. 311, (Tokyo, Japan, 26-30 Nov. 2007); also see www.lutw.org .
3. Shuji Nakamura and Gerhard Fasol, *"The blue laser diode",* Springer Publications, (1997).
4. Michael S. Shur, "Solid state lighting: toward superior illumination," *Proc. of the IEEE*, **93,** 10, 1691 (2005).
5. Shuji Nakamura *et al*., "Recent Performance of Nonpolar/semipolar/polar GaN-based emitting devices and bulk crystal growth (plenary)", *Proc. The First International conference on White LED and Solid State Lighting*, p. 64, (Tokyo, Japan, 26-30 Nov. 2007).
6. Y. S. Liu, "Impacts of Nano-Science on the Commercialization of Light Sources: from Light Bulbs, Lasers to Solid State Lighting", *Proc. The 2nd International conference on Display and Solid State Lighting (DSSL'2008),* (Seoul, Korea, 1/30-2/1, 2008) p. 119,
7. Y. S. Liu, "From Light Bulbs to Solid State Lighting: Impacts of Nanotechnologies to the development of solid state lighting and impacts on earth, energy and environment", *Proc. the 3rd Asia-Pacific Workshop on Wide-gap Semiconductors,* (Jeonju, Korea, 2007).
8. Y. S. Liu, *"From Light Bulbs, Semiconductor Lasers to solid State lighting – the impacts of nano-technologies," China International Forum on Solid State Lighting",* (Shenzhen, China, 2006).
9. US Patent 2,239,040 (1938).
10. "Light emitting diodes (LEDs) for general illumination", An OIDA technology roadmap update (2002).
11. R. N. Hall *et al*., "Coherent light emission from GaAs junctions", *Phys. Rev. Lett.*, **9,** 366 (1962).
12. E. F. Schubert, *"Light-Emitting Diodes",* Cambridge University Press, 2nd Edison, (2006).
13. S. Nakamura *et al*., "P-GaN/n-InGaN/GaN double heterostructure blue light emitting diodes", *Jpn. J. Appl. Phys*. **32**, L8 (1993).
14. S. Nakamura *et al.*, "High-brightness InGaN/AlGaN double-hetero-structure blue-green- light-emitting-diodes", *J. of Applied Physics*, **34**, L797 (1995).
15. *"Vision 2000 Lighting Technology Roadmap", EPRI Report*, TR-106022, (1995).
16. Wu Ling, "Solid State Lighting in China", *Proc. The First International conference on White LED and Solid State Lighting,* p. 55, (Tokyo, Japan, 26-30 Nov. 2007).

17. *Photonics Industry Development Association, Display, No. 2, Special Issue on LED*, (2007).
18. Y. S. Liu *et al*., "Solid state lighting technology development," *Symposium on Solid State Lighting*, Photonics West, SPIE, San Jose, CA, USA (2003).
19. Y. S. Liu, "GaN Research and the Industry development in Taiwan," *First Asia-Pacific Workshop on Wide-Gap Semiconductors*, (APWS-2003), Hyogo, Japan (2003).
20. Y. S. Liu, "Recent Development of solid State Lighting Devices and Applications," *International Forum on Solid State Lighting,"* (Xiamen, China, 2005).
21. Y. S. Liu, "Progress in Solid State Lighting in and Development of the GaN industry in Taiwan", *Proc. The First International conference on White LED and Solid State Lighting*, p. 64, (Tokyo, Japan, 26-30 Nov. 2007).

CHAPTER 2

HIGH PRESSURE BULK CRYSTAL GROWTH OF (Ga,Al)N

Peter Geiser, Jan Jun, Bertram Batlogg, Janusz Karpinski

Laboratory for Solid State Physics
Swiss Federal Institute of Technology Zurich, Switzerland
E-mail: peter.geiser@alumni.ethz.ch

This chapter reviews the synthesis of (Ga,Al,In)N bulk single crystals. A brief introduction of the field is presented in the first part with an emphasis on methods developed for bulk single crystal growth. The second part summarizes thermodynamic, kinetic and defect formation aspects relevant for the growth of crystals by direct synthesis and their subsequent characterization. Two crystal growth techniques and the corresponding technical set-up and growth procedures are described in the third part. One technique involves the growth from a metallic melt under high nitrogen pressure (high nitrogen pressure solution growth, HNPSG), an established method for the direct synthesis of GaN at temperatures up to 1600°C and pressure up to 15 kbar. The other method, new for this study, is based on a cubic anvil cell (CAC) with tungsten carbide pistons, a solid medium for pressure transmission and nitride powders serving as a nitrogen source. The temperature can be as high as 1850°C and a maximum pressure of 35 kbar is applied. In the fourth part, recent results in bulk $Al_xGa_{1-x}N$ growth with the CAC method and results from HNPSG experiments are discussed.

1. Introduction

Light generation by recombination of electrons and holes in semiconductors is technically exploited since the 1950s. With the aim to cover the entire visible spectrum, an intense search for suitable semiconductor materials was conducted at the beginning of the 1970s

including SiC, ZnSe, ZnO and GaN as promising candidates. During the 1970s and 1980s substantial progress was made using SiC and ZnSe resulting in commercially available devices. However, since the end of the 1980s, GaN and its cousins AlN and InN showed their superiority over the other materials with respect to device fabrication and market potential. The reasons are manifold: SiC is mainly limited by an indirect band gap and the resulting limited device efficiency. ZnSe suffers from short device life time limiting consumer application. ZnO is still a subject of intense research as material properties are expected to be superior to those of the III-nitrides. Yet challenges remain on the way to device fabrication (e.g. p-type doping). For more information the interested reader may consult.[1]

By the end of the 1980s two important findings mark the breakthrough for GaN: The introduction of AlN [2] and GaN [3] buffer layers deposited at low temperatures led to a significant reduction of the lattice mismatch problems. The other important discovery relates to p-type doping. It was found that Mg impurities can be activated, using electron irradiation (LEEBI)[4] or thermal treatment,[5] resulting in p-type material.

Optoelectronic devices became available and their quality quickly improved. The history of the high brightness LED and LD is reviewed in Ref. 6. Still, dislocation density was a serious limiting factor for device reliability. Kim *et al.*[7] advanced the field in 1997 by developing the "lift-off" technology, lowering the dislocation density to $10^7\,cm^{-2}$. Another relevant approach yielding similar dislocation densities is the so-called epitaxial lateral overgrowth method (ELOG) introduced by Usui *et al.*[8] Nowadays the growth of group-III nitrides with metal organic vapor phase epitaxy (MOVPE) and molecular beam epitaxy (MBE) on sapphire and SiC substrates is the prevailing approach in industry. Further details on that subject can be found in Refs. 9 and 10. Still, dislocations remain a limiting factor for device quality and life time. A density lower than 10^4 defects per cm^2 is considered the magic number to fabricate defect free devices.[11] The aspect of substrate quality will remain critical in the near future: Modern nitride devices are built from ternary or quaternary nitride layers with high contents of Al or In. As the lattice parameters are changing with the composition, the choice of a suitable substrate will

remain challenging. Substrates for group-III nitride epitaxy were reviewed by Liu and Edgar.[12]

Attempts were made to grow single crystals for homoepitaxy. The thermodynamics of Ga-N-GaN and Al-N-AlN pose a big challenge, as a high temperature and in case of GaN also a high pressure is needed to grow single crystals. Several methods were used to grow bulk single crystals,[13,14] and the growth from molten nitrides (Na, Li, Ca melts) at moderate temperature and pressure yielded high quality material.[15] The growth of GaN using supercritical ammonia has attracted attention in recent years. Large crystals have been grown[16] and the method is considered as a candidate for scaling up GaN bulk crystals. A successful method for GaN bulk single crystal growth was developed by Karpinski *et al.* at the beginning of the 1980s.[17] Crystals grown by this method have been widely investigated at the High Pressure Research Center "Unipress" in Warsaw, PL.[18,19,20,21,22] Despite the intense work on binary compounds, little is known about the feasibility to grow ternary nitride crystals employing these methods.

2. The group-III nitrides AlN, GaN and InN

Growth of high quality group-III nitride single crystals is difficult, especially for InN and the ternary compounds. Therefore material data are often extracted from measurements on heteroepitaxially grown nitride layers. For GaN this is less problematic as bulk single crystals have been available for some time. Therefore the following explanations emphasize GaN, however, the general statements are also valid for AlN and InN.

2.1. *Crystal structure*

As summarized by Trampert *et al.*, the group-III nitrides crystallize in three different structures: Zinc-blende, rock-salt and wurtzite.[23] The zinc-blende structure is meta-stable and is grown heteroepitaxially on suitable substrates like Si (001), GaAs (100) or MgO. The rock-salt phase is observed only at high pressure. As the maximum pressure reached with the equipment of the present study does not exceed 4 GPa, the samples

studied by us are in the wurtzite phase. Both zinc-blende and wurtzite structures lack a center of inversion and possess a polar axis which determines lattice orientation. These are the [0001] direction for wurtzite and [111] for zinc-blende respectively. As a result the crystals are e.g. piezoelectric and properties of the (000-1) and (0001) crystal faces differ significantly. To make the crystals ready for epitaxy GaN bulk single crystals are therefore treated with different procedures for each side. It is also commonly observed that the properties of the epitaxially grown layers depend on lattice orientation. Determining the orientation is not straight-forward and must be done for each type of sample as it depends on growth conditions, substrates or doping. It is emphasized again, that the lattice orientation addresses a true bulk property. It is not related to the terminating atom layer or the bonding situation at the crystal surface. To underline this, the expressions "polarity" or "polar face" are commonly used. See also Ref. 24.

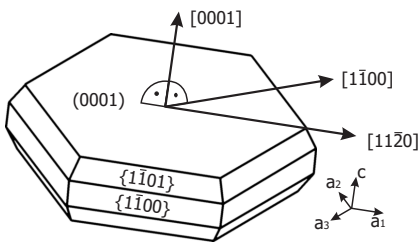

Fig. 1. Wurtzite crystal orientation: Faces and directions.

2.2. *Material properties, defects and dopants*

Binding energies in the group-III nitrides are large compared with other compounds: the values are 11.52, 8.96 and 7.72 eV/atom for AlN, GaN and InN respectively while it is 6.52 eV/atom only for GaAs (Ref. 25 and references therein). Additionally, the bond length is comparably small (1.89, 1.94 and 2.15Å respectively) which yields a set of interesting material properties. The semiconductors have wide band-gaps and show excellent chemical and physical stability. The compounds are also known for their good thermal conductivity. The possibility to grow ternary nitride layers with tailor made properties such as the gap energy or the

refractive index is another important feature. This makes the group-III nitrides suitable compounds for high temperature and optoelectronic devices.

Band structure: Calculations indicate that the group-III nitrides in the wurtzite and cubic phase have all direct energy band gaps.[26] At room temperature the value of E_g is 6.13 eV for AlN,[27] 3.44 eV for GaN[28] and less than 2 eV for InN. For InN the gap energy was reported to be 1.89 eV.[29] However, recent work indicated that the gap energy is rather 0.65-0.7 eV (Ref. 30 and references therein), and the subject is under discussion. The unusual scatter in the measured values may be due to the material quality. Heteroepitaxially grown InN thin films contain high densities of structural defects and impurities (e.g. oxygen). Only micrometer sized InN crystallites have been grown so far.[31] Their gap energy was estimated to be 2.2 eV.

Defects and impurities: Control of the impurity concentration, defects and dopants, including their distribution, is at the very core of the commercial semiconductor application. Such questions have been at the focus of numerous studies since the late 1960s. GaN, in bulk or thin film form, is usually a strong n-type conductor. The carrier concentration can be as high as 10^{20} per cm^3. The origin of this autodoping has been discussed in detail and nitrogen vacancies were considered as a source for these free carriers[32,33] as demanding growth conditions force to grow the material in a nitrogen deficient environment.[34] This interpretation held for almost three decades and was the generally accepted view until Neugebauer and Van de Walle presented their work on formation of native defects.[35] Their study is based on first principle total-energy calculations and covers the electronic structure of defects, the atomic geometry and formation energies in a group-III nitride lattice. The formation energy is defined as[36]

$$E^f[X^q] = E_{tot}[X^q] - E_{tot}[GaN,bulk] - \sum_i n_i\mu_i + q[E_F + E_v + \Delta V] \; . \quad (1)$$

For an impurity X with charge q the quantities $E_{tot}[X^q]$ (total energy of the lattice with impurity) and E_{tot}[GaN,bulk] (total energy of the undisturbed lattice) are taken from supercell calculations (Density-

functional theory with local density approximation). The expression takes into account the energy change upon removal or addition of atoms (number n_i with the chemical potential μ_i) as well as the dependence of the formation energy on the Fermi level E_F. Both E_v and ΔV are correction factors required for the model. The consideration of different charge states and the influence of the Fermi level on the formation energy leads to a detailed assessment of the defect and impurity properties.

Point defects: The group-III nitrides have in common, that self-interstitials and anti-site defects have high formation energies of several eV regardless of the Fermi level (Fig. 2.1). The presence of these defects in relevant concentrations *c* is usually excluded as this quantity is calculated according the expression

$$c = N_{sites} N_{config} \exp(-E^f/kT) \, . \qquad (2)$$

The exception to that rule is the Al interstitial in AlN. In all other cases, vacancies are the point defects with the lowest formation energies. The most striking result of the investigation is the observation, that for a Fermi level high in the gap (n-type) it is not the nitrogen vacancy (singly charged shallow donor) that will form. Instead, Neugebauer and Van de Walle found that the formation of the gallium vacancy (triply charged deep acceptor) is more probable under these conditions. Positron annihilation experiments by Saarinen *et al.* subsequently confirmed the presence of V_{Ga} in n-type samples.[37] The presence of V_{Ga} is also associated with impurity complex formation and a parasitic impurity band often found in luminescence measurements, the so called “yellow luminescence”, which is discussed below. For p-type material, the nitrogen vacancy (now in 3+ charge state) is the energetically most favored point defect and may act as a compensating center.

N-type GaN: As the nitrogen vacancy is not likely to form in n-type GaN, other residual impurities must be present to explain the high concentration of free carriers in GaN. With their lower formation energies, Si_{Ga} and O_N are considered to be the shallow donors causing the high n-type background (Fig. 1.2).[38] Si, most important for intentional

n-type doping, can be excluded as an autodopant according to Kim *et al.*[39] Oxygen however, was found to be present in virtually every environment used for GaN growth. Growth substrates, impurity traces in the precursor gases and oxide ceramics used for thermally loaded areas of the growth reactor are possible sources. According to Krukowski *et al.* oxygen is also easily incorporated in the growth melt used in HNPSG experiments.[40] Both Si and O have low ionization energies in the range of 20 to 30 meV and are usually assumed to be fully ionized at room temperature.[41,42,43] The presence of these dopants can be associated with features commonly observed in photoluminescence spectra. If no special measures are taken, bulk GaN grown by HNPSG is a degenerate semiconductor. With the Fermi-level shifted into the conduction band, a blue-shift of the band-to-band transition is observed (Burstein-Moss effect). The effect is very pronounced in GaN and a shift by 0.1 eV is not unusual.[44] The so-called yellow luminescence (YL) refers to a broad luminescent transition around 2.2 eV. Several models have been proposed to explain the YL including different shallow and deep levels.[45,38,46,47,48]

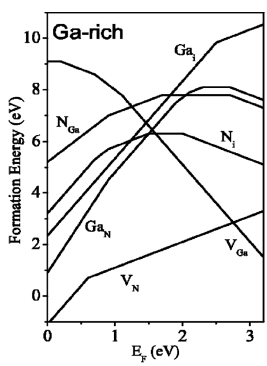

Fig. 2.1. Point defect formation energy for GaN as a function of the Fermi level. The slope indicates the charge state, with positive values for donor like behavior.[36]

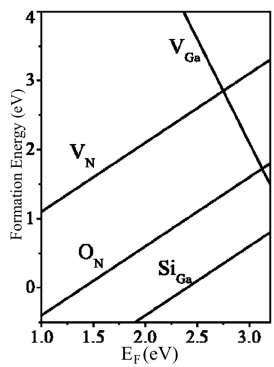

Fig. 2.2. Formation energies of donors in comparison to the most probable native defects. The Fermi energy is measured from the top of the valence band.[36]

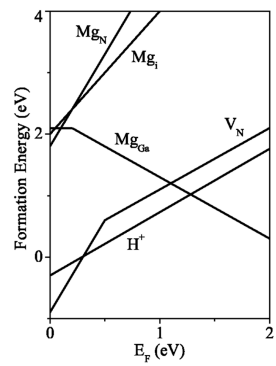

Fig. 2.3. Formation energy of Mg in different configurations. For comparison energies of hydrogen and nitrogen vacancies are shown as well.[36]

P-type GaN: 35 Elements were investigated by Pankove *et al.*, using ion implantation and thermal annealing to introduce the impurities into the GaN lattice.[46] Among the eight elements identified as luminescent centers, Mg is the most significant one for current applications. Electrical characterization was not possible, as the ion implanted films were highly resistive. This was most probably due to the generation of compensating point defects. Mg predominantly substitutes on the Ga atom position. According to Neugebauer and Van de Walle, Antisite (Mg_N), interstitial or configurations off the substitutional site ("AX"-center) are not likely to form. At room temperature the achievable hole concentration hardly exceeds 10^{18} cm^{-3}, for two reasons. The solubility of Mg in the GaN lattice is limited to about 10^{20} atoms/cm^3 as for higher concentrations Mg_3N_2 will form. In addition, Mg is far from being an ideal acceptor with an ionization energy as large as 200 meV. At room temperature only about 1% of the acceptor atoms are ionized.

GaN bulk single crystals can be doped by adding Mg to the growth melt in the HNPSG process. Litwin-Staszewska *et al.* report the growth of Mg doped GaN. They found crystals with different properties which were assigned to two groups.[49] Both types of crystals are highly resistive, but in one case, determination of the sign of the thermoelectric power indicated p-type material. More detailed studies show, that this material is heavily compensated and that more than one defect may be responsible for that. The hole concentration was reported to be $3 \times 10^{14}\,cm^{-3}$ with a mobility of 5 cm^2/Vs at room temperature.[50]

Ternary nitrides: Substitution of Ga with In and Al is a standard procedure in group-III nitride device fabrication. With varying composition of the ternary nitride layers, the characteristics of native defects and dopants change. For the $Al_xGa_{1-x}N$ ternary nitride a meta-stable lattice configuration is of interest. The so-called DX-transition is known from other III-V semiconductors. As discussed by Queisser and Haller,[51] Si as a shallow donor in AlAs-GaAs was found to undergo a transition into a deep defect for $Al_xGa_{1-x}As$ with $x > 0.22$. Initially the effect was explained with the formation of deep centers by combining the shallow donors D with an unknown defect X, hence the name DX center or DX transition. Calculations by Chadi and Chang[52] provided a

better and now generally accepted explanation. Two different bonding configurations exist for an impurity. Depending on material composition or by application of high pressure, the formation of one of these configurations is energetically favored. As reviewed by Neugebauer and Van de Walle, a similar effect was discovered for oxygen in $Al_xGa_{1-x}N$. For $x > 0.3$ or at a corresponding hydrostatic pressure of about 20 GPa, the impurity will change its bonding configuration and turn from a shallow donor into a deep acceptor. Therefore, the presence of oxygen in high Al substituted ternary nitrides must be avoided as oxygen may render other donors ineffective when undergoing the DX transition. Other technically relevant dopants, Si and Mg in particular, and their behavior in $Al_xGa_{1-x}N$ have been studied as a function of the composition. As a general trend it was found that their electronic levels move deeper into the gap with increasing Al content, rendering the dopants less effective. Although theoretically predicted for Si, a DX like transition was not confirmed experimentally for x up to 0.44.[43,53]

Implications for the present study:

(i) High concentrations of shallow donor impurities will affect material characterization measurements. When interpreting a measured luminescence blue shift of the near band-gap transition, it is necessary to consider a possible Burstein-Moss shift in addition to the widening of the band gap due to Al substitution in GaN.

(ii) A similar complication exists for x-ray diffraction measurements, where the change of the lattice parameters does not only depend on Al incorporation but also on the presence of impurities: It is not (only) the size effect of these impurities that influences the lattice parameters but rather the free electrons they contribute. These effects are discussed and quantified for $Al_xGa_{1-x}N$ bulk single crystals in section 4.2.

(iii) For the samples investigated, with an Al content of less than 30%, it can be excluded that the donor impurities will undergo a transition from a shallow to a deep state with increasing Al content.

(iv) A special concern may be the high growth temperatures applied in the cubic anvil cell. This will result in increased concentrations of native defects and impurities.

(v) The information that interstitial and anti-site native defects have too high formation energy to be present in relevant concentrations is important to calibrate mass-spectrometric measurements. The method yields element ratios and thus it is crucial for calibration of the data (internal standardization) that the total number of atoms is known to be equal to the number of cation lattice sites.

2.3. *Direct synthesis of group-III nitrides*

Comparing the bonding energies of group-III nitrides with those of other semiconductors one would expect to find properties between those of SiC on one side, and GaAs on the other side. However, the thermodynamic properties of group-III nitrides differ significantly. With G as the Gibbs free energy, the stability criterion for GaN can be written as

$$\Delta G = G_{GaN} - G_{Ga} - \tfrac{1}{2} G_{N2} < 0 \quad (3)$$

as the direct formation of the group-III nitrides follows the reaction

$$Me + \tfrac{1}{2}N_2 \leftrightarrow MeN \quad (4)$$

The nitrogen molecule has a very high bonding energy of about 9.8 eV/molecule. This lowers the Gibbs free energy of the constituents and shifts the equilibrium to the left side in equation 1.4. Very high melting temperatures (e.g. $T_m^{GaN} \sim 2200°C$ [55]) must be assumed for group-III nitrides, based on calculations[54] or projection of experimental data.[17,55] With increasing temperature the Gibbs free energy, defined as

$$G = H - TS \quad (5)$$

is lowered faster for the constituents than for the crystal. This further shifts the reaction equilibrium to the left hand side in equation 1.4. Thus an increase of the nitrogen pressure is required to counter this tendency. In fact a very high N_2 equilibrium pressure has been reported for group-III nitrides at high temperature, exceeding 1000 bar.[56] Based on calculations assuming ideal behavior, the equilibrium pressure was estimated to be several hundred kbar close to the melting temperature.[57] This is far beyond the gas pressure range that can be technically controlled. At pressures of up to 20 kbar the interaction between nitrogen

molecules becomes significant, and the behavior deviates from the predictions made by the ideal gas law. In particular, as shown by Karpinski,[58] this interaction at high pressure increases the chemical potential of the nitrogen (repulsion) and gives rise to a contribution which is defined as

$$\Delta\mu = kT \ln a\,(p_{N2},T) \tag{6}$$

The activity a (also denoted as fugacity for gaseous species) is equal to the pressure for an ideal gas. For real nitrogen, it reaches values orders of magnitude larger (in dimensionless units) than the real pressure. This contribution substantially lowers the equilibrium pressure: For a temperature as high as 1700°C the equilibrium pressure of GaN was reported to be rather 20 kbar than 650 kbar as calculated for nitrogen as an ideal gas.[17]

Although a pressure of 20 kbar might be controlled in an autoclave, the resulting equilibrium temperature at this pressure is still far away from the conditions estimated for a congruent melting. However, at elevated temperature and pressure the solubility of nitrogen in gallium quickly increases. As shown by Karpinski *et al.*,[17] it becomes feasible to crystallize GaN in a gallium melt taking advantage of the increasing nitrogen concentration at high p and T. Similar investigations of the thermodynamic properties have been made for AlN and InN, which must be taken into account when considering the growth of ternary group-III nitrides.

Using the ideal solution approximation, Grzegory *et al.* calculated the amount of N dissolved in Ga, Al and In melts (Fig. 4).[34] For Al and In they additionally considered a deviation from the ideal behavior which would shift the amount of nitrogen dissolved as indicated by arrows in Fig. 4. Although this effect increases the solubility of N in Al, the growth of AlN remains problematic with respect to the growth temperature required. Experimental facilities are limited to approximately T = 2000°C and p = 20 kbar. Even at such a high temperature the molar fraction of nitrogen dissolved in the Al growth melt remains small, ending up in a slow crystal growth of AlN. The solubility of N in an In melt, however, rises quicker with temperature than in Ga and Al. Although the real behavior of the system will probably lead to lower

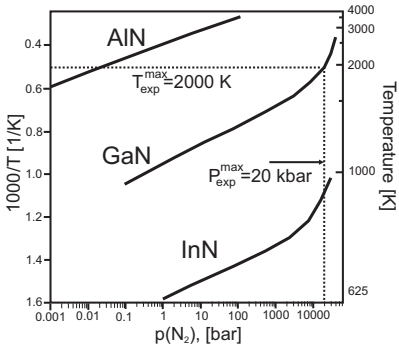

Fig. 3. The equilibrium pressure of group-III nitrides compared to technical limitations for crystal growth (dashed lines). Figure based on Ref. 34.

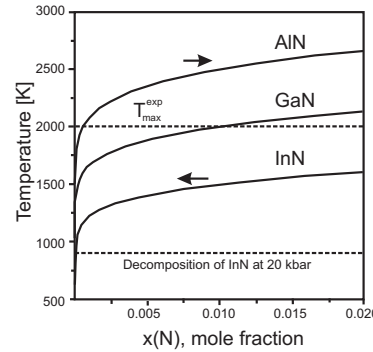

Fig. 4. Liquidus curves for group-III nitrides calculated in the ideal solution approximation. Arrows indicate the trend for non-ideal behavior of Al and In. Figure based on Ref. 34.

concentrations than expected for the ideal case, the limiting factor for InN growth is a different one: the equilibrium partial pressure is extremely high even at low temperatures. The maximum pressure controllable with HNPSG is not sufficient to increase the equilibrium temperature significantly, thus InN growth is considered not feasible.[34]

The formation of (In,Ga)N films grown with MOVPE was studied by Matsuoka.[59] In addition, theoretical considerations were made for the (In,Al,Ga)N system. GaN-AlN compounds are reported to be miscible over the entire range of composition. For compounds containing InN, the conclusion was that stable mixing is not possible over a large composition range.

Another important feature was reported by Boćkowski (Ref. 60 and refs. therein): Synthesis of group-III nitrides directly from their constituents strongly depends on the kinetics of the first reaction step. This is the dissolution of the nitrogen molecule in the metallic growth melt. It was found that nitrogen has to overcome a substantial energy barrier when approaching the melt surface. The values reported for this barrier are 5.8, 4.8 and 3.2 eV for InN, GaN and AlN respectively. The experimental observations are in line with these values: For molten Al under high nitrogen pressure a combustion synthesis takes place.

Boćkowski reports that if the pressure is within a range of about 0.1 to 6.5 kbar, aluminum shows a strong exothermic reaction with nitrogen, and polycristalline AlN powder is formed with a high yield rate. Above about 1 kbar the reaction is increasingly controlled by the thermal conductivity of the nitrogen, which leads to extinction of the reaction above 6.5 kbar. The growth of single crystalline AlN material with HNPSG was reported subsequently (Ref. 61 and refs. therein). However, the crystals exhibit features typical for cellular growth or seem to include cavities. Two aspects are considered as problematic for the growth of good quality AlN single crystals: (1) the nitrogen transport mechanism (convection rather than diffusion) (2) a strong nitrogen supersaturation and the formation of an AlN layer at the beginning of the growth procedure that suppresses growth. It seems that high temperatures and large temperature gradients may be a way to overcome this problem.

The combustion reaction is not reported for GaN, but also in this case, the reaction kinetics at the gas/liquid interface is important. A thin layer of GaN forms at the surface of the growth melt exposed to the nitrogen atmosphere, which subsequently dissolves and releases nitrogen into the growth melt. The direct synthesis of InN is hardly possible. With an energy barrier of 5.8eV for dissolution, very high temperatures are needed to achieve the nitrogen concentration in the In melt. Such high temperatures in turn require an extremely high pressure for InN phase stabilization. The range of 20 kbar that can be addressed with HNPSG is not sufficient for that purpose.

No information is available for ternary nitrides or binary melts. Considering the different aspects of binary compound growth laid out in this section, the growth of ternary compounds can be assumed to be a challenging task.

3. Growth of group-III nitride bulk single crystals

As shown in the previous section, high pressure is required for the growth of group-III nitride bulk single crystals near the thermodynamic equilibrium. For GaN a technical realization is the high nitrogen pressure solution growth (HNPSG) method. Equipment design and the growth method were developed at the beginning of the 1980s by Karpinski *et al.*

at UNIPRESS in Poland[17] and by now it is an established tool for GaN bulk single crystal growth. Its potential for $Al_xGa_{1-x}N$ crystal growth was studied in this project. In addition a new assembly was developed, based on an cubic anvil cell with a solid pressure-transmitting medium (CAC). Crystal growth facilities and the experimental procedures are discussed in the following sections.

3.1. *High nitrogen pressure apparatus for crystal growth* (*HNPSG*)

Facility description: The single atmosphere autoclave (SAA) design is based on a double-walled steel cylinder closed with plugs from both sides. To optimize the construction for highest pressure, the bore diameter of the autoclave (pos.1, Fig. 5) is quite small (30 or 40 mm), limiting the forces in the cylinder. The autoclaves used in the present study can be safely operated up to 15 or 12 kbar respectively.

A second key feature of this design is the heater (pos.7, Fig. 5), being placed entirely inside the pressure vessel. This is a significant difference to other constructions (see e.g. Ref. 62) where the pressurized volume is heated externally. The advantage is obvious: there is no thermal load on the mechanically stressed vessel. To keep the

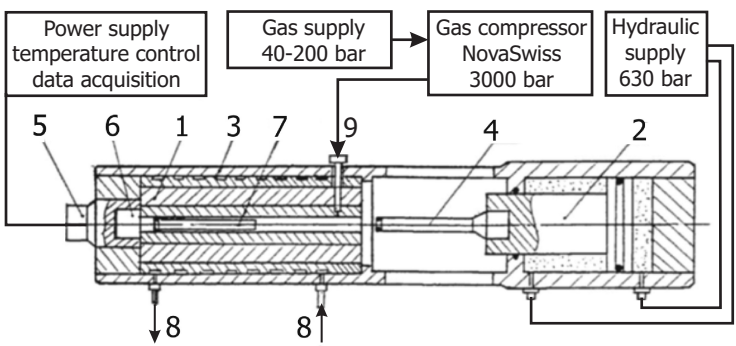

Fig. 5 Cross-sectional view of the single atmosphere high pressure gas autoclave. The pressure cell consists of a double-wall pre-stressed steel cylinder. External control and support facilities are shown, including first stage gas and second stage oil compressor. 1) pressure vessel; 2) oil hydraulics; 3) cooling jacket; 4) pressure intensifier; 5) catch; 6) plug with electrical feed-through or capillary connection for autoclave extension; 7) heater and crucible; 8) cooling water in/outlet; 9) capillary from first stage compressor.

temperature of the assembly low, the pressure cell is actively cooled with an external water-cooling jacket (pos.3, Fig. 5). Further, and equally important, a high maximum heater temperature can be handled with this setup: 1600°C can be kept for up to 1000 hours with a three stage heater constructed from alumina and PtRh30 wire. The temperature can be stabilized within ± 0.5°C at gradients as large as 20°C/cm. Centering rings at both ends of the assembly avoid direct contact of the heater and autoclave wall. The cylindrical volume available for crystal growth is 8 or 12 mm in diameter and is about 50 mm long.

As shown in Fig. 5, a number of auxiliary installations are required to operate the autoclave. The temperature is controlled by a programmable unit (Eurotherm 2704) with independent feedback loops for all three heater stages. The gas is pressurized in two stages: The first stage is a 3 kbar industrial compressor (e.g. Nova Swiss) with a 200 bar standard bottle as gas supply. For reliable operation the compressor requires a minimal input pressure of about 50 bar. The 3 kbar outlet of the compressor is connected to the SAA by a capillary (0.3 mm inner diameter). The second pressure stage uses an oil hydraulic compressor with a maximum oil pressure of 630 bar.

Experimental procedure (GaN growth): Pure gallium is used as starting material. Standard quality gallium without a certificate of purity and 7N quality from Alfa Aesar were used. The latter was used to grow reference crystals that were studied with mass spectrometry measurements (LA-ICPMS). The measurements indicate a similar purity of the GaN bulk single crystals grown from either starting material. Compared to the reference crystals, only slightly higher impurity concentrations were found in crystals grown from the gallium standard quality, e.g. Sn with a few ppm.

The starting material is placed in a pyrolytic BN crucible. This container is manufactured from high grade starting material (AX05, Saint-Gobain) which is further purified by heating *in vacuo* in an RF or e-beam furnace (1600°C for about 1 hour). For the standard experiments, all preparation steps are performed in air. The handling is performed, however, in an argon drybox for experiments where the raw material is heated, alloyed with Al, Mg or other elements (Unilab, MBraun;

$O_2 < 1$ ppm, $H_20 < 1$ ppm). The exposure to oxygen and water from the laboratory environment is minimized by tight packing of the crucible/heater assembly for the transfer from the drybox to the autoclave. Immediate evacuation of the autoclave with a turbo molecular pump after the transfer was performed for all experiments. To support the evacuation of the autoclave, in particular to heat out the adsorbed moisture, the assembly is slowly heated up to 300°C. This temperature should not be exceeded when the vessel is evacuated as otherwise an unwanted tempering of the autoclave wall might locally lower the stability of the vessel.

Table 1. Standard temperature program for GaN growth experiments in the single atmosphere autoclave. The temperature values given are typical, and should be considered as an example only.

		stage target temp. [°C]				
		bottom	middle	top		
step	description	(b)	(m)	(t)	duration	
1	stabilization	300	300	300	1	min
2	ramp up	1500	1500	1500	2	hours
3	stabilize	1500	1500	1500	10	min
4	set gradient	1500	1525	1525	20	min
5	set gradient	1500	1525	1550	20	min
6	dwell	1500	1525	1550	150	hours
7	close gradient	1500	1525	1525	10	min
8	close gradient	1500	1500	1500	10	min
9	ramp down	300	300	300	2	hours
10	dwell	300	300	300	48	hours

In the next step, the autoclave is pressurized to the maximum pressure of the first stage. The pressure level is subsequently adjusted to the desired starting pressure of the experiment by further moving in the pressure intensifier (2nd stage) into the autoclave bore. An increase of almost 4 kbar must be considered when the temperature is subsequently increased from 300°C to 1575°C ± 25°C. A typical growth run follows the program steps listed in Table 1.

The experiment ends with depressurizing and disassembling the autoclave and heater. The crystals can be retrieved from the crucible by etching the excess gallium with hydrochloric acid and aqua regia.

Although GaN does not dissolve in acids, selective etching of the (000-1) face may occur if the acid is too hot (~ 50°C).

3.2. *Cubic anvil cell for $Al_xGa_{1-x}N$ crystal growth (CAC)*

Multi anvil cell setups are installed in many research laboratories around the world to study high pressure phase transformations and material properties. Depending on the specific need, the sample cell varies in shape and size. Hemispherical, cubic and octahedral assemblies (referring to the sample volume) with a diameter/truncation edge length from one inch down to a few millimeters are in use. Tungsten carbide or diamond anvils transfer the load to the sample volume and enable either resistive or laser heating. For in situ sample investigation, some multi anvil cells are integrated in larger facilities.

Rather few applications of the anvil technology to the group-III nitrides are reported. Karpinski *et al.*[17] used a hemispherical anvil cell for determination of the equilibrium pressure of GaN. More recent work from Utsumi, Saitoh *et al.* focusses on congruent melting of GaN [55] and $Al_xGa_{1-x}N$ solid phase reactions[63] Growth of nitride crystallites in a laser heated diamond anvil cell was reported by Hasegawa *et al.*[64]
A new assembly for nitride crystal growth was developed in this study. The resistively heated cubic anvil cell (CAC) with solid pressure medium uses nitride compounds as nitrogen source. As shown in section 4, the method was successfully used to grow $Al_xGa_{1-x}N$ bulk single crystals for the first time.

Facility description: The set-up is based on a commercially available pressure cell with tungsten carbide pistons as shown in Fig. 6. The truncation edge length is 22 mm. Pressure is built up with a 1600 ton oil hydraulic press working against the two base plates of the pressure cell. A set of wedge-shaped steel parts transmits this force through six tungsten carbide pistons to the sample volume in a quasi isostatic way. A pyrophyllite (alumosilicate) cube acting as solid pressure medium and thermal isolation represents the experimental volume of about one cubic inch. The external load ring and both base plates are water cooled to prevent the anvils from being overheated. The assembly has a one stage

heater (shown in Fig. 7). The current for heating is supplied through the appropriately isolated steel parts and tungsten carbide pistons.

Pressure and temperature are calibrated in separate runs. The pressure is monitored externally by measuring the oil hydraulic pressure. This value is calibrated, using phase transitions of metals (resistivity change). In the present cell a pressure up to 35 kbar can be reached. The temperature is measured with type B thermocouples. This temperature is related to the power dissipated in the pressure cell, as this quantity can easily be determined from the applied current and tension. The temperature calibration must be performed each time the heater or thermal isolation dimensions have been changed. The maximum temperature used in this study was 1850°C.

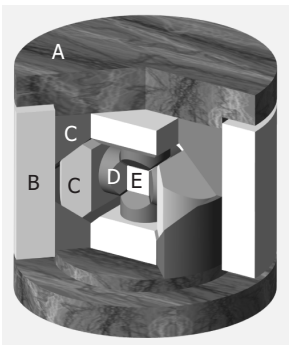

Fig. 6. Cubic anvil cell setup. Water cooled parts: A) base plate, B) load ring. Pressure transmission: C) wedge-shaped steel parts, D) tungsten carbide pistons. The growth experiment assembly including the heater is placed in the sample volume E.

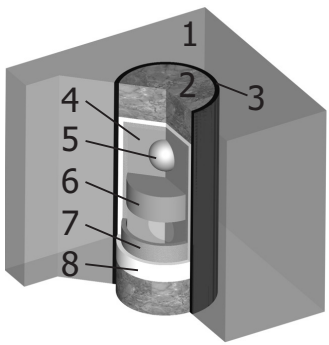

Fig. 7. Assembly for bulk $Al_xGa_{1-x}N$ single crystal growth. The pyrophyllite cube 1) represents the sample volume from Fig. 6. and serves together with 2) as thermal and electrical insulation. 3) graphite heater; 4) Gallium melt; 5) Aluminum; 6) nitride precursor; 7) gold encapsulation; 8) BN crucible.

Experimental procedure: The nitrogen required for crystal growth in a cubic anvil setup has to be provided from inside the reaction volume – a key difference in comparison with HNPSG. Nitride precursors, usually GaN powders, are sintered in the gas autoclave to reduce the oxygen and water content. Then the powder is pressed into pellets and stored under

argon. The detailed experimental assembly is shown in Fig. 7. The nitride precursor is placed in a gold capsule together with the other raw materials (gallium, aluminum) in the desired concentrations. The encapsulation is necessary to prevent a loss of (liquid) gallium when building up the pressure at the beginning of an experiment. At higher temperature (~ 1400°C), gold forms an alloy with the other metallic starting materials. The melting point of Au is shifted due to the high pressure applied (30-35 kbar). The gold capsule is placed in a BN crucible, serving as electrical isolation against the surrounding graphite heater.

In a typical experiment, a pressure of $p = 30$ kbar is applied at ambient temperature. While keeping the pressure stable, the temperature is ramped up within 60 min to the maximum value of $T = 1750$°C, and is then held for 12 to 60 hours. At the end of the dwell phase, the temperature is lowered to room temperature within 30 min and the pressure is subsequently released. After the experiment, the pyrophyllite cube must be broken apart to gain access to the BN crucible. Hydrochloric acid and aqua regia are used to remove the metallic compounds in the crucible.

4. Results and discussion

4.1. *$Al_xGa_{1-x}N$ bulk single crystals, growth results*

$Al_xGa_{1-x}N$ and GaN crystals form during the experiment and their composition is measured by several methods. The crystals grow near the top and the bottom of the BN crucible. These locations are obviously the coolest spots in the crucible. This supports the picture of a growth mechanism involving nitrogen transport driven by a temperature and/or concentration gradient. At the center of the assembly, which is the hottest zone during the experiment, sintered pieces of the initially supplied nitride can be found. The precursor is transformed into $Al_xGa_{1-x}N$ with high Al content (see below).

The crystals grown with the CAC are hexagonal and their habitus varies from platelets to needles. The size of crystals having well defined

growth facets is in the range of tenth of a millimeter. A good quality sample is shown in Fig. 8. Larger crystallites with up to 1 mm length have well defined crystal faces and may be single crystalline, but they usually exhibit irregular growth features such as dendritic structures or skeletal growth. The crystals are shiny, transparent and usually slightly brown, with changing intensity across the crystal.

Fig. 8. $Al_xGa_{1-x}N$ bulk single crystals. Grid spacing is 1 mm.

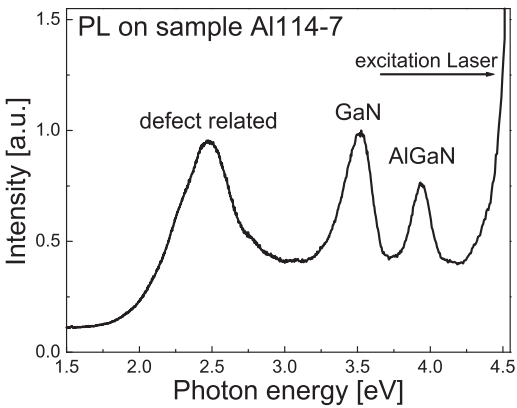

Fig. 9. Photo luminescence spectrum measured on sample Al114-7 (4.66 eV excitation). Two distinct peaks are attributed to near band-gap transitions of both pure GaN (3.5 eV) and $Al_xGa_{1-x}N$ (3.9 eV). The broad luminescent emission around 2.5 eV is attributed to defects (yellow luminescence).

Suitable crystals are selected for the subsequent analysis. Room temperature photoluminescence measurements are used to evaluate the near band-gap transition energy. If the luminescence energy is found to be higher than that for pure GaN, the crystals are selected for further studies. As the excitation laser used has an excitation energy of 4.66 eV, a reliable detection of near band-gap transitions of $Al_xGa_{1-x}N$ crystals is possible for an Al content up to x ~ 0.4. Crystals of sufficient size and of regular shape (platelet) are selected in order to ensure a defined orientation {0001} and a sufficiently large area for PL and LA-ICPMS measurements. Figure 9 shows the emission spectrum measured on the larger crystal shown in Fig. 8. Several features are distinguished: defect related luminescence (yellow luminescence (YL)) around 2.5 eV, near

band-gap transitions between 3.5 eV and 4 eV and the shoulder of the laser line (4.66 eV). The PL spectra of $Al_xGa_{1-x}N$ crystals reflect the blue-shifted near-band-edge transition due to the Al incorporation into the bulk of the crystal, and (sometimes) also the unshifted PL line of GaN. The latter originates in a thin GaN capping layer which covers the $Al_xGa_{1-x}N$ crystals. This feature is the subject of more detailed studies but can be summarized here as a result of a strong temperature dependence of the Al solubility in GaN in conjunction with the experimental procedure.

4.2. *Material characterization*

XRD analysis: Single crystal x-ray diffraction is used to measure the lattice parameter, (four-cycle Siemens P4 diffractometer). The measurements confirm the wurtzite structure. The Al content of the ternary nitride is calculated by assuming a linear dependence of the lattice parameter on the Al content, known as Vegard's law.[65] The assumption of Vegard's law holds well as shown e.g. by Angerer *et al.*[27] For the present study the lattice parameter values used to calculate the Al content are c = 5.1851 Å for GaN and c = 4.98 Å for AlN. In doped samples, secondary effects may play a role. They lead to an underestimation of the Al content by XRD. As discussed by Leszczynski *et al.*[68,69] a high concentration of free carriers, attributed to shallow donors such as O and Si, yield a lattice expansion. This expansion is not expected when just taking into account the size effect: the Si atomic radius is smaller than the Ga atom replaced, and a lattice contraction would be expected. Si and O can be detected in samples grown with the CAC process. The most probable source is the thermal isolation (Pyropyhllite, an alumosilicate). For the $Al_xGa_{1-x}N$ crystals studied, the Si content was measured using LA-ICPMS. A calibration function for XRD measurements was determined based on the work of Prystawko *et al.*[66] The solid line in Fig. 10 represents the lattice parameters calculated with Vegard's law and the dashed lines correspond to the corrected Al content for two different concentrations of Si. X-ray diffraction (XRD) measurements show, that the contraction of the lattice is significant and an Al content of more than

25% is determined. The small expansion due to Si related doping is a minor effect compared to the dominant expansion due to Al substitution.

In Fig. 10. a range of lattice parameters (indicated by a cross) is shown for GaN crystals grown by the HNPSG method (n-type, oxygen background about $5 \times 10^{19}\,\mathrm{cm}^{-3}$). As indicated, such crystals have a slightly larger lattice parameter c (up to 5.1864 [67]) than the generally accepted value for GaN (c = 5.185 e.g. Ref. 70). This secondary effect on lattice parameters was not quantified in the present study. However, the deviation for GaN bulk material shows that, similar to silicon doping, the unintentional doping of $Al_xGa_{1-x}N$ with oxygen will lead to a slight underestimation of the Al content. In this context it is worth noting that for $Al_xGa_{1-x}N$ samples with $x < 0.3$ the nature of these impurities is of a shallow donor type and full ionization is assumed. Following section 2.2. a DX transition of oxygen is not expected.

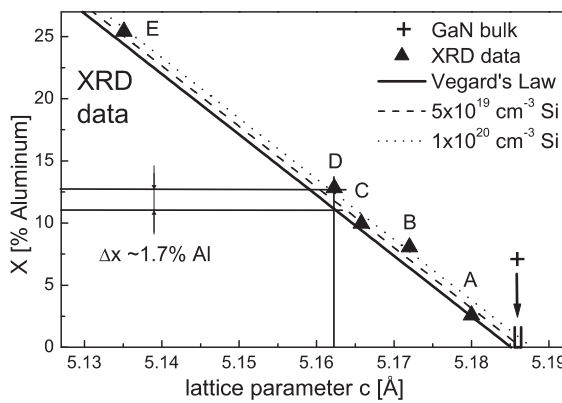

Fig. 10. Determination of x in AlxGa1-xN using XRD data. The solid line represents Vegard's law. The presence of free electrons yields a systematic underestimation of the Al content. The dashed lines represent a modified calibration curve taking into account the presence of Si as described quantitatively by Prystawko *et al.*[66] Data for pure GaN taken from.[67]

Photoluminescence studies: The dominant transitions are of excitonic type (free, donor or acceptor bound). The spectrometer CCD used for the photoluminescence measurements in this study has a resolution of 4 meV at 3.5 eV, suitable to detect shifts of the transitions as a function of the

aluminum content (room temperature measurement). With its energy close to the band to band transition the excitonic feature is referred to as "near band-gap". The band-gap energy does, in general, not depend linearly on the Al content in $Al_xGa_{1-x}N$. It rather follows Eq. (7)

$$E_{peak}^{AlxGa1-xN}(x) = (1 - x)\, E_{peak}^{GaN} + x\, E_{peak}^{AlN} - b\, x\, (1 - x) \qquad (7)$$

where the deviation from a linear interpolation is incorporated in a parabolic contribution, parametrized by the "bowing parameter" b. The bowing parameter b was the subject of a number of investigations. The values determined range from – 0.8 eV to 2.6 eV as summarized by Lee *et al.*[71] For the analysis of the present data, a bowing parameter b = 1.3 eV was used, following Angerer *et al.*[27]

This choice appears appropriate because the samples in that study were investigated with complementary measurements and the strain in thin films was also carefully taken into account. In Fig. 11 the function derived experimentally by Angerer *et al.* is shown as a dashed line. The data for equation (7) are based on room temperature measurements of the absorption coefficient. The PL peak position is known to be by 0.03 eV lower in energy than the peaks identified in absorption measurements.[72] To account for this difference, the values measured in this work are denoted as E_{peak} and are corrected accordingly.

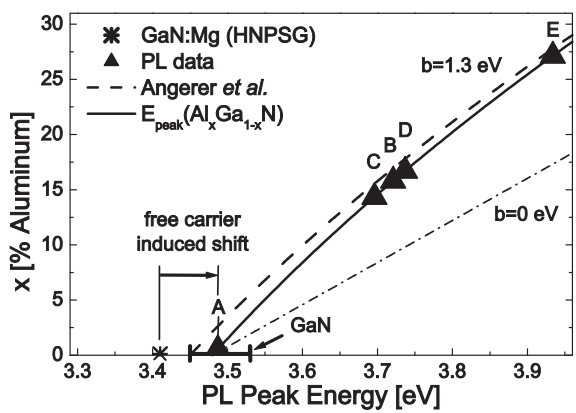

Fig. 11. Determination of x in $Al_xGa_{1-x}N$ from PL data. The blue-shifted near band-gap transitions (see inset) are evaluated using a modified calibration curve (solid line) based on investigations by Angerer *et al.* [27] (dashed line)

The resulting value of $E_{peak}^{GaN} = 3.42$ eV agrees well with the data measured on semi-isolating Mg doped GaN (indicated by "x" in Fig. 11). For the value of E_{peak}^{GaN} the high concentration of free carriers is further taken into account. As indicated on the x-axis in Fig. 11, GaN grown with HNPSG exhibits a blue-shifted peak energy (relative to Mg doped samples) due to the Burstein-Moss effect. For the calculation of the Al content a value of $E_{peak}^{GaN} = 3.48$ eV was chosen. The Al content determined via the PL for the $Al_xGa_{1-x}N$ bulk single crystals has an uncertainty of a few percent.

Composition from mass spectrometry: Laser ablation inductively coupled plasma mass spectrometry (LA-ICPMS) has been used to determine the composition of the crystals. Despite the large Au concentration in the growth melt an incorporation into the crystal could hardly be detected (at the detection limit of a few ppm). Only Si was detected as a significant trace element, with concentrations in the range of 10^3 ppm, typically several hundred ppm, ~ 3000 ppm at most in a single case. Oxygen, carbon (as dopants, few percent range), or nitrogen (relevant for stoichiometry estimates, 50% range) cannot be detected due to a high background. More details on LA-ICPMS and data treatment can be found in Refs. 73, 74, 75.

The mass spectrometry results for five crystals are shown in Fig. 12. A closer inspection leads to the following conclusions. First, a substantial

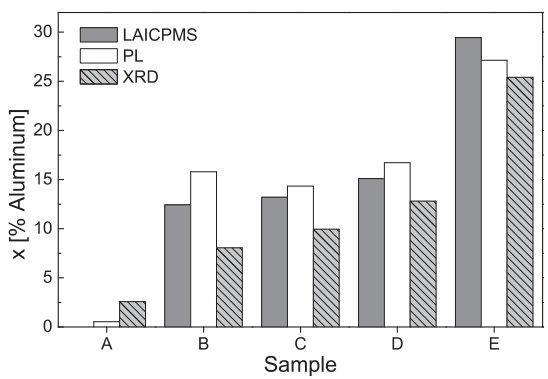

Fig. 12. Al content of five samples as determined by three independent methods.

incorporation of Al into the GaN lattice is confirmed also by this method, reaching up to 30% Al with an uncertainty of a few percent (absolute). All three methods to determine the Al content are in substantial agreement. Second, evaluation of the blue-shift of PL transitions using equation 1.7 with a bowing parameter b = 1.3 eV yields an Al content that is comparable with concentrations determined with LA-ICPMS. Corrected values for E^{GaN} and E^{AlN} are required to take into account the blue-shift caused by a high concentration of free carriers in the investigated samples. Third, XRD measurements and subsequent evaluation of the lattice parameter using Vegard's law tend to underestimate the Al content. This is in agreement with observations reported by Angerer *et al.*[27] Secondary effects related to impurities play a role as indicated by the deviation of the XRD data of sample A.

4.3. *Parameters influencing the Al content in $Al_xGa_{1-x}N$*

The Al content in $Al_xGa_{1-x}N$ can be influenced by the proper choice of the ratio of the starting materials (Ga/Al alloy, nitride precursor). Upon closer analysis of the LA-ICPMS data, we find two parameters to be relevant. The first is the Al concentration in the $Ga_{1-y}Al_y$ alloy (molar fraction).

$$R_1 = Al/(Al + \mathbf{Ga}) \, . \qquad (8)$$

This ratio was determined for seven experiments and crystals were taken from these to measure the resulting Al content. This Al content is shown in figure 13 as a function of the ratio R_1. The key observation is that a low concentration of Al in the Ga/Al alloy is sufficient to reach a high Al concentration in the $Al_xGa_{1-x}N$ bulk single crystal. An extrapolation of the trend line suggests that a ratio $R_1 = 10$ would be sufficient for 100% substitution (pure AlN). However, for $R_1 > 4$ it turned out to be difficult to grow crystals like those shown in Fig. 8. Several explanations are possible.

- Additional factors beside the ratio R_1 control the Al content in $Al_xGa_{1-x}N$. High Al content $Al_xGa_{1-x}N$ only forms when all requirements are met, which is not the case for the samples with $R_1 = 8$ to 10 in Fig. 13.

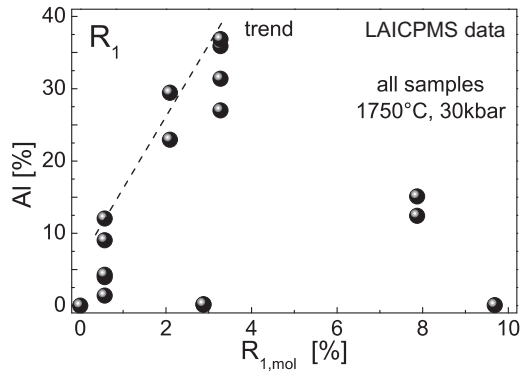

Fig. 13. Al content control: Al concentration in the Ga melt; R_1= Al/(Al + Ga)).

- The growth of $Al_xGa_{1-x}N$ with the HNPSG turned out to be impossible for $Ga_{1-y}Al_y$ alloys with $y > 0.01$. This is due to a dense AlN layer that does not dissolve in the Ga/Al alloy at the temperature chosen (see below) and a similar barrier may play a role in CAC growth if an alloy with a high Al content is used.
- An uncertainty is introduced by the sample selection process, based on a visual pre-selection and a crosscheck with photoluminescence (4.66 eV excitation energy ~ $x < 0.4$). Powder XRD data shown below indicate that there is in fact $Al_xGa_{1-x}N$ with $x > 0.7$ forming. However, larger crystallites with such a composition do not form.

The second parameter important to control the Al content is the ratio of Al to the nitrogen available in the crucible (molar mass of the nitride precursor in form of GaN)

$$R_2 = \mathrm{Al}/(\mathrm{Al}+\mathbf{GaN}) \, . \tag{9}$$

A clear trend towards a higher Al content in $Al_xGa_{1-x}N$ is found for higher values of R_2, as shown in Fig. 14. The trend line indicates that for a given ratio R_2 the Al content in the $Al_xGa_{1-x}N$ crystal approaches, but does not exceed the value of R_2. Other than for R_1, the ratio R_2 does not seem to have an upper value limiting the crystal growth.

The third and probably most important parameter is the temperature and the temperature gradient. For all crystals investigated, the growth conditions were 1750°C and 30 kbar, with variations of ± 30°C and

+2/–1 kbar during the dwell phase of a single experiment. The scattering of the Al content for one specific ratio R_1 or R_2 can be explained by these fluctuations and an unknown gradient of the temperature in the crucible given by the single-stage heater setup of the CAC.

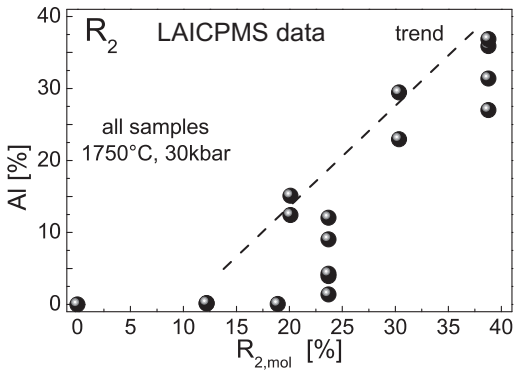

Fig. 14. Al content control: Al in relation to the GaN precursor; R_2 = Al/(Al + GaN)).

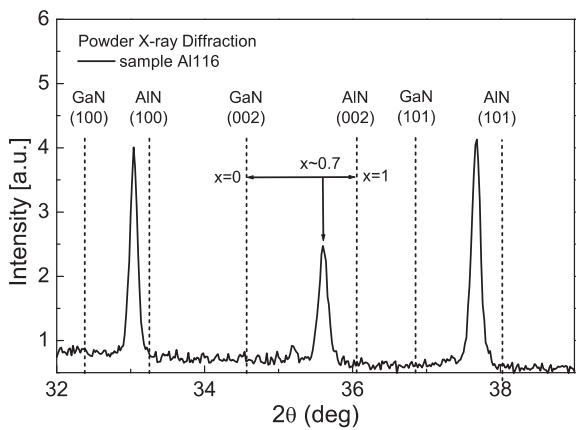

Fig. 15. Powder X-ray diffraction analysis (CuK_{a1}-radiation) of the gallium nitride precursor after the experiment. Peak positions of GaN and AlN are indicated with dashed lines. On the basis of Vegard's law, an Al substitution up to 70% was measured.

As mentioned earlier, pieces of the nitride precursor pill can be retrieved after the experiment. The material is partially sintered and has a higher mechanical stability than the original pill. Further, the color changed from slightly yellow to a light gray. In Fig. 15, a powder x-ray

diffractogram from such a sample is shown. The positions of several reflections are indicated for pure GaN and AlN respectively (taken from the analysis software of the Stoe diffractometer). The partially sintered nitride powder was originally supplied as GaN precursor. For sample Al116 the pronounced shift towards AlN is obvious. After determination of the lattice parameters and application of Vegard's law, one finds an Al substitution as high as 70%. This leaves room for further optimization of the single crystal growth process as it indicates that the maximum Al solubility at 1750°C is higher than estimated from single crystal growth.

4.4. *Suppression of crystal growth in $Ga_{1-y}Al_y$ alloys with y > 0.01*

It was planned to grow $Al_xGa_{1-x}N$ with the HNPSG method. Using the 15 kbar autoclave and $Ga_{1-y}Al_y$ alloys with $y = 0.3$ and 0.5 led to the observation of a strong overshoot of the temperature while ramping up to the dwell conditions (step 2, table 1.1). The material extracted from the crucible at the end of the experiment was mainly polycrystalline AlN with some inclusions of the solution alloy. A small amount of GaN and $Al_xGa_{1-x}N$ also forms, but its exact composition was not possible to control. This observation is in good agreement with the literature reporting a combustion synthesis for pure Al under high nitrogen pressure.[60] This makes it hardly possible to grow crystals with the common HNPSG approach. Nevertheless, the polycrystalline AlN blocks resulting from the combustion reaction were of some use when cut into sticks. In this form they served as precursor material for the first exploratory experiments that subsequently led to the development of the CAC setup.

To avoid the combustion, alloys with a lower Al content were used. For $Ga_{1-y}Al_y$ alloys with $y < 0.1$ used as growth melt the combustion synthesis was no longer observed, yet no crystalline material grows at conditions known to be suitable for pure GaN growth. Rather, a very thin grey layer crystallizes on the crucible walls and at the alloy/gas interface. When the Al concentration in the initial alloy is higher than 1%, this layer forms over the entire temperature range accessible with the HNPSG autoclave (1600°C max.).

To further clarify that issue, a molybdenum based heater with $T_{max} = 1700°C$ was constructed. An autoclave with a separated atmosphere (Argon) for the heater is necessary, as Molybdenum reacts with nitrogen at (p,T) required for the experiment. The pressure range available (< 2 kbar) in this larger autoclave is not sufficient to stabilize the GaN phase at such a high temperature. Still, with only a few hundred bars required for AlN phase stabilization, the pressure range would also leave room for $Al_xGa_{1-x}N$ compositions close to AlN. However, the key focus of this experiment is to search for signs of nitrogen mass transport. For this purpose, an alloy with a few percent of Al was used. The result is similar to the standard HNPSG experiments: a thin polycrystalline layer forms at the alloy/gas interface. Powder x-ray diffraction revealed the composition of that layer to be a mixture of AlN and Al_2O_3. No other nitrides were forming in this experiment, in particular no crystals were found in the cooler zones of the experimental setup. In addition, CAC experiments were performed, using AlN powder rather than GaN powder as a nitrogen source. No indications for nitrogen transport in the melt could be found even at a temperature as high as 1750°C, and a pressure of 30 kbar that was otherwise sufficient for pure GaN phase stabilization. This indicates the low solubility of AlN in Ga/Al alloy at such extreme conditions.

To summarize these results, two aspects are worth noting: First, the reaction kinetics promotes the formation of AlN if gaseous nitrogen is present, even at low Al concentrations in the growth alloy. For high Al content alloys this reaction is very fast, not to say violent, and yields AlN powder. The crystallization of good quality single crystals is considered very difficult under such conditions. Second, as indicated by the results of this study, the solubility of AlN in Ga or $Ga_{1-y}Al_y$ alloys is extremely small, independent of the crystallization process. The growth of GaN from Ga is possible no matter whether GaN is stable at the alloy/gas interface or not. But as soon as AlN is involved, either as a thin layer (HNPSG) or powder (CAC), no nitrogen transport and subsequent crystallization takes place.

4.5. *GaN bulk single crystals*

Throughout this study GaN bulk single crystals grown with the HNPSG method (see section 3.1) were a valuable reference either as unintentionally doped crystals or doped with Mg (see Fig. 11). High quality crystals are shown in Fig. 16. Such crystals are grown in a process lasting 100 hours or more at a temperature of 1400 +/–50 °C and a pressure in the range of 10 kbar. By limiting the temperature gradient in the crucible, crystal growth in the c-direction can be suppressed. Platelet shaped crystals grow up to a size of $5 \times 3 \times 0.3$ mm reflecting the preferred growth along the a directions under these conditions. The crystals can either be used as bulk samples or as substrates for thin film (MOCVD or MBE) deposition – the latter after a suitable polishing step.

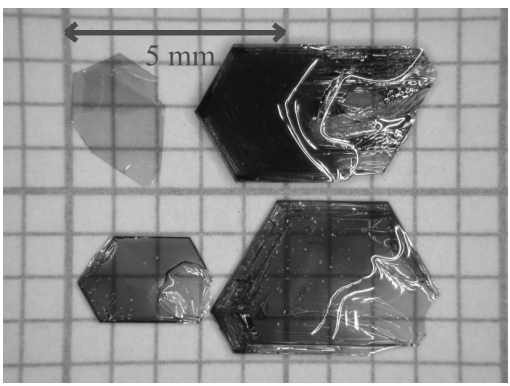

Fig. 16. GaN bulk single crystals grown with the HNPSG method. An autoclave with 40mm inner diameter was used, running at T = 1400 +/–50°C for 150 hours.

Crystals grown from a pure Ga melt under nitrogen pressure are transparent and have a slightly brown color. This indicates an elevated background of free carriers, mainly due to oxygen. Hall effect measurements in the van der Pauw geometry yield free electron concentrations in the range from 5×10^{19} to 9×10^{19} per cm^3. Below this range, the control of the free carrier concentration in GaN bulk single crystals is hardly possible due to e.g. adsorbed moisture in the autoclave or the trace impurities in the supplied nitrogen.

The presence of the free carriers manifests itself also through the Burstein-Moss-shift of the transitions measured in photoluminescence studies (see Fig. 11). This blues-shift can be suppressed by doping the GaN crystals with divalent elements. The most common element for that purpose is Mg. When we use the HNPSG method to grow crystals we have added ~ 1% of Mg to the Ga melt and find the crystals to be completely colorless and to be highly resistive.

5. Conclusions and outlook

In this study the feasibility to grow group-III ternary nitride bulk single crystals was intensively investigated, starting from (Ga,Al)N compounds. A new growth setup was developed using a cubic anvil cell (CAC) and nitride powder precursors as a nitrogen source. With the CAC facility, $Al_xGa_{1-x}N$ bulk single crystals have been successfully grown at a temperature of 1750°C and a pressure of 30 kbar. The Al content is as high as 30% for bulk samples and approached 70% for polycrystalline (sintered) material, indicating a potential for further developments. The CAC facility may also be used to prepare polycrystalline $Al_xGa_{1-x}N$ precursors in a controlled way. The Al content in the crystals was confirmed by XRD, photo luminescence and mass spectrometry and the results are in good agreement with the existing literature on $Al_xGa_{1-x}N$ thin films. It was possible to identify experimental parameters that influence the Al content of the crystals.

Ternary nitride crystal growth turned out to be more challenging with the high nitrogen pressure solution growth (HNPSG) method although it is an established tool for GaN and AlN. Two impediments to the growth of $Al_xGa_{1-x}N$ bulk single crystals have been identified: (1) The formation of an AlN cap layer with low solubility in Ga/Al alloys, and (2) a propensity of Al and N to form AlN in a strongly exothermic reaction, when nitrogen is present in gas form. These obstacles render the ternary nitride crystal growth impossible with the classical setup of HNPSG. Crystals can be grown, however, from Ga/Al alloys with a low Al content (less than one percent). The highest Al concentration measured in a bulk crystal was about 2% (grown at 1575 ± 25°C).

A number of important questions related to ternary nitride bulk crystal growth remain to be clarified. In particular, before assessing the scalability of the crystal size with a particular approach, the underlying questions on thermodynamics and kinetics should be investigated in detail.

The key question concerns the equilibrium pressure necessary to thermodynamically stabilize the $Al_xGa_{1-x}N$ phase. Comparing GaN and AlN properties it is expected that the pressure necessary for phase stabilization drops with increasing Al content in the ternary nitride. The exact knowledge of this dependence is required in order to assess the potential of different growth methods for industrial application. When performing such experiments, kinetic barriers that could influence the decomposition must be carefully considered. Of similar importance is the further study of the temperature dependence of the Al solubility in GaN and its impact on Al distribution in the crystal as a function of the experimental procedure.

Acknowledgments

LA-ICPMS measurements were performed at the Institute for Isotope Geochemistry and Mineral Resources at ETH Zürich. We would like to thank Prof. Ch. Heinrich and L. Klemm for providing their expertise and equipment. This study was supported by ETH Zürich under project number TH-16/99-4 and by the Swiss National Science Foundation through NCCR pool MaNEP.

References

1. S. J. Pearton, D. P. Norton, K. Ip, Y. W. Heo, and T. Steiner, *J. Vac. Sci. & Tech. B* **22,** 932-948 (2004).
2. H. Amano, I. Akasaki, K. Hiramatsu, N. Koide, and N. Sawaki, *Thin Solid Films* **163,** 415-420 (1988).
3. S. Nakamura, *Jpn. J. Appl. Phys.* **30,** L1705-1707 (1991).
4. H. Amano, M. Kito, K. Hiramatsu, and I. Akasaki, *Jpn. J. Appl. Phys.* **28,** L2112-L2114 (1989).
5. S. Nakamura, T. Mukai, M. Senoh, and N. Iwasa, *Jpn. J. Appl. Phys.* **31,** L139-142 (1992).

6. S. Nakamura, S. Pearton, and G. Fasol, *The blue laser diode - The complete story*, 2nd ed. (Springer-Verlag, Berlin, Heidelberg, New York, 2000).
7. S. T. Kim, Y. J. Lee, D. C. Moon, C. H. Hong, and T. K. Yoo, *J. Cryst. Growth* **194,** 37-42 (1998).
8. A. Usui, H. Sunakawa, A. Sakai, and A. A. Yamaguchi, *Jpn. J. Appl. Phys.* **36,** L899-902 (1997).
9. S. J. Pearton, J. C. Zolper, R. J. Shul, and F. Ren, *J. Appl. Phys.* **86,** 1-78 (1999).
10. S. C. Jain, M. Willander, J. Narayan, and R. Van-Overstraeten, *J. Appl. Phys.* **87,** 965-1006 (2000).
11. S. Porowski, I. Grzegory, S. Krukowski, M. Leszczynski, P. Perlin, and T. Suski, *Europhysics news* **35,** 69-73 (2004).
12. L. Liu and J. H. Edgar, *Materials Science & Engineering R* **R37,** 61-127 (2002).
13. E. Ejder, *J. Cryst. Growth* **22,** 44-46 (1974).
14. H. Yamane, M. Shimada, T. Sekiguchi, and F. J. DiSalvo, *J. Cryst. Growth* **186,** 8-12 (1998).
15. B. J. Skromme, K. Palle, C. D. Poweleit, H. Yamane, M. Aoki, and F. J. DiSalvo, *J. Cryst. Growth* **246,** 299-306 (2002).
16. M. P. D'Evelyn, K. J. Narang, D. S. Park, H. C. Hong, M. Barber, S. A. Tysoe, J. Leman, J. Balch, V. L. Lou, S. F. LeBoeuf, Y. Gao, J. A. Teetsov, P. J. Codella, P. R. Tavernier, D. R. Clarke, R. J. Molnar, H. Min-Ng, M. Wraback, K. Hiramatsu, and N. Grandjean, in *Growth and characterization of bulk GaN crystals at high pressure and high temperature*, 2004 (Materials Research Society), p. 275-280.
17. J. Karpinski, J. Jun, and S. Porowski, *J. Cryst. Growth* **66,** 1-10 (1984).
18. I. Grzegory and S. Krukowski, *Phys. Scr.* **T39,** 242-249 (1991).
19. J. Prywer and S. Krukowski, *MRS Internet J. Nitride Semicond. Res.* **3** (1998).
20. I. Grzegory and S. Porowski, *Thin Solid Films* **367,** 281-289 (2000).
21. I. Grzegory, *J Phys-Condens Mat* **13,** 6875-6892 (2001).
22. I. Grzegory, M. Bockowski, B. Lucznik, S. Krukowski, Z. Romanowski, M. Wroblewski, and S. Porowski, *J. Cryst. Growth* **246,** 177-186 (2002).
23. A. Trampert, O. Brandt, and K. H. Ploog, in *Gallium Nitride GaN I*; Vol. 50, edited by J. I. Pankove and T. D. Moustakas (Academic Press, San Diego, 1998), p. 167-192.
24. E. S. Hellman, MRS Internet J. Nitride Semicond. Res. **3** (1998).
25. W. A. Harrison, *Electronic structure and the properties of solids* (W.H. Freeman and Company, San Francisco, 1980).
26. N. E. Christensen and I. Gorczyca, *Physical Review B Condensed Matter* **50,** 4397-4415 (1994).
27. H. Angerer, D. Brunner, F. Freudenberg, O. Ambacher, M. Stutzmann, R. Hopler, T. Metzger, E. Born, G. Dollinger, A. Bergmaier, S. Karsch, and H. J. Korner, *Appl. Phys. Lett.* **71,** 1504-1506 (1997).
28. B. Monemar, *Phys. Rev. B* **10,** 676-681 (1974).
29. T. L. Tansley and C. P. Foley, *J. Appl. Phys.* **59,** 3241-3244 (1986).

30. B. Maleyre, S. Ruffenach, O. Briot, B. Gil, and A. Van der Lee, *Supperl. and Microstr.* **36,** 517-526 (2004).
31. I. Grzegory, J. Jun, S. Krukowski, P. Perlin, and S. Porowski, *Jap. J. Appl. Phys.* **32,** 343-345 (1993).
32. H. P. Maruska and J. J. Tietjen, *Appl. Phys. Lett.* **15,** 327-329 (1969).
33. R. A. Logan and C. D. Thurmond, *J. Electrochem. Soc.* **119,** 1727-1735 (1972).
34. I. Grzegory, J. Jun, M. Bockowski, S. Krukowski, M. Wroblewski, B. Lucznik, and S. Porowski, *J. Phys. Chem. Sol.* **56,** 639-647 (1995).
35. J. Neugebauer and C. G. Van de Walle, *Phys. Rev. B* **50,** 8067-8070 (1994).
36. C. G. Van de Walle and J. Neugebauer, *J Appl Phys* **95,** 3851-3879 (2004).
37. K. Saarinen, T. Laine, S. Kuisma, J. Nissila, P. Hautojarvi, L. Dobrzynski, J. M. Baranowski, K. Pakula, R. Stepniewski, M. Wojdak, A. Wysmolek, T. Suski, M. Leszczynski, I. Grzegory, and S. Porowski, *Phys Rev Lett* **79,** 3030-3033 (1997).
38. J. Neugebauer and C. G. Van de Walle, *Appl. Phys. Lett.* **69,** 503-505 (1996).
39. W. Kim, A. E. Botchkarev, A. Salvador, G. Popovici, H. Tang, and H. Morkoc, *J. Appl. Phys.* **82,** 219-226 (1997).
40. S. Krukowski, M. Bockowski, B. Lucznik, I. Grzegory, S. Porowski, T. Suski, and Z. Romanowski, *J Phys-Condens Mat* **13,** 8881-8890 (2001).
41. W. Seifert, R. Franzheld, E. Butter, H. Sobotta, and V. Riede, *Cryst. Res. Tech.* **18,** 383-390 (1983).
42. W. Götz, N. M. Johnson, C. Chen, H. Liu, C. Kuo, and W. Imler, *Appl. Phys. Lett.* **68,** 3144-3146 (1996).
43. C. Wetzel, T. Suski, J. W. Ager, E. R. Weber, E. E. Haller, S. Fischer, B. K. Meyer, R. J. Molnar, and P. Perlin, *Phys. Rev. Lett.* **78,** 3923-3926 (1997).
44. H. Teisseyre, P. Perlin, T. Suski, I. Grzegory, S. Porowski, J. Jun, A. Pietraszko, and T. D. Moustakas, *J. Appl. Phys.* **76,** 2429-2434 (1994).
45. T. Ogino and M. Aoki, *Jap. J. Appl. Phys.* **19,** 2395-2405 (1980).
46. J. I. Pankove and J. A. Hutchby, *J. Appl. Phys.* **47,** 5387-5390 (1976).
47. R. Armitage, W. Hong, Y. Qing, H. Feick, J. Gebauer, E. R. Weber, S. Hautakangas, and K. Saarinen, *Appl. Phys. Lett.* **82,** 3457-3459 (2003).
48. J. W. P. Hsu, F. F. Schrey, and H. M. Ng, *Appl. Phys. Lett.* **83,** 4172-4174 (2003).
49. E. Litwin-Staszewska, T. Suski, I. Grzegory, S. Porowski, P. Perlin, J. L. Robert, S. Contreras, D. Wasik, A. Witowski, D. Cote, and B. Clerjaud, *Phys. Status Solidi B* **216,** 567-570 (1999).
50. E. Litwin-Staszewska, T. Suski, R. Piotrzkowski, I. Grzegory, M. Bockowski, J. L. Robert, L. Konczewicz, D. Wasik, E. Kaminska, D. Cote, and B. Clerjaud, *J. Appl. Phys.* **89,** 7960-7965 (2001).
51. H. J. Queisser and E. E. Haller, *Science* **281,** 945-950 (1998).
52. D. J. Chadi and K. J. Chang, *Phys Rev Lett* **61,** 873-876 (1988).
53. M. D. McCluskey, N. M. Johnson, C. G. Van-de-Walle, D. P. Pour, M. Kneissl, and W. Walukiewicz, *Phys Rev Lett* **80,** 4008-4011 (1998).
54. J. A. Van Vechten, *Phys. Rev. B* **7,** 1479-507 (1973).

55. W. Utsumi, H. Saitoh, H. Kaneko, T. Watanuki, K. Aoki, and O. Shimomura, *Nature Materials* **2,** 735-738 (2003).
56. J. B. MacChesney, P. M. Bridenbaugh, and P. B. O'Connor, *Mat. Res. Bull.* **5,** 783-791 (1970).
57. C. D. Thurmond and R. A. Logan, *J. Electrochem. Soc.* **119,** 622-626 (1972).
58. J. Karpinski and S. Porowski, *J. Cryst. Growth* **66,** 11-20 (1984).
59. T. Matsuoka, *J. Cryst. Growth***,** 19-23 (1998).
60. M. Bockowski, *Physica B* **265,** 1-5 (1999).
61. M. Bockowski, M. Wroblewski, B. Lucznik, and I. Grzegory, *Mat. Sci. Semicond. Proc.* **4,** 543-548 (2001).
62. F. Kawamura, T. Iwahashi, M. Morishita, K. Omae, M. Yoshimura, Y. Mori, and T. Sasaki, *Jpn. J. Appl. Phys.* **42,** L729-731 (2003).
63. H. Saitoh, W. Utsumi, H. Kaneko, and K. Aoki, *Jpn. J. Appl. Phys.* **43,** L981-983 (2004).
64. M. Hasegawa and T. Yagi, *J. Cryst. Growth* **217,** 349-354 (2000).
65. L. Vegard, *Zeitschr. Phys.* **5,** 17 (1921).
66. P. Prystawko, M. Leszczynski, B. Beaumont, P. Gibart, E. Frayssinet, W. Knap, P. Wisniewski, M. Bockowski, T. Suski, and S. Porowski, *Phys. Stat. Sol. (b)* **210,** 437-443 (1998).
67. I. Grzegory, M. Bockowski, B. Lucznik, M. Wroblewski, S. Krukowski, J. Weyher, G. Nowak, T. Suski, M. Leszczynski, H. Teisseyre, E. Litwin-Staszewska, S. Porowski, F. A. Ponce, S. P. DenBaars, B. K. Meyer, S. Nakamura, and S. Strite, in *Ga} crystals: growth and doping under pressure*, 1998 (Mat. Res. Soc.), p. 15-26.
68. M. Leszczynski, H. Teisseyre, T. Suski, I. Grzegory, M. Bockowski, J. Jun, S. Porowski, K. Pakula, J. M. Baranowski, C. T. Foxon, and T. S. Cheng, *Appl. Phys. Lett.* **69,** 73-75 (1996).
69. M. Leszczynski, P. Prystawko, T. Suski, B. Lucznik, J. Domagala, J. Bak-Misiuk, A. Stonert, A. Turos, R. Langer, and A. Barski, *J Alloys and Comp.* **286,** 271-275 (1999).
70. T. Detchprohm, K. Hiramatsu, K. Itoh, and I. Akasaki, *Jpn. J. Appl. Phys.* **31,** L1454-1456 (1992).
71. S. R. Lee, A. F. Wright, M. H. Crawford, G. A. Petersen, J. Han, and R. M. Biefeld, *Appl. Phys. Lett.* **74,** 3344-3346 (1999).
72. G. Y. Zhao, H. Ishikawa, H. Jiang, T. Egawa, T. Jimbo, and M. Umeno, *Jpn. J. Appl. Phys.* **38,** L993-995 (1999).
73. D. Günther, A. Audétat, R. Frischknecht and C.A. Heinrich, *J. Anal. At. Spec.* **13** (4), 263-270 (1998).
74. C.A. Heinrich, T. Pettke, W.E. Halter, M. Aigner-Torres, A. Audétat, D. Günther, B. Hattendorf, D. Bleiner, M. Guillong and I. Horn, *Geoch. et Cosmoch. Acta*, **67** (18), 3473-3496 (2003).
75. T. Pettke, C.A. Heinrich, A.C. Ciocan and D. Günther, *J. Anal. At. Spec.*, **15** (9), 1149-1155 (2000)**.**

This page intentionally left blank

CHAPTER 3

STRUCTURAL AND OPTICAL PROPERTIES OF InGaN/GaN MULTIPLE QUANTUM WELL LIGHT EMITTING DIODES GROWN BY METALORGANIC CHEMICAL VAPOR DEPOSITION

Zhe Chuan Feng

Institute of Photonics & Optoelectronics, and Department of Electrical Engineering, National Taiwan University, Taipei, Taiwan 106, ROC
E-mail: zcfeng@cc.ee.ntu.edu.tw

Jer-Ren Yang

Department of Materials Science and Engineering, National Taiwan University, Taipei, Taiwan 106, ROC

Alan Gang Li

ShenZhen Fangda GuoKe Optronics Technical Co. Ltd., Nanshan, ShenZhen, 518055 China

Ian T. Ferguson

School of Electrical & Computer Engineering, Georgia Institute of Technology, Atlanta, GA 30332-0250, USA

A comprehensive review on the materials analysis of structural and optical properties of InGaN/GaN multiple quantum well light emitting diodes grown on sapphire by metalorganic chemical vapor deposition is presented. High resolution x-ray diffraction and transmission electron microscopy, and a variety of photoluminescence (PL) spectroscopy including temperature and excitation dependent PL, PL excitation and time resolved PL are mainly employed to study our high quality wafers. Penetrating analysis and discussion are given.

1. Introduction

Energy-efficient and environmentally friendly solid-state light sources, in particular GaN-based light emitting diodes (LEDs), are currently revolutionizing an increasing number of applications, and bring apparent benefits to vast areas of development, such as lighting, communications, biotechnology, imaging, and medicine.[1] It is expecting that LEDs may replace the traditional light bulbs and tubes to open a new lighting era.[2]

Research and developments on GaN-based compound semi-conductors and structures for optoelectronic and electronic applications have been very active in recent years. GaN and related III-nitride semiconductors possess large direct band gaps, extremely high hardness, very large heterojunction offsets, high thermal conductivity and high melting temperature, and great breakthroughs have been achieved in recent years for their materials growth and device manufactures in applications in blue-UV light emitting diode (LED), laser diode (LD) and other optoelectronic and electronic devices.[1–9] InGaN-based LED and LD grown on sapphire are now available commercially. InGaN/GaN multiple quantum wells (MQWs) are attracting much research interest currently, acting as the active layer in above high brightness III-Nitride LED and cw blue-green laser diode LD.[2–4] InGaN/GaN heterostructures can exhibit intense photoluminescence (PL) and electroluminescence (EL) despite of a high dislocation and defects density existed,[3,10] and have advantages, such as, lowering the threshold current density for LDs and reducing the device sensitivity to temperature.[11] More research efforts have been made on InGaN/GaN multiple quantum wells.[12-34] among which, most of InGaN/GaN MQWs were prepared by the metalorganic chemical vapor deposition (MOCVD) technique, that has been approved a powerful technology for R&D and industry production of III-nitride materials and devices.

InGaN/GaN multiple quantum wells are the key components of these commercial devices emitting UV-green and white light, acting as the active layer, which can exhibit intense luminescence despite of a high dislocation and defects density existed.[3] However, despite an impressive commercial success, the mechanism of luminescence from InGaN/GaN is not yet well-understood[1] and the physical origin of efficient light generation is unveiled incompletely.[1,3]

Since mid-1990s, a turbo-disk technology has been employed in manufacturing MOCVD systems on III-Nitrides. It uses a vertical growth configuration with a high speed rotation platter for multiple sample wafers. This chapter reviews our MOCVD growth and comprehensive investigation of InGaN-GaN MQW blue-green LED structures on sapphire substrates using such vertical growth systems, manufactured by Emcore and Veeco companies.

Analytical techniques of high-resolution (HR) X-ray diffraction (XRD), HR transmission electron microscopy (TEM), photo-luminescence (PL), temperature (T) and excitation power dependent PL, photoluminescence excitation (PLE), time resolve photoluminescence (TRPL), etc. have been employed to investigate their structural and optical properties.

2. Experimental

A large number of high quality InGaN/GaN MQW LEDs were grown on (0001)-plane (c-face) sapphire substrate by low pressure (LP) MOCVD. Trimethylgallium (TMGa), Trimethy-lindium (TMIn), and ammonia NH_3 were used as precursors for Ga, In, and N, with carrier gas of H_2 and N_2, respectively. The substrates were initially treated in H_2 at 1173^{o}C, and 30 nm thick GaN buffer layer was grown on sapphire at 520^{o}C. Followed, 2 µm thick GaN was grown at 1020^{o}C, and 800 nm InGaN layer and 5-8 periods of InGaN/GaN QWs were grown at 800^{o}C. Different designed MQW structures lead to different color LEDs.

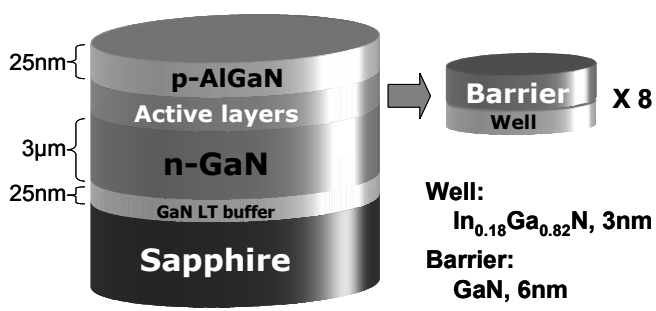

Fig. 1. Schematic drawing of the typical InGaN/GaN MQW LED sample structure.

A typical MQW LED structure is shown as in Figure 1. A series of samples with similar structures but mainly varied QW parameters (size, composition, and numbers) are selected to involve within this review chapter.

3. Structural Properties of InGaN/GaN MQWs

3.1. *High Resolution X-ray Diffraction* (*HRXRD*)

HR-XRD is a sensitive technology to characterize the fine structural features of MQW samples. Figure 2 shows the HR-XRD 2θ–ω scans of (0002), (0004) and (0006) GaN patterns, from two MOCVD-grown InGaN-GaN MQW samples on sapphire. One is for an initially grown sample with 5-QWs which exhibits poor XRD scanned patterns with only 1-2 satellite bands. The right figure shows the development from a 10-QW sample after the improvements of growth conditions. The 1st-order pattern exhibits a broad GaN 2θ peak at 34.6° and only two MQW satellite bands while the 2nd-order shows three satellite bands. The 3rd order (0006) patterns exhibits five satellite bands with the n = 0 observable. Indeed, this is from an old sample grown a few years ago.

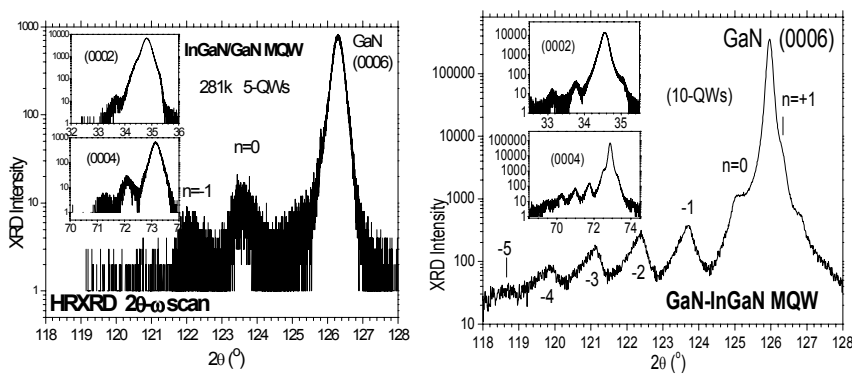

Fig. 2. HR-XRD (0002), (0004) and (0006) patterns from two MOCVD-grown InGaN/GaN MQWs on sapphire, (upper) 5-QWs in the initial growth and (lower) 10-QWs from the improved growth.

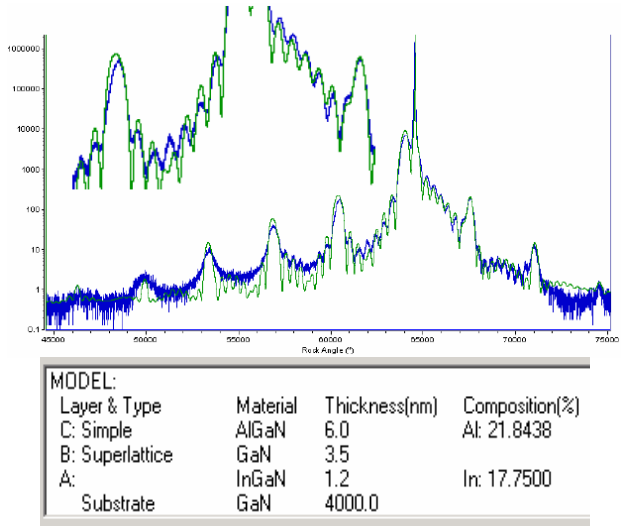

Fig. 3. HR-XRD pattern and simulation from a MOCVD-grown InGaN-GaN MQW on sapphire (8-QWs for blue LED).

The continual efforts have been made on further improvements of the MOCVD growth and parameter optimization for growth parameters, including growth temperature, pressure, V/III ratio, In source flow, carrier gas flow etc. Good improvements have been realized. Figure 3 provides such evidence, where the GaN peak is very sharp and all satellite bands are narrow. More fine structures are seen between satellite peaks and can be fitted well based on the dynamical theory.[25,35] These indicate the excellent layer crystalline perfection and sharp interfaces between all multiple layers. The computer simulation leads to the precise determination of layer parameters of the thickness and composition, as shown in the right side of the figure for this sample. These show that great improvements have been achieved on the MOCVD growth of high quality InGaN-GaN MQW LED wafers.

Figure 4 is the HR-XRD ω-2θ scans for the (0002) reflection from another sample, a green color 5-QW LED (G978). High order satellites up to 11th can be clearly distinguished, showing very good InGaN/GaN interfaces. Such high order satellites were scarcely seen in the literature.[28,32] The GaN peak localized at the angle of 34.56° is very sharp and all satellite bands are narrow. More fine structures are seen between satellite peaks.[25] These indicate the excellent layer crystalline perfection

and sharp interfaces between all multiple layers. Well/barrier width and average indium composition were estimated to be around 4/40 nm and 18% by using Philips X'pert Epitaxy and Smoothfit Program.

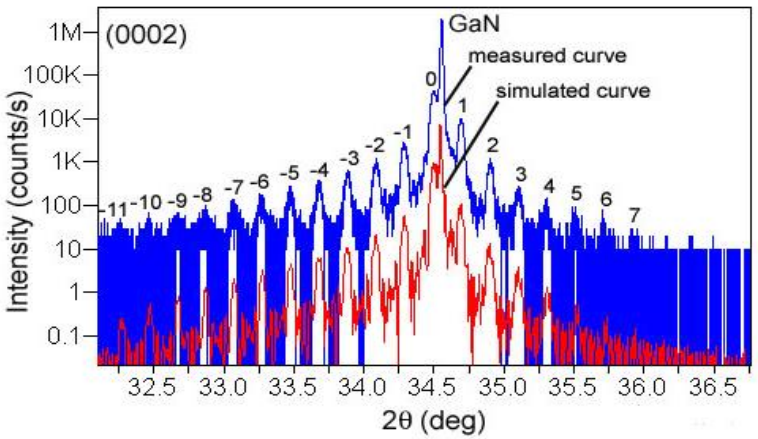

Fig. 4. HRXRD ω-2θ (0002) scans for a 5-QW InGaN/GaN green LED wafer (G978). The lower curve is the simulation result.

3.2. *High Resolution Transmission Electron Microscopy* (*HRTEM*)

Figure 5 shows the high resolution (HR) transmission electron microcopy (TEM) cross section images from a MOCVD-grown InGaN-GaN MQW on sapphire (QW8a) for blue LED. Figure 6 exhibits HRTEM images for another green MQW (5-QWs) LED (G978). The measurements were performed with an acceleration voltage of 200 kV. All high-resolution micrographs were taken at Scherzer defocus, performed under short times of irradiation to prevent electron beam-induced artifacts.[36]

Structural features of 8-QWs in Fig. 5 and 5-QWs in Fig. 6 are clearly seen from these cross-sectional TEM micrographs. The interfaces between InGaN and GaN layers in the MQWs are abrupt. The widths of the well and barrier can be determined. The In-rich precipitates caused by alloy fluctuation appeared as the regions with a dark contrast can be attributed to the In-poor region. The HR image shows no threading dislocation at this area, but some strain field around the well, which sometimes may induce V-shape defects and high density of stacking faults.[21]

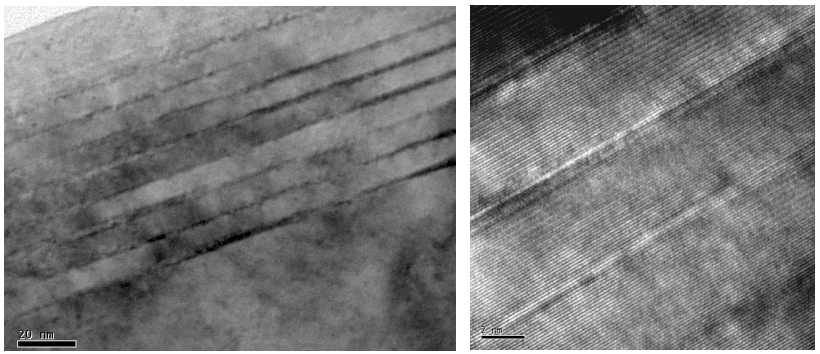

Fig. 5. Cross-sectional high resolution TEM micrographs of an InGaN/GaN MQWs containing 8 QW pairs for blue LED, with the scale of 20 nm (left) and 2 nm (right).

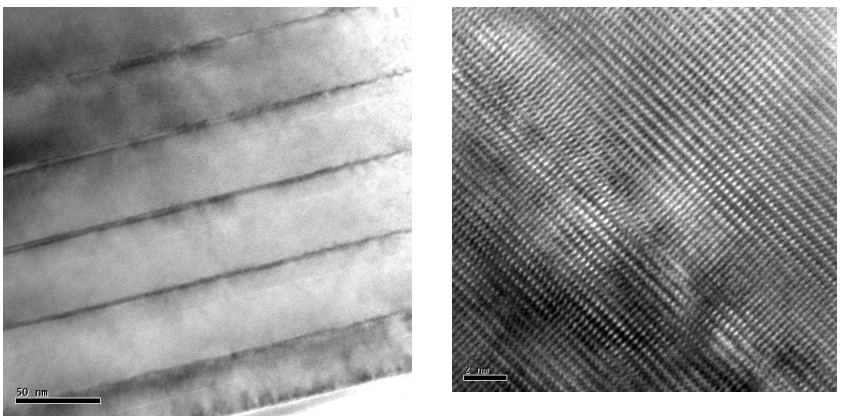

Fig. 6. Cross-sectional high resolution TEM micrographs of an InGaN/GaN MQWs (5-QWs) green LED, with the scale of 50 nm (left) and 2 nm (right).

3.3. *High-Angle Annular Dark Field* (*HAADF*) *Images*

Figure 7 shows two cross-sectional low magnified high-angle annular dark field (HAADF) STEM[20,29] images in two regions of two capped InGaN/GaN MQWs, which were simulated from the original TEM pictures by computer. HAADF STEM contrast is mainly due to thermal diffuse scattering, whose intensity is almost proportional to the square of atomic number. Bright stripes parallel to the basal plane are InGaN layers and dark ones are GaN layers. Eight and five QW structures can

be clearly identified from the cross-sectional HR-TEM observation and HAADF graphs. The dark contrast clearly shows that the QW is not uniform. The well and barrier widths were determined to be 3/10 nm for 8-QW sample QW8a in (a) and 4/40 nm for 5-QW G978 in (b), which are in good agreement with the XRD measurements and simulation results, described previously.

The left side HAADF-STEM micrograph of the InGaN/GaN MQWs structure in Fig. 7 exhibits also the typical V-defect starting at about the fourth quantum well. Threading dislocation, which were formed from the big lattice misfit between the GaN and sapphire, are seen with bright contrast due to large distortion around the defects. Threading dislocation would disrupt the InGaN/GaN MQWs and initiate the V-defects, which have inverted hexagonal pyramid-shaped {10-11} side walls and a strong influence on the optical properties of InGaN/GaN MQWs.

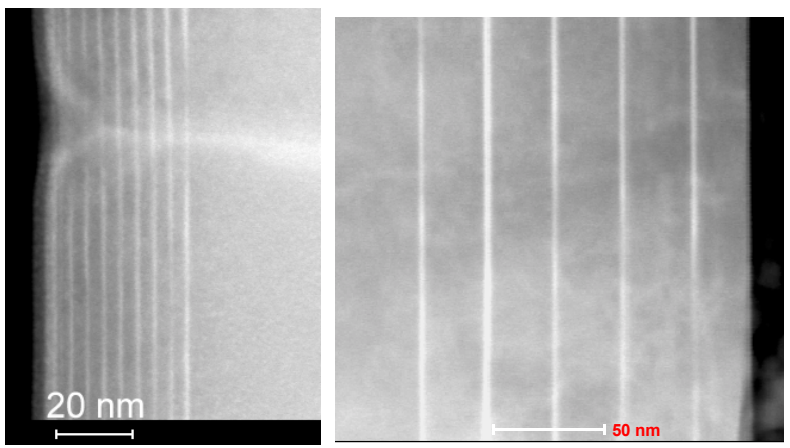

Fig. 7. Cross-sectional low magnified high-angle annular dark field (HAADF) STEM micrographs of two MOCVD-grown InGaN/GaN MQW wafers, containing 8-QW pairs (left for blue LED) and 5-QWs (right for green LED).

4. Optical Properties of InGaN/GaN MQW LEDs

4.1. *Temperature Dependent Photoluminescence*

Figure 8 shows the Temperature (T)-dependent (9-300K) PL spectra of a MOCVD-grown InGaN-GaN MQW (8-QWs) on sapphire, with XRD and TEM data exhibited in Figs. 3-5. The strong and broad emissions

between 2.4-3.0 eV are from the InGaN quantum wells. The full width at half maximum (FWHM) of the QW peak for the LED structure were found 176.8 meV at 9 K. Such large inhomogeneous broadening was due to the compositional fluctuation which is inherently present in the InGaN ternary system.

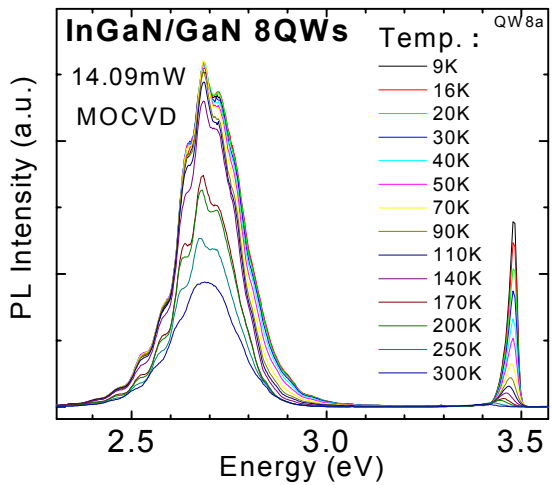

Fig. 8. Temperature (9-300K) dependent PL spectra of a MOCVD-grown InGaN/GaN MQW (8-QWs) on sapphire.

4.2. *PL Band Shifts and Quantum Efficiency*

Figure 9 shows the T-dependent PL peak shifts of both the GaN and QW emissions, and the integrated PL intensity of QW emission peak versus inverse temperature, obtained from Fig. 8. The T-dependent PL peak shifts for GaN band follow the variation of the GaN energy gap versus T. With increasing temperature the band gap shrinks due to the temperature-dependent dilation of the lattice and electron–lattice interaction, and the peak position of PL spectrum exhibits only the red-shift. This can be described by the Varshni equation:[19]

$$Eg = E(0) - \frac{\alpha T^2}{T + \beta} \tag{1}$$

where E_g denotes the energy gap at temperature T; E(0) at 0 K, and α and β constants. The constants α and β are considered in principle

dependent on the sample compositions, but independent of the growth method and the well width. The values of α and β were evaluated from the linear interpolation from the values for GaN and InN. The values of α and β are 0.77 meV (0.69 meV) and 600 K for GaN.[19]

But the T-shifts of the QW band exhibit a special behavior: from 9 K to 150 K, it keeps almost a constant, and from 150-300 K, it decreases in energy only very slightly. The unique T-behavior of PL spectra is due to the quantum dot like structure features within the MQW structures.

The activation energy, E_A, is deduced to be 80 meV from the slope of data for the integrated PL intensity of QW emission peak versus inverse temperature, in the temperature range of 140-300 K from Fig. 9. This large value of E_A (80 meV) indicates the localization of the carriers in the structure.[15] Assuming that the internal quantum efficiency equals unity at 9 K, we obtained the internal quantum efficiency of 34.8% at room temperature for this LED.

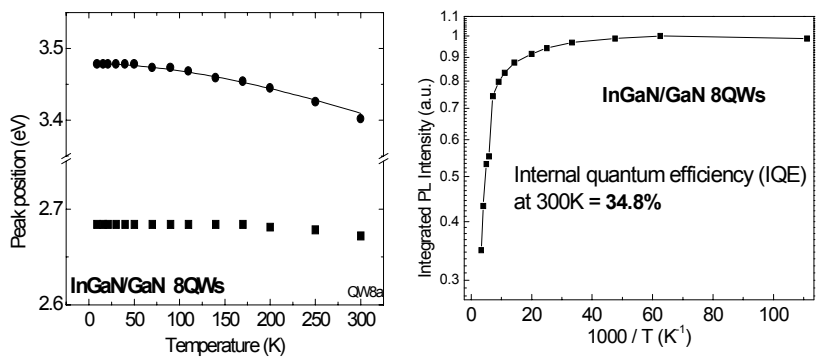

Fig. 9. PL peak shifts (left) and intensity-reciprocal temperature (right) dependence, obtained from Fig. 8, of a MOCVD-grown InGaN-GaN MQW (8-QWs) on sapphire.

4.3. *Excitation-Power-Dependent Photoluminescence of InGaN/GaN Green LED Wafer*

Figure 10 shows the excitation power-dependent PL spectra for a 5-QWs green LED wafer. With increasing the excitation power from 0.07 to 33.1 mW, the emission shows a clear blue-shift. Figure 11 shows the excitation power dependence of the emission peak energy in (a) and the full width at half maximum (FWHM) in (b) of the main emission, respectively. A blue-shift of ~163 meV for the QW peak is evident in

Fig. 11 (a) as the excitation power increases from 0.07 mW to 33.1 mW. For the blue-shift of emission energy in this sample, normally, there are two possible explanations. One refers to the piezoelectric field-induced QCSE,[11] and another is related to the band-filling effect at the self-organized small In-rich regions.[37]

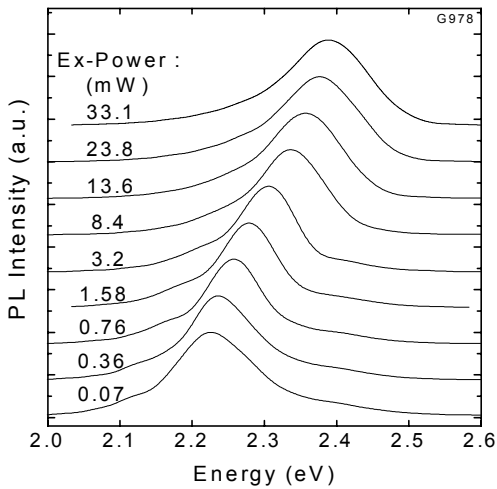

Fig. 10. Low temperature PL spectra of the InGaN/GaN green LED under different excitation intensities. All spectra are normalized and shifted vertically for clarity.

In addition, in Fig. 11 (b) the FWHM of the emission peak decreases with increasing excitation power from 0.07 to 3.2 mW, and then increases with increasing excitation power up to 33.1 mW. Such anomalous excitation power dependence of the emission linewidth behavior is rarely seen in literatures, but monotonous increasing or decreasing phenomena of the emission peak linewidth for InGaN/GaN QW structure were observed by another group.[38] Our results can be well explained in the terms of the QCSE along with the state filling effect. Due to the lattice mismatch between InGaN and GaN, the InGaN wells were under biaxial stress. In such a case, a piezoelectric field is induced since group III nitrides have large piezoelectric constants along the [0001] orientation.[39] Therefore, the optical properties are strongly affected by this piezoelectric field, which produces QCSE. Due to the QCSE, the emission peak will show a red-shift and the peak linewidth will be broadened, which has been observed earlier in the GaAs system.[40]

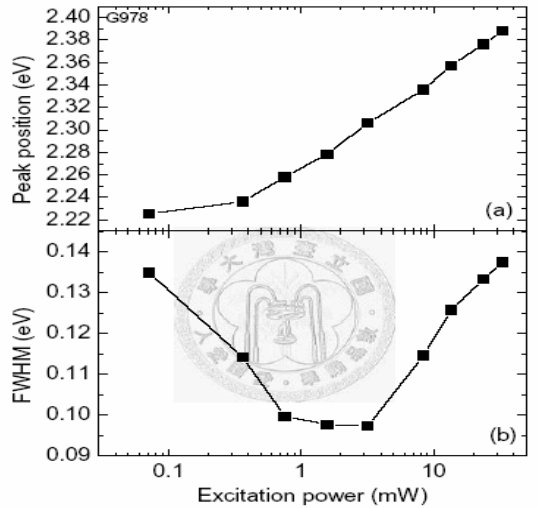

Fig. 11. Excitation power dependence of the peak position (a) and the FWHM (b) for the InGaN/GaN 5-QWs green LED structure.

The piezoelectric field can be screened by photo-generated carriers. The increase of the excitation power from 0.07 to 3.2 mW weakens the QCSE and thus increases the transition energy, resulting in a blueshift, and decreases the FWHM of the peak at the same time. At higher excitation power more than 3.2 mW, the piezoelectric field seems to be fully screened, which the linewidth doesn't decrease any more. Then, the band-filling were the dominant effect, which can cause the emission energy blue-shift also. On the other hand, the band filling can explain the broadening of the emission linewidth. At high level excitation, radiative recombination from high higher energy states will occur because there are more injected carriers and the possibility of higher energy states being filled with the excited carriers is larger. Most of these excited carriers at the higher energy states relax to the ground states and the ground state recombination still dominate the PL emission, while only a small amount can directly recombine and emit light of larger energy. It can cause the PL emission blueshift and broader as the excitation power is further increased.

4.4. *Different T-behavior of Photoluminescence from InGaN/GaN Green and Blue LED Wafers*

Our experiments showed quit different T-behaviors of PL from different InGaN/GaN MQW LEDs. Figure 12 shows the T-dependent PL spectra for the InGaN/GaN green LED sample from 9 to 300 K. In each case, the excitation power was fixed at ~20 mW. Different from previous blue LED MQW sample, single peak emission was observed over all temperatures, and the decrease of peak intensity is slow with an increase in temperature. The PL peak positions of QW-related band for this sample exhibit a monotonous red-shift. In general, with increasing temperature the band gap shrinks due to the temperature-dependent dilation of the lattice and electron–lattice interaction. Thus, the peak position of PL spectrum exhibits only the red-shift, which can be well described by the Varshni formula (1).[19]

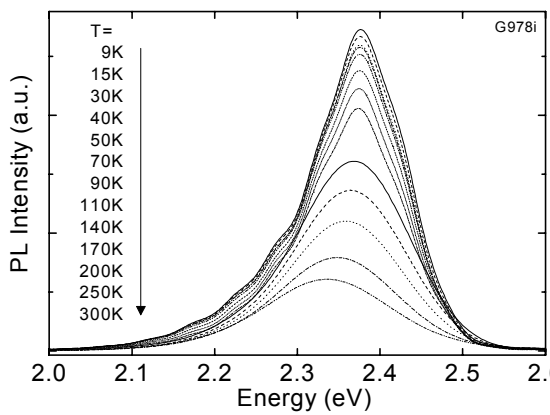

Fig. 12. PL spectra from an InGaN/GaN 5-QWs green LED structure in the temperature range from 9 to 300 K.

The indium fraction for this sample is 18 % determined by XRD measurement. The energy gap *E(T)* variations of $In_{0.18}Ga_{0.82}N$ with temperature are shown together with the experimental data in Figure 13 (a). The values of α and β are 0.77 meV/K and 600 K for GaN and 0.245 meV/K and 624 K for InN, respectively.[19,20]

As shown in Fig. 13 (a), the deviation of the PL peak position from the Varshni's characteristics appears, which is considered due to the thermal broadening of carrier distribution, the delocalization of carriers,

the dissociation of the exciton, and the piezoelectric field intensity with temperature change.[41] The points in Fig. 13 (b) show a W-shaped temperature dependence of the full width at half maximum (FWHM) with a characteristic kink at about 140 K. The W-shaped temperature behavior of the linewidth is known to be a signature of exciton hopping over randomly dispersed localized states with a crossover from a non-thermalized to a thermalized distribution function of the exciton.

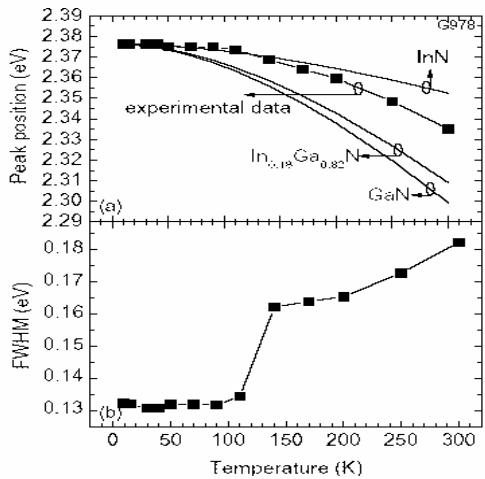

Fig. 13. Temperature dependence of the peak position (a) and the FWHM (b) for the InGaN/GaN 5-QWs green LED structure.

Furthermore, some more InGaN/GaN MQW LED wafers showed a third type of PL spectral variation with temperature, redshift-blueshift-redshift, i.e. a so-called S-shape shift, of the peak energy (E_{PL}) of the InGaN related PL emission with increasing temperature.[10] Figure 14 shows such an example for a MOCVD-grown InGaN/GaN MQW (5-QWs) LED, RE41, which consists of 5-QWs with well width x_{In} = but same barrier width of d_b=11.8 nm and same In compositions of x_{In} = 18%, has the similar S-shape T- E_{PL} behavior.

This behavior is conventionally interpreted as a sign of localization due to inhomogeneities of the potential and the carrier localization in its band-tail states, due to the fluctuations in In composition, layer thickness and possibly defects in the quantum wells, including QD-like and nano-structures.[42,43] It is thus of interest to consider how the behavior and these effects vary with emission energy. Since the band-tail model is

applicable for the temperatures above 30 K, we focus on the study of the PL spectra at temperatures higher than 30 K. In the case of this sample, the emission energy increases with increasing temperature from about 30 K to around 120 K, and then decreases with further increase of temperature up to room temperature (RT). This is a fingerprint of the excitation localization effect. The experimental data can be fitted using the band-tail equation:[42,43]

$$E(T) = E(0) - \frac{\alpha T^2}{T + \beta} - \frac{\sigma^2}{K_B T}. \quad (2)$$

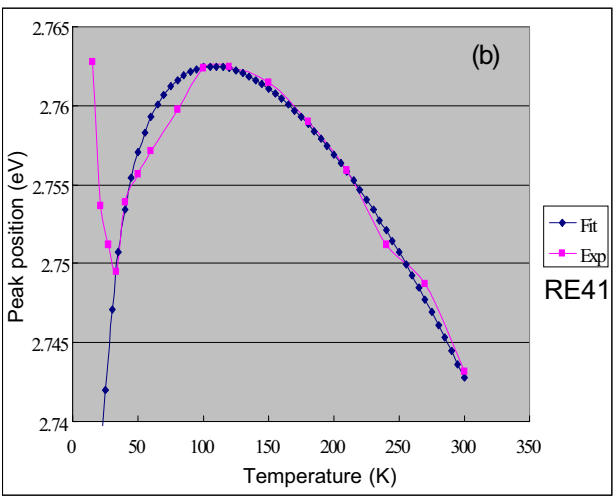

Fig. 14. Temperature dependence of the peak position of a MQW LED (RE41).

The first term in Eq. (2) describes the energy gap at zero temperature; α and β are known as Varshini's fitting parameters, which appear in Eq. (1). The third term comes from the localization effect, indicating the degree of localization effect, i.e. a large value of σ means a strong localization effect. k_B is Bolzmann's constant. In addition, because this model is based on the assumption of non-degenerate occupation, the absolute value of σ is strongly dependent on the excitation power. Therefore, from this model, one can only obtain a relative value, i.e. one can only relatively compare the values of σ in different samples under identical measurement conditions, in order to compare their exciton localization effects. The σ value of sample RE26 with $d_w = 2.85$ nm is about 12.5 meV and that of sample RE41 with $d_w = 1.6$ nm is about

8.2 meV. This indicates that the exciton localization effect is stronger in MQW sample with wider well width.

5. Special Electron Microscopy of InGaN/GaN MQWs

5.1. *V-shape Defects*

It is found that the most troublesome defects in the InGaN/GaN MQWs are V defects or inverted hexagonal pyramid (IHP) defects.[21,44,45] They cause undesirable long-wavelength small emissions in addition to the main emission.[44] High-angle annular dark-field (HAADF) scanning transmission electron microscopy (STEM) is a good technology to investigate the V and IHP defects and related fine structural features of MQW samples.

Figure 15 (a) shows a HR TEM image of a V-defect region from a MOCVD-grown InGaN-GaN MQW green LED on sapphire. It exhibits the threading dislocation originating from GaN/sapphire interface to disrupt the InGaN/GaN MQW, and to initiate the V-shaped pit defect, which have inverted the hexagonal pyramid-shaped {10-11} side walls. The cross sectional HAADF STEM image can be seen from the right figure (b), where QW InGaN-well layers appeared as thin bright bands and black-grey areas are for QW GaN barriers.

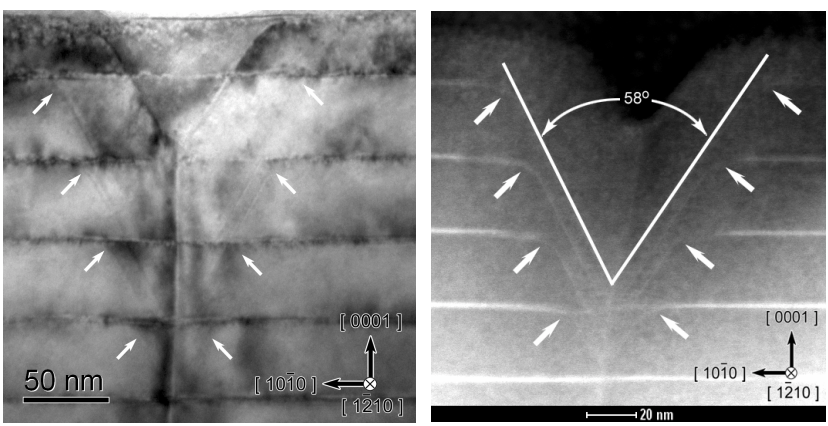

(a) (b)

Fig. 15. HRTEM and HAADF STEM images of a V-defect region from a MQW green LED.

From these two figures for a V-shaped pit, it showed that the V defects were observed nucleating on a threading dislocation (TD) crossed with the InGaN QW just above the underlying GaN layer. HAADF-STEM gave undoubted evidence that the V defects have a thin six-walled structure with InGaN/GaN $\{10\bar{1}1\}$ QWs. The sidewall would be thin InGaN layers on the {10-11} planes, where InGaN and GaN layers were epitaxially grown successively, similar to the growth on the (0001) plane. The InGaN QWs on the pyramid planes have similar thickness as the QWs on the (0001) planes. However the inclined GaN barriers have a thinner thickness compared in the (0001) QWs. The segregation of In atoms was observed at the starting points of the V defects, by HRTEM and HAADF-STEM. This might work as the In-rich mask which induced the $\{10\bar{1}1\}$ facets on the GaN crystal grown at the low temperature, as proposed in the formation mechanism of the V defects.[44]

When the QWs are capped with either GaN or AlGaN, the V-defects are filled with GaN (or AlGaN) and the central TD propagates to the free surface. The angle between the (0001) plane and the InGaN well of the left side and right side is different. This phenomenon changes the period thickness of the superlattice (well + barrier) within the MQWs, and it would have an influence on the optical properties of InGaN/GaN MQWs.

The corners connecting the $\{10\bar{1}1\}$ interfaces on the walls of a V defect with the (0001) interfaces in the main MQWs were curved. This is explained as a result of the layer-by-layer growth on the (0001) and $\{10\bar{1}1\}$ surfaces where each monolayer did not cover over its under-monolayer for lack of atom. The successive growth of these monolayers formed an interface with step-wise lattices near the corner, which is observed as the curved corner of the QW in the low-magnified HAADF-STEM images.

5.2. *TEM Digital Analysis of Lattice Images* (*DALI*)

A so-called digital analysis of lattice images (DALI) technique from cross-section HR-TEM can be performed in order to reveal the QW layer, thickness, indium composition, and well-to-well inhomogeneity. It is indeed an image of strain state analysis (SSA).[27,48] To avoid specimen degradation during electron-beam irradiation, the exposure time before image recording was kept smaller than 1 min,[49] and even much shorter as 5-10 seconds.[27] Figure 16 provides such TEM DALI images of the

studied green LED, showing the color-coded map of the local In concentration in this InGaN/GaN MQW structure containing 5 InGaN well layers. The left pattern is from QW1 just next to the capping layer and the right one is from QW5 at the bottom of the active layer. The clustering nanostructures[27,48] or quantum dot (QD)-like structures[20,50] around the In-rich areas are formed, which is the cause of strong luminescence from InGaN/GaN MQWs.

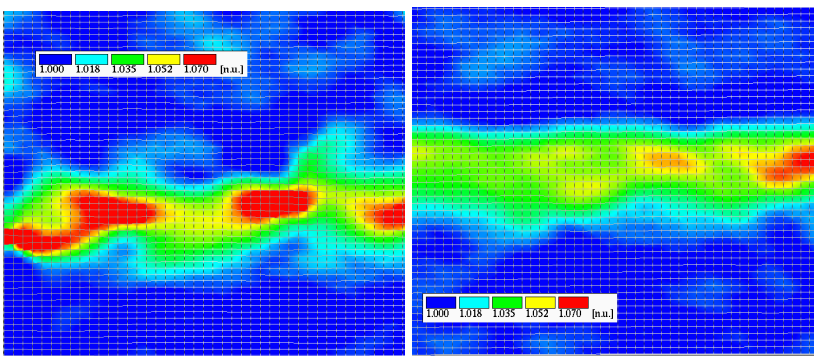

Fig. 16. TEM DALI images of an InGaN MQW with left pattern from QW1 just next to the capping layer and the right one is from QW5 at the bottom of the active layer.

5.3. *Different TEM Studies on InGaN-based LEDs*

There appears a hot discussion on the mechanism or origin of luminescence from InGaN/GaN system.[1,49–51] In all other traditional light-emitting semiconductors (except for III-nitrides), crystal defects (dislocations) in the semiconductors or LEDs reduce radiative recombination severely and light emission is quenched if the dislocation density exceeds about 10^3 cm^{-2}. However, although with the dislocation density of about 10^8-10^{10} cm^{-2}, i.e. one million times higher than this value, InGaN emit strong blue and green light (it is also known that dislocations in InGaN act as non-radiative recombination center).[32,52] It is considered by many researchers that the clustering in $In_xGa_{1-x}N$ layer and the nano-meter scale In-inhomogeneities and dot-like structures in InGaN well region play a main rule, even not all, for the intense light emissions from InGaN/GaN QW structures.[25,27,32]

However, controversy arguments and opinions exist. C. J. Humphreys and co-authors have suggested that the contrast observed in many HRTEM images is to a large extent a consequence of exposure to the electron beam and is not due to the presence of In-clustering, that strong luminescence from the carrier localization is possible due to monolayer well width fluctuations with a lateral scale of about 2 nm.[51] They also postulate, by observing the gross well-width fluctuations in single InGaN/GaN QWs and interlinking strips of InGaN with In-rich centers, that excitons are localized at these In-rich regions preventing them reaching threading dislocations.[51]

6. Special Luminescence Spectroscopy of InGaN/GaN MQWs

6.1. *Photoluminescence Excitation* (*PLE*) *Spectroscopy*

Photoluminescence Excitation (PLE) Spectroscopy is a combination of luminescence and absorption measurement. It fixes the detection wavelength at a distinguished emission and scans the excitation photon energy above this emission, i.e. the intensity of a given PL band is recorded as a function of excitation photon energy. It is usually recognized that the PLE spectrum exhibits an absorption-like profile. The PLE spectrum, therefore, reflects the absorption characteristics of the luminescent layer.[53] PLE has advantages over optical absorption techniques. It does not require the substrate material to be transparent at the excitation energy and is not dependent on the thickness of the active layer. PLE is a particularly sensitive technology to measure the Stokes shift between absorption and emission of a specific emission line, which is an indication of energy relaxation of carriers to lower energy states following optical excitation and prior to the luminescence process examined. PLE technique has been used to investigate InGaN/GaN MQWs.[54-59]

Figure 17 shows RT InGaN-related PL spectrum, and PLE spectra measured with four different detection photon energies E_{detect} of 2.748, 2.479, 2.274, and 2.039 eV, respectively, for the sample RE26, with 5-QWs, d_w = 2.85 nm, d_b = 11.8 nm and x_{In} = 18%. The PL spectrum was excited by a 325 nm (3.81 eV) light source using a 450 W Xenon lamp dispersed by a monochromator. The PL spectrum for this MQW LED sample exhibits two emission bands located at 2.49 and 1.97 eV with weak multiple fine structures due to Fabry-Perot interference fringes.

This emission is identified as the yellow-band (YB). The yellow band emission is similarly defect-related and correlated with the presence of threading dislocations and other related structural defects.[60,61]

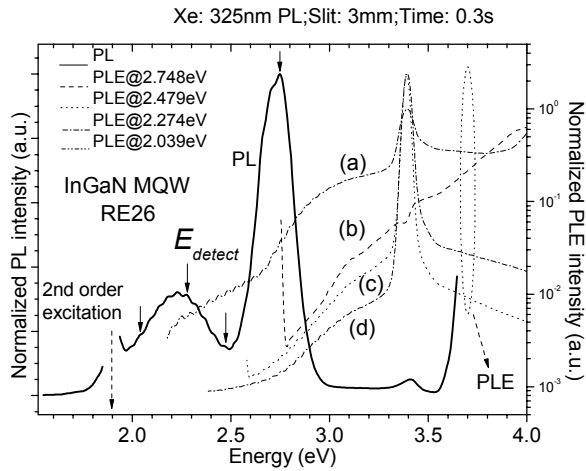

Fig. 17. PL and PLE spectra at RT of InGaN/GaN 5-QWs blue LED sample (RE26). The PL measurement was excited with a xenon lamp coupled with a monochromator (325nm). PLE spectrum was taken at energies indicated by the red arrows.

The PLE spectra taken under four detection energies marked by arrows are normalized in Fig. 17. In each PLE spectrum, the contributions from the InGaN wells and the GaN barriers are clearly distinguishable. It is noted that the carrier generation ratio of the InGaN wells to the GaN barriers achieves the maximum when the PLE detection energy was set at the PL peak energy (curve *a*). When the detection energy is below the InGaN main emission peak (curve *b*), the contributions of the GaN regions are enhanced compared to the curve *a*. These facts imply that for E_{detect} (detection energy) > $E_{g,GaN}$ (E_g of the GaN barriers), the lower-energy side of the InGaN main emission peak is governed mainly by carrier generation in the GaN barriers and subsequent carrier transfer to the InGaN wells. From the different PLE contributions for the higher- and lower-energy sides of $E_{p,InGaN}$, we can expect different recombination mechanisms for various excitation energies.

As the PLE detection energy is monitored at (d) 2.039 and (c) 2.274 eV for the YB emission, the contribution of the GaN barrier

layer is noticeably increased. These facts indicate that the main source of the YB emission does not predominantly originate from the InGaN wells but originates from the GaN barrier layers.

6.2. *PLE Fitting and Quantum Confined Stokes Effect*

A large energy difference between the band-edge absorption and emission was observed from the QW LED structure, i.e. due to the quantum confined Stokes effect (QCSE). Theoretical simulation helps to describe the QCSE behavior. PLE spectrum near the absorption edge can be fitted to a sigmoidal formula:[54,55,57]

$$\alpha = \alpha_0/[1 + \exp((E_{eff} - E)/\Delta E)] \quad (3)$$

where α_0 is a constant, E_{eff} the effective band gap, and ΔE the broadening parameter which indicates a distribution of absorption states, and E the excitation energy at which the intensity of emission. We obtained E_{eff} values of 3.030 eV, and ΔE value of 15.2 meV, for this InGaN/GaN MQW sample with well width of 2.85 nm, as shown in Fig. 18.

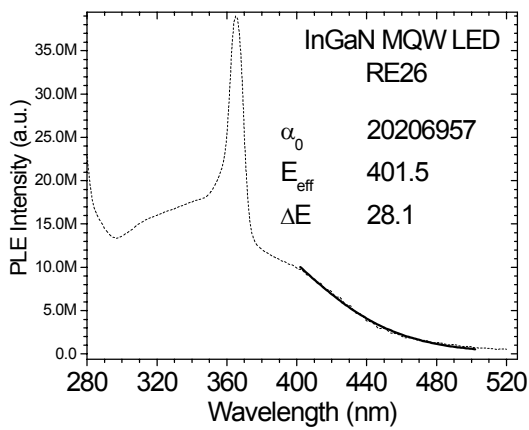

Fig. 18. Sigmoidal plot of the PLE intensity for the InGaN/GaN MQW (RE26) with the average In composition of 21%. The solid line is a fitting curve.

For another comparative MQW sample with well width of 1.6 nm and all other growth parameters same as above sample, we have obtained an E_{eff} value of 3.088 eV and ΔE value of 28.1 meV. With increasing well width, the InGaN-related PLE band edge redshifts and becomes

broadened. With the precise determination of the effective band gap, E_{eff}, the difference between E_{eff} and the PL peak energy, i.e. the Stokes' shift can be determined accurately, as shown in Fig. 19, to be 300 and 340 meV, respectively, for these two MQW LEDs. It is seen that the Stokes' shift is larger for MWE with wider well width. We obtained the Stokes' shift as high as 340 meV, which is consistent with the large value of activation energy associated with the strong localization of the carriers in this MQW-structure.

It is worthy to point out that most of PLE measurements on the QCSE shifts, reported in the literature,[54–57] were performed at low temperature range below 20 K (C. L. Yang *et al*.[58] measure PLE at 11K and 50-250K showing GaN peak only beyond 100 K; Y. C. Lu *et al*.[59] studied enhanced PLE over 10-200K for SiN/Ag coated InGaN/GaN QW with surface plasmon coupling), while our measurements for PLE-QCSE were successfully performed at RT condition, which is also an indication of the high quality of our MOCVD grown InGaN/GaN MQW samples with excellent characteristics.

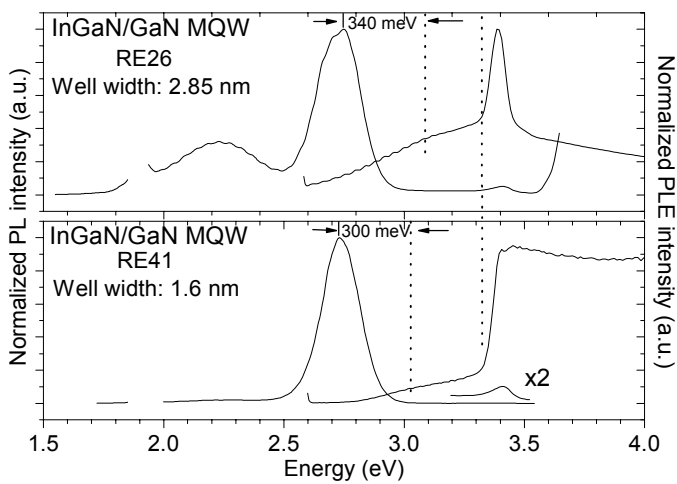

Fig. 19. PLE spectra at room temperature for the InGaN/GaN MQW RE26 and RE41 blue LED structures.

6.3. *Temperature Dependent Time Resolved Photoluminescence*

Time-resolved spectroscopy provides a method for the direct measurement of exciton and carrier lifetimes in semiconductors and

semiconductor structures. Lifetimes are critical to device efficiency and therefore overall device performance. An understanding of the fundamental physics underpinning such phenomena is essential for the improvement of nitride semiconductor devices. In particular, the room temperature (RT) behavior of these systems at high carrier concentration is directly relevant for device operation.

Time-resolved photoluminescence (TRPL) has been used to examine nitride semiconductor multiple quantum wells (MQWs).[62–65] Time-resolved spectroscopy provides a method for the direct measurement of exciton and carrier lifetimes in semiconductors and semiconductor structures. Lifetimes are critical to device efficiency and therefore overall device performance. Detailed analysis and discussion are helpful to understand the emission dynamics properties.

Here TRPL studies are presented on two typical MOCVD-grown InGaN/GaN MQW LEDs, which were investigated by PLE in last two sub-sections. Their PL peak vs temperature, E_{PL}-T, shows a S-shape behavior as mentioned previously. PL spectra vs T for MQW sample RE26 (d_w = 2.85 nm) is shown in Fig. 20 with a S-shape variation of PL peak vs T.

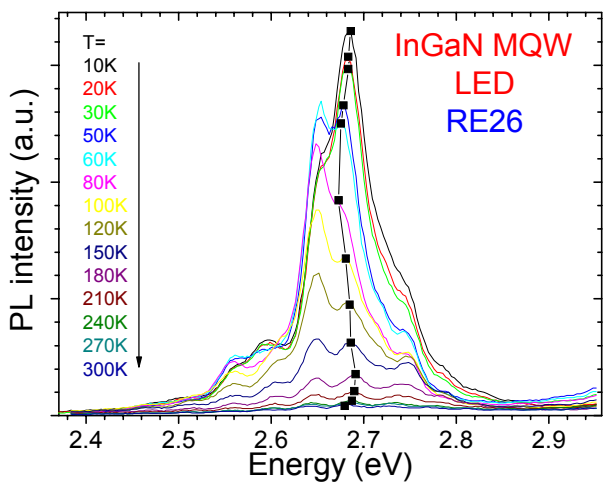

Fig. 20. The PL spectra for an InGaN/GaN MQW in the temperature range from 10 to 300 K. The main emission peak shows an S-shaped shift with increasing temperature (solid squares). All spectra are normalized and shifted in the vertical direction for clarity.

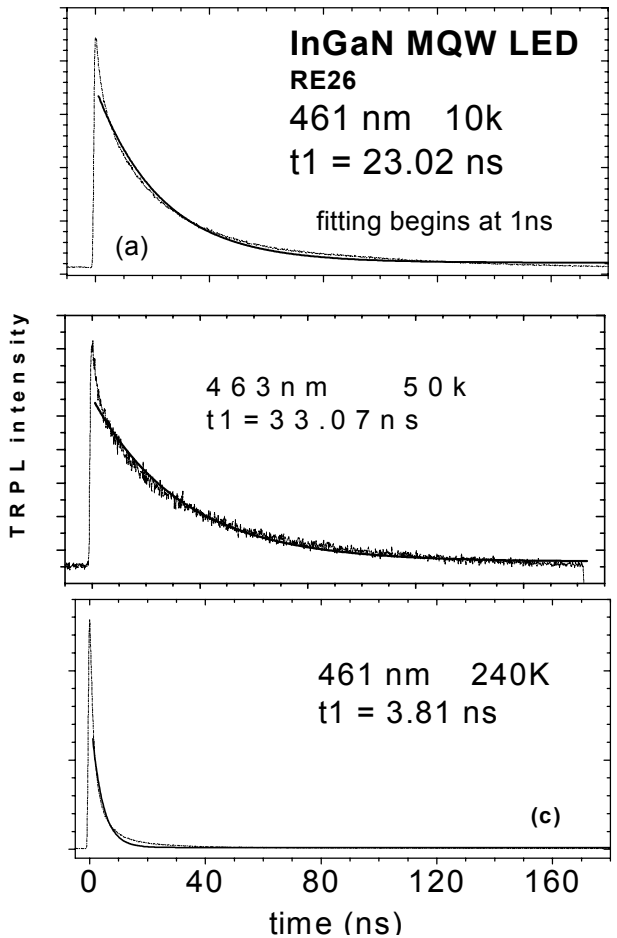

Fig. 21. Typical TRPL data and fittings for MQW RE26 at three temperatures of 10, 50 and 240 K, respectively.

Time-resolved photoluminescence (TRPL) measurements on this MQW sample were performed in 10-300 K. Typical TRPL data and fittings at three temperatures of 10, 50 and 240 K, respectively, are shown in Fig. 21. When we are performing fits, we let the fitting begins at about 1 ns after the laser pulse peak, to avoid the laser response.

6.4. *Decay Time versus Temperature*

Figure 22 shows the dependence of lifetime on the temperature from 10 K to 300 K. The time constants are obtained from the single exponential fit as a function of temperature at the luminescence peak. As the temperature was raised from 10 to 50 K, the measured lifetime increase from 23.02 to 33.07 ns. All of these data show a bimolecular characteristic. These results suggest that at low temperature, the band-edge luminescence is dominated by radiative free carrier recombination. At temperatures greater than 50 K, the measured luminescence lifetimes start to decrease with decreasing luminescence intensities. The measured lifetime decreases down to 20.44 ns at a temperature of 100 K. This result indicates that the carrier recombination is no longer dominated by radiative processes at temperatures higher than 50 K. The measured TRPL can no longer be fit to a bimolecular recombination mechanism. Detailed information about nonradiative channels requires further study. At temperatures higher than 100 K, the luminescence intensity decreases with increasing temperature while the measured lifetimes remain roughly constant around 19.23–2.65 ns.

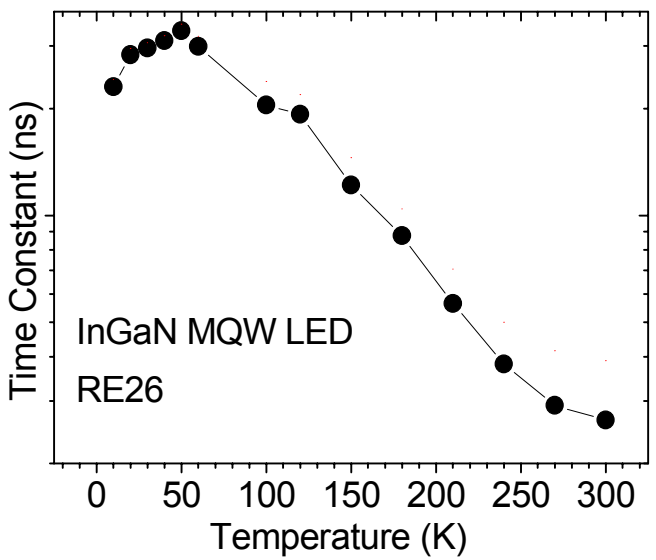

Fig. 22. The PL lifetime as a function of temperature. Measurements are performed at the PL peak wavelength 462 nm. A single-exponential fit was used to determine the lifetime.

6.5. *Detection Energy Dependent Time Resolved Photoluminescence*

To further clarify the emission properties of InGaN/GaN MQWs, we perform TRPL measurements with varying the detection energy, E_{detect}, across the MQW emission band. Decay times at each E_{detect} can be obtained similarly as done in Fig. 21. The detection energy dependence of τ_{PL} at RT can be obtained. Fig. 23 shows this dependence of τ_{PL} vs E_{detect} for sample RE41. The normalized PL spectrum is also exhibited in the figure. PL has a main peak around 2.715 eV for MQW RE41. The PL decay time was dependent on the detection photon energy and it is shorter (~ 1.75 ns) on the higher energy side than that (~ 5 ns) on the lower energy side for RE26; shorter (~ 1.1 ns) on the higher energy side than that (~ 4.5 ns) on the lower energy side for RE41. In other words, the τ_{PL} values increase with decreasing photon energy.

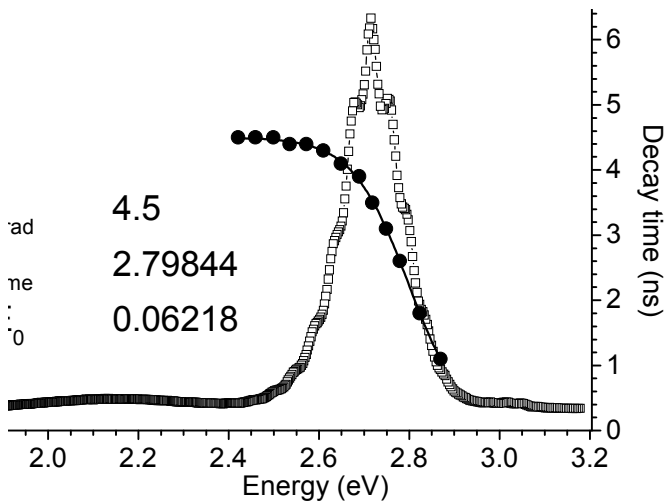

Fig. 23. Detection energy dependence of PL lifetime τ_{PL} for an InGaN/GaN MQW blue LED, RE41 (d_w = 2.85 nm), between 418 to 512 nm, i.e. 2.42 to 2.97 eV at RT. The integrated PL spectrum (open square symbols) is also shown in the figure.

This energy dependence is due to the energy transfer from higher energy localized state to lower one. This is characteristic of the localized system, where the decay of exciton consists of both radiative recombination and the transfer process to tail states. The depth of

localization can be evaluated by assuming the exponential distribution of the density of tail states and by fitting the photon energy dependence of the τ_{PL} values using the following equation:[66,67]

$$\tau_{PL}(E) = \frac{\tau_{rad}}{1 + \exp\dfrac{E - E_{me}}{E_0}} \tag{4}$$

where τ_{rad}, E_{me}, and E_0 are the radiative lifetime, the energy similar to the mobility edge, and the depth of localization, respectively. By fitting, τ_{rad} = 4.5 ns, E_{me} = 2.798 eV and E_0 = 62.18 meV were obtained for the sample RE41 (d_w = 2.85 nm). Similarly, τ_{rad} = 4.92 ns, E_{me} = 2.76 eV, and E_0 = 39.3 meV were obtained for RE26 with a narrower well width (d_w = 1.6 nm).

The lifetime at the low-energy side of the InGaN peaks is longer for larger well width, as expected from the larger Stokes shift,[68] discussed in section ***6.2***. At RT, the samples have different lifetimes because of thermally activated nonradiative recombination. In this case, the majority of excitons in InGaN QWs on the sample RE41 is delocalized from the shallow potential minima and recombines radiatively at around RT. On the other hand, InGaN QWs on the sample RE26, which have a deeper localization depth of 84.5 meV. TRPL study further indicated that the radiative lifetime was decreased with the decreased well width. In general, growing a thicker well with a longer growth time could easily cause fluctuation of In diffusion path and form worse interfaces between wells and barriers. The more degree of In separation could result in the more localized states between conduction band and valence band, i.e. more nano-structural centers. Therefore, more localized states in the thicker well could trap parts of carriers transited from higher levels to lower levels.[69]

7. Summary

We have reported on the MOCVD growth of InGaN/GaN multiple quantum well (MQW) green light emitting diode (LED) structures on sapphire substrates. Analytical investigation by photoluminescence, photoluminescence excitation, time resolved photoluminescence, high-resolution X-ray diffraction and transmission electron microscopy has shown the excellent optical and structural properties. Up to 10th order

QW XRD satellite peaks were observed plus the fine fringes corresponding nanometer scale thickness variation. Transmission electron microscopy confirmed the sharp MQW structures and dimensional parameters as well as nano-structural features.

Detailed and penetrating studies of luminescent properties have been performed via a variety of photoluminescence spectroscopic measurements. Three types of temperature dependence behaviors of the InGaN-QW emission peak energy were observed from various InGaN/GaN MQW LEDs, including near Varshni-type, near flat-variation and an S-shaped (redshift-blueshift-redshift) behavior with increasing temperature. The unique P (excitation power) and T behaviors of PL spectra are due to quantum confined Stokes Effect (QCSE) and filling effect of band-tail states within the MQW structures. A large Stokes shift was observed from the comparison of PL and PLE measurements which arises due to inhomogeneities in the InGaN-based material.

Time-resolved PL properties of MOCVD grown InGaN/GaN MQWs have been studied over the temperature range of 10 to 300 K and across the QW emission peak. The relationships of the carrier decay lifetime as a function of temperature and detection energy are obtained, which reveal that the InGaN-related emission is strongly affected by the change in carrier recombination dynamics with increasing temperature for the InGaN/GaN MQWs and emission mechanisms below or beyond the QW emission peak.

This penetrating investigation is helpful to better understand the luminescent mechanisms and find ways to further improve the material design and growth of InGaN/GaN MQWs for the wide spectral LED applications.

Acknowledgments

The authors acknowledge the supports and help in this work from Profs. (Drs.) C. C. Yang, L. C. Chen, K. H. Chen, Y. F. Chen, I. T. Ferguson, W. Lu, P. Li and H. L. Tsai, as well as my students of J. H. Chen, Z. S. Lee, and T. W. Kuo. The work at National Taiwan University was supported by several funds from National Science Council of Republic of China, NSC 93-2218-E-002-011, 93-2215-E-002-035, 94-2215-E-002-019, 95-2221-E-002-118 and 96-2221-E002-166.

References

1. S. M. de S. Pereira, K. P. O'Donnell and E. J. da C. Alves, *Advanced Functional Mat.* **17**, 37 (2007).
2. Zhe Chuan Feng, ed., *GaN-Based Materials: Growth and Characterization,* Imperial College Press, London, 2006.
3. S. Khatsevich, D. H. Rich, S. Keller and S. P. Denbaars, *Phys. Rev. B* **75**, 035324 (2007).
4. S. Nakamura, S. Pearton and G. Fasol, *The Blue Laser Diode – the complete story*, Springer, Berlin, 2000.
5. J. I. Pankove and T. D. Moustakas ed., *Gallium Nitride (GaN) I and II*, *Semiconductors and Semimetals,* ed. R. K. Willardson and E. R. Weber, Vol. 50 and 58, Academic, San Diego, 1998 & 1999.
6. H. Morkoc, *Nitride Semiconductors and Devices,* Springer, Berlin, 1999.
7. S. Nakamura and S. G. Chichibu ed., *Introduction to Nitride Semiconductor Blue Lasers and Light Emitting Diodes*, Taylor & Francis, London, 2000.
8. E. T. Yu and M. O. Manasreh ed., *III-V Nitride Semiconductors: Applications & Devices*, Vol. 16 in M. O. Manasreh ed., *Optoelectronic Properties of Semiconductors and Superlattices*, Taylor & Francis, New York, 2003.
9. M. O. Manasreh and I. T. Ferguson ed., *III-V Nitride Semiconductors: Growth*, Vol. 19 in M. O. Manasreh ed., *Optoelectronic Properties of Semiconductors and Superlattices*, New York, Taylor & Francis, 2003.
10. K. S. Ramaiah, Y. K. Su, S. J. Vhang, B. Kerr, H. P. Liu, L. G. Chen, *Appl. Phys. Lett.* **84**, 3307 (2004).
11. H. Gotoh, T. Tawara, Y. Kobayashi, N. Kobayashi, T. Saitoh, *Appl. Phys. Lett.* **83**, 4791 (2003).
12. T. Wang, H. Saeki, J Bai, T. Shirahama, M. Lachab, S. Sakai, P. Eliseev, "Effect of silicon doping on the optical and transport properties of InGaN/GaN multiple-quantum-well structures", *Appl. Phys. Lett.* **76**, 1737 (2000).
13. H. H. Cho, J. Y. Lee, C. S. Kim, G. M. Yang, N. Sharma and C. Humphreys, "Microstructural characterization of InGaN/GaN multiple quantum wells with high indium composition", *J. Crystal Growth* **231**, 466 (2001).
14. S. Watanabe, N. Yamada, M. Nagashima, Y. Ueki, C. Sasaki, Y. Yamada, T. Taguchi, K. Tadatomo, H. Okagawa, and H. Kudo,"Internal quantum efficiency of highly-efficient $In_xGa_{1-x}N$-based near-ultraviolet light-emitting diodes", *Appl. Phys. Lett.* **83**, 4906 (2003).
15. Y. C. Cheng, C. M. Wu, H. S. Chen, C. C. Yang, Z. C. Feng, G. A. Li, J. R. Yang, A. Rosenauer & K. J. Ma, "Effects of emission properties of interface thin layers in InGaN/GaN quantum well structures", *Appl. Phys. Lett.* **84**, 5422 (2004).
16. K. S. Ramaiah, Y. K. Su, S. J. Chang, C. H. Chen, and F. S. Juang, H. P. Liu ,and I. G. Chen, "Studies of InGaN/GaN multi-quantum-well green-light-emitting diodes grown by metalorganic chemical vapor deposition", *Appl. Phys. Lett.* **85**, 401 (2004).
17. Y. D. Qi, H. Liang, D Wang, Z. D. Lu, W. Tang, and K. M. Lau,"Comparison of blue and green InGaN/GaN multiple-quantum-well light-emitting diodes grown by metalorganic vapor phase epitaxy", *Appl. Phys. Lett.* **86**, 101903 (2005).
18. J. H. Chen, Z. C. Feng, J. C. Wang , H. L. Tsai, J. R. Yang, A. Parekh, E. Armour, P. Faniano, "Study of carrier locali-zation in InGaN/GaN quantum well blue light emitting diode structures", *J. Crystal Growth* **287**, 354-358 (2006)

19. J. H. Chen, Z. C. Feng, H. L. Tsai, J. R. Yang, P. Li, C. Wetzel, T. Detchprohm and J. Nelson, "Optical and structural properties of InGaN/GaN multiple quantum well structure grown by metalorganic chemical vapor deposition", *Thin Solid Films* **498**, 123-127 (2006).
20. Z. C. Feng, J. Chen, H. Tsai, J. Yang, P. Li, C. Wetzel, T. Detchprohm, J. Nelson, and I. T. Ferguson, "Optical and structural investigation on InGaN/GaN multiple quantum well light-emitting diodes grown on sapphire by metalorganic chemical vapor deposition", *Proc. SPIE* **6337**, 63370D 1-10 (2006).
21. H. L. Tsai, T. Y. Wang, J. R. Yang, C. C. Chuo, J. T. Hsu, Z. C. Feng and M. Shiojiri, "Observation of V Defects in Multiple InGaN/GaN Quantum Well Layers", *Materials Transactions,* **48**, 894 (2007).
22. Y. H. Cho, Y. P. Sun, H. M. Kim, T. W. Kang, E. K. Suh, H. J. Lee, R. J. Choi and Y. B. Hahn, *Appl. Phys. Lett.* **90**, 011912 (2007).
23. C. Y. Chen, Y. C. Lu, D. M. Yeh and C. C. Yang, *Appl. Phys. Lett.* **90**, 183114 (2007).
24. N. K. van der Laak, R. A. Oliver, M. J. Kappers and C. J. Humphreys, *Appl. Phys. Lett.* **90**, 121911 (2007).
25. M. Krysko and M. Leszczynski, *Appl. Phys. Lett.* **91**, 061915 (2007).
26. A. K. Viswanath, J. J. Lee, S. T. Kim, G. M. Yang, H. J. Lee and D, Kim, *Thin Solid Films* ***515***, 4401 (2007).
27. Y. C. Lu, C. Y. Chen, H. C. Wang, C. C. Yang and Y. C. Cheng, *J. Appl. Phys.* **101**, 063511 (2007).
28. J. W. Ju, E. S. Kang, H. S. Kim, L. W. Jang, H. K. Ahn, J. W. Jeon, I. H. Leea and J. H. Baek, *J. Appl. Phys.* **102**, 033519 (2007).
29. M. J. Caltrey, and A. Cerezo, *Appl. Phys. Lett.* **92**, 041904 (2008).
30. K. C. Shen, C. Y. Chen, C. F. Huang, J. Y. Wang, Y. C. Lu, Y. W. Kiang, C. C. Yang and Y. J. Yang, *Appl. Phys. Lett.* **92**, 013108 (2008).
31. M. Funato, T. Kondou, K. Hayashi, S. Nishiura, M. Ueda, Y. Kawakami, Y. Narukawa and T. Mukai, *Appl. Phys. Express.* **1**, 011106 (2008).
32. M. S. Kumar, J. Y. Park, Y. S. Lee, S. J. Chung, C. H. Hong and E. K. Suh, *Jpn. J. Appl. Phys.* **47**, 839 (2008).
33. L. Rigutti, A Castaldini, M Meneghini and A Cavallini, *Semicond. Sci. Technol.* **23**, 025004 (2008).
34. L. X. Zhao, E. J. Thrush, C. J. Humphreys and W. A. Phillips, *J. Appl. Phys.* **103**, 024501 (2008).
35. D. K. Bowen and B. K. Tanner, *High Resolution X-ray Diffraction and Topography*, Taylor & Francis, London, 1998.
36. T. M. Smeeton, M. J. Kappers, J. S. Barnard, M. E. Vickers and C. J. Humphreys, *Appl. Phys. Lett.* **83**, 5419 (2003)
37. A. Statake, Y. Masmoto, T. Miyajima, T. Asatsuma, F. Nakamura, and M. Ikeda, *Phys. Rev. B* **57**, R2041 (1998).
38. S. Khatsevich and D. H. Rich, X. Zhang, W. Zhou, and P. D. Dapkus, *J. Appl. Phys.* **95**, 1832 (2004).
39. T. Takeuchi, S. Sota, M. Katsuragawa, M. Komori, H. Takeuchi, H. Amano, and I. Akasaki, *Jpn. J. Appl. Phys.*, Part 2, **36**, L382 (1997).
40. D. A. B. Miller, D. S. Chemla, T. C. Damen, A. C. Gossard, W. Wiegmann, T. H. Woodand, and C. A. Burrus, *Phys. Rev. Lett.* **26**, 2173 (1984).
41. C. F. Li, Y. S. Huang, L. Malikova, and F. H. Pollak, *Phys. Rev. B* **55**, 9251 (1997).

42. P G Eliseev, P Perlin, J Lee and M Osinski, *Appl. Phys. Lett.* **71,** 569 (1997).
43. T. Wang, in Zhe Chuan Feng, ed., *GaN-Based Materials: Growth and Characterization,* p. 305-343 (Imperial College Press, London, 2006).
44. M. Shiojiri, C. C. Chuo, J. T. Hsu, J. R. Yang and H. Saijo, "Observation of V Defects in Multiple InGaN/GaN Quantum Well Layers", *J. Appl. Phys.* **99**, 073505 (2006).
45. A. Yong, C. Soh, X. Zhang, S. Y. Chow and S. J. Chua, *Thin Solid Films* **515**, 4496 (2007); F. Lin, N. Xiang, P. Chen, S. Y. Chow and S. J. Chua, *J. Appl. Phys.* **103**, 043508 (2008).
46. Y. C. Cheng, E. C. Lin, C. M. Wu, C. C. Yang, J. R. Yang, A. Rosenauer, K. J. Ma, S. C. Shi, L. C. Chen, C. C. Pan and J. I. Chyi, *Appl. Phys. Lett.* **84**, 2506 (2004).
47. B. Witzigmann,_ V. Laino, M. Luisier, U. T. Schwarz, G. Feicht, W. Wegscheider, K. Engl, M. Furitsch, A. Leber, A. Lell, and V. Härle, *Appl. Phys. Lett.* **88**, 021104 (2006).
48. Y. L. Lai, C. P. Liu and Z. Q. Chen, *Appl. Phys. Lett.* **86**, 121915 (2005).
49. S. Khatsevich, D. H. Rich, S. Keller and S. P. Denbaars, Phys. Rev. B **75**, 035324 (2007).
50. M. J. Galtrey, R. A. Oliver, M. J. Kappers, C. J. Humphreys, D. J. Stokes, P. H. Clifton and A. Cerezo, *Appl. Phys. Lett.* **90**, 061903 (2007).
51. N. K. van der Laak, R. A. Oliver, M. J. Kappers and C. J. Humphreys, *Appl. Phys. Lett.* **90**, 121911 (2007).
52. C. J. Humphreys, *Microscopy and Analysis*, p. 5-8, November (2007).
53. H. Takeuchi, Y. Yamamoto, Y. Kamo, T. Kunii, T. Oku, T. Shirahama, H. Tanaka and M. Nakayama, *J. Appl. Phys.* **102**, 043510 (2007).
54. R. W. Martin, K. P. O'Donnell, P. G. Middleton, W. Van der Stricht, *Appl. Phys. Lett.* **74**, 263 (1999).
55. Y. H. Kwon, G. H. Gainer, S. Bidnyk, Y. H. Cho, J. J. Song, M. Hansen and S. P. DenBaars, *Appl. Phys. Lett.* **75**, 2549 (1999).
56. H. C. Yang, P. F. Kuo, T. Y. Lin, Y. F. Chen, K. H. Chen, L. C. Chen and J. I. Chyi, *Appl. Phys. Lett.* **76**, 3712 (2000).
57. M. E. White, K. P. O'Donnell, R. W. Martin, S. Pereira, C. J. Deatcher, and I. M. Watson, Mater. Sci. Eng. B **93**, 147 (2002)
58. C. L. Yang, L. Ding, J. N. Wang, K. K. Fung, W. K. Ge, H. Liang, L. S. Yu, Y. D. Qi, D. L. Wang, Z. D. Lu, and K. M. Lau, *J. Appl. Phys.* **98**, 023703 (2005).
59. Y. C. Lu, C. Y. Chen, K. C. Shen, D. M. Yeh, T. Y. Tang, and C. C. Yang, *Appl. Phys. Lett.* **91**, 183107 (2007).
60. J. Elsner, R. Jones, M. I. Heggie, P. K. Sitch, M. Haugk, Th. Frauenheim, S. Oberg, and P. R. Briddon, *Phys. Rev. B* **58**, 12571 (1998).
61. X. Li, P. W. Bohn, J. Kim, J. O. White, and J. J. Coleman, *Appl. Phys. Lett.* **76**, 3031 (2000).
62. Y. Narukawa, Y. Kawakami, Sz. Fujita, Sg. Fujita, and S. Nakamura, *Phys. Rev. B* 55, R1938 (1997).
63. Y. Sun, Y. H. Cho, E. K. Suh, H. J. Lee, R. J. Choi, and Y. B. Hahn. *Appl. Phys. Lett.* **84**, 49 (2004).
64. T. Onuma, A. Chakraborty, B. A. Haskell, S. Keller, S. P. DenBaars, J. S. Speck, S. Nakamura, U. K. Mishra, T. Sota, and S. F. Chichibu, *Appl. Phys. Lett.* **86**, 151918 (2005).

65. S. M. Olaizola, W. H. Fan, S. A. Hashemizadeh, J.-P. R. Wells, D. J. Mowbray, M. S. Skolnick, A. M. Fox, and P. J. Parbrook. *Appl. Phys. Lett.* **89**, 072107 (2006).
66. Cheng-Yen Chen, Dong-Ming Yeh, Yen-Cheng Lu, and C. C. Yang, *Appl. Phys. Lett.* **89**, 203113 (2006).
67. S. Nagahara, M. Arita, and Y. Arakawa, *Appl. Phys. Lett.* **88**, 083101 (2006).
68. Y. H. Cho, J. J. Song, S. Keller, M. S. Minsky, E. Hu, U. K. Mishra, and S. P. Denbaars, *Appl. Phys. Lett.* **73**, 1128 (1998).
69. T. S. Ko, T. C. Lu, T. C. Wang, M. H. Lo, J. R. Chen, R. C. Gao, H. C. Kuo, and S. C. Wang, *Appl. Phys. Lett.* **90**, 181122 (2007).

CHAPTER 4

MOCVD GROWTH AND EFFICIENCY IMPROVEMENT FOR ULTRAVIOLET LIGHT EMITTING DIODES

Seong-Ju Park and Min-Ki Kwon

Nanophotonic Semiconductors Laboratory,
Department of Materials Science and Engineering,
Gwangju Institute of Science and Technology, Gwangju 500-712, Korea
E-mail: sjpark@gist.ac.kr

Ultraviolet light emitting diodes(UV-LEDs) have much attention for white LEDs (when combined with phosphors), counterfeit detection, air and water purification, biohazard detection, biomedical instruments, and many others. Although UV-LED has many applications and potentials, it had yet achieved substantially commercial success. This can be attributed to the low efficiency, lifetime, and high-cost for commercialization of UV-LED. In this chapter, many techniques to improve the internal, external quantum efficiency and reliability of UV-LED are discussed.

1. Introduction

There are various application and potential application for GaN ultraviolet light emitting diodes (UV-LEDs), including white LEDs (when combined with phosphors), counterfeit detection, air and water purification, biohazard detection, biomedical instruments, and many others. The global market for UV-LED devises based on wide bandgap semiconductor in 1998 was worth only US$0.33 million, which will rise with an overall average growth rate of 79 % to over US$4.2 million in the year 2003.[1] The present market is dominated by apparatus which comprises a low pressure gas within a glass tube for the use of largely restricted to fixed, main voltage-powered installations such as in hotel

kitchens and supermakets. However, by far the largest potential market is for white LEDs, with market size measured in the billion-dollar range. Present generation of white LEDs is based on blue LEDs with yellow YAG phosphor. On the other hands, UV-LEDs seem better suited to this than the existing blue LED by virtue of higher light conversion efficiency. This is one of the crucial factors in the further market penetration of the white LED in the general lighting market. Phosphor technology is already available since this is in use within the commonplace fluorescent discharge tube. The UV-LED based white LED would, therefore, in effect become a solid-state equivalent of this traditional light source. In addition, the development of a compact, robust, milliwatt-level deep-UV light source would greatly impact a number of commercial applications including fluorescence-based biological agent detection, water purification, sterilization and decontamination, non-line-of-sight (NLOS) communications and thin film curing.

Although UV-LED has many applications and potentials, it had yet achieved substantial commercial success. Nichia has already demonstrated examples of such a component in the mid-1990s and offers a limited range of these components on the open market. There are, however, very few other manufactures of UV-LEDs. This can be attributed to the low efficiency, lifetime, and high-cost for commercialization of UV-LED. Therefore, many studies for high efficiency UV-LED are needed.

2. Issue of InGaN, AlInGaN, AlGaN Material System

2.1. *InGaN*

The main phosphor-based approach to white LED lighting uses a near-UV (380-410 nm) pump LED in combination with a RGB mix of phosphors that produce a broad spectral output over the visible range. This is potentially the best source of white lighting in terms of CRI(Color Rendering Index) and color stability, and potentially could be reasonably efficient as well. Also, it is highly flexible in terms of setting the CCT (Correlated Color Temperature) at a desirable point. Although there are

as yet no commercial offerings of UV/RGB devices, several companies (e. g. Nichia, Toyoda Gosei, Cree) are offering UV way on this approach at several organizations. However, in order to achieve the full promise of this approach, high efficiency UV sources are indispensible. Several promising development in this regard have been announced. In 1999, Nitres, Inc (which later was purchased by Cree and became Cree lighting) announced that it had achieved 20 % external quantum efficiency and 12 mW output power from a near UV (405 nm) InGaN emitter. In 2000, the external quantum efficiency was increased to 28 % corresponding to a wall plug efficiency of 21 %, by this same group.[2] Cree lighting has more recently reported UV outputs as high as 300 mW from its XBright Power large area UV chip, corresponding to a wall plug efficiency of 23.2 %.[2] Nichia also reported that the external quantum efficiency InGaN UV-LED at the wavelength of 400 nm was increased to 35.5 % by patterned substrate, mesh electrode and filp chip geometry on sapphire substrate.[3] GE had achieved 33.7 % of the external quantum efficiency by the use of GaN substrate.[4] Mitsubishi shows the best result which the external quantum efficiency of InGaN based UV-LED at the wavelength of 405 nm was increased to 43.1 % by patterned substrate and filp chip geometry on sapphire substrate.[5] Many research center and group have been also reported results for improvement of internal and external quantum efficiency of InGaN based UV-LED.

2.2. *AlInGaN*

UV-LEDs with emission in the range of 300-350 nm are ideal for pumping the fluorescent film of full color display devices. In addition, from the view point of environmental friendliness such as water purification, it is necessary to develop a 350 nm UV-LED.[6] The most promising material for active layer of such UV emitter is ternary AlGaN because the direct transition energy can be adjusted between 6.2 eV (AlN) and 3.4 eV (GaN). However, UV-LEDs with AlGaN active layer are typically less efficient than those based on InGaN active layer due to the poor crystal quality, whereas the performance of InGaN active layer based blue LEDs is not so sensitive to the crystal quality due to an

exciton localization effect in In-rich region. By introducing In into AlGaN, an effect similar to that obtained in InGaN active layer is expected for quaternary AlInGaN. With the development of AlInGaN quaternary growth technology, the quantum efficiency of AlInGaN quaternary film is greatly improved, and can be comparable to the InGaN ternary film.[7,8] However, to date, a 350 nm UV-LED with an optical power of 1 mW at 50 mA injection in cw operation mode has been achieved,[6] which is still much lower than that of InGaN based UV-LED. It can be attributed to self absorption of UV emission in substrate and epi-layer and lower crystal quality of AlInGaN active layer than InGaN active layer yet. To slove these problems, many researchers are studding about growth of high quality AlInGaN active layer, transparent substrate, GaN free structure etc.

2.3. *AlGaN layer*

The development of a compact, robust, milliwatt-level deep-UV light source would greatly impact a number of applications including fluorescence-based biological agent detection, water purification, sterilization and decontamination, non-line-of-sight (NLOS) communications and thin film curing. Recently, there have been reports of LEDs using AlGaN alloys with emission wavelengths below 300 nm.[9–15] Particular note are the results of Zhang *et al.*[10] where a relatively high power of 0.47 mW has been achieved at 278 nm under DC current injection. This result was achieved from a 1×4 array of 200 μm^2 devices operated at 260 mA. Also notable is the demonstration of LED emission wavelengths as short as 267 nm by Yasan *et al.*[14] These results were also obtained from a 4-element array, and output powers as high as 165 μW at 450 mA of input current under DC operation and 4.5 mW at 1 A of input current under pulsed operation have been achieved. However, efficiency of UV-LED based on AlGaN active layer is still lower than that of InGaN active layer because AlGaN layer has poor crystal quality, lack of composition fluctuation and high resistivity which can induce self heating of the device.

3. Substrate Issue

Commercially available III-nitride LEDs are now grown hetero-epitaxially on sapphire or SiC substrate due to the lack and high-cost of native GaN or AlN crystal. The mismatch in lattice constant and thermal expansion coefficient between the epi-layer and the substrate give rise to a high density of threading dislocations in the LED structure. The dislocation in GaN and its alloys are believed to be carrier scattering[16] and trap centers,[17,18] leakage current source,[19,20] and impurity diffusion paths.[21] In addition, the heteroepitaxial LEDs also suffer from excess structural strain which may lead to the formation of cracks and strong built-in electrostatic field.[22,23] These drawbacks can be overcome by growing the devices homoepitaxially. With conducting homo-substrate, vertical geometry in combination with the high thermal conductivity allows the LEDs to operate at much higher current densities.

3.1. *Homoepitaxy on GaN substrate*

X. A. Cao *et al.*[4] demonstrated blue and near UV InGaN/GaN MQW LEDs grown on GaN homo-substrate and sapphire hetero-substrate. The densities of surface and bulk defects in the homoepitaxially grown LEDs were substantially reduced, leading to a decrease in reverse currents by more than six orders of magnitude as shown Fig. 1. This is resulted from the lower surface defect and bulk defect density in LED based on GaN than that based on sapphire as shown in Fig. 2. The LED on sapphire exhibits 1×10^8 cm^{-2} so-called V defects with a typical size of 50~150 nm. The apexes of these defects are connected to threading dislocations with mixed or pure screw character.[24,25] In contrast, the homoepitaxial LED surface is defect free, and a terrace-step structure is clearly seen. The improvement of material quality on GaN was also confirmed by transmission electron microscopy measurements, which showed that the dislocation density in the homoepitaxially grown LEDs was more than two orders of magnitude lower.

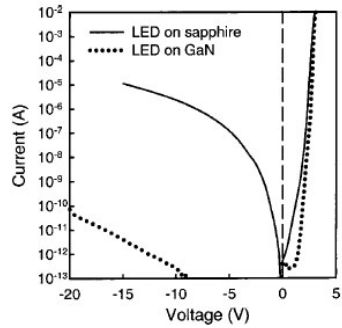

Fig. 1. Typical *I-V(current-voltage)* characteristic of the LED image of the LEDs grown on sapphire and GaN (from X. A. CaO *et al.* [4], reprinted with permission of the American Institute of Physics).

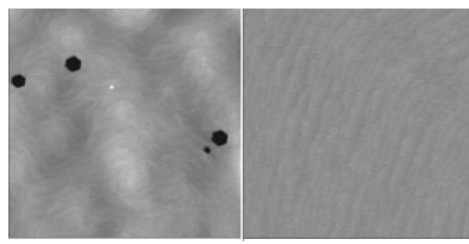

Fig. 2. Representative 2×2 μm2 AFM image of LEDs grown on sapphire(left) and GaN(right) (from X. A. CaO *et al.* [4], reprinted with permission of the American Institute of Physics).

Figure 3 shows *L-I* (light output power – input current) characteristics of the blue and UV-LEDs on sapphire and GaN. At a typical operating current of 20 mA, the internal quantum efficiency of the UV-LED on GaN was twice as high compared to that of the UV-LED on sapphire, whereas the performance of the blue LEDs was found to be comparable. For the blue LEDs, the homoepitaxial LED significantly outperforms the LED on sapphire only at high current (> 100 mA), largely due to better heat dissipation and current spreading through the GaN substrate. It can be attributed to the absorption in GaN substrate because GaN substrate is slightly opaque while sapphire substrate is transparent. However, light output power of UV-LED is significantly improved with the use of GaN substrate and never saturated at high

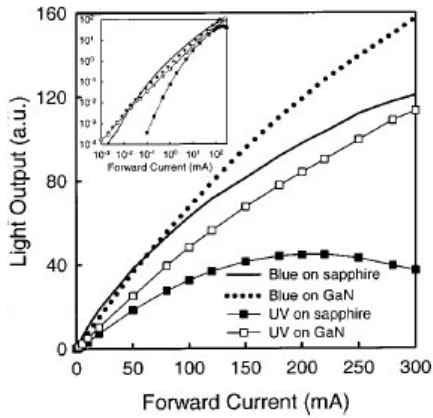

Fig. 3. L-I characteristic of the blue and UV-LED (from X. A. CaO *et al*. [4], reprinted with permission of the American Institute of Physics).

current operation. It can be attributed to the decrease of dislocation density and heat dissipation through the GaN substrate. They suggest that the high-density dislocations are of greater influence on the light emission of the UV-LEDs due to less In-related localization effects.

Recently, Yasan *et al.*[26] also demonstrated 340 nm AlGaN LEDs grown on GaN substrate, and the device showed an output power one order of magnitude higher than that grown on sapphire. The *I –V* (*input current – voltage*) characteristics of the UV-LED grown on sapphire and GaN are shown in Fig. 4. The UV-LED grown on GaN substrate shows a lower turn-on voltage with a differential series resistance of 13 Ω than that of UV-LED grown on sapphire with a differential series resistance of 40 Ω. The leakage currents of UV-LEDs grown on GaN and sapphire at –3 V are 2 and 120 μA, respectively. This indicates that the LED grown on GaN substrate has higher material quality than that of sapphire, due to lower defect density.

Figure 5(a) shows the output power of UV-LED grown on GaN substrate and on sapphire in pulsed injection mode. An enhancement of more than one order of magnitude has been achieved for the peak power of the UV-LED grown on GaN substrate due to higher material quality. Also the slope efficiency for the UV-LED grown on GaN substrate is one order of magnitude higher as shown in Fig. 5. Power increases with a

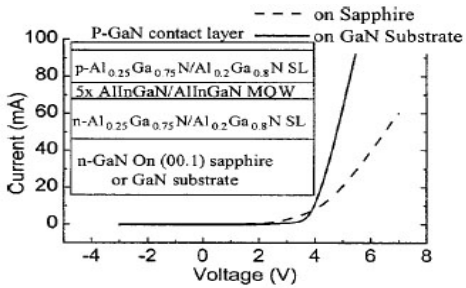

Fig. 4. I-V characteristic of UV-LED (from A. Yasan *et al.* [26], reprinted with permission of the American Institute of Physics).

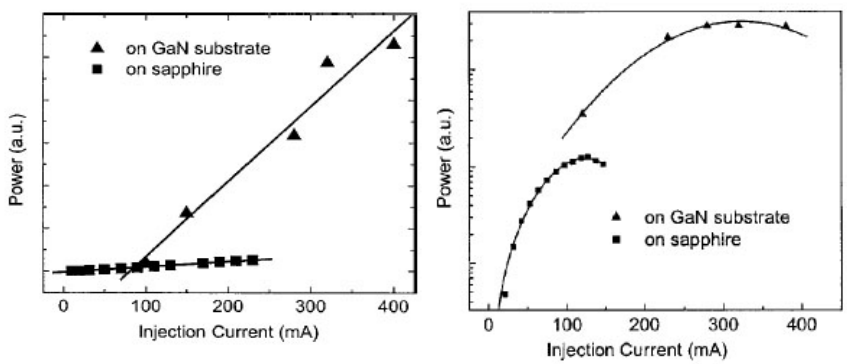

Fig. 5. Output power of UV-LED (a) linear scale, (b) log scale (from A. Yasan *et al*. [26], reprinted with permission of the American Institute of Physics).

slope of 0.18 mW/mA as opposed to the value of 0.012 mW/mA for the UV-LED grown on sapphire. In addition, GaN substrate provides better heat dissipation, as for the UV-LED grown on sapphire, power saturates at a current of higher than 120 mA in cw injection mode due to heating inside the device, however, for the UV-LED grown on GaN substrate, the output power in cw injection mode does not saturate for the injection currents up to 350 mA as shown in Fig 5(a). This is understandable by the fact that the thermal conductivity of GaN is about five times higher than that of sapphire. Figure 5(b) shows the output power of semilog scale versus injection current of these two devices in cw injection mode. Maximum output power for the UV-LED grown on GaN substrate is more than 20 times higher than the UV-LED grown on sapphire.

3.2. *AlN substrate*

After early developments decades ago,[27,28] the technology of growing bulk AlN is now entering a new era. Good structural, thermal, and chemical compatibility of this material with many III-nitride structures containing high-aluminum-content layers sets up bulk AlN single crystal as a desirable substrate material. The recent progress has resulted in production of larger AlN single crystals exceeding 1 cm in length and 0.5 cm in diameter, and having a dislocation density of less than 104 cm^{-2}.[29]

R. Gaska *et al.*[30] demonstrated the high-quality AlGaN/AlN multiple quantum wells (MQWs) emitting in deep UV region (265 nm). They show that luminescence PL intensity of the MQW structure grown on bulk AlN substrate is higher than that of the sample grown on SiC by a factor of 28 as shown in Fig. 6. They insist that this enhancement of PL intensity results from the decrease of dislocation density with the use of AlN substrate.

T. Nishida *et al.*[31] also demonstrated the UV-LED at emission peak wavelength of 345~347 nm grown on the bulk AlN substrate. They shows that optical output power of LED linearly increases with a saturation injection of 300 mA, which is two times higher than that of the reference device using sapphire substrate because heat dissipation of the highly thermal conductive AlN substrate. However, the maximum output power of LED with bulk AlN substrate is not improved compared to that of LED with sapphire substrate. This is partially due to the slightly colored substrate and partially due to the insufficient optimization of the growth condition for the LED structure on the AlN substrate.

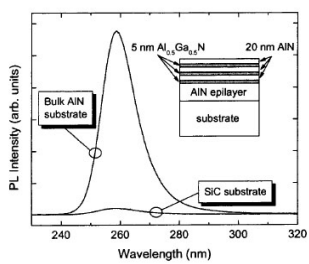

Fig. 6. PL spectra of MQW grown on SiC and AlN substrate (from R. Gaska *et al.* [30], reprinted with permission of the American Institute of Physics).

4. Defect Control of Epi-Layer

In the blue LED, reduction dislocation density is not issue because high efficiency due to localized energy state formed by alloy compositional fluctuation of the InGaN layer.[32,33] The output power of blue LEDs grown on the ELO (epitaxy lateral over-growth) was almost same as that of blue LEDs grown directly on a sapphire.[34] However, LED in the UV length has low or In-free materials due to the requirement of a wide band gap. The localized energy state which are well known for recombination site in blue LED are not formed or a little formed with the small depth of energy state. Therefore, carriers can easily diffuse into nonradiative recombination centers at or around treading dislocation which can induce scattering, trap, leakage current and impurity diffusion. To prevent the nonraditative recombination, reduction of dislocation density in LED structure is indispensable.

4.1. *Epitaxial lateral over-growth* (*ELOG*)

A process known as epitaxial lateral over-growth (ELOG) was recently developed to reduce dislocations in GaN layers. In this method, the GaN layer is partially covered with a mask. Growth starts exclusively in the remaining openings and the layer laterally overgrows the mask regions. Almost dislocation free material is obtained above the masked regions but dislocations remain above the open areas and at the intersections of merging growth fronts. The procedure can be repeated to remove dislocations by placing the mask on the former openings and intersections. The resulting GaN epitaxial layers are of high quality. However, the fabrication process involves several alternating growth and processing steps and very thick GaN films are deposited.

T. Mukai *et al*.[35] demonstrated that output power of UV InGaN and GaN LEDs as a function of forward current. The UV GaN LED on ELOG has a much higher (about two fold) output power than that on sapphire as shown in Fig 7. This is because the number of dislocation densities of a GaN LED on ELOG is much smaller than that on sapphire. However, a near-UV GaN LED on ELOG showed a small increase in output power (25 %) in comparison with that on sapphire at 20 mA. This

is related to the localized energy state formed by alloy composition fluctuation. When electrons and holes are injected into the GaN active layer of the UV GaN LED on sapphire, they are captured by nonradiative recombination centers formed by a large number of dislocations. Thus, the output power of a UV GaN LED on sapphire is very low. When the dislocation density is reduced by using ELOG, the output power of a UV GaN LED grown on sapphire can be increased drastically to twice its initial value. On the other hand, when electron and hole are injected into the InGaN active layer of a UV InGaN LED grown on sapphire, the carriers are easily captured by deep localized states formed by alloy composition fluctuation, then recombined radatively before they are captured by nonradiative recombine center formed by a large number of dislocations. However, when the depth of the localized energy states in small, such as that in UV InGaN LEDs due to a small In mole fraction in the InGaN well layer some carrier overflow from the localized energy states with increasing current and reach nonradiative recombination center formed by a large number of dislocations. Thus, the output power of 380 nm UV-LED can be increased by reducing the number of dislocations using ELOG.

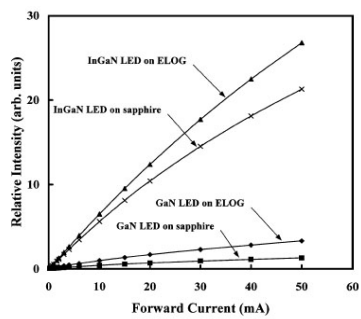

Fig. 7. Relative optical output power of InGaN and GaN LED grown on ELOG and Sappahire (from T. Mukai *et al*. [35], reprinted with permission of the The Japan Society of Applied Physics).

4.2. *Delta doping*

K. H. Kim *et al*.[36] demonstrated that delta doping in *p,n*-GaN and AlGaN has improvement not only the conduction, but also significantly suppresses the dislocation densities. They shows that dislocation density

of *n*-AlGaN template can be reduced by a factor of more than 2 by AFM images as shown in Fig. 8. Figure 9 shows that the *L-I* characteristics of interconnected μ-disk UV (340 nm) LED for δ-doped and uniform-doped structures under a pulsed driving current (pulse frequency 20 MHZ, pulse width 50 ns, duty cycle 1 %). The optical output power of UV-LED is 1.6 times improved by the use of delta doped p-GaN and n-AlGaN layer at the current of 400 mA.

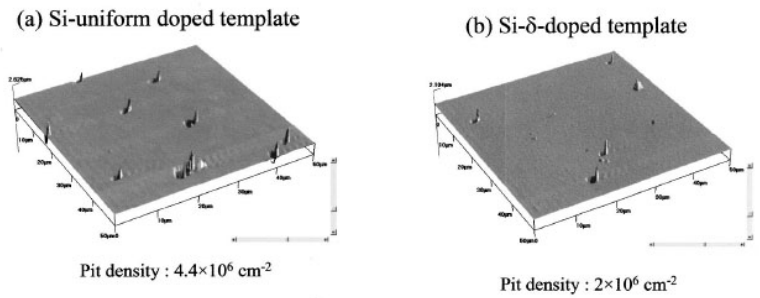

Fig. 8. AFM image of Si uniform doped and delta doped n-AlGaN tmplate (from K. H. Kim *et al.* [36], reprinted with permission of the American Institute of Physics).

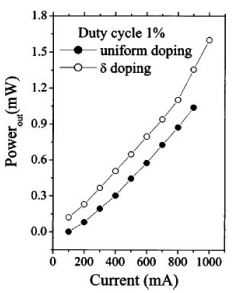

Fig. 9. L-I characteristic of UV-LEDs for delta doped and uniform-doped structures. (from K. H. Kim *et al.* [36], reprinted with permission of the American Institute of Physics).

4.3. *Facet control technique*

The fabrication of highly luminescent AlGaN has been difficult, because all dislocation types act as nonradiative sources.[37] To reduce all type of threading dislocations in GaN, a novel growth technique named ELO has

been developed and has successfully realized growth and a very low dislocation density.[38] Unfortunately, due to the strong adhesion of AlN on the mask surface, polycrystalline AlGaN is deposited on the mask, which prohibits epitaxial lateral overgrowth of AlN-containning alloys.[39] Moreover, this technique also present the problem of crack generation on the AlGaN suface due to the tensile stress introduced during growth.

M. Iwaya *et al*.[40] shows that reduction of treading dislocation is very important in realizing high-efficiency UV-LEDs. They also suggest the facet control (FC) technique reduces dislocation of AlGaN film. The growth procedure follows: All samples were grown by organometallic vapor phase epitaxy on a sapphire (0001) substrate covered with a LT-GaN buffer layer. After depositing the LT GaN buffer layer to about 20 nm thickness at 500°C, 3 μm-thick GaN was grown at 1,100°C. Periodic SiO_2 stripe masks along the (1-100) axis, where the width and spacing are both 3 μ m, were formed on the GaN surface. In the 2nd step, the facet-controlled GaN seed crystals were selectively grown on the window. In the cross-sectional view, they have a triangular shape with (11-22) facets, as shown in Fig. 10. Dislocations in GaN seed crystals maintaining (11-22) facets during growth bent horizontally, and only a few dislocations propagated vertically, as shown in Fig. 10. In the 3nd step, Low dislocation density AlGaN over the entire AlGaN layer is grown on GaN seed crystal grown by FC technique. Furthermore, the LT-AlN interlayer makes it possible to relax the tensile stress in the AlGaN layer,[41] therefore, cracks are not formed on the overgrown AlGaN layer.

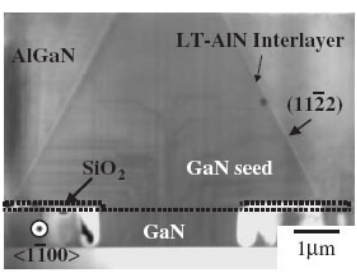

Fig. 10. Cross-sectional TEM image of AlGaN on FC GaN with LT-AlN interlayer (from M. Iwaya *et al*. [40], reprinted with permission of the The Japan Society of Applied Physics).

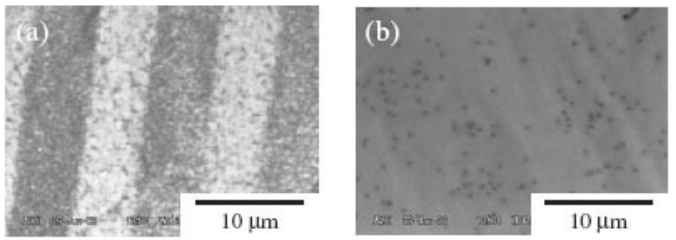

Fig. 11. CL image of GaN/AlGaN:Si MQW (a) grown on AlGaN using ELOG on a periodically grooved GaN and an LT-AlN interlayer (b) grown on low dislocation density AlGaN using FC technique (from M. Iwaya *et al.* [40], reprinted with permission of the The Japan Society of Applied Physics).

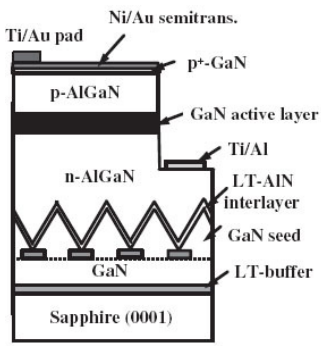

Fig. 12. schematic diagram of UV-LED (from M. Iwaya *et al.* [40], reprinted with permission of the The Japan Society of Applied Physics).

Figure 11 (a) shows a cathodoluminescence (CL) image of a GaN/$Al_{0.08}Ga_{0.92}$N:Si MQW grown on AlGaN using ELOG on periodically grooved GaN and a LT-AlN interlayer. Several dark spots, which correspond to dislocations, can be observed in the grooved region while the terrace region is entirely dark. On the other hand, as shown in Fig. 11(b), the CL image of a GaN/$Al_{0.08}Ga_{0..92}$N:Si MQW grown on low-dislocation-density AlGaN using the facet control technique shows dark spot density as low as 2×10^7 cm^{-2} over the entire wafer.

Figure 12 shows the schematic of the UV-LED grown by FC technique. Figure 13 shows *L–I* and *I-V* curves of UV-LED. The *L–I* curve indicates that the light output increases almost linearly with increase of the forward current. The operating voltage of 4.2 V at a

forward current of 20 mA is slightly higher than that of conventional InGaN-based blue LED. The output power is as high as 1.2 mW at 50 mA. Although this UVLED has the highest efficiency ever reported in UV-LEDs with wavelengths shorter than 370 nm, the quantum efficiency of this LED is still lower than those of conventional GaInN visible LEDs. Moreover, the *L–I* curve is somewhat superlinear, which means it is still limited by nonradiative components such as point defects. Further improvement of crystalline quality may be necessary to achieve a much higher performance UV emitter.

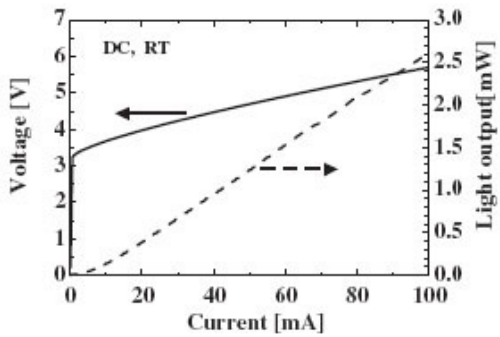

Fig. 13. L–I and I-V curves of UV-LED (from M. Iwaya *et al.* [40], reprinted with permission of the The Japan Society of Applied Physics).

4.4. *Superlattice buffer*

A. Chitis *et al.*[42] demonstrated that LED with peak emission at 324 nm is fabricated on low-defect density n^+ $Al_{0.2}Ga_{0.8}N$ buffer layer using strain-relieving AlN/AlGaN superlattice as shown in Fig. 14. This superlattice buffer approach results in materials with a threading dislocation density a factor of 5 less than that of the 1-μm-thick n^+ $Al_{0.2}Ga_{0.8}N$ buffer layer. The *I–V* characteristics for a 300×300 μm^2 device is shown in the inset of Fig. 15. A turn-on voltage of 5 V and a series resistance of 25 Ω were measured. The turn-on voltage is somewhat 0.5~1 V larger than that expected from the bandgap of the active region. It can be attributed to the relatively low doping of high Al-content cladding layers. This turn-on voltage can be further decreased by optimizing the bottom n-and the top

p-AlGaN layers. Also included in Fig. 15 is the emitted power as a function of wavelength for input current of 200 mA. The LED emission is peaked at 324.4 nm with a full- width at half maximum (FWHM) of only 8 nm. The position of this peak agrees very well with that of the PL emission from the active region quantum well.

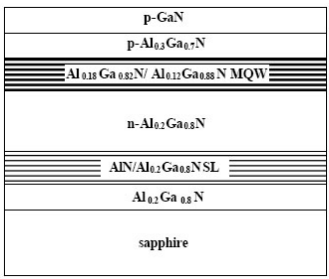

Fig. 14. schematic diagram of UV-LED (from A. Chitnis *et al*. [42], reprinted with permission of the The Japan Society of Applied Physics).

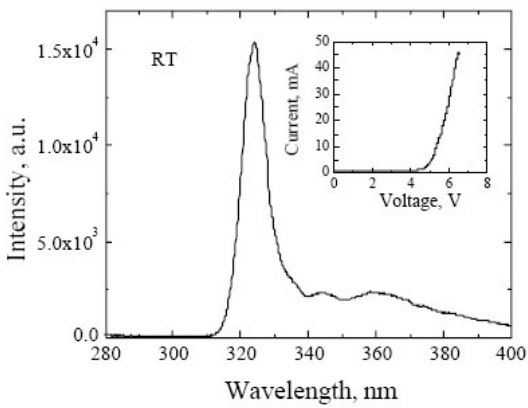

Fig. 15. EL spectrum of UV-LED, Inset shows the I-V characteristic of UV-LED (from A. Chitnis *et al.* [42], reprinted with permission of the The Japan Society of Applied Physics).

5. Internal Quantum Efficiency

LEDs in the UV range contains low or In-free materials due to the requirement of a wide band gap. We can not expect that the localized energy state formed by alloy fluctuation. Therefore, it is necessary to

improve the internal quantum efficiency of UV-LEDs by increasing the carrier injection to the quantum well layer, carrier confinement and decrease in non radiative recombination in the InGaN/GaN MQW.

5.1. *Band offset between well and barrier layer*

H. X. Wang *et al.*[43] demonstrates that internal quantum efficiency is improved by increase in band offset between barrier and well layer. They shows that by using high-Al content and symmetric composition n- and p-side barriers, the output efficiency of AlGaN/InGaN SQW (single quantum well) LED with emission peak at 370 nm has been greatly improved. Figure 16 shows schematic diagram of UV-LED. In the active layers, both n- and p-side AlGaN barriers were grown with three group different TMA flow rates, the details of which are shown in Table. 1. For simplicity, these samples were denoted as samples A, B, and C. Fig. 17 shows the L-I characteristics of LEDs of samples A, B, and C, which have the SQW active layer with different barrier compositions. When both side barriers were grown with the TMA flow rate of 2.6 μmol/min, the output power of sample A saturates even at a low injection current of 50 mA. When the n-side barrier was grown with a TMA flow rate of 2.6 μmol/min, and that of the p-side was 4.3 μmol/min, the output power of sample B shows a very small value with the injection current below 20 mA. Then sample B shows almost linear I-L characteristics with the injection current above 20 mA. When the injection current was above 50 mA, the output power of sample B was higher than that of sample A. When both side barriers were all grown with a TMA flow rate of 4.3 μmol/min, sample C shows a higher output power even at the low injection current, and also addresses an almost linear L-I characteristics. In the case of sample A, the low Al content barriers have the small band offset which cannot confine a larger injection current. Therefore, injection current was very easily spilled over from the well region to the other sides, as shown in the inset of Fig. 17. In the case of sample B, only a certain part of the holes can be injected into the well, and the other part of the holes directly flows to the other side of the barrier. Therefore, the

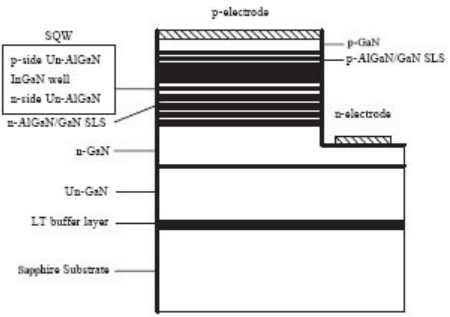

Fig. 16. Schematic diagram of UV-LED (from H. X. Wang *et al*. [43], reprinted with permission of Elsevier).

Table 1. Different TMA flow rate of three groups (from H. X. Wang *et al*. [43], reprinted with permission of Elsevier).

Sample no.	A (μmol/min)	B (μmol/min)	C (μmol/min)
n-Slide barrier	2.6	2.6	4.3
p-Slide barrier	2.6	4.3	4.3

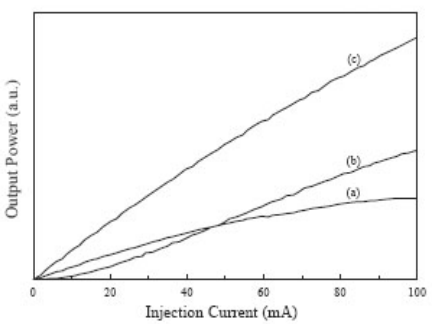

Fig. 17. L-I characteristics of UV-LED samples with a SQW active layer with different compositions of undoped n- and pside barriers. (a) An InGaN well layer sandwiched by low Al content symmetry composition barriers, (b) an InGaN well layer sandwiched by a low Al-content n-side barrier and a high Al-content p-side barrier, (c) an InGaN well sandwiched by a high Al-content symmetry composition barrier. (from H. X. Wang *et al.* [43], reprinted with permission of Elsevier).

net injection ratio of holes to the well would be smaller, i.e., compared with the case of SQW LED with symmetric barrier, only a certain part of the injection hole can be injected into well of SQW LED with asymmetric barrier, leading to a decrease in the light emission efficiency. In the case of sample C, the higher performance could be contributed to the larger band-offset to decrease the carriers spillover, and also to the symmetric composition barrier to increase the carrier confinement, leading to an enhancement of the light emission efficiency, as shown in inset of Fig. 17.

5.2. *Pulsed atomic layer epitaxy* (*PALE*)

J. Zhang *et al.* [44] demonstrate that the PALE approach allows the layer thickness and the alloy composition to be precisely controlled by the number of unit growth-cell repeats and the number of precursor pulses in it. In addition, PALE can be helpful to growth of AlInGaN alyer with Al mole fraction in excess of 40 % at 200-300°C lower temperature than convetional MOCVD growth.

Figure 18 shows the growth sequence by PALE technique. As can be seen, 6 sec long pulse of the TMA, TMI, TMG, and NH_3 precursor were introduced alternately into the low pressure MOCVD reactor. An ammonia pulse always followed the metalorganic pulses. As an example, the unit cell in Fig. 18 consisted of three repeats of Al and N pulses, followed by one In and N and one Ga and N pulse. They refer to the resulting $Al_xIn_yGa_{1-x-y}N$ layer as the $(3_{Al},1_{In},1_{Ga})_{150}$ or, simply, as a $(3,1,1)_{150}$ layer. The subscript 150 denotes the number of unit cell repeats. The precursor fluxes in individual pulses were adjusted in such a way that the deposited thickness in each unit cell, determined from the total layer thickness divided by the number of unit cell repeats, was around 6 Å.

Figure 19 shows the room-temperature PL spectra for the quaternary $Al_xIn_yGa_{1-x-y}N$ films with unit cell configurations of (3,0,1), (3,1,1), (3,3,1), $(3,3^+,1)$, (2,2,1),(1,3,1), and $(1,3^+,1)$. (Here the superscript '+' denotes pluses with the In-metal organic flux doubled) The growth temperature for all samples was 760 °C. The data show the PL signal for

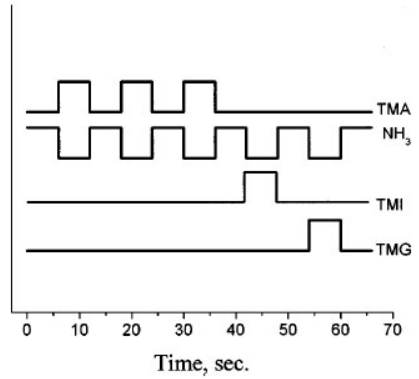

Fig. 18. Repesenative growth sequence of a unit cell using PALE. They donate this cell as (3Al,1In,1Ga) (from J. Zhang *et al.* [44], reprinted with permission of the American Institute of Physics).

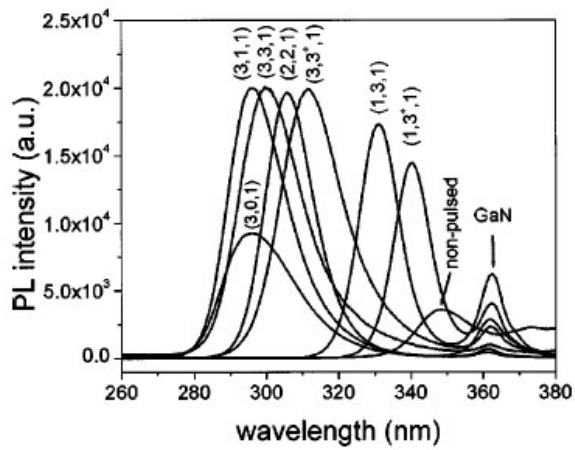

Fig. 19. Room-temperature eximer laser excited PL spectra of the quaternary sample (from J. Zhang *et al.* [44], reprinted with permission of the American Institute of Physics).

PALE quaternary layers to be much stronger than that of the conventional MOCVD grown sample. Also, the PALE samples show no deep level emissions. The data further establish that addition of Al in the unit cell blueshifts the PL peak positions. The addition of In, on the contrary, results in a redshift. This is to be expected from the known

band gaps of AlN, InN, and GaN. The optical quality is improved by increasing the In. It can confirm by comparing the PL signal strength from the (3,0,1) and the (3,1,1) samples. Furthermore, in contrast to conventional $Al_xGa_{1-x}N$ films, the PL peak intensity for the quaternary layers does not degrade with increasing the Al-mole fraction. This is true even for the material with a cutoff wavelength of 280 nm.

5.3. *Ga droplet layer*

Y. B. Lee *et al.* [45] demonstrates that Ga droplet underlying layer below AlGaN/GaN single quantum wll (SQW) can improve the optical output power of LED because thin Ga droplet layer cause a spatial and compositional fluctuation on the SQW active layer.

The mechanism by which the Ga droplet layer causes the exciton localization effect as illustrated in Fig. 20. The region of the AlGaN barrier grown on the Ga droplet is marked A, while that grown without the Ga droplet is marked B. Since the diffusion length and adsorption rate of reactant adatoms depend on the surface material and its roughness, the aluminum composition of the AlGaN barrier in region A can be different from that of structure B. Further, the strain variation on the rugged layer can also be attributed to the aluminum compositional fluctuation, as reported by Darowski *et al.*[46] This compositional fluctuation of aluminum would affect the potential barrier height. In addition, as the QW layer is grown on the Ga droplet layer, the thickness (marked C and D in Fig. 2) of a few monolayers in the well-barrier interface can be fluctuated, which changes the energy states in the active

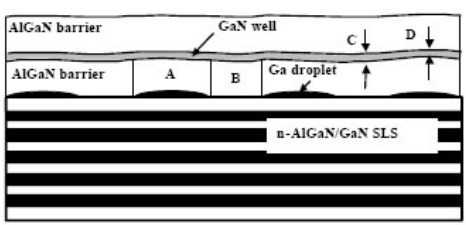

Fig. 20. Schematic of the proposed mechanism by which the Ga droplet layer introduces the exciton localization effect. (from Y. B. Lee *et al.* [45], reprinted with permission of the The Japan Society of Applied Physics).

layer. These two potential fluctuations of barriers and well caused by the Ga droplet layer lead to the potential minima in the GaN active layer. Consequently, the excitons generated by current injection can radiatively recombine through the localized centers similarly to the alloy fluctuation in InGaN QW, as schematically shown in Fig. 21.

Figure 22 shows the optical output power as a function of the injection current (*L–I*) up to 100 mA for these structures. In order to measure only the optical output power in the UV region, the *L–I* characteristics were measured using the filter with the cutting range from 480 nm to 700 nm. The turn-on voltages in both samples are shown to be below 3.5 V in the inset of Fig. 22. The optical output power of the UV-

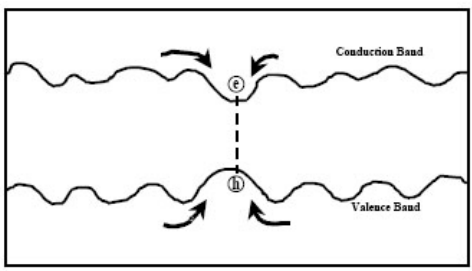

Fig. 21. Schematic of band structure showing random potential fluctuation (from Y. B. Lee *et al.* [45], reprinted with permission of the The Japan Society of Applied Physics).

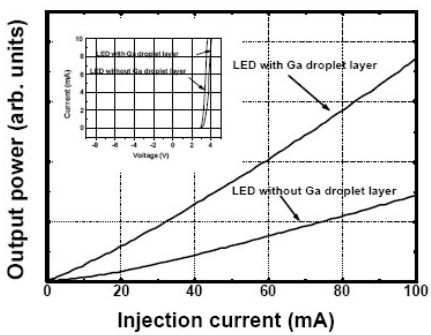

Fig. 22. Optical output power in UV region of these UV-LEDs as a function of injection current under CW injection-current operation at room temperature. The inset shows current versus voltage (*I –V*) characteristics of the UV-LEDs (from Y. B. Lee *et al.* [45], reprinted with permission of the The Japan Society of Applied Physics).

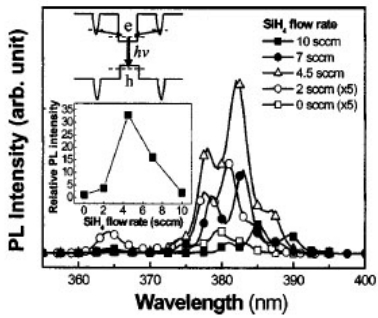

Fig. 23. PL intensity of InGaN/GaN MQW with Si delta doped barrier as a function of SiH_4 flow rate (from M.-K. Kwon *et al*. [47], reprinted with permission of the American Institute of Physics).

LED with the Ga droplet layer is almost three times higher than that of the UV-LED without the Ga droplet layer over the entire measured current range. Since the only difference between the two structures is the introduction of the Ga droplet layer, this indicates that the fluctuation of the barrier-well potential caused by the Ga droplet layer induces the exciton localization and enhances the optical output power.

5.4. *Si delta doped barrier layer*

M. K. Kwon *et al.*[47, 48] demonstrate that the Si delta doped barrier can improved interanl quantum efficiency of UV-LED with an emission peak at 385 nm. The effect of Si delta doping in the GaN barrier on the PL properties of InGaN/GaN MQWs is shown in Fig. 23. The SiH_4 flow rate for Si delta doping was varied from 2 to 10 sccm. The SiH_4 flow rate for maximum PL intensity was 4.5 sccm, where the PL intensity at the main peak position was 33 times larger than that of the MQW without delta doping. The increase in PL intensity is attributed to the efficient supply of electrons in the potential well of the Si delta-doped barrier region into the InGaN well layer and an increase in hole capturing by the higher-energy barrier in the valence band, as shown in the inset of Fig. 23. Figure 24 shows the output power of UV as function of input current under CW injection-current operation at room temperature. The optical

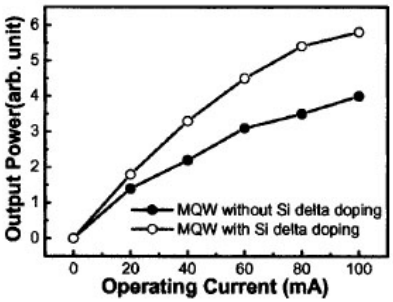

Fig. 24. Output power of UV-LED with and without Si delta doped barrier in MQW (from M.-K. Kwon *et al.* [47], reprinted with permission of the American Institute of Physics).

output power of InGaN/GaN UV-LED is 40 % increased at the input current of 100 mA by the use of Si delta doped barrier in the MQW.

6. External Quantum Efficiency

Recently, high-efficiency white LEDs have gained much interest because the replacement of fluorescent lamps will be realistic in the near future. State-of-the-art efficiency of white LEDs ~74 lm/W[49] is almost the same as that of ordinary fluorescent lamps ~75 lm/W. There are two principal approaches for improving LED efficiency: the first is increasing the internal quantum efficiency (η_i), which is determined by crystal quality and epitaxial layer structure, and the second is increasing light extraction efficiency. High values of internal quantum efficiency have already been reported, and so further improvements may not be readily achieved: a typical η_i value for blue LEDs has reached more than 70 %,[50] and a recently-grown UV-LED grown on a low-dislocation GaN substrate has shown an η_i of about 80 %.[51] However, there is much room for improvement of the light extraction efficiency. Considering the refractive indices of GaN ($n' = 2.5$)[52] and air, the critical angle for the light escape cone is about 23°. Assuming that light emitted from sidewalls and backside is neglected, one expects that approximately only 4 % of the internal light can be extracted from a surface. The light outside the escape cone is reflected into the substrate and is repeatedly reflected,

then reabsorbed by active layers or electrodes, unless it escapes through the sidewalls.

6.1. *Patterned sapphire substrate* (*PSS*)

M. Yamada *et al.* and K. Tadotomo *et al.*[3,53] demonstrate that patterned sapphire substrate are very helpful for light extraction in high power UV-LED application. Table 2 shows the comparison of the PSS UV-LED and conventional non-patterned sapphire substrate (CSS) UV-LED with an emission peak at 400 nm. The output power of UV-LED with PSS and CSS substrate are summarized on the Table 2. The output power of UV-LED with PSS is approximately fivefold higher than that of UV-LED with CSS. When the PSS is used, the direction of the propagating light is changed from the regular direction to an almost random one by the slope of the PSS as shown in Fig. 25. The propagating light can more efficiently exit into the sapphire substrate than in the case of CSS. One of the lights in the sapphire propagates to the side edge without reflection at the *p*-electrode and the others to the nitride films, the light is not absorbed within the sapphire substrate. This induced the increase in the output power. In addition, the number of non radiative recombination center, i.e, dislocation and point defects, of the UV-LED with PSS substrate is lower than that of the UV-LED with CSS substrate. This is also confirmed that leakage current of UV-LED with PSS is lower than that of UV-LED with CSS.

Table 2. Comparison of the PSS UV-LED and CSS UV-LED (from K. Tadatomo *et al.* [53], reprinted with permission of the The Japan Society of Applied Physics).

	Sample A	Sample B
Substrate	PSS $(1\bar{1}00)_{sapphire}$	CSS
	$(11\bar{2}0)_{GaN}$	
Dislocation density	1.5×10^8 cm^{-2}	4×10^8 cm^{-2}
Die bonding	Flip chip	Standard
Operating voltage at forward current 20 mA	3.4 V	3.4 V
Output power P_o (@ 20 mA)	15.6 mW	~3.5 mW
External quantum efficiency η_e (@ 20 mA)	24%	~5.4%
Voltage at reverse bias current of 100 μA	17.8 V	11.5 V

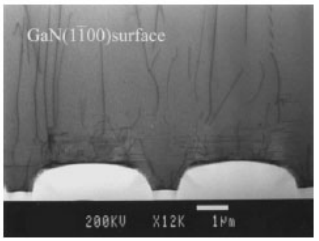

Fig. 25. Cross-sectional TEM image of a GaN layers grown on the PSS (from M. Yamada *et al.* [3], reprinted with permission of the The Japan Society of Applied Physics).

6.2. *Mesh electrode*

Conventional LED structure, transparent metal is generally used for current spreading in p-GaN layer. However, the propagating light generated by MQW is absorbed by the transparent metal. When the mesh electrode as transparent metal layer is used, the light generated in the active layer can exit into the epoxy resine through the window area of the electrode.[3] As a result, the density of light re-absorbed in the nitride films decreases by reflection between p-GaN and metal and the optical absorption by the electrode is reduced. Moreover, it is possible to further improve the extraction efficiency by increasing the aperture ratio (Ra) value of *p*-electrode without bond pad area because window area is increase by decreasing the Ra.

6.3. *DBR*

For UV-LED below 365 nm, the method preventing the internal absorption in the GaN layer is indispensable. By using an AlN substrate, the internal absorption issue can be solved. However, it is much more expensive, and it is impossible for mass-production. Therefore, sapphire is best choice to growth of UV-LED. And also, the internal absorption in the GaN layer can be prevented by the use of highly reflective DBR mirror. Highly reflective DBR mirror is generally formed from a repeated periodic stack of alternating high and low index quarter-wavelength layer. Figure 26 shows the 300 K reflectivity spectrum of the

25 pair DBRs, the calibration sample containing 36.5 nm of $Al_{0.49}Ga_{0.51}N$ and 34.5 nm of $Al_{0.16}Ga_{0.84}N$ in each pair. This shows DBR reflector can successfully reflect the light a factor of 90 % in the range form 340 to 360 nm. T. Wang *et al*.[54] demonstrates that the output power of UV-LED is increased to 2.3 times at 100 mA injection current by the use of DBR mirror as shown in Fig. 27.

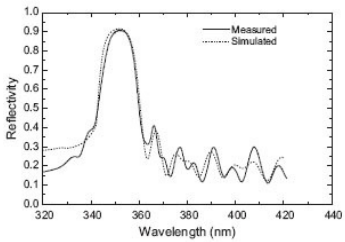

Fig. 26. Measured (full) and simulated (dashed) 300 K reflectivity spectra of DBRs (from T. Wang *et al.* [54], reprinted with permission of Elsevier).

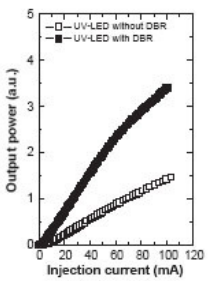

Fig. 27. Output power of UV-LED with and without DBR (from T. Wang *et al.* [54], reprinted with permission of Elsevier.

6.4. *Photonic crystal* (*PC*)

Periodic arrays of holes are typically etched in semiconductors to realize 2D PCs that forbid certain electromagnetic radiation in the lateral direction creating so called “photonic band gaps” in the plane. 2D PCs enhance the light output from LEDs by extracting lateral guided modes of light in the vertical direction.

J. Shakaya *et al*.[55] demonstrates that the output power of LED at the wavelength 333 nm is enhanced by the use of photonic crystal. Figure 28(a) shows the schematic diagrams of our 333 nm UV-LED structure with LED mesa and contact pads. Figure 28 shows the schematic diagram of hexagonal mesh for 2D PCs. The hexagonal mesa of side length 120 μm, as shown in Fig. 29(a), was defined by electron-beam (e-beam) lithography and etched by inductively coupled plasma (ICP) dry etching. A hexagonal *p*-contact pad with 60 μm side length was deposited at the center of the LED mesa. To improve the electrical transport, a 10 μm wide *n*-type ohmic contact was deposited around the mesa along with a 100×100 μm^2 *n*-contact pad. The PCs with triangular lattice patterns of circular holes with varying diameter $d = 100$ nm to $d = 200$ nm and periodicity $a = 300$ nm to $a = 600$ nm were fabricated using e-beam lithography and ICP dry etching. Extraction of guided light traveling along Γ–*K* direction can be as much as three times more than the light traveling along Γ–*M* direction of the PCs in the nitride quantum well. For efficient extraction of the guided light, Γ–*K* direction of the PCs was set perpendicular to the sides of the mesa. An atomic force microscopy (AFM) image of the PCs on UV-LED with $a = 600$ nm and $d = 200$ nm is shown in Fig. 28(b). The targeted etching depth of the holes was 200 nm. The AFM image revealed that the depth of the etched holes varied from 175 nm to 190 nm and that the holes with a larger diameter were etched relatively deeper. This indicates that most of the holes were etched through to the active layers. Figure 28(c) shows the SEM (scanning electron microscopy) image of the PCs with $a = 300$ nm and $d = 100$ nm etched on UV-LED. Figures 29(b) and 2(c) show the optical microscopy images of UV-LEDs in action at 20 mA current injections. The less bright image in Fig. 29(b) is the LED without PCs. The LED with PCs ($a = 600$ nm, $d = 200$ nm) is shown in Fig. 29(c), which clearly shows a significant enhancement of light output compared with the LED without PCs. The current was injected by probing with a needle hence, the darker area in the right bottom side of both of the images is due to the light obstruction by the probe tip.

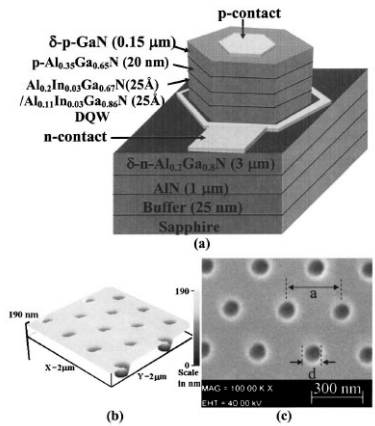

Fig. 28. (a) Schematic diagram of 333 nm UV-LED structure showing mesa and contact pads. (b) AFM image of the PCs on UV-LED with $a = 600$ nm and $d = 200$ nm. The etch depth is around 190 nm. (c) The SEM image of the PCs on UV-LED with lattice constant $a = 300$ nm and hole diameter $d = 100$ nm. (from J. Shakay *et al.* [55], reprinted with permission of the American Institute of Physics).

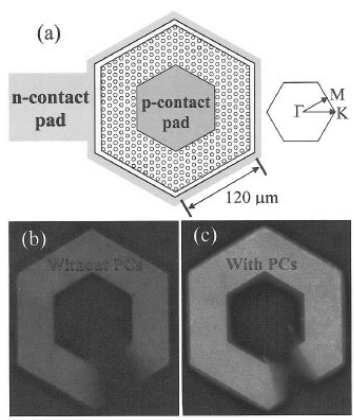

Fig. 29. (Color) (a) Schematic top view diagram of the hexagonal mesa. The *p*-contact pad side length is 60 mm. Triangular array of holes were etched on top of mesa all around *p*-contact pad with G–*K* direction of PCs perpendicular to the side of mesa. The change coupled device images of UV-LEDs at 20 mA current injections (b) without PCs and (c) with PCs s$a = 600$ nm, $d = 200$ nmd. The darker area in the right bottom side of both of the images is due to the light obstruction by the *p*-contact probe. (from J. Shakay *et al.* [55], reprinted with permission of the American Institute of Physics).

6.5. *PEC etching* (*phtoelectrochemical etching*)

In general, for conventional GaN-bsed LEDs, the internal quantum efficiencies are close to 100 %. But, the external quantum efficiency is only 5~10 % in most commercial LEDs. This large discrepancy is originated from the fact that the light extraction efficiency of most conventional LEDs is limited by the total internal reflection of the generated light in the active region of the LED, which occurs at the semiconductor-air interface. This is due to the large difference in the refractive index between the semiconductor and air. For GaN-based LEDs, the refractive indexes of GaN (nGaN) and the air (nair) are 2.5 and 1, respectively.[56] In this case, the critical angle ($\theta_c = \sin^{-1}(n_{air}/n_{GaN})$) for the light generated in the active region to escape is about 23°. Because the light emission from the active region of an LED is a directionally isotropic and the light can escape from the chip if the angle of incidence to the chip wall is less than the critical angle, a small fraction of light generated in the active region of the LED can escape to the surrounding air. Therefore, for a conventional GaN-based LED, the external quantum efficiency limits to a few % due to the high refractive index of GaN as well as the absorption in the metal pad for current injection and free carriers, even if the internal quantum efficiency close to 100 % is reached. Roughening of the top surface of an LED is one of the methods for improving the light extraction.[57-59] The roughened top surface reduces internal light reflection and scatters the light outward. The PEC process used to produce the roughened surface must give the appropriate surface morphology for efficient light extraction without damaging the electrical or optical properties of the material. T. Fujii shows that the output power of UV-LED is significantly improved with surface roughning by PEC process.[60] They combine laser LLO with PEC etching to produce a roughened LED surface with con-like features. LLO method has been established for detaching a sapphire substrate from a GaN film grown on it.[61,62] Utilizing filp-chip technology[63] and the LLO method, a substrate-free n-side-up structure can be made. The flipped n-GaN also reveals the (0001) nitrogen face, which is the more readily etched surface for the PEC process.[64] Figure 30 shows a photomicrograph of a device processed up to this stage. Finally, in order

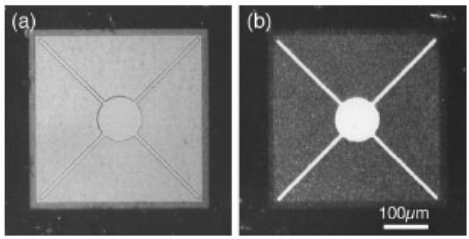

Fig. 30. Plan-view microphotographs of an LLO-LED boned on a Si substrate (a) before roughening the surface and (b) after roughening the surface ((from T. Fujii *et al.* [59], reprinted with permission of the American Institute of Physics).

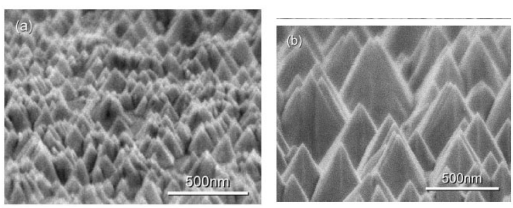

Fig. 31. SEM micrographs of an N-face GaN surface etched by a KOH based PEC method (a) 2min (b) 10 min etching (from T. Fujii *et al.* [59], reprinted with permission of the American Institute of Physics).

to roughen the top of surface, PEC wet etching was used. A KOH solution and a Xe lamp were used as electrolyte and light source, respectively.

Shown in Fig. 31 are scanning electron micrograph images of the *N*-face of GaN after PEC etching for different etching times. Notice that the PEC-etched *N*-face GaN surfaces show hexagonal conelike features, which is distinct from the PEC-etched Ga-face GaN surfaces. This difference is considered to be due to the surface polarity of GaN. A similar phenomenon was observed by Ng *et al.*[65] In comparing the 2-min-etched surface (Fig. 31(a)) and the 10-min etched one (Fig. 31(b)), the size of the features increases and the facets of the hexagonal cones become more defined. The ‘‘mirrorlike’’ surface before PEC etching becomes degraded as the etching time increases. If a highly reflective metal is deposited on the other side of a GaN film, the surface appears white, otherwise it is dark. This is believed to be due to the light-

reflection restraint at the air/GaN boundary, and if there is a highly reflective metal on the backside of the GaN, the light passing into GaN comes out again, scattering at the roughened surface. Figure 31(b) presents a photomicrograph of an LED with a roughened surface. Because the *n*-electrode prevents GaN from being exposed to the electrolyte and blocks UV light during PEC etching, the GaN beneath it is not etched and the electrode remains on the GaN after the etching process. Figure 32 shows upward EL output power from the surface of the chip versus dc injection current (*L-I*) characteristics for the LEDs with different etching times at RT. These data were obtained from the same device before and after PEC etching, so that any factor causing this difference except the surface morphology could be neglected. All *L-I* curves showed linear characteristics up to 50 mA. Because of the higher thermal conductivity of Si compared to sapphire, these devices are advantageous for high-power operation. The output power at a given current increased with increasing PEC etching time. As compared with the output power for a flat-surface LED and the 10-min-etched surface LED, this roughening treatment resulted in an increase of output power by a factor of 2.3 from the top surface. From other measurements on different devices, the power also showed a twofold to threefold increase after the roughening process.

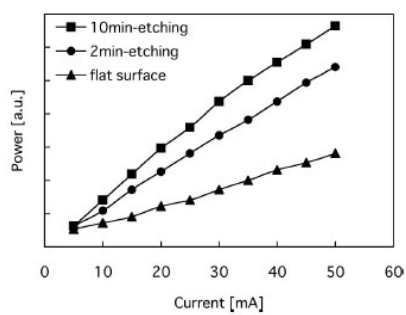

Fig. 32. Output power measured from the top surface of the surface roughened LED's with different PEC etching times as a function of the forward dc current ((from T. Fujii *et al*. [59], reprinted with permission of the American Institute of Physics).

7. Summary

The main phosphor-based approach to white LED lighting uses a near-UV (380–410 nm) pump LED based on InGaN active layer in combination with a RGB mix of phosphors that produce a broad spectral output over the visible range. This is potentially the best source of white lighting in terms of CRI and color stability, and potentially could be reasonably efficient as well. Also, it is highly flexible in terms of setting the CCT at a desirable point. UV-LED with emission in the range of 300–350 nm are ideal for pumping the fluorescent film of full color display devices. In addition, from the view point of environmental friendliness, it is necessary to develop a 350 nm UV-LED. For high efficiency of UV-LED, AlInGaN quaternary barrier which can produce the composition fluctuation is suggested. The development of a compact, robust, milliwatt-level deep-UV light source based on AlGaN active layer would greatly impact a number of applications including fluorescence-based biological agent detection, water purification, sterilization and decontamination, non-line-of-sight communications and thin film curing. Although UV-LED has many applications and potentials, UV-LED has not yet commercialized. This can be attributed to the low efficiency, lifetime, and high cost commercialization of UV-LED. Therefore, many ideas are suggested to make the high efficient UV-LED. First, to reduce dislocations in LED structure which can occur nonradiative recombination, GaN and AlN substrate are studied. And LED structure grown on GaN and AlN substrate can operate at more high current than that on sapphire substrate because of better heat dissipation and current spreading through the GaN substrate. In addition, ELOG, delta doping, facet control technique, superlattice buffer also studied for reduction of dislocation in LED structure. To improvement of internal quantum efficiency, techniques of the increase in band offset between well and barrier layer, pulsed atomic layer epitaxy, Ga droplet layer and Si delta doped barrier layer in MQW are presented. To increase in external quantum efficiency, processes of patterned sapphire substrate, mash electrode, DBR, photonic crystal, PEC etching are suggested. Although efficiency of UV-LED is greatly improved by many ideas, it is not low to commercial application.

Therefore, considerable improvements in device efficiency and operating characteristics are required to commercialize high efficient UV-LED. Thus, many significant advances in UV-LED can be expected in the future that will enable many applications.

References

1. *Gallium nitride & related wide bandgap materials & divice* edited by R. Szweda (Elsevier Science Ltd, UK, 2000).
2. http://www.cree.com
3. M. Yamada, T. Mitani, Y. Narukawa, S. Shioji, I. Niki, S. Sonobe, K. Deguchi, M. Sano and T. Mukai, *Jpn, J. Appl. Phys*., **41**, L1431 (2002).
4. X. A. Cao, S. F. LeBoeuf, M. P. D'Evelyn, S. D. Arthur, and J. Kretchmer, C. H. Yan and Z. H. Yang, *Appl. Phys. Lett*., **84**, 4313 (2004).
5. H. Kudo *et al*., International conference on nitride semiconductor (ICNS-5), Nara, Jjapan (2003).
6. T. Wang *et al*., *Appl. Phys. Lett*., **81**, 2508 (2002).
7. Z. P. Zhang *et al*., *Appl. Phys. Lett*., **79**, 925 (2000).
8. T. Wang, *Phys. Sat. Sol* (*c*), **0**, 2019 (2003).
9. J.P. Zhang, A. Chitnis, V. Adivarahn, S. Wu, V. Mandavilli, R. Pachipulusu, M. Shatalov, G. Simin, J.W. Yang, M. Asif Khan, *Appl. Phys. Lett.*, **81**, 4910 (2002).
10. V. Adivarahan, S. Wu, A. Chitnis, R. Pachipulusu, V. Mandivilli, M. Shatalov, J. P. Zhang, M. Asif Khan, G. Tamulaitis, A. Sereika, I. Yilmaz, M.S. Shur, R. Gaska, *Appl. Phys. Lett*., **81**, 3666 (2002).
11. A. Yasan, R. McClintock, K. Mayes, S.R. Darvish, P. Kung, M. Razeghi, *Appl. Phys. Lett.* **81**, 801 (2002).
12. G. Kipshidzhe, V. Kuryatkov, B. Borisov, S. Nikishin, M. Holtz, S.N.G. Chu, H. Temkin, *Phys. Stat. Sol. A*, 192, 286 (2002).
13. A. Hanlon, P. M. Pattison, J. F. Kaeding, R. Sharma, P. Fini, S. Nakamura, *Jpn. J. Appl. Phys*., **42**, L628 (2003).
14. A. Yasan, R. McClintock, K. Mayes, D. Shiell, L. Gautero, S.R. Darvish, P. Kung, M. Razeghi, *Appl. Phys. Lett.*, **83**, 4701 (2003).
15. A.J. Fischer, A. A. Allerman, M. H. Crawford, K. H. A. Bogart, S. R. Lee, R. J. Kaplar, W. W. Chow, S. R. Kurtz, K. W. Fullmer, J. J. Figiel, *Appl. Phys. Lett*., **84**, 3394 (2004).
16. N. Weimann, L. F. Eastman, D. Doppalapudi, H. M. Hg, and T. D. Moustukas, Appl. Phys. Lett., **83**, 3656 (1998).
17. S. M. Lee, M. A. Belkhir, X. Y. Zhu, Y. H. Lee, Y. G. Hwang, and T. Frauenheim, Phys. Rev. B, **61**, 16033 (2000).

18. S. J. Rosner, E. C. Carr, M. J. Ludowise, G. Girolami, and H. I. Erikson, *Appl. Phys. Lett.*, **70**, 420 (1997).
19. P. Kozodoy, J. P. Ibbetson, H. Marchand, P. T. Fini, S. Keller, J. S. Speck, S. P. DenBaars, and U. K. Mishra, *Appl. Phys. Lett.*, **73**, 975 (1998).
20. B. S. Simpkins, E. T. Yu, P. Waltereit, and J. S. Speck, J. *Appl. Phys*., **94**, 1448 (2003).
21. C. Sasaoka, H. Sunakawa, A. Kimura, M. Nido, A. Usui, and A. Sakai, *J. Cryst. Growth*, **189-190**, 61 (1998).
22. J. S. Im, H. Kollmer, J. Off, A. Sohmer, F. Scholz, and A. Hangleiter, *Phys. Rev. B* **57**, R9435 (1998).
23. S. Ghosh, P. Waltereit, O. Brandt, H. T. Grahn, and K. H. Ploog, *Phys. Rev. B*, **65**, 075202 (2002).
24. D. Cherns, S. J. Henley, and F. A. Ponce, *Appl. Phys. Lett.*, **78**, 2691 (2001).
25. X. H. Wu, C. R. Elsass, A. Abare, M. Mack, S. Keller, P. M. Petroff, S. P. DenBaars, J. S. Speck, and S. J. Rosner, *Appl. Phys. Lett*., **72**, 692 (1998).
26. A. Yasan, R. McClintock, K. Mayes, S. R. Darvish, H. Zhang, P. Kung, M. Razeghi, S. K. Lee, and J. Y. Han, *Appl. Phys. Lett*., **81**, 2151 (2002).\
27. G. A. Slack, *J. Phys. Chem. Solids* **34**, 321 (1973).
28. G. A. Slack and T. McNelly, *J. Cryst. Growth*, **34**, 263 (1976); **42**, 560 (1977).
29. J. C. Rojo, G. A. Slack, K. Morgan, B. Raghothamachar, M. Dudley, and L. J. Schowalter, *J. Cryst. Growth*, **231**, 317 (2001).
30. R. Gaska, C. Chen, J. Yang, E. Kuokstis, and A. Khan, G. Tamulaitis, I. Yilmaz, M. S. Shur, J. C. Rojo and L. J. Schowalter, *Appl. Phys. Lett.*, **81**, 4658 (2002).
31. T. Nishida, T. Makimoto, H. Saito and T. Ban, *Appl. Phys. Lett*, 84, 1002 (2004).
32. S. Nakamura; *Science*, **281**, 956 (1998).
33. S. Chichibu, H. Marchand, M. S. Minsky, S. Keller, P. T. Fini, J. P. Ibbetson, S. B. Fleischer, J. S. Speck, J. E. Browers, E. Hu, U. K. Mishra, S. P. DenBaars, T. Deguchi, T. Sota, and S. Nakamura, *Appl Phys. Lett*., **74**, 1460 (1999).
34. T. Muka, K. Takekawa and S. Nakamura, *Jpn. J. Appl. Phys*., **37**, L 839 (1998).
35. T. Mukai and S. Nakamura, *Jpn. J. Appl. Phys*., **38**, 5735 (1999).
36. K. H. Kim, J. Li, S. X. Jin, J. Y. Lin and H. X. Jiang, *Appl. Phys. Lett.* **83**, 566 (2003).
37. M. Iwaya, R. Nakamura, S. Terao, T. Ukai, S. Kamiyama, H. Amano and I. Akasaki, *Proc. Int, Workshop on Nitride Semiconductors* (IPAP, Tokyo, 2000) IPAP Conf. Ser. **1**, 833.
38. A. Usui, H. Sunakawa, A. Sakai and A. A. Yamaguchi: *Jpn. J. Appl. Phys.*, **36**, L899 (1997).
39. Y. Kato, S. Kitamura, K. Hiramatsu and N. Sawaki: *J. Cryst. Growth* **144**, 133 (1994).
40. M. Iwaya, S. Takanami, A. Miyazaki, Y. Watanabe, S. Kamiyama, H. Amano and I. Akasaki , *Jpn. J. Appl. Phys*., **42**, 400 (2003).

41. M. Iwaya, S. Terao, N. Hayashi, T. Kashima, H. Amano and I. Akasaki, *Appl. Surf. Sci*., **159-160**, 405 (2000).
42. A. Chitnis, J. P. Zhang, V. Adivarahan, W. Shuai, J. Sun, M. Shatalov, J. W. Yang, G. Simin and M. A. Khan, *Jpn. J. Appl. Phys.*, **41**, L450 (2002).
43. H. X. Wang, H. D. Li, Y. B. Lee, H. Sato, K. Yamashita, T. Sugahara and S. Sakai, *J. Crystal. Growth*, **264**, 48 (2004).
44. J. Zhang, E. Kuokstis, Q. Fareed, H. Wang, J. Yang, G. Simin, M. Asif Khan, R. Gaska and M. Shur, *Appl. Phys. Lett.*, **79**, 925 (2001).
45. Y. B. Lee, T. Wang, Y-H. Liu, J-P. Ao, H-D. Li, H. Sato, K. Nishino, Y. Naoi and S. Sakai, *J. Jpn. Appl. Phys*., **41**, L1037 (2002).
46. N. Darowski, U. Pietsch, U. Zeimer, V. Smimitzki and F. Bugge, *J. Appl. Phys*., **84**, 1366 (1998).
47. M. -K. Kwon, I. -K. Park, S. -H. Baek, J. -Y. Kim, and S. –J. Park , *J. Appl. Phys*., **97**, 106109, (2005).
48. M. K. Kwon, I. K. Park, S. H. Beak, J. Y. Kim, and S. J. Park, *Phys. Stat. Sol*.(*a*), **202**, 859 (2005).
49. http://www.cree.com/News/news175.asp
50. Y. Kawakami, Y. Narukawa, K. Omae, S. Fujita, and S. Nakamura, *Phys. Status Solidi A* **178**, 331 (2000).
51. T. Nishida, H. Saito, and N. Kobayashi, *Appl. Phys. Lett*., **79**, 711 (2001).
52. A. Billeb, W. Grieshaber, D. Stocker, E. F. Schubert, and R. F. Karlicek, Jr., *Appl. Phys. Lett*., **70**, 2790 (1997).
53. K. Tadatomo, H. Okagawa, Y. Ohuchi, T. Tsunekawa, Y. Imada, M. Kato, and T. Taguchi, *Jpn. J. Appl Phys*., **40**, L583 (2001).
54. T. Wang, P. J. Parbrook, C. N. Harrison, J. P. Ao and Y. Ohno, *J. crystal. Growth* **267,** 583 (2004).
55. J. Shakay, K. H. Kim, J. Y. Lin and H. X. Jiang, *Appl. Phys. Lett.*, **85**, 142 (2004).
56. J. V. Smith, *Geometrical and Structural Crystallography* (Wiley, New York, 1982), p. 449.
57. A. A. Bergh, M. Hill, R. H. Saul, and S. Plains, U. S. Patent No 3, 739, 217 (1973).
58. C. Huh, K. S. Lee, E. J. Kang, S. J. Park, *J. Appl. Phys.* **93**, 9383 (2003).
59. T. Fujii, Y. Gao, R. Sharma, E. L. Hu, S. P. DenBaars, and S. Nakamura, *Appl, Phys. Let*t. **84**, 855 (2004).
60. W. S. Wong, T. Sanda, N. W. Cheung, M. Kneissl, D. P. Bour, P. Mei, L. T. Romano, and N. M. Johnson, *Appl, Phys. Lett.* **72**, 1999 (1998).
61. P. R. Tavernier and D. R. Clarke, *J. Appl. Phys.*, **89**, 1527 (2001).
62. C. -F. Chu, C. -C. Yu, H. -C. Cheng, C, -F. Lin, and S. -C. Wang, *Jpn. J. Appl. Phys.* Part 2 **42,** L147 (2003).
63. J. J. Wierer, D. A. Steigerwald, M. R. Krames, J. J. O'Shea, M. J. Ludowise, N. F. Gardner, R. S. Kern, and S. A. Stockman, *Appl. Phys. Lett*. **78**, 3379 (2001).

64. T. Palacios, F. Calle, M. Varela, C. Ballesteros, E. Monroy, F. B. Naranjo, M. A. Sanchez-Garacia, E. Calleja, and E. Munoz, *Semicond. Sci. Technol.*, **15**, 996 (2000).
65. H. M. Ng, N. G. Weimann, and A. Chowdhury, *Appl. Phys. Lett.*, **94**, 650 (2003).

This page intentionally left blank

CHAPTER 5

FABRICATION OF GAN LIGHT EMITTING DIODES BY LASER LIFT-OFF TECHNIQUE

Chen-Fu Chu, Jung-Tang Chu, Hao-Chung Kuo*, and S. C. Wang

1001 Ta Hsueh Road, Hsinchu, Taiwan 300
National Chiao Tung University
**E-mail: hckuo@faculty.ieo.edu.tw*

The GaN-based wide band gap semiconductors have been employed for blue light emitting diodes (LEDs) and laser diodes. These devices were grown heteroepitaxially onto dissimilar substrates such as sapphire and SiC because of difficulties in the growth of bulk GaN. However, due to the poor electrical and thermal conductivity of sapphire substrate, the device process steps are relatively complicated compared with other compound semiconductor optoelectronic devices. Therefore, fabrication of GaN-based light emitting devices on electrically and thermally conducting substrate by separating sapphire substrate is most desirable. Several techniques were used to achieve this process including, metallization and wafer bonding, lift-off, and layer transfer. In this thesis, we report the research results on the fabrication of free standing GaN LEDs on conductivity substrate. In this chapter, the establishment of laser lift-off (LLO) conditions for freestanding GaN thin film was presented. By combing the LLO process, new p-type ohmic contact metallization, and wafer bonding techniques, the performance of freestanding LLO-LEDs on copper substrate with p-side up and p-side down configuration, and a large-area-emission LEDs were demonstrated.

1. Introduction

The GaN-based wide band gap semiconductors are widely used for optoelectronic devices such as blue light emitting diodes (LEDs) and laser diodes (LDs). These devices were grown heteroepitaxially onto dissimilar substrates such as sapphire and SiC because of difficulties in the growth of bulk GaN. Sapphire is the most commonly used substrate

because of its relatively low cost. However, due to the poor electrical and thermal conductivity of sapphire substrate, the device process steps are relatively complicated compared with other compound semiconductor devices. Therefore, GaN optoelectronics devices fabricated on electrically and thermally conducting substrate by separating sapphire substrate are most desirable. The separation of hydride vapor phase epitaxy grown 2 inch GaN wafer from the sapphire substrate was first demonstrated[1] by using the laser lift off (LLO) technique. The pulsed, high power UV laser of third harmonic of Q-switched Nd:YAG laser with 355 nm wavelength was used to irradiate through the transparent sapphire substrate to lift off the GaN film. The physical process responsible for the lift-off appears to be dominated by rapid thermal decomposition of GaN near the sapphire interface. Recently, The LLO technique has been used to fabricate the freestanding InGaN LEDs and LDs.[2-4] These include p-side up GaN LEDs with Ti/Al as p- and n-contact, the p-side down $In_xGa_{1-x}N$ LEDs on Si substrates with Pd-In as p-GaN contact and bonding metal, and p-side up InGaN laser diodes on copper substrates.

Freestanding GaN optoelectronic devices without sapphire substrate are most desirable. The transformation of GaN with other substrates could take advantages of the favorable function of different material systems. For fabrication freestanding GaN light emitting devices, several techniques may be used to achieve including material deposition, bonding of different elements, thermal stable of p-type ohmic contact for device fabrication, wafer bonding, lift-off, and layer transfer. In these techniques, the combination of wafer bonding and device layer lift-off present the major part to join the GaN device layer with dissimilar materials.

In our recently report,[5] we compared the performance of p-side up and p-side down LLO-LEDs on Copper substrate with the same p-GaN contact metals, and demonstrated superior performance p-side down configuration of GaN LEDs over the p-side up LEDs. The result suggests the p-side down LLO-LEDs can enhance the light output power, operate at high current and increase the heat capacity of GaN-based LEDs. In this chapter, we presented the detail investigation results of the GaN LLO process and the establishment of GaN LLO conditions, the demonstration of the LLO-GaN light emitting devices.

2. Current Issues of Conventional LED

2.1. *Thermal stable metallization of P-type ohmic contact*

Good ohmic contacts with low contact resistance are essential for GaN-based optoelectronic devices. For n-type GaN, ohmic contact with relatively low contact resistance of 10^{-5}~10^{-8} Ω-cm^2 using alloy composition such as Ti/Au, Ti/Al, and Ti/Al/Ni/Au,[6-8] have been achieved. However, for p-type GaN, it is difficult to obtain a low resistance ohmic contact on p-type GaN layer due to the following two major reasons. First, it is difficult to achieve a high hole carrier concentration in p-type GaN. The p-type GaN is typically achieved by doping magnesium (Mg) in metal-organic chemical vapor deposition (MOCVD) or molecular beam epitaxy (MBE). Mg has the relative high optical activation energy of around 250meV[9] compared to other acceptors.[10] The formation of Mg-H complexes[11,12] during MOCVD growth was generally suggested to be responsible for the low activation efficiency of Mg that results in the relative low p-type GaN carrier concentration. Second, the absence of suitable metals that have higher work function than that of p-type GaN (~7.5 eV) resulting the specific contact resistance only around 10^{-2} ohm-cm^2. Many attempts have been reported thus far in finding ways of lowering the contact resistance in p-type GaN materials. For fabrication of GaN-based light-emitting devices, the Au-based metallization for p-type GaN ohmic contact was commonly used for metal wire-bond process. Recently various Au-based ohmic contacts using metallization[13-21] have been reported. However, for the wafer bonding process of fabrication freestanding GaN light emitting devices, a stable and useful p-type GaN metallization was also desirable.

During the GaN LED operation, the large voltage drop across the p-GaN/metal interface, which leads to poor devices performance. For fabrication of GaN-based light-emitting devices, Ni/Au metallization scheme annealed in oxide ambient was commercially used for the p-type contact metallization., a thermal stable and useful p-type GaN metallization was desirable for the fabrication of freestanding GaN light emitting devices in particular in the wafer bonding process. In our recently report,[22] we applied a new metallization scheme of Ni/Pd/Au to form the ohmic contact on p-GaN and obtained the specific contact resistance as low as 10^{-4} Ω-cm^2. More recently, H. W. Jang[23] also reported a low-resistance thermally stable ohmic contact on p-type GaN using a thin contact scheme of Pd/Ni. The specific contact resistance was

around 10^{-4} to 10^{-5} Ω-cm^2 for the contact annealed at 500°C under an oxidizing ambient. They concluded the NiO that formed at the surface prevented Pd atoms from outdiffusing, promoting the formation of Pd gallides, Ga_2Pd_5 and Ga_5Pd. This reaction produces Ga vacancies below the contact, leading to enhancement of the thermal stability as well as reduction of the contact resistivity.

2.2. *Growth substrate*

The semiconductors GaN, AlN, and InN have been grown primarily on sapphire, most commonly the (0001) orientation, but also on the a- and r- planes.[24] In addition, the group-III-V nitrides have been grown on SiC, Si, GaAs. With the exception of SiC, the interest in using these substrates has slowly decreased. The primary reason for the decline in interest in the zincblende substrates is the inherent difficulty in growing high quality GaN in the cubic phase. In addition, the high growth temperature involved usually precludes the use of materials with low decomposition temperatures such as GaAs. Due to the reactivity of nitrogen with Si, amorphous Si3N4 layers typically form before the GaN deposition, preventing high-quality GaN films on Si[25-26] substrates. Currently, the SiC materials system is challenging the GaN/sapphire system for dominance in both the optoelectronic and electronic arena.[27] SiC offers a higher electrical and thermal conductivity compared to sapphire and is available in the hexagonal crystal structure. Despite these advantages, SiC suffers from being substantially more expensive compared to sapphire. The large cost of using SiC has limited its usefulness and availability to only a small number of groups.

The preference for sapphire substrates can be ascribed to its wide availability, hexagonal symmetry, low coast, 2-inch-diameter crystals of good quality, transparent nature, and its ease of handling and pre-growth cleaning. Sapphire is also suitable at high temperatures (~1000℃) required for epitaxial growth using the various CVD techniques commonly employed for GaN growth.

However, due to the poor electrical (Electrical resistivity = 10^{11}-10^{16} ohm-cm) and thermal conductivity (35 W/m-K) of sapphire substrate, the device process steps are relatively complicated compared with other compound semiconductor devices. For devices processed on sapphire substrates, all contacts must be made from the topside. This configuration complicates contact and packaging schemes, resulting in a

spreading-resistance penalty and increased operating voltages.[28] The heat dissipation of sapphire substrate was poor, therefore the commercial available GaN blue LEDs was typically operated under low current operation conditions.

Therefore, GaN optoelectronics devices fabricated on electrically and thermally conducting substrate by separating sapphire substrate are most desirable. The separation of hydride vapor phase epitaxy (HVPE) grown 2-inch GaN wafer from the sapphire substrate was first demonstrated[29] by using the laser lift off (LLO) technique. The pulsed, high power UV laser of third harmonic of Q-switched Nd:YAG laser with 355 nm wavelength was used to irradiate through the transparent sapphire substrate to lift off the GaN film. For the LED grown on GaN substrate, the performance of high light output power and high current continuous wave operation condition was reported.[30] However, the GaN substrate fabricated by combining HVPE growth and LLO process was substantially more expensive compared to sapphire.

2.3. *Light output power*

2.3.1. *Emitting area of GaN LEDs*

The emission area of conventional GaN-based LEDs on sapphire with the p-side up configuration was limited because the p-GaN and MQW layers required etching away to expose the n-GaN layer for n-type contact and wire bond purpose. In Figure 1, the electrical contacts to the p- and n-layers are both on the top surface of the device because of the insulating sapphire substrate. An important consequence for LEDs on sapphire is that since most of the light generated at the junction escapes the device through the top surface, the large-area p-contact[31] has to be made as transparent as possible outside the area where electrical bond wires are attached. Typically the p-contact pad with square or circular size of 80-100 μm was fabricated.

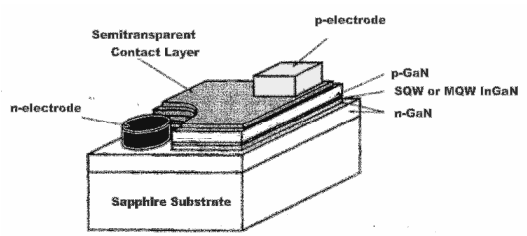

Fig.1. The basic structure of GaN LED.

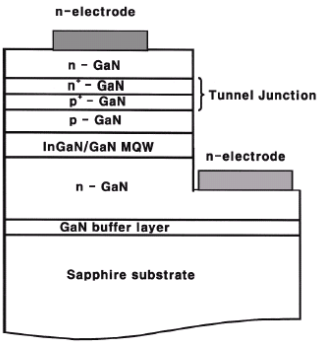

Fig. 2. Schematic structure of an InGaN/GaN MQW light-emitting diode with a tunnel contact junction structure. (from Jeon *et al.*[33], reprinted with permission of the American Institute of Physics).

The p-type ohmic contact of conventional LED devices with semi transparence is required to spread current from the p-bonding pad across the junction area because of the very low conductivity of GaN:Mg.[32] This is typically done by deposited a semitransparent ohmic contact metallization across the GaN:Mg surface. Although the technology has matured, there still exist challenges in optimizing the growth of high p-type doping and in device fabrication aspects.

Recently, S. R. Jeon et al.[33] demonstrated a buried tunnel contact junctions on the p-side with n-side up configuration to eliminate lateral hole excitation currents as shown in Figure 2.

A reverse biased tunnel junction (TJ) supplies holes to the p-type crystal above the active region by lateral electron currents. Furthermore, this concept allows the use of a low-resistivity n-type GaN instead of a high-resistivity p-type GaN as a top contact layer. Thus, the n-type ohmic contact can be used instead of the p-type ohmic contact of conventional LED devices.

Figure 3(a)[33] shows the light emission of the conventional LEDs with no semitransparent p-electrode onto the p-GaN layer is occurring just around the p-contact electrode. The localized EL image means that the current is crowed around p-electrode due to the low conductivity of p-type layer. Figure 3(b)[33] shows the blue LED with buried tunnel contact junction has a light emission throughout the entire surface of the n-type layer.

S. R. Jeon concluded that the tunnel junction allows the use of n-type GaN instead of p-type GaN as a top contact layer in GaN-based

devices. The top-emitting light output power of the TJ LED with a lateral current spreading is two times higher than that of the conventional LED with semitransparent metal onto p-type layer. The TJ LEDs also induce a spatially uniform luminescence. Although the turn voltage of these TJ LEDs was still higher than that of the conventional LEDs, the configuration of n-side up GaN LEDs could be a very good idea to obtain a large-area-emission GaN LEDs due to its good current effect of n-type GaN layer.

By increasing the emitting area, other technologies are developed, for example, an interdigitated mesa geometry was recently reported.[34] However, the emitting area was still limited due to the current spreading length of p-GaN layer.[35] The current spreading length was critical depended on the ratio of semitransparent contact resistance and its thickness.[36] In addition, the interdigitated finger circuit patterns on the top of p-GaN as shown in Figure 4 also confine the active light of emission area.

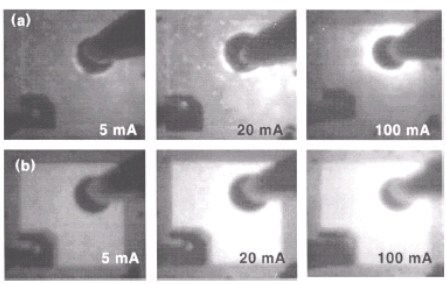

Fig. 3. Light emission images of (a) conventional blue LEDs (without semitransparent electrode) and (b) TJ blue LEDs tested at 5, 20, and 100 mA. (from Jeon *et al.*[33], reprinted with permission of the American Institute of Physics).

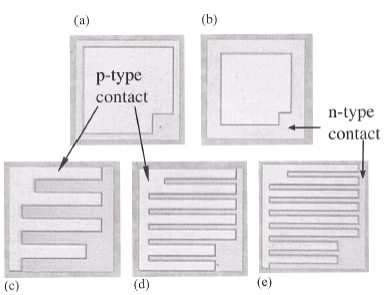

Fig. 4. Micrograph of InGaN/GaN LEDs with (a) large square-shaped pattern; (b) small square-shaped pattern; (c)large finger interdigitated pattern; (d) medium finger interdigitated pattern; and (e) small finger interdigitated pattern. (from Guo *et al.*[34], reprinted with permission of the American Institute of Physics).

More recently, the flip chip bonding technique for backside emission of GaN LEDs was reported.[37] A large emitting size of about 1 mm× 1mm and high extrication output power from the backside polished sapphire substrate was achieved by flip chip bonding techniques. However, the processes steps of these techniques were relatively complicated.

2.3.2. *The reflectivity of GaN/material interface*

The reflectivity of GaN/material interface also plays an important role to enhance the light extrication. The reflectivity from the interface of material/GaN interface can be estimated by using the well-known Fresnel expression:

$$R = \frac{(n_s - n_m)^2 + {k_m}^2}{(n_s + n_m)^2 + {k_m}^2} \tag{1}$$

where n_s is the refractive index of semiconductor, n_m is the refractive index of material, and k_m is extinction coefficient of metal. Table 1[38-41] gives the parameters for different material and GaN material at the wavelength 470 nm, and 550 nm. The calculated reflectivity (R) of GaN/material interface was also listed in Table 1. For the blue GaN LEDs, the standard emission wavelength is at bout 470 nm. The light extrication of the conventional GaN LEDs was limited due to the reflectivity of GaN/sapphire was only about 2 %. Higher light output extrication was desired to enhance the light output power by increasing the reflectivity of GaN/material. The flip chip bonding techniques can provide a high reflectivity of GaN/silver to enhance the light output power.[42] However, the processes steps of the flip chip bonding techniques for the fabrication of GaN LEDs were relatively complicated due to the n-, and p- electrode were both fabricated on the top surface of the devices.

2.4. *Laser lift-off setup and process conditions*

2.4.1. *Laser system*

Figure 5 shows the schematic diagram of the setup for conducting LLO experiment. A KrF excimer laser (Lambda Physick LPX210) at wavelength of $\lambda = 248$ nm with pulse width of 25 ns was used for LLO.

The laser output energy can be varied from 10 nJ to 25 mJ. The laser beam is reshaped and homogenized using a special optical system to form a highly uniform (± 5% RMS) beam profile of 12×12 mm^2 after the mask plane. A beam splitter then splits the laser beam into a LLO beam and a monitor beam. The LLO processing beam passed through a projection system of 10× with 0.2 numerical aperture, and then focuses onto the sample with a square spot size of 1.2×1.2 mm^2. The monitor beam is incident on a beam analyzer for real-time monitoring of the laser beam quality. The samples were placed on the top of working station which can be moved 1.2 mm step by step to scan a typical sample size of 2 cm × 2 cm by using the computer controlled stepper motor. The CCD camera was used to in-situ monitoring of the LLO process.

Table 1. The calculated reflectivity (R) of GaN/material interface.

λ / Material	470 nm			550 nm		
	n	k	R (GaN/ Material)	n	k	R (GaN/ Material)
GaN	2.48	0~0.01	0%	2.42	0~0.01	0%
Al_2O_3	1.77	0	2%	1.77	0	2%
Ni	1.78	3.12	37%	2.00	3.36	37%
Ti	2.32	3.10	30%	2.54	3.44	33%
Pd	1.46	3.38	46%	1.64	3.85	49%
Au	1.18	1.86	31%	0.34	2.37	75%
Ag	0.05	2.6	96%	0.05	3.32	97%
Cu	1.16	2.55	42%	1.0	2.93	52%
Al	0.54	4.51	82%	0.76	5.32	81%

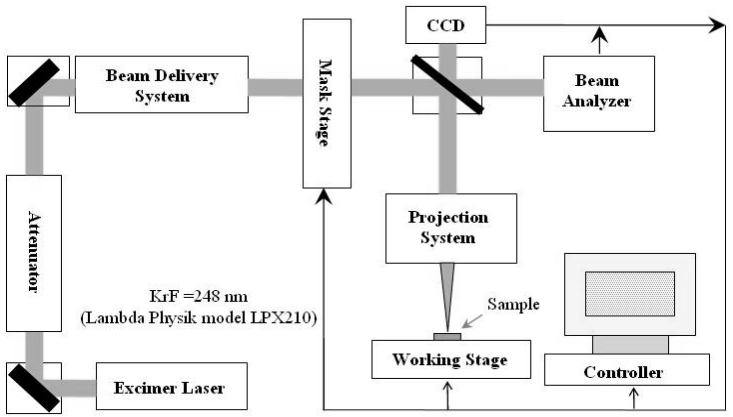

Fig. 5. The schematic diagram of laser etching and laser lift-off process setup.

2.4.2. *Laser interaction on GaN material*

For establishing LLO conditions for GaN, the effect of laser fluence on the ablation of GaN materials under different environment was investigated first. A bare un-doped GaN sample of 14.9 μm thick was irradiated with the laser beam under two pressure conditions: one atmosphere pressure and 10^{-3} torr. The laser fluence was varied from 0.2 to 1.0 J/cm^2 at constant number of pulses. The laser irradiation causes the decomposition of GaN into gaseous nitrogen and gallium droplets, following the equation:

$$GaN \Leftrightarrow Ga + \frac{1}{2} N_{2(g)} \tag{2}$$

The GaN sample after laser irradiation tends to show some material residues such as Ga, Ga oxide. These residues were then clean up by dilute acid solution such as HCl or H_2SO_4/H_2O_2 before measurement of etched depth.

Figure 6 shows the rate of removable of GaN or etching rate as a function of laser fluence for the two different pressure conditions. The etching rates increase with increasing laser fluence under both conditions. At the incident laser fluence of 1.0 J/cm^2, the etching rate was about 35 nm/pulse, and 60 nm/pulse for one atmosphere pressure and 10^{-3} torr, respectively.

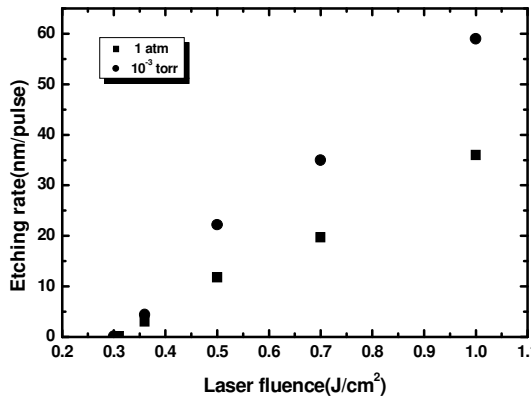

Fig. 6. The rate of removable of GaN or etching rate as a function of laser fluence for the two different pressure conditions.

According to the chemical kinetic theory,[43] a system in stable chemical equilibrium subjected to the influence of an exterior force tends to cause variation in its pressure. For GaN sample irradiated under low pressure of 10^{-3} torr, which is lower compared with the one atmosphere condition, the decomposition rate of GaN should be higher than that of the sample placed in one atmosphere condition. Thus higher etching rate was obtained in low-pressure condition. Based on the laser etching of GaN sample, we obtained the threshold laser fluence for ablation of GaN surface to be about 0.3 J/cm^2. From the etching rate and the incident laser fluence relationship, the GaN material absorption coefficient at KrF laser wavelength can also be estimated based on the widely accepted formula of Beer's law:[44]

$$d = \left(\frac{1}{\alpha}\right)\ln\left(\frac{E_i}{E_{th}}\right) \tag{3}$$

where d is the etched depth per pulse, α is the absorption coefficient, E_i is the incident laser fluence, and E_{th} is the threshold laser fluence for material removal. By plotting the etching rate versus logarithm of incident fluence E_i, we obtained an absorption coefficient of about $2.5(\pm 2.0) \times 10^5$ cm^{-1} from the slopes of the plot. This value is in agreement with the reported data for GaN obtained from the optical measurement method.[45]

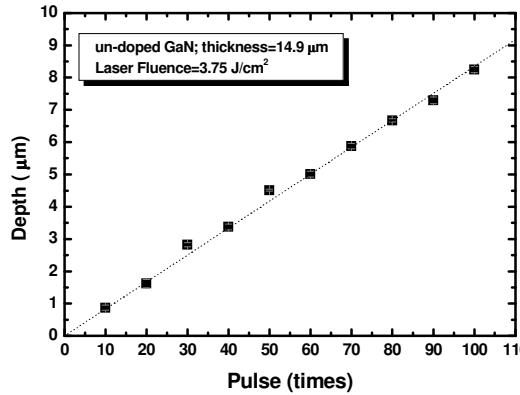

Fig. 7. The etching rate as a function of pulse numbers at the laser fluence of 3.75 J/cm^2 under the atmosphere condition.

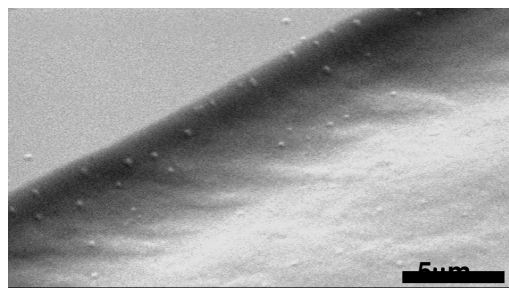

Fig. 8. The SEM picture of the etched sidewall.

The dependence of the etched depth on the numbers of pulses at higher laser fluence of 3.75 J/cm^2 was also investigated to establish the optional LLO condition. Figure 7 shows the etched depths as a function of pulse numbers.

The etched depth increases linearly with the numbers of pulses. This dependence is similar to the reported elsewhere.[46] Form this data, the higher etching rate as high as 82 nm/pulse was obtained at higher laser fluence.

Figure 8 shows a SEM picture of the etched sidewall. The etched surface morphology was also obtained by AFM measurement in contact mode operation with a scan area of 5 μm^2.

Figure 9 shows the typical AFM images for the samples under these two different conditions. The root mean square (RMS) roughness

of the surface morphology is around 4~14 nm for the sample processing in the atmosphere pressure condition, and around 30~36 nm for the sample processing under low pressure condition. These results show that the decomposition of GaN material under the atmosphere pressure condition has relatively better surface morphology. Therefore, the GaN LLO was conducted process under the atmosphere environment.

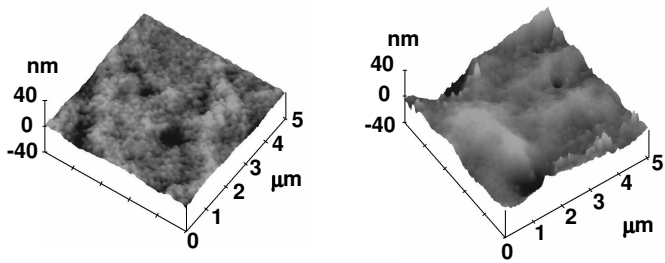

(a) Atmosphere Pressure (b) Low-Pressure

Fig. 9. The typical AFM images for the samples under these two different onditions. (a) The atmosphere condition. (b) Low pressure of 10^{-3} torr.

2.4.3. *Thermal model of laser interactions*

Determination of the temperature rise of the irradiated GaN thin films was done using the one-dimensional heat flow equation,

$$I(z,t) = I_0(t)(1-R)e^{-\alpha z} \tag{4}$$

$I(z,t)$ is the power density of the incident laser light at a depth z and time t. The variables T, ρ, C_p, k, and α are the temperature, density, specific heat, thermal conductivity and optical absorption coefficient, respectively, of GaN. Assuming the thin film is a homogeneous absorbing medium, the incident power density can be written as:

$$T(z,t) = \frac{I_a \xi}{K} \sum_{n=-\infty}^{\infty} ierfc\left[\frac{2nL - z}{\xi}\right](1-R) \tag{5}$$

where $I_0(t)$ is the output laser power density and R is the reflectivity. The heat equation can then be solved analytically assuming the thermal and optical parameters are invariant with temperature, the GaN film is of a semi-infinite thickness, and no phase change occurs during the laser pulse. The solution is given as:[47-48]

For notational convenience, we introduce the diffusion length: $\xi = \sqrt{2Kt}$. For a uniform surface source of incident power density, we have:[49]

$$T(0.t) = I_a \frac{\xi}{K\sqrt{\pi}}(1-R) \tag{6}$$

For a single 38 ns pulse from a KrF laser,[50] equation 6 reveals that a laser fluence of approximately 400 mJ/cm^2 is needed to raise the surface of the GaN film to the decomposition temperature of 900°C. The values for ρ, *Cp*, *k*, *R* and α used in the calculations were 6.11 g/cm^3, 9.745 cal/mol-K, 1.3 W/cm-K, 0.3 and 4.4×10^5 cm^{-1} respectively. A simulated temperature profile for a single 38 ns, 400 mJ/cm^2 pulse from a KrF laser as a function of time and depth is shown in Figure 10.[50]

Figure 10 shows the temperature rise, coupled with a large temperature gradient across the thickness of the GaN film, occurs in a highly localized heated area that is within 100 nm below the irradiated GaN/sapphire interface. This selective localized heating allows for the formation of a thin interfacial layer to yield separation of the GaN film from the sapphire substrate.

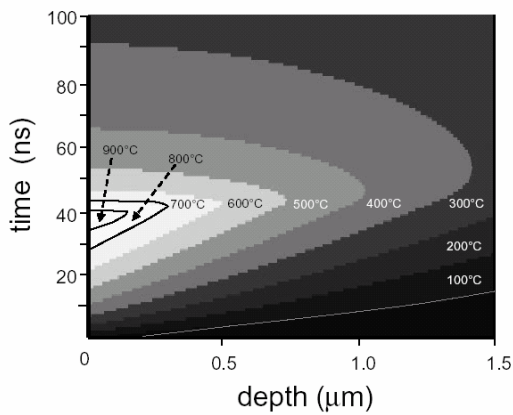

Fig. 10. A simulated temperature profile for a single 38 ns, 400 mJ/cm2 pulse from a KrF laser. The temperature rise, coupled with a large temperature gradient across the thickness of the GaN film, occurs in a highly localized heated area that is within 100 nm below the irradiated GaN/sapphire interface (referenced at 0 mm depth).

In particular, for the semi-infinite solid (for $L = \infty$), the temperature at the irradiated surface is:[49]

$$\frac{\partial T}{\partial t} = \frac{\alpha}{\rho C_p} I(z,t) + \frac{1}{\rho C_p} \frac{\partial}{\partial z}\left(\kappa \frac{\partial T}{\partial t}\right) \tag{7}$$

where $\xi = 2(Dt)^{1/2}$ is the diffusion length, and the thermal diffusivity $D = K/C_p\rho$, K is the thermal conductivity, C_p is the heat capacity, ρ is density, t is the pulse duration, and R is the reflectivity. For GaN material, the decomposition temperature (T) is about 900ºC-1000ºC,[51-53] K = 1.3 W/cm-K, C_p = 9.75 cal/mol-K, ρ = 6.11 g/cm^3, t = 25 ns, and R = 0.3.[54-56] Using these values, the absorbed laser fluence required for decomposition of GaN is about 0.3 J/cm^2, which is in agreement with the experiment value.

2.4.4. *LLO process*

The LLO process was first conducted using an un-doped GaN sample grown on sapphire substrate. The backside of sapphire was first polished by various size of diamond paste from 3 μm to 1 μm, then cut to a sample size of 1 cm × 1 cm. The sample was bonded to a Si wafer using cyanoacrylate ($C_6H_7NO_2$)-based ester adhesive forming a sapphire/u-GaN/epoxy/Si structure. The sample was placed on the top of workstation in air. Figure 11 shows the LLO process sequence for fabrication of freestanding un-doped GaN.

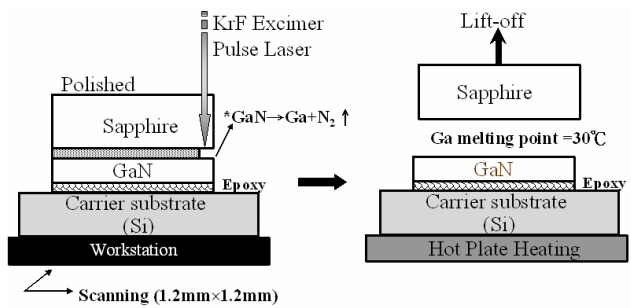

Fig. 11. The process scheme for fabrication of the LLO un-doped GaN.

The pulsed KrF excimer laser with a spot size of 1.2 mm × 1.2 mm was directed through the backside of the polished transparent sapphire substrate. Since the attenuation of the KrF excimer laser through the 0.5 mm thick sapphire substrate is approximately 20-30 %[57] and the reflection of the interface of sapphire/GaN at 248 nm is approximately

20 %,[46] the incident laser fluence was set to a value of 0.6 J/cm^2, corresponding to a laser fluence of about 0.3 J/cm^2 at the interface.

With the incident fluence of 0.6 J/cm^2, the metallic silver color with size of 1.2 mm × 1.2 mm was clearly appeared in the interface of GaN and sapphire with ejection of some dust like particles from the edge of sample, indicating the decomposition of Ga interfacial layer between the GaN and sapphire. By heating the irradiated samples at Ga melting point of 30ºC, the GaN film was then easily separated from sapphire substrate and transferred onto the Si supported carrier and the metallic Ga residues was removed to complete the LLO process.

The LLO GaN sample was characterized by using SEM, AFM, x-ray rocking curve (XRC), and PL spectrum measurements. Figure 12 shows a typical cross-sectional SEM micrograph of the LLO GaN sample. The structure of GaN/epoxy/Si was clearly depicted. The thickness of LLO-GaN film was measured around the value of 14.9 μm indicating the reduction in thickness is relatively small after LLO process.

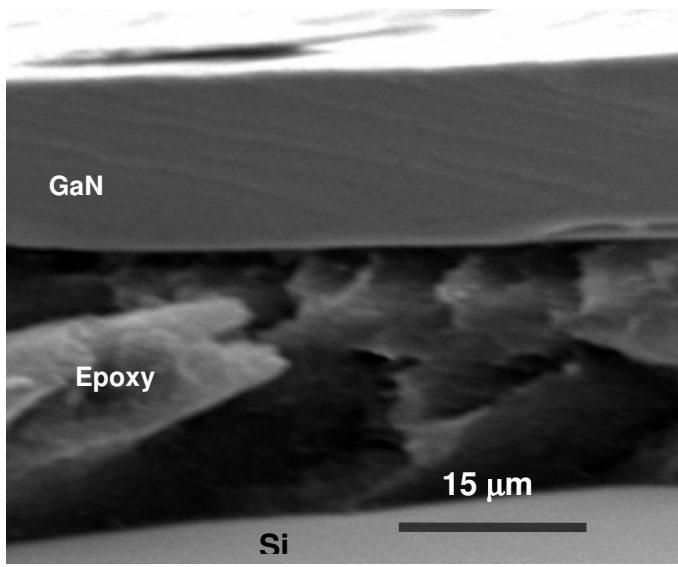

Fig. 12. A cross-sectional SEM micrograph of 14.9 μm thick un-doped sample.

Figure 13 shows the typical AFM images of the LLO-GaN film surface. The uneven and whiskers like micro-pole structures were formed as the result of lift off process. The root mean square values (RMS) of

the GaN surface roughness were around 12 nm, which is consistent with the results of the GaN etched surface for the sample etching in the atmosphere pressure condition. The RMS value of 12 nm compared to the value of 0.3 nm for the sample before LLO was larger due to thermal decomposition occurred in the interface of the GaN and sapphire.

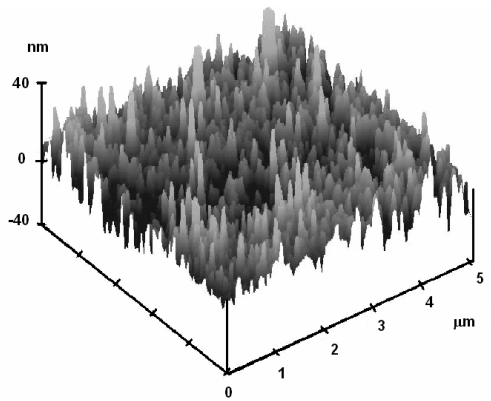

Fig. 13. A typical AFM image of the LLO un-doped GaN film surface.

Figure 14 shows the XRC spectrum of the GaN sample before and after lift-off. The full width at half maximum (FWHM) value of LLO film is about 528 arcsec, which is slightly larger than that of the conventional GaN film of 412 arcsec. The increasing in the FWHM of the rocking curve maybe due to the thermally induced lattice disorder carried by the laser irradiation.[58]

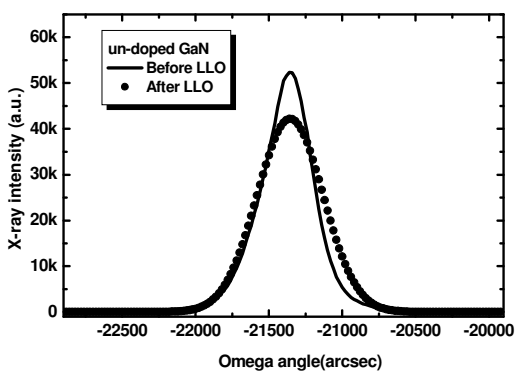

Fig. 14. The x-ray rocking curve (XRC) spectrum of the un-doped GaN before and after LLO.

Figure 15 shows the PL spectrum of the GaN sample before and after LLO process. The emission peak of LLO-GaN is at 364 nm, which is slightly red shift compared to the emission peak before LLO. A similar red-shift was reported previously[58] and attributed to the induced localized defects in the GaN/sapphire interface caused by LLO process.

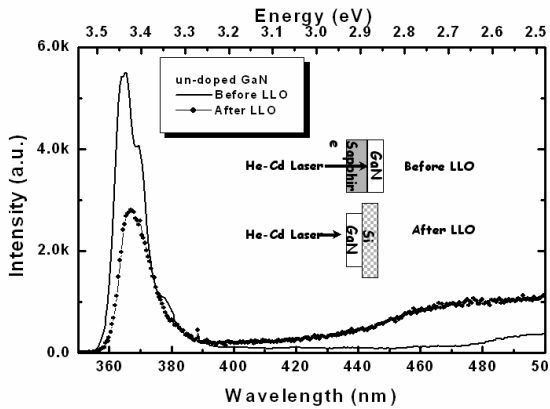

Fig. 15. The PL spectrum of the un-doped GaN before and after LLO.

3. Major Considerations and Approaches for LLO of GaN LEDs

3.1. *Laser energy requirements and modification*

For the fabrication of freestanding GaN-based LEDs, the quality of device thin film for light emitting was very important. Due to the thickness of freestanding GaN LED thin film was only about 4-6 μm, the completed interfacial decomposition was needed to obtain the accomplished device thin film during the lift-off process. For KrF excimer laser, the laser fluence and beam uniformity strongly influenced by the gas mixture. It is not only affected by the initial gas recipe, but also by the evolution of mixture during laser operation due to halogen depletion and production of reaction products. In our experiment, the output laser energy of KrF excimer laser has about ± 2-10 % difference for each laser pulse. Therefore, the laser energy should be added to complete the GaN decomposition in the interface of GaN/sapphire after scanning the entire sample.

For the fabrication of freestanding GaN LEDs, the incident laser fluence was modified to a value of 800 mJ/cm^2, corresponding to a laser

fluence of about 500 mJ/cm^2 at the interface. By simulating the temperature distribution of GaN device thin film irradiated on the GaN surface under an fluence of 0.5 J/cm^2, the temperature decreases rapidly to 100ºC [59] at the depth of about 2 μm suggesting the MQW region of GaN LED will not be affected after laser irradiation.

3.2. *Selection of substrate and bonding metal*

Recently, many groups attempt to try different substrate as the transferred substrate. The transferred substrate should be taken both electrical and thermal conductivities into account. For example, Si[3,50], GaAs, and Cu[60] have been published to be the substrate in the previously reports.

The copper (Cu) metal was selected to be a transferred substrate for the fabrication of GaN-LLO-LEDs due to it has relatively high thermal conductivity compared with other metals. Cu is an available metal, which can also provide a flat plate for device bonding process.

WS Wong *et al*. reported the PdIn3 (as shown in Figure 16) metal bonding process to fabricate the LLO-LEDs.[60] Wuu *et al*. reported conductive glue (as shown in Figure 17) as a low temperature bonding material.[61]

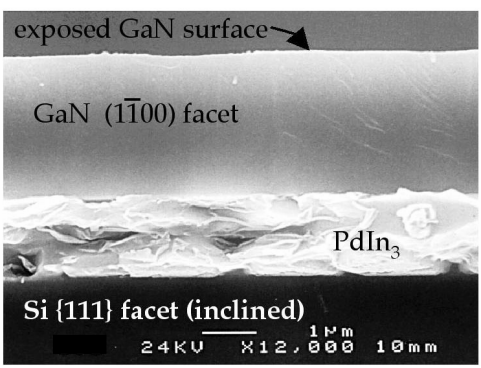

Fig. 16. The TEM of $PdIn_3$ metal bonding (from Wong *et al.*[60], reprinted with permission of the Minerals, Metals & Materials Society)

Nakamura *et al*. reported the characteristics of the MCLED by bonding and LLO technique as shown in figure 18.[62] The bonding is processed by Au-Sn bonding. In our previously report,[63] Indium (In)

metal was used as a bonding metal to fabricate the GaN LLO-LEDs. Indium has relatively soft and low melting temperature (T_m = 156ºC) that can adherent different metals and GaN easily to simplify the fabrication process steps of GaN LLO-LEDs. More recently, we reported a new metal bonding process (Cu-Ni) for fabrication of GaN LLO-LEDs.

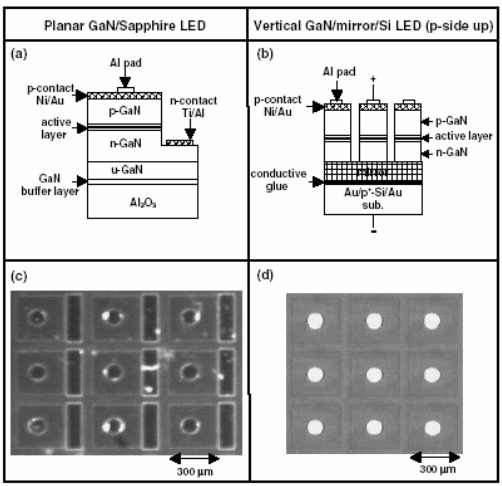

Fig. 17. Device configurations of (a) GaN/sapphire LED with planar electrodes, (b) GaN/mirror/Si LED with vertical electrodes. The corresponding device photographs are shown in (c) and (d), respectively. (from Wuu *et al.*[61], reprinted with permission of the Institute of Pure and Applied Physics).

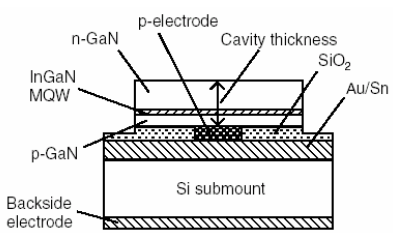

Fig. 18. MCLED fabricated by LLO and Au-Sn metal bonding process (from Fujii *et al.*[62], reprinted with permission of the Institute of Pure and Applied Physics).

The metal phase of Ni is the same as the transferred Cu substrate. Figure 19 shows the Cu-Ni phase diagram. The Cu-Ni solid solution was easily formed at low temperature of about 355ºC which is lower than the p-type GaN contact metallization annealing temperature of 550ºC.

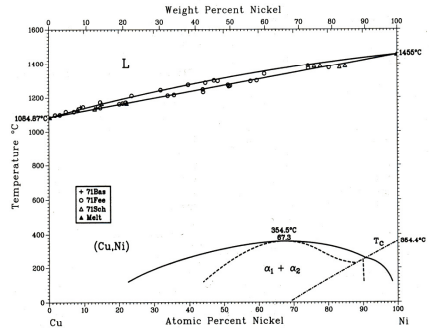

Fig. 19. The Cu-Ni phase diagram.

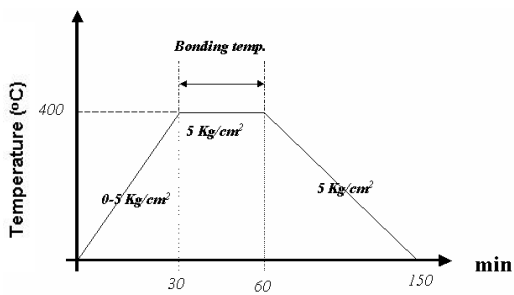

Fig. 20. The processing temperature and bonding pressure versus time.

The Ni-coated GaN LED sample and the receptor of Ni-coated Cu substrate were both immersed and softly mounted together in de-ionized water to prevent particles creating in air. The softly mounted sample was then blown by N_2 gas for drying and subsequently put into a thermal bonder. The thermal bonder has independent top and bottom graphite. Both top and bottom of the bonded graphite were heated and forced. The processing temperature and bonding pressure versus time was plot in Figure 20.

On heating to the processing temperature of 400ºC, the compressive stress on the GaN and Cu samples was increased to be 5Kg/cm^2 and keep this pressure and temperature for metallization in 30 min. Then, lowing down the temperature very slowly and keep the compressive pressure to the room temperature. Figure 21 shows the SEM pictures of the Cu-Ni bonding interface. The shredding force of Cu-Ni bonding was about 4.5×10^7 Pa.

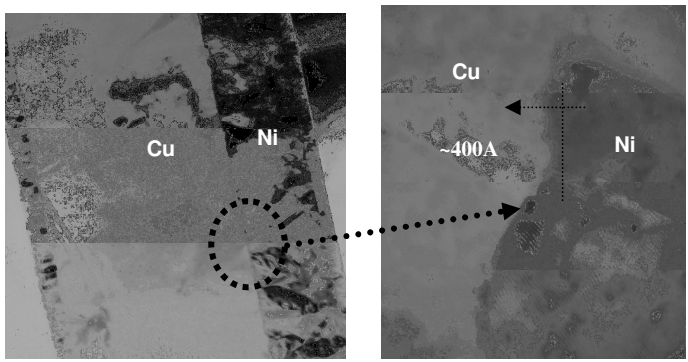

Fig. 21. The SEM pictures of the Cu-Ni bonding interface.

3.3. *Two types of LLO-LEDs configurations*

3.3.1. *P-side up GaN LLO-LEDs*

Figure 22(a) shows the simple scheme of double transfer process for the fabrication of GaN LLO-LEDs with p-side up configuration. The conventional p-side up GaN LEDs on sapphire substrate was first fabricated and then transferred to a supported glass carrier by LLO process. The lift-off film with LED devices was then double transferred to conductive substrate by indium metal bonding. Then, a freestanding p-side up GaN LLO-LEDs on conductive substrate was fabricated.

.

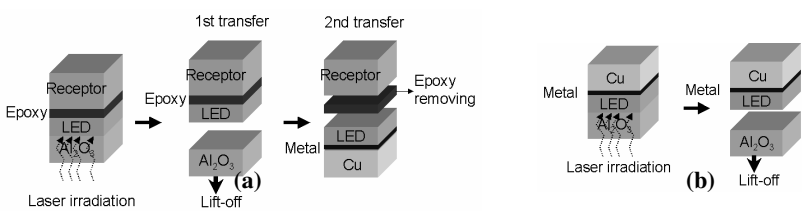

Fig. 22. (a) The simple scheme of double transfer process for fabrication of GaN LLO-LEDs with p-side up configuration. (b) The simple scheme of one transferred process for the fabrication of GaN LLO-LEDs with p-down configuration.

3.3.2. *P-side down GaN LLO-LEDs*

Figure 22(b) shows the simple scheme of one transferred process for the fabrication of GaN LLO-LEDs with p-down configuration. The GaN

LED wafer with p-type metallization on the top of LED wafer was transferred to conductive substrate by LLO process. The GaN LEDs were then fabricated on conductive substrate. Then, a freestanding p-side down GaN LLO-LEDs on conductive substrate was fabricated

4. Fabrication of LLO-LEDs

4.1. *Fabrication of freestanding P-side up GaN LLO-LEDs on conductive cubstrate*

The LED wafer structure was grown by metalorganic chemical vapor deposition (MOCVD) on (0001) sapphire substrate. The LED structure consists of a 25-nm-thick GaN low-temperature buffer layer, a 1.5-μm-thick un-doped u-GaN layer, a 1.5-μm-thick highly conductive n-type GaN layer, a MQW region consisting of five periods u-GaN 2/5-nm-thick InGaN/GaN multiple quantum wells, and a 0.3-μm-thick p-type GaN layer. Conventional GaN LEDs on sapphire were first fabricated. Figure 23 shows the scheme of the conventional LEDs, which has a Ni/Au semitransparent layer and the wire bond p- and n- contact metal. The conventional GaN LEDs on sapphire has the emission area of about 50 % compared to the entire mesa range (300μm × 300 μm). The normal light output power has about 38 mcd at 470 nm under 20 mA.

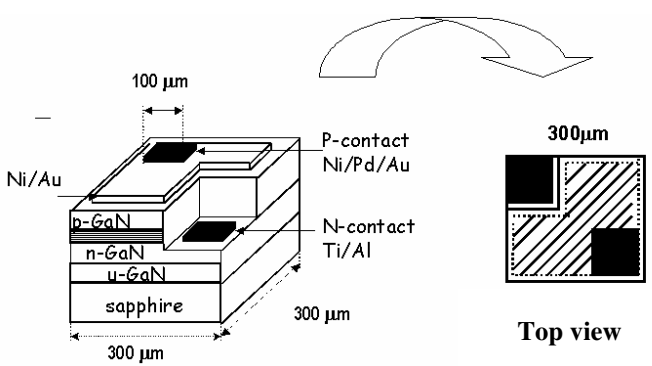

Fig. 23. The scheme of the conventional LEDs.

For fabrication of p-side up LLO-LEDs on Cu substrate, the schematics of the fabrication steps, which involve LEDs fabrication first followed by LLO process and an additional transfer process, are shown in Figures 24 (a)-(h).

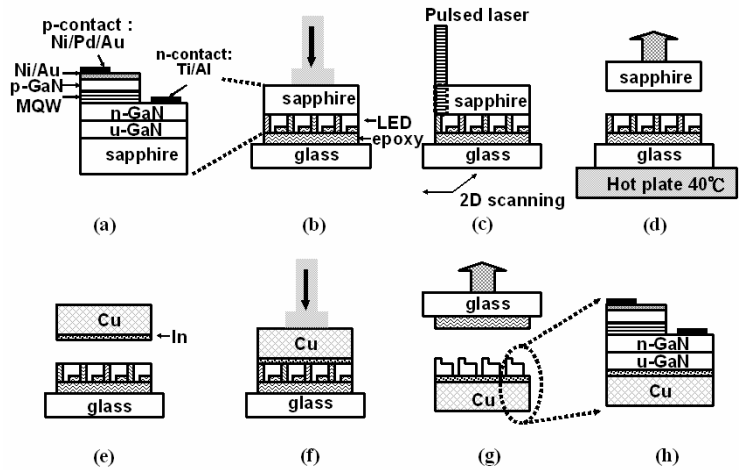

Fig. 24. The schematic diagram of the fabrication steps for the p-side up LLO-LEDs on Cu substrate. (a) The structure of p-side up LEDs on sapphire. (b) First bonding process. (c) Laser processing. (d) Separation. (e) Metal deposition. (f) Second bonding. (g) Epoxy stripping. (h) Freestanding p-side up LLO-LED structure.

The conventional GaN LEDs sample on sapphire with the backside polished was bonded to a supported glass carrier by using cyanoacrylate ester adhesive to form a structure of glass/epoxy/GaN-LEDs/sapphire. The bonded structure was then subjected to the LLO process as described previously and transferred the GaN LEDs from the sapphire substrate to the glass carrier and forming a structure of glass/epoxy/LLO-GaN LEDs.

The lift-off LED structure with u-GaN exposed was then subjected to the double transfer process. The u-GaN layer oflift-off LED thin film was first deposited Al as a reflected metal and then bonded onto an indium-coated Cu substrate forming a structure of glass/epoxy/ GaN-LEDs/Al/In/Cu on the Cu substrate. By dipping the structure into an acetone solution to remove the glass carrier, a freestanding p-side up LLO-LED on Cu was produced.

The normal light output has about 69 mcd at 470 nm under 20 mA, which has about 80% higher than that of the conventional LEDs on sapphire. This result is in agreement with the light enhancement of about 80% by the reflectivity of GaN/Alumni. The similar results were also reported by Dong-Sing Wuu et al. Figure 25[61] showed the normal light output-current-voltage characteristics of the vertical GaN (p-side up) LLO-LEDs by depositing the different reflected metals on the LLO n-GaN surface.

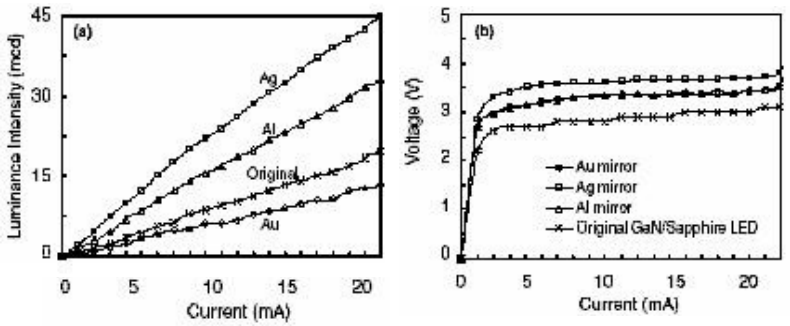

Fig. 25. The L-I-V characteristics of different reflected metals on p-side up vertical GaL LED. (from Wuu *et al*.[61], reprinted with permission of the Institute of Pure and Applied Physics).

4.2. *Fabrication Steps of P-side down LLO-LEDs on Cu*

The fabrication process of the LLO-LEDs on Cu substrate is shown in Figure 26 (a)-(h).

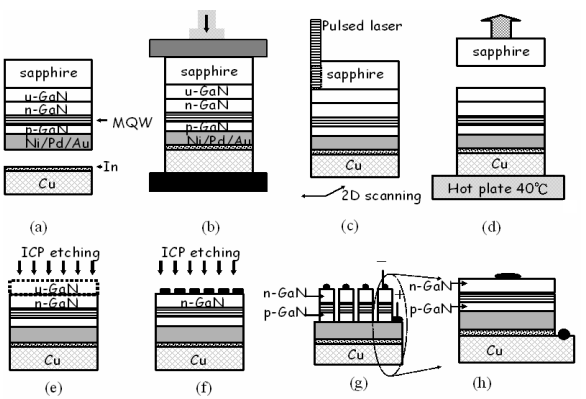

Fig. 26. The schematic diagram of the fabrication process for the LLO-LEDs on Cu substrate. (a) P-type metal deposition. (b) Cu substrate bonding. (c) Laser processing. (d) Separation. (e) Etching of u-GaN layer. (f) 300 μm square mesa formation and device isolation. (g) N-type contact deposition. (h) Freestanding p-side down LLO-LEDs on Cu.

The process involves the LLO of LED wafer process first followed by the fabrication of LEDs on Cu substrate. The GaN LED wafer sample was deposited with the p-contact metallization using Ni/Pd/Au (20nm/20nm/100nm)[68] as p-GaN contact and the backside of sapphire

substrate was polished. Then the sample was annealed in oxygen at 550ºC for 5 minutes first to form the p-type ohmic contact. The sample was then bonded onto an indium-coated Cu substrate at 200ºC to form a structure of sapphire/GaN LED/Ni/Pd/Au/In/Cu. In this process, the Ni/Pd/Au p-type contact is also served as the bonding material without using any other bonding substance. The bonded structure was then subjected to the LLO process as described earlier to form a u-GaN/ n-GaN/MQW/p-GaN structure on Cu substrate. Then the u-GaN was etched away by inductively coupled plasma reactive ion etching (ICP/RIE) to expose the n-GaN layer. The typical rough and uneven surface of the u-GaN after LLO process was also even out by the ICP etching process to form a relatively smooth surface for the n-contact formation. Then, a square mesa of 300 μm × 300 μm was created by ICP/RIE for current isolation purpose. Finally, a Ti/Al with a diameter of 100 μm circular pad was deposited as the n-type contact on the center of square mesa without any other semitransparent contact layer. The completed top and side view of the LLO-LEDs is shown in Figure 27.

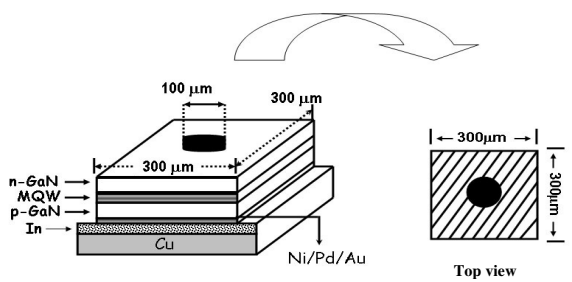

Fig.27. The completed top and side view of the LLO-LEDs on Cu.

It has a low resistivivity n-GaN top layer facilitates better current spreading[69] without the need of an additional semitransparent ohmic contact metallization typical of the conventional LEDs on sapphire substrate. The LLO-LED on Cu has a lager emission area of about 90 % compared to the entire mesa range (300μm × 300 μm).

4.3. *Performance of P-side down LLO-LEDs on Cu*

Figure 28 shows the light output power-current-voltage (*L-I-V*) characteristics under low current continuous wave (CW) operation

conditions for the LLO-LEDs on Cu, and the conventional LEDs on sapphire.

The voltage at 20 mA is about 4.2 V for the conventional LEDs on sapphire and 6.5 V for the LLO-LEDs on Cu. The higher operating voltage of the LLO-LEDs on Cu could be caused by the degradation in the p-contact after the bonding process. Nevertheless, the light output power of the LLO-LEDs on Cu was about 4 times larger than conventional LEDs on sapphire at the operated current of 20 mA. The increase in the output power could be due to several factors. First, the effect light emitting area of the LLO-LEDs on Cu has about 1.8 times larger than that of the conventional LEDs on sapphire. Second, the GaN/Ni interface has higher reflectivity of about 37 %[70-72] at LED wavelength of 470 nm than that of the GaN/sapphire interface of 2 %. The light output has about 34 % enhancement for the LLO-LEDs on Cu.

Third, the LLO-LEDs on Cu with n-side up configuration without semitransparent metal has about 1.6 times higher light output power than that of the conventional GaN LEDs on sapphire due to no light absorption by the semitransparent contact metal. Finally, according to the reported,[70] the GaN LEDs with n-side up configuration tends to have higher light output power compared to the conventional GaN LEDs on sapphire because of no current crowding effect. Furthermore, the LLO-LEDs on Cu require no additional semitransparent metal layers, which simplify the fabrication process.

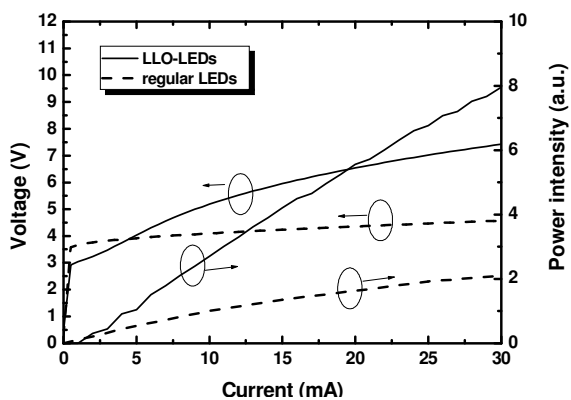

Fig. 28. The light output power-current-voltage (L-I-V) characteristics for the LLO-LEDs and regular LEDeds.

Figure 29 shows the comparison of the *L-I* characteristics for the LLO-LEDs on Cu, and the conventional LEDs on sapphire under high current CW operation conditions.

The light output power of the conventional LEDs on sapphire increased with increasing current up to about 225 mA and saturated around 225 mA and gradually degraded when the operation current exceeds 270 mA. On the other hand, the light output power of the LLO-LEDs on Cu increases with increasing current up to about 225 mA and maintained the same power level after exceeding and still operational up to 400 mA suggesting superior heat dissipation with the Cu substrate and also allowing higher current operation with higher light output.

These results indicate the LLO-LEDs on copper substrate do provide much better heat dissipation capability than the conventional LEDs on sapphire substrate, and allows higher current operation.

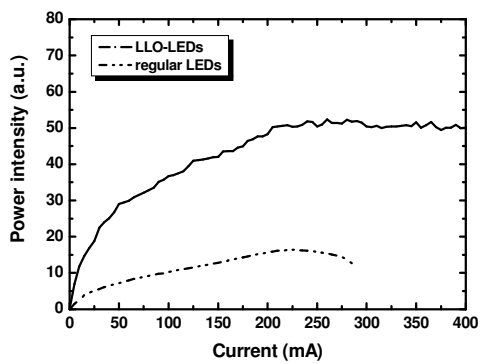

Fig. 29. Comparison of the L-I characteristics for the LLO-LEDs on Cu, and the conventional LEDs on sapphire under high current continuous wave operation conditions.

References

1. M. K. Kelly, O. Ambacher, B. Dahlheimer, G. Groos, R. Dimitrov, H. Angerer, and M. Stutzmann, *Appl. Phys. Lett.* **69**, 1749 (1996).
2. W. S. Wong, T. Sands, N. W. Cheung, M. Kneissl, D. P. Bour, P. Mei, L. T. Romano, and N. M. Johnson, *Appl. Phys. Lett.* **75**, 1360 (1999).
3. W. S. Wong, T. Sands, N. W. Cheung, M. Kneissl, D. P. Bour, P. Mei, L. T. Romano, and N. M. Johnson, *Appl. Phys. Lett.* **77**, 2822 (2000).
4. M. Kneissl, W. S. Wong, D. W. Treat, M. Teepe, N. Miyashita, and N. M. Johnson, *Phys. Stst. Sol. A* **188**, 23 (2001).
5. C. F. Chu, C. C. Yu, H. C. Cheng, C. F. Lin, and S. C. Wang, *Jpn. J. Appl. Phys.* **42**, L417, (2003).

6. J. S. Foresi and T. D. Moustakas, *Appl. Phys. Lett.* **62**, 2859 (1993).
7. M. E. Lin, Z. Ma, F. Y. Huang, Z. F. Fan, L. H. Allen, and H. Morkoc, *Appl.Phys. Lett.* **64**, 1003 (1994).
8. Z. Fan, S. Mohammad, and W. Kim, *Appl. Phys. Lett.* **68**, 1672 (1996).
9. S. Strite and H. Morkoc, *J. Vac. Sci. Technol.* B **10**, 1237 (1992).
10. S. Nakamura, T. Mukai, and M. Senoh, *Jpn. J. Appl. Phys.* **30**, L1998 (1991).
11. C. H. Park and D. J. Chadi, *Phys. Rev. B* **55**, 12995 (1997).
12. C. G. Van De Walle, *Phys. Rev. B* **56**, 10020 (1997).
13. T. Kim, M. C. Yoo, and T. Kim, *Mate. Res. Soc. Symp. Proc.* **449**, 1061 (1997).
14. J. K. Ho, C. S. Jong, C. C. Chiu, C. N. Huang and K. K. Shih, *Appl. Phys. Lett.* **74**, 1275 (1999).
15. Y. Koide, T. Maeda, T. Kawakami, S. Fujita, T. Uemura, N. Shibata, and M. Murakami, *J. Electron. Mater.* **28**, 341 (1999).
16. A. K. Fung, J. E. Borton, M. I. Nathan, J. M. Van Hove, R. Hickman, P. P. Chowand A. M. Wowchak, *J. Electron. Mater.* **28**, 572 (1999).
17. J. K. Kim, J. L. Lee, J. W. Lee, H. E. Shin, Y. J. Park, and T. Kim, *Appl. Phys. Lett.* **73**, 2953 (1998).
18. T. Kim, J. Khim, S.Chae, and T. Kim, *Mater. Res. Soc. Symp. Proc.* **468**, 427 (1997).
19. J. S. Jang, K.H. Park, H. K. Jang, H. G. Kim, and S. J. Park, *J. Vac. Sci. Technol.* B **16**, 3105 (1998).
20. J. S. Jang, I.-S. Chang, H.-K. Kim, T.-Y. Seong, S. Lee, and S. J. Park, *Appl. Phys. Lett.* **74**, 70 (1999).
21. L. Zhou, W. Lanford, A. T. Ping, I. Adesida, J. W. Yang and A. Khan, *Appl. Phys. Lett.* **76**, 3451 (2000).
22. C. F. Chu, C. C. Yu, Y. K. Wang, J. Y. Tsai, F. I. Lai, and S. C .Wang, *Appl. Phys. Lett.* **77**, 3423 (2000).
23. H. W. Jang, K. H. Kim, J. K. Kim, S. W. Hwang, J. J. Yang, K. J. Lee, S. J. Son and J. L. Lee., *Appl. Phys. Lett.* **79**, 1822 (2001).
24. S. Strite, H. Morkoc, *J. Vac. Sci. Technol.* B **10**, 1237 (1992).
25. S.A. Nikishin, N.N. Faleev, V.G. Antipov, S. Francoeur, L. Grave de Peralta, G.A. Seryogin, H. Temkin, T.I. Prokofyeva, M. Holtz, and S.N.G. Chu, *Appl. Phys. Lett.* **75**, 2073 (1999).
26. Chuong A. Tran, A. Osinski, R.F. Karlicek, Jr., I Berishev, *Appl. Phys. Lett.* **75**, 1494 (1999).
27. S. Sriram, G. Augustine, A. Burk, R. Glass, H. Hobogood, P. Orphanos, L. Rowland, T. Smith, C. Brandt, M. Driver, and R. Hopkins, *IEEE Electron. Device Lett.* **17**, 369 (1996).
28. D. L. Barton, M. Osinski, C. J. Helms, N. H. Berg, and B. S. Phillips, *SPIE Int. Soc. Opt. Eng.* **64**, 2694, (1996).
29. M. K. Kelly, O. Ambacher, B. Dahlheimer, G. Groos, R. Dimitrov, H. Angerer and M. Stutzmann, *Appl. Phys. Lett.* **69**, 1749 (1996).
30. A. Yasan, R. McClintock, K. Mayes, S. R. Darvish, H. Zhang, P. Kung, M. Razeghi, S. K. Lee and J. Y. Han, *Appl. Phys. Lett.* **81**, 2151 (2002).
31. T. Mori, T. Kozawa, T. Ohwaki, Y. Taga, S. Nagai, S. Yamasaki, S. Asama, N. Shibita, and M. Koite, *Appl. Phys. Lett.* **69**, 3537 (1996).
32. H. Amano, N. Sawaki, I. Akasaki, and Y. Toyoda, *Jpn. J. Appl. Phys.* **28**, 2112 (1989).

33. S. R. Jeon, Y. H. Song, H. J. Jang, and G. M. Yang, *Appl. Phys. Lett.* **78**, 3265 (2000).
34. X. Guo, and E. F. Schubert, *Appl. Phys. Lett.* **78**, 3337 (2001).
35. X. Guo, and E. F. Schubert, *J. Appl. Phys.* **90**, 4191 (2001).
36. H. Kim, S. J. Park, H. Hwang, N. M. Park, *Appl Phys. Lett.* **81**, 1326, (2002).
37. J. J. Wierer, D. A. Steigerwald, M. R. Krames, J. J. O'Shea, M. J. Ludowise, G. Christenson, Y.-C. Shen, C. Lowery, P. S. Martin, S. Subramanya, W. Götz, N. F. Gardner, R. S. Kern, and S. A. Stockman., *Appl. Phys. Lett.* **78**, 3379 (2001).
38. J. Goldhahn, S. Scheiner, T. Shokhovets, U. K. Frey, D. J. As, and K. Lischka, Appl. Phys. Lett. **76**, 291 (2000).
39. W. J. Tropf and M. E. Thomas in *"Handbook of Optical Constants of Solids*" III Ed. Palik, Academic Press, (1998).
40. M. A. Ordal, R. J. Bell, R. W. Alexander, Jr., L. L. Long, and M. R. Querry, Appl. Opt. **24**, 4493 (1985).
41. P. B. Johnson and R. W. Christy, *Phys. Rev. B* **9**, 5056 (1974).
42. J. J. Wierer, D. A. Steigerwald, M. R. Krames, J. J. O'Shea, M. J. Ludowise, G. Christenson, Y.-C. Shen, C. Lowery, P. S. Martin, S. Subramanya, W. Götz, N. F. Gardner, R. S. Kern, and S. A. Stockman, *Appl. Phys. Lett.* **78**, 3379 (2001).
43. F. Battaglia, and T. F. George, "*Fundamentals in Chemical Physics",* Boston, Mass, Kluwer Academic, (1998).
44. Leonard Migliore, "*Laser Materials Processing",* Markcel Dekker, Inc, (1996).
45. J. F. Muth, J. H. Lee, I. K. Shmagin, R. M. Kolbas H. C. Casey, Jr., B. P. Keller, U. K. Mishra, S. P. DenBaars, *Appl. Phys. Lett.* **71**, 2572 (1997).
46. H. Chen, R.D. Vispute, V. Talyansky, R. Enck, S. B. Ogale, T. Dahmas, S.Choopun, R. P. Sharma, T. Venkatesan, A. A. Iliadis, L. G. Salamanca-Riba, K. A. Jones, *Mater. Res. Soc. Symp. Proc.* **482,** 1015 (1998).
47. K. Osamua, K. Nakajima, Y. Murakami, *Solid State Commun.* **11**, 617 (1972).
48. G. A. Slack, *J. Phys. Chem. Solids* **38**, 330 (1977).
49. Martin Von Allmen and Andreas Blastter, *Laser-Beam Interactions with Materials, Physical Principles and Applications (Second Edition)*, Springer-Verlag, Berlin (1995).
50. W. S. Wong, J. Kruger, Y. Cho, B. P. Linder, E. R. Weber, N. W. Cheung, and T. Sands, *Proceedings of the Symposium on LED for Optoelectronic Applications and the 28th State of the Art Programs on Compound Semiconductors* **98**, 377 (1998).
51. R. Groh, G. Gerey, L. Bartha, and J. I. Pankove, *Phys. Stat. Sol. A* **26**, 353 (1974).
52. C.J. Sun, P. Kung, A. Saxler, H. Ohsato, E. Bigan, and M. Razeghi, *J. Appl. Phys.* **76**, 236 (1994).
53. M. E. Lin, B. N. Sverdlov, and H. Morkoç, *Appl. Phys. Lett.* **63**, 3625 (1993).
54. O. Knacke, O. Kubaschewski, and K. Hesselmann, editors, "*Thermochemical Properties of Inorganic Substances*," Springer Verlag, Berlin (1991).
55. K. Osamua, K. Nakajima, Y. Murakami, *Solid State Commun.* **11**, 617 (1972).
56. G. A. Slack, *J. Phys. Chem. Solids* **38**, 330 (1977).
57. F. Benabid, M. Notcutt, V. Loriette, L. Ju and D. G Blair, *J. Phys. D: Appl. Phys.* **33,** 589 (2000).
58. W. S. Wong, T. Sands, and N. W. Cheung, *Appl. Phys. Lett.* **72**, 599 (1998).
59. Chen-Fu Chu, " Study of GaN Light Emitting Devices Fabricated by Laser Lift-off Technique", PhD dissertation(2003).

60. W. S. Wong, A. B. Wengrow, Y. Cho, A. Salleo, N. J. Quitoriano, N.W. Cheung, and T. Sands, *J. Electron. Mater.* **28**, 1409 (1999).
61. D. S. Wuu, S. C. Hsu, S. H. Huang, C. C. Wu, C. E. Lee and R. H. Horng, *Jpn J. Appl. Phys.* **43**, 5239 (2004).
62. T. Fujii, A. David, C. Schwach, P. M. Pattison, R. Sharma, K. Fujito, T. Margalith, S. P. Denbaars, C. Weisbuch and S. Nakamura, *Jpn J. Appl. Phys.* **43**, L 411 (2004).
63. C. F. Chu, F. I. Lai, J. T. Chu, C. C. Yu, C. F. Lin, H. C. Kuo and S. C. Wang, *J. Appl. Phys.* **95**, 15 (2004).
64. Z. S. Luo, Y. Cho, V. Loryuenyong, T. Sands, N. W. Cheung, and M. C. Yoo, *IEEE Photo. Tech. Lett.* **14**, 1440 (2002).
65. P. Perlin, C. Kisielowski, V. Lota, B. A. Weinstein, L. Mattos, N. A. Shapiro, J. Kruger, E. R. Weber, and J. Yang, *Appl. Phys. Lett.* **73**, 2778 (1998).
66. T. Wang, T. Sugahara, S. Sakai, and J. Orton, *Appl. Phys. Lett.* **74**, 1376 (1999).
67. H. Morkoc, *Nitride Semiconductors and Devices* (Springer Berlin, 1999).
68. C. F. Chu, C. C. Yu, Y. K. Wang, J. Y. Tsai, F. I. Lai, and S. C .Wang, *Appl. Phys. Lett.* **77**, 3423 (2000).
69. S. R. Jeon, Y. H. Song, H. J. Jang, and G. M. Yang, *Appl. Phys. Lett.* **78**, 3265 (2000).
70. J. I. Pankove, "*Optical Processes in Semiconductors*", (New York: Dover, 1975).
71. P. B. Johnson and R. W. Christy, Phys. Rev. B. **9**, 5056 (1974).
72. Palik, "*Handbook of Optical Constants of Solids III' Ed"*. (Academic Press,1998).

This page intentionally left blank

CHAPTER 6

HIGH-RESOLUTION ELECTRON MICROSCOPY OBSERVATIONS OF GAN-BASED LASER DIODES

Makoto Shiojiri*

Kyoto Institute of Technology, Kyoto 606-8585, Japan
E-mail: shiojiri@pc4.so-net.ne.jp

Our recent investigations of InGaN/GaN multiple quantum wells (MQWs) and AlGaN/GaN strained-layer superlattice (SLS) claddings in GaN-based violet laser diodes (LDs) are reviewed. They have been performed by high-angle annular dark-field (HAADF) scanning transmission electron microscopy (STEM) and high-resolution field-emission gun scanning electron microscopy (FEG-SEM). The physics of HAADF-STEM imaging is also interpreted.

1. Introduction

As well-known, the lifetime of light emitting diodes (LEDs) and laser diodes (LDs) with InGaN/GaN multiple quantum wells (MQWs) has exceeded more than 10000 h,[1] which has been achieved by the epitaxial lateral overgrowth (ELOG) of GaN contact layer on the sapphire substrate and the cladding of AlGaN/GaN strained-layer superlattices (SLSs). ELOG greatly reduces the dislocation density in the GaN contact layers and consequently decreases lattice defects in its successive layers.[2,3] For optical confinement, the devices need thick AlGaN cladding layers. The formation of the thick AlGaN layers is, however, impossible because cracks and dislocations are induced by lattice mismatch between the AlGaN and GaN. By using an AlGaN/GaN multilayer architecture, the formation of these defects is suppressed, thus

*Professor Emeritus, Present address: 1-297 Wakiyama, Kyoto 618-0091, Japan.

allowing the growth of thick cladding layers.[1] Additionally, Mg-doped *p*-AlGaN/GaN SLSs have the hole concentration enhanced over 3×10^{18} cm^{-3} at room temperature, which exceeds more than ten times the value available in bulk AlGaN layers.[4,5]

The nanostructures of MQW InGaN/GaN active layers and SLS cladding layers greatly influence the final laser properties. Since the *in-situ* monitoring in the most processing equipment is still absent, atomic-scale analysis is demanded for the understanding of the real structure in the final product, including the thickness and the composition of each layer. High-resolution transmission electron microscopy (HRTEM) has been a very successful analytical method for studying structures of crystals and defects in various materials. Therefore, HRTEM would be expected to be the most powerful tool for characterization of these nanostructures because other existing techniques for determining atomic structure are generally limited in spatial resolution. However, it is very hard to make an atomic structural and compositional analysis of the ultrathin layer materials even by analytical HRTEM. Hence, there have been very few nanostructural investigations of the InGaN/GaN layers and AlGaN/GaN layers. At present, high-angle annular dark-field (HAADF) scanning transmission electron microscopy (STEM) is only a possible technique for the analysis.

HAADF-STEM is a quite new technique, and has been used to analyze lattice defects as well as crystal structures.[6] HAADF-STEM images are sensitive to atomic number and do not give rise to contrast reversal with change in focus and specimen thickness, unlike conventional transmission electron microscopy (CTEM) images. We examined systematically the influence of the optical parameters; the spherical aberration of the probe-forming lens C_s, the defocus Δf, the semi-angle of the probe α,[7,8] and the collection angle range of the annular detector D,[9,10] on the HAADF-STEM images, developing a new scheme for STEM image simulation.[9] We also demonstrated that image artifacts are typical of the influence and may mislead the structure analysis unless one finds them from image simulation.[11,12] Then, we illustrated that atomically resolved HAADF-STEM can provide the structural and compositional information of every atomic column along the incident beam with the aid of image simulation, using As-doped Si wafers[13] and Bi-doped $SrTiO_3$ ceramic condensers.[14]

The HAADF-STEM is said to be incoherent imaging, being completely different from CTEM imaging due to coherent scattering. Therefore, the first part of this paper is devoted to physics to understand HAADF-STEM imaging and interprets *why HAADF-STEM imaging is incoherent.*[15] We take *coherence* and *incoherence,* for that purpose, into reconsideration on the basis of quantum mechanism. Then, we review our HAADF-STEM investigations of GaN-based violet LDs,[16,21] together with our high-resolution field-emission scanning electron microscopy (FEG-SEM) observations.[22,23]

2. HAADF-STEM Imaging

In the text book by Born and Wolf [24] the optical interference and coherence are defined as follows. 'If light from a source is divided by suitable apparatus into two beams which are then superposed, the intensity in the region of superposition is found to vary from point to point. This phenomenon is called *interference*. The superposition of beams of strictly monochromatic light always gives rise to interference. If the two beams originate in the same source, the fluctuations of the amplitude and phase in the two beams are in general correlated, and the beams are said to be completely or partially *coherent* depending on whether the correlation is complete or partial. In beams from different sources, the fluctuations are completely uncorrelated, and the beams are said to be mutually incoherent'. This is typical of the prevailing definitions, but seems to not grasp the inner meaning of the phenomena behind the outward form. We then treat them on the basis of quantum wave optics.[15]

It is a fundamental concept of quantum mechanism that a quantum particle also behaves as a wave. In the well-known Young's experiment, light waves from the two slits interfere with each other to show fringes. The interference also occurs between electron waves elastically scattered by different atoms. According to quantum mechanism, the interference never occurs between waves of different electrons.[25] Thus, the interference takes place only between the waves for 'a single electron' with the same wavelength. The electron is observed in terms of the intensity I, which gives a probability of the existence. The position of the

detected electron does not show its definite place but only indicates one of probable places where it can be captured. For the visualization of the whole probable position of electron we need the detection of many electrons that are described by the same probability wave. These electrons or the waves of these electrons are 'coherent' with each other, and do image a physically valuable intensity distribution (such as interference fringes or diffraction spots) as a result of the cooperation. Tonomura's experiment definitely demonstrated this phenomenon.[26,27] Thus, 'interference' is a term showing the intra-electron relation of waves, while the term of 'coherence' or 'incoherence' would be used for showing the inter-electron relation between the waves that belong to different electrons. In other words, the interference is described as $I_j = |\Phi_j|^2 = |\Sigma_i \phi_{ij}|^2$, where ϕ_{ij} is the wave function of an electron j elastically scattered by the atom i, while the coherence and incoherence are described using total intensity $I_T = \Sigma_j I_j = \Sigma_j |\Phi_j|^2$. The coherence is in the case that $|\Phi_j|^2 = |\Phi|^2$ and then $I_T = n|\Phi|^2$, where n is the number of electrons. It should thereby be noted that the terms coherence and incoherence show, by nature, *the mutual relation between the electrons in a beam rather than the relation between the beams*. The beam composed of coherent electrons may be called a coherent electron beam.

The electrons from the same source are mutually coherent when they are emitted with the same energy. The coherence, incoherence, and partial coherence can be much easily understood if we assume flying classic particles, as illustrated using missile's orbit in Fig. 1.[15] Missiles 1 in Figs 1(a) and 1(b) are coherent with each other since they are launched with the same energy (velocity) from the same pad and hit the same target point, flying in the same orbit. Missile 2 in Fig. 1(c) that is launched from a different pad with the same energy is incoherent with missile 1. It can be said that missile 3 hitting a given target area is partially coherent with missile 1. This is spatial-coherent. Missile 2 in Fig. 1(d) that is launched with different energy from the same pad is incoherent with missile 1. Missile 3 hitting the target area is also partially coherent with missile 1 and is said to be time-coherent. A field-emission gun can supply a high coherent electron beam because it provides the same source at the top of the tip and gives the same energy to the emitting electrons. We can use the term of 'partial coherence' when the

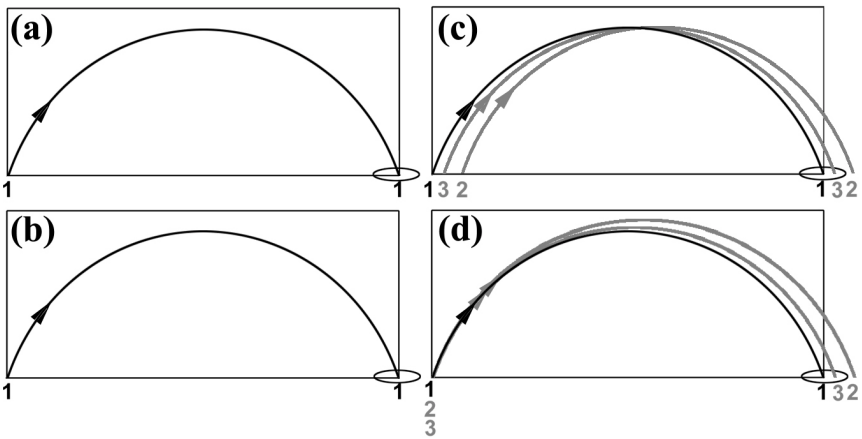

Fig. 1. Coherence, incoherence and partial time- or spatial-coherence of classic particles.[15] Missiles 1 in (a) and (b) are coherent with each other since they are launched with the same energy (velocity) from the same pad and run in the same orbit. Missile 2 in (c) that is launched from a different pad with the same energy is incoherent with missile 1. Missile 3 hitting a given target area is partially spatial-coherent with missile 1. Missile 2 in (d) that is launched with different energy from the same pad is incoherent with missile 1. Missile 3 hitting the target area is partially time-coherent with missile 1.

source position and/or energy of electrons are the same only within a permissible limit given by the Rayleigh criterion, that is, when the spatial coherence and/or the time coherence are not completely but partially satisfied to recognize the interference fringes.

All atoms in the specimen vibrate thermally around their equilibrium positions. The waves of electrons that are elastically scattered by atoms having the same displacement corresponding to their equilibrium positions are completely coherent with each other. Hereafter we call the elastically coherent scattering 'Bragg scattering', which causes Bragg reflections in the crystal. The atoms differently displaced from the equilibrium positions also do elastically scatter electrons. The waves of these electrons are mutually incoherent because of spatial difference of the resources. The frequency of the thermal lattice vibration, which is in the order of 10^{13} Hz, is the fifth power of 10 times as small as a frequency of incident electron wave, ~10^{18} Hz, so that the displacements are observable using the electron beam. The scattering from the displaced atoms, thus, gives diffuse intensity distribution. This is

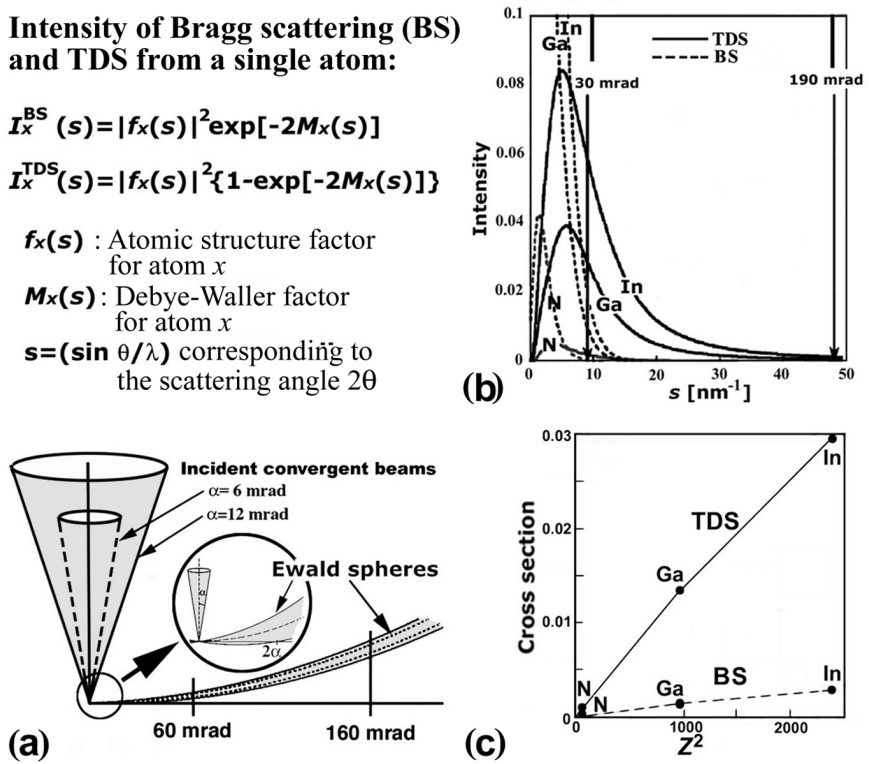

Fig. 2. Intensities of Bragg scattering (BS) and thermal diffuse scattering (TDS) for a single atom. (a) Schematic Ewald sphere construction of HAADF-STEM, indicating the relation between the incident convergent beam and the annular detector.[7,10] The case for the beam probe with semi-angle α=6 or 12 mrad and the collecting range of the detector D = 60 ~160 mrad is indicated. (b) Intensities of Bragg scattering and TDS from single N, Ga and In atoms as a function of scattering angle.[10] (c) Cross section, which is the detection intensity integrated over a detector range of D = 30~190 mrad used in Tecni F30. This shows that TDS is predominant in HAADF-STEM imaging.

'thermal diffuse scattering' (TDS). We assume Einstein model where the atoms moving independently with each other. By taking the mean squared displacement, the Debye-Waller factor was led.[28] Then, the intensities of Bragg scattering and TDS are given by the formulae shown in Fig. 2. Frozen phonon method is another approach, where thermal vibration of atoms is simulated on a computer and then the intensities of Bragg scattering and TDS are numerically deduced by summing up those

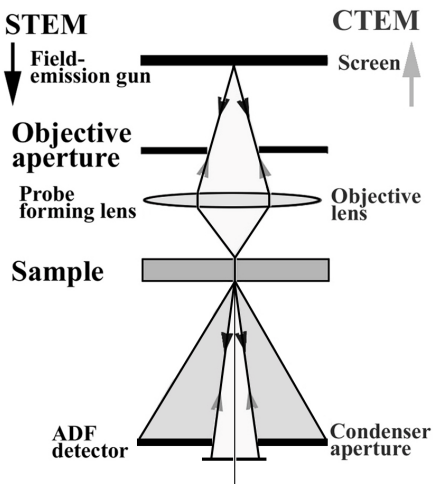

Fig. 3. Ray diagram for STEM and CTEM.[10] The beams run in reverse between STEM and CTEM. Coherent bright field STEM imaging is the same with the CTEM imaging, according to the principle of reciprocity. But HAADF-STEM mainly uses TDS and is completely different in imaging mechanism from CTEM.

intensities at several moments.[29] On the other hand, the incident electrons may be considered to interact inelastically with phonons, which are quantized particles representing the lattice vibration, losing or gaining energy ΔE, during the collision. Since the energy of phonons is in the order of 10^{-1} eV or less (~infrared radiation) and the energy of the incident electrons is 10^{5} eV, ΔE should be negligibly small. Hence, the TDS can be treated as elastic, incoherent scattering, while Bragg scattering is elastic, coherent scattering.

The electron beam runs in reverse between STEM and CTEM modes, as shown in Fig. 3. A STEM image is a focal signal recorded on the detector as a function of the probe position. Bright field (BF) STEM imaging is explained to be equivalent to CTEM imaging in terms of the reciprocity rule (strictly in case of use of an ideal point detector),[30] and it is greatly influenced by the imaging condition; defocus, thickness and so on. The high-angle annual detector was invented to exclude Bragg scattering and eliminate this phase problem.[31] This is seen in Fig. 2a. All the reciprocal points within a scattering angle of 2α in the zero-order

Laue zone (ZOLZ), where α is the semi-angle of probe, are placed on one of Ewald spheres and thereby Bragg reflections take place. In a high angle range, the reciprocal points not only in ZOLZ but also in low higher-order Laue zone (HOLZ) do not cross with any Ewald sphere. Furthermore, the intensity of the Bragg scattering exceedingly reduces with increasing scattering angle as shown in Fig. 2(b), comparing with TDS intensity. Therefore, Bragg reflections scarcely influence HAADF-STEM imaging. TDS is an origin of undesirable background, particularly in a high angle range, in electron diffraction and X-ray diffraction, but it plays the principal part in HAADF-STEM imaging.

In atomically resolved HAADF-STEM images, the contrast of an atom column is obtained as the integrated intensity for exposure, since the atoms in the column vibrate thermally and scatter electrons incoherently as TDS. This is one of the reasons why HAADF-STEM imaging is incoherent, and the contrast may be called 'laterally incoherent'. Another reason of the incoherent imaging is ascribed to scanning of the convergent incident beam. The electrons scattered from an atom column might be different from electrons scattered from different atom columns because time is different. Therefore, the columns laterally separated are incoherently imaged, that is, STEM imaging is transversally incoherent by nature. Thus, HAADF-STEM imaging is both laterally and transversally incoherent.

The contrast of the HAADF-STEM image is given by the sum of the intensity of TDS electrons collected on the detector. We assume that each atom ejects TDS electrons, the number of which depends on the wave field of the incident electrons in the crystal. The cross section for TDS depends on atom species, as shown in Fig. 2(c). The intensity in HAADF-STEM images, hence, depends on the atomic number Z and the number of atoms along atom columns in the specimen. On the basis of this principle, one can write a STEM image simulation program. We have developed a program for BF-STEM and ADF-STEM simulations,[9] whose flowchart and formalism are illustrated in Fig. 4. The algorithm is based on Bethe method using two kinds of optical potentials,[32] and contains calculation programs for the Bragg scattering and TDS. Our scheme reduces drastically the computing time,[10,33] and allows routine works of ADF-STEM image simulation, accordingly.

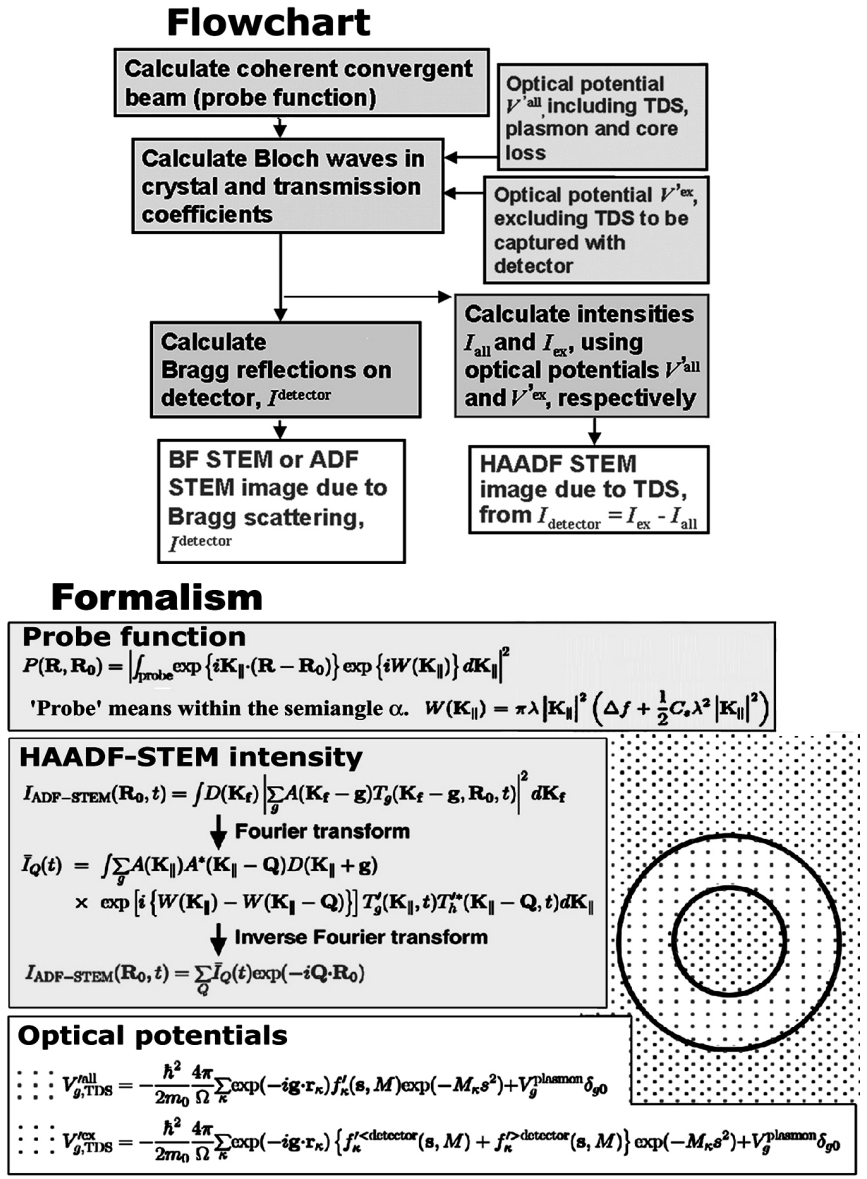

Fig. 4. Flowchart and formulae indicating the algorism of a new scheme for HAADF-STEM image simulation.[10] Details and notations are shown in Ref. 9. A drawing indicates ranges for potentials V'^{all} and V'^{ex} in respct with the detection range enclosed by two circles.

The incident probe influences HAADF-STEM image, more or less. Then, experimental images do not always provide so-called *Z*-dependent contrast images. Sometimes artifact appears in experimental images by the convolution influence of the probe.[11,12] Furthermore, today's field-emission gun scanning transmission electron microscopes still have some instrumental and environmental instability, and experimental images are often deformed, accordingly. We developed deconvolution processing technique for HAADF-STEM images which provides almost real projected atomic structure images with Z-contrast, by reforming the systematic distortion and eliminating the effects of the probe.[33-35] Thus, atomically resolved HAADF-STEM allows a valuable compositional analysis of every atomic column along the incident beam,[13,14,28,33-36] and is the most potential technique for nanostructual analysis. A lens aberration (C_S) corrector is much more effective for HAADF-STEM than for HRTEM, which has a problem that no phase contrast could be obtained in the just-focus image. The improving scanning transmission microscopes in stability and resolution would supply directly atomically resolved *Z*-contrast images using a larger probe semi-angle α, although some problems occur.[7]

3. Structural and Compositional Analysis of MQW InGaN/GaN Layers and Strained AlGaN/GaN Superlattices

We have applied the HAADF-STEM techniques to the nanostructural analysis of the heterostructures, which cannot be achieved by CTEM and HRTEM. By metalorganic vapour phase epitaxy, different MQW layers with various In contents [for example, $In_{0.25}Ga_{0.75}N$(2.5 nm)/GaN(8 nm)] and/or $Al_{0.14}Ga_{0.86}N$(3 nm)/GaN(3 nm) SLS layers were grown directly on an *n*-GaN:Si layer deposited on the (0001) sapphire substrate.[37, 38] The specimens were similar to the prototype wafer of the violet LD structured as shown in Fig. 5(a), which had demonstrated a strong emission peak at about 415.5 nm with two small peaks between 416 nm and 417 nm as shown in Fig. 5(b). In the specimens used in the present experiments, some upper layers were not deposited. The samples for STEM were prepared by mechanical polishing, followed by ion milling.[39] STEM and

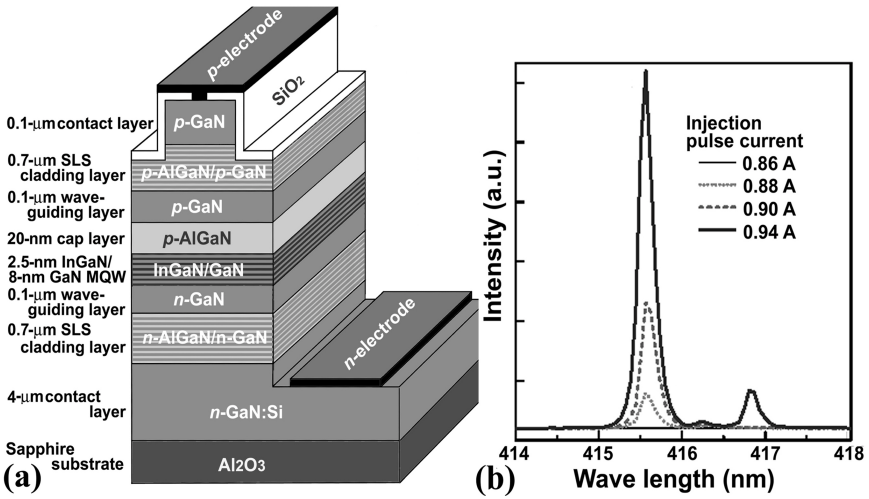

Fig. 5. GaN-based violet laser diode.[37,38] (a) Structure of a standard laser diode which displays the position of MQW InGaN/GaN layer and SLS $Al_{0.14}Ga_{0.86}N$/GaN cladding layers. (b) Room temperature emission spectra of the 10 μm × 1000 μm ride-waveguide laser diode measured under pulsed operation. At the injection pulse current above the threshold current of 870 mA, the strong stimulated emission appears at 415.5 nm with a FWHM of 0.2 nm, together with two small peaks between 416 nm and 417 nm.

HRTEM observations were performed with a Tecnai F30 (for MQW InGaN/GaN) and a JEM 2010F TEM/STEM (for AlGaN/GaN SLS). The Tecnai F30, operated at $V = 300$ keV, was equipped with a lens of $C_S = 1.2$ mm, and all of the HAADF-STEM images were recorded in a detector range of $D = 36$~190 mrad using a convergent electron probe with a semiangle of $\alpha = 26$ mrad. The JEM 2010F TEM/STEM, operated at 200 keV, was equipped with a lens of $C_S = 0.48$ mm, and the HAADF-STEM images were recorded with $\alpha = 10$ mrad and $D = 100$~220 mrad. HRTEM image simulations were made in a conventional multislice program, while HAADF-STEM image simulations were made using a scheme developed by Watanabe *et al*.[9] FEG-SEM observations were performed with a Hitachi S-5200, which was employed to the secondary electron mapping as well as the backscattered electron mapping. It is capable of reolving 1.8 nm at 1 keV and 0.5 nm at 30 keV.

3.1. *MQW InGaN/GaN layers*

We first observed MQW $In_{0.2}Ga_{0.8}N$ (2.5 nm) /GaN (8 nm) active layers by HAADF-STEM. As seen in HAADF-STEM images in Figs 6(a) and 6(b), the $In_{0.2}Ga_{0.8}N$ layers appear as bright bands while the GaN layers appear as dark bands, which were confirmed by energy dispersive X-ray spectroscopy (EDS) nanoanalysis in Fig. 6(c).[16] This is caused by the high TDS cross-section of In atoms shown in Fig. 2(c). Figure 7 shows

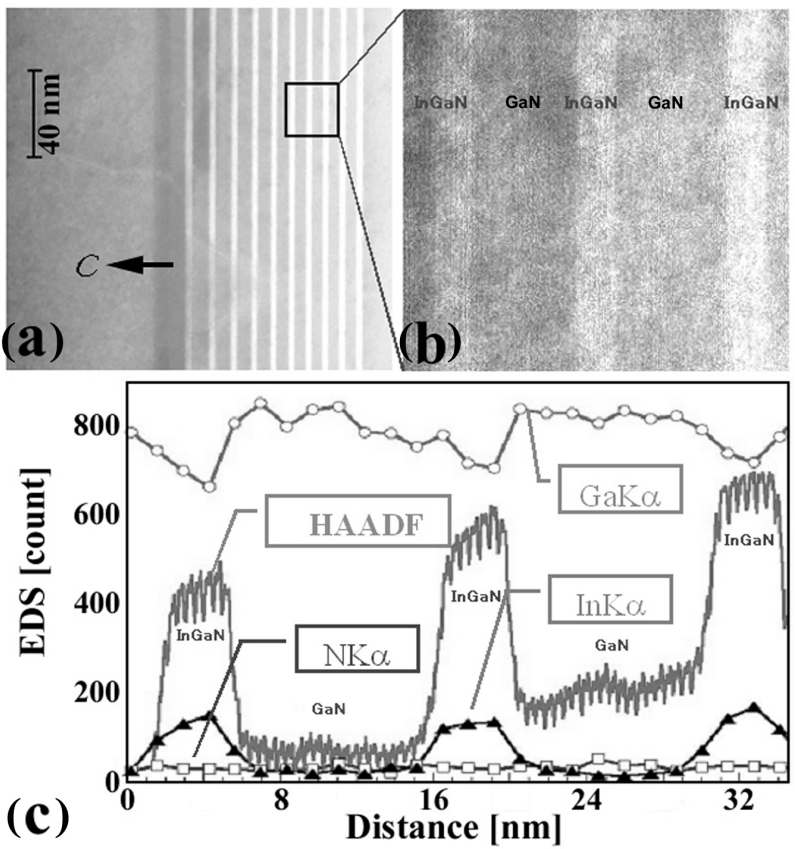

Fig. 6. (a) Low-magnification cross-sectional HAADF-STEM image of the MQW active region. (b) Enlarged image of the area enclosed by square in (a). (c) EDS intensity profiles of Ga-Ka, In-Ka and N-Ka and HAADF-STEM image contrast profile on the same line, which show that InGaN layers appear as bright bands and GaN layers as dark bands in the HAAD-STEM image.[16]

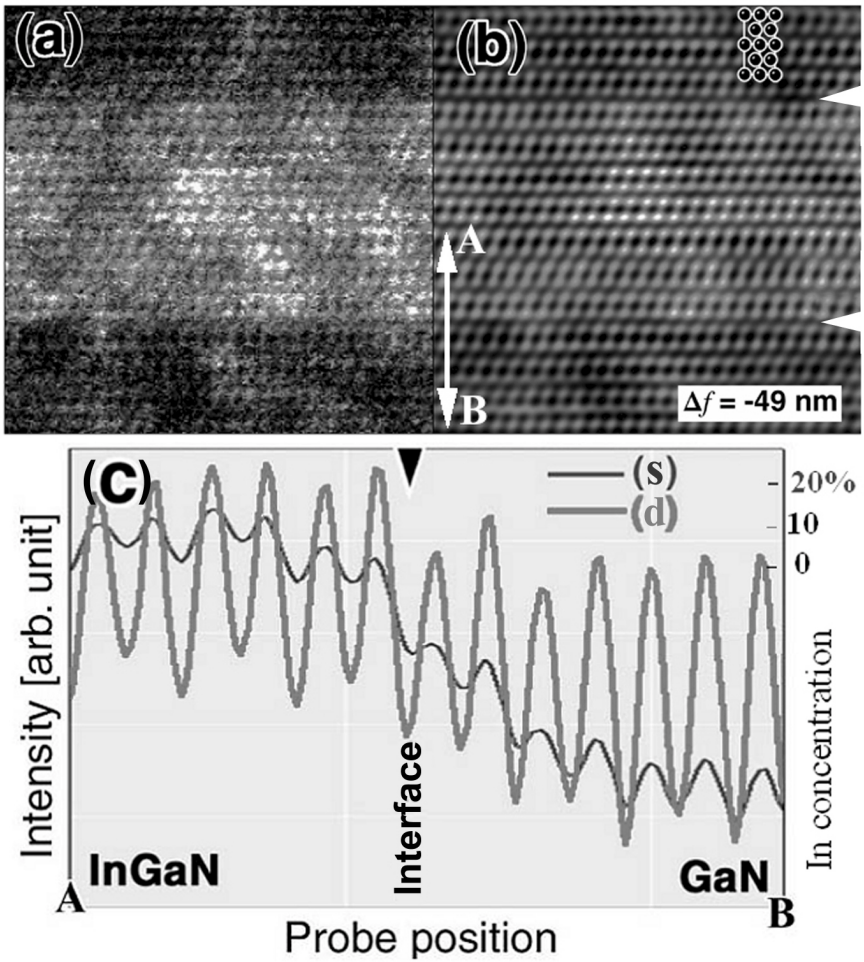

Fig. 7. High-resolution HAADF-STEM images of InGaN/GaN MQW. (a) Experimental image. (b) Deconvoluted image of (a), inserting [1210] projection of the GaN crystal. The defocus of the probe-forming lens was evaluated to be Δf = -49 nm in the deconvolution processing. Arrow heads indicate the interfaces between GaN and InGaN layers. (c) Intensity profiles in the image processed by a simple noise-filtering **s** and in the deconvoluted image **d**, along A = B. The interface between InGaN and GaN layers is distinguished by intensity profile in deconvoluted image.

that a high-resolution HAADF-STEM image, processed by a de-convolution method,[34] defines clearly the interface between the InGaN and GaN layers at atomic scale.[16]

Threading defects or dislocations, which were formed by large lattice mismatch between the GaN:Si and sapphire substrate, appear as bright lines along the *c* axis in Fig. 8(a). The random static atomic displacements around dislocation cores give rise to diffuse scattering of electrons, similar to the thermal diffuse scattering which is caused by thermally agitated random displacements of atoms, and consequently cause strong intensity in HAADF-STEM images.[6] Hence, the bright contour lines indicate the exact position of the dislocations, unlike diffraction contrast dislocation images in CTEM.

V-defects or inverted hexagonal pyramid (IHP) defects can be seen in Fig. 8(a).[17] The apex of the V-defect corresponds to the position at which a threading dislocation crosses an $In_{0.2}Ga_{0.8}N$ QW (in most cases in the first one). The names originate from the fact that empty pyramidal pits, with hexagonal openings at the growth surface and sidewalls parallel to $\{10\bar{1}1\}$ planes, are formed during the MQW growth.[40] These are subsequently filled during growth of the *p*-type GaN capping layer to form an IHP.[41] Two different structural models were proposed for the $\{10\bar{1}1\}$ sidewalls of the IHPs; one is that the sidewalls include thin InGaN/GaN layers,[42] the other is that the InGaN QWs end abruptly at the surfaces of the pits and these are then filled by the GaN capping layer with no InGaN/GaN sidewall layers.[40,41,43] This fundamental issue had not been resolved before our observations[17,20,22] because it was very hard to perform an atomic-scale structural or compositional analysis of such ultra-thin layers even by conventional analytical HRTEM.

Figure 8(b) shows an enlarged image of the V-defect in Fig. 8(a), wherein several inclined brighter stripes can be seen, especially on the left-hand side of the V. These thin stripes terminate on horizontal InGaN QWs, successively decreasing the number of the sidewall stripes with increasing height in the V. The apical angle of the V is approximately 56°, which corresponds to the angle between the $(10\bar{1}1)$ and $(\bar{1}011)$ planes. Thus, the thin bright stripes on the sidewalls would be InGaN layers on $(10\bar{1}1)$ and $(\bar{1}011)$ planes. This result supports the structural model proposed by Wu *et al.*,[42] in which the V-defect includes the buried sidewall QWs on the $\{10\bar{1}1\}$ planes and the open hexagonal inverted pyramid that is defined by the six $\{10\bar{1}1\}$ planes and filled with capping

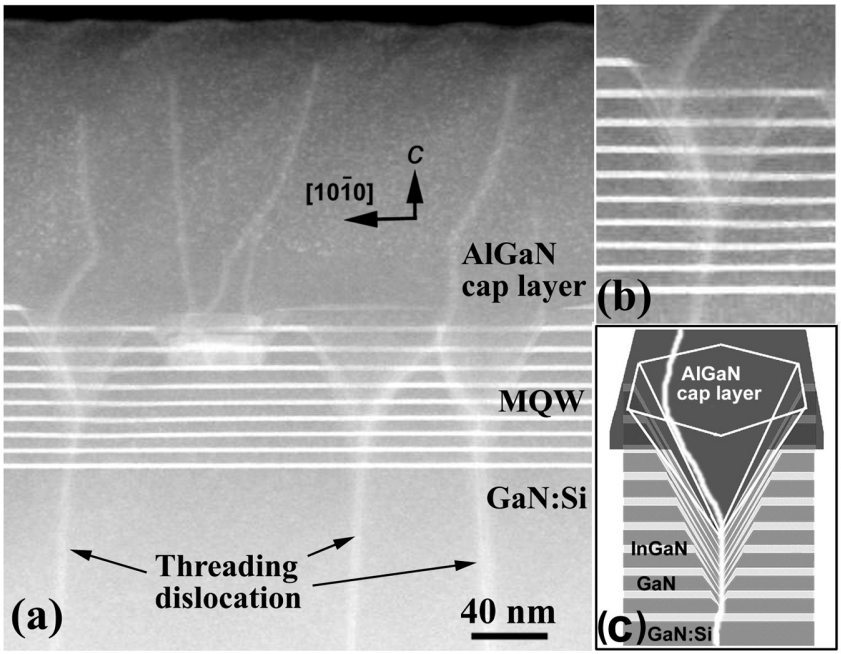

Fig. 8. (a) Cross-sectional low magnified HAADF-STEM image of capped MQW $In_{0.2}Ga_{0.8}N$ (2.5 nm)/GaN (8 nm) layers, taken in the [1$\bar{2}$10] axis.[20] Ten bright stripes parallel to the basal plane are InGaN layers. Threading dislocations appear as bright lines along the [0001] axis. *V*-defects nucleate at the dilocations in the first InGaN layer. (b) Enlarged image of the *V*-defect on the left side in (a). The *V*-defect grew in the form of a thin six-walled structure with InGaN/GaN {10$\bar{1}$1} layers. (c) Schematical representation of the structure of the *V*-defect.

matrix afterward. The structure of the V-defect is illustrated in Fig. 8(c), showing six symmetric {10 $\bar{1}$ 1} planes with thin QWs and the incorporated dislocation. Hence, the *Z*-contrast in the HAADF-STEM image gave the definitive evidence for the sidewall QWs of the V-defect, although Wu *et al*.[42] had not indicated any persuasive microscopy image. Thus, we concluded that these side-wall InGaN/GaN QWs are an origin of undesirable long-wavelength small emissions like the emissions between 416 nm and 417 nm caused in the 415-nm LD shown in Fig. 5(b). Figure 8 also shows that the threading dislocation propagates to the free surface through the V-defect, which was reported by Wu *et al.*[42] and Sharma *et al.*[41]

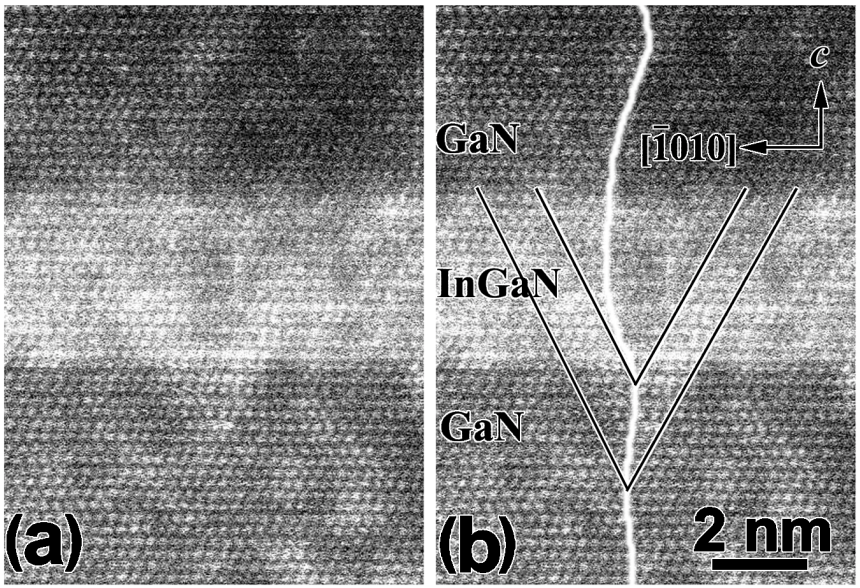

Fig. 9. (a) High-resolution HAADF-STEM image of an $In_{0.2}Ga_{0.8}N$ QW between the GaN barrier layers, taken in the [1210] axis at around Scherzer focus. (b) The same image with lines added to indicate the positions of the sidewall QWs on the (10$\bar{1}$1) and ($\bar{1}$011) planes in the V-defect, and the incorporated dislocation.[20]

Figure 9(a) shows an atomically resolved HAADF-STEM image of an $In_{0.2}Ga_{0.8}N$ QW between the GaN barrier layers in the same sample.[20] The $In_{0.2}Ga_{0.8}N$ QW exhibits strong intensity, showing distinctly the difference in composition from the GaN. In spite of the noise in this image we can see the brighter sidewall QWs on the (10$\bar{1}$1) and ($\bar{1}$011) planes and the darker inside of the V-defect as compared with the matrix QW, and these are indicated in Fig. 9(b). Away from this V-defect, Fig 9(a) shows that the QW lattice was apparently coherent with the GaN barrier lattice. That is, the lattice in the $In_{0.2}Ga_{0.8}N$ QW as thin as a few nanometers (in this case the nominal thickness was 2.5 nm but the thickness estimated from the image was approximately 3.6 nm which is corresponding to 14 monolayers) was strained to match the GaN lattice on the (0001) interfaces. Complementarily the $In_{0.2}Ga_{0.8}N$ lattice was, as a whole, extended along the *c*-axis. In addition, there was local fluctuation of expansion, which corresponded to local fluctuation of In

atom in the $In_{0.2}Ga_{0.8}N$ QW, as mentioned later.[18] The In-rich regions, considered as quantum dots, caused large expansion along the [0001] direction.

On the basis of these observations, we explained the formation of the V-defects by analogy with the epitaxial lateral overgrowth (ELOG).[20] The GaN:Si underlying layer in our sample was deposited at a high reactor temperature of 1150°C, at which the layer might grow layer by layer keeping the smooth (0001) surface, as reported by Hiramatsu *et al*.[44] To suppress re-evaporation of In, the multiple InGaN/GaN QW layers were deposited at a reactor temperature as low as 820~850°C; for which the poor surface diffusion of Ga atoms, and particularly In atoms, might impede the layer-by-layer growth. If any mask were placed on the underlying GaN:Si surface, the MQW InGaN/GaN layers would grow with the $\{10\bar{1}1\}$ facets, similar to GaN crystals formed by ELOG at the same temperature.[44] Indium atoms, as a foreign element, play an important part in the formation of the V-defect, making the small mask (the nucleus of the V-defect) by trap and segregation in the strained field (or Cottrell atmosphere) around the core of a threading dislocation. The mask hinders Ga atoms from migrating on the (0001) layer to make a smooth monolayer, and then causes the termination on the six $\{10\bar{1}1\}$ planes of the InGaN and GaN layers successively grown, which become to the side-walls of the forming V-shape pit. During successive MOVPE the layer growth also occurs on the new surfaces of the six $\{10\bar{1}1\}$ sidewalls, although the growth rate is slower compared with the (0001) face, and consequently the thin sidewall InGaN and GaN layers are formed. The unburied V-pit is filled with the capping layer material deposited at the high temperature of 1150°C, whose lattice is connected on the $\{10\bar{1}1\}$ interface, coherently with the lattice of thin InGaN or GaN layers [see Figs 8(c) and 9]. When the materials in V-defect are buried with the coherent lattice relation to the matrix InGaN/GaN QWs, the incorporated dislocation appears as the survivor within the V-defect and is taken over in the upper layer. We previously found that V-defects start even at In-rich dots in the QW,[17] and also found that the In-rich regions correspond with lattice expansion along the *c* axis.[18] The wide In-rich region might behave the masking effect. In this formation mechanism, In atoms help the nucleation of V-defect, which is consistent with the idea

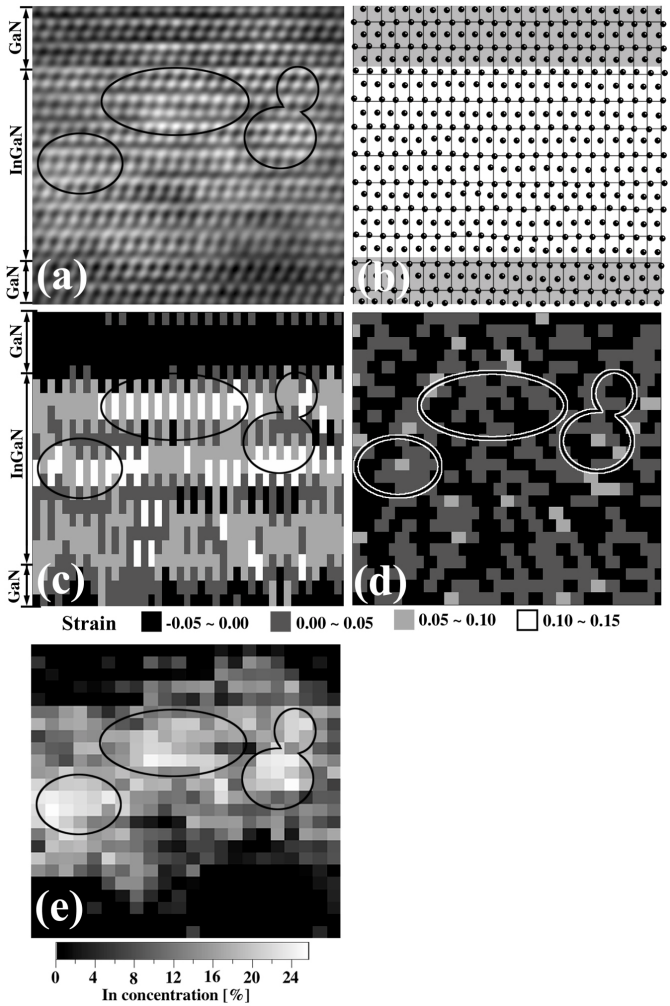

Fig. 10. **(**a**)** Experimental deconvolution-processed high-resolution HAADF-STEM image of the MQW $In_{0.25}Ga_{0.75}N$ (2.5 nm)/GaN (13.9 nm) layers.[18] The defocus of the probe-forming lens was evaluated to be Δf = –44 nm using the maximum_entropy method in deconvolution process. Bright dots are Ga(In) columns along the [1210] axis. (b**)** Projected atomic column positions derived from (a). (c) Strain field maps along the [0001] axis evaluated from (b). (d) Strain field maps along the [1010] axis evaluated from (b). The distortion hardly occurred along the [1010] direction. (e**)** Two-dimensional In atom distribution evaluated from the intensity in (a). There is local fluctuation of In atoms in the InGaN layers, and the In-rich regions enclosed by circles, considered as quantum dots, cause large expansion only along the [0001] axis.

by Wu *et al.*[42] and Chen *et al.*,[40] but the formation of the six $\{10\bar{1}1\}$ sidewalls is ascribed to the growth kinetics of the GaN crystal, independently of the presence of In atoms. In fact we have detected no V-defects in a cladding layer of a strained $Al_{0.14}Ga_{0.86}N$(3 nm) and GaN (3 nm) superlattice grown at 1150°C on the GaN:Si underlying layer, although we have observed threading dislocations, as shown in the next section.

Figure 10(a), which is a HAADF-STEM image processed by two-dimensional smoothing and deconvolution, provides the precise position of the atom columns (Fig. 10(b)) and the clearly *Z*-dependent contrast (Fig. 10(e)), thereby allowing us to map both the strain field and In atom distributions in successive GaN and InGaN layers.[18] As a rule, the lattice expanded largely along the *c* axis as seen in Fig. 10(c) but hardly along the $[10\bar{1}0]$ direction (Fig. 10(d)), in the $In_{0.2}Ga_{0.8}N$ layers. We concluded from Figs 10(c) and 10(e) that there is a local fluctuation of In atoms in the InGaN layers and the In-rich regions, considered as quantum dots, cause large lattice expansion only along the [0001] direction. Before our observation, Gerthen *et al.*[45] and Ruterana *et al.*[46] had reported In-concentration maps in ultrathin InGaN layers using strain distribution extracted from HRTEM images, wherein the linear dependence of the strain on In composition was employed simply assuming the Vegard law approximation. Kisielowski *et al.*[47] had also shown a similar map obtained from the variation of crystal potential in an HRTEM image, assuming that In concentration in the center of an ultrathin layer is the intended In content. In any case, these concentration maps were only indirectly deduced.

We also observed the MQW active layer by FEG-SEM.[22] MQW $In_{0.25}Ga_{0.75}N$ (2.5 nm) and GaN (13.9 nm) layers were resolved in a secondary electron image (Fig. 11(a)) and a backscattered electron image (Fig. 6(b)). The backscattered electron image, giving compositional mapping without surface effects such as cleaved steps, distinguishes definitely between the two layers. The image reproduced the *V*-defects and confirmed the thin six-walled structure with InGaN/GaN $\{10\bar{1}1\}$ layers.[20,22] The merit of the SEM observations is in the very simple specimen preparation that is just cleaving the sapphire substrate with the upper epilayers.

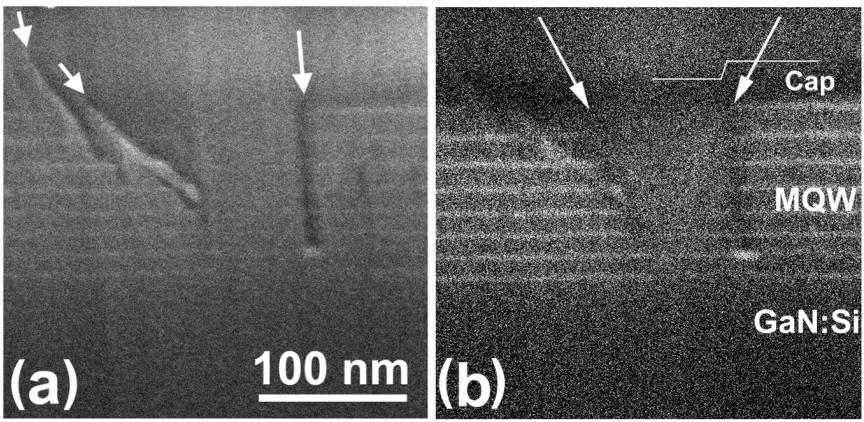

Fig. 11. FEG-SEM images of a capped multiple MQW $In_{0.25}Ga_{0.75}N$ (2.5 nm)/GaN (13.9 nm) QW layer grown on the GaN:Si underlying layer, obtained with the beam direction parallel to [1210].[20,22] (a) Secondary electron image. Arrowheads indicate the position of surface defects, which were caused by cleaving the sample wafer to prepare the SEM specimen. (b) Back scattering electron image.Arrowheads indicate a V-defect. These two images were taken at an accelerating voltage of 10 kV.

3.2. *Strained AlGaN/GaN superlattices*

The nanostructure of the SLS cladding greatly influences the final laser properties. However, there have been very few structural investigations of the SLS AlGaN/GaN cladding. Bremser *et al.*[48] and Pecz *et al.*[49] used TEM to observe $Al_{0.2}Ga_{0.8}N$/GaN and $Al_{0.06}Ga_{0.94}N$/GaN layers. The layers could be observed in the diffraction contrast caused by small strain fields along their interfaces. However, it was impossible to identify the AlGaN and GaN layers in the images or to evaluate their exact thickness. The InGaN and GaN layers in the MQW active layer were resolved in HRTEM images.[20,45–47,50] However, the AlGaN and GaN layers in the SLS cladding could never be distinguished in HRTEM images, as seen in Fig.12(a), since Al incorporation on Ga sites in the AlGaN introduced only minimal phase shift.[21] The cross correlation factors between the $Al_{0.14}Ga_{0.86}N$ and GaN images are 96% for Δf=0 and 98%~99% for other defoci. If HAADF-STEM contrast is described as the *Z*-contrast proportional to the square of the atomic number, the intensity ratio of the N column to the Ga(Al) column in the $Al_{0.14}Ga_{0.86}N$ and to the Ga

column in the GaN would be 5:82:100. In the HAADF-STEM images the Ga columns appear bright, whilst the N columns are dark, just above the noise level [Fig. 12(b)]. According to the low thermal diffuse scattering cross-section of Al atoms, the intensity of $Al_{0.14}Ga_{0.86}$ columns is weaker than that of Ga columns in the corresponding images.

First, we performed FEG-SEM observations of the SLS cladding layer,[23] using the *n*-$Al_{0.14}Ga_{0.86}N$ (3 nm)/*n*-GaN (3nm) layers. With the aid of image processing, the AlGaN and GaN layers were definitely

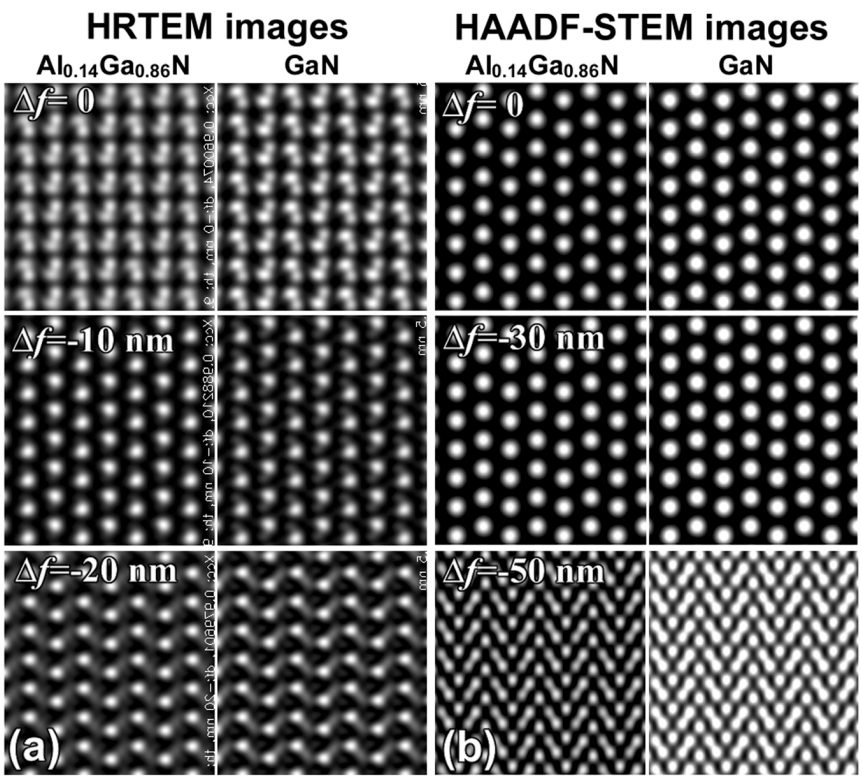

Fig. 12. Image simulations of the $[1\bar{2}\bar{1}0]$-oriented $Al_{0.14}Ga_{0.86}N$ and GaN crystals, using the optical parameters of JEOL-2010F TEM/STEM. (a) HRTEM images of the crystals 30 nm thick calculated at different defoci Δf. No difference can be distinguished between the $Al_{0.14}Ga_{0.86}N$ and GaN. (b) Atomic resolved HAADF-STEM images of the same crystals at different Δf. The difference in the absolute intensities between the two compositions is observable.

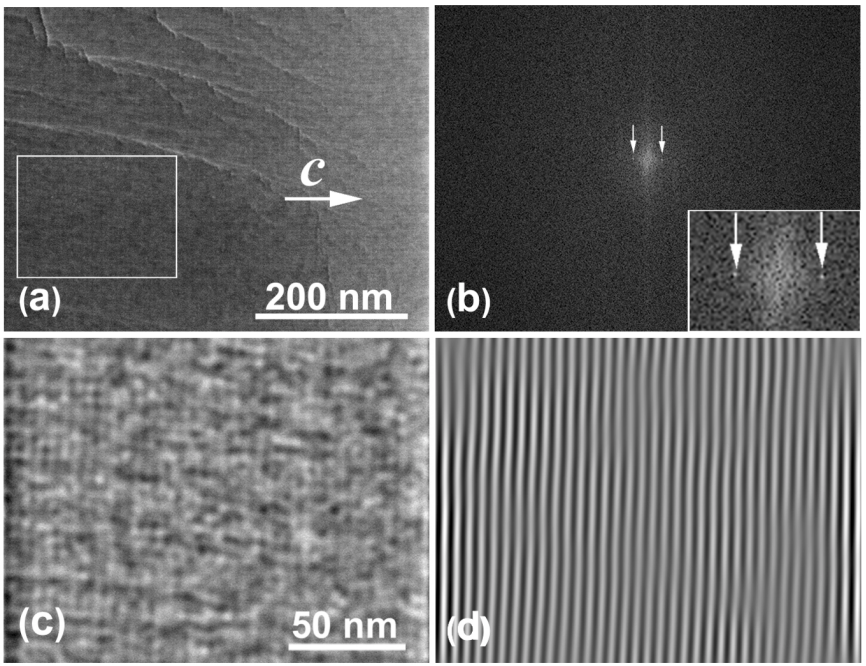

Fig. 13. FEG-SEM image of SLS *n*-$Al_{0.14}Ga_{0.86}N$ (3 nm)/*n*-GaN (3 nm) layers. The specimen for SEM was simply prepared by cleaving the sapphire substrate with the upper epilayers.[23] (a) Original secondary electron image, taken at V=10.0 keV. (b) Computer diffractogram of the area in (a) with its enlarged central part in the inset. (c) High and low pass band noise-filtered image reconstructed from the diffractogram (b). Bright and dark fringes with a spacing of about 3 nm correspond to the *n*-$Al_{0.14}Ga_{0.86}N$ and *n*-GaN layers, respectively. (d) Image reconstructed using the diffraction spots indicated by arrowheads in (b), with the contrast of superlattices enhanced and the surface structure suppressed.

resolved as bright and dark fringes in the mapping of secondary electrons, as shown in Fig. 13. The back-scattered electron images, however, undistinguished between the $Al_{0.14}Ga_{0.86}N$ and GaN layers, because the mass difference between $Al_{0.14}Ga_{0.86}N$ and GaN is too small to identify them in the bulk specimen. The secondary emission yield greatly depends on the surface state of materials so that the *n*-$Al_{0.14}Ga_{0.86}N$ and *n*-GaN layers might be distinguishable with each other in the secondary electron images. We also observed *p*-$Al_{0.14}Ga_{0.86}N$/*p*-GaN SLS cladding layer at the same imaging conditions. However, the

contrast fringes were detected neither in the secondary electron images nor in the backscattered images. Difference in the secondary emission yields seems to be very small between *p*-$Al_{0.14}Ga_{0.86}N$ and *p*-GaN.

Then, we observed the same sample with the TEM/STEM. Figs 14(a) and 14(b) are experimental HRTEM and HAADF-STEM images of the $Al_{0.14}Ga_{0.86}N$ and GaN layers in the SLS cladding.[21] The images were processed by a noise-filtering method, which was done on the images using Bragg mask in the fast Fourier transform (FFT) images. The calculated images that correspond to the experimental images are also shown in Fig. 14. It is impossible to distinguish between the two layers in Fig. 14(a). In Fig.14(b) it is still hard but possible to do so by identifying them from the low magnification HAADF-STEM image, as shown later.

A BF-STEM image in Fig. 15(a) indicates the whole structure of the sample.[19,21] Figure 15(b) shows a HAADF-STEM image of the SLS cladding layer, where about 2×200 individual $Al_{0.14}Ga_{0.86}N$ and GaN layers are clearly resolved. The $Al_{0.14}Ga_{0.86}N$ layers were identified as dark bands while the GaN were identified as bright bands. This difference in intensity was readily confirmed by the calculation shown in Fig. 12(b). In the corresponding BF-STEM image, shown in Fig. 15(c), the $Al_{0.14}Ga_{0.86}N$ and GaN layers are also visible as faint bright and dark bands as a result of both, the coherent phase effect and some incoherent scattering. Dislocations appear as strong dark contours by diffraction contrast in the BF-STEM image. Figs 15(d) and 15(e) are a BF-STEM and a HAADF-STEM images of the area enclosed by the rectangle in Fig. 15(a), respectively. The dislocations either parallel or perpendicular to the *c* axis are clearly detected in the HAADF-STERM image in Fig. 15(e). They appeared as bright lines, indicating the areas just having random static atomic displacements around the dislocations. Therefore, the HAADF-STEM image indicated very exactly the position of the dislocation. It was also found that dislocations reverted from running along the *c* direction to lying in the basal plane. The converted dislocations would not reach the upper MQW layer. This evidently shows a role of the SLS of suppressing the defect propagation, which results in the overall reduction of the structural defects in the active MQW layer.

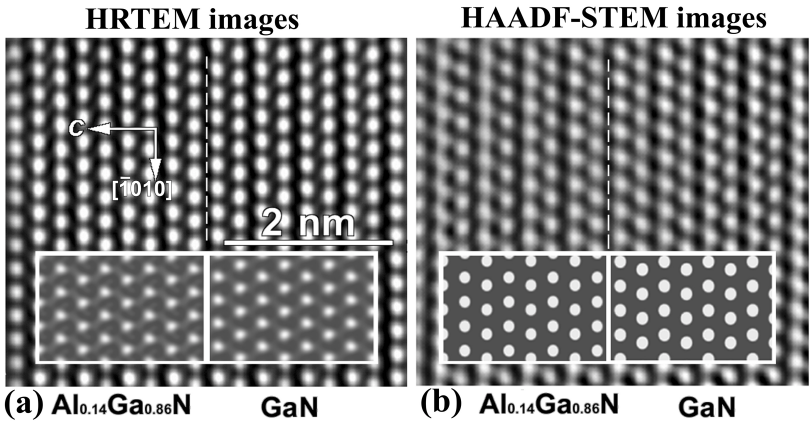

Fig. 14. High-resolution images of $Al_{0.14}Ga_{0.86}N$ and GaN layers in the SLS cladding.[21] Experimental imaged were processed by noise-filtering.[21] (a) HRTEM image. Calculated images of $Al_{0.14}Ga_{0.86}N$ and GaN crystals 30 nm thick at $\Delta f = -15$ nm are inset. (b) HAADF-STEM image. Calculated images of the crystals at $\Delta f = -20$ nm are inset. The dotted lines indicate the interface between the $Al_{0.14}Ga_{0.86}N$ and GaN layers.

Semi-quantitative EDS analysis was performed in areas **A**-**D** in Fig. 15(e). The results are shown in Table 1. As seen in Fig. 15(f), if the analyzed area includes the same number of $Al_{0.14}Ga_{0.86}N$ and GaN layers, the average composition in the area should be $(Al_{0.035}Ga_{0.465})N_{0.5}$. The measured Al concentration in the SLS matrix areas **B** and **D** was 3.5 ± 0.1 %, which confirmed the composition of the $Al_{0.14}Ga_{0.86}N$, accordingly. Somewhat higher Al concentration was measured in the areas **A** and **C**, where the EDS spectra were acquired from dislocations parallel to the *c* direction and in the basal plane, which suggested precipitation of Al atoms around the dislocations in the SLS.

With the aid of image processing shown in Fig. 16, the averaged thicknesses of the $Al_{0.14}Ga_{0.86}N$ and GaN layers in the *n*-SLS were determined to be 2.24 ± 0.09 nm and 2.34 ± 0.15 nm, respectively, which correspond to nine atomic planes in the *c* direction. The lattice parameters of the $Al_{0.14}Ga_{0.86}N$ and GaN crystals were evaluated from these values and HRTEM and HAADF-STEM images as shown in Fig. 14, and are indicated in Table 2, together with that of the pure GaN crystal. The $Al_{0.14}Ga_{0.86}N$ lattice shrunk for ~4 % along the *c* direction

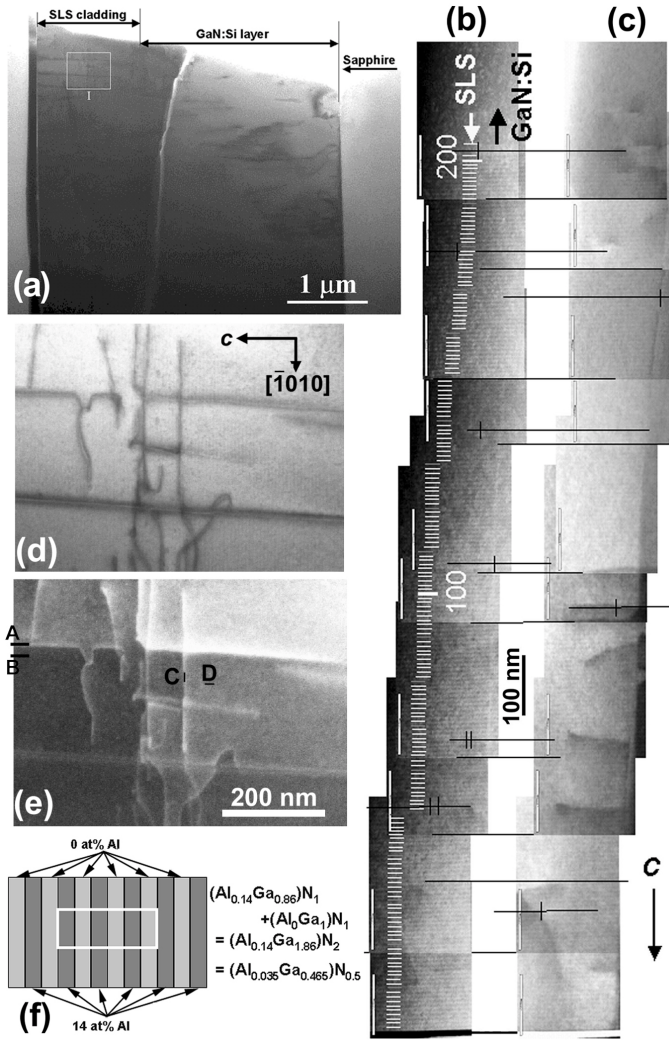

Fig. 15. **(**a) BF-STEM image of *n*-$Al_{0.14}Ga_{0.86}N$/*n*-GaN SLS cladding layer and *n*-GaN:Si layer on the sapphire substrate. (b) Experimental HAADF-STEM image of the SLS. About 200 pairs of $Al_{0.14}Ga_{0.86}N$ (dark bands) and GaN layers (bright bands) are clearly resolved and the $Al_{0.14}Ga_{0.86}N$ layers are numbered. (c) BF-STEM image of the same area. Dislocations are visible in strong diffraction contrast. (d) BF-STEM image of the area I in (a). (e) HAADF-STEM image of the same area. The defects appear as sharp bright contours, which localized them much exactly. (f) The composition of AlGaN/GaN layers in the SLS in view of Al concentration.

Table 1. EDS analysis of the SLS cladding layer.
The areas **A**-**D** are shown in Fig. 15(e).

Area	at% Al	at% Ga	at% N	Area
A	40 nm×5 nm	3.6±0.1	46.4±0.5	**A**
B	40 nm×5 nm	3.5±0.1	46.5±0.5	**B**
C	1 nm×20 nm	3.7±0.1	46.3±0.5	**C**
D	20 nm×1 nm	3.5±0.1	46.5±0.5	**D**

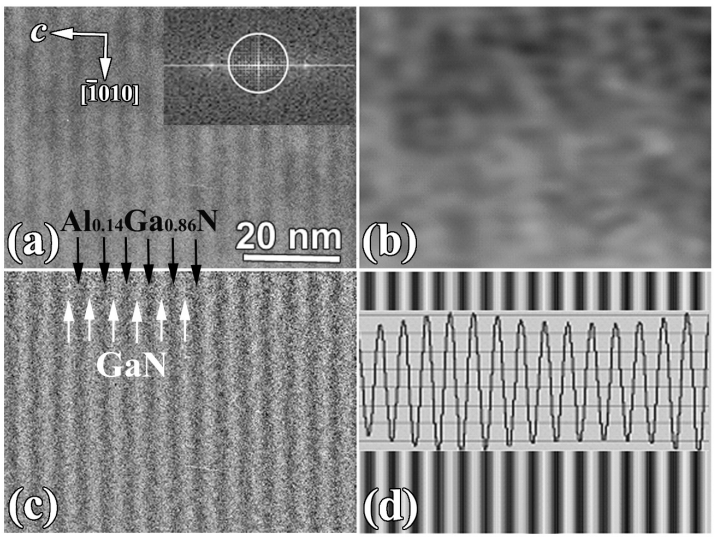

Fig. 16. (a) Experimental HAADF-STEM image of the SLS cladding. The dark bands are $Al_{0.14}Ga_{0.86}N$ layers and bright bands are GaN layers. Inset is the computer diffractogram. (b) Low-frequency HAADF-STEM image reconstructed using the low-pass mask filter shown by the circle in (a). (c) Normalized HAADF-STEM image by subtracting image (b) from image (a). (d) Averaged filtered normalized HAADF-STEM image and the corresponding intensity line profile. The thickness of the layers was determined according to the FWHM criterion, from the line profile.

while no change was measured in the basal plane, as compared with the GaN lattice. This is a direct illustration of the strained lattice in the cladding layer. Namely, a good lattice matching in the basal plane between the $Al_{0.14}Ga_{0.86}N$ and the GaN suppresses the generation of misfit dislocations on the $Al_{0.14}Ga_{0.86}N$/GaN interfaces in the SLS as well as on the interface between the $Al_{0.14}Ga_{0.86}N$ and GaN:Si layers.

Table 2. Thicknesses and lattice parameters of the $Al_{0.14}Ga_{0.86}N$ and GaN layers in the *n*-SLS Cladding.

	Thickness (nm)	Lattice parameters (nm)	
		a	*c*
$Al_{0.14}Ga_{0.86}N$	2.24 ± 0.09	0.32±0.01	$Al_{0.14}Ga_{0.86}N$
GaN	2.34 ± 0.15	0.32±0.02	GaN
Pure bulk GaN		0.319	Pure bulk GaN

In this chapter, the structural and compositional analyses of GaN-based violet laser diodes, which cannot be obtained even by conventional high-resolution analytical transmission microscopy, have been presented. Functional devices, such as quantum well (QW) lasers, tunneling devices, random access memories and high electron mobility transistors, usually comprise nano-scale multi-layer heterostructures that exploit quantum confinement effects. Since the *in-situ* monitoring in the most processing equipment is still absent, atomic-scale analysis is demanded for understanding of the real structure in the final product, including the thickness and composition of each layer. HAADF-STEM would become the most powerful tool for the analysis of nanostructure of these devices.

Acknowledgments

The present electron microscopy observations of the LDs were performed in collaboration with J. T. Hsu, R. C. Tu and C. C. Chuo, Opto-Electronics and Systems Laboratories, Taiwan, K. Inoke and E. Kobayashi, FEI Japan, M. Nakagawa and M. Yamada, Hitachi Science Systems, Japan, M. Čeh and S. Šturm, Jožef Stefan Institute, Slovenia, T. Yamazaki and N. Nakanishi, Tokyo University of Science, Japan, K. Watanabe, Tokyo Metropolitan College of Technology, Japan, J. R. Yang, National Taiwan University, and H. Saijo, Kinki University, Japan, to whom deep thanks are owing.

References

1. S. Nakamura, M. Senoh, S. Nagahara, N. Iwasa, T. Yamada, T. Matsushita, H. Kiyoku, Y. Sugimoto, T. Kozaki, H. Uemoto, M. Sano and K. Chocho, *Appl. Phys. Lett.* **72**, 211 (1998).

2. A. Usui, H. Sunakawa, A. Sakai and A. Yamaguchi, *Jpn. J. Appl. Phys*. Part 2 **36,** L899 (1997).
3. O. H. Nam, M. D. Bremser, T. Zheleva and R. Davis, *Appl. Phys. Lett*. **71,** 2638 (1997).
4. K. Kumakura, T. Makimoto and N. Kobayashi, *Jpn. J. Appl. Phys*. **39**, 2428 (2000).
5. P. Kozodoy, M. Hansen, S. P. DenBaars, U. K. Mishra and J. Kauffman, *Appl. Phys. Lett*. **74**, 3681 (1999).
6. For example: S. J. Pennycook and P.D. Nellist P D, in: D. G. Rickerby, G. Valdre and U. Valdre (Eds.), *Impact of electron and scanning probe microscopy on materials research*, (Kluwer Academic Publishers, Dordrecht, 1999), pp.161-207.
7. K. Watanabe, N. Nakanishi, T. Yamazaki, M. Kawasaki, I. Hashimoto and M. Shiojiri, *Phys. Status, Solidi (b)* **235,** 179 (2003).
8. S. Šturm, A. Rečnik, M. Kawasaki, T. Yamazaki, K. Watanabe, M. Shiojiri and M. Čeh, JEOL News **37E**, 22 (2002).
9. K. Watanabe, T. Yamazaki, I. Hashimoto and M. Shiojiri, *Phys. Rev.* B **64,** 115432 (2001).
10. M. Shiojiri and T. Yamazaki, *JEOL news* **38**, 54 (2003).
11. K. Watanabe, T. Yamazaki, Y. Kikuchi, Y. Kotaka, M. Kawasaki, I. Hashimoto and M. Shiojiri, *Phys. Rev.* B **63,** 085316 (2001).
12. T. Yamazaki, M. Kawasaki, K. Watanabe, I. Hashimoto and M. Shiojiri, *J. Electron microsc.* **50,** 517 (2001).
13. T. Yamazaki, K. Watanabe, Y. Kikuchi, M. Kawasaki, I. Hashimoto and M. Shiojiri, *Phys. Rev*. B **61,** 13833 (2000).
14. M. Kawasaki, T. Yamazaki, S. Sato, K. Watanabe and M. Shiojiri, *Philos. Mag.* A**81,** 245 (2001).
15. M. Shiojiri and H. Saijo, *J. Microsc.* in print.
16. K. Watanabe, J.R. Yang, N. Nakanishi, K. Inoke and M. Shiojiri, *Appl. Phys. Lett*. **80**, 761 (2002).
17. K. Watanabe, J. R. Yang, S. Y. Huang, K. Inoke, J. T. Hsu, R. C. Tu, T. Yamazaki, N. Nakanishi and M. Shiojiri, *Appl. Phys. Lett*. **82**, 718 (2003).
18. K. Watanabe, J. R. Yang, S. Y. Huang, K. Inoke, J. T. Hsu, R. C. Tu, T. Yamazaki, N. Nakanishi and M. Shioijiri, *Appl. Phys. Lett.* **82**, 715 (2003).
19. M. Shiojiri, M. Čeh, S. Šturm, C.C. Chuo, J.T. Hsu, J.R. Yang, and H. Saijo, *Appl. Phys. Lett.* **87,** 031914 (2005).
20. M. Shiojiri, C.C. Chuo, J.T. Hsu, J.R. Yang, and H. Saijo, *Appl. Phys.* in print.
21. M. Shiojiri, M. Čeh, and H. Saijo, *Proc. 7th Multinational Congress on Microscopy,* (Portoroz, Slovenia, 2005), 91.
22. H. Saijo, J.T. Hsu, R. C. Tu, M. Yamada, M. Nakagawa, J. R. Yang and M. Shiojiri, *Appl. Phys. Lett*. **84**, 2271 (2004).
23. H. Saijo, M. Nakagawa, M. Yamada, J.T. Hsu and R. C. Tu, J. R. Yang and M. Shiojiri, *Jap. J. Appl. Phys.* **43**, 968 (2004).

24. M. Born and E. Wolf, *Priciples of Optics*, 4th Edition, (Pergamon Press, Oxford, 1970).
25. P.A.M Dirac, *The principles of quantum mechanics*, 3rd Edition, (Oxford University Press, London, 1947).
26. A. Tonomura, J. Endo, T. Matsuda, T. Kawasaki and H. Ezawa, *Am. J. Phys.* **57**, 117 (1989).
27. A. Tonomura, *The quantum world unveiled by electron waves*, (World Scientific, Singapore, 1998).
28. R.W. James, *The optical principles of the diffraction of X-rays*, (G. Bell and Sons, London, 1948).
29. R.F. Loane, P. Xu and J. Silcox, *Acta Crystallogr.* **A47,** 267 (1991).
30. J. M. Cowley, *Appl. Phys. Lett.* **15,** 58 (1969).
31. A. Howie, J. Microsc. **117,** 11 (1979).
32. P. B. Hirsch, *Proc. Roy. Soc. of London* A **286,** 158 (1965).
33. T. Yamazaki, N. Nakanishi, A. Rečnik, M. Kawasaki, K. Watanabe, M. Čeh and M.Shiojiri, *Ultramicroscopy* **98**, 305 (2004).
34. K. Watanabe, Y. Kotaka, N. Nakanishı, T. Yamazaki, I. Hashimoto and M. Shiojiri, *Ultramicroscopy* **92**, 191 (2002).
35. N. Nakanishi, T. Yamazaki, A. Rečnik, M. Čeh, M. Kawasaki, K. Watanabe and M. Shiojiri, *J. Electron Microsc*. **51,** 383 (2002).
36. S. Šturm, A. Rečnik, M. Čeh, T. Yamazaki, M. Kawasaki and M. Shiojiri, *Proc. 8th Asia-Pacific Conference of Electron Microscopy*, (Kanazawa, 2004), 546.
37. R. C. Tu, W. H. Kuo, T. C. Wang, C. J. Tun, F. C. Hwang, J. Y. Chi and J. T. Hsu, *Proc. 4th Int. Symp. Blue Laser and Light Emitting Diode*, (Cordoba, Spain, 2002), 1.
38. R. C. Tu, C. J. Tun, J. K. Sheu, W. H. Kuo, T. C. Wang, C. E. Tsai, J. T. Hsu, J. Chi and G. C. Chi, *Electronics Device Lett. IEEE* **24,** 206 (2003).
39. M. Gec, M. Čeh and M. Shiojiri, *Proc. 7th Multinational Congress on Microscopy,* (Portoroz, Slovenia, 2005), 385.
40. Y. Chen, T. Takeuchi, H. Amano, I. Akasaki, N. Yamada, Y. Kaneko and S.Y. Wang, *Apply. Phys. Lett*. **72**, 710 (1998).
41. N. Sharma, P. Thomas, D. Tricker and C. Humphreys, *Appl. Phys. Lett.* **77,** 1274 (2000).
42. X. H. Wu, C. R. Elsass, A. Abare, M. Mack, S. Keller, P. M. Petroff, S. P. DenBaars, and J. S. Speck, *Appl. Phys. Lett*. **72**, 692 (1998).
43. Liliental-Weber, Y. Chen, S. Ruvimov, and J. Washburn, *Phys. Rev. Lett.* **79,** 2835 (1997).
44. K. Hiramatsu, K. Nishiyama, A. Motogaito, H. Miyake, Y. Iyechika, and T. Maeda, *Phys. Status, Solidi* **A 176,** 535 (1999).
45. D. Gerthsen, E. Hahn, B. Neubauer, A. Rosenauer, O. Schön, M. Heuken, and A. Rizzi, *Phys. Status Solidi* A **17**7,144 (2000).
46. P. Ruterana, S. Kret, A. Vivet, G. Maciejewski and P. Dluzewski, *J. Appl. Phys*. **9**1, 8979 (2002).

47. C. Kisielowski, Z. Liliental-Weber and S. Nakamura, *Jpn. J. Appl. Phys.*, Part 1 **3**6, 6932 (1997).
48. M. D. Bremser, W. G. Perry, T. Zheleva, N. V. Edwards, Q. H. Nam, N. Parikh, D. E. Aspnes, and R. F. Davis, *MRS Internet J. Nitride Semicond. Res*. **1,** 8 (1996).
49. B. Pecz, Zs Makkai, M.A. di Forte-Poisson, F. Huet, and R.E. Dunin-Borkowski, *Appl. Phys. Lett.* **78,** 1529 (2001).
50. Y. Narukawa, Y. Kawakami, M. Funato, S. Fujita, S. Fujita and S. Nakamura, Appl. Phys. Lett. **70**, 981 (1997).

CHAPTER 7

GROWTH AND DEVELOPMENT OF III-NITRIDE PHOTODETECTORS

Uttiya Chowdhury

Depts of Chemical and Materials Engg and Electrical Engg.
Arizona State University, Tempe, AZ 85287-6006 USA
E-mail: ucy@asu.edu

Charles J. Collins

US Army Research Laboratories
AMSRD-ARL-SE-EM,
2800 Powder Mill Road, Adelphi, MD 20783 USA

Peng Li

School of Electrical and Computer Engineering
Georgia Institute of Technology
Atlanta, GA 30332-0250 USA

The AlGaN material system, being a direct bandgap semiconductor alloy covering a bandgap-equivalent wavelength range from 365 nm (GaN) to 200 nm (AlN), is attractive for miscellaneous near and deep-UV photo-detection applications. Since AlGaN has a wide-bandgap, devices made out of it have a low thermal noise and can therefore deliver higher detectivity compared to UV photodetectors made out of narrow-bandgap materials (such as Si). In addition, because of the fact that photodetectors are insensitive to sub-bandgap luminescence, nitride photodetectors can be used where insensitivity to certain longer-wavelength range is required. Examples of such requirements are "visible-blind" and "solar-blind" response and such photodetectors are attractive for many commercial, scientific and defence applications.

1. Introduction

1.1. *Applications*

Presently, the biggest commercial interest in III-nitride semiconductor technology is in light emitters followed by AlGaN/GaN heterostructure field effect transistors (HFETs). The scenario is expected to remain so for the near future due to the relative demand volumes of the associated products. However, nitride-based photodetectors also have created their place in the pantheon of semiconductor devices because of their unique suitability to cover the ultra-violet (UV) spectral range with high responsivity, detectivity and wavelength selectivity.

Nitride-based photodetectors are generally suitable for two important spectral ranges in the UV. These are the "visible-blind" and the "solar-blind" ranges. A visible-blind photodetector (VBD) is one that is insensitive to visible wavelength range (~400 nm to ~650 nm), but is sensitive to shorter wavelengths. GaN-based photodetectors are generally used for this purpose. With the GaN bandgap being ~365 nm, a GaN-based photodetector will be insensitive to longer wavelengths while giving a sharp rise in photoresponse at shorter wavelengths. One of the unique capabilities of such detectors is their ability to detect the UV signature of flames against a high temperature ambient. Presence of flame in a hot furnace, for example, can be detected by such a photodetector.

A solar-blind photodetector (SBD) similarly, is insensitive to wavelengths longer than ~280 nm but is sensitive to shorter wavelengths. The reason behind this naming is that due to strong absorption in the terrestrial ozone layer at ~280 nm, shorter wavelength constituents of the solar spectra get strongly absorbed and can not reach the earth surface. The solar spectra at the earth surface is thus virtually devoid of photons with wavelength shorter than ~280 nm. As a result, in a photodetection application on the earth surface, any photodetector sensitive to wavelengths longer than ~280 nm will suffer from a strong baseline of solar radiation noise. Any UV signal to be detected above the background signal will be seriously limited in signal-to-noise ratio (SNR). On the other hand, an SBD, consisting of an $Al_{\sim 0.45}Ga_{\sim 0.55}N$

active layer is insensitive to the solar spectra because the photon energy is less than the bandgap energy and is incapable of exciting electron hole pairs (EHPs). As a result, it will have a much lower noise signal from the solar-radiation and consequently, a much higher SNR.

SBDs are of high defence interest due to their ability to detect missile exhaust plume with a high SNR from an observation site situated on earth's surface. Another defence application of the technology is to detect orbiting satellites from sites located outside earth's atmosphere from the solar UV reflected from the orbiting craft. The detectors are also useful for detecting heavenly bodies and thus have astronomical applications.

1.2. *Suitability*

While a narrow bandgap semiconductor such as silicon can generally be used for detection of higher energy photons, considerable limitations exist in this route. The biggest fundamental limitation of using a narrow bandgap semiconductor in detecting higher energy photon arises from thermal noise considerations. At a given ambient temperature, in any scheme of photodetection, a semiconductor with a comparatively narrower bandgap will have higher thermal noise due to higher thermal regeneration of EHPs. The thermally generated EHPs are indistinguishable from photo-generated EHPs and thus contribute to the dark current (dark current is the noise current in a photodetector in absence of exciting illumination). As a result, from the consideration of obtaining a high SNR, it is the best to use a semiconductor that has a bandgap only slightly smaller in energy than the photons to be detected. Accordingly, the AlGaN alloy system with bandgap equivalent wavelength ranging from ~200 to ~365 nm is fundamentally more suitable than semiconductors with a narrower bandgap for UV photodetection applications. In addition, generally speaking, the absorption coefficient of a semiconductor is very high at photon energies much larger than the bandgap. This essentially means that incident photons with higher energy are absorbed within a very short distance into the semiconductor. Particularly for Schottky and *p-n* junction photodetectors, this requires the depleted active photodetection region to be within the range of photon penetration. These considerations lead to

special design and processing requirements commonly known as UV-enhancement. Besides these limitations, the only way to obtain spectral selectivity, such as visible-blindness or solar-blindness, from a narrow bandgap semiconductor is by the use of an expensive and cumbersome optical filter which makes the detector unsuitable for a wide range of applications.

In addition to this, the entire AlGaN material system has a relatively small lattice mismatch, making fabrication of heterostructures possible. The availability of heterostuctures gives an extra degree of freedom for the design of the device structure. Particularly, this enables the placement of non-absorbing layers of higher bandgap energy in the path of the photons to the active photodetection region as necessary for design considerations. Moreover, since the entire AlGaN alloy system is direct bandgap, a sharp spectral selectivity with sharp fall of responsivity at bandgap is obtained. Also, sapphire, which is currently the most popular substrate for growth of AlGaN, is UV-transparent over the entire spectral range of interest. With this large list of advantages, it is no surprise that the AlGaN material system enjoys high interest from UV photodetector researchers.

While the technology holds much promise, its implementation is not without challenges. During the early phase of nitride photodetector research, most of the work was concentrated on the development of GaN-based VBDs. The main challenges at that time were obtaining high material quality, low unintentionally doped carrier concentration, and good *p*-type doping. Subsequent research was aimed at gradually pushing the cut-off wavelength shorter by using higher Al-content AlGaN alloys. At that stage, the requirement for high material quality became even more important. Additionally, high *n*-type doping, which usually is easy to achieve in GaN, was found to be difficult to obtain for high Al-content AlGaN. We describe more on the challenges and their step-by-step overcoming in the next sections.

1.3. *Types of photodetectors*

For UV photodetection applications, relevant devices are photo-conductors, Schottky junction photodiodes, *p-n* junction photodiodes,

avalanche photodiodes and phototransistors. Of these, photoconductors, avalanche photodetectors and phototransistors are gain devices: under proper operating conditions, the electron flux can be higher than the incident photon flux. The other devices have a sub-unity gain and the electron current is always smaller than the photon flux. In the present state of the technology, nitride photoconductor, Schottky and *p-i-n* photodiode development can be considered to have matured. However, major difficulty was encountered in the development of avalanche photodiodes and phototransistors.

A photoconductor is essentially a bar of lightly doped semiconductor with two ohmic contacts made on the two sides. When illuminated, the conductivity of the material increases because of the increase in free carrier concentration by the photogeneration of EHPs. When biased with a small voltage then, the current across the device increases with illumination and the increase in current is interpreted as the photogenerated signal. Photoconductors suffer from the problem of a need for external bias. Also, since in nitride semiconductors, the minority carriers have relatively long lifetime, photoconductors suffer from a very slow photoresponse time and therefore, a slow speed. The long lifetimes also lead to persistent photoconductivity (PPC) where even after the removal of optical excitation, the conductivity does not fall to initial values for a very long time. Nitride photoconductors have also been reported to have non-linear photoresponse which is yet another drawback for many practical applications.

p-n junction photodetectors act by sweeping out the photogenerated electrons and holes in opposite directions by the built-in field in the depletion region. If the two terminals of the diode are shorted, a photocurrent is obtained. For epitaxially grown structures, a *p-n* structure is grown, and mesas are isolated by etching down to the bottom *n*-layer. Ohmic contacts are made on the *p* and *n*-material forming the diode. Light can be introduced either from the top or the bottom side and is converted into photocurrent mainly in the depleted region at the junction. So, it is desirable to loose as few photons as possible on the path of the photons to the depletion region. This seems to favor a thin *p*-layer and top illumination, since for devices made from epitaxial AlGaN, on the bottom side, a thick layer of material is needed to reduce the threading

dislocation density (TDD) originating at the heteroepitaxial nucleation layer. However, the problem with top illumination is that the *p*-metallization can block the path of light. One good solution to the problem is to use a heterostructure design where the bottom *n*-layer is made of a higher bandgap semiconductor through which light can pass unabsorbed to the depletion region. Also, the amount of photons absorbed in the depletion region is dependent on the depletion width. For a *p-n* junction, the depletion width is usually not thick enough to absorb a sizable portion of the incident photon. An improvement to this design is the use of a *p-i-n* structure whereby the depletion width is approximately the same as the *i*-layer thickness. An appropriate thickness of *i*-layer is chosen so that most of the photons are absorbed in the layer as determined by the absorption coefficient of the *i*-layer material.

Schottky barrier photodiodes also work using a similar principle. Here, the built-in field of the Schottky barrier of a rectifying metal-semiconductor junction is used. *p-n* and Schottky junction detectors both fall under the classification of photovoltaic detectors.

Schottky junction detectors can be made in a number of configurations. One ohmic and one Schottky metallization can be formed on top of a high-resistivity semiconductor layer by use of suitable metallization schemes. Alternatively, an epitaxial structure of an *n*-layer followed by an *i*-layer can be used. Here, the ohmic contact is formed on the *n*-layer after a mesa-etch. Yet another alternative device is the metal-semiconductor-metal or MSM structure consisting of two back-to-back Schottky junctions formed by two rectifying metallizations on top of an *i*-layer. The MSM photodetector is operated by applying a bias voltage whereby one junction is forward biased and the other is reverse biased. While MSM photodetectors are simpler to fabricate, the need for external bias is a major disadvantage. Both Schottky junction and MSM devices can also show photoconductive gain due to carrier trapping effects modifying the Schottky barrier height and, in case of lateral devices, due to bulk material conductivity changes.

In a Schottky junction, the barrier height is generally lower compared to that in a *p-n* junction. Additionally, the thermionic emission mechanism being an efficient process causes the reverse leakage current in a Schottky diode to be generally higher than that in a *p-n* junction

detector. As we discuss shortly, this higher reverse leakage translates into an inferior noise performance.

For photodetectors, the Fresnel reflection at the interface between the device and ambient air causes a reduction of photons actually getting into the device. This Fresnel reflection can be minimized by the use of a dielectric anti-reflective (AR) coating. However, the design and fabrication of the AR coating is a rather straight-forward problem, modularly separate from the issues of designing a photodetector. As a result, most researchers are seen to report device performance without the AR coating, with implicit acknowledgement that an additional small improvement of responsivity can be obtained by the application of the coating.

1.4. *Performance criteria*

The most commonly used performance criteria for photodetectors are responsivity spectrum (which directly gives the external quantum efficiency or EQE spectrum), detectivity and speed. Responsivity is defined by the amount of photocurrent obtained per incident radiant power and has a unit of Amps./Watt. EQE describes the number of photoelectrons generated per incident photon and is given in percentage. Said differently, EQE is the ratio of photocurrent to the photon flux in percentage unit. It is important to note that devices with gain can have an EQE greater than 100%. Since photon energy is immediately obtained from it's wavelength using the equation $\varepsilon=hc/\lambda$, photon flux can be converted into incident radiant power, which can then be used to relate EQE to responsivity.

Detectivity is defined by the inverse of noise-equivalent power. The noise-equivalent power is the amount of radiant power required to obtain a unity SNR at the output of a detector under given modulating frequency, operating wavelength and effective noise conditions. It is usually indicated by the symbol D and has a unit of $Hz^{1/2}Watt^{-1}$. It is more common in fact, to use the specific detectivity D^* which is the detectivity normalized per unit area and bandwidth and has a unit of $cm.Hz^{1/2}Watt^{-1}$. As we can see, the responsivity term is simply an indication of gain and does not tell anything about the lowest radiant

power the photodetector can detect as limited by inherent noise. For example, a photodetector that has a high detectivity, but also a high dark current will be severely limited in terms of the minimum radiant power it can detect. This is because with small radiant power incident on the photodetector, the increase in photocurrent will not register above the already high dark current. For applications where detection of low intensity signal matters, the D^* term becomes an important performance criteria. It is to be noted here that for wide bandgap photodetectors such as the ones under discussion, it is customary to assume that thermal noise dominates over other forms of noise. Therefore, noise-equivalent power can be obtained from the zero-volt resistance R_0 under no-illumination condition. This essentially means that a photodiode is required to have a low reverse leakage in order to have a high detectivity.

Detector speed can be described in a number of ways – one example being the specification of the rise time and fall time when a square-wave modulated optical signal is incident on the photodetector. Photodetector speed is obviously a very important performance criterion for fiber optic telecommunication applications. Such applications mainly require photodetectors in the infrared range and are dominated by conventional III-V semiconductor devices. The application of UV photodetectors on the other hand, are mainly in imaging, sensing and space-related spectroscopy. For these applications, the detector speed is generally of a secondary importance.

Responsivity measurement of photodiodes is done by comparing the photocurrent of the device under test and a calibrated reference photodetector (usually a UV-enhanced Si photodiode) under identical illumination conditions. Light from a broad-spectrum source is monochromated by use of optical gratings. The monochromatic light is then focused on the photodetector through appropriate optics. The photodetector is put in a closed circuit with or without an external DC bias. The photocurrent in the loop is measured for the photodetector under measurement. Since for the reference photodetector, the relationship between the output current and incident radiant power is known at all wavelengths in the range of measurement, one can calculate the responsivity of the test photodetector. In order to reduce noise contributions, the incident light on the photodetector is usually chopped

using a mechanically-rotating slitted-wheel optical chopper and only the component from the photocurrent that has the same frequency and phase as the chopped incident light is measured by using a lock-in amplifier.

In this section, we have presented only a brief overview of photodetector technology while in the next sections, we go mostly over a survey of the progression of nitride photodetector research. Readers interested in the details of the theory of device operation and performance can refer to a number of textbooks and review articles.[1]

2. Visible-Blind Photodetectors

2.1. *Early work*

In the early 1990s, group III-nitrides were considered a semiconductor with much potential, but fraught with many challenges. As grown unintentionally doped GaN had too high a residual *n*-type doping – too high even for the fabrication of photoconductors. Schottky junction photodetectors were even more challenging since even lower residual doping is required to obtain a Schottky junction. *p*-type doping was only emerging with researchers establishing growth and acceptor activation conditions for Mg-doping.

The first report on a III-nitride based photodetector was made in 1992 by Khan *et al.* who developed a GaN photoconductor.[2] This work was made possible by the achievement of relatively high resistivity GaN by use of a novel switched atomic layer epitaxy (SALE) technique. The devices demonstrated a linear *I-V* characteristics, a nearly flat responsivity spectra from 200 nm to 365 nm, and a sharp cut-off at the bandgap energy. The responsivity spectra is shown in Fig. 1**.** Using neutral density filters, a large (but unquantified) dynamic range was reported. Response to pulsed laser irradiation was used to determine a response time of 1 ms. At 5 V bias, a high responsivity of 2000 A/W was obtained, which is representative of a high photoconductive gain.

After this first report, the next challenge at hand was the demonstration of photovoltaic detectors based on GaN. The same research group also demonstrated the first Schottky barrier photodetector which is also the first photovoltaic detector in the material system.[3] They

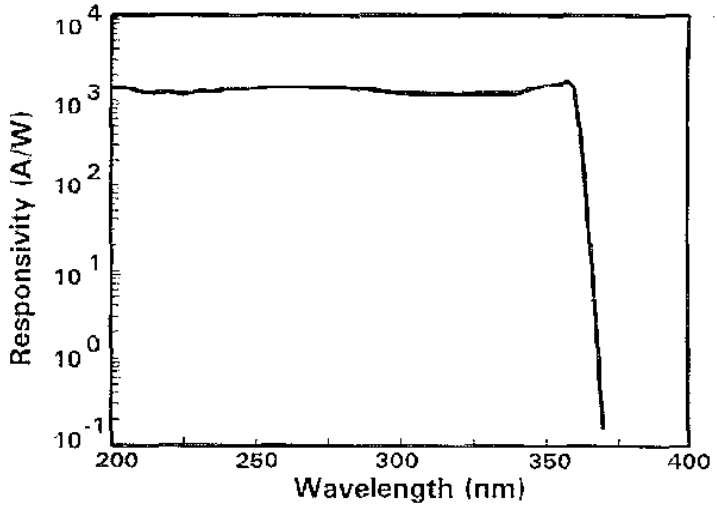

Fig. 1. The responsivity spectra of the first GaN photoconductor developed by Khan *et al*.[2] (Reused with permission from M. Asif Khan, J. N. Kuznia, D. T. Olson, J. M. Van Hove, M. Blasingame, and L. F. Reitz, Applied Physics Letters, 60, 2917 (1992). Copyright 1992, American Institute of Physics.)

succeeded in adequately compensating the residual *n*-type conductivity in as grown GaN by the use of Mg-doping. A Schottky barrier was achieved with a Ti/Au metalization that showed a forward turn-on at 1.5 V and reverse breakdown at 3 V. A zero bias responsivity of 130 mA/W was obtained under back-illuminated configuration, for a normalized area of 1 mm^2. Spectral responsivity again, was almost flat between 200 to 365 nm with a sharp drop-off at 365 nm.

The first report of III-nitride *p-n* junction photodetector was also by the same research group. In 1995, Chen *et al*. reported on MOCVD grown *p-n* photodiode structures.[4] Both *p*-on-*n* and *n*-on-*p* structures were fabricated in back-illumination configurations. Devices showed a responsivity of 90 mA/W. Turn-on was at 3 V and a low leakage current was published with zero volt resistance exceeding 20 MΩ for 16 mm^2 mesa area. Rise and fall times measured in response to pulsed laser was reported to be 0.4 ms. Both the *p*-on-*n* and *n*-on-*p* devices showed similar performance characteristics except that while the *p*-on-*n* devices showed a fairly flat responsivity spectra for wavelengths down to 200 nm,

the *n*-on-*p* devices showed a small decrease in responsivity at shorter wavelengths. This presumably is because of relative material quality degradation resulting from growing a thick *p*-layer first. For GaN, due to small acceptor ionization, obtaining of p-type material requires a large [Mg] in the range of $\times 10^{20}$ cm^{-3}. Such high doping causes degradation of material quality.

Although nitride photoconductors are of a lesser practical importance, significant early research was performed to study the properties of photoconductor operation. Kung *et al*. published results on the time response of GaN photoconductors.[5] The authors noted a sublinear photoresponse and dependence of response time with radiant power. Binet *et al.* presented a detailed analysis of the recombination mechanisms in GaN photoconductors.[6] Using experimental data and theoretical modeling, the authors identified two competing recombination mechanisms that lead to an intensity-dependence of response time. The high photoconductive gain and long response time (> 1 ms) were related to the presence of deep levels in compensated GaN material. In order to study the influence of material quality on photoconductor performance, Smith *et al*. compared photoconductors fabricated from MOCVD GaN on sapphire, SiC and thick GaN substrates grown by hydride vapor-phase epitaxy (HVPE).[7] SiC and HVPE GaN substrates yielded an improved material quality as determined by X-ray diffractometry (XRD), transmission electron microscopy (TEM) and atomic force microscopy (AFM). The devices grown on SiC and HVPE GaN substrates had an improvement of responsivity by a factor of 4.6 and 7.8 respectively compared to devices grown on sapphire substrates. The improvement of responsivity was attributed to a longer carrier lifetime resulting from better material quality. The devices on SiC and HVPE GaN also had sharper cut-off of responsivity at bandgap.

More recently, Katz *et al*. reported on persistent photoconductivity in GaN Schottky photodetectors.[8,9] Gain saturation and persistent photoconductivity were observed and modeled theoretically. The two effects were shown to be related and arising from the modification of Schottky barrier height from carrier trap-related effects at the Schottky junction interface.

Carrano *et al*. developed GaN MSM photodetectors with a high responsivity of 120 mA/W in the bias range of 5 to 20 V.[10] Furthermore, they found very little bias dependence of the responsivity indicating an absence of photoconductive gain. The devices also had reverse leakage at record low levels making them a major milestone in GaN MSM device performance. This high performance was attributed to the high material quality of the GaN layers obtained from optimized growth. Monroy *et al.* fabricated planar Schottky GaN photodetectors using the epitaxial lateral overgrowth (ELOG) technique and observed significant improvement in spectral rejection and reverse leakage.[11] The improved performance was attributed to the reduction of TDD by the use of the ELOG technique.

In order to solve the problem of blockage of incident light by the metalization in Schottky barrier detectors, Chen *et al*. developed a thin Pd-based transparent Schottky metalization scheme.[12] For vertical geometry devices, a 5 nm thick Pd contact was found to give UV transmission ~70 % resulting in a high responsivity of 180 mA/W. The devices also had a fast response time of 118 ns. The authors also performed noise measurements on the devices and demonstrated that 1/f noise is the dominant source of noise for these devices. This was the first study of the nature of noise in GaN Schottky photodetectors. The same group also performed a study of noise in GaN *p*-π-*n* photodetectors.[13,14] They used a low Mg-doping in the *i*-layer to compensate the native *n*-conductivity and called the resulting material as "π-type". The noise was found to be an order of magnitude lower compared to GaN Schottky devices. Reverse current was found to scale with device area indicating that the main source of leakage is the bulk material rather than mesa-etch sidewall. Carrano *et al*. performed modeling of Schottky barriers in GaN and found that a trap-assisted field emission process dominates the dark current in GaN MSM photodetectors.[15,16]

Carrano *et al.* reported on the development of high performance GaN *p*-*i*-*n* photodetectors with low dark current.[17] A high responsivity of 100 mA/W was obtained along with a record low dark current density of 2.8 nA/cm^2. The same group also reported on record high speed performance of GaN *p*-*i*-*n* with a rise time of 90 ps and a bandwidth of 1.6 GHz at 30 V reverse bias.[18]

Earlier we discussed the advantages of a heterostructure design for *p-n* junction photodetectors. Xu *et al*. made the first report on the incorporation of this idea in a *p-i-n* photodetector and performed a detailed analysis of the benefits of the heterostructure design.[19] They fabricated heterojunction *P-i-n* photodiodes with an AlGaN *p*-layer on top of a GaN *i-n* structure. However, when compared to devices with *p*-GaN layers, the *p*-AlGaN-based devices were found to have a higher leakage current which the authors attributed to the lower material quality of *p*-AlGaN. Due to the high electron affinity of *p*-AlGaN, it is difficult to make ohmic contact to the *p*-AlGaN layer. Li *et al*. approached this problem by designing a similar structure but with the addition of a *p*-GaN cap.[21] The contact metalization is made on the *p*-GaN, but a recessed window, with the *p*-GaN layer etched away, is formed in the rest of the device area to eliminate the problem of absorption in the *p* layer. However, in this design, effects of current crowding was a major problem because of the high resistivity of the *p*-AlGaN material. To circumvent this problem, the same group developed a new design – a thin unrecessed *p*-GaN cap layer on the *p*-AlGaN with a current spreading semi-transparent *p*-metalization.[21] Kuryatkov *et al*. performed noise and detectivity measurement based on these structures[22] and noted results similar to that reported previously for *p-i-n* diodes.[13]

A better solution to the problem is obtained if illumination is from the substrate-side and the bottom dislocation reduction layer is of a higher bandgap. Zhang *et al*. fabricated back illuminated AlGaN/GaN MSM heterostructure photodetectors.[23] Due to backside illumination, the contact metalization does not block the light. Also, since the active absorption material is GaN, and the thick underlayer is AlGaN, photons with energy in-between the two bandgap energies can get to the absorption region without significant loss. One feature of this design is that instead of having a flat spectral response on the short wavelength side, the responsivity spectra is peak shaped with a cut-off on the shorter wavelength side also. This is because the AlGaN underlayer acts as an optical filter that prevents shorter wavelength photons from getting to the active region. The MSM devices fabricated by Zhang *et al*. had a long wavelength cut-off at 365 nm and a short wavelength cut-off at 343 nm. The devices also showed photoconductive gain. Torvik *et al*. studied the

effects of dislocation density, Mg-doping and etching for fabrication of recessed window in GaN *p*-*i*-*n* diodes by using photoconductive spectroscopy.[24] They identify the importance of a thin *p* or *n*-layer on the path of photons to the active *i*-layer to maximize responsivity. They discuss different device structure possibilities, such as *p*-on-*n*, *n*-on-*p* and back-illuminated heterostructure designs and comment on their relative advantages and disadvantages.

2.2. *AlGaN based devices – Towards solar-blindness*

With the development of GaN-based photodetectors, research also progressed on the use of AlGaN for the active region in order to push the cut-off wavelength shorter. Walker *et al*. reported on the development of AlGaN-based photoconductors using a wide range of Al compositions.[25] The device performance however, was generally poor.

Omnès *et al*. reported on visible-blind photoconductor and Schottky photodiode fabrication using MOCVD grown AlGaN.[26] Variation of AlGaN composition gave sharp cut-off in the wavelength range from 362 to 293 nm. Devices made of higher Al content AlGaN (i.e. devices of shorter cut-off wavelength) were seen to have smaller responsivity, which was found to go down from 54 mA/W to 10 mA/W with a transition from GaN to $Al_{0.35}Ga_{0.65}N$. The photoconductors consistently showed PPC and response non-linearity. Monroy *et al*. developed high responsivity AlGaN-based MSM photodetectors based on $Al_{0.25}Ga_{0.75}N$ with a cut-off wavelength at 310 nm.[27,28]

It is generally found that of the different III-nitride alloys, GaN can be grown with the highest material quality. In the quaternary InAlGaN system, one can find an InAlGaN alloy that is lattice matched to GaN but has a bandgap energy much larger than that of GaN. Due to the lattice match with GaN, the alloy can theroretically be grown on GaN with relatively lower defect density when compared to AlGaN of equivalent bandgap energy. However, for MOCVD growth, incorporation of In requires a nitrogen atmosphere and relatively low growth temperature which makes obtaining high material quality difficult. Oder *et al.* performed MOCVD growth of quaternary InAlGaN alloy on GaN layers for UV photoconductor applications.[29] A wide range of alloy

compositions, nominally lattice matched to GaN were grown. The fabricated devices had a cut-off wavelength varying from 345 nm to 290 nm. However, because of absorption and conduction in the underlying GaN layer, some devices had photoresponse at the GaN bandedge. Also, the responsivity cut-off was not found to be very sharp.

2.3. *Devices grown on Si substrates*

Besides the mainstream development efforts using sapphire substrates, significant work was also dedicated towards the growth of devices on Si substrates. Since Si has a cubic crystal structure and the nitrides are hexagonal, practically all nitride growth on Si is done on the (111) face which has the requisite 3-fold symmetry. Also, generally, GaN has inadequate wetting on Si, which makes it essential for growth to begin with an AlN nucleation layer.

In any case, due to large mismatch in the coefficient of thermal expansion (CTE) and lattice constant, the quality of nitride material grown on Si is generally inferior compared to that on sapphire. The epitaxial layers tend to form cracks when cooling from the high growth temperature to room temperature because of the CTE mismatch. Nevertheless, lower cost, availability of larger substrates, and the possibility of integration with Si MOS circuitry, act as significant motivating factors for the development of any device on Si substrates.

The first report of a nitride photodetector grown on Si substrate was made by Stevens *et al*.[30] The devices were photoconductors made from MBE grown GaN:Mg layers and had a responsivity of 12 A/W at 4V bias. Zhao *et al.* reported on GaN-based photoconductors with interdigitated finger configuration fabricated using MOCVD grown GaN on Si.[31] A peak responsivity of 6.9 A/W at 357 nm wavelength at 5 V bias was obtained along with a response time of 4.8 ms. Both performances are poor compared to GaN photoconductors on sapphire of the time. GaN-based Schottky photodetectors on Si substrates were reported by Osinsky *et al*.[32] The GaN:Si epitaxial layer was grown using MBE and lateral geometry Schottky diodes were fabricated using one ohmic and one Schottky contact. The devices had a peak responsivity of 100 mA/W at 4 V reverse bias. Pau *et al*. reported on the development of

photoconductors and Schottky and *p-n* junction photodiodes using both GaN and AlGaN.[33,34] Significantly inferior device performance was reported for the AlGaN-based devices compared to the devices fabricated from GaN.

2.4. *Avalanche detectors and phototransistors*

There exists a high interest in photodetectors with internal gain because a very high responsivity can be obtained without the use of external amplifiers. The simplest gain mechanism is the photoconductive gain which can be achieved in both photoconductor and MSM configurations. However, photoconductors do not have high detectivity and are therefore not suitable for detecting low intensity signals. In addition, photoconductors are slow and they also have bad linearity. Because of these factors, practical applications of such devices are limited.

Avalanche photodetectors (APDs) have a high gain resulting from the avalance multiplication process. This is a fast and low-noise process and is therefore technologically attractive. However, since heteroepitaxially grown III-nitride materials have a high TDD, under high field conditions leakage current is seen to dominate over any avalanche processes. Additionally, avalanche breakdown is seen to occur in conjunction with the creation of microplasmas because of the high electric field along the threading dislocations.

Osinsky *et al.* reported on the first APD operation in III-nitrides and on optical and electrical measurements to study the formation of microplasma.[48] Due to the microplasma formation over threading dislocations, avalanche breakdown in actual device area was weak. Carrano *et al.* also reported on the evidence of avalanche gain in their high performance *p-i-n* diodes.[17] McIntosh *et al.* reported on the development of microplasma-free APDs based on low-defect-density GaN grown by hydride vapor-phase epitaxy.[49] A uniform multiplication gain of 10 was measured in the wavelength range from 320 to 360 nm. Carrano *et al.* reported on the observation of microplasma-free APDs by using relatively small mesa sizes.[50] It is estimated that when the device diameter is very small (< 25 μm), some of the fabricated devices contain

no threading dislocations, which leads to the elimination of microplasma formation. Devices showed a stable and uniform gain > 25. This technique however, has the inherent disadvantage of low device yield and unavailability of large-area devices.

The first conclusive report of strong avalanche multiplication was reported by Yang *et al*. using similar small diameter devices.[55] The breakdown voltage had the temperature dependence predicted by the theory of avalanche multiplication and this conclusively proved avalanche operation. The avalanche gain obtained was 23. More recently, Limb *et al*. have reported much improved performance data based on similar device structure – except in this case, use of HVPE-grown bulk GaN substrate led to a much lower TDD and hence the improved performance.[51] With a homojunction *p-i-n* structure with an i-layer thickness of 300 nm, mesa-structure diodes were fabricated in 30 and 50 μm diameter sizes. Devices had a breakdown voltage between 80 and 90 V and an extremely low dark-current. Stable optical gain > 1000 was obtained without any evidence of microplasma formation along mesa-edge or threading dislocations. Devices also showed a positive temperature coefficient of breakdown voltage which confirms avalanche operation.

Other than APDs, high speed gain is also obtained from phototransistors. The gain mechanism in these devices is the same as in a bipolar junction transistor (BJT). The photogenerated carriers provide the equivalent of base current, which is multiplied by transistor action. Both BJT and phototransistor development in GaN has been found to be difficult because of low *p*-type doping, high junction leakage and Mg-related *p*-doping memory effect.

Yang *et al*. reported on high ($> 10^5$) gain phototransistor operation based on AlGaN/GaN heterostructures.[56] However, the gain was mostly due to the photoconductive effect. Chernyak *et al.* reported on phototransistor action based on AlGaN/GaN heterojunction bipolar transistor (HBT) in *N-p-n* configuration.[57] Device measurement was performed with electron beam illumination instead of optical illumination and yielded a transistor action gain of $\beta \sim 2.5$.

2.5. *Vacuum UV performance*

Besides the applications described thus far, GaN-based photodetectors are also useful in the 10 nm to 200 nm wavelength range known as the vacuum UV (VUV). The main application of the technology is in space science for a number of spectral measurement and imaging applications. These applications generally demand an outstanding noise performance and radiation hardness (i.e. devices should not degrade from the high levels of radiation dosage in space). GaN-based photodetectors are an ideal solution for this purpose. Since for these applications, the photon energy is much higher than the semiconductor bandgap, absorption occurs within a very short distance of the surface. Since unlike a *p-n* diode, the junction in a Schottky diode is right at the semiconductor surface, Schottky barrier photodetectors in different configurations are most suited for this application. Photoconductors are not suitable because of their inferior noise performance.

Research in the VUV wavelength range however, requires a very different set of characterization tools compared to UV-visible-near infra-red equipment. Appropriate light source, monochromator and miscellaneous optical components are required for measurement of responsivity in the VUV range. Motogaito *et al*. reported on the characterization technique and performance results of Schottky barrier photodiodes fabricated from GaN.[58,59] For this work, a BL7B synchrotron radiation source was used as the light source in the wavelength range from 564 nm to 41 nm. Since at high photon energies, material photoemission also contributes to the device current, the authors performed separate measurements of photoemision current of GaN and the Au Schottky metal. Responsivity in the VUV range was in the range of 10 mA/W and was found to increase with increasing reverse bias. Compared to Schottky junction diode, MSM structures generally provide a lower dark current which is an important benefit for space application. Monroy *et al*. measured the VUV performance of GaN MSMs using a Super-ACO synchrotron source.[60] The authors compared devices grown using GaN and AlN nucleation layers and found that due to lower residual doping, devices on AlN nucleation layer have a significantly lower dark current. VUV responsivity was calibrated using two different

calibrated photodetectors and a responsivity in excess of 100 mA/W was obtained at a 5 V reverse bias.

2.6. *Other miscellaneous works*

Besides the work discussed thus far, significant research has also occured in other areas that can improve device performance. Among these, the problem with top-illumination with metal covering much of the surface was addressed by Ozelo *et al*. They demonstrated a polymer microlens fabricated between the MSM fingers that focuses the light incident over the entire surface into the openings between the fingers.[35] Kim *et al.* reported on the successful use of an IrO_2-based Schottky contact on GaN.[36] The higher barrier from the use of IrO_2 translates into lower leakage current (and thus, higher detectivity) and also higher penetration of the photons of interest ($\lambda \sim 360$ nm) through the contact layer to the active absorption region of the photodiode. The first photodetector array in the material system was reported by Huang *et al*. who reported on a 1×16 element linear array of GaN MSM photodetectors.[37] Kishino *et al.* developed the first resonant cavity photodetector in the material system.[38] Using a structure consisting of 20 period $Al_{0.06}Ga_{0.94}N$/AlN bottom DBR, GaN active region and 2 period ZrO_2/SiO_2 top DBR, sharp peaks were obtained in the responsivity spectra at 363 nm and 352 nm.

It was mentioned earlier that low dark current is required from a photodetector for noise performance purposes. It has been proposed that a major source of the dark current is the surface states created in mesa-isolation from plasma etching. Adivarahan *et al*. developed a mesa-etch free lateral Schottky device structure coupled with a PECVD-deposited SiO_2-based surface passivation technology.[39] This led to reduction of reverse current by 2 to 4 orders of magnitude in the 10 to 20 V reverse bias range. A similar effort to reduce dark current in *p-n* junction photodetector by elimination of mesa etch was directed by Sheu *et al*., who reported on a novel planar GaN *p-n* photodetector fabrication technique by Si triple implantation in *p*-GaN.[40] However, dark currents measured on the fabricated devices did not show significant improvement over conventional epitaxially defined *p-n* structures. This is

presumably because of material quality degradation from ion-implantation damage.

Seo *et al.* made the first report on the development of GaN MSM photodetector on $LiGaO_2$ substrate.[41] The principal motivation behind the use of the $LiGaO_2$ substrate was smaller TDD owing to smaller lattice mismatch with GaN. Also, the $LiGaO_2$ substrate can be selectively removed by HF:H_2O wet etch which enables various material integration possibilities. A responsivity of 105 mA/W was reported at 20 V reverse bias at 308 nm wavelength.

Responsivity performance of MSM photodetectors require narrow finger-to-finger distance to allow reduction of hole transit time and improve hole collection at the cathode. This requirement favours microlithography technique which is not under widespread use for photodetector fabrication. Joshi presented results on Monte-Carlo simulation for graded AlGaN submicron MSM photodiodes and showed that improved photoresponse is expected from such structures.[42] On the practical side, Palacios *et al*. fabricated submicron MSM devices with finger-width and pitch down to 0.5 μm using e-beam lithography.[43] A superlinear improvement of responsivity with reduction of feature size, consistent with theoretical prediction was obtained.

A number of research groups developed heterostructure photo-conductors based on AlGaN/GaN heterostructures similar to high electron mobility transistors (HEMT). Khan *et al*. reported on the use of AlGaN/GaN HEMTs as gated photoconductors.[44] Li *et al*. reported on the observation of PPC in AlGaN/GaN heterostructure photoconductor using pulsed laser excitation.[45] Zhou *et al*. developed AlGaN/GaN single and multi-layer photoconductor and studied the influence of polarization field on the device performance.[46]

Ghosh *et al*. reported on theoretical prediction of the dependence of the absorption coefficient on the polarization of the normally incident light for the case of GaN layers with *M*-plane strain.[47] The authors predict that in certain range of strain, this polarization dependence of absorption coefficient can be used to develop polarization sensitive photodetector.

3. Solar-Blind Photodetectors

3.1. *Schottky devices and top-illuminated p-i-n devices*

After the successful development of GaN-based VBDs and related devices, the next major spectral milestone was the devolopment of SBDs using an AlGaN active region. The first report of an SBD however, is not easy to pinpoint because the wavelength selectivity criteria to define an SBD has not been accurately established. The first photodetectors with the requisite spectral selectivity were developed in AlGaN photoconductor configurations which are essentially not suitable for any of the key SBD applications and thus are usually not taken into consideration. In adition, as researchers developed photodetectors with progressively shorter cut-off wavelengths, terms such as "true solar blind"[61] begin to appear in the literature which again does not contribute much towards the precise definition of an SBD.

Another problem in following SBD research lies in the disagreement among researchers regarding AlGaN bandgap bowing parameter. As a result, the Al composition of AlGaN reported by different researchers can not be directly compared – only an approximate comparison can be made by comparing the cut-off wavelength.

Osinsky *et al.* reported AlGaN Schottky photodetector operation with a fairly flat responsivity spectra between 290 and 260 nm and a sharp cut-off on the long wavelength side.[62] The device was of a vertical geometry with a thin *i*-Schottky contact layer grown on top of a thick *n*-contact layer. This was essentially a top-illumination device.

Li *et al.* reported on the development of top-illuminated AlGaN SBD in MSM configuration based on MOCVD grown material.[63] The AlGaN device structure was grown on top of a thick GaN defect reduction layer. At a relatively high reverse bias of 90 V, the devices were found to have a peak responsivity of 107 mA/W at 272 nm. A sharp cut-off on the long wavelength side was also obtained. Noise measurement showed a $D^* = 3.3 \times 10^{10}$ cm.$Hz^{1/2}W^{-1}$ which is comparable to other AlGaN *p-i-n* detectors of that time. Soon after this report, the same group also reported on the development of back-illuminated MSM SBDs. Yang *et al.* reported on a high responsivity of 105 mA/W at 262 nm under 12 V

reverse bias.[64] The dark current from the devices was also very low. After the nucleation layer, a high-Al-content window layer was grown for TDD reduction. Because of the use of an AlGaN window instead of GaN, the structure allowed back-side illumination. In addition, a heterostructure design was used where the Al content of the window layer was higher than that of the active region. As a result, the photons with wavelengths of interest could get to the active region without getting absorbed in the thick defect-reduction layer. Biyikli *et al.* reported on high-speed top-illuminated MSM SBD fabrication using MOCVD grown AlGaN material.[65] The AlGaN device layers were grown on a thick GaN defect reduction layer. The peak responsivity was 1.6 A/W at 264 nm which included the effect of a high photoconductive gain. The time response was measured by use of a pulsed laser and a fast oscilloscope. Despite the presence of significant photoconductive effect, the devices showed impressive time response. A fast rise along with exponentially decaying fall was observed. The maximum 3 dB bandwidth was 5.4 GHz at 5 V bias. The bandwidth was found to go down with increasing bias voltages.

Pernot *et al*. reported on the development of front-illuminated AlGaN *p-i-n* SBD on GaN TDD reduction layer.[66] The peak responsivity obtained was 12 mA/W and the spectral cut-off was at 270 nm. The devices also had a very low leakage current which gave a high detectivity of $D^*>1.2\times10^{13}$ cm.$Hz^{1/2}W^{-1}$. Walker *et al*. reported on the development of top-illuminated *p-i-n* SBD grown on thick GaN defect reduction layer with very short cut-off wavelength.[67] The group used a semi-transparent Ni/Au *p*-metalization scheme to improve light collection. Under 5 V reverse bias, the peak responsivity obtained was 110 mA/W at a wavelength of 232 nm.

Since heteroepitaxial GaN material has a high TDD originating at the nucleation layer, researchers developed different variations of the lateral epitaxial overgrowth (LEO) technique that gave a significant reduction in TDD. For photodetector applications, the lower TDD is expected to improve the time response and also the detectivity by the reduction of dark current. Parish *et al*. reported on front illuminated AlGaN *p-i-n* SBDs grown on LEO GaN that showed reduction of dark current by orders of magnitude when compared to similar devices fabricated on

traditional heteroepitaxial GaN.[68] Dark current densities as low as 10 nA/cm^2 was obtained at 5 V reverse bias. A peak responsivity of 50 mA/W was obtained at a wavelength of 285 nm. The impulse-response fall time for the devices were in the range of 4.5–6.5 ns compared to 30 ns for devices fabricated on traditionally grown GaN.

Pau *et al.* reported on visible and solar-blind MSM and Schottky barrier photodiode fabrication on (111) Si substrates.[69] An AlGaN/GaN superlattice buffer layer was used to suppress crack formation and improve material quality. The superlattice also acted as an electrical insulator between the device and the Si substrate. The cut-off wavelength varied from the GaN bandedge to ~ 285 nm. While the GaN Schottky and MSM devices demonstrated good responsivity, the AlGaN devices, including those that were solar-blind, had very low responsivities.

3.2. *Back-illuminated p-i-n devices and focal-plane array*

For imaging application, significant interest exists towards the development of focal-plane arrays (FPA) of solar-blind photodetectors to be flip-chip mounted on Si electronics for defence applications such as missile detection. These devices should have a high responsivity and detectivity at zero volt-bias in order to eliminate the need for large power supply. This essentially means that only *p-n* or Schottky barrier photodetectors were relevant. Additionally, *p-n* junction photodetectors are more suitable because of the high detectivity requirement. Since flip-chip mounting si desired, the array also needs to be of a back-illuminated configuration. Additionally, inherent insensitivity to solar radiation is required in order to eliminate the need for cumbursome external optical filters. Also, in the imaging array, the performance uniformity of the individual elements of the array needs to be high.

The device design suitable for this purpose was essentially a heterostructure *p-i-n* design with the thick defect-reduction AlGaN underlayer having a somewhat larger bandgap compared to the *i*-region so that most of the photons of interest can reach the active *i*-region unabsorbed (Fig. 2). Ideally, the *n*-layer should also be of larger bandgap since photons absorbed in the *n*-layer do not contribute to the photocurrent because of the absence of collecting electric field. Also, the

n-layer generally needs to be quite thick in order to reduce the spreading resistance. If the spreading resistance is high, then the short-circuit current under illumination is reduced which essentially reduces the responsivity. However, with the high Al-containing alloys involved, obtaining a high *n*-doping was found to be difficult[70] and much of the initial work did not use a heterostructure design with an *n*-layer of higher bandgap. Optical transmittance measurement was found to be a very useful characterization technique for the purpose of optimizing the window, *i* and *n*-layers so that they have appropriate absorption wavelengths.

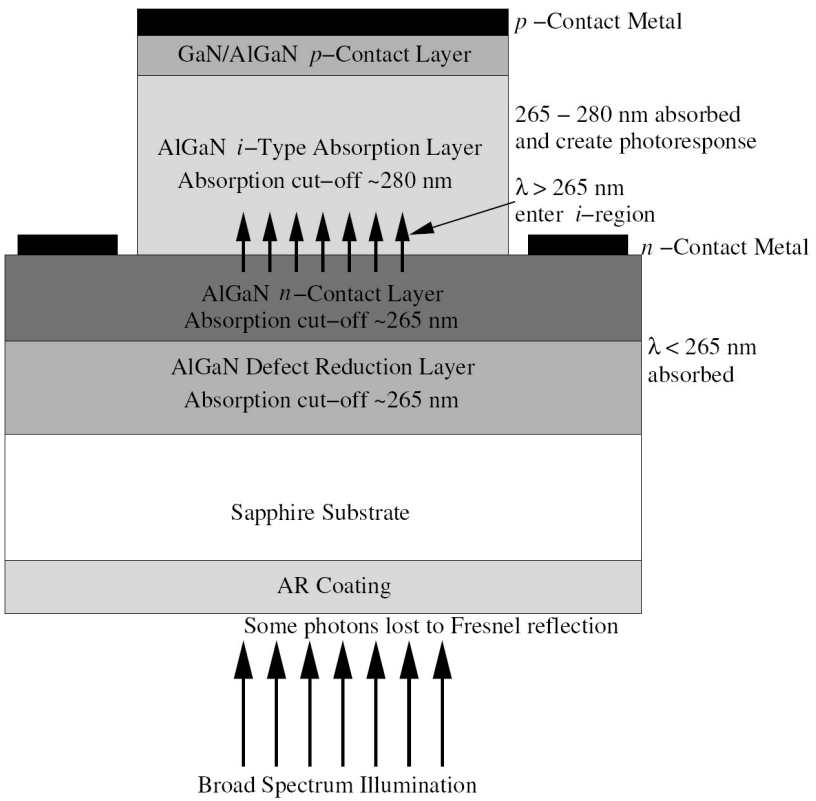

Fig. 2 A Schematic structure of heterostructure p-i-n SBD is shown. Note the absorption cut-off wavelengths of the relevant layers that lead to the responsivity spectra in the wavelength range of ~265 nm to ~280 nm.

Sandvik *et al*. reported on the development of front and back-illuminated *p-i-n* SBD structures grown using MOCVD.[71] The top-illuminated devices had LEO GaN and the back-illuminated devices had thick AlGaN buffer layers for the purpose of TDD reduction. A wide range of Al compositions were used for top-illuminated structures to obtain various cut-off wavelengths. For the back-illuminated structures, a peak responsivity of 35 mA/W was obtained at 278 nm. Brown *et al*. reported on development of high performance *p-i-n* SBDs of heterostructure design.[72] The peak responsivity reported was 51 mA/W at 273 nm. The authors reported on the development of an optimized AlGaN:Mg doping condition that led to reduction in dark current. As a result, a high detectivity of $D^*=3.5\times10^{12}$ cm.$Hz^{1/2}W^{-1}$ was obtained for the SBD devices. Lambert *et al*. reported on the development of back-illuminated *p-i-n* SBD using MOCVD grown AlGaN structure.[73] Improved growth optimization led to a peak responsivity of 79 mA/W at a wavelength of 278 nm under a reverse bias of 60 V. The device structure was not of a heterostructure design. Although *p-i-n* photodetectors are not theoreticaly expected to have a responsivity dependent on the reverse bias, these devices showed a strong bias-dependent responsivity. In order to verify that the photoresponse was from the *p-n* junction and did not result from a Schottky barrier at the *p*-metalization, the authors performed C-V measurement of a number of devices with various mesa and contact area. The capacitance was found to scale with the mesa area and not with the metal contact area, which demonstrated that the photoresponse originates at the *p-n* junction.

Tarsa *et al*. introduced a new design concept for back-illuminated *p-i-n* SBD design.[61] They proposed that if the *p*-side of the device consists solely of a thin *p*-GaN layer instead of a *p*-AlGaN/*p*-GaN structure, the device will still not have GaN related photoresponse due to the energy barrier created at the heterointerface (Figure \ref{banddiag}). The authors fabricated front-illuminated photodiodes consisting of a *p*-GaN/*i*-AlGaN/*n*-GaN structure and back-illuminated *p*-GaN/*i*-AlGaN/*n*-AlGaN structures that showed no GaN related photoresponse. This design eliminated the problems of obtaining high *p*-doping concentrations in the AlGaN material. The authors reported a peak responsivity of 33 mA/W at a wavelength of 275 nm for the back-illuminated design.

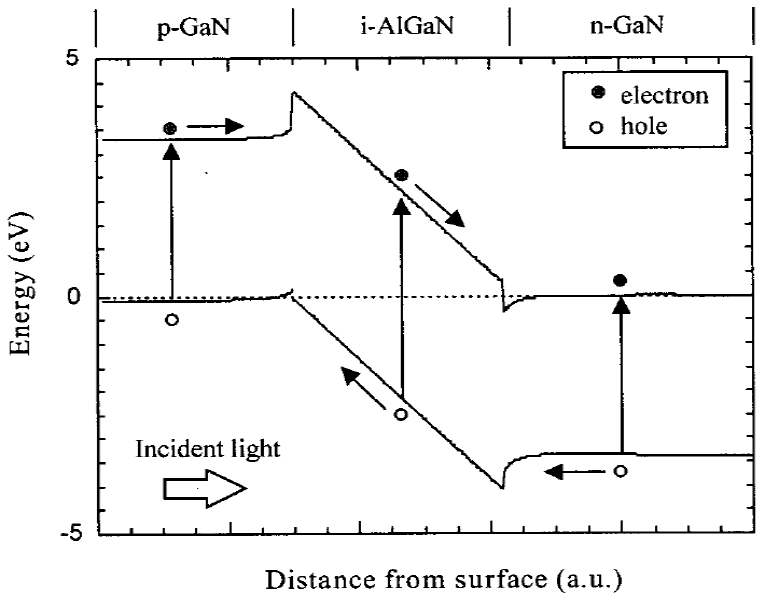

Fig. 3 Band diagram simulation indicating that even with the p-layer consisting solely of GaN, the band alignment prevents any GaN-related photoresponse. (Reused with permission from E. J. Tarsa, P. Kozodoy, J. Ibbetson, B. P. Keller, G. Parish, and U. Mishra, Applied Physics Letters, 77, 316 (2000). Copyright 2000, American Institute of Physics.

Collins *et al*. reported on the development of high doping condition in high Al-content AlGaN and its use in back-illuminated heterostructure *p-i-N* SBD.[75] With the increased photon collection coupled with a reduction of ohmic loss in the *n*-layer, the authors demonstrated a high responsivity of 90 mA/W at 269 nm. Due to the high material quality, the devices also demonstrated a low dark current leading to a high detectivity of $D^*\sim 2.0 \times 10^{14}$ cm.Hz$^{1/2}$W^{-1}. With further refinement, the same group developed improved devices with a responsivity of 120 mA/W at a slightly longer wavelength of 275 nm.[76] These devices had a record detectivity of $D^*\sim 3.0 \times 10^{14}$ cm.Hz$^{1/2}$W^{-1} which is comparable to that of the photocathode of a photomultiplier tube.[76]

The same research group reported on further optimization of the devices leading to a peak responsivity of 130 mA/W at 274 nm.[77,78] The

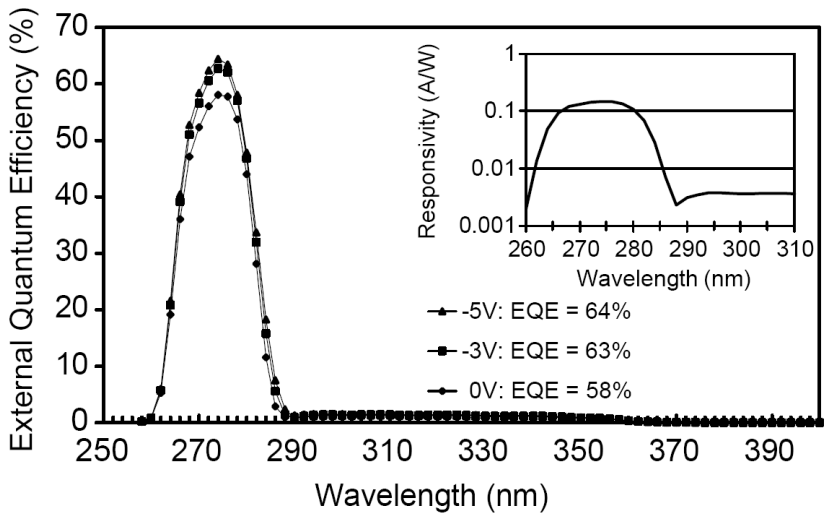

Fig. 4 The responsivity spectra of the first GaN photoconductor developed by Khan *et al*.[2] (Reused with permission from M. Asif Khan, J. N. Kuznia, D. T. Olson, J. M. Van Hove, M. Blasingame, and L. F. Reitz, Applied Physics Letters, 60, 2917 (1992). Copyright 1992, American Institute of Physics.)

responsivity and EQE spectrum is reproduced here in **Fig. 4**. After obtaining high performance back-illuminated SBDs, the group reported on the fabrication of high performance FPA using the same epitaxial structures. A high response uniformity with σ/μ=6% was obtained for a 256×256 element array.[78]

4. Conclusion

To summarize, III-nitride photodetector technology has seen significant advancement with demonstration of a wide range of devices and gradual improvement of device performance and understanding of underlying mechanisms. High performance solar-blind focal plane photodetector arrays made from AlGaN *p-i-n* structures have been demonstrated.

Presently, with the increased availability of bulk GaN and AlN substrates, the research community seems to be interested in the development of avalanche devices. The lower TDD afforded by these substrate makes it possible, on one hand, the realization of higher gain

and lower dark current and on the other hand, devices of larger area – since if the TDD is high, devices of large area fail with microplasma breakdown over the large number of dislocation covered by the device area. However, the high cost of these bulk substrates act as a significant barrier to research efforts on this topic. Nevertheless, a significant effort is going on towards the development of high-performance avalanche photodetectors in the AlGaN material system and it is hoped that solar-blind avalanche photodetectors will be realized in the near future.

On the phototransistor side, low free-hole concentration in *p*-GaN material act as a fundamental limitation as base spreading resistance remain excessively high. Due to the same limitation, III-nitride based heterojunction bipolar transistor (HBT) technology has also failed to mature. Recently, researchers from NTT Corporation in Japan have demonstrated significant progress in nitride HBT technology using *p*-InGaN material which enjoys a higher free-hole concentration. Makimoto *et al*. from NTT have recently demonstrated high performance HBT operation with high current gain β.[79] Although the use of an InGaN base essentially limits how short the responsivity cut-off wavelength can be, with the successful demonstration of InGaN-base HBT, it can be hoped that high performance nitride phototransistors can also be realized.

References

1. M. Razeghi and A. Rogalski, "Semiconductor Ultraviolet Detectors", *J. Appl. Phys.* **79**, 7433–7473, (1996).
2. M. A. Khan, J. N. Kuznia, D. T. Olson, J. M. Van Hove, M. Blasingame, and L. F. Reitz, "High-responsivity Photoconductive Ultraviolet Sensors Based on Insulating Single-Crystal GaN Epilayers", *Appl. Phys. Lett.* **60**, 2917–2919, (1992).
3. M. A. Khan, J. N. Kuznia, D. T. Olson, M. Blasingame, and A. R. Bhattarai, "Schottky Barrier Photodetector Based on Mg-Doped *p*-Type GaN Films", *Appl. Phys. Lett.* **63**, 2455–2456, (1993).
4. Q. Chen, M. A. Khan, C. J. Sun, and J. W. Yang, "Visible-Blind Ultraviolet Photodetectors Based on GaN *p-n* Junction", *Electron. Lett.* **31**, 1781–1782, (1995).
5. P. Kung, X. Zhang, D. Walker, A. Saxler, J. Piotrowski, A. Rogalski, M. Razeghi, "Kinetics of Photoconductivity in *n*-type GaN Photodetector", *Appl. Phys. Lett.*, **67**, 3792–3794, (1995).
6. F. Binet, J. Y. Duboz, E. Rosencher, F. Scholz, and V. Härle, "Mechanisms of Recombination in GaN Photodetectors", *Appl. Phys. Lett.*, **69**, 1202–1204, (1996).

7. G. M. Smith, J. M. Redwing, R. P. Vaudo, E. M. Ross, J. S. Flynn, and V. M. Phanse, "Substrate Effects on GaN Photoconductive Detector Performance", *Appl. Phys. Lett.*, **75**, 25–27, (1999).
8. O. Katz, V. Garber, B. Meyler, G. Bahir, and J. Salzman, "Gain Mechanism in GaN Schottky Ultraviolet Detectors", *Appl. Phys. Lett.* **79**, 1417–1419, (2001).
9. O. Katz, G. Bahir, and J. Salzman, "Persistent Photocurrent and Surface Trapping in GaN Schottky Ultraviolet Detectors", *Appl. Phys. Lett.* **84**, 4092–4094, (2004).
10. J. C. Carrano, T. Li, P. A. Grudowski, C. J. Eiting, R. D. Dupuis, and J. C. Campbell, "High Quantum Efficiency Metal-Semiconductor-Metal Ultraviolet Photodetectors Fabricated on Single-Crystal GaN Epilayers", *Electron. Lett.* **33**, 1980–1981, (1997).
11. E. Monroy, F. Calle, E. Muñoz, B. Beaumont, F. Omnès, and P. Gibart, "High UV/Visible Contrast Photodiodes Based on Epitaxial Lateral Overgrown GaN Layers", *Electron. Lett.* 35 1488–1489, (1999).
12. Q. Chen, J. W. Yang, A. Osinsky, S. Gangopadhyay, B. Lim, M. Z. Anwar, M. A. Khan, D. Kuksenkov, and H. Temkin, "Schottky Barrier Detectors on GaN for Visible-Blind Ultraviolet Detection", *Appl. Phys. Lett.* **70**, 2277–2279, (1997).
13. A. Osinsky, S. Gangopadhyay, R. Gaska, B. Williams, M. A. Khan, D. Kuksenov, and H. Temkin, "Low Noise *p-π-n* GaN Ultraviolet Photodetectors", *Appl. Phys. Lett.* **71**, 2234–2236, (1997).
14. D. V. Kuksenkov, H. Temkin, A. Osinsky, R. Gaska, and M. A. Khan, "Low-Frequency Noise and Performance of GaN *p-n* Junction Photodetectors", J. Appl. Phys. **83**, 2142–2146, (1998).
15. J. C. Carrano, T. Li, P. A. Grudowski, C. J. Eiting, R. D. Dupuis, and J. C. Campbell, "Current Transport Mechanisms in GaN-Based Metal-Semiconductor-Metal Photodetectors", *Appl. Phys. Lett.*, **72**, 542–544, (1998).
16. J. C. Carrano, T. Li, P. A. Grudowski, C. J. Eiting, R. D. Dupuis, and J. C. Campbell, "Comprehensive Characterization of Metal-Semiconductor-Metal Ultraviolet Photodetectors Fabricated on Single-Crystal GaN", *J. Appl. Phys.* **83**, 6148–6160 (1998).
17. J. C. Carano, T. Li, P. A. Grudowski, C. J. Eiting, D. Lambert, J. D. Schaub, R. D. Dupuis, and J. C. Campbell, Low Dark Current *pin* Ultraviolet Photodetectors Fabricated on GaN Grown by Metal Organic Chemical Vapour Deposition", *Electron. Lett.* **34**, 692–694, (1998).
18. J. C. Carrano, T. Li, D. L. Brown, P. A. Grudowski, C. J. Eiting, R. D. Dupuis, and J. C. Campbell, "High-Speed *pin* Ultraviolet Photodetectors Fabricated on GaN", *Electron. Lett.* **34**, 1779–1781, (1998).
19. G. Y. Xu, A. Salvador, W. Kim, Z. Fan, C. Lu, H. Tang, H. Morko\c c, G. Smith, M. Estes, B. Goldenberg, W. Yang, and S. Krishnankutty, "High Speed, Low Noise Ultraviolet Photodetectors Based on GaN *p-i-n* and AlGaN(*p*)-GaN(*i*)-GaN(*n*) Structures", *Appl. Phys. Lett.* **71**, 2154–2156, (1997).

20. T. Li, A. Beck, C. Collins, R. D. Dupuis, J. C. Campbell, J. C. Carrano, M. J. Schurman, and I. A. Ferguson, "Improved Ultraviolet Quantum Efficiency Using a Semitransparent Recessed Window AlGaN/GaN Heterojunction *p-i-n* Photodiode", *Appl. Phys. Lett.* **75**, 2421–2423, (1999).
21. C. J. Collins, T. Li, A. L. Beck, R. D. Dupuis, J. C. Campbell, J. C. Carrano, M. J. Schurman, and I. A. Ferguson, "Improved Device Performance Using a Semi-Transparent *p*-contact AlGaN/GaN Heterojunction Positive-Intrinsic-Negative Photodiode", *Appl. Phys. Lett.* **75**, 2138–2140, (1999).
22. V. V. Kuryatkov, H. Temkin, J. C. Campbell, and R. D. Dupuis, "Low-Noise Photodetectors Based on Heterojunctions of AlGaN-GaN", *Appl. Phys. Lett.* **78**, 3340–3342, (2001).
23. S. K. Zhang, W. B. Wang, I. Shtau, F. Yun, L. He, H. Morkoç, X. Zhou, M. Tamargo, and R. R. Alfano, "Backilluminated GaN/AlGaN Heterojunction Ultraviolet Photodetector with High Internal Gain", *Appl. Phys. Lett.* **81**, 4862–4864, (2002).
24. J. T. Torvik, J. I. Pankove, S. Nakamura, I. Grzegory, and S. Porowski, "The Effect of Threading Dislocations, Mg Doping, and Etching on the Spectral Responsivity in GaN-Based Ultraviolet Detectors", *J. Appl. Phys.* **86**, 4588–4593, (1999).
25. D. Walker, X. Zhang, P. Kung, A. Saxler, S. Javadpour, J. Xu, and M. Razeghi, "AlGaN Ultraviolet Photoconductors Grown on Sapphire", *Appl. Phys. Lett.* **68**, 2100–2101, (1996).
26. F. Omnès, N. Marenco, B. Beaumont, Ph. de Mierry, E. Monroy, F. Calle, and E. Muñoz, "Metalorganic Vapor-Phase Epitaxy-Grown AlGaN Materials for Visible-Blind Ultraviolet Photodetector Applications", *J. Appl. Phys.* **86,** 5286–5292, (1999).
27. E. Monroy, F. Calle, E. Muñoz, and F. Omnès, "AlGaN Metal-Semiconductor-Metal Photodiodes'', *Appl. Phys. Lett.* **74**, 3401–3403, (1999).
28. E. Muñoz, E. Monroy, J. L. Pau, F. Calle, E. Calleja, F. Omnès, and P. Gibart, "(Al,Ga)N Ultraviolet Photodetectors and Applications", *Phys. Stat. Sol. A,* **180** 293–300, (2000).
29. T. N. Oder, J. Li, J. Y. Lin, and H. X. Jiang, "Photoresponsivity of Ultraviolet Detectors Based on $In_xAl_yGa_{1-x-y}N$ Quaternary Alloys", *Appl. Phys. Lett.* 77, 791–793, (2000).
30. K. S. Stevens, M. Kinniburgh, and R. Beresford, "Photoconductive Ultraviolet Sensor Using Mg-Doped GaN on Si(111)", *Appl. Phys. Lett.*, **66**, 3518–3520, (1995).
31. Z. M. Zhao, R. L. Ling, P. Chen, D. J. Xi, Z. Y. Luo, R. Zhang, B. Shen, Z. Z. Chen, and Y. D. Zheng, "Metal-Semiconductor-Metal GaN Ultraviolet Photodetectors on Si(111)", *Appl. Phys. Lett.* **77**, 444–446, (2000).
32. A. Osinsky, S. Gangopadhyay, J. W. Wang, R. Gaska, D. Kuksenkov, H. Temkin, I. K. Shmagin, Y. C. Chang, J. F. Muth, and R. M. Kolbas, "Visible-Blind GaN

Schottky Barrier Detectors Grown on Si(111)", *Appl. Phys. Lett.* **72**, 551–553, (1998).

33. J. L. Pau, E. Monroy, E. Muñoz, F. B. Naranjo, F. Calle, M. A. Sánchez-García, and E. Calleja, "AlGaN Photodetectors Grown on Si(111) by Molecular Beam Epitaxy", *J. Crystal Growth*, **230**, 544–548, (2001).
34. J. L. Pau, E. Monroy, F. B. Naranjo, E. Muñoz, F. Calle, M. A. Sánchez-García, and E. Calleja, "High Visible Rejection AlGaN Photodetectors on Si(111) Substrates", *Appl. Phys. Lett.* **76**, 2785–2787, (2000).
35. H. F. B. Ozelo, L. E. M. de Barros, Jr., B. Nabet, L. G. Neto, M. A. Romero, A. C. S. Ramos, and J. W. Swart, "MSM Photodetector with an Integrated Microlens Array for Improved Optical Coupling", *Microwave Opt. Tech. Lett.* **26**, 357–360, (2000).
36. J. K. Kim, H. W. Jang, C. M. Jeon, and J.-L. Lee, "GaN Metal-Semiconductor-Metal Ultraviolet Photodetector with IrO_2 Schottky Contact", *Appl. Phys. Lett.* **81**, 4655–4657, (2002).
37. Z. C. Huang, J. C. Chen, D. B. Mott, and P. K. Shu, "High Performance GaN Linear Array", *Electron. Lett.*, **32,** 1324–1325, (1996).
38. K. Kishino, M. Yonemaru, A. Kimuchi, and Y. Toyoura, "Resonant-Cavity-Enhanced UV Metal-Semiconductor-Metal (MSM) Photodetectors Based on AlGaN System", *Phys. Stat. Sol. A*, **188**, 321–324, (2001).
39. V. Adivarahan, G. Simin, J. W. Yang, A. Lunev, M. A. Khan, N. Pala, M. Shur, and R. Gaska, "SiO_2-Passivated Lateral-Geometry GaN Transparent Schottky-Barrier Detectors", *Appl. Phys. Lett.* 77, 863–865, (2000).
40. J. K. Sheu, M. L. Lee, L. S. Yeh, C. J. Kao, C. J. Tun, M. G. Chen, G. C. Chi, S. J. Chang, Y. K. Su, and C. T. Lee, "Planar GaN n^+-p Photodetectors Formed by Si Implantation into p-GaN", *Appl. Phys. Lett.* **81**, 4263–4265, (2002).
41. S. W. Seo, K. K. Lee, S. Kang, S. Huang, W. A. Doolittle, N. M. Jokerst, and A. S. Brown, "GaN Metal-Semiconductor-Metal Photodetectors Grown on Lithium Gallate Substrates by Molecular-Beam Epitaxy", *Appl. Phys. Lett.* **79**, 1372–1374, (2001).
42. R. P. Joshi, "Simulations for the Transient Response of Graded $(Al_xGa_(1-x)N)$ Submicron Photodetectors", *J. Appl. Phys.* **76**, 4434–4436, (1994).
43. T. Palacios, E. Monroy, F. Calle, and F. Omnès, "High-Responsivity Submicron Metal-Semiconductor-Metal Ultraviolet Detectors", *Appl. Phys. Lett.* **81**, 1902–1904, (2002).
44. M. A. Khan, M. S. Shur, Q. Chen, J. N. Kuznia, and C. J. Sun, "Gated Photodetector Based on GaN/AlGaN Heterostructure Field Effect Transistor", *Electron. Lett.* **31**, 398–400, (1995).
45. J. Z. Li, J. Y. Lin, H. X. Jiang, and M. A. Khan, "Effects of Persistent Photoconductivity on the Characteristic Performance of an AlGaN/GaN Heterostructure Ultraviolet Detector", *Appl. Phys. Lett.* **72**, 2868–2870, (1998).

46. J. J. Zhou, R. L. Liang, B. Wen, L. Y. Liang, X. Li Ji, B. Shen, R. Zhang, and Y. D. Zheng, "Influence of AlGaN/GaN Interface Polarization Fields on the Properties of Photoconductive Detectors", *J. Appl. Phys.* **95**, 5925–5927, (2004).
47. S. Ghosh, O. Brandt, H. T. Grahn, and K. H. Ploog, "Strained M-Plane GaN for the Realization of Polarizaton-Sensitive Photodetectors", *Appl. Phys. Lett.* **81**, 3380–3382, (2002).
48. A. Osinsky, M.S. Shur, R. Gaska, and Q. Chen, "Avalanche Breakdown and Breakdown Luminescence in *p-π-n* GaN Diodes", *Electron. Lett.* **34**, 691–692, (1998).
49. K. A. McIntosh, R. J. Molnar, L. J. Mahoney, A. Lightfoot, M. W. Geis, K. M. Molvar, I. Melngailis, R. L. Aggarwal, W. D. Goodhue, S. S. Choi, D. L. Spears, and S. Verghese, "GaN Avalanche Photodiodes Grown by Hydride Vapor-Phase Epitaxy", *Appl. Phys. Lett.* **75**, 22, 3485–3487, (1999).
50. J. C. Carrano, D. J. H. Lambert, C. J. Eiting, C. J. Collins, T. Li, S. Wang, B. Yang, A. L. Beck, R. D. Dupuis, and J. C. Campbell, "GaN Avalanche Photodiodes", *Appl. Phys. Lett.* **76**, 924–926, (2000).
51. J. B. Limb, D. Yoo, J. H. Ryou, W. Lee, S. C. Shen, R. D. Dupuis, M. L. Reed, C. J. Collins, and M. Wraback, "GaN Ultraviolet Avalanche Photodiodes With Optical Gain Greater Than 1000 Grown on GaN Substrates by Metal-Organic Chemical Vapor Deposition", *Appl. Phys. Lett.* **89**, 11112, (2006).
52. US Army Research Laboratory, AMSRL-SE-EM, 2800 Powder Mill Road, Adelphi, Maryland 20783-1197
53. D. Hanser, E. Preble, N. M. Williams, and K. Evans
54. Kyma Technologies, Inc., 8829 Midway West Road, Raleigh, North
55. B. Yang, T. Li, K. Heng, C. Collins, S. Wang, J. C. Carrano, R. D. Dupuis, J. C. Campbell, M. J. Schurman, and I. T. Ferguson, "Low Dark Current GaN Avalanche Photodiodes", *IEEE J. Quant. Elec.*, **71**, 1389–1391, (2000).
56. W. D. Yang, T. E. Nohava, S. Krishnankutty, R. Torreano, S. McPherson, and H. Marsh, "High gain GaN/AlGaN Heterojunction Phototransistor", *Appl. Phys. Lett.* **73**, 978–980, (1998).
57. L. Chernyak, A. Osinsky, S. J. Pearton, and F. Ren, "Phototransistor Measurements in AlGaN/GaN HBTs", *Electron. Lett.* **37**, 1411–1412, (2001).
58. A. Motogaito, M. Yamaguchi, K. Hiramatsu, M. Kotoh, Y. Ohuchi, K. Tadatomo, Y. Hamamura, and K. Fukui, "Characterization of GaN-Based Schottky Barrier Ultraviolet (UV) Detectors in the UV and Vacuum Ultraviolet (VUV) Region Using Synchrotron Radiation", *Jpn. J. Appl. Phys.* **40**, L368–L370, (2001).
59. A. Motogaito, K. Ohta, K. Hiramatsu, Y. Ohuchi, K. Tadatomo, Y. Hamamura, and K. Fukui, "Characterization of GaN Based UV-VUV Detectors in the Range 3.4–25 eV by Using Synchrotron Radiation", *Phys. Stat. Sol. A,* **188**, 337–340, (2001).
60. E. Monroy, T. Palacios, O. Hainaut, F. Omnès, F. Calle, J.-F. Hochedez, "Assessment of GaN Metal-Semiconductor-Metal Photodiodes for High-Energy Ultraviolet Photodetection", *Appl. Phys. Lett.* **80**, 3198–3200, (2002).

61. E. J. Tarsa, P. Kozodoy, J. Ibbetson, B. P. Keller, G. Parish, and U. Mishra, "Solar-Blind AlGaN-Based Inverted Heterostructure Photodiodes", *Appl. Phys. Lett.* **77**, 316–318, (2000).
62. A. Osinsky, S. Gangopadhyay, B. W. Lim, M. Z. Anwar, M. A. Khan, D. V. Kuksenkov, and H. Temkin, "Schottky Barrier Photodetectors Based on AlGaN", *Appl. Phys. Lett.* **72**, 742–744, (1998).
63. T. Li, D. J. H. Lambert, A. L. Beck, C. J. Collins, B. Yang, M. M. Wong, U. Chowdhury, R. D. Dupuis, and J. C. Campbell, "Solar-Blind $Al_xGa_{1-x}N$-Based Metal-Semiconductor-Metal Ultraviolet Photodetectors", *Electron. Lett.*, **36**, 1581–1583, (2000).
64. B. Yang, D. J. H. Lambert, T. Li, C. J. Collins, M. M. Wong, U. Chowdhury, R. D. Dupuis, and J. C. Campbell, "High-Performance Back-Illuminated Solar-Blind AlGaN Metal-Semiconductor-Metal Photodetectors", *Electron. Lett.* **36**, 1866–1867, (2000).
65. N. Biyikli, I. Kimukin, T. Kartalogu, O. Aytur, and E. Ozbay, "High-Speed Solar-Blind AlGaN-Based Metal-Semiconductor-Metal Photodetectors", *Phys. Stat. Sol. C*, **0**, 2314–2317, (2003).
66. C. Pernot, A. Hirano, M. Iwaya, T. Detchprohm, H. Amano and I. Akasaki, "Solar-Blind UV Photodetectors Based on GaN/AlGaN *p-i-n* Photodiodes", *Jpn. J. Appl. Phys.* **39**, L387–L389, (2000).
67. D. Walker, V. Kumar, K. Mi, P. Sandvik, P. Kung, X. H. Zhang, and M. Razeghi, "Solar-Blind AlGaN Photodiodes with Very Low Cutoff Wavelength", *Appl. Phys. Lett.* **76**, 403–405, (1998).
68. G. Parish, S. Keller, P. Kozodoy, J. P. Ibbetson, H. Marchand, P. T. Fini, S. B. Fleischer, S. P. DenBaars, U. K. Mishra, and E. J. Tarsa, "High-Performance (Al,Ga)N-Based Solar-Blind Ultraviolet *p-i-n* Detectors on Laterally Epitaxially Overgrown GaN", *Appl. Phys. Lett.* **75**, 247–249, (1999).
69. J. L. Pau, E. Muñoz, M. A. Sánchez-García, and E. Calleja, "Visible and Solar-Blind AlGaN Metal-Semiconductor-Metal Photodetectors Grown on Si(111) Substrates", *Phys. Stat. Sol. A*, **192**, 314–319, (2002).
70. C. Stampfl and C. G. Van de Walle, "Doping of $Al_xGa_{1-x}N$", *Appl. Phys. Lett.* **72**, 459–461, (1998).
71. P. Sandvik, F. Shahedipour, R. McClintock, A. Yasan, P. Kung, and M. Razeghi, "$Al_xGa_{1-x}N$ for Solar-Blind UV Detectors", *J. Crystal Growth*, **231**, 366–370, (2001).
72. J. D. Brown, J. Li, P. Srinivasan, J. Matthews, and J. F. Schetzina, "Solar-Blind AlGaN Heterostructure Photodiodes", *MRS. Internet J. Nitride Semicond. Research*, **5**, 9, (2000).
73. D. J. H. Lambert, M. M. Wong, U. Chowdhury, C. Collins, T. Li, H. K. Kwon, B. S. Shelton, T. G. Zhu, J. C. Campbell, and R. D. Dupuis, "Back Illuminated AlGaN Solar-Blind Photodetectors", *Appl. Phys. Lett.* 77, 1900–1902, (2000).

74. P. Lamarre, A. Hairston, S. P. Tobin, K. K. Wong, A. K. Sood, M. B. Reine, M. Pophristic, R. Birkham, I. T. Ferguson, R. Singh, C. R. Eddy Jr., U. Chowdhury, M. M. Wong, R. D. Dupuis, P. Kozodoy, and E. J. Tarsa, "AlGaN UV Focal Plane Arrays", *Phys. Stat. Sol. A* **188**, 289–292, (2001)
75. C. J. Collins, U. Chowdhury, M. M. Wong, B. Yang, A. L. Beck, R. D. Dupuis, and J. C. Campbell, "Improved Solar-Blind Detectivity Using an $Al_xGa_{1-x}N$ Heterojunction *p-i-n* Photodiode", *Appl. Phys. Lett.* **80**, 3754–3756, (2002).
76. C. J. Collins, U. Chowdhury, M. M. Wong, B. Yang, A. L. Beck, R. D. Dupuis, and J. C. Campbell, "Improved Solar-Blind External Quantum Efficiency of Back-Illuminated $Al_xGa_{1-x}N$ Heterojunction *pin* Photodiodes", *Electron. Lett.* **38**, 824–825, (2002).
77. U. Chowdhury, M. M. Wong, C. J. Collins, B. Yang, J. C. Denyszyn, J. C. Campbell and R. D. Dupuis, "High-performance Solar-Blind Photodetector Using an $Al_{0.6}Ga_{0.4}N$ *n*-Type Window Layer", J. Crystal Growth, **248**, 552–555, (2003).
78. U. Chowdhury, "MOCVD Growth for UV Photodetectors and Light Emitting Diodes", doctoral dissertation, University of Texas at Austin, Dec. 2002.
79. T. Makimoto, Y. Yamauchi, and K. Kumakura, "High-Power Characteristics of GaN/InGaN Double Heterojunction Bipolar Transistor", *Appl. Phys. Lett.* **84**, 1964–1966, (2004).

CHAPTER 8

LASER DIODES GROWN ON BULK GALLIUM NITRIDE SUBSTRATES

P. Perlin, M. Leszczyński, P. Prystawko, M. Boćkowski, I. Grzegory, C. Skierbiszewski, T. Suski

Institute of High Pressure Physics, Polish Academy of Sciences, Sokolowska 29/37, 01-142 Warsaw, Poland
e-mail:piotr@Unipress.waw.pl

1. Introduction

Gallium nitride laser diodes are at present the shortest-wavelength semiconductor-based emitters of the coherent light. Thanks to their high photon energy, they not only can compete with and replace conventional gas and solid state lasers but they also inspire engineers to use semiconductors lasers for the creation of brand new devices which may change the technological landscape of the modern civilization. The development of the "blue laser" technology is due to the pioneering works of Pankove, Maruska, Illegems, Monemar[1] (1967-1978) followed by two crucial discoveries of Amano and Akasaki (low temperature buffer layer 1986 [2] and p-type doping (1989)[3] . We due the solution of many technical problems related to the fabrication of the nitrides green/blue/violet light emitters to Shuji Nakamura from Nichia Chemicals. His motivation, talent and the vision facilitated the fast conversion of scientific achievements into the industrial products. In 1993-1994, his team released first industrial grade blue InGaN light emitting diode.[4] Only two years later (fall 1995) he demonstrated first current injection laser diode setting up the world record for the shortest light emitting semiconductor laser diode (417 nm).[5] The active area of this device was composed from 26 InGaN quantum wells! The lasing was achieved at a very elevated voltage close to 30 V which clearly prohibited the continuous wave (CW) operation. This latter parameter (voltage) was gradually improved together with the whole laser design.

In the mid 1996 the ridge geometry was introduced by the same team.[6] The voltage has been reduced to 20 V, threshold current density to 3 kA/cm^2 and the number of quantum wells to 5. By the end of 1996 Nakamura *et al.* demonstrates the first CW operation of violet InGaN laser diode.[7] The lifespan of the device was only one second but the threshold voltage of this device was further reduced to 8 V. By the end of 1996 the lifetime of continues wave operated devices was extended to 27 h,[8] the threshold voltage reduced to 5.5 V and the threshold current density kept at the level of 3.6 kA/cm^2. During the year 1997, the laser lifetime was further extended to 300 hours.[9] Very steep learning curve observed during 1996 and 1997 brought promises of almost immediate commercialization of the violet laser diodes, so much needed for new generation of optical storage system (DVD). However, the reality turned out to be much more complex. The InGaN lasers structures mentioned above were grown on the sapphire substrates, which (because of the large lattice and thermal mismatch to GaN) resulted in generation of threading dislocation of density 10^8-10^9 cm^{-2}. This is a well known mystery of nitrides, that InGaN active layer can act as an efficient emitter in spite of large density of dislocations. The explanation, based on carrier localization, was proposed by Chichibu *et al.*[10] and still is accepted description of radiative transitions in InGaN alloys. In this model, the potential fluctuation caused by inhomogeneous In distribution localize the carriers and thus prevent them from diffusing to nonradiative recombination centers. While it was experimentally proven that InGaN quantum wells may efficiently emit light even in presence of 10^{10} cm^{-2} of dislocation, it turned out that such high defect density has a tremendous influence on the laser diode lifetime. In 1997, it was clear for Nakamura and the researchers from the other groups, that without a substantial improvement in the crystalline quality of the laser structures, the required reliability standards will never be met. Not having at this time good quality GaN crystals available for substrates, the researchers turned into finding an adequate dislocation filtering method. The technique they employed at that time is called ELOG (Epitaxial Lateral Overgrowth) known also under other acronyms like ELO and LEO [11]. The method consists in interrupting GaN layer growth, deposition of oxide or metal mask in the form of stripes (e.g. 5 μm wide stripe with periodicity of 13 μm[12]). After this step the wafer returns to MOVPE reactor where the mask is overgrown by relatively thick layer of GaN (e.g. 12-20 μm[12]). The regions above the mask (wings) are characterized by much lower

dislocation density than the areas not masked by an oxide. The structure prepared in this way is called "ELOG substrate" and is a starting point for laser diode manufacturing. The second improvement introduced to the laser diode design was the replacement of AlGaN claddings by GaN/AlGaN Strained – Layer-Superlattice.[1]. This structure consisted of the sequence of GaN and AlGaN layers of thicknesses between 1.5 and 4 nm. The introduction of this structure helped a great deal in the elimination of cracks induced by the presence of large tensile strain in the claddings layers of the laser diode. Both mentioned above improvement (realized between 1997-1998) helped in demonstration the laser diode lifetime reaching 10 000 h.[12,13] Meanwhile, other Japanese and US groups succeeded in fabrication of pulse operated InGaN lasers. These were among others: Toshiba group (1996[14]), Fujitsu team (1997[15]), XEROX group (1997,[16] Cree and North Carolina State University team (1997)[17])).

The advancement in ELOG technology did not remove however all the obstacles hampering the proliferation of nitride laser diodes technology. The nitride ELOG structure fabricated on the sapphire was thick enough to cause the wafer bowing which made the laser diode processing very difficult. Also the method of mirror fabrication by the dry etching could not produce mirrors (at least at this time) equal in the quality to these fabricated by cleavage in the standard materials. Consequently, the need for the use of sapphire free substrates for laser diode epitaxy was already at that time very clear.

Nichia team[12] was probably the first to prepare free standing gallium nitride substrate for laser diode fabrication. These wafers were fabricated by applying the following steps[12]:

1.) The growth of 2 μm thick GaN layer on C-face sapphire substrate.
2.) Deposition of 2 μm thick SiO_2 layer and its pattering into 3 μm wide (13 μm period) stripes.
3.) Overgrowth of the mask by 20 μm thick GaN layer.
4.) The growth of additional 80 μm layer of GaN (most likely by HVPE technique though it was not specified in Reference 12).
5.) Removal of the sapphire substrate by mechanical polishing

Free-standing pseudo-wafers prepared by this method were subsequently used for MOVPE epitaxy of laser diode structures. The main modification introduced by Nichia group was to increase the thickness of lower AlGaN/GaN superlattice serving as a cladding layer.[12]

The reason for this was the need for suppressing the electromagnetic mode leakage into the substrate area. In contrast to sapphire based laser diodes, in that case there is no additional reflecting interface (sapphire/GaN). Though the authors did not report the improvement in the threshold parameters of laser diodes made on free standing GaN material, the lifetime of these devices seemed to be improved and to exceed 10 000 h. The first step towards the production of laser diodes on GaN substrates was made!

2. GaN Substrates for Laser Diodes Applications

From the very beginning of its history, the nitride epitaxial technology seeks for the method of crystallizing large boule-like gallium nitride single crystals in order to slice them into well oriented GaN wafers of lateral dimensions of 2-3 inches. However due to extreme melting conditions of GaN, this material cannot be grown from its stoichiometric melt by the standard Czochralski or Bridgman methods. Gallium nitride melts at high nitrogen pressure (6 GPa) and high temperature (2497 K).[18] It implicates that the practical method of growth should imply pressures and temperatures lower than these characteristic for the melting point of this semiconductor.

Among the most promising method of growing GaN substrates, Hydride Vapor Phase Epitaxy (HVPE) plays, at present, the most prominent role. HVPE growth consists in GaN deposition on foreign substrates (sapphire, GaAs, SiC) at temperatures about 1323 K and at ambient pressure. The foreign substrate is removed from the sample by etching or laser lift off technique and then a large diameter free-standing GaN wafer may be obtained. The big advantage of this method is relatively fast growth rate in c-direction, exceeding sometimes 100-200 μm/h.[19,20,21] Very high quality free standing quasi-bulk GaN crystals have been grown in Sumitomo Electric. They used a combination of HELO (Heteroepitaxial Lateral Overgrowth)[22,23] which relies on the direct HVPE epitaxy on SiO_2 masked GaAs. The next step of this method is called DEEP – Defect Elimination by the Epitaxial growth with inverse-pyramidal Pits. The essence of this method is the to localize and concentrate the threading dislocations in the center of inverse-pyramidal pits, growing spontaneously under properly chosen growth conditions. It is worth noticing here that the localization of the pits is independent on the initial distribution of the HELO mask openings.[23] In

spite of inhomogeneous dislocation density varying from $5 \times 10^5 cm^{-2}$ to $5 \times 10^8 cm^{-2}$ in Sumitomo's crystals high quality laser structures have been grown on these substrates by both MOCVD[24] and MBE[25] methods. It should also be noticed that Nichia reported frequently on growing their laser structures on ELOG/HVPE free-standing substrates.[26] Unfortunately, it is difficult to say what technology is used for the production purposes. The next method, recently strongly developed, is crystallization from solutions in supercritical NH_3 [27,28] also called ammonothermal method. Herein, the typical pressure and temperature ranges are 0.1-0.3 GPa and 673–873 K respectively. Both, the spontaneous growth resulting in a few millimeter size crystals and the growth seeded with the free standing HVPE-GaN wafers have been studied. The typical dislocation densities in the GaN crystals obtained from supercritical ammonia are $10^4 cm^{-2}$-$10^5 cm^{-2}$. However, a real bulk crystals exceeding 1 cm grown entirely by this method have never been officially reported. It seems the main problem encountered in this approach is the low growth rate of the order of 0.1 mm per day. Another problem is to find adequate mineralizer (usually alkali metal) to the solution in order to support dissolution of GaN.

Gallium nitride can be also grown using the Na flux method at temperatures from 973 K to 1273 K and nitrogen pressure up to 5 MPa. This method has been developed in Tohoku University[29] and Osaka University[30] and yields bulk GaN single crystals with a size of few millimeters and defect density of order of $10^4 cm^{-2}$. Various flux composition like Ca-Na and Li-Na have been also studied.[31] Recently, the liquid phase epitaxy (LPE) technique applied to the Ca-Na flux system has been reported.[32] 150 μm GaN thick layer with the dislocation density of order of 2×10^5 cm^{-2} has been deposited on MOCVD sapphire/GaN template. Up to our knowledge no device or epitaxial structure grown on the crystals by sodium flux method has been so far reported in the literature.

The crystals with the lowest dislocation density- 10^2 cm^{-2} have been obtained by High Nitrogen Pressure Solution (HNPS) method and used with success as substrates for lasers diodes.[33] The HNPS method is based on direct synthesis reaction between liquid gallium and nitrogen at high temperature (up to 2000 K) and high nitrogen pressure (up to 2 GPa). The spontaneous growth of GaN by this method results in crystals having form of hexagonal platelets (up to 3 cm^2 in diameter) or needles with length up to 1 cm. The high-pressure directional crystallization method

(technique similar to LPE), with GaN hexagonal platelets as a seed, has been also intensively examined and resulted in 100 μm of new deposited GaN with stable morphology and good quality.[34] Bigger crystals seeded with high pressure GaN (HNP-GaN) have been obtained using Hydride Vapor Phase Epitaxy (HVPE) method.[35] However in this case, in new deposited material the dislocations are often generated and the method requires further optimization.

In this chapter the present status of the GaN growth by HPNS method will be reviewed. The attempts of growing low dislocation density bulk GaN crystals, combining HPS and HVPE technologies, will be also presented.

2.1. *High nitrogen pressure solution growth method and its experimental set up*

The High Nitrogen Pressure Solution method is a temperature gradient growth method based on direct reaction between gallium and nitrogen at high temperature and high nitrogen pressure.

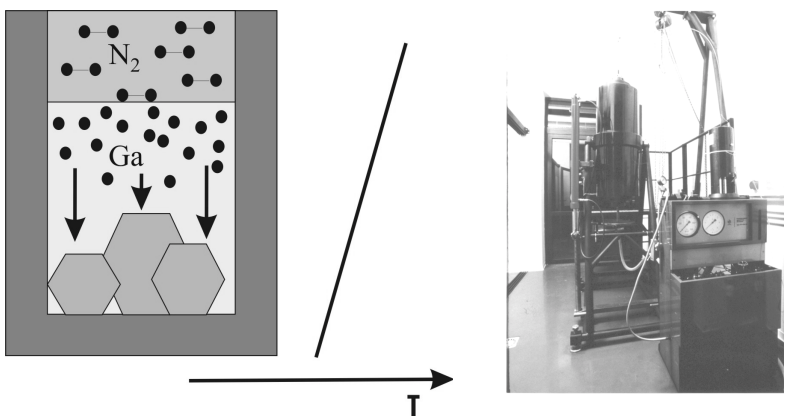

Fig. 1. a) Schematic illustration of the crystallization of GaN from the solution in a temperature gradient b) A general view of the experimental system for crystal growth of GaN at N_2 pressure.

Figure 1a presents schematic illustration of the crystallization by HPNS method. Nitrogen molecules dissociate on gallium surface and dissolve in the metal. Therefore, the crystals are grown from the solution of atomic nitrogen in liquid gallium. Supersaturation, the driving force

for the crystallization process, is created by the application of temperature gradient along the liquid gallium. Thus the HPNS method consists of three stages: i/ dissociative adsorption of nitrogen on liquid metal surface, ii/ dissolution and transport of nitrogen atoms from the hot end of the solution to the cooler one, iii/ crystallization process. The first stage has been analyzed in details by quantum mechanical calculations.[36] The nitrogen molecule approaching the metal surface is repelled by the metal, which results in a potential barrier. If the molecule has enough energy to overcome this barrier, it gets closer to the metal and dissociates into two nitrogen atoms, forming new bonds with the metal. The potential barrier is lower than the binding energy in the nitrogen molecule (9.8 eV/molecule). However, its value is quite high-4.8 eV, which suggests the dissociation process can be kinetically controlled even for relatively high temperatures. It should be noted that for oxygen interacting with gallium, there is no potential barrier and therefore one can always expect the oxygen atoms in the metal during crystal growth experiments.

Due to temperature gradient in the system, the atomic nitrogen is transported from the hot end of the solution to the cooler part. The convection mechanism plays the dominant role in the transport phenomenon. This follows from the simple estimation based on comparison of nitrogen flows induced by diffusion and convection.[37,38] The equilibrium curve, nitrogen pressure-temperature, have been determined by Karpinski *et al*.[39] One of the typical experimental system for crystal growth of GaN at nitrogen pressure is shown in Fig. 1b. This system (two visible high-pressure chambers) is connected to the central pressure line where 1 GPa of nitrogen can be obtained by a set of membrane compressors and intensifiers. Vertically or horizontally positioned technological gas pressure chamber (reactor) of internal diameter of 4, 6 or 10 cm is connected by a capillary to the special gas compressor, which serves as a reservoir of nitrogen and allows to stabilize the pressure in the chamber during experiments. The multi-zone cylindrical graphite furnace, capable of reaching temperatures up to 2000 K, is placed inside the gas pressure reactor. The high pressure chamber is equipped with additional systems necessary for: annealing in vacuum, cooling of the reactor, electronic stabilization and programming of pressure and temperature.

The typical crystal growth experiment is that the metal (Ga), placed in the crucible, is heated in the furnace inside high pressure chamber with a

constant rate to the given temperature gradient. Then the system is annealed at these conditions under high nitrogen pressure during 100-150 hours. The pressure and temperatures in the whole sample correspond to the nitride stability range. During the crystallization process gallium nitride crystals grow spontaneously from the walls of the crucible perpendicular to the wall surfaces.[40]

2.2. *Habit and morphology of HNP-GaN crystals grown without seeding*

The dominating morphological form of GaN crystals grown by the high pressure method described in the previous section is a thin hexagonal platelet (see Fig. 2).

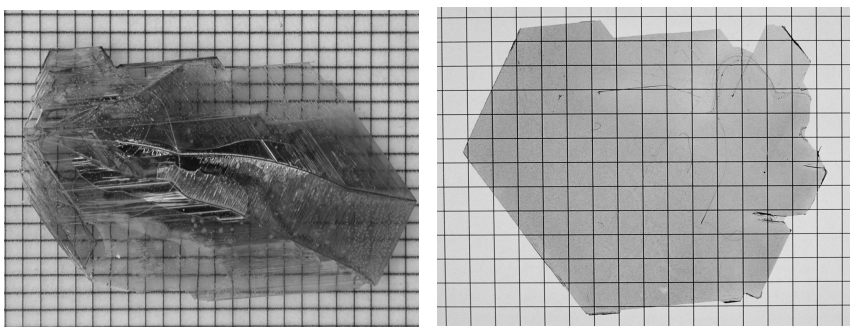

A B

Fig. 2. GaN crystals obtained from the solution in liquid gallium a) as grown, b) after epi-ready preparation. Grid: 1 mm.

The large hexagonal surfaces of the platelets correspond always to {0001} polar crystallographic planes of the wurzite structure. The side faces of the crystals are the polar {10-11} and also non-polar {10-10} planes. The maximum lateral size of the platelets for 100-150 h processes, is up to 3 cm^2, whereas the thickness is about 100 μm. The crystals in the form of hexagonal platelets grown slowly, with a rate < 0.1mm/h into {10-10} directions (perpendicular to the c-axis), are single crystals. They are slightly gray or transparent, very often with flat

mirror like faces. The habit of the crystals does not change for solutions containing impurities like Mg, Be, Zn, Fe, Mn, Gd or Er.

For crystals grown without an intentional doping (strongly n-type) the unstable surface always corresponds to the Ga-polar (0001) face of GaN, whereas for crystals doped with Mg (semi-insulating) it is always the opposite N-polar (000-1) face. The polarity of the crystal surfaces was identified by etching in hot alkali water solutions since the Ga-polar surface is inert to etching whereas the N-polar one etches very well for both types of crystals. The method was calibrated by CBED[41,42] and XPS[43] measurements.

2.3. *Seeded growth by HNPS method*

The main disadvantage of the spontaneous crystal growth method is its poor reproducibility of the size and distribution of GaN crystals in the crucible. Better control of these two parameters may be achieved by growth with a seed crystals introduced intentionally into the solution.

The directional crystallization method (technique similar to LPE i.e. deposition of GaN on the substrate to force the growth in particular direction) with hp-GaN platelets and/or MOCVD GaN/sapphire templates as seeds has been examined recently[34]. Figures 3a and 3b present a general view and the cross section of the samples deposited on MOCVD GaN/sapphire template, respectively.

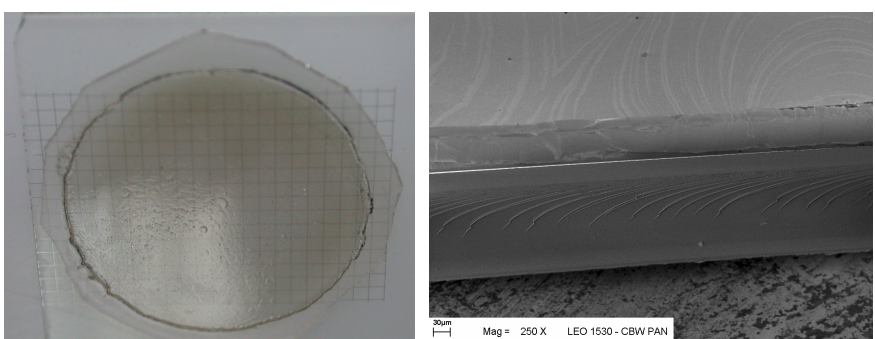

A B

Fig 3. SEM and optical images of the samples deposited on MOCVD GaN/sapphire templates a) general view of 100 μm thick GaN layer b) the cross section.

It has been shown that there are two factors responsible for GaN growth in c-direction.[34] For short time the growth rate is governed mainly by nitrogen transport to the crystallization zone. In longer time, even at big temperature gradients, the surface kinetics factor becomes more important. The formation of macrosteps and terraces slow down the GaN growth in c-direction. Thus, the main problem of the crystallization in the c-direction on HNP-GaN is the small growth rate (1-2 μm/h). The dislocation density in new deposited material is the same as in the seed: 10^2 cm^{-2}. For longer than 200 h processes the parasitic nucleation i.e. the GaN crystals nucleation from the wall of the crucible and the baffle plate slows down the seeded growth in c-direction even more what is the biggest disadvantage of this method.

2.4. *HVPE growth on HNP-GaN crystals*

As mentioned the HVPE, in contrast to HPNS method, allows crystallization of GaN with a considerably higher rate in the c-direction. Thus it seems to be extremely suitable to increase the size of high quality pressure grown crystals using this technology. The HVPE system used by our group is the horizontal home-made quartz reactor with the rotating quartz susceptor. The growth temperature of 1300-1350 K, temperature of GaCl synthesis of about 1150 K, HCl flow in the range of 18-24 mls/min. diluted in 500 mls/min of N_2, NH_3 flow of 1200 mls/min. and 3000 mls/min. of N_2 as a carrier gas are applied for runs of 1 to 24 h. The prolongation of the processes is always associated with the parasitic deposition of GaN outside of the substrate what leads to significant changes in growth conditions during the process. The growth rates observed for geometry and the set of conditions presented above have varied from 100 to 200 μm /h.[35] Recently, it was possible to demonstrate by this method the growth of the almost dislocation free crystals of the thickness approaching two millimeters.

3. Homoepitaxial MOVPE Growth of Laser Structures on Bulk GaN Substrates

It is quite obvious that the ideal substrate for the growth of high quality GaN layers is high quality gallium nitride. However, this material is not available in the form of “boules” which is a reason for the severe problem with upscaling the laser diode production. The most common

sort of free standing GaN material is obtained by deposition of thick GaN buffer followed by removing foreign substrate, typically sapphire-Al_2O_3, SiC or GaAs. The subsequent growth of GaN/AlGaN/InGaN layers on these substrates is commonly referred as homoepitaxy (semantically this name is quite misleading and disagrees with the terminology used in standard III-V materials technology). The growth of the most of freestanding GaN material originate from many spatially separated nucleation sites which results in mosaic structure on the GaN surface with crystallites not perfectly aligned. The boundaries between crystallites have therefore some dislocations present due to this imperfection in "seed" region. In the case of GaN substrates prepared from high-pressure synthesis (HNPS, see the previous chapter for the complete description) we deal with the monocrystalline material which allows to study MOVPE growth without perturbations caused by high density of dislocations. Despite the limited HNPS-substrate area (~1cm^2) available for epitaxy, the MOVPE technique indeed can produce GaN layers with the best optical and structural properties ever reported,[44] low optical pumping threshold,[45] long PL decay under high excitation[46]). It is also well known that the growth conditions can affect the optical, structural and electrical characteristics of AlInGaN alloys. Therefore, optimized growth conditions of Separate Confinement Heterostructure (SCH) lasers using monocrystalline GaN substrates significantly differ from heteroepitaxial growth on sapphire and SiC. In comparison to the epitaxy on heteroepitaxial-origin freestanding GaN, the difference is less pronounced but still there are differences regarding atomic steps spacing what can result in different growth-and-segregation in kinetically affected regime of growth (i.e. low temperature InGaN).

In order to produce multilayer structure of laser diode, it is necessary to grow single-crystal layers with precisely controlled thickness, composition and doping. The small lattice mismatch of the layer and substrate materials ($\Delta a/a$ ~1%) can be allowed without introducing any defect up to a certain thickness. After critical thickness is exceeded, misfit defects are generated to relieve the built-in strain. Under the tensile strain, a thick layer of AlGaN on GaN usually cracks while under compressive strain the dislocations are rather formed.

The growth of laser structures using organometallic vapor-phase epitaxy (OMVPE, MOVPE, MOCVD) technique is performed in flowing gas close but not exactly at equilibrium conditions. These conditions help in removing the surface damage at the onset of the growth and is also

known to provide high quality interfaces generally important in devices. In fact MOVPE is used for the manufacturing of most laser diodes regardless of the semiconductor system used. Nitride MOVPE system contain gas-handling part to obtain the proper mixtures to be provided into the growth chamber. The substrate is positioned on a graphite susceptor SiC- and eventually AlN-coated which is heated by rf-inductive or by resistive heater. Both near-atmospheric pressure and low-pressure conditions are used, typically 50÷800 Torr. The source of nitrogen for epitaxy is ammonia NH_3 and is always separated from the group-III precursor flow, what reduces the interaction between those two. At atmospheric pressure the reactant gases are consumed more effectively. Low pressure is more desired where very abrupt interfaces between layers are needed and where high aluminium-containing layers are grown to avoid previously mentioned interaction with ammonia. The other than NH_3 sources typically used for Nitride-MOVPE consist of a combination of organometallic liquids and solids, which are used to saturate an N_2 or H_2 carrier gas. There are trimethyl- and triethyl-gallium, trimethyl-aluminium, trimethyl-indium (solid chemical). Dopants are delivered from other hydrides (monosilane SiH_4 or disilane Si_2H_6) or solid source for Mg (biscyclopentadienyl-magnesium) for n- or p-type respectively. The carrier gas is nitrogen especially for indium containing layers and/or hydrogen, important for p-type layers.

Typically, the SCH laser structure (for devices operating t 405 nm) is grown on slightly ~0.5º miscuted toward a- or M-plane (0001) GaN surface of 60÷90-μm-thick highly n-type substrate starting from Si-doped GaN buffer to burry the interface contaminated with oxygen etc. This buffer is followed by 0.6-μm-thick n-type cladding layers consisting of strained layer superlattice (SLs) of 120 periods of Si-doped GaN and $Al_{0.16}Ga_{0.84}N$ heterostructures or single bulk $Al_{0.08}Ga_{0.92}N$ cladding. On top there is deposited 0.1-μm-thick n-type GaN optical guiding layer, MQW active region consisting of 2 to 5 periods of 5÷10nm-thick Si-doped $In_{0.02}Ga_{0.98}N$ barriers and 2.5÷5-nm-thick undoped $In_{0.09}Ga_{0.91}N$ wells (for ~408nm emission), a 1.5nm undoped GaN spacer, a 20-nm-thick p-type $Al_{0.22}Ga_{0.78}N$:Mg electron blocking layer, 0.1-μm-thick p-type GaN:Mg optical guiding layer, a 0.3÷0.5-μm-thick p-type strained layer superlattice (SLs) cladding layer consisting of GaN:Mg and $Al_{0.16}Ga_{0.84}N$(:Mg) heterostructures and 50-nm-thick p-type GaN:Mg contact layer. The n-type side layers are grown at about 1020÷1070˚C, active region at above 800ºC, while electron blocking layer and the other

Mg doped layers about 120÷200ºC higher. For some LD structures, the $In_{0.02}Ga_{0.98}N$:Si additional layer (50÷200-nm-thick) is added prior to the growth of MQW to reduce nonradiative recombination centers and increase luminescence. This layer also acts as a compliance layers for structures with increased Al-compositions and/or thickness' in claddings. The MQW region is grown in pure nitrogen carrier gas and with gas phase composition very reach in indium, usually >75%. It provides very uniform, small scale segregation of indium. Typically, the Mg concentration is kept below solubility limit at about $2\div4\cdot10^{19}cm^{-3}$ what means 10÷300 Ga/Mg ratio in the gas phase depending on the growth chamber and conditions used. For reduced Mg-related absorption within optical waveguide the core is lightly doped or even completely undoped. From technological point of view the most difficult layer to be grown is the AlGaN:Mg electron blocking layer due to the very high doping level required along with the good structural properties what favors growth conditions very much different and therefore danger to the underlaying InGaN layers. The active region with electron-blocking layer is the place where there are important differences in growth kinetics on perfect and heteroepitaxial substrate due to the relatively low growth temperature.

The other important part of the LD device is p-type contact layer. It can be GaN doped in very thin layer up to about $1.2\cdot10^{20}\,cm^{-3}$ Mg or even InGaN:Mg can be applied to allow tunneling through or reducing the barrier height to the contact metal correspondingly.

In conclusion, it is very well established that the optimized MOVPE technique can be used for fabrication of violet and blue laser diodes based on GaN semiconductor system. Regardless of the complex character of chemical and physical reactions involved, this method is chosen because of the very good reproducibility and control of alloys composition and doping. This epitaxial technique also allows for controlling the thicknesses and interface abruptness in-situ using optical methods (reflectivity, light scattering, bowing measurement).

4. Laser Diodes Grown on Bulk GaN by Molecular Beam Epitaxy

Major developments in wide band gap III-N semiconductors which have led to the commercial production of high brightness light emitting diodes (LEDs) and laser diodes (LDs) operating at continuous wave (CW) conditions have been all done by metal organic vapour phase epitaxy (MOVPE) growth technique [see the previous chapters]. On the other

hand, molecular beam epitaxy (MBE), which in principle gives more precise growth control, up until recently lagged considerably behind MOVPE in the field of nitride based optoelectronic devices.[47-48] These difficulties were often explained using thermodynamic argument which sets the optimum temperature for epitaxial deposition to about $0.5 \cdot T_M$, where T_M is the melting temperature of the material in question. According to such estimates, growth at much lower temperatures results in poor adatom kinetics, which leads to 3D growth mode and rough surfaces. For GaN experimentally determined T_M is 2540 K (for 6 GPa)[18] and theoretically predicted 2800 K,[49] which would set the minimum temperature for good epitaxy to about 1300 K–1400 K (1000ºC– 1100ºC). However, in vacuum required for MBE growth, GaN starts decomposing at temperatures already well below 800ºC. Further increase of the temperature accelerates decomposition rate exponentially and matching overpressure of active nitrogen species is needed to stabilize the surface and to promote the growth of the layer. In MOVPE, ammonia overpressure in mbar-bar range prevents GaN decomposition for temperatures in excess of 1000ºC. Clearly for MBE, which relies on the negligible interaction of the atomic beams, such conditions are unattainable. Still, some groups working in the nitrides managed to push the growth conditions in the MBE reactors fairly close to these used in the MOVPE by growing at temperatures as high as 950ºC using very high ammonia flows (up to 200 sccm). Owing to the nitrogen precursor used, this technique is often referred to as ammonia MBE. Recently, Hooper *et. al.*[50] from Sharp Laboratories of Europe demonstrated the first MBE grown "violet" LDs. In spite of its potential advantages for both optoelectronic[51] and electronic [52] devices, ammonia MBE has not been the technique of choice for the majority of nitride MBE community. Indeed, corrosive nature of ammonia compounded by its large flows creates additional hazards and technological challenges as well as leads to often undesirable high hydrogen background during the epitaxial process. In the more widely employed plasma assisted MBE (PAMBE),[48] purified nitrogen gas is activated using an RF-plasma and supplied to the growing surface at typical flow rates of 1-2 sccm. The technique already proved its potential for the growth of high quality structures for electronic components,[53] but up until now only limited success was reported in the area of optoelectronic devices.[54] The turning point for GaN growth with PAMBE was the discovery that Ga rich conditions are necessary for growth of high quality GaN and AlGaN/GaN

heterostructures. High quality layers and interfaces were demonstrated at temperature range of 650-750ºC, much lower than required for the growth of similar structures with ammonia.[55-59] In our earlier works we optimized the growth conditions for high quality GaN and AlGaN/GaN heterojunctions in Ga rich regime, and demonstrated (i) the record high electron mobility of two-dimensional electron gas at AlGaN/GaN interface and (ii) very narrow photoluminescence lines from GaN epitaxial layers.[55-59] Extensive study of the growth of nitride structures with In as surfactant enabled us to grow first InGaN LDs by PAMBE.[60] Recent *ab-inito* calculations explains that smooth, step-flow growth of GaN (AlGaN, InGaN) achieved at relatively low temperatures is possible thanks to existence of a very efficient lateral diffusion channel for adatoms on semiconductor surface just below the dynamically created thin (two or one layer) Ga or In film.[61-63] Surprisingly small activation energies for this so called adlayer enhanced lateral diffusion (AELD) enable high quality epitaxy at temperatures much lower than expected from mentioned earlier estimates based on GaN melting point. In this work, we investigate parameters of LDs with different number of InGaN QWs grown by this new PAMBE technique.

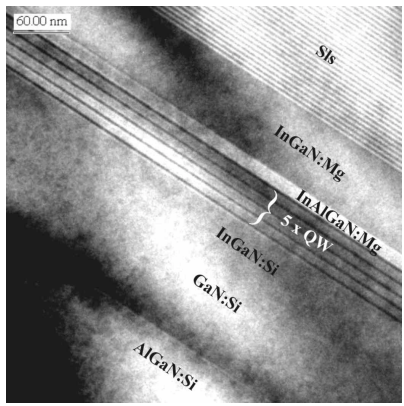

Fig. 4 TEM picture of MBE grown 3QWs laser diode structure.

The laser diode structures were grown in custom designed V90 Oxford based MBE system. Ultra-high purity gas handling manifold together with Veeco UniBulb RF Plasma cell was used as a source of activated nitrogen. The LDs structures were deposited on conductive, very low dislocation density, high-pressure-grown GaN bulk substrates (see previous sections). The epi-ready bulk substrates were prepared in the three-step process of mechano-polishing, dry etching and deposition of 2 μm GaN:Si buffer layer in the MOVPE reactor. The back sides of the substrates were coated with 0.7 μm of molybdenum layer to improve the thermal coupling for radiative heating. Special holders capable of accommodating small irregularly shaped substrates (5×5 to 10×10 mm approximate size) and designed to minimize edge effects ensured high

temperature uniformity across the entire substrate area. The LDs structures consisted of the following sequence of layers. The 200 nm of GaN:Si buffer layer was followed by 0.55 μm $Al_{0.08}Ga_{0.92}N$:Si cladding layer. The wave guide was asymmetric with lower part consisting of 100 nm GaN:Si and 40 nm $In_{0.01}Ga_{0.99}N$:Si. Depending on the structure, five, three or two undoped 4 nm thick $In_{0.09}Ga_{0.91}N$ Quantum Wells (QW) with 7 nm $In_{0.01}Ga_{0.99}N$:Si barriers were deposited in the active region. 14 nm $In_{0.01}Al_{0.16}Ga_{0.83}N$:Mg blocking layer was followed by 70 nm $In_{0.01}Ga_{0.99}N$:Mg upper wave guide. The upper cladding consisted of 80 pairs of uniformly Mg doped $In_{0.01}Ga_{0.99}N/In_{0.01}Al_{0.16}Ga_{0.83}N$ short period superlattice (2.5/2.5 nm). The contact layer was 100 nm GaN:Mg or InGaN:Mg. Doping levels for n-type layers was $5 \cdot 10^{18}$ cm^{-3}. The acceptor Mg concentration detected by SIMS was in the range 3-10$\cdot 10^{19}$ cm^{-3}. The growth temperature for GaN and AlGaN layers was 710ºC (growth at Ga-rich regime), while QWs and p-type cladding were grown at 590ºC (growth at In-rich regime). To enable high quality growth, the excess Ga and In fluxes were precisely chosen to form dynamically stable metal film on semiconductor surface which enhance lateral adatom mobility.[58-61] We used solid sources (high purity Si and Mg) for n and p type doping. No post growth annealing was necessary to activate p-type conductivity. In Figure 4 we show state of the art of the PAMBE technology – transmission electron microscope (TEM) picture of laser diode structure containing 3 InGaN/InGaN QWs. The laser diode devices were processed as ridge-waveguide, oxide-isolated lasers. The mesa structures were etched out in the wafers down to a depth of 0.35 μm. The laser structures were then isolated by e-beam deposition of a 0.2 μm layer of SiO_x. The final devices had the stripe width of 15 μm and the resonator length of 500 μm. The oxidized Ni/Au ohmic contacts were deposited on the top surface of the devices, while Ti/Au contacts were deposited on the backside of the highly conducting n-GaN substrates. The tested devices had cleaved uncoated mirrors.

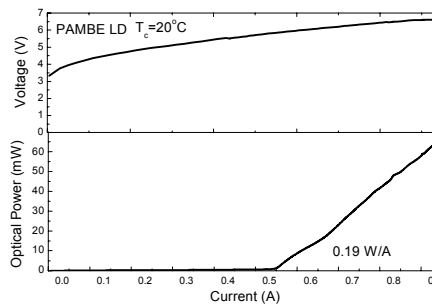

Fig. 5. Current voltage and light current characteristics of CW operated PAMBE grown laser diodes.

Our recent progress in the p-type contact layer growth led to demonstration of continuous wave operation of the PAMBE grown blue-violet LDs [64]. Parameters of these diodes: threshold current density 4.2 kA/cm^2, voltage 5.4V, optical output power of 60 mW (see Fig. 5) and lifetime exceeding 5 hours proves great potential of PAMBE as a viable technology in the field of nitrides.

5. Performance of Nitride Laser Diodes Grown on Bulk Gallium Nitride Substrates

5.1. *Overview*

Most of the leading group working in the field of nitride laser technology reported fabrication of their lasers on bulk or bulk-like GaN substrates. What concerns the commercially available devices manufactured by Nichia Chemical, Sony and Sanyo, none of these companies released the information about the exact type of substrate material used for the production. Nevertheless, basing on the officially published information we can describe the present situation (2006) in the following way:

Nichia Chemicals claims to fabricate their own ELOG substrates by the method described in the first chapter (however it is not clear whether sapphire substrate removal is always performed). The additional feature in comparison to the early publication[12] is the introduction of the second ELOG step after the growth of thick HVPE layer and sapphire substrate lift-off.[65] The use of ELOG substrate is reported by Mukai *et al*. from Nichia.[66,67] It is worth to note the use of very thick (5 μm) AlGaN layer as a first layer on ELOG substrate. This layer denoted a "contact layer" probably also is important for limiting the laser mode leakage into the substrate.

Sony, having a strategic partnership with Nichia Chemical is probably sharing at least a part of a technological know-how with this latter company. They reported on using Nichia-like ELOG substrate (the substrate removal not mentioned)[68]. However, in the other publication they reported on the use of free standing GaN crystals (Sumitomo substrates) for growth of wide-stripe, high power laser diodes.[69,70] Using this type of substrate they established probably the best result in terms of optical output power – 0.9 W measured under CW operation with 10 μm stripe device.[69] However, no data about the lifetime of such a devices were published.

The group from Samsung Advanced Institute of Technology (SAIT) reported also on nitride lasers grown on free standing HVPE substrate[71] They compared the lifetime of devices grown on ELOG/sapphire substrates and on free standing material. Surprisingly enough the lifetime of ELOG/sapphire devices was much larger (10 000 h) than these grown on free standing material (few hundreds hours). The author explains this observation by much larger concentration of dislocation in the free standing substrates. SAIT group presented also very good parameters of their laser diodes. The threshold current density was in the range of 2.5 kA/cm^2, the threshold voltage 4.25 V and the differential efficiency slightly above 1 W/A.[71] Very recently SAIT demonstrated laser diodes with threshold voltage value around as low as 3.8 V,[72] indicating almost perfect electrical properties of the diode.

5.2. *High-pressure grown GaN substrates for the future generation of high power laser diodes*

High pressure grown GaN crystal thanks to their almost dislocation free character provide the optimum platform for the construction of large area (wide stripe devices) needed for high power application such as: large area color displays (e.g. laser projection TV), high-speed printing, photochemical processing and photolithography. For these applications the required level of optical power is between 200 mW and 1 W. Below we present the description of the current status of wide stripe laser diode technology developed with the use of low dislocation density, high-pressure grown bulk GaN substrate.[73-77]

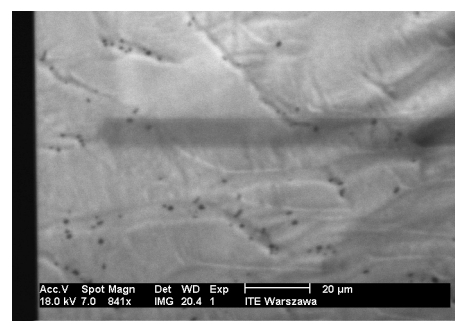

Fig. 6. Cathodoluminescence measurements of the threading dislocation density indicating $6*10^5$ cm^{-2} dislocation. The dark shadow marks the position of the laser stripe.

GaN/AlGaN/InGaN laser structures were grown in a home-made vertical flow MOVPE reactor using TMGa, TEGa, TMAl, TMIn, CP_2Mg, SiH_4 and ammonia as precursors. The substrates used for epitaxy are GaN bulk crystals obtained by high-pressure synthesis. The initial density of dislocations in the substrate is at the level of 10^2cm^{-2}. The

active layer of the device is composed of one to five $In_{0.1}Ga_{0.9}N$ quantum wells of a width of 40 Å. The quantum barriers were $In_{0.02}Ga_{0.98}N$:Si layers of a thickness of 70 Å. The quantum well system is followed by a 200Å-thick $Al_{0.2}Ga_{0.8}N$:Mg electron blocking layer. 0.07 μm-thick undoped upper and 0.1 μm-thick n-type lower GaN layer form the device waveguide. A 0.5 μm-thick *n*-type $Al_{0.16}Ga_{0.84}N$/GaN superlattice (110×24Å/24Å) was used as bottom cladding and 0.37 μm- thick p-type $Al_{0.15}Ga_{0.85}N$/GaN superlattice (80×23Å/23Å) as upper cladding to confine the light emitted from the active region of the InGaN MQW structure. A 40nm-thick *p*-type GaN layer was used as a contact layer of the *p*-electrode.

The devices were processed as ridge-waveguide, oxide-isolated lasers. The mesa structure was etched out in the wafer down to a depth of 0.3 μm (roughly to the middle of the upper cladding layer). The laser structure was then isolated by the e-beam deposition of a 0.1 μm layer of ZrO_2. Ni/Au contacts, of typical contact resistance between 10^{-3}-10^{-4} $\Omega \cdot cm^2$, were deposited on the top surface of the device, while Ti/Au contacts were deposited on the backside of the highly conducting n-GaN substrate crystal. The stripe width was set to 20 or 50 μm and the resonator length was 500 or 1000 μm. The mirrors were coated with quarter-wavelength layers of SiO_2/TiO_2 to increase the mirror reflectivity. The structures were characterized by a density of dislocations at the level of around $5 \cdot 10^4$–10^5 cm^{-2} (see the result of selective etching procedure showed in Fig. 6). The origin of additional dislocation is large mechanical strain existing in cladding and blocking AlGaN layers. One of the most important conditions for the successful operation of high-power laser diodes is the removal of the large amount of heat dissipated during diode operation. Nitride laser diodes are characterized by a 10-fold larger threshold current density and two times larger threshold voltage as compared with their GaAs counterparts. This results in a more than 20 times higher electrical power consumption at threshold comparing to GaAs based devices. In case of our wide-stripe laser we have the electrical power density at threshold in the range of 24-30 kW/cm^2.

Three types of wide-stripe laser of the following dimensions has been tested:

A: 20 μm × 500 μm stripe device

B: 20 μm × 1000 μm stripe device

C: 50 μm × 500 μm stripe device

All these diodes were mounted p-side down on metalized diamond heat-spreaders. The optical parameters of these devices are shown in Fig. 7. These lasers are characterized by the threshold current density between 4 and 5 kA/cm^2, which implies that the device current remains proportional to the stripe area. The dissipated power roughly varies between 2.5 W and 8 W, depending on the stripe geometry. This large amount of heat forces us to use an active thermoelectric cooling system. Our measurements indicate that the temperature roll-off of L-I characteristics occurs for an electrical power density of 80 kW/cm^2.

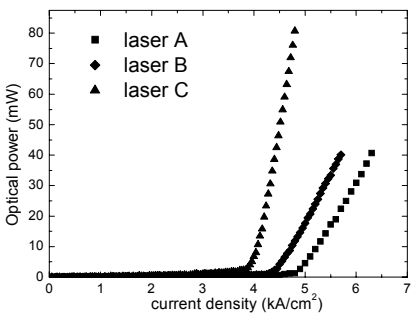

Fig. 7. Light-current characteristics of the lasers of different stripe geometries. Lasers were measured at room temperature under pulsed current conditions (100 kHz, 50 ns).

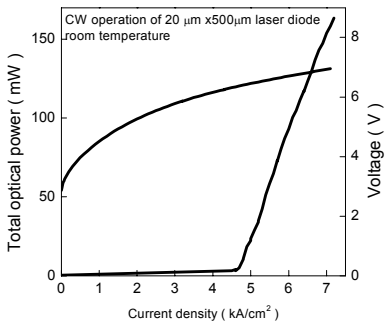

Fig 8. Light-current and current-voltage characteristics of a laser diode of type "A" measured under CW conditions at room temperature.

In Fig. 8 we present the optical and electrical characteristics of a type "A" laser (operated in CW regime). So far slightly higher optical output powers were achieved by using a 20 μm device. The maximum ratings of our lasers are so far limited by the slope efficiency and by the thermal resistance of the package, which should both be improved.

Until now, laser "C" was not successfully tested under CW operation because of thermal management problems. However, we believe that, with an improved mounting scheme, this type of laser may provide a good solution for the 1 W emission range. Figure 9 shows the pulsed current test performance of a class "A" device. We could demonstrate over 2.5 W of optical power on the output mirror. The failure of this device for larger power can be attributed to catastrophic optical damage of the mirror and coincides with the typical level of around 50 MW/cm^2.

We expect that type "C" devices would be able to emit over 5 W of radiation from a single stripe (at least under pulse operation).

We can conclude this short description of the properties of nitride lasers grown on high-pressure substrate by stating: Though the present technology still needs improvement the results are quite encouraging, and seems to indicate that after the optimization of heat management and the diode efficiency 1 Wat range of optical power may be achievable.

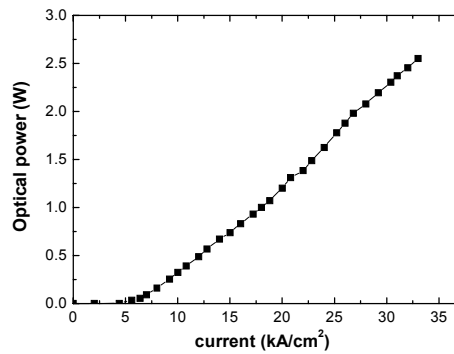

Fig. 9 Light-current characteristic measured under pulsed current conditions (5 kHz, 20 ns). Highly reflective coating causes almost all emission to exit through the output mirror.

6. Crystallographic defects in laser diode structures

The defects existing in the nitride laser structures are of the crucial importance for the lifetime of these devices. Their origin is related to the substrate material quality but also (especially for high quality growth on bulk GaN) to the details of the epitaxial growth. There are three main origins of crystallographic extended defects in nitride laser diodes:

i) high lattice mismatch of AlGaN claddings and electron blocking layer to GaN,
ii) high magnesium content in p-type part of the epi-structure,
iii) segregation tendency of indium in InGaN quantum wells.

Below, these three factors will be discussed.

6.1. *Mismatch problem of AlGaN layers*

In order to achieve a good optical confinement in the waveguide, the AlGaN claddings should contain as much Al as possible and should be as thick as possible. Additionally, the electron blocking layer (ebl) should contain even more aluminum, however, in that case (layer is very thin), p-doping is more severe issue than defect creation. Unfortunately, the large lattice mismatch between AlGaN layers and GaN substrates causes

limitations for both, Al-composition and thickness of claddings and electron blocking layer. This mismatch causes a strain that could be entirely or partially relaxed by bowing, creation of dislocation or macroscopic cracking. Figure 10 shows theoretical predictions for cracking[78] and dislocation[79] creation as a function of Al-composition and AlGaN layer thickness. Both curves were obtained for very simplified models that do not take into account, for example, the thickness of the substrate. However, the experimental data we obtained confirm roughly the position of both curves. In the figure, it is shown the values for claddings (lower+upper) and ebl we are using for 415 nm devices. It can be seen that the claddings are very close to the critical conditions for defect creation.

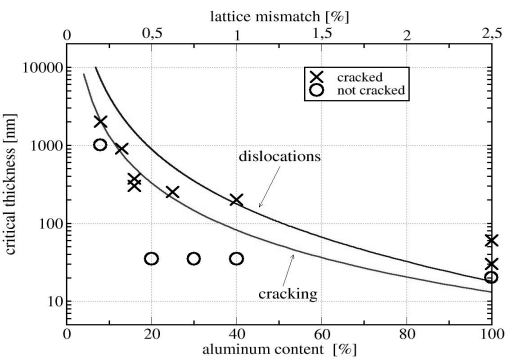

Fig. 10. Cracking and dislocation generation in AlGaN/GaN structures.

To obtain crack-free and dislocation-free devices it is necessary not only to optimize the Al content and cladding thickness, but also to optimize the substrate thickness, as when it is small it may accommodate part of the stress by bowing. However, the bowing can not be too large because of processing difficulties. Figure 11 shows the radius of bowing for three different substrate thickness versus Al content. It can be seen that for the 60 micrometer substrate, the experimental points are exactly on the theoretical curve (Stoney equation[80]) what means that the samples are fully strained and without dislocations and cracks. However, the bowing radius is too small to use such samples for device fabrication. For 120 micrometer substrate, the sample gets cracked (see Fig. 11) for Al content of about 8%. Therefore, the optimum thickness of the substrate is around 90 micrometer for which Al content of 8% and total AlGaN thickness of about 1 micrometer is possible. In the real LD epi-structure, the dislocations are created at the interfaces of: the GaN substrate and the AlGaN lower cladding (most harmful as they cross the active region), at the interface of MQW and the ebl, the upper waveguide

and the upper cladding. For 415 nm LDs, the total dislocation density (as observed by selective etching and TEM[76]) is of 10^5 cm^{-2}-10^6 cm^{-2} with 20-30% of dislocations crossing the active region. However, it should be stressed that such low dislocation density and lack of cracks can be obtained in expense of the reduction of the optical confinement of the laser mode.

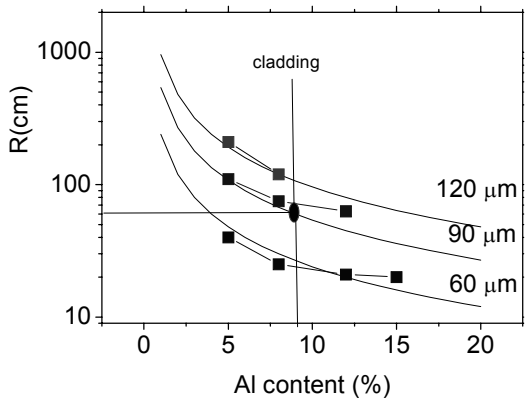

Fig. 11. Bowing radius for 1 micron thick AlGaN layer versus the Al content and GaN substrate thickness. The deviation of the experimental points from the theoretical curves arise from lattice relaxation by dislocations and cracking.

6.2. *Mg-related defects*

P-doping of nitride semiconductors is a crucial factor for operation of LDs. Because of a large activation energy of Mg acceptors, only a small fraction (around 1%) of these atoms are ionized in GaN (even less in AlGaN) at room temperature. To achieve reasonable hole concentrations, it is necessary to use very high Mg concentration what leads to creation of many structural defects. Hommel *et al.* [96] reported for a highly doped GaN:Mg layers a creation of triangular defects of size 3-5 nm formed as a superlattice with spacing of about 150 nm. Presence of such defects was accompanied by a drop of p-type conductivity in the layers. For even higher Mg concentration, the polarity reversing is observed.[81] In that case, the incorporation of Mg is decreased in nitrogen-polar phase. Figure 12

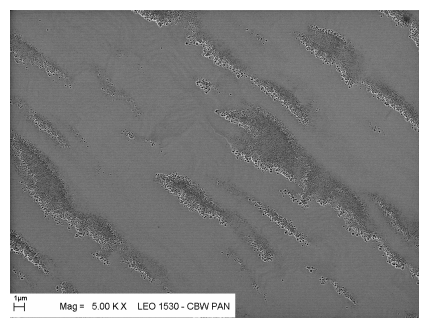

Fig.12. Bands of inversion domains related to very high doping of $Al_{0.18}Ga_{0.82}N$ layer with magnesium revealed by selective etching.

shows the bands of such inversion domain defects present in the LD structure when the Mg-doping and Al-content in p-type AlGaN cladding and electron blocking layer are too high (revealed by selective etching).

6.3. *In-related defects*

The issue still not well understood is a role of indium in GaInN layers. This compound decomposes at rather low temperatures (InN: about 500^{o}C at atmospheric pressure). Therefore, these layers are grown at a very high N/III ratio of 20000-50000 (ten times higher than GaN) and much higher In:Ga mole ratio than it could be derived from the chemical composition of the InGaN layer.

Big differences in ionic radii of these three elements are the main cause of an easy segregation and creation of quantum-dot-like objects. Cho and Stringfellow[82] calculated (using a modified valence-force-field model) the binodal and spinodal curves for InGaN. At a typical growth temperature of 800^{o}C, the solubililty of In in GaN was calculated to be less than 6%, however, during the epitaxic growth, the situation is much more complex. The In segregation can be observed almost in every scale: a few nanometers, a few tens of nanometers, as well as in micrometer scale. Adding to that very strong electric fields (induced by spontaneous and piezoelectric polarization) present in these compounds, it is not unlikely that two quantum wells of the same average composition and thickness can emit light of wavelength different by 100 nm! It is a common opinion that the segregation of indium plays a positive role in green and blue LEDs, enabling to produce efficient emitters despite a very high dislocation density in structures on foreign substrates. For LDs, the situation is less clear, as a lasing action depends on many parameters and there are some indications that active region of the LDs should be uniform. However, the growth of InGaN quantum wells of homogeneous composition and with sharp interfaces is extremely difficult, and depends on many factors (some of them listed by Gerthsen, *et al.*[83]), as growth rate, presence of strains below the quantum wells, substrate miscut, growth temperature of the subsequent layers, and others.

7. Reliability of Nitride Laser Diodes

The reliability of nitride laser diode was a key issue of this technology from the very beginning of its history. The lifetime of the first devices

characterized by very high defect concentration was very short. For example the first CW operated laser demonstrated by Nakamura lived only one second.[7] With the improvement introduced by ELOG technology and because of the use of free standing GaN substrates the lifetime of nitride laser diodes has been expanded in some cases even above 10 000 hours.[12] The problem of pin-pointing the physical mechanism of the laser degradation is very difficult in its nature, in case of arsenide and phosphide laser it took decades to work out a consistent model of degradation mechanism.

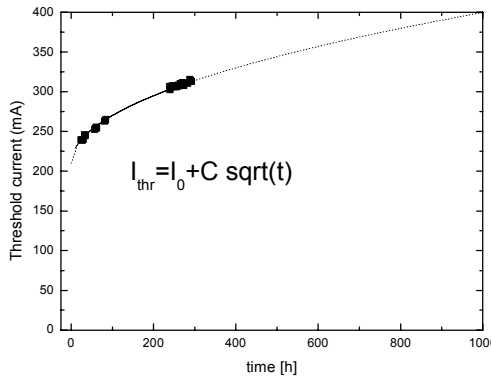

Fig 13. The evolution of the threshold current density for InGaN laser diode during the aging process. The dotted line depicts square-root function of time.

In the middle of 2000 Kneissl *et al.*[84] described the aging experiment performed on ELOG laser diodes. He discovered that the aging is thermally activated with characteristic energy around 0.5 eV (see also Ref. 85) and it is manifested by increase of threshold current density and decrease of the laser gain[86] He also postulated that the degradation process is fotoactivated.[84]

Kummler *et al.* argued that the main reason for the degradation is large current and not the elevated temperature of the junction.[87]

Nam *et al*.[71] pointed out that the magnesium profile seems to undergone diffusion related evolution during aging and this may cause device degradation.

Tomiya *et al*.[88] demonstrated that the degradation of GaN based laser diode is not accompanied dislocation multiplication and dark line formation.

Schoedl *et al.* indicated the importance of the facet degradation for the device reliability.[89]

Takeya *et al*.[90] suggested that diffusion (probably Mg) may be responsible for the degradation. He also demonstrated a square root dependence with time of the degradation of laser devices.

Finally the measurement performed by Marona *et al*.[91] on the devices fabricated on high-pressure grown crystals lead to the following conclusions:

1) The degradation of laser diodes occurs mostly by the increase of the threshold current due possibly (but not necessarily) to creation of new nonraditive recombination centers.
2) The degradation follows the square-root law (see Fig. 13) indicating the importance of diffusion process.
3) The degradation processes are not photo-activated.[92]

References

1. J. Pankove, in *Optoelectronic Properies of Semiconductors and Superlattice*, ed. O. Manasreh, "GaN and related Materials" vol 2, p 1, Gordon and Breach Science Publishers 1997.
2. H. Amano, N. Sawaki, I. Akasaki, Y. Toyoda, *Appl. Phys. Lett.* **48**, 353 (1986).
3. H. Amano, M. Kito, K. Hiramatsu, I. Akasaki, *Jap. J. Appl. Phys*. **28**, L2112 (1989).
4. S. Nakamura, *J. Cryst. Growth* **145**, 911 (1994).
5. S. Nakamura, M. Senoh, S. Nagahama, N. Iwasa, T. Yamada, T. Matsushita, H. Kiyoku, Y. Sugimotu, *Jpn. J. Appl. Phys*. **35**, L74, (1996).
6. S. Nakamura, M. Senoh, S. Nagahama, N. Iwasa, T. Yamada, T. Matsushita, Y. Sugimoto, H. Kiyoku, *Appl. Phys. Lett.* **69** 1477, (1996).
7. S. Nakamura, M. Senoh, S. Nagahama, N. Iwasa, T. Yamada, T. Matsushita, Y. Sugimoto, H. Kiyoku, *Appl. Phys. Lett*. **69**, 4056 (1996).
8. S. Nakamura, M. Senoh, S. Nagahama, N. Iwasa, T. Yamada, T. Matsushita, Y. Sugimoto, H. Kiyoku, *Appl. Phys. Lett*. **70**, 1417 (1997).
9. S. Nakamura, M. Senoh, S. Nagahama, N. Iwasa, T. Yamada, T. Matsushita, Y. Sugimoto, H. Kiyoku, *Jpn. J. Appl. Phys*. **36**, L1059 (1997).
10. S. Chichibu, T. Azuhata, T. Sota, and S. Nakamura, *Appl. Phys..Lett*. **69**, 4188 (1996).
11. P. Gibart, *Rep. Prog. Phys.* **67**, 667 (2004).
12. S. Nakamura, *J. Mater. Res*. **14**, 2716 (1999).
13. S. Nakamura, M. Senoh, S. Nagahama, N. Iwasa, T. Yamada, T. Matsushita, H. Kiyoku, Y. Sugimoto, T. Kozaki, H. Umemoto, M. Sano, K. Chocho, *J. Jpn. Appl. Phys.* **37**, L309 (1998).
14. K. Itaya, M. Onomura, J. Nishio, L. Sugiura, S. Saito, M. Suzuki, J. Rennie, S. Nuonue, M. Yamamoto, H. Fujimoto, Y. Kokubun, Y. Ohba, G. Hatakoshi, M. Ishikawa, *Jpn. J. Appl. Phys*. **35**, L1315 (1996).
15. A. Kutamata, K. Domen, R. Soejima, K. Horino, S. Kubota, T. Tanahashi, *Jpn. J. Appl. Phys.* **36,** L1130 (1997).
16. M. Kneissl, D.P. Bour, N.M. Johnson, L.T. Romano, B.S. Krusor, R. Donaldson, J. Walker, C. Dunrowicz, *App. Phys. Lett.* **72**, 1539 (1998).
17. J.T. Brown, J.T. Swindell, M.A.L. Johnson, Y. Zhongai, J.F. Schetzina, G.E. Bulman, K. Doverspike, S.T. Sheppard, T.W. Weeks, M. Leonard, H.S. Kong,

H. Dieringer, C. Carter, J.A. Edmond, *Nitride-Semiconductors-Symposium*. 1998: 1179-84, Mater. Res. Soc, Warrendale, PA, USA, Ed. F.A. Ponce; S.P. DenBaars; B.K. Meyer; S. Nakamura; S. Strite.
18. W. Utsumi, H. Saitoh, H. Kaneko, T. Watanuki, K. Aoki, O. Shimomura, *Nature Materials*, Vol. 2, November (2003), 735.
19. H. P. Maruska and J. J. Titjen, *Appl. Phys. Lett.* **15**, 327 (1969).
20. W. Seifert, G. Fitzl and E. Butter, *J. Cryst. Growth* **52**, 257 (1981).
21. A. Usui, H. Sunakawa, A. Sakai and A. Yamaguchi, *Jpn. J. Appl. Phys*. **36**, L899 (1997).
22. Y. Kumagai, H. Murakami, H. Seki, A. Koukitu, *J. Cryst Growth*, **246**, (2002), 215.
23. K. Motoki, T. Okahisa, S. Nakahata, N. Matsumoto, H. Kimura, H. Kasai, K. 34 Takemoto, K. Uematsu, M. Ueno, Y. Kumagai, A. Koukitu, H. Seki, *J. Cryst Growth* **237** (2002) 912.
24. S. Goto, M. Ohta, Y. Yabuki, Y. Hoshina, S. Uchida and M. Ikeda, in *Proceedings of ICNS 5*, May 2003, Nara, Japan.
25. J. F. Heffernan, M. Kauer, S.E. Hooper, V. Bosquet, J. Windle, T. Smeeton, C. Zellweger, J. Barnes, presented on *Photonics West 2006 Conference* 6133, 21-26 January 2006, San Jose, USA.
26. T.Kozaki, H. Matsumura, Y. Sugimoto, S. Nagahama, T. Mukai, presented on *Photonics West 2006 Conference* 6133, 21-26 January 2006, San Jose, USA.
27. H. C. Hong, D. S. Park, K. J. Narang, S. F. LeBoeuf, M. P. D'Evelyn, P. R. Tavernier, D.R. Clarke and R. J. Molnar, presented on the *8th Wide BandgaP III-Nitride Workshop*, Sept. 29 – Oct. 1, 2003, Richmond, Virginia, USA.
28. A. Yoshikawa, E. Ohshima, T. Fukuda, H. Tsuji and K. Oshima, *J. Cryst. Growth* **260**, (2004) 67–72.
29. M. Aoki, H. Yamane, M. Shimada, S. Sarayama, F.J. DiSalvo, *J. Cryst. Growth* **242** (2002) 70.
30. F. Kawamura, M. Morishita, K. Omae, M. Yoshimura, Y. Mori, T. Sasaki, *J Mat. Sci.: Materials in Electronics* **16** (2005) 29.
31. M. Morishita, F. Kawamura, M. Kawahara, M. Yshimura, Y. Mori, T. Sasaki, *J. Cryst. Growth* **284** (2005) 91.
32. F. Kawamura, T. Iwahashi, M. Morishita, K. Omae, M. Yoshimura, Y. Mori, T. Sasaki, *Jpn. J. Appl. Phys*. **42** (2003) L729.
33. I. Grzegory, M. Boćkowski and S. Porowski, "GaN bulk substrates grown under pressure from solution" in *Bulk Crystal Growth of Electronic, Optical and Optoelectronic Materials*, ed. by P. Capper, Wiley&Sons, (2005), 173.
34. M. Boćkowski; I. Grzegory; J. Borysiuk; G. Kamler; B. Lucznik, M. Wróblewski, P. Kwiatkowski, K. Jasik S. Krukowski, S. Porowski, *J. Crystal Growth* **281** (2005) 11.
35. B. Lucznik, B. Pastuszka, I. Grzegory, M. Boćkowski, G. Kamler, E. Litwin-Staszewska, S. Porowski, *J. Cryst. Growth* **281** (2005) 38.
36. S. Krukowski, M. Bockowski, B. Łucznik I. Grzegory, S. Porowski T. Suski Z. Romanowski, *J. Phys. Condensed Matter* **13** (2001) 8881.
37. I. Grzegory, M. Bockowsk, B. Lucznik, S. Krukowski, Z. Romanowski, M. Wroblewski, S. Porowski, *J. Cryst Growth* **246** (2002) 177.
38. I. Grzegory, M. Bockowski, J. Jun, P. Figurny, *High Pres. Res*., **7-8 (**1991) 248.
39. J. Karpinski., J. Jun and S. Porowski,, *J.Cryst. Growth*, **66**, (1984) 1-10.
40. M. Bockowski, *Cryst. Res&Techn*, **36**,8-10, (2001) 771.

41. Z. Liliental-Weber, EMIS Datareview Series No23, published by INSPEC, The Institution of Electrical Engineers, London, 1999, 230.
42. J. L. Rouviere, J. L. Weyher, M. Seelmann-Eggebert, S. Porowski, *Applied Physics Letters*, **73** (1998) 668.
43. M. Seelmann-Eggebert, J. L. Weyher, H. Obloh, H. Zimmermann, A. Rar, S. Porowski, *Appl. Phys. Lett*. **71** (1997) 18.
44. Thonke-Ulm], K. Kornitzer, T. Ebner, K. Thonke, R. Sauer, C. Kirchner, V. Schwegler, M. Kamp, M. Leszczynski, I. Grzegory, S. Porowski, *Phys. Rev. B* **60**, 1471, (1998).
45. Yu. Ivanov, M. Godlewski, H. Teisseyre, P. Perlin,R. Czernecki, P. Prystawko, M. Leszczynski, I. Grzegory, T. Suski, S. Porowski, *Appl. Phys. Lett*. **81**, 3735 (2002).
46. S. Jursenas, N. Kurilcik, G. Kurilcik, A. Zukauskas, P. Prystawko, M. Leszczynski, T. Suski, P. Perlin, I. Grzegory, S. Porowski, *Appl. Phys. Lett*. **78**, 3776 (2001).
47. H. Morkoc, *Journal of Material Science: Materials in Electronics* **12**, 677 (2001).
48. T.D. Moustakas, E. Iliopoulos, A.V. Sampath, H.M. Ng, D. Doppalapudi, M. Misra, D. Korakakis, R. Singh, *Journal of Crystal Growth*, **227-228**, 13, (2001).
49. A. Van Vechten, *Phys. Rev. B* **7**, 1479-507 (1973).
50. Kauer, S.E. Hooper, V. Bousquet, K. Johnson, C. Zellweger, J.M. Barnes, J. Windle, T.M. Smeeton and J. Heffernan, *Electronic Letters* **41**, No.13, 23 (2005).
51. N. Grandjean, B. Damilano, and J. Massies, *J. Phys.: Condens. Matter* **13,** 6945-6960 (2001).
52. J. A. Bardwell, Y. Liu, H. Tang, J. B. Webb, S. J. Rolfe, and J. Lapointe, *Electron. Lett.* **39,** 564-566 (2003).
53. M. J. Manfra, K. W. Baldwin, M. Sergent, R. J. Molnar and J. Caissie, *Appl. Phys. Lett.* **85**, 1722 (2004).
54. P. Waltereit, H. Sato, C. Poblenz, D. S. Green, J. S. Brown, M. McLaurin, T. Katona, S. P. DenBaars, and J. S. Speck, J.-H. Liang, M. Kato, H. Tamura, S. Omori, and C. Funaoka, *Appl. Phys. Lett*. **84**, 2748 (2004).
55. C.T. Foxon, TS Cheng, SV Novikov, D Korakakis, NJ Jeffs, I Grzegory, S Porowski, *Journal of Crystal Growth*, **207**, 1 (1999).
56. B. Heying, I. Smorchkova, C. Poblenz, C. Elsass, P. Fini, and S. Den Baars, U. Mishra, J. S. Speck, *Appl. Phys. Lett.* **77**, 2885 (2000).
57. C. Adelmann, J. Brault, D. Jalabert, P. Gentile, H. Mariette, Guido Mula, and B. Daudin, *J. of Appl. Phys*. **91**, 9638 (2002).
58. C. Skierbiszewski, Z. Wasilewski, M. Siekacz, A. Feduniewicz, B. Pastuszka, I. Grzegory, M Leszczynski, S. Porowski, *Physica Status Solidi A*, **201**, 320 (2004).
59. C. Skierbiszewski, K. Dybko, W. Knap, J. Łusakowski, M. Siekacz, W. Krupczyński, G. Nowak, M. Boćkowski, Z. Wasilewski, D. Maude, T. Suski, and S. Porowski, *Appl. Phys. Lett*. **86**, 102106 (2005).
60. C. Skierbiszewski, Z. Wasilewski, M. Siekacz, A. Feduniewicz, P. Perlin, P. Wisniewski, J. Borysiuk, I. Grzegory, M. Leszczynski, T. Suski and Porowski S., *Appl. Phys. Lett*. **86**, 011114 (2005).
61. J. Neugebauer, T. K. Zywietz, M. Scheffler, J. E. Northrup, H. Chen and R.M. Feenstra, *Phys. Rev. Letters* **70**, 56101 (2003).
62. J. E. Northrup, J. Neugebauer, R. M. Feenstra, A. R. Smith, *Phys. Rev. B* **61**, 9932 (2000).
63. T. Zywietz, J. Neugebauer, M Scheffler, *Appl. Phys. Lett*. **73**, 487 (1998).

64. C. Skierbiszewski; P. Wisniewski; M. Siekacz; P. Perlin; A. Feduniewicz-Zmuda; G. Nowak, I. Grzegory; M. Leszczynski S. Porowski, "60 mW continuous-wave operation of InGaN laser diodes made by plasma-assisted molecular-beam epitaxy", *Appl. Phys.Lett.* **88**, 221108-1-3 (2006).
65. T. Mukai, S. Nagahama, T. Yanamoto, M. Sano, *Phys. Stat. Sol. A* **192**, 261 (2002).
66. S. Nagahama, T. Yanamoto, M. Sano, T. Mukai, *Appl. Phys. Lett.* **79**, 1948, (2001).
67. T. Mukai, S. Nagahama, T. Kozaki, M. Sano, D. Morita, T. Yanamoto, M. Yanamoto, M. Yamamoto, K. Akashi, S. Masui, *Phys. Stat. Sol.* (a) **201**, 2712 (2004).
68. T. Asano, M. Takeya, T. Tojyo, T. Mizuno, S. Ikeda, K. Shibuya, T. Hino, S. Uchida, M. Ikeda, *Appl. Phys. Lett.* **80**, 3497, (2002).
69. S. Goto, M. Ohta, Y. Yabuki, Y. Hoshina, K. Naganuma, K. Tamamura, T. Hashizu, M. Ikeda, *Phys. Stat. Sol*. (a) **200**, 122, (2003).
70. S. Goto, M. Ohta, Y. Yabuki, Y. Hoshina, K. Naganuma, K. Tamamura, T. Hashizu, M. Ikeda, *Phys. Stat. Sol*. (a) **200**, 122, (2003).
71. O.H. Nam, K.H. Ha, J.S. Kwak, S.N. Lee, Y. J. Sung, H.S. Paek, J.H. Chae, T. Sakong, J.K. Son, H. Y. Ryu, Y.H. Kim, Y. Park, *Phys. Stat. Sol.* (a) **201,** 2717 (2004).
72. H.Y. Ryu, K.H. Ka, S.N. Lee, K.K. Choi, T. Jang, J.K. Son, J.H. Chae, S.H. Chae, H.S. Paek, Y.J. Sung, T. Sakong, H.G. Kim, K.S. Kim, Y.H. Kim, O.H. Nam, Y.J. Park, Photonics Technology Letters, *IEEE*, **18,** 101, (2006).
73. P. Perlin, L. Marona, T. Swietlik, M. Leszczynski, P. Prystawko, P. Wisniewski, R. Czernecki, G. Franssen, S. Grzanka, G. Kamler, J. Borysiuk, J. Weyher, I. Grzegory, T. Suski, S. Porowski, T. Riemann, J. Christen, *Proc. SPIE*, **5738**, 72 (2005).
74. P. Wisniewski R. Czernecki P. Prystawko, M. Maszkowicz, M. Leszczynski, T. Suski, I. Grzegory, S. Porowski, M. Marona, T. Swietlik, P. Perlin, *Proc. SPIE*, **6133**, 168 (2006).
75. L. Marona, P. Wisniewski, P. Prystawko, S. Porowski, T. Suski, M. Leszczynski, I. Grzegory, R. Czernecki, P. Perlin, T. Riemann, J. Christen, *Proc. SPIE* **6184**, 131, (2006).
76. P.Perlin, P. Wisniewski, R. Czernecki, P. Prystawko, M. Leszczynski, T. Suski, I. Grzegory, L. Marona, T. Swietlik, K. Komorowska, S. Porowski, *Proc. SPIE* **6184**, 139 (2006).
77. T. Swietlik, G. Franssen, P. Wisniewski, S. Krukowski, S.P. Lepkowski, L. Marona, M. Leszczynski, P. Prystawko, I. Grzegory, T. Suski, S. Porowski, P. Perlin, R. Czernecki, A. Bering-Staniszewska, P.G. Eliseev, *Appl. Phys. Lett.* **88**, 071121 (2006).
78. T. Boettcher, S. Figge, S. Einfeldt, R. Chierchia, R. Kroeger, Ch. Peter, Ch. Zellweger, H. J. Buehlmann, M. Diesselberg, D. Rudloff, J. Christen, H. Heinke, P. L. Ryder, M. Ilegems, D. Hommel, *Phys. Stat. Sol*. (a) 0 no 6, 1846 (2003).
79. R. People and R.C. Bean, *Appl. Phys. Lett*. **47**, 322 (1985).
80. G. G. Stoney, *Proc. R. Soc. London Ser A* **82**, 172 (1909).
81. L. T. Romano, J. E. Northrup, A. J. Ptak and T. H. Myers, *Appl. Phys. Lett.* **77**, 2479 (2000).
82. I. Cho, G. B. Stringfello, *Appl. Phys. Lett*. **69**, 2701 (1996).

83. D. Gerthsen, E. Hahn, B. Neubauer, V. Potin, A. Rosenauer, M. Schowalter, *Phys. Stat. Sol.* (a) 0 no 6, 1668 (2003).
84. M. Kneissl, D. Bour, L. Romano, Ch. Van de Walle, J. Northrup, W. Wong, D. Treat, M. Teepe, T. Schmidt, N. Johnson, *Appl. Phys. Lett*, **77**, 1931 (2000).
85. S. Nakamura, *MRS Bull*. **23**, 37 (1998) .
86. L.L. Goddard, M. Kneissl, D.P.Bour, N.M. Johnson, *Appl. Phys. Lett*. **88**, 3820 (2000).
87. V. Kummler, G. Bruderl, S. Bader, S. Miller, A. Weimar, A. Lell, V. Harle, U.T. Schwartz, N. Gmeinwieser, W. Wegscheider, *Phys. Stat. Sol*. (a) **194**, 419 (2002).
88. S. Tomiya, S. Goto, M. Takeya, M. Ikeda, *Phys. Stat. Sol*. (a) **200**, 139 (2003).
89. T. Schoedl, U.T. Schwartz, V. Kummler, M. Furitch, A. Leber, A. Miler, A. Lell, V. Harle, *J. Appl. Phys.* **97**, 123102, (2005).
90. M. Takeya, T. Hashizu, M. Ikeda in "Novel in plane Semicoductor lasers" edited by C. Mermeistein, D.P. Bour, *Proceedings of SPIE* **5738**, p 63.
91. L. Marona, P. Wisniewski, P. Prystawko, I. Grzegory, T. Suski, S. Porowski, P. Perlin, M. Leszczynski, R. Czernecki, *Appl. Phys. Lett*. **88**, 201111 (2006).
92. L. Marona *et al*., in *Proceedings of Photonics West Conference*, 2007.

CHAPTER 9

III-NITRIDE LIGHT-EMITTING DEVICES ON SI

N. C. Chen, C. F. Shih

Institute of Electro-Optical Engineering,
Department of Electronic Engineering Chang Gung University,
Tao-Yuan, Taiwan, R. O. C.
E-mail: ncchen001@mail.cgu.edu.tw

1. Introduction

The search for a substrate other than sapphire or SiC for use in III-V nitride devices has attracted substantial attention. Although both sapphire and SiC substrates are already available in 2" diameters, researchers continue to seek larger substrates (with diameters >4") to promote high-volume commercialization of GaN. Si has long been a promising candidate for obvious reasons. Si circuit technology has developed rapidly and produced large Si wafers (up to 12"), with a high electrically conductivity, low cost, high thermal conductivity and high crystalline quality. Large-area wafers are suitable for use in large-junction devices for general lighting. Electrically conducting wafers can be used in vertical transport devices, saving the cost of lithography. One of the contacts is made on the backside of the substrate, subsequently reducing the cost of the chip package. Because the cleavage directions between GaN and Si (111) substrates are parallel, laser diodes (LD) can be fabricated effectively. The possibility of integrating GaN-based electro-optical devices with the advanced Si-based electronics is also of great interest. GaN-on-Si technology supports a broad range of product applications, such as optoelectronics, microwave and millimeter-wave high-power electronics, optical and mechanical sensors, high-

temperature and radiation-tolerant electronics and high-voltage rectifiers. This work focuses on the growth and characteristics of LEDs-on-Si.

Many attempts had been made to GaAs/Si and InP/Si systems. However, these efforts have been little success because of large amounts of intrinsic defects. In contrast, the degradation of performance of GaN-based light-emitting diodes (LEDs) is relatively insensitive to the presence of threading dislocations due to the exciton localization effect or the existence of the quantum dots in the active region. Therefore, hetero-substrates like Si, might be able to be used to make high-performance GaN-based LEDs.

In 1971, Manasevit *et al*. reported the growth of AlN film on Si (111) by metalorganic vapor phase epitaxy (MOVPE).[1] Nevertheless, investigations of the epitaxy of III-V nitrides on Si in the following two decades are scarce. However, in the 1990s, epitaxial schemes for growing GaN on sapphire, involving the low-temperature nucleation layers, successful p-type doping and high-quality InGaN quantum well have been used effective to achieve high-brightness LEDs for commercialization. Although sapphire-based LEDs have overshadowed research of Si-based LEDs, in 1998, Guha and Bojarczuk demonstrated the first GaN-based double heterostructure (DH) violet LED on Si grown by molecular beam epitaxy (MBE).[2,3] The DH structure consisted of Si (111)/8 nm AlN/n-$Al_xGa_{1-x}N$ (Si doped)/6 nm GaN/p-$Al_xGa_{1-X}N$ (Mg doped) /15 nm p-GaN with x = 0.05-0.09. Unlike in the fabrication of sapphire-based LEDs, the n-contact can be formed on the backside of Si substrate. These results not only demonstrate the possibility of making GaN-based vertical transport light emitters on Si, but also motivated the subsequent research activities.

2. Growth

2.1. *Challenge of growing GaN on Si*

The hexagonally arranged Si (111) face is generally the preferred substrate for use in GaN epitaxy. The growth of GaN on Si (111) causes problems with respects to the material properties (Table 1). (1) The high lattice mismatch between GaN and Si (17%) yields a high dislocation

density of typically over $10^{12}cm^{-2}$. (2) The Ga-Si reaction usually causes so-called meltback etching phenomenon at the interface. Hence, once meltback etching, the surface becomes rough and the crystallinity is poor[4]. (3) The thickness of the GaN buffer layer is an important parameter for in III-nitrides applications. A thicker GaN buffer layer can eliminate more misfit defects initiated from the hetero-substrate. However, a large difference between the thermal expansion coefficients (TEC) of GaN and Si inhibits the growth of sufficiently thick GaN on Si. The TEC introduces a large biaxial tensile stress to the GaN layer and accumulates gradually as the thickness is increased. Therefore, crack networks always appear during cooling when the thickness of the grown GaN exceeds its critical value (<1 μm). (4) Si, which is a material with small band gap, absorbs light whose energy exceeds its band gap. (~1.1 eV).

Table 1. Material parameters of GaN and potential hetro-substrates for GaN epitaxy.

Material	Lattice constant (Å)	TEC (10^{-6}/K)	Lattice mismatch (refer to GaN, %)	Thermal mismatch (refer to GaN, %)
GaN	a = 3.189 c = 5.185	5.59 3.17	–	–
AlN	a = 3.111 c = 4.978	4.20 5.30	2.4	25
Si (111)	a = 5.430 a_{eff} = 3.840	3.59	–16.9	54
ZnO	a = 3.2496 c = 5.2065	5.2065	1.8	7
Sapphire	a = 4.758 c = 12.99 a_{eff} = 2.747	7.50 8.5	16	-34
6H-SiC	a = 3.080 c = 15.120	4.2	3.5	25

"1" is not a severe problem because the growth of GaN on sapphire suffers from a similar amount of lattice mismatch but with the opposite sign. The techniques used to reduce the number of dislocations of GaN on sapphire, like the use of superlattices and ELOG, among others, can be expected to be applicable to GaN on Si. In solving problem "2", an

appropriate nucleation layer or buffer layer can be adopted to minimize the interface reaction that will be discussed in section 2.2. With respect to "4", the wafer lift-off technique and the use of distributed Bragg reflector (DBR) will be helpful. Section 3 will demonstrate another method for tackling the substrate absorption problem. The worst problem is the third, which can only be solved with more academic work in relation to the strain engineering, which will be partially described in section 2.3.

2.2. *Nucleation layers*

Limitations of using conventional GaN used as a nucleation layer (NL) have motivated attempts to use various NLs such as AlAs,[5] nitrided GaAs,[6] ZnO,[7] 3C-SiC[8], AlN[9] and HfN,[10] to prevent Si from undergoing nitridation and to overcome the large difference between the lattice constants of Si and GaN. AlN shows superior advantages to others. First, the subsequently growth of GaN-based devices can be grown using the same process, i.e., MOVPE. Additionally, the AlN layer promotes strain relaxation following GaN growth. For MOVPE, the V-group source is usually ammonia, immediately forming SiN_x when exposed to the silicon surface particularly at higher temperature. The appearance of SiN_x always leads to a poor crystallinity. Therefore, the inlet valve of ammonia source should be closed prior to grow at high temperature. Exposure of the Si surface to Al has been reported to be necessary before AlN growth. Chen *et al.*[11] studied the effect of Al pre-treatment of a Si surface on the following high-temperature (HT, 1100°C) NL growth of AlN (Fig.1). They showed that the optimal Al pre-treatment time was as short as 5 s, resulting in subsequent step-by-step growth for the following AlN and GaN. They also found that the Al pre-treatment time was critical; treatment for too long causes Al to accumulate on the Si surface while insufficient treatment is detrimental to the morphology and crystal quality, because nitridation of Si occurs. Liu *et al.*[12] demonstrate the growth of a high quality GaN grown on low-temperature (LT) AlN (720°C). A highly coherent LT AlN/ Si interface was observed. The lattice images indicated an abrupt interface at which the misfit dislocations appeared with an average separation of about 5.3

$\{1\bar{1}00\}_{AlN}$ planes, which equals 4.3 $\{111\}_{Si}$ planes (Fig. 2). In our experience, when Al pre-treatment was performed at ~700°C and LT AlN was grown at the same temperature, the pre-treatment window at this low temperature was much broader. However, no significant evidence suggested that the pretreatment time was related to the crystalline quality in the range of 5-40 s.

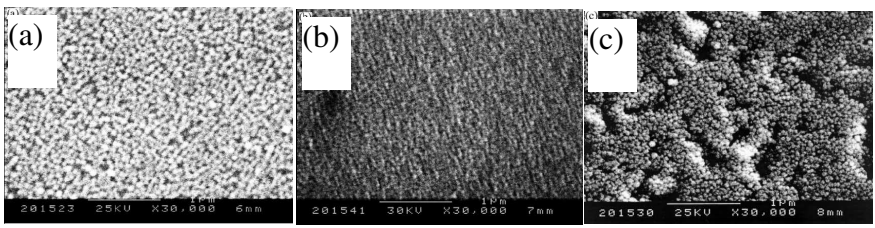

Fig. 1. The surface of 150 nm AlN buffer layers on Si(1 1 1) substrate with pre-treatment Al for 0 s (a), 5 s (b) and 10 s (c), respectively. GaN achieves 2 dimensional growth only on (b). J. Cryst. Growth 225, 150-154 (2001). With the permission for reproduction from Elsevier.

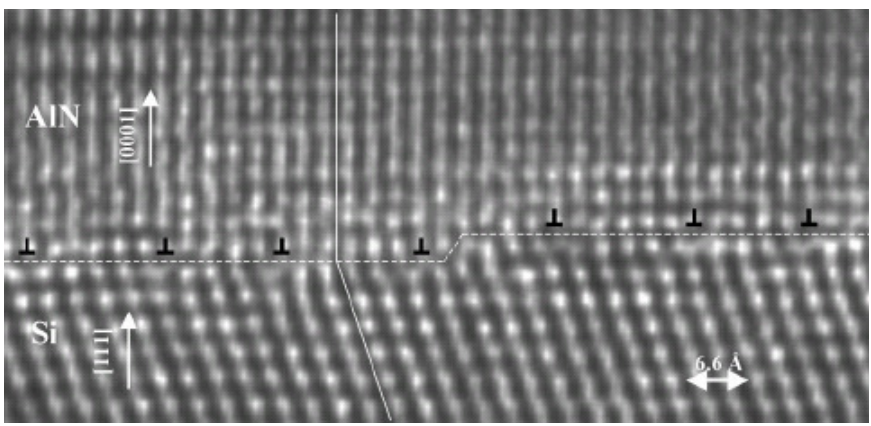

Fig. 2. The lattice images at AlN/Si interface observed by HRTEM for AlN grown at 720°C with a TMAl pretreatment. (Appl. Phys. Lett. 83, 860 (2003).) With the permission for reproduction from American Institute of Physics (AIP)

In the literature, the growth temperatures of AlN NL can be simply divided into two categories- HT above 1000°C or LT of around 700°C. Currently, the better choice is unclear. Intuitively, better crystal quality of an AlN NL should lead to better quality of GaN. A higher bonding energy between III and V ions typically corresponds to a higher growth temperature required to obtain a high crystalline quality. Therefore, high quality AlN is rarely obtained at growth temperatures of below 1000°C.[13] Lowering the growth temperature causes toward poly-crystallinity of the AlN and small grain size. Zamir[13] found a dramatic transition of AlN (002) preferred orientation at 760°C. They observed that the HT-grown AlN on Si (111) had larger grains and was of higher quality than the LT grown one. Lahrèche[14] examined AlN NL grown at HT (950-1200°C) and found that the quality of GaN was optimized when the AlN NL was grown at a temperature in the middle of that range (1050°C). Unfortunately, the HT growth risked re-depositing species from the reactor wall or the susceptor, and promoted the chemical reaction between ammonia and non-covered Si surface.[15] The GaN films grown on an AlN NL at HT were usually locally polluted because of these unexpected effects, even when the temperature-ramping process was ammonia free and conducted in a hydrogen atmosphere. The HT AlN promotes the two-dimensional (2D) growth of GaN, inhibiting the coarsening of the above the AlN fine grains. The coalescence of grains of the GaN NL on sapphire is well known to be critical in improving crystalline quality. An LT-deposited AlN layer has the same columnar grains as an HT-deposited AlN layer, but is more defective and each small grain is smaller. Fortunately, the growth parameters, such as the V/III ratio and the temperature, can be tuned to grow GaN subsequently in a process that is like the two-step growth of GaN on sapphire. Finally, the quality of GaN on the LT-grown AlN is as high as that on the HT-grown AlN, with a threading dislocation density of around 10^9-10^{10} cm^{-2}.

Properly choosing the growth temperature of the AlN NL depends on extensive knowledge including of how to improve the quality of the crystal itself, the crystalline quality of the following buffer layer, the effect of strain relaxation and the reproducibility of epitaxy. Among these considerations, the crystalline quality of the bulk GaN is not the main concern, because it can be improved by many methods. The LT-

grown AlN is more reproducible because the weaker chemical reaction between Si and ammonia. A clean and uniform GaN epi-layer was easily obtained on Si using an LT-grown AlN NL rather than an HT-grown AlN NL.

2.3. *Control of stress and reduction of dislocations*

Controlling stress of the GaN thin film grown on proper buffer layers is the most important issue in producing effective devices. It depends on the knowledge of the origins and mechanisms of the stress. As stated in the literature, the intrinsic and extrinsic tensile stresses of the epitaxial GaN on Si mainly arise from four causes- (1) lattice mismatch[16,17], (2) TCE mismatch,[18] (3) Si doping[19] and (4) three-dimensional (3D) grain coalescence,[20] all of which are listed in Table 2. The listed data show that the cracking thickness of a GaN layer on Si is less than 1 μm because the fracture stress of GaN is around 1GPa.

Table 2. Stress of epitaxial GaN on Si.

Origin of stress	Stress level
Lattice mismatch	0.1-0.2 GPa/μm
TEC mismatch	0.7 GPa/μm
Si doping (~10^{18}cm^{-3})	0.1 GPa/μm
3-D islands coalescence	0.2 GPa/μm

The stress of lattice mismatched GaN grown on sapphire is known to change from compressive to tensile through a grain coalescence process.[21] An *in-situ* measurement tool is necessary to elucidate further the stress transition during a GaN/Si growth. Krost *et al*.,[20] Raghavan *et al.*[22-24] and Han *et al*.[25] adopted a normally incident focus laser beam as a light source; the beam was split using an etalon and then passed through a semitransparent mirror. Subsequently, the split laser beams are reflected, being analyzed by a detector.[20] A film under tensile stress caused by either TEC or lattice mismatch, normally exhibits concave bending. Thus, the *in situ* stress evolution can be derived from the curvature-thickness vs. growth time relation curve, using the Stoney equation[26] or the Freund equation.[27] *Ex-situ* in-plane X-ray diffraction

(XRD) is also another powerful method for determining the stress of as-grown films.

The lattice mismatch between GaN and AlN is –2.6%, yielding a theoretical compressive stress in GaN of around –12 GPa, if a biaxial modulus of 470 GPa[29] is assumed. However, regardless of the growth temperature of AlN NL, the maximum biaxial compressive stresses of the GaN on AlN were between –1.5[23] and –1.8 GPa[29] partially because AlN NL was also tensile stress caused by the lattice mismatch between AlN and Si. However, the mismatch strain was calculated to be ~1.5 GPa. The origins of the extra 10 GPa require future study. With the help of *in-situ* or *ex-situ* stress measurement, the strain relaxation mechanisms reported by Raghavan and Krost were similar. That is, an initial compressive stress is followed immediately by a tensile stress. However, they used different AlN NLs. Krost (LT AlN, 720°C) obtained a hydrostatic compressive stress during the very early stage of GaN growth (<40 nm) on LT AlN. The onset of the tensile stress was obtained during the coalescence of islands (Fig. 3). The hydrostatic compressive stress gradually changed to a biaxial tensile stress, accompanied by changes in the surface morphology. This change was explained in terms of a zipping mechanism. In contrast, using an HT AlN (1100°C) as an NL, Raghavan *et al*. did not observe such a transformation. Instead, they suggested that the onset of the tensile stress was associated with step-by-step growth, during which the lateral grain size of the individual islands increased, before full coalescence (Fig. 4). They attributed their observations to the annihilation of free volume caused by the elimination of grain boundaries or dislocations. These two different observations are attributed herein to the different quality and morphology of AlN NLs. In an LT AlN NL, the Al atoms cannot easily diffuse on surface so the crystal is highly defective, and the AlN grains are discontinuously distributed over the Si wafer in three-dimensions. Therefore, the subsequently grown GaN are initially discontinuous. Coalescence is delayed until the discrete islands meet each other. The thickness is usually exceeds 100 nm to achieve a fulfill coalescence, and is somewhat modified by such growth parameters as the V/III ratio. However, the HT AlN NL has a better crystalline quality and a smother surface. The coalescence was complete within the first few tens of nanometers, so the

HT AlN NL has more grain boundaries and dislocations than the LT-AlN. The numbers of grain boundaries and dislocations fall only during the step-by-step growth, and so are related to the thickness of the film. More efforts must be made to characterize GaN on various AlN NLs.

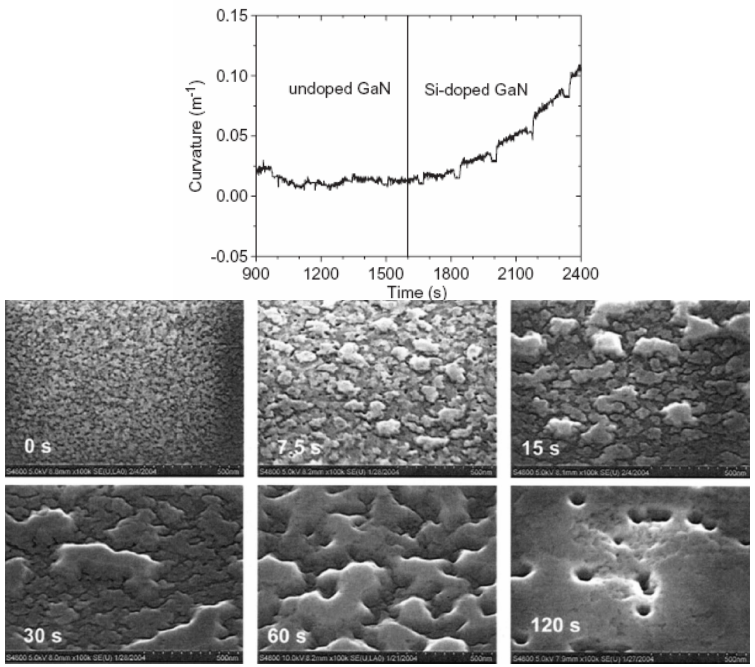

Fig. 3. (Upper figure) *In-situ* curverture measurement of GaN growth on Si using LT AlN NL. (J. Cryst. Growth 275, 209 (2005).) (Lower figure) The corresponding surface morphologis observed by SEM during the initial GaN growth on LT AlN/Si (Appl. Phys. Lett. 85, 3441 (2004)). With the permission for reproduction from American Institute of Physics (AIP) and Elsevier.

Many successful studies concerning the strain problems, including the insertion of strain relaxation layers, patterning substrate[30,31] and compliant SOI substrates have been performed.[32] The latter two usually uses patterned SiO_2 (or SiN_x) to define the mask or etched trench. The cracks are guided into the mask/trench regions, so the remaining GaN regions can be very thick and crack-free.

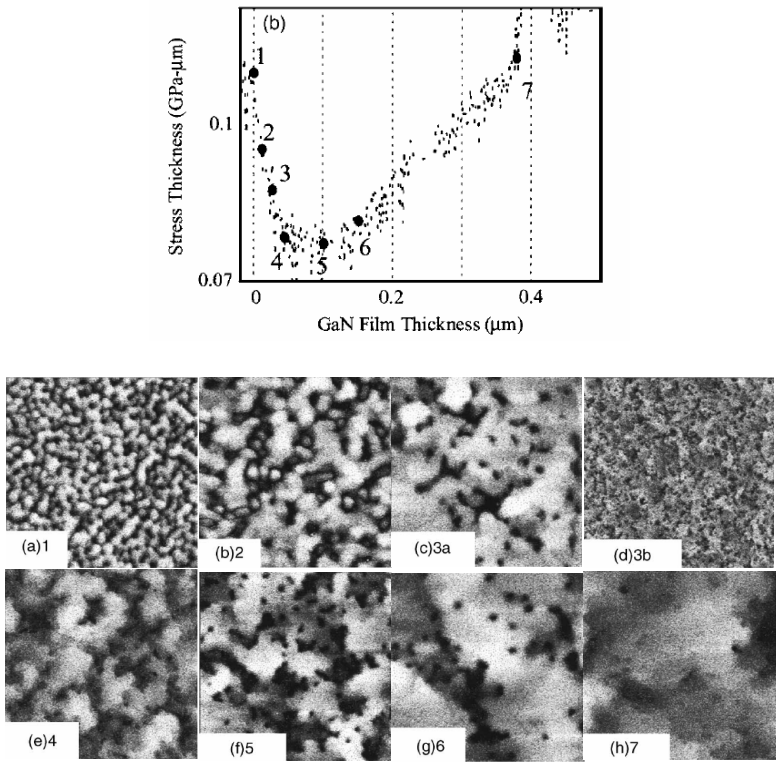

Fig. 4. (Upper) *In-situ* curverture measurement of GaN growth using LT AlN /Si(111). (Lower) The corresponding surface morphologis observed by AFM during the initial GaN growth on LT AlN/Si. Scan image size (a)-(c): 1×1 μm, (d)-(h): 5×5 μm. (J. Appl. Phys. 98, 023514 (2005).) With the permission for reproduction from American Institute of Physics.

This article concentrates on the epitaxial techniques for GaN grown directly on clean Si substrate, because such approaches are the most cost-effective and reproducible in commercial uses, and can be completed only in a MOVPE reactor. Interlayers (IL), such as the LT AlN,[22,24] AlGaN/GaN superlattices,[33,34] the SiN_x,[35,36] and graded AlGaN between AlN NL and bulk GaN,[22] have significantly reduced stress, particularly in the LT AlN interlayer. Such methods were initially developed by Amano to increase the critical thickness of AlGaN on a GaN layer.[37] Inserting a 10-nm-thick LT AlN into the GaN contributes to an increase

in the critical thickness of about 0.5-1 μm.[38] Accordingly, the total thickness of numerous AlN/GaN stacks can easily exceeds 4 μm, which is the typical thickness of sapphire LEDs.

The growth temperature of LT AlN IL has been shown to affect importantly the stress relaxation. Growing AlN IL over a broad range of temperatures from 550 to 1100°C, Bläsing found that the tensile stress dropped.[39] As a terminal condition, the high-temperature (HT) GaN or AlGaN grown on a LT AlN (550°C) was almost stress and crack-free at room temperature. *Ex-situ* x-ray reciprocal space mapping also confirmed that the lattice changed from pseudomorphic to relaxated as the growth temperature of LT AlN was reduced. Han[25] studied the AlGaN interlayers with compositions that varied from AlN to GaN at 800°C. They showed that the critical thickness of HT 0.9 μm-thick-$Al_{0.2}Ga_{0.8}N$ layers grown on LT $Al_xGa_{1-x}N$ interlayers with x = 0, 0.35-0.42 and 0.62 increased by a factor of zero, four and 30, respectively, and that of a layer grown on an interlayer with x = 1 was fully compressive during growth. That is, the LT GaN almost does not affect the strain relaxation. The induced compressive stresses increased with increased the lattice mismatch between the interlayers and the HT layers. Cong[40] recently proposed more detailed growth parameters, including the number of pairs and the thickness of LT AlN. The stress and the crystal quality decline as the AlN thickness increases. The optimized thickness of the LT AlN was around 16 nm, which is consistent with the results in Dadgar's report.

Notably, an interesting relationship exists between the strain relaxation and the improvement in crystalline quality of GaN/Si grown by MOVPE. ILs or buffer layers applied to relax the lattice and thermal strain were usually found also to reduce the dislocation density. For instance, LT AlN ILs, AlGaN/GaN superlattices, and *in-situ* SiN_x masks[41] effectively reduced the numbers of threading dislocations. Only experimental data have so far revealed the relationship. Figure 5 presents cross-sectional transmission electron microscope (XTEM) images, in which HT GaN is divided into two regions by inserting an LT AlN IL grown at 580°C. Obviously, dislocation density was much reduced through the insertion of a LT AlN IL, except few dislocations were generated within the upper GaN or penetrate the LT AlN IL.

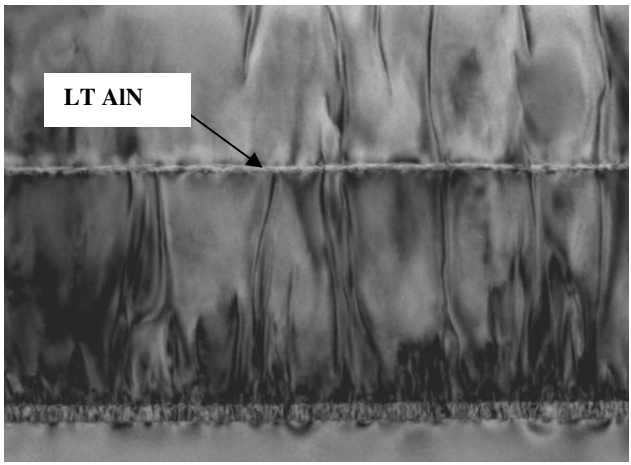

Fig. 5. XTEM image showed that the LT AlN insertion between HT GaN.

3. Recent development of the LEDs on Si

The performance of LEDs grown by MOVPE on Si has been improved in recent years as the crystalline quality has been improved. In 2002, Dadgar *et al*. demonstrated that the vertically conducting blue LED with an output power of 152 μW at a current of 20 mA with *in-situ* deposited SiN_x masks. Turn-on voltages of as low as 2.8 V and a series resistance of 55 Ω were also obtained (Fig. 6). In the same year, Zhang and Egawa *et al.* employed HT AlN NL and AlN/GaN multilayers with a thin AlN/AlGaN buffer layer to grow LEDs. The lateral and vertical LEDs with operating voltages of 3.7V and 4.2V, respectively, and output powers of 34.8 μW and 34.5 μW were presented. The forward series resistances of the lateral and vertical conducting LEDs were 33Ω and 42 Ω, respectively (Fig. 7). The reported operating voltages were sufficiently good for commercial use, but the output powers were still much lower than those of sapphire-based LEDs.

In 2005, we utilized similar epitaxial techniques, developed by Dadgar, successfully made the blue and green LEDs on Si with average output powers of around 0.7 mW.[42] We also fabricated a white LED

using a Si substrate by converting blue emission using yellow phosphor. Figure 8 compares the white LED with both blue and green LEDs grown on Si, and a blue LED grown on sapphire. Figure 9 displays both top and side views of LED/Si chips before and after the current was injected. The intensity of light was strong enough to be visible even at a small driving current.

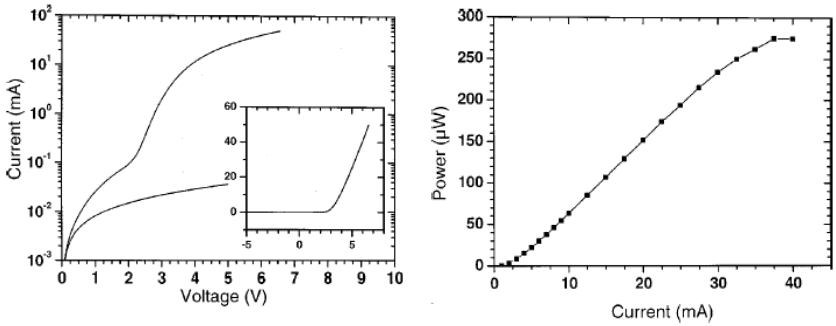

Fig. 6. I-V(Left) and L-I (right) curves of blue LED (455 nm, 14 mil) reported by Dadgar *et al*. (Appl. Phys. Lett. 80, 3670, (2002)). With the permission for reproduction from American Institute of Physics.

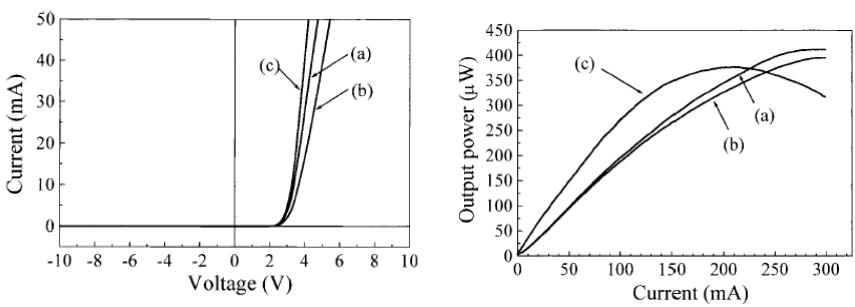

Fig. 7. I-V and L-I curves of blue LEDs reported by Egawa *et al*.. (Jpn. J. Appl. Phys. 42, L226, 2003) (a) lateral conduction LED/Si (b) vertical conduction LED/Si(c) LED/sapphire. With the permission for reproduction from Japanese Journal of Applied Physics.

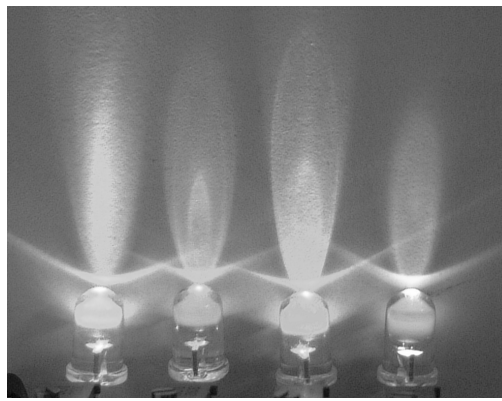

Fig. 8. Photograph of four LEDs using Si and sapphire substrates. From left to right: LED A using sapphire substrate with an output power of 5 mW; LED B using Si substrate with an emission at 430 nm and an output power of 0.7 mW; LED C using Si substrate with an emission at 490 nm and an output power of 0.5 mW; LED D, a white one, achieved by coating an LED similar to B with yellow phosphor.

Table 3. Recent progress of the blue and green LEDs on Si(111).

wavelengths (nm)	Lop	Vf (V)	Year	References
365	0.0015 mW	15 V at 35 mA	2000	43
455	0.152 mW	5 V at 20 mA	2002	44
505	0.02 mW	7 V at 20 mA	2002	45
453	0.0348 mW	3.7 V at 20 mA	2003	46
505	0.6-0.8 mW	~6 V at 20 mA	2005	42
470	0.6-0.8 mW	~5 V at 20 mA	2005	42
460	20 mcd	3.8 V at 20 mA	2005	47

The measured output powers of the LEDs/Si herein exceeded the best result reported to date by a factor of four to five. The marked improvement in output powers may be related to many factors, like the film thickness, the quantum structures, the quality of the p-type layer, the optimization of each layer and the LED chip process, among others. Notably, our subsequent studies routinely obtained output powers of over 1 mW. Table 3 briefly summarizes the LEDs/Si research activities of recent years.

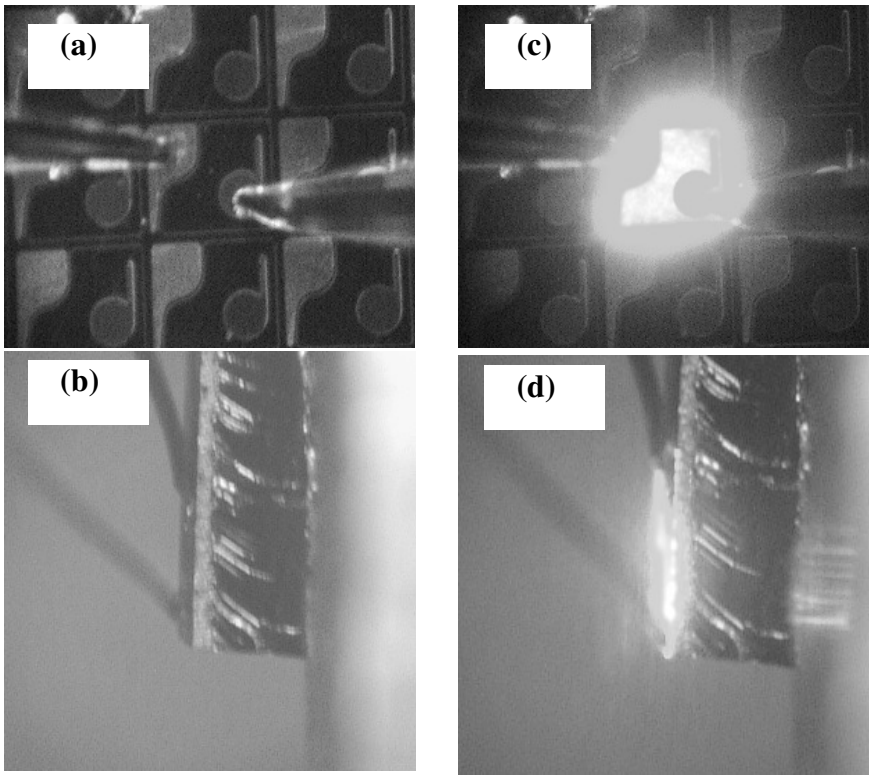

Fig. 9. LED on Si (a) (b) before and (c) (d) after the 20 mA current injection, where (a)(c) were viewed from the top side and (b)(d) were from the cross section.

Electroluminescence, output power-current (L-I) properties, current-voltage (I-V) properties, life time test and TEM were used to elucidate further the presented high-brightness LEDs. Figure 10 shows the EL spectra of three LEDs with different wavelengths, labeled Sample A, B, and C, respectively. The spectra showed only very small blue shifts.

Figure 11 plots the L-I and I-V characteristics of the same LEDs. As presented in Fig. 11 (a), the output power of these LEDs ranged from 0.5 mW to 0.7 mW at a forward current of 20 mA. The turn-on voltage was around 4-6 V for all three LEDs, with a small reverse leakage current of between 10^{-8} and 10^{-9} mA at –5 V, as shown in Fig. 11 (b).

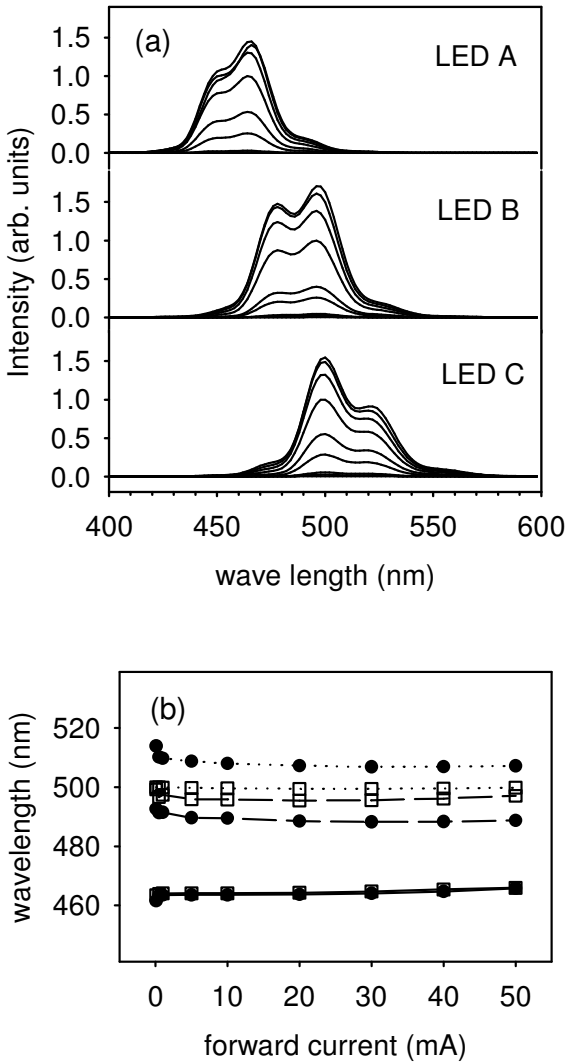

Fig. 10. Electroluminescence and emission wavelengths of the three LEDs. (a) Electroluminescence spectra at different driving currents: from bottom up, 0.1 mA, 0.5 mA, 1 mA, 5 mA, 10 mA, 20 mA, 30 mA, 40 mA and 50 mA. (b) Peak wavelengths and dominant wavelengths at different driving currents. Open square: peak wavelength; Solid circle: dominant wavelength. LED A: solid line; LED B: dashed line; LED C: dotted line.

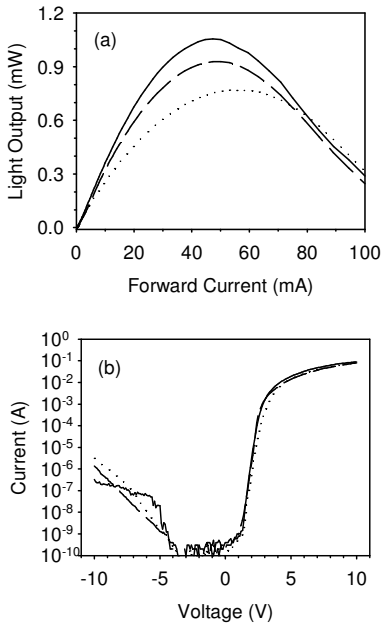

Fig. 11. (a) L-I and (b) I-V characteristics of the three LEDs shown in Fig. 1. LED A: solid line; LED B: dashed line; LED C: dotted line.

A comparison of the LEDs grown with identical structures on Si and sapphire is of interest. Two unique characteristics are observed. First, although the LEDs/Si had a weaker output powers and much poorer crystal quality than LEDs/sapphire, the former had a longer life time than the latter because the thermal conductivity of Si (1.5W/cm K) exceeds that of sapphire (0.3–0.4W/cm-K). As indicated in Fig. 12, the decrement of output powers of the blue or green LEDs/Si were in the range 0-15 % after a long-term test (1000 hrs) with the inject of 20 mA current. However, the output powers of the LEDs on sapphire fell by ~60 % in just the first 100 hrs. An obvious accelerated degradation of the LEDs/sapphire began after a few hours, as clearly revealed when represented the life-time in logarithmic scale (inset of Fig.12). The quantum wells and barriers of the LEDs/Si revealed by cross-sectional TEM (XTEM) showed gradually became thicker from the bottom up during growth (Fig. 13). For example, a GaN-InGaN MQW grown on Si,

which consisted of ten periods of quantum-wells with an intended barrier thickness of 10 nm, had first and last barrier layers with thicknesses of 10.5 and 18.0 nm, respectively. The mechanism of this unique phenomenon is still under investigation. Consequently, the LED grown on Si exhibited a consistent shift in emission toward longer wavelengths, as determined by comparison with that from LED grown on sapphire. For example, the emission wavelength changed of the LED grown on Si was 480 nm, in contrast to the 430 nm for that grown on sapphire. A similar large redshift in emission wavelength was repeatedly observed. The redshift in emission wavelength for the structures grown on Si, as compared with that from LEDs grown on a sapphire substrate, was related to the observed gradual increase in the thickness of the layer grown in the MQW.

An important issue must be considered seriously to increase further the external efficiency. Si absorbs much light from the active layer because the substrate is not transparent to light from blue to UV wavelengths. Given the absorption at the GaN/Si interface, inserting the distributed Bragg reflector (DBR) between the active region and the substrate enhances the optical output power of an LED on Si.

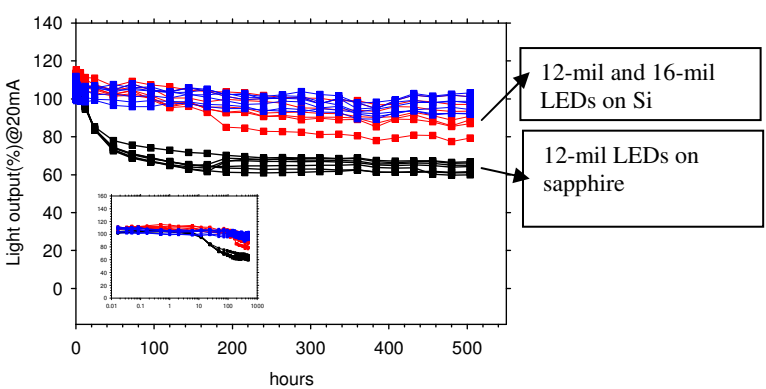

Fig. 12. Lifetime test of two LED structures grown on Si and one using a sapphire substrate at room temperature with a constant driving current of 20 mA.

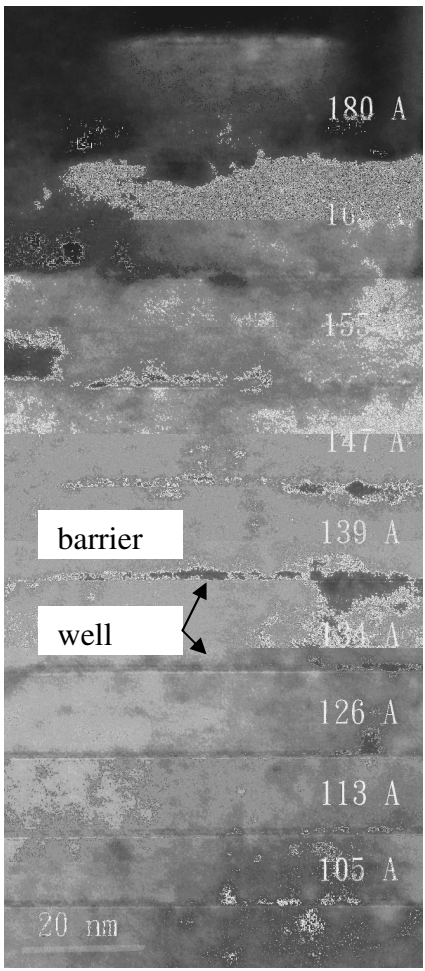

Fig. 13. XTEM of the InGaN/GaN multiple quantum-wells on Si.

Nakada *et al.* reported considerably higher output power from an InGaN multiple quantum-well LED when DBR was inserted between the LED structure and the sapphire substrate.[48] Ishikawa demonstrated that the insertion of three DBR pairs between GaN and Si increased the output power by three times.[49] Figure 14 displays simulated reflectance spectra, based on the assumption that DBR with various Al contents and DBR pair numbers was sandwiched between Si and the active layer/air.

The DBR clearly increased the reflectivity. Unfortunately, the additional strain generated by introducing DBR limited the number of pairs of DBR. In our experience, crack-free GaN can only be made on DBR/Si when DBR pairs less than three. However, it was helpless to the extraction efficiency. Additionally, wavy interfaces of DBR were easily formed by the penetration by threading dislocations. The presence of uneven interfaces destroyed the constructive interference. Hence, the application of using DBR for LEDs on Si remains difficult.

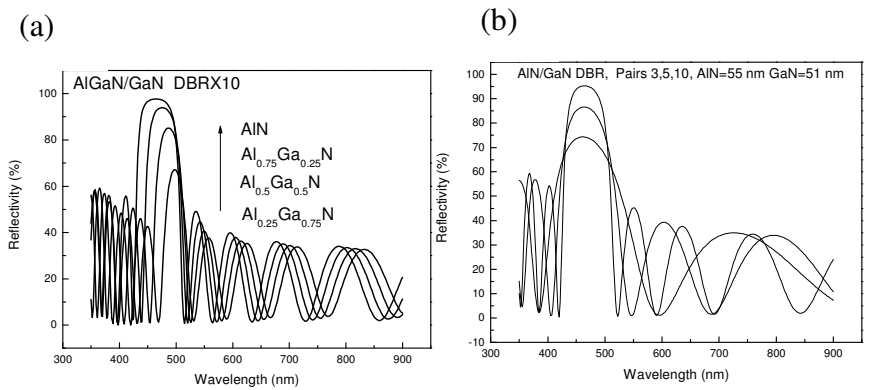

Fig. 14. (a) Reflectivity as a function of the Al content in AlGaN/GaN DBR. (b) Reflectivity as a function of AlN/GaN DBR pair numbers. Note: the simulation assumes that the light incidents the wafer from air.

The use of rocksalt-type titanium nitride (TiN) as a nucleation layer on Si is proposed to ease the substrate absorption problem. TiN has been used in many Si-based semiconductor device technologies in recent years, such as in gate electrodes in field-effect transistors and in advanced metallization schemes of ultralarge scale integrated applications.[50-52] Additionally, TiN has also been proven to be an excellent Ohmic or Schottky contact for n-type and p-type GaN, respectively.[53] This material is shiny and yellowish with a very high conductivity. The lattice mismatches between TiN (111) (a = 0.2998 nm) and AlN (001) (a = 0.3111 nm) and between TiN and GaN (001) (a = 0.3189 nm) are as low as 3.7 % and 6.3 %, respectively.

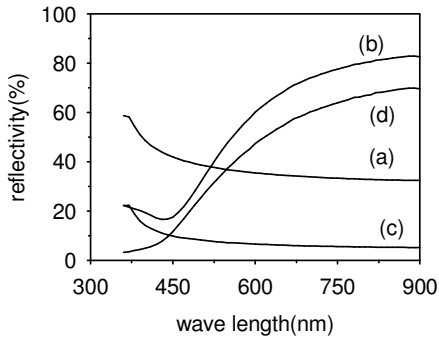

Fig. 15. Reflectivity as functions of wavelengths for (b) & (d) TiN buffered Si and (a) & (c) without TiN buffered Si. The simulation assumed lights generated from (a) & (b) air, (c) & (d) GaN.

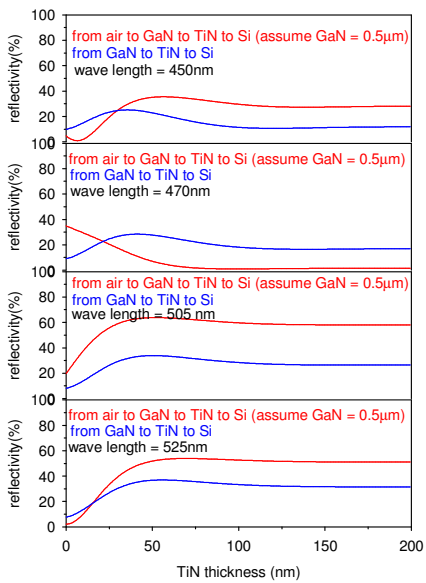

Fig. 16. Reflectivity as a function of TiN thickness simulated from 525 to 450 nm (bottom up). Lower and upper curves in each set represent the reflectivity simulated by assuming the light generated from GaN and air, respectively.

For LEDs or LDs, light is excited from the quantum wells within GaN. Thus, using the air or GaN as the top layer to simulate the reflectivity of TiN-buffered Si yielded significantly different results. As indicated by the curves plotted in Fig. 15(a) and (b), the reflectance of the air/Si interface exceeds than that of the air/TiN interface between 450 nm and 480 nm. Replacing the refractive index and extinction coefficient of air with those of GaN yields very different simulated results. The curves in Figs. 15 (c) and (d) show that the reflectance of GaN/TiN interface exceeds that of the GaN/Si interface at all wavelengths of interest. For example, the reflectivity at 500 nm is increased from 8% to 25% when a TiN layer is inserted. The simulated results (Fig. 16) also reveal that optimal thickness of TiN on Si is 50 nm, beyond which the reflectivity remained constant for a wide range of wavelengths from 450 nm to 525 nm.

Figure 17 presents the cross-sectional images of the MOVPE-grown Si/TIN/AlN/AlGaN sample observed by high-resolution TEM. The X-ray $\theta/2\theta$ diffraction (XRD) pattern, depicted in the inset of Fig. 17(a) shows that the TiN(111), AlN (002) and GaN (002) faces are parallel to the Si(111) face. The selected area electron diffraction (SAED) pattern of the Si/TiN/AlN interface, which is displayed in another inset of Fig. 17(a), confirms that the epitaxial relationships are Si(1,1,1)//TiN(1,1,1)//AlN(0,0,1), Si[1,1,0]//TiN[1,1,0] and Si[0,0,1]//TiN[0,0,1]. Figures 17(b) and (c) show lattice images of the Si/TiN and TiN/AlN/AlGaN interfaces, respectively. The large lattice mismatch exists between TiN (111) and Si (111) can be relieved by introducing a periodic array of misfit dislocations, as observed in Fig. 17 (b). The result that the distance across around four {111}Si planes equals that across five {111}TiN planes is consistent with the theoretical lattice mismatch ~20%. Only a few misfit dislocations are observed near the abrupt interface (Fig. 17(c)). A more detailed discussion and presentation of data will be reported elsewhere.[54]

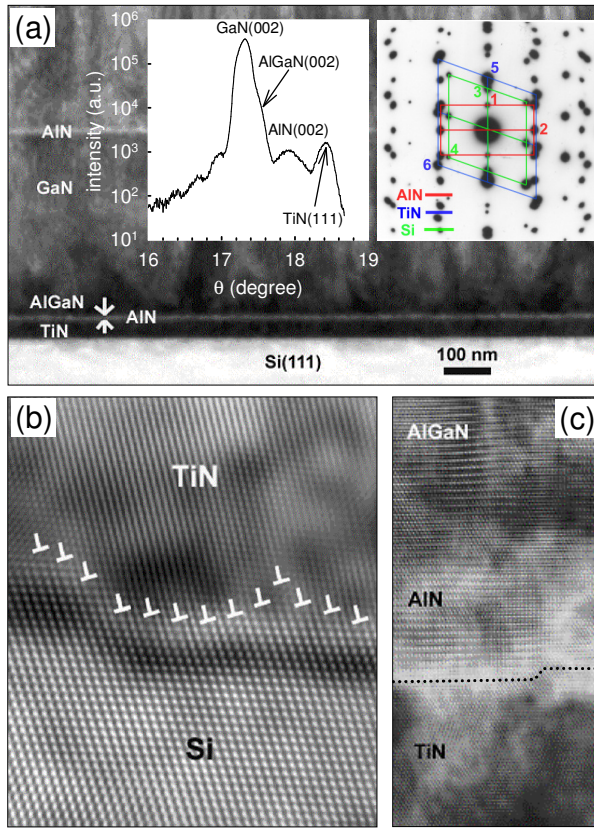

Fig. 17. (a) Cross-sectional image of III-nitrides grown on Si. Insets show the XRD diffraction patterns of LED grown on Si and the SAD pattern of the Si/TiN/AlN interface. The index of numbers 1-6 represent the AlN (0,0,0,1), AlN (-1,1,0,0), Si(1,1,1), Si(-2,0,0), TiN(1,1,1) and TiN(-2,0,0), respectively. The incident electron beam is parallel to Si[-1,1,0]. (b) HR-TEM images near the TiN/Si interface. Misfit dislocations are indicated by "⊥". (c) HR-TEM images near the TiN/AlN/AlGaN interfaces. The dotted line marks the coherent interface of $\{111\}_{TiN}/\{001\}_{AlN}$.

Finally, a proposal of Funato *et al.*[55] is considered. They used a so-called wafer bonding technique for transferring the as-grown GaN from GaAs to Si substrate through an AuGe binding layer. Unlike laser lift-off using an excimer laser, which removes the GaN film from sapphire substrate, only mechanical polishing and chemical etching should be used to remove the GaAs substrate. However, the cost and poor device

performance are the main problems. Recently, Egawa *et al.* futher modified wafer bonding technique into a technique called "selective lift-off" (SLO) technique[56]. The as-grown LED/Si was mounted on a Cu substrate, between deposited a high reflective metal reflector (Al/Au). This method increases output power by 49% and reduces the operating voltage from ~4 V to 3.6 V at 20 mA. Besides, similar methods that increase the performance of AlInGaP LEDs to that of Si-based LEDs can be used.

4. Conclusion

This article reviewed several works of GaN on Si. Based on knowledge of nitridation prevention, strain controlling, dislocation elimination and substrate absorption reduction, it revealed an improvement in GaN quality and performance of LEDs on Si. Hopefully, the mass production of blue or green LEDs on Si may be realized in the near future when the light output power satisfies the requirements of the market. Until that time, the remaining problem will be in production yield. Fortunately, well-established Si technologies can accelerate improvements in yield. Besides, GaN on Si technology will continue to be of great interest with possible applications to other devices, like transistors.

Reference

1. H. M. Manasevit, F. M. Erdmann, and W. J. Simpson, *J. Electrochem. Soc*. **118**, 1867 (1971).
2. S. Guha and N. A. Bojarczuk, *Appl. Phys. Lett.* **72**, 415 (1998).
3. S. Guha and N. A. Bojarczuk, *Appl. Phys. Lett.* **73**, 1487 (1998).
4. H. Ishikawa, K. Yamamoto, T. Egawa, T. Soga, T. Jimbo, and M. Umeno, *J. Cryst. Growth* **189/190**, 178 (1998).
5. N. P. Kobayashi, J. T. Kobayashi, P. D. Dakus, W. J. Choi, and A. E. Bond, *Appl. Phys. Lett.* **71**, 3569 (1997).
6. J.W. Yang, J.S. Sun, Q. Chen, M.Z. Anwar, M. Asif Khan, S.A. Nikishin, G.A. Seryogin, A.V. Osinsky, L. Chernyak, H. Temkin, C. Hu, S. Mahajan, Appl. *Phys. Lett.* **69** 3566 (1996).
7. W. Lee, S. W. Park, J. B. Yoo, *Phys. Stat. Sol*. (a) **176**, 583 (1999).
8. C.I. Park, J.H. Kang, K.C. Kim, K.S. Nahm, E. K. Suh, K.Y. Lim, *Thin Solid Film*, **401**, 60 (2001).

9. S. Zamir, B. Meyler, E. Zolotoyabko, J. Salzman, *J. Cryst. Growth*, **218**, 181 (2000).
10. X. Xu, R. Armitage, Satoko Shinkai and Katsutaka Sasaki, C. Kisielowski, E. R. Weber, *Appl. Phys. Lett*. **86**, 182104 (2005).
11. P. Chen, R. Zhang, Z.M. Zhao, D.J. Xi, B. Shen, Z.Z. Chen, Y.G. Zhou, S.Y. Xie, W.F. Lu, Y.D. Zheng, *J. Cryst. Growth* **225**, 150 (2001).
12. R. Liu, F. A. Ponce, A. Dadgar, and A. Krost, *Appl. Phys. Lett*. **83**, 880 (2003).
13. S. Zamir, B. Meyler, E. Zolotoyabko, J. Salzman, *J. Cryst. Growth* **218**, 181 (2000).
14. H. Lahrèche, P. Vennégues, O. Tottereau, M. LauK gt, P. Lorenzini, M. Leroux, B. Beaumont, P. Gibart, *J. Cryst. Growth* **217**, 13 (2000).
15. I. H. Lee, S. J. Lim, and Y. Park, *J. Cryst. Growth* **235**, 73 (2002).
16. S. Hearne, *et al.*, *Appl. Phys. Lett*. **74**, 356 (1999).
17. H. Amano *et al.*, *Jpn. J. Appl. Phys*. **37**, L1540 (1998).
18. L. T. Romano, *J. Appl. Phys*. **87**, 7745 (2000).
19. J. A. Floro, *MRS Bull*. **27**, 19 (2002).
20. A. Krost, D. Dadgar, F. Schulze, J. Blässing, G. Strassburger, R. Clos, A. Diez, P. Veit, T. Hempel, J. Christen, *J. Cryst. Growth* **275**, 209 (2005).
21. S. Hearne, E. Chason, J. Han, J. A. Floro, J. Figiel, J. Hunter, H. Amano, I.S.T. Tsong, *Appl. Phys. Lett*. **74**, 356 (1999).
22. S. Raghavan, and J. M. Redwing, *J. Appl. Phys*. **98**, 023514 (2005).
23. S. Raghavan, and J. M. Redwing, *J. Appl. Phys*. **98**, 023515 (2005).
24. S. Raghavan, X. Weng, E. Dickey, and J. M. Redwing, *Appl. Phys. Lett*. **87**, 142101 (2005).
25. J. Han, K. E. Waldrip, S. R. Lee, J. J. Figiel, S. J. Hearne, G. A. Petersen, and S. M. Myers, *Appl. Phys. Lett*. **78**, 67 (2001).
26. G. Stoney, *Proc. R. Soc. London, Ser. A* **82** 172 (1909).
27. L. B. Freund, J. A. Floro, E. Chason, *Appl. Phys. Lett.* **74**, 1987 (1999).
28. A. F. Wright, *J. Appl. Phys*. **82**, 2833 (1997).
29. A. Krost, A. Dadgar, J. Blläsing, A. Diez, T. Hempel, S. Petzold, J. Christen, and R. Clos, *Appl. Phys. Lett*. **85**, 3441 (2004).
30. C. H. Chen, C. M. Yeh, J. Hwang, T. L. Tsai, C. H. Chiang, C. S. Chang, and T. P. Chen, *J. Appl. Phys*. **98**, 093509 (2005).
31. L. Macht, P. R. Hageman, S. Haffouz, and P. K. Larsen, *Appl. Phys. Lett*. **87**, 131904 (2005).
32. R. F. Davis, T. Gehrke, K. J. Linthicum, P. Rajagopal, A. M. Roskowski, T. Zheleva, E. A. Preble, C. A. Zorman, M. Mehregany, U. Schwarz, J. Schuck, and R. Grober, *MRS Internet J. Nitride Semicond. Res*. **6**, 14 (2001).
33. S. Hwan Jang, and C. Ro Lee, *J. Cryst. Growth*, **253**, 64 (2003).
34. E. Feltin, B. Beaumont, M. Laügt, P. de Mierry, P. Vennégues, H. Lahrèche, M. Leroux, and P. Gibart, *Appl. Phys. Lett.* **79**, 3230 (2001).
35. T. A. Rawdanowicz and J. Narayan, *Appl. Phys. Lett*. **85**, 133 (2004).
36. K. J. Lee, E. H. Shin, and K. Y. Lim, **85**, 1502 (2004).

37. H. Amano, M. Iwaya, N. Hayashi, T. Kashima, S. Nitta, C. Wetzel, and I. Akasaki, *Phys. Status Solidi B* **216**, 683 (1999).
38. A. Krost and A. Dadgar, *Mater. Sci. Eng. B* **93**, 77 (2002).
39. J. Bläsing, A. Reiher, A. Dadgar, A. Diez, and A. Krost, *Appl. Phys. Lett*. **87**, 2122 (2002).
40. G. Cong , Y. Lu, W. Peng, X. Liu, X. Wang, Z. Wang, *J. Cryst. Growth* **276**, 381 (2005).
41. A. M. Poschenrieder, A. Reiher, J. Bläsing, J. hristen, A. Krtschil, T. Finger, T. Hempel, A. Diez, and A. Krost, *Appl. Phys. Lett*. **82**, 28 (2003).
42. C. F. Shih, N. C. Chen, C. A. Chang, and K. S. Liu, *Jpn. J. of Appl. Phys*. **44**, L140 (2005).
43. M. A. Sánchez-García, F. B. Naranjo, J. L. Pau, A. Jiménez, E. Calleja, and E. Muñoz, *J. Appl. Phys*. **87**, 1569 (1999).
44. T. Egawa, B. Zhang, N. Nishikawa, H. Ishikawa, T. Jimbo, and M. Umeno, *J. Appl. Phys*. **91**, 528 (2002).
45. Baijun Zhang, Takashi Egawa, Hiroyasu Ishikawa, Yang Liu and Takashi Jimbo, *Jpn. J. Appl. Phys*. **42**, L226 (2003).
46. C. Mo, W. Fang, Y.Pu, H. Liu, F. Jiang, *J. Cryst. Growth* **285**, 312-317 (2005).
47. N. Nakada, M. Nakaji, H. Ishikawa, T. Egawa, M. Umeno, T. Jimbo, *Appl. Phys. Lett.* **76**, 1804 (2000).
48. H. Ishikawa, , B. Zhanga, K. Asanoa, T. Egawaa, T. Jimbob, *J. Cryst. Growth* **272**, 322 (2004).
49. Gurtej S. Sandhu, Scott G. Meikle, and Trung T. Doan, *Appl. Phys. Lett.* **62**, 240 (1993).
50. S.C. Sun and M.H. Tsai, *Appl. Phys. Lett.* **68**, 670 (1996).
51. P. Patsalas and S. Logothetidis, *J. Appl. Phys*. **93**, 989 (2003).
52. C. A. Dimitriadis, Th. Karakostas, S. Logothetidis, G. Kamarinos, J. Brini, and G. Nouet, *Solid-State Electron*. **43**, 1969 (1999).
53. *Appl. Phys. Lett.* (In revised).
54. Mitsuru Funato, Shizuo Fujita, and Shigeo Fujita, *Appl. Phys. Lett*. **77**, 3959 (2000).
55. B. Zhang, T.i Egawa, H. Ishikawa, Y. Liu, and T. Jimbo, *Appl. Phys. Lett*. **86**, 071113 (2005).

CHAPTER 10

NITRIDE MICRODISPLAY AND MICRO-SCALE LIGHT EMITTING DIODE ARRAYS

Hoi Wai Choi

Department of Electrical and Electronic Engineering,
University of Hong Kong, Pokfulam Road, Hong Kong
E-mail: hwchoi@eee.hku.hk

The evolution, current developments and future trends of Gallium Nitride based micro-light emitting diodes will be summarized in this chapter. Micron-scale LEDs were initially developed to maximize light extraction efficiencies to overcome the large amount of light trapped in the device structure due to total internal reflection. However, it was later discovered that by grouping micro-LEDs into arrays, their functionality goes beyond illumination purposes. The first reported use of GaN emissive micro-arrays was a micro-display. Moreover, the high optical power output of these emissive arrays also makes them potentially competitive in the projection display market. Arrays emitting at ultra-violet wavelengths have also been demonstrated to be useful for chemical and biological fluorescence excitation. On the other hand, interconnected micro-disk LED arrays have also made dramatic progress. Arrays employing novel geometries, including rings and hexagons have been introduced to optimize extraction efficiencies and packing densities. Down-scaling of dimensions to nano-scale levels have also been reported to maximize the aspect ratios of the structures. Random roughening of the GaN surface, usually by chemical wet etching, has been demonstrated to aid in light extraction. Periodic nanostructures, typically patterned by electron beam lithography, have been incorporated into GaN LED structures as photonic crystals to exploit the photonic bandgap. Major milestones and breakthroughs in the research and development of GaN-based micro-LED arrays will be highlighted.

1. Introduction

Progress in Gallium Nitride (GaN) based light-emitting diodes (LEDs) has been tremendous in the past decade. From the early demonstration of candela class LEDs[1] emitting at visible wavelengths in the mid 1990s to the recent achievement of broadband white light LEDs capable of producing over 80 lumens/watt,[2] it can be seen that considerable research efforts around the world, both by academics and industrialists, have been invested in the development and perfection of a light source which can revolutionize the way our world is illuminated.

Such efforts can generally be categorized into four main areas: physics, epitaxy, processing and packaging. Significant progress has been made in each of these areas which contributed to the success of GaN. Physicists have, through extensive material characterization, improved our understanding of the physical and optical properties of the material. Growers have devised novel methods to combat lattice mismatch between GaN and common substrates to produce high-quality materials. Engineers have been working towards optimizing device

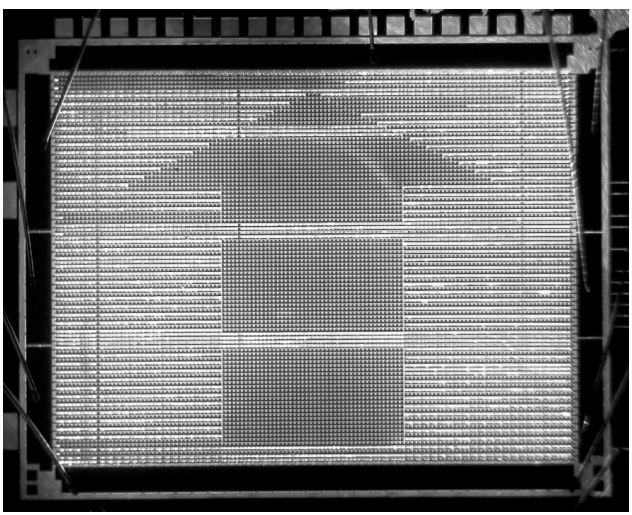

Fig. 1. Optical microscope image of a 128 x 96 pixels blue GaN micro-display in action displaying an arrow pattern, demonstrating the potential and capabilities of a semiconductor emissive micro-display (with permission for reproduction from Institute of Electrical and Electronics Engineers).

structures for maximum light extraction. Finally, innovative packaging techniques have increased the efficiency of heat dissipation dramatically, resulting in the high current operation of LEDs and their improved optical output.

The combined efforts of research and development in the various aspects mentioned above have resulted in the tremendous growth of the GaN lighting industry. However, the main focus of this chapter will be on the processing of GaN LEDs. One well-known factor which limits the efficiency of LEDs is the amount of light which gets trapped in the device mesa structure due to total internal reflection. This phenomenon is equally, if not more, important in nitride LEDs. One possible way of overcoming this problem is the structuring of the mesa into multiple interconnected micron-scale or even nano-scale regions. Such techniques have been employed in LEDs based on other material systems such as AlInGaP[3] with great successes. The first report of micro-structuring in GaN LEDs by Jin et al.[4] at Kansas State University paved the way for a field of research in micro-light-emitting diodes, or micro-LEDs. Since then, GaN micro-scale devices have grown in diversity and complexity, and the emissive micro-display, as shown in Fig. 1, looks set to revolutionize the imaging and display markets.

2. Light Extraction in Nitride Materials

There are two main factors which determine how well an LED can perform, namely internal quantum efficiency and external light extraction efficiency. External quantum efficiencies as high as 20% have been reported for InGaN/GaN LEDs emitting at visible wavelengths,[5] although the performance of AlGaN-based ultra-violet (UV) LEDs is still some way behind that of their InGaN counterparts.[6]

On the other hand, light extraction efficiency is largely dependent on the optical properties of the material and the geometry of the LED mesa structure. Photons generated within the active multi-quantum well (MQW) region of the LED are emitted randomly in all directions. However, only photons which eventually manage to escape the LED structure are useful. The emitted photons are either reflected at the semiconductor-air interface or re-absorbed by the semiconductor

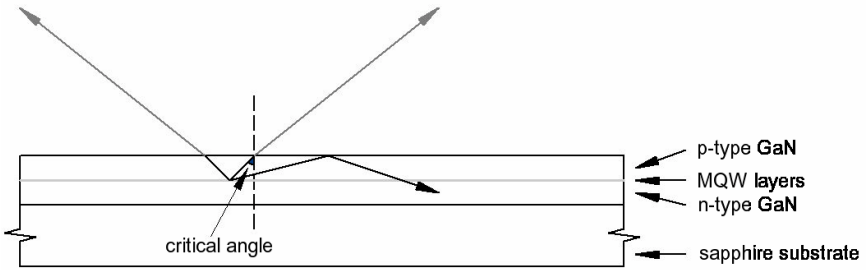

Fig. 2. A schematic illustration of total internal reflection in a GaN LED structure. Photons emitted at an angle beyond the critical angle will be reflected at the semiconductor-air interface.

material after traveling long distances within the device structure. Therefore, the refractive index and the absorption coefficient are key parameters in determining the amount of light that can be extracted.

Figure 2 illustrates the cross-sectional view of a typical GaN light emitting diode. Photons are generated at the MQW region below the p-type cap layer, usually 20 to 300 nm below the semiconductor-air interface. The escape cone is defined by twice the critical angle, which is approximately 46^{o} (using the value of 2.5 for the refractive index of GaN at 470 nm). Photons traveling in other directions may be reflected at the interfaces or extracted from the sidewall of the mesa structure, provided it is not reabsorbed into the GaN. GaN has an absorption coefficient of 10^3 cm^{-1}, or a mean absorption length of 10 μm.[7] In other words, if a photon remains within the device structure after traveling 10 μm, then the likelihood of it being extracted is slim. This realization has given rise to the concept of micro-light emitting diodes.

3. Micron-Scale Light Emitting Diodes

As explained above, a reduction in the dimension of the LED structure can potentially increase its light extraction efficiency. This increase is mainly due to additional light extraction through the sidewalls of the structure. In a study reported by Choi *et al.*,[8] an experiment was conducted to verify this postulation. A focused electron beam was directed towards the centre of a 12 μm diameter micro-disk structure

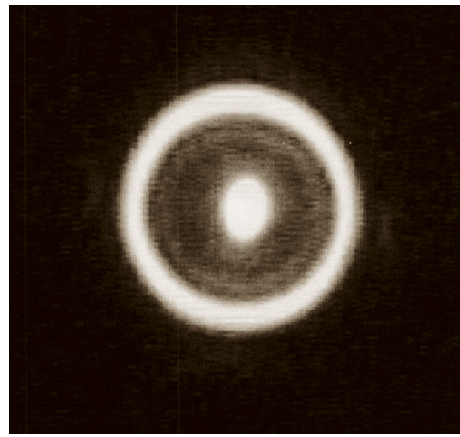

Fig. 3. A micro-disk MQW structure excited by a focused electron beam. The spot in the centre corresponds to the position of the incident electron beam. A bright ring of light at the periphery of the micro-disk was observed, attributable to light extraction through the sidewall with permission for reproduction from American Institute of Physics).

containing MQW. Naturally, the electrons generated luminescence at the spot upon which the electron beam was directed, as shown in Fig. 3. At the same time, a bright ring of light was observed at the periphery of the micro-disk. This ring of light was caused by photons which had escaped the micro-disk through the sidewall, and was greater in intensity than the spot in the middle. It was then apparent that fabricating LEDs with smaller dimensions and larger aspect ratios was beneficial to light extraction.

Micro-LEDs are typically of dimensions in the scale of microns to tens of microns. This size advantage is illustrated in the plot optical power density vs current in Fig. 4. Micro-structures with the smallest feature sizes emits with the highest optical density. Although a micro-LED has very high light extraction efficiency, its light generating active area remains small and each device produces tens of micro-watts of optical power only at a drive current in the micro-ampere region. In order to make micro-LEDs useful and practical, they must be connected into array formats.

Two forms of micro-LED arrays have since been reported. Two-dimensional arrays of micro-LEDs (such as the device in Fig. 5(a)),

whether individually addressable or matrix addressable, have been demonstrated and potentially have diverse applications ranging from imaging science to biological and chemical sensing. On the other hand, micro-LEDs interconnected and emitting at the same time, like the one shown in Fig. 5(b), makes very efficient LEDs for illumination uses.

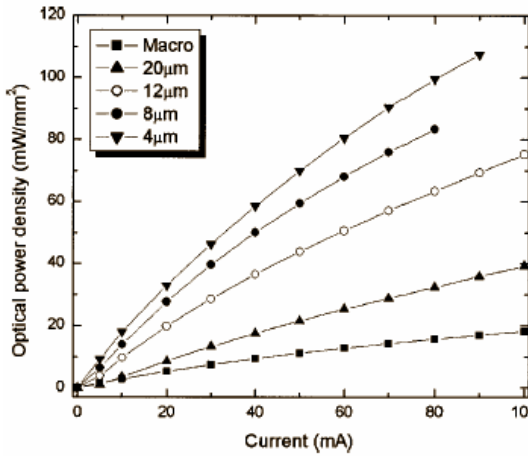

Fig. 4. Normalized optical power densities vs current characteristics of micro-LEDs with different dimensions (with permission for reproduction from American Institute of Physics).

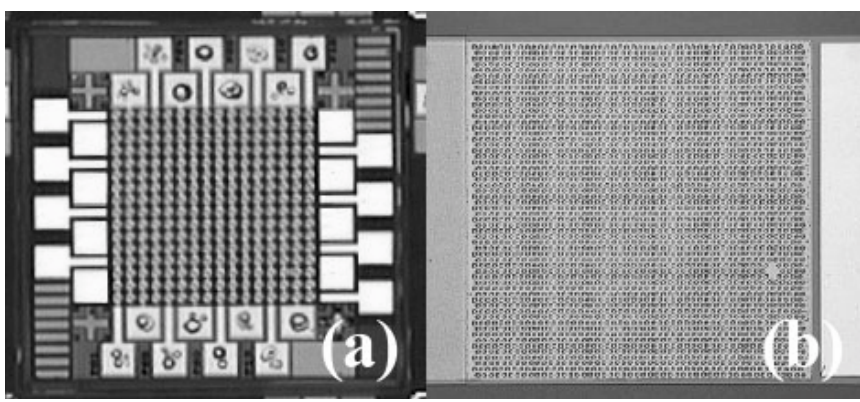

Fig. 5. Two main forms of micro-LED arrays have been developed. Matrix-addressable arrays, like the one in (a), serves as versatile micro-displays, while the interconnected micro-LEDs in (b) act as efficient light sources (with permission for reproduction from Institute of Electrical and Electronics Engineers).

.

4. Micro-LED Processing

In the simplest cases, the processing of a micro-LED involves an additional etch step not required for conventional broad-area LEDs. The active light-emitting region is sectioned into multiple micro-scale structures. This is typically achieved by photolithography followed by plasma etching. The individual micro-LEDs are interconnected via a semi-transparent current spreading layer that spans the entire micro-structured area. To avoid short-circuiting the p-n junction, the gaps between the active regions must be isolated with a dielectric, usually SiO_2, prior to metal deposition.

The fabrication of micro-arrays is invariably more complex, and the level of complexity depends on the dimension, scale and addressing scheme of the pixels. Consider the fabrication of a matrix addressable array. The first step involves creating isolated columns of GaN material by plasma etching. The etch must terminate at the sapphire layer to ensure proper isolation. Current conduction for pixels in a column is via the n-type GaN layer. Subsequently micro-LEDs are formed on top of the columns to act as the pixels of the array. These micro-LEDs must be etched through the MQW region, with the result that each pixel is typically 0.5 μm to 1 μm in height. To prevent the overlying metal layers from shorting the p-type and n-type regions, a thin layer of dielectric material, usually SiO_2, is deposited to cover the sidewalls of the pixels. Finally, pixels in a row (in the direction orthogonal to the columns) are interconnected by deposited metal lines.

Figure 6 shows a schematic diagram of an array fabricated using this process. A prominent issue regarding metal interconnection is the conformal coverage of the metal layer across the etched columns with step heights of several microns. As such, the sidewalls are deliberately etched to be inclined to the vertical by 25^o to 40^o to facilitate conformal metal coverage.[9] This can be achieved by adjusting the inductively-coupled plasma (ICP) etching parameter. The degree of inclination to the vertical can be increased by increasing the ICP power and reducing the plate power, producing an isotropic dry etch. Figure 7(a) illustrates a scanning electron microscope (SEM) image of a GaN mesa structure with sidewall inclination angle of 25^o. In Fig. 7(b), interconnection metal lying conformally across the mesas and ridges is illustrated.

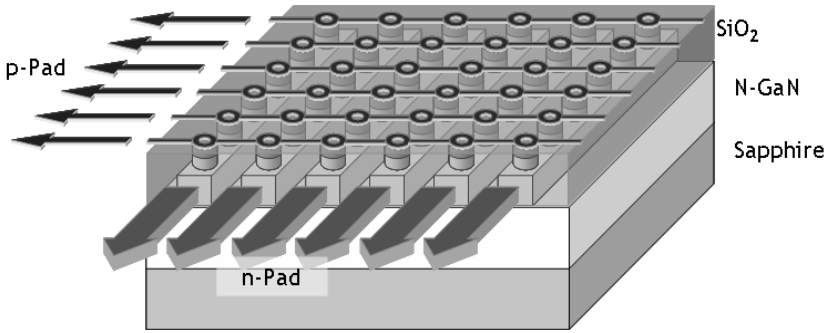

Fig. 6. A schematic diagram illustrating the interconnection scheme in a matrix addressable micro-LED array. Pixels in a column are interconnected via n-type GaN material, while metal lines connect pixels in a row.

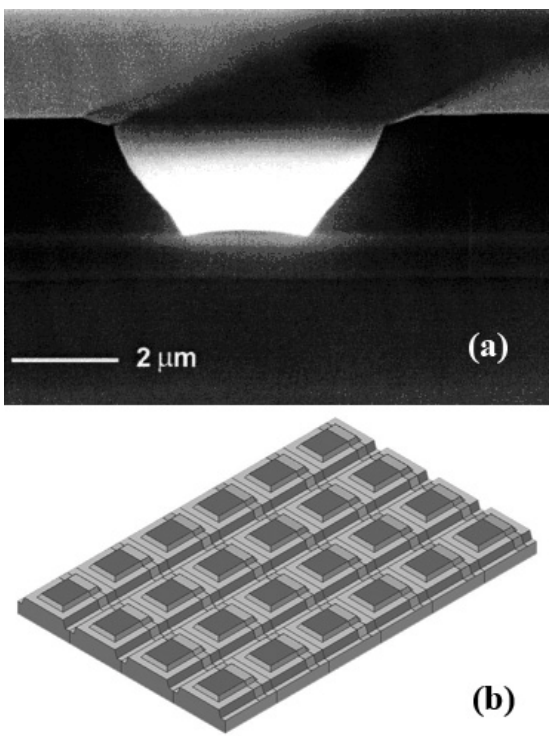

Fig. 7. (a) SEM image showing the sidewalls of GaN mesas which have been etched to produce an inclination of 25° to the vertical. This is to facilitate conformal metal coverage for metal lines across the columns. (b) Schematic diagram of an array with metal lines running across mesas with sloped sidewalls. (with permission for reproduction from American Institute of Physics).

5. Micro-Displays

The first report of an individually addressed GaN micro-array portrays the device as a micro-display. Indeed, there is great potential in this type of devices for the display and imaging market. In that report, a 10 by 10 array of 12 μm micro-disk fabricated on 450 nm emitting LED material, each with its own control pad, was demonstrated to display single characters[10] (as shown in Fig. 8). The dimension of the display region was 0.5 mm by 0.5 mm, but the overall chip size was approximately four times larger due to the large number of control pads. Although such micro-displays can be controlled by a simple circuitry, the individually addressing scheme imposes great limitations on the scalability of the array. Subsequently, matrix-addressable nitride micro-arrays were reported, using a similar addressing scheme to that employed in Liquid Crystal Displays (LCDs). Ozden *et al*. fabricated a display scheme of 1024 matrix-addressable elements whereby pixels are interconnected by row and column.[11] The number of bond pads necessary is thus reduced from n^2 (where n is the number of pixels in a column) to $2n$.

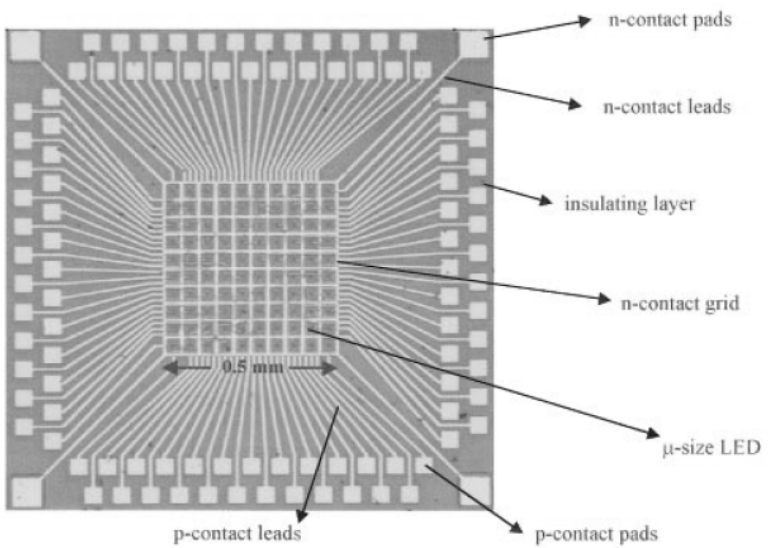

Fig. 8. The first demonstrated GaN micro-display, consisting of 10 × 10 12 μm diameter micro-disks. Each pixel can be individually by its own control pad. As a result the overall chip area was about four times the dimension of its display area. (with permission for reproduction from American Institute of Physics).

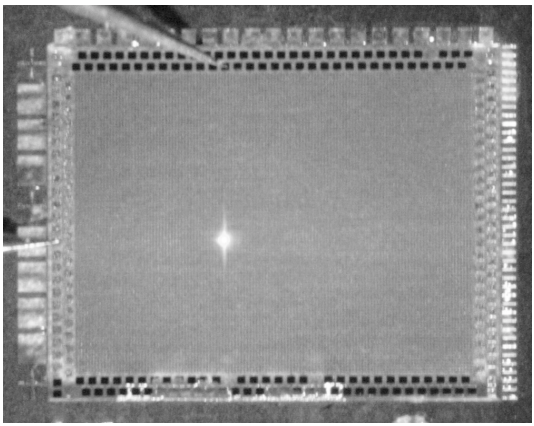

Fig. 9. A 128 x 96 pixel matrix-addressable blue microdisplay packed into a chip area of 3mm × 2mm.

Presently, the largest reported micro-display, by Choi *et al*.,[12]consists of 128 × 96 matrix-addressable elements packed into a 3 mm by 2 mm chip area, shown in Fig. 9. With a pitch of 22 μm the device is capable of emitting with 1200 dpi resolution. While most of the devices are fabricated in visible light emitting materials, arrays emitting at ultra-violet wavelengths have also been reported. Jeon *et al*.[13] demonstrated a 64 × 64 elements micro-array emitting at 368 nm using AlInGaN-based material. An image of the array in action, together of an emission spectrum from a single pixel, is displayed in Figs. 10 (a) and (b). Short wavelength-emitting arrays can potentially be used for fluorescence excitation in micro-assays.

In order to drive these arrays, suitable driving circuits must be designed to meet certain requirements associated with GaN devices. These include voltage and current levels, timing issues and transient responses. Figure 11 illustrates the letters "IOP" being displayed on a 64 × 64 pixels microplay using an in-house developed circuit.

6. Interconnected Micro-LEDs

Micro-LEDs were initially developed to increase light extraction efficiencies, and interconnected arrays of micro-LEDs serve just this

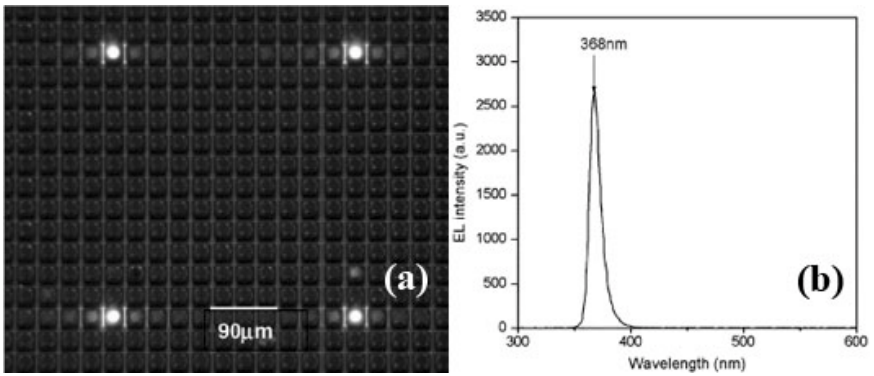

Fig. 10. (a) 4 illuminated pixels on a 370-nm emitting micro-array. (b) Spectrum showing the spectral peak at 370 nm (with permission for reproduction from Institute of Electrical and Electronics Engineers).

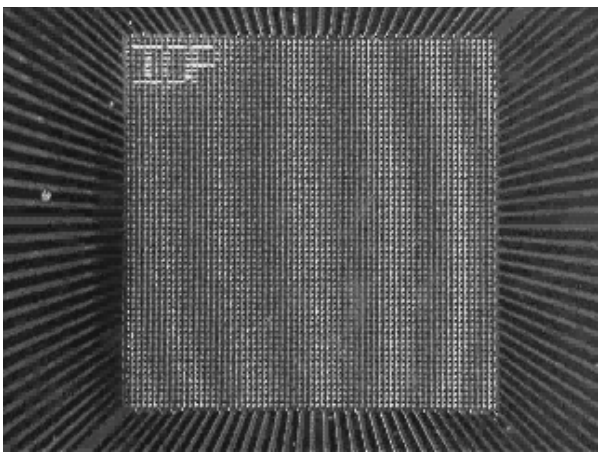

Fig. 11. Letters "IOP" displayed on a 64×64 microdisplay using an in-house developed control circuitry

purpose. Before electroluminescent micro-LED arrays were reported, numerous studies were made of the optical properties of fabricated GaN microstructures. The most prominent features are the observation of whispering gallery (WG) modes and radial modes in micro-disk cavities[14] (Mair *et al*.) and WG-like optical resonance modes in GaN

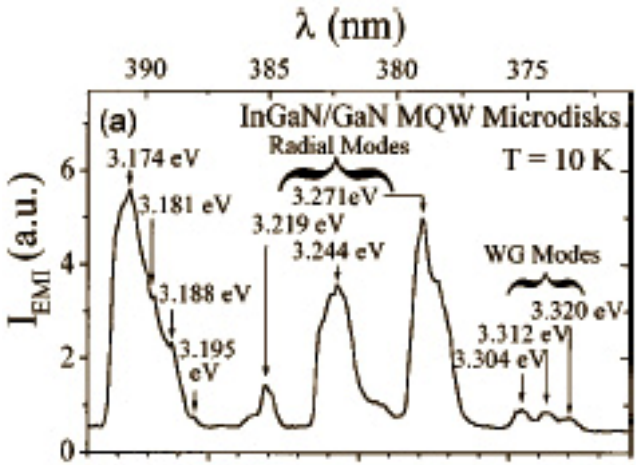

Fig. 12. Cavity modes, including radial modes and whispering gallery (WG) modes, prominent in the photoluminescence spectrum of InGaN/GaN MQW microdisks (with permission for reproduction from American Institute of Physics).

pyramidal microcavities[15] (Jiang *et al.*). Examples of such cavity modes are plotted in the spectrum in Fig. 12. Subsequently an electroluminescent interconnected micro-disk LED was reported by Jin *et al.*[16] (see Fig. 13(a)). Since then, similar techniques have been employed to boost optical power from GaN LEDs, including a parallel addressed micro-LED array[17] (Choi *et al.*, Fig. 13(b)), an surface-textured indium-tin-oxide (ITO) LED[18] (Pan *et al.*, Fig. 13(c)) and a micro-pixel 280 nm UV LED[19] (Adivarahan *et al*., Fig. 13(d)). In all cases, improvements in optical output of as much as 100% have been reported (Fig. 14).

Besides the widely-reported improvements in optical output, several additional benefits of micro-LEDs have also been identified. As a result of the increase in surface area (which helps to enhance light extraction), heat dissipation is also facilitated. Choi *et al.*[20] reported an increase in the current at which optical power saturated, from 80 mA to 120 mA under the same external heat-sinking conditions. The device series resistance dropped from 40 ohms in a square geometry UV LED to less than 10 ohms in the micro-pixel LED. Additionally, improved current spreading via the n-type layer was reported by Choi *et al*.[21] in a 370 nm

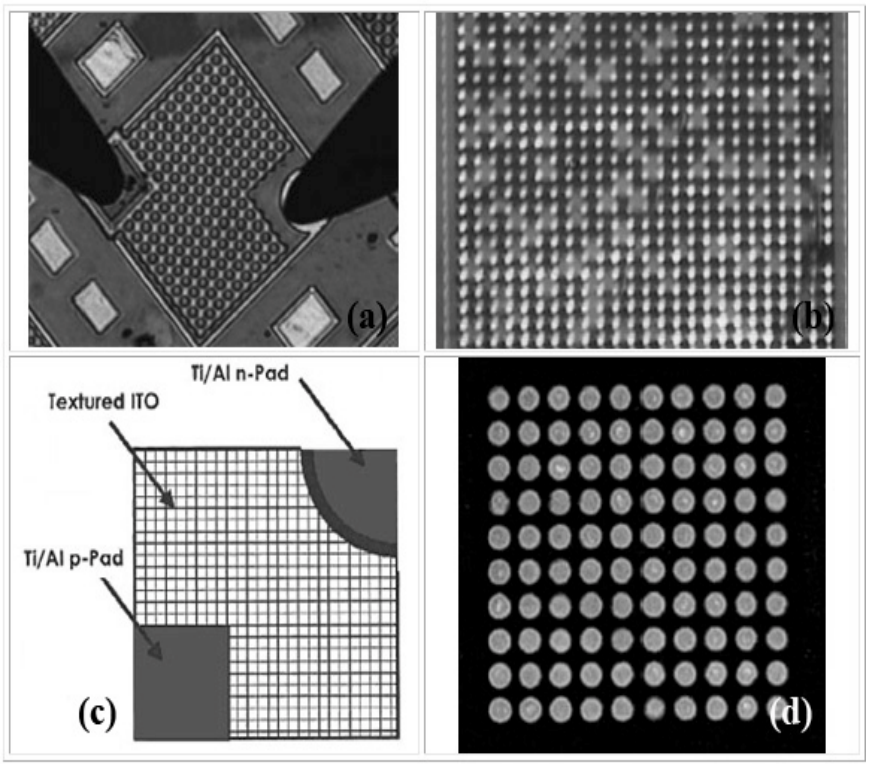

Fig. 13. (a) The initial interconnected micro-disk LED. (b) High-brightness parallel-addressed micro-LED array. (c) Micro-structured ITO layer LED. (d) Micro-pixel 280nm deep UV LED. (with permission for reproduction from American Institute of Physics).

interconnected micro-array LED, as illustrated in Fig. 15. Micro-sectioning of the active region reduces the contribution of the high-resistance AlGaN/GaN superlattice to the mechanism of current spreading, leading to an overall improvement in emission uniformity of the near-UV LED.

It is apparent that sidewalls contribute significantly to light extraction in micro-LEDs. However, the effect of varying sidewall profile to light extraction efficiency has not been studied in details. Kao *et al.* reported on an LED with 22^{o} undercut sidewall which slants inwards as compared to typical sidewall profiles which slopes

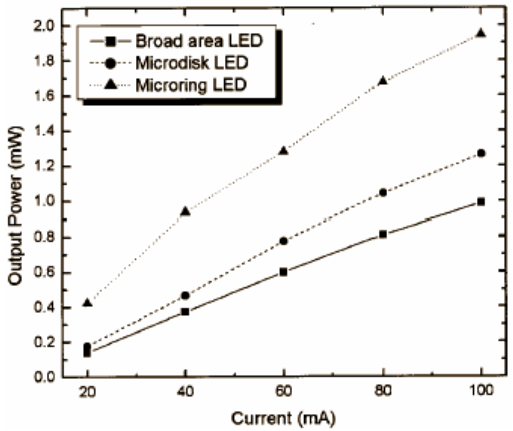

Fig. 14. Significant improvement to the optical output from micro-LED arrays compared to broad-area LEDs (with permission for reproduction from American Institute of Physics).

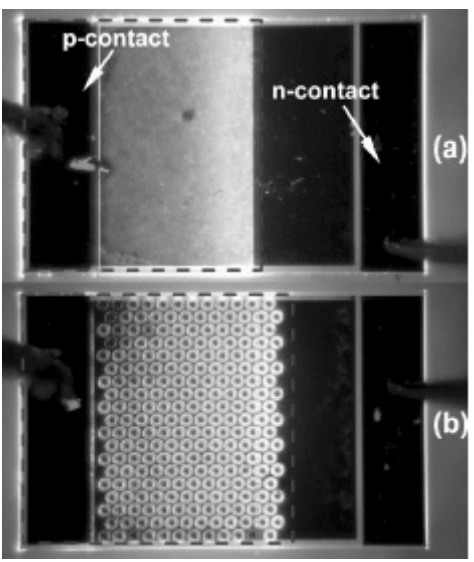

Fig. 15. (a) Light emission confined to the edge close to the n-contact. (b) Improved current spreading achieved with a micro-structured light emitting active region. (with permission for reproduction from American Institute of Physics).

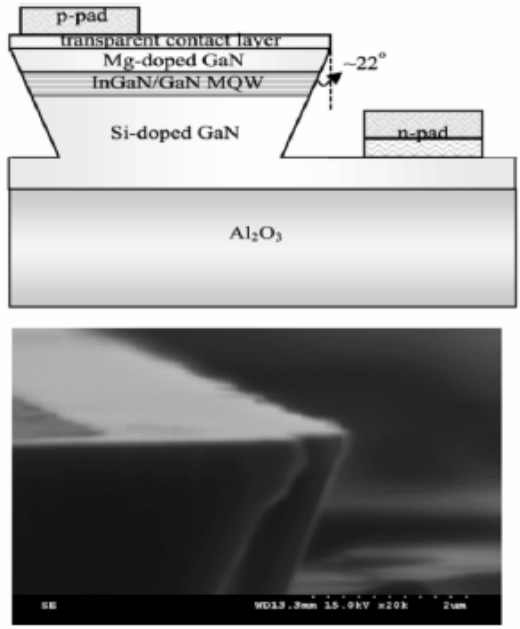

Fig. 16. Schematic diagram of an LED with 22° undercut sidewall. The inset shows an SEM image of the sidewall profile (with permission for reproduction from American Institute of Physics).

outwards,[22] which the authors claim could enhance the probability of photons escaping from the mesa. Such a profile was achieved by a controllable ICP etching process. A schematic diagram and an SEM image of this geometry are shown in Fig. 16. Based on ray-tracing simulation and device measurements, an enhancement in optical output by a factor of 1.7 was observed.

7. Micro-Optics and its Integration to Micro-LEDs

One of the major shortcomings of LED arrays arise from the fact that LEDs are Lambertian emitters. While light emitted in the forward direction (perpendicular to the device) is most useful, laterally propagating photons are hard to collect, and may be absorbed by the adjacent pixel, resulting in severe cross-talk. Griffin *et al*.[23] studied the

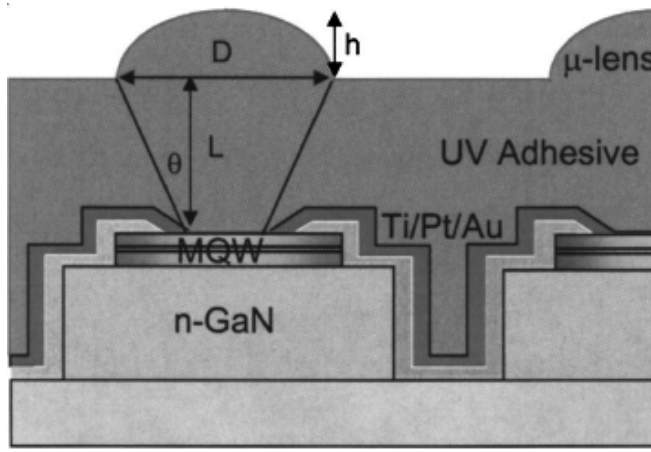

Fig. 17. Polymer microlens array fabricated directly onto the micro-LED array for optical coupling and focusing (with permission for reproduction from American Institute of Physics).

emission characteristics of micro-LEDs using confocal microscopy. It was found that micro-LEDs typically have a divergence angle in the range of 65° to 75°. The integration of microlenses may improve the directionality of light. Jeon *et al.*[24] reported on a UV-emitting micro-array containing an integrated microlens array fabricated using polymer, as illustrated in Fig. 17. The polymer layer was spin-coated onto the device and subsequently hardened by UV curing. A layer of photoresist was spin-coated on top and patterned into micro-disks. Resist-reflow transforms the disks into lenticular structures. The microlenses are aligned to each pixel, enabling each lens to focus light from each micro-LED element to a focal point.

The devices developed to date emit light from the GaN surface of the LED wafer. A flip-chip GaN micro-array, with a polished sapphire surface, was reported by Choi *et al.*[25] A schematic diagram of this configuration is shown in Fig. 18(a). Additionally, a 128x96 microlens array, matched to an emissive matrix-addressable micro-LED array of the same dimension,[26] was fabricated onto the sapphire surface to improve light collection and for beam manipulation. The sapphire

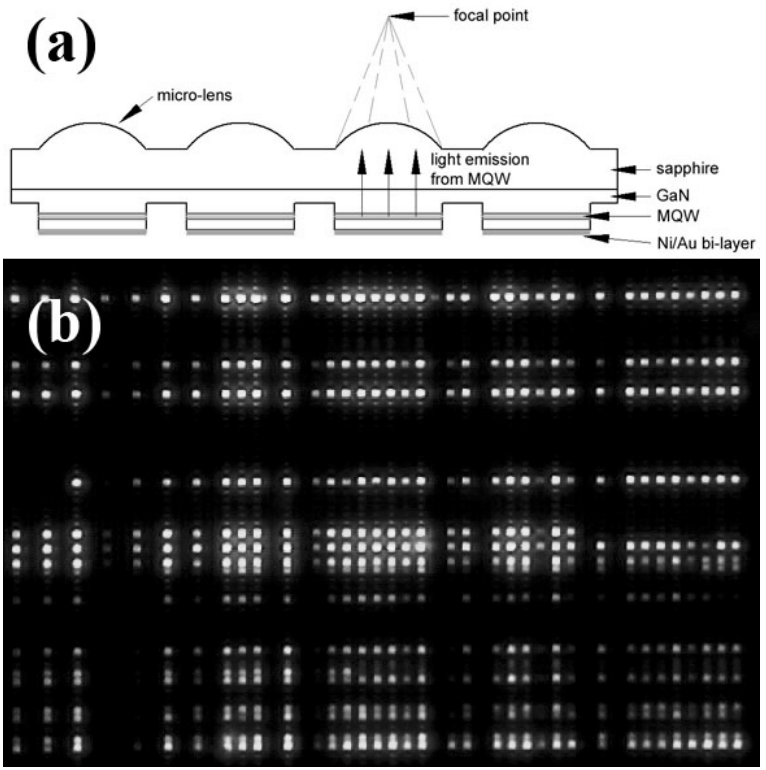

Fig. 18. (a) Microlens array fabricated on the polished sapphire face of a GaN interconnected micro-LED array. (b) A 128x96 microlens array integrated into a 128x98 matrix-addressable micro-LED array (with permission for reproduction from American Institute of Physics).

microlens array was fabricated by resist reflow followed by plasma etching. Emission from this array is illustrated in Fig. 18(b).

8. Novel Geometry and Configuration of micro-LEDs

Apart from micro-disk structures, novel geometries have been proposed to further enhance the performance of micro-LED arrays. Given that the aspect ratio and sidewall area are important parameters in extraction light from the device, the micro-ring structure was proposed and micro-ring array LEDs emitting at visible and near-UV wavelengths [see Fig. 19(a)]

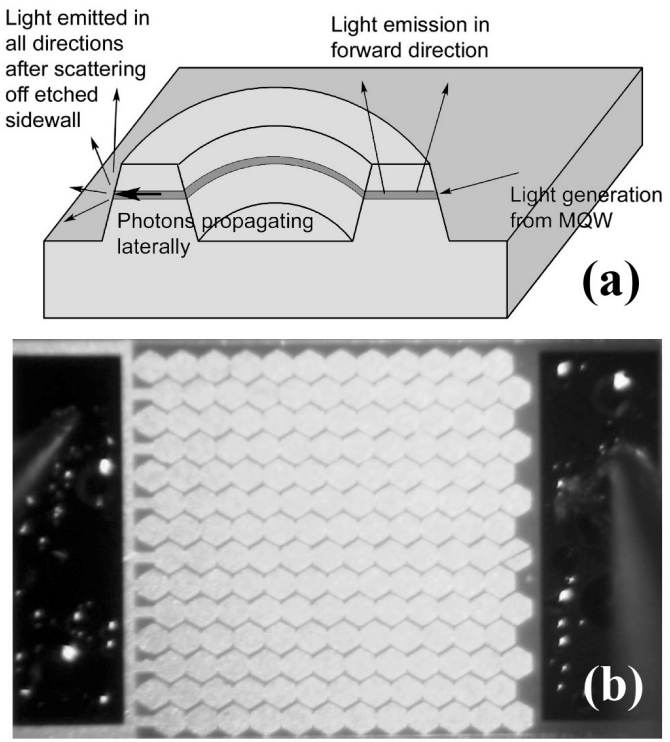

Fig. 19. (a) Schematic diagram of a micro-ring element, illustrating the light escape pathways. (b) A high-packing density hexagonal micro-LED. (with permission for reproduction from American Institute of Physics).

have been reported[20,21]. The ring structure provides twice the amount of sidewall than a micro-disk, but the major drawback lies in the reduction in active area. An attempt to maximize the packing density of micro-LED structures resulted in the hexagonal micro-LED array.[27] Each micro-element is hexagonal in shape, as shown in Fig. 19(b), and the separation between each element was reduced to 2 μm. This design provides a tradeoff between sidewall area and active area.

Nano-scale structures have also been incorporated into GaN to boost light extraction efficiencies. Fujii *et al*.[28] created an n-side up surface-roughened LED by laser lift-off followed by anisotropic wet etching. An increase in output by a factor of 2.3 was recorded. Huang *et al*.[29]

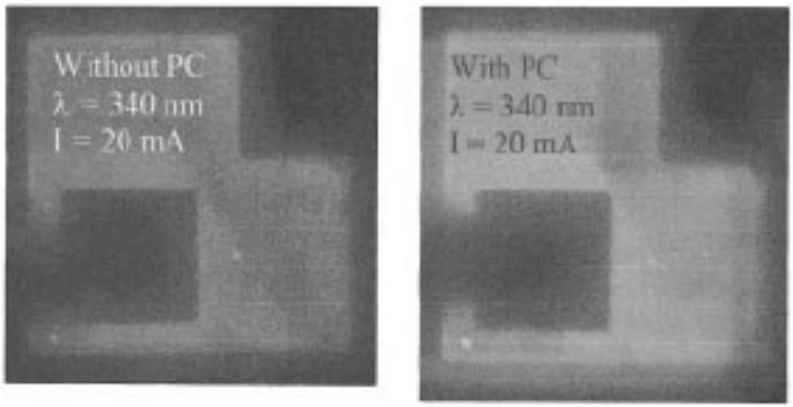

Fig. 20. Enhanced light emission from LEDs with integrated photonic crystal array (with permission for reproduction from American Institute of Physics).

employed a similar wet etch technique to create nanostructures, but they also processed the p-type GaN surface, achieving a 45% increase in output.

Beside random nanostructures created by wet etching, periodic nanostructures were fabricated by deep UV lithography or electron beam lithography to integrate a photonic crystal (PC) array into a GaN LED to exploit the photonic bandgap (PBG). Oder et al[30] patterned triangular arrays of PCs by electron beam lithography and etched the structure onto the surface of visible (460 nm) and UV (340 nm) LEDs by plasma etching. An increase of 63% and 93% in intensity has been claimed for the visible and UV devices respectively. The increase in brightness is apparent from Fig. 20.

More recently, the band-structure and specific emission properties of PCs formed onto GaN waveguides have been studied by photoluminescence (PL) by David *et al*.[31] at the University of California, Santa Barbara. The same group has also fabricated PC GaN LEDs with tailored guided modes distribution[32] and GaN LEDs with Archimedean lattice PCs.[33]

A technique based on the Fresnel diffraction effect for the fabrication of nano-scale site-controlled ring structures in InGaN/GaN multi-quantum well structures has been demonstrated.[34] The ring structures have an internal diameter of 500 nm and a wall width of 300 nm. A

1 cm^{-1} Raman shift has been measured, signifying substantial strain relaxation from the fabricated structure. The 5 nm blue shift observed in the cathodoluminescence spectra can be attributed to band-filling and/or screening of the piezoelectric field. A light emitting diode based on this geometry has been demonstrated, as illustrated in Fig. 21.

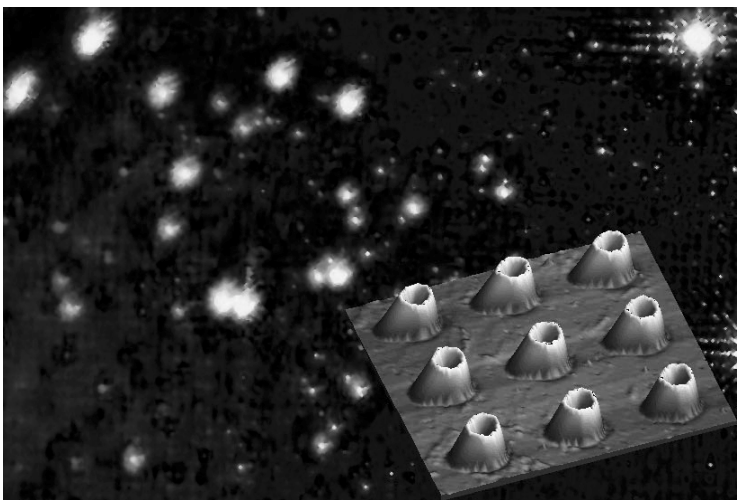

Fig. 21. Light emission from single pixels of a nano-ring LED array. The diagram in the inset shows an AFM image of the nano-rings, with an internal diameter of 500 nm and a wall width of 300 nm (with permission for reproduction from American Institute of Physics).

9. Applications of Micro-LED Arrays

Visible wavelength matrix-addressable arrays are strong contenders in the display and imaging market. Being emissive in nature, they stand out against conventional micro-displays technologies like liquid crystal displays (LCDs) or Liquid Crystal on Si (LCoS). While organic light-emitting diode (OLED) technology can also be adopted for micro-displays, it suffers from severe limitations in terms of luminous efficiency and lifetime. There is no doubt that GaN-based micro-displays are superior in every aspect.

However, the applications of GaN micro-arrays go beyond displays. It is believed that UV-emitting versions of these arrays can potentially be useful for a wider range of applications, including optical biochips and biological and/or chemical agent sensing. In fact, a 470 nm emitting 64 × 64 pixel emissive micro-array, operated in pulsed mode, has been used for fluorescence excitation of a range of biological dyes and the fluorescence lifetime was successfully measured using this technique.[35] An example of the excitation and fluorescence spectra for the mitochondria-staining dye Rhodamine 123 excited by the pulsed blue micro-LED is shown in Fig. 22, highlighting the rapid response speed of the micro-LED devices.

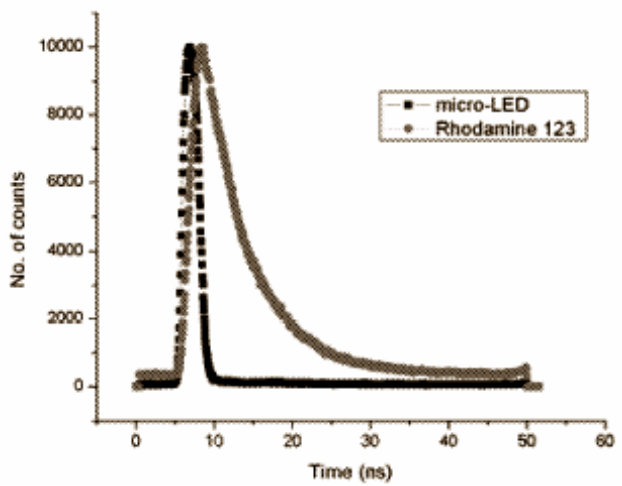

Fig. 22. (a) The excitation and fluorescence spectra of Rhodamine 123 using a 460-nm micro-LED as an excitation source (with permission for reproduction from Institute of Electrical and Electronics Engineers).

Similar work has been carried out at Brown University. Pan *et al.* reported on aerosol fluorescence detection using a visible GaN linear array,[36] and more recently single airborne particles have been detected using a 32-element linear LED array emitting at deep UV wavelengths.[37] Figure 23 shows the device being used for the excitation.

On the other hand, the high efficiencies of interconnected micro-LED arrays can be exploited for high-brightness visible LEDs for

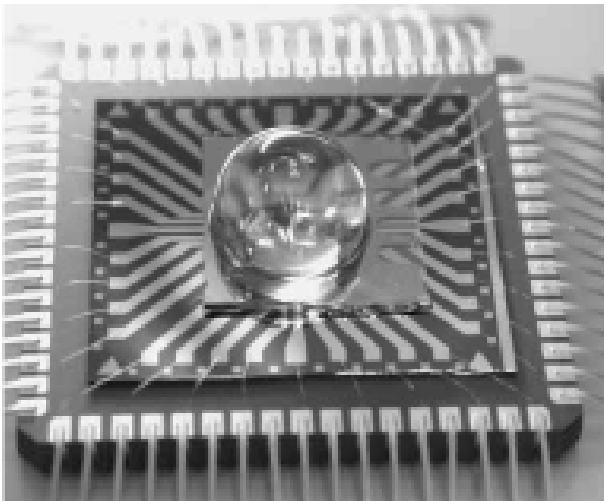

Fig. 23. A packaged 32-element linear LED array used for the detection of single airborne particles. (with permission for reproduction from the Optical Society of America).

illumination, and to improve the performance of relatively weak UV LEDs.

The use of a matrix-addressable micro-pixellated AlInGaN UV micro-LED array for mask-free photolithographic exposure has also been proposed recently.[38] The device was a 64×64 elements array with integrated polymer microlenses emitting at 370 nm. This wavelength is suitable for exposing typical i-line photoresists. The authors attempted to transfer the pattern displayed on the micro-array to a wafer coated with Shipley S1805 i-line photoresist. The image was successfully transferred, as shown in Fig. 24, opening up yet another exciting direction for GaN emissive micro-arrays.

10. The Future of Micro-LEDs

Many of the major recent advances in micro-LED development have been described in this chapter, though its coverage does not claim to be comprehensive. Although micro-LEDs arrays have yet to become commercialized products, their rapid development promises a bright future for the coming generations of optoelectronic devices. Since the

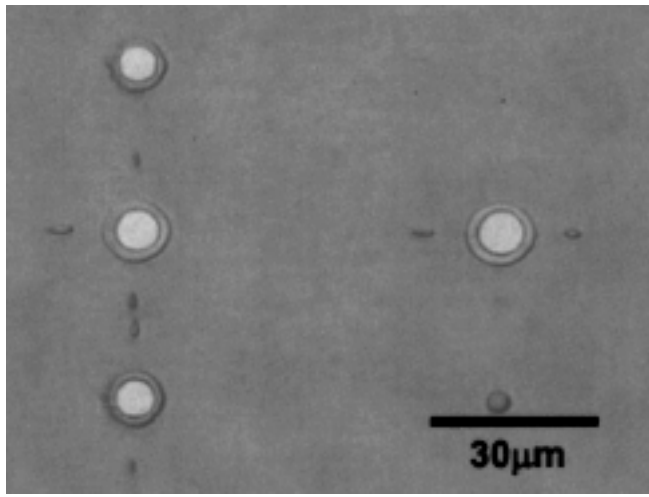

Fig. 24. Optical micrograph of i-line photoresist after development. The resist was exposed with an AlInGaN micro-array emitting at 370 nm. (with permission for reproduction from the American Institute of Physics).

first micro-LED array was reported, more and more research groups are engaging in this new field of device development. Several start-up companies around the globe have begun efforts to develop products based on GaN emissive micro-arrays for a range of display and imaging applications. One of the imminent targets is to demonstrate GaN micro-arrays with VGA resolutions and above. Dimensional downscaling of individual pixels is another important trend to look out for. In conclusion, micro-displays look set to compete strongly with existing display technologies such as LCDs in the coming years.

Acknowledgments

This work was carried out at the University of Strathclyde, United Kingdom and at the University of Hong Kong. I would like to thank M.D. Dawson for the opportunity to work on micro-LEDs, and the support of S.J. Chua for my research work in Hong Kong. Credits also go to D. Wilmshurst of HKU for proofreading my manuscript.

References

1. S. Nakamura, T. Mukai and M. Senoh, *Appl. Phys. Lett*. **64**, 1687 (1994).
2. M.S. Shur and A. Zukauskas, *Proc. IEEE* **93**, 1691 (2005).
3. M. R. Krames, M. Ochiai-Holcomb, G. E. Höfler, C. Carter-Coman, E. I. Chen, I.-H. Tan, P. Grillot, N. F. Gardner, H. C. Chui, J.-W. Huang, S. A. Stockman, F. A. Kish, M. G. Craford, T. S. Tan, C. P. Kocot, M. Hueschen, J. Posselt, B. Loh, G. Sasser, and D. Collins, *Appl. Phys. Lett*. **75**, 2365 (1999).
4. S.X. Jin, J. Li, J.Z. Li, J.Y. Lin and H.X. Jiang, *Appl. Phys.Lett*. **76**, 631 (2000).
5. T. Mukai, M. Yamada and S. Nakamura, *Jap J. Appl. Phys* Part 1. 38, 3976 (1999).
6. J.P. Zhang, X. Hu, Yu. Bilenko, J. Deng, A. Lunev, M.S. Shur, R. Gaska, M. Shatalov, J.W. Yang and M.A. Khan, *Appl. Phys.Lett*. 85, 5532 (2004).
7. O. Ambacher, W. Rieger, P. Ansmann, H. Angerer, T.D. Moustakas and M. Stutzmann, *Solid State Commun*. **97**, 365 (1996).
8. H.W. Choi, C.W. Jeon, M.D. Dawson, P.R. Edwards, R.W. Martin and S. Tripathy, *J. Appl. Phys*. **93**, 5978 (2003).
9. H.W. Choi, C.W. Jeon and M.D. Dawson, *J. Vac. Sci. Technology* **23**, 99 (2005).
10. H.X. Jiang, S.X. Jin, J. Li, J. Shakya and J.Y. Lin, *Appl. Phys. Lett*. **78**, 1303 (2001).
11. I. Ozden, M. Diagne, A.V. Nurmikko, J. Han and T. Takeichi, *Phys Stat. Solidi* (a) **188**, 139 (2001).
12. H.W. Choi, C.W. Jeon and M.D. Dawson, *IEEE Elect. Dev. Lett*. **25**, 277 (2004).
13. C.W. Jeon, H.W. Choi, E. Gu and M.D. Dawson, *IEEE Photon. Tech. Lett*. **16**, 2421 (2004).
14. R.A. Mair, K.C. Zeng, J.Y. Lin, H.X. Jiang, B. Zhang, L. Dai, A. Botchkarev, W. Kim, H. Morkoç and M.A. Khan, *Appl. Phys. Lett*. **72**, 1530 (1998).
15. H.X. Jiang, J.Y. Lin, K.C. Zeng and W. Yang, *Appl. Phys. Lett*. **75**, 763 (1999).
16. S.X. Jin, J. Li, J.Y. Lin and H.X. Jiang, *Appl. Phys. Lett*. **77**, 3236 (2000).
17. H.W. Choi, C.W. Jeon, M.D. Dawson, P.R. Edwards and M.D. Dawson, *IEEE Photon. Tech. Lett*. **15**, 510 (2003).
18. S.-M. Pan, R.-C. Tu, Y.-M. Fan, R.-C. Yeh and J.-T. Hsu, *IEEE Photon. Tech. Lett.* **15**, 649 (2003).
19. V. Adivarahan, W. Wu, W.H. Sun, V. Mandavilli, M.S. Shatalov, G. Simin, J.W. Yang, H.P. Maruska and M.A. Khan, *Appl. Phys. Lett*. **85**, 1838 (2004).
20. H.W. Choi, M.D. Dawson, P.R. Edwards and R.W. Martin, *Appl. Phys. Lett*. **83**, 4483 (2003).
21. H.W. Choi and M.D. Dawson, *Appl. Phys. Lett*. **86**, 053504 (2005).
22. C.-C. Kao, H.-C. Kuo, H.-W. Huang, J.-T. Chu, Y.-C. Peng, Y.-L. Hsieh, C.Y. Luo, S.-C. Wang, C.-C. Yu and C.-F. Lin, *IEEE Photon. Tech. Lett*. **17**, 19 (2005).
23. C. Griffin, E. Gu, H.W. Choi, C.W. Jeon, G. McConnell, J.M. Girkin and M.D. Dawson, *Appl. Phys. Lett*. **86**, 041111 (2005).

24. C.W. Jeon, E. Gu, C. Liu, J.M. Girkin and M.D. Dawson, *IEEE Photon. Tech. Lett*. **17**, 1887 (2005).
25. H.W. Choi, C. Liu, C. Griffin, E. Gu, G. McConnell, I.M. Watson, J.M. Girkin and M.D. Dawson, *Appl. Phys. Lett*. **84**, 2253 (2004).
26. H.W. Choi, E. Gu, J.M. Girkin and M.D. Dawson, *Phys Stat. Solidi* (c) **2**, 2903 (2005).
27. H.W. Choi and S.J. Chua, *J.Vac. Sci Tech*. **24**, 800 (2006).
28. T. Fujii, Y. Gao, R. Sharma, E.L. Hu, S.P. DenBaars and S. Nakamura, *Appl. Phys. Lett*. **84**, 855 (2004).
29. H.-W. Huang, C.C. Kao, J.T. Chu, H.C. Kuo, S.C. Wang and C.C. Yu, *IEEE Photon. Tech. Lett*. **17**, 983 (2005).
30. T.N. Oder, K.H. Kim, J.Y. Lin and H.X. Jiang, *Appl. Phys. Lett*. **84**, 466 (2004).
31. A. David, C. Meier, R. Sharma, F.S. Diana, S.P. DenBaars, E. Hu, S. Nakamura, C. Weisbuch and H. Benisty, *Appl. Phys. Lett*. **87**, 101107 (2005).
32. A. David, T. Fujii, R. Sharma, K. McGroddy, S. Nakamura, S.P. DenBaars, E.L. Hu, C. Weisbuch and H. Benisty, *Appl. Phys. Lett*. **88**, 061124 (2006).
33. A. David, T. Fujii, E. Matioli, R. Sharma, S. Nakamura, S.P. DenBaars, C. Weisbuch and H. Benisty, *Appl. Phys. Lett*. **88**, 073510 (2006).
34. H.W. Choi, C.W. Jeon, C. Liu, I.M. Watson, P.R. Edwards, R.W. Martin, S. ripathy and S.J. Chua, *Appl. Phys. Lett*. **86**, 021101 (2005).
35. C. Griffin, E. Gu, H.W. Choi, C.W. Jeon, O.J. Rolinski, D.J.S. Birch, J.M. Girkin and M.D. Dawson, *Proc.LEOS 2004*, vol 2, 896 (2004).
36. Y.L. Pan, V. Boutou, R.K. Chang, I. Ozden, K. Davitt and A.V. Nurmikko, *Optics.Lett*. **28**, 1707 (2003).
37. K. Davitt, Y.K. Song, W. R. Patterson, A.V. Nurmikko, M. Gherasimova, J. Han, Y.L. Pan and R. Chang, *Optics Express*. **13**, 9548 (2005).
38. C.W. Jeon, E. Gu and M.D. Dawson, *Appl. Phys. Lett*. **86**, 221105 (2005).

This page intentionally left blank

CHAPTER 11

III-NITRIDE FILMS AND DEVICES ON LITHIUM METAL OXIDES BY MOLECULAR BEAM EPITAXY

Gon Namkoong[1,*], Sa Huang[2] and W. Alan Doolittle[2]

[1]*Department of Electrical & Computer Engineering, Old Dominion University, Applied Research Center, 12050 Jefferson Ave, Newport News, VA 23693.*
[2]*Department of Electrical & Computer Engineering*
Georgia Institute of Technology, 777 Atlantic Drive, N.W., Atlanta, GA 30332
[*] *gnamkoon@odu.edu*

Lithium Metal Oxide (LMO) substrates offer new advantages over sapphire (Al_2O_3) and silicon carbide (SiC) substrates, such as better lattice matching, easier lift-off process and multifunctional device integration. As LMO substrates, lithium gallate ($LiGaO_2$) and lithium niobate ($LiNbO_3$)/lithium tantalate ($LiTaO_3$) substrates have been described for III-nitride growth and device applications. Lithium gallate ($LiGaO_2$) which is closely lattice- matched with GaN can be a choice to produce lower dislocation density of GaN, resulting in superior performance of MSM devices. On the other hand, lithium niobate ($LiNbO_3$)/lithium tantalate ($LiTaO_3$) substrates are widely used for nonlinear optical modulators and can be integrated with the multifunctional high power AlGaN/GaN devices, resulting in compact device size and fast device operation.

1. Introduction

The technology of III-nitride materials and device has matured over the last one and a half decades with commercially available products, such as light emitting devices (LEDs) already available in the market. However, there are some issues in III-nitride materials and device performance to be addressed. Especially, III-nitride materials contain a high dislocation density of around 10^9~10^{10} cm^{-2} due to a large lattice mismatch between

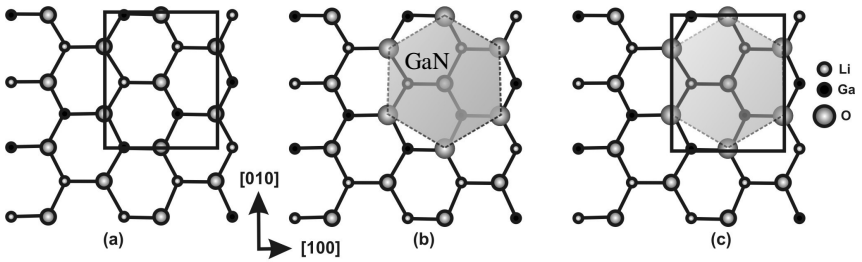

Figure 1. (a) $LiGaO_2$ crystal structure looking along the c-axis. (b) Same view with the GaN unit cell superimposed. (c) Both unit cells superimposed.

III-nitride materials and substrates. The minimization of the dislocation density by lattice matching is critical for reducing the non-radiative recombination and dark current for nitride based optoelectric devices. Furthermore, the use of LMO substrates of $LiGaO_2$ which can be easily etched with simple wet chemistry offers the flexibility of heterogeneous integration onto metal mirrors/heat sinks and optionally, substrate micro-machining, facilitating unprecedented control over device design and allowing higher input power to be tolerated by advanced thermal management. Another advantage of using LMO substrates, lithium niobate ($LiNbO_3$) and lithium tantalate ($LiTaO_3$), is that they provide multi-functional devices where the properties of substrate are fully utilized along with the unique properties of the III-nitride and related materials. For example, AlGaN/GaN high power transistors can be integrated with nonlinear optical materials such as lithium niobate ($LiNbO_3$) and lithium tantalate ($LiTaO_3$) substrates. That integration technology can reduce nonlinear optical modulator size, resulting in significant reduction of production cost while providing advanced on-board intelligence not currently possible with the present technology[1].

2. III-Nitride Optoelectronic Devices on $LiGaO_2$

2.1. *Lithium gallate ($LiGaO_2$) substrates*

$LiGaO_2$ has the space group of $\boldsymbol{Pna2_1}$ (no. 33) and an orthorhombic crystal structure with lattice constants of $\boldsymbol{a} = 5.402^2$ (5.407^3), $\boldsymbol{b} = 6.372$

(6.379), and $\boldsymbol{c}$ = 5.007 (5.014) Å. Figure 1 shows the projected GaN structure onto $LiGaO_2$ substrate illustrating GaN hexagonal symmetry ($\boldsymbol{a}$ = 3.189 Å) aligned to subatomic layers of $LiGaO_2$. While $LiGaO_2$ proves to be an excellent substrate choice for GaN, it is not an obvious choice. Specifically, $LiGaO_2$ has an orthorhombic unit cell[a] while GaN is hexagonal. However, it is easily shown (see Figure 1) that $LiGaO_2$ possesses hexagonal sub-symmetry that very closely lattice matches GaN and matches AlGaN in the range of aluminum compositions. The unit cell of $LiGaO_2$ is shown looking down the c-axis in Figure 1(a). Note the rectangular unit cell. The same surface is shown in Figure 1(b), but with the unit cell of GaN superimposed. Both crystals' unit cells are superimposed in Figure 1(c) showing close lattice matching. Note that the GaN atoms align nearly directly on top of the $LiGaO_2$ atoms. This lattice matching results because the orthorhombic unit cell is merely a slightly distorted version of the hexagonal unit cell arising from the fact that there are two cations (Li and Ga) of differing size. This leads to the slight distortion of the hexagons as shown in Figure 1(a). However, the oxygen sub-lattice is not distorted and is hexagonal in shape. Only the cation placement varies. Thus, for the cation-terminated surface, the nitrogen atoms of GaN align nearly exactly over the buried undistorted oxygen hexagonal sub-lattice. This near perfect alignment of the nitrogen atoms over the undistorted hexagonal oxygen sub-lattice allows GaN to be epitaxially grown directly off the surface of the $LiGaO_2$ without the need for a defective buffer layer as required by other technologies. It should be noted that the same approach, alignment of the GaN on the oxygen sub-lattice, is used to grow GaN on sapphire but results in a huge lattice mismatch of ~16%.

The crystalline relationship between GaN and $LiGaO_2$ has been determined as $[0001]_{GaN} \| [001]_{LiGaO2}$, $[11\ \bar{2}\ 0]_{GaN} \| [010]_{LiGaO2}$, and $[1\ \bar{1}\ 00]_{GaN} \| [100]_{LiGaO2}$[3]. Therefore, the in-plane misfit parameters of GaN epitaxial layer on $LiGaO_2$ can be expressed as

$$f_a = \frac{\bar{a}_{GaN} - a_{LiGaO_2}}{a_{LiGaO_2}} \tag{1}$$

[a] Orthorhombic implies a≠b≠c but all angles = 90° forming a rectangular box.

and

$$f_b = \frac{\bar{b}_{GaN} - b_{LiGaO_2}}{b_{LiGaO_2}} \tag{2}$$

where $\bar{a}_{GaN} = 2a_{GaN}\cos(30°)$ and $\boldsymbol{a}_{LiGaO2}$ are the parameter projected into $\boldsymbol{a}$-axis $LiGaO_2$ and $\boldsymbol{a}$-axis $LiGaO_2$ lattice parameter, and $\bar{b}_{GaN} = 2a_{GaN}$ and $\boldsymbol{b}_{LiGaO2}$ are the parameter projected into $\boldsymbol{b}$-axis $LiGaO_2$ and $\boldsymbol{b}$-axis $LiGaO_2$ lattice parameter. Therefore, along the [001] $\boldsymbol{a}$-axis of $LiGaO_2$, the lattice mismatch is only 2.15%, while along the [010] $\boldsymbol{b}$-axis, it is -0.015%, resulting in an average biaxial lattice mismatch of only 2.14% at the room temperature. This small lattice mismatch makes $LiGaO_2$ a very attractive substrate for achieving low dislocation densities in III-nitride materials compared with alternative substrates such as Al_2O_3 and SiC.

Furthermore, $LiGaO_2$ is very soluble in a number of acids[4,5,6,7] and can be selectively removed while GaN is inert to most of chemical etching. Contrarily, the two most common substrates used for III-Nitride growth, Al_2O_3 and SiC, are very hard, chemically inert and are difficult to etch or even mechanically grind. This feature prevents the easy removal of the substrates or the backside patterning of such substrates. $LiGaO_2$ is unique in that, not only can it be etched, it can be etched quickly. An entire 0.5 mm thick substrate can be chemically wet etched in a few minutes[5]. Therefore, GaN thin film devices can be lifted off and transferred onto various host substrates. This heterogeneous integration technology could allow the development of power devices with heat dissipation pipes or the integration onto low cost, high thermal conductivity materials such as copper.[8]

2.2. *Polarity*

Wurtzite GaN has noncentrosymmetric structure, leading to polar materials.[9,10] Thus, a basal plane GaN surface should be either Ga- or N-polarity, as shown in Figure 2(a). $LiGaO_2$ is also a polar substrate like SiC and ZnO substrates, which has cation (Li and Ga) terminated face and anion (O) terminated face, as shown in Figure 2 (b). Therefore, it is

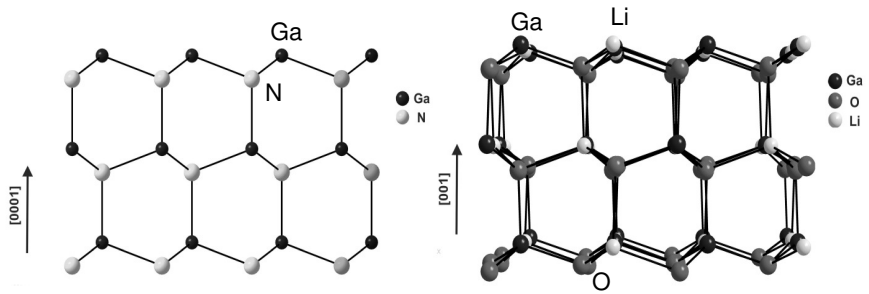

Figure 2. Polarity of (a) GaN and (b) $LiGaO_2$ along c-axis.

expected that GaN polarity can be controlled easily by proper choice of the growth face of the $LiGaO_2$. However, delamination of GaN films from the $LiGaO_2$ after growth has been observed depending on the selected surface polarity of $LiGaO_2$ by molecular beam epitaxy (MBE) growth. Thick GaN films could only be grown on the cation (Li and Ga) face of $LiGaO_2$ while GaN films grown on the anion (O) face of $LiGaO_2$ peeled under vacuum or shortly after exposure to air. GaN films grown on cation face $LiGaO_2$ result in single Ga-polarity films based on chemical wet etching method.[11] Cation face $LiGaO_2$ are Li and Ga terminated so that "Ga-Ga" and "Li-Ga" (cation-cation) bonding are weak and unstable compared to the more ionic ("Ga-N" and "Li –N") cation-anion bonds. This implies that the chemistry of the $LiGaO_2$ / GaN interface uniquely requires the GaN film polarity for the cation (Ga and Li)-face $LiGaO_2$ substrates to be Ga-polarity while resulting in weak adhesion of purely N-polar GaN grown on the anion (O) face $LiGaO_2$ substrates.

2.3. *Strain in III-nitrides on $LiGaO_2$*

$LiGaO_2$ has anisotropic thermal expansion coefficients with temperature (see Table 1) while III-nitride materials show thermal expansion coefficients that, while not isotropic, only vary in the a and c-axis directions. To calculate the lattice mismatch between various III-Nitride materials used for heteroepitaxial buffer layers and $LiGaO_2$ at the growth temperature, the linear thermal expansion coefficient for a-axis GaN[12]

Table 1. Comparison of the linear thermal expansion coefficients.

	Rawn[14]	Nanamatsu [15]	Neumann [3]	Ishii [16]
α_a (10^{-6} K^{-1})	7.0±0.3	6	12.6	1.7
α_b (10^{-6} K^{-1})	15.6±0.4	9	15.7	11.0
α_c (10^{-6} K^{-1})	10.7±0.1	7	7.5	4.0
anisotropy	$\alpha_a<\alpha_c<\alpha_b$	$\alpha_a<\alpha_c<\alpha_b$	$\alpha_a<\alpha_c<\alpha_b$	$\alpha_a<\alpha_c<\alpha_b$

and AlN[13] was used while a polynomial of third order expression was used for $LiGaO_2$ from Ref. [3]. Figure 3 shows the strain (ε_a=-f_a and ε_b=-f_b) for the relaxed lattice parameters of $Al_xGa_{1-x}N/LiGaO_2$ (x = 0~1) after calculating the relative changes in in-plane lattice misfit parameters at the growth temperature of T:

$$f_a = \frac{(\bar{a}_{Al_xGa_{1-x}N}[T] - a_{LiGaO_2}[T])}{a_{LiGaO_2}[T]} \tag{3}$$

and

$$f_b = \frac{(\bar{b}_{Al_xGa_{1-x}N}[T] - b_{LiGaO_2}[T])}{b_{LiGaO_2}[T]} \tag{4}$$

where $\bar{a}_{AlGaN} = 2a_{AlGaN}\cos(30°)$ and $\bar{b}_{AlGaN} = 2a_{AlGaN}$ are the parameter projected into ***a***- and ***b***-axis $LiGaO_2$. The linear value of 5.59 and 4.15×10^{-6} K^{-1} for the thermal expansion coefficient (TEC) of GaN[12] and AlN[13] was used, respectively.

Following the conventional notation, positive and negative values of strain indicates tensile and compressive strain, respectively. Therefore, $Al_xGa_{1-x}N$ films along the *a*-axis of $LiGaO_2$ shown in Figure 3 are under compressive strain while tensile strain is dominant along the *b*-axis of $LiGaO_2$ for temperature ranges of 300K-1400K. With increased growth temperature, the compressive strain along *a*-axis of $LiGaO_2$ decreases while the tensile strain increases along the *b*-axis of $LiGaO_2$. The strain-

energy in the $Al_xGa_{1-x}N$ film/$LiGaO_2$ substrate was calculated following the procedure described in Ref. [17]. After considering the crystalline structure of $Al_xGa_{1-x}N$ on orthorhombic $LiGaO_2$, the resulting strain energy per unit volume for $Al_xGa_{1-x}N$ on $LiGaO_2$ is written from Ref. [17] as

$$U = \frac{s_{11}(\varepsilon_a^2 + \varepsilon_b^2) - 2\varepsilon_a \varepsilon_b s_{12}}{2(s_{11}^2 - s_{12}^2)} \ . \tag{5}$$

The compliance constants of s_{11} and s_{12} have been calculated from relationship with stiffness constants reported in Refs. [18], [19], [20]. The resulting strain-energy density between the $Al_xGa_{1-x}N/LiGaO_2$ systems has been plotted in Figure 4. The strain-energy density for $GaN/LiGaO_2$ decreases with increased growth temperature and vanishes around 1025K (727°C) which is in range of typical MBE growth temperatures.

To calculate the lattice parameters and strain in GaN films, two dimensional (2D) x-ray diffraction reciprocal space mapping has been measured. The lattice parameters for a Bragg reflection (h k l) are calculated using the following relationship:

$$a = \frac{\lambda}{2Q_x}\sqrt{\frac{4}{3}(h^2 + k^2)} \tag{6}$$

where Q_x, is the in-plane component of reciprocal lattice vector, λ is the wavelength of the x-ray, which is 1.5406 Å in the present case. The unstrained in-plane GaN lattice parameter $\boldsymbol{a}_{GaN,\phi}$ has to be the same in all directions due to a hexagonal symmetry, where $\phi = 0$, 60, 120, 180, 240, and 300° are symmetric.[21] On the other hand, the in-plane $LiGaO_2$ lattice parameter has a slightly distorted wurtzite structure. Therefore, $LiGaO_2$ is not six-fold symmetric but slightly elongated along the ***b***-axis. Consequently, when GaN is grown on $LiGaO_2$, this same distorted hexagonal structure of $LiGaO_2$ is transferred into distorted GaN. Thus, the in-plane lattice parameter of GaN on $LiGaO_2$ can be discriminated into two groups: $\boldsymbol{a}^*_{GaN}$ was measured with $\phi = 60$, 120, 240, and 300° while $\boldsymbol{b}^*_{GaN}$ parallel to ***b***-axis $LiGaO_2$ was measured $\phi = 0$ and 180°.

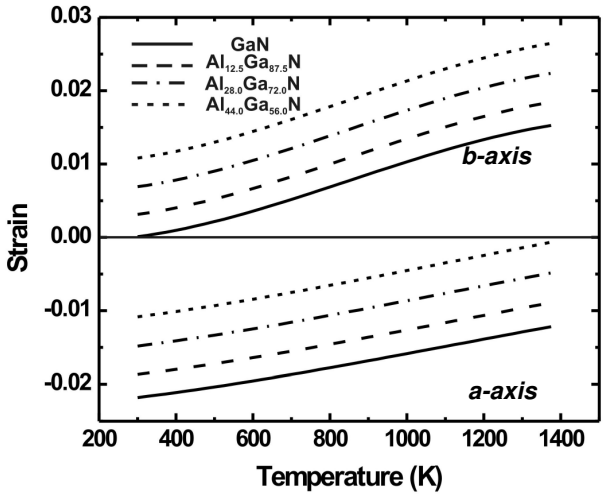

Figure 3. Calculated strain at different growth temperatures from relaxed lattice parameters of III-nitrides and $LiGaO_2$.

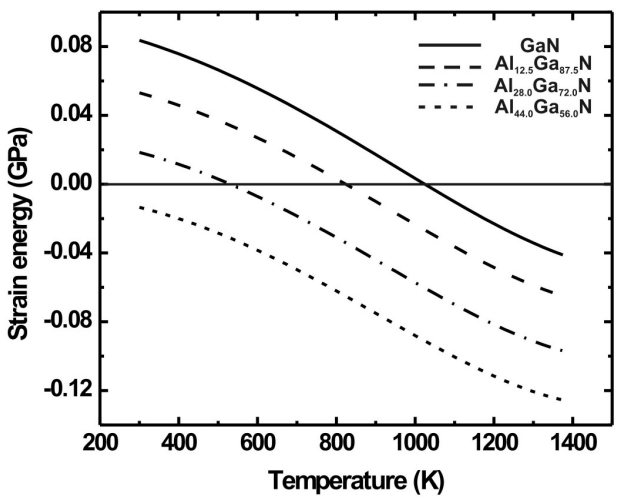

Figure 4. Calculated thermal strain energy between III-nitrides and $LiGaO_2$ at different growth temperatures.

Figure 5(a) shows the GaN in-plane lattice parameters grown on $LiGaO_2$ with different thicknesses as measured by x-ray diffraction reciprocal space mapping. The measured in-plane lattice parameters were discriminated as two groups, representing a^*_{GaN} and b^*_{GaN}. The component of lattice parameter along the *a*- and *b*-axes of $LiGaO_2$ was also shown as a reference by the broken-dash horizontal line. When the thickness of GaN film is 5 nm, in-plane lattice parameters of GaN films ($\boldsymbol{a}^*_{GaN} = 3.1336$ Å and $\boldsymbol{b}^*_{GaN} = 3.1878$ Å) almost lattice-matches with equivalent in-plane lattice parameters of $LiGaO_2$ ($\boldsymbol{a}_{LiGaO2}/\sqrt{3} = 3.1212$ Å and $\boldsymbol{b}_{LiGaO2}/2 = 3.1895$ Å) resulting in low strain-energy in GaN/$LiGaO_2$, shown in Figure 5(b). It is inferred from Figure 5 that 5~10 nm GaN films are grown pseudomorphically on $LiGaO_2$ and for over 10 nm thickness, a sudden relaxation of the in-plane lattice parameters was observed. *Huang et al.*,[21] indicates that the critical thickness of GaN on $LiGaO_2$ is around 10 nm thickness. When GaN films are very thin, compared with the in-plane lattice constants of $LiGaO_2$ substrates, a^*_{GaN} is longer and b^*_{GaN} is shorter than the *a*-and *b*-lattice parameters of $LiGaO_2$, respectively. The a^*_{GaN} increases along with the film thickness while the b^*_{GaN} decreases. Therefore, the anisotropic strain of the GaN films becomes more intense along the primary axis of $LiGaO_2$. Along the *a*-axis of $LiGaO_2$ the GaN films are under compressive strain while under tensile strain along the *b*-axis relative to $LiGaO_2$ substrates. On the other hand, compared with the lattice parameters of fully relaxed GaN films, the in-plane lattice parameters ($\boldsymbol{a}^*_{GaN} = 3.1687$ Å and $\boldsymbol{b}^*_{GaN} = 3.1627$ Å) of 1.0 μm thick GaN films are far from the relaxed GaN lattice parameter $a_{GaN} = 3.1889$ Å, indicating considerable compressive strain/stress in GaN films. Both components of the anisotropic strained GaN lattice parameter do not completely coincide with a relaxed GaN films. This shows that there is an anisotropic and strong deformation of the GaN crystal lattice expanded in the *a* direction and contracted in the *b* direction, as shown in Figure 6. The measured strain-energy of 0.04 GPa for 1.0 μm thick GaN is two times less than calculated stain-energy of 0.084 GPa for relaxed GaN on $LiGaO_2$ indicating only partial relaxation has occurred.

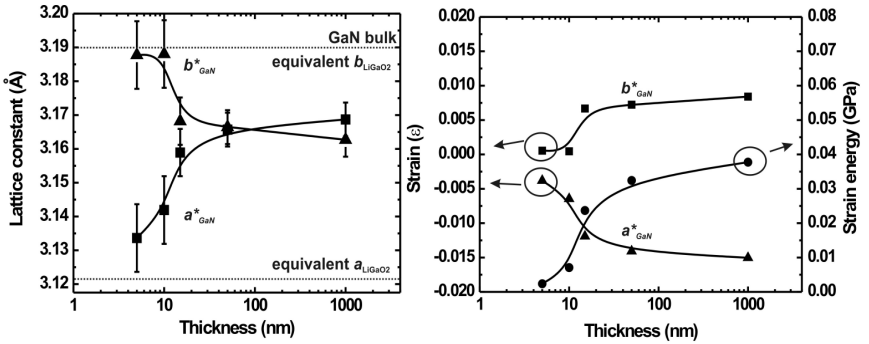

Figure 5. (a) In-plane lattice parameters and (b) strain and strain energy of 5 nm to 1.0 μm thick GaN on $LiGaO_2$.

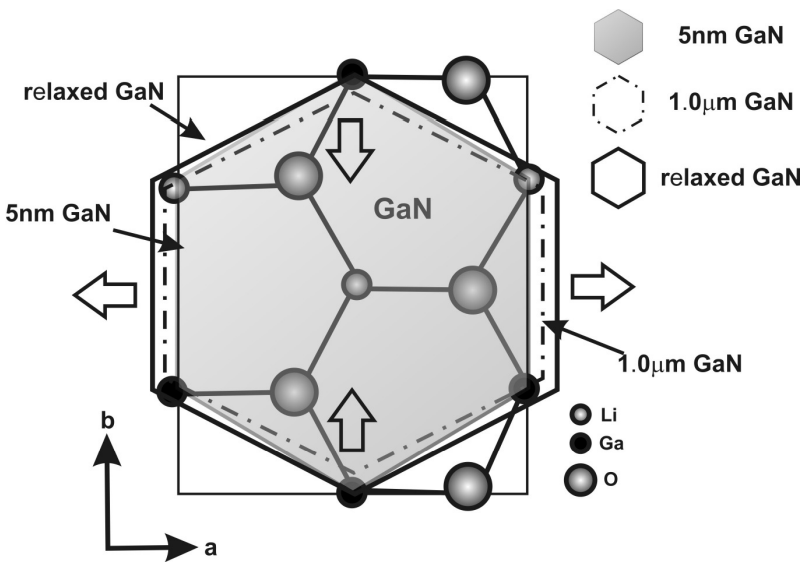

Figure 6. Development of the GaN structure with different thickness on $LiGaO_2$.

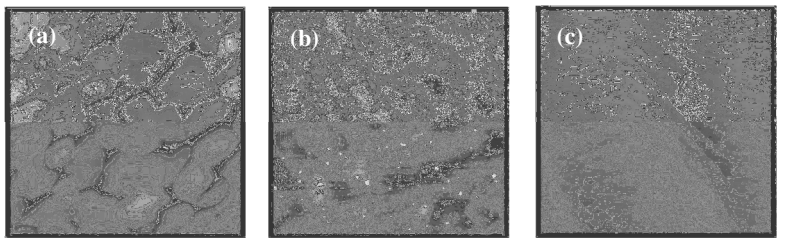

Figure 7. AFM images of 0.4μm GaN grown (a) without a buffer; (b) with a low temperature GaN buffer; (c) with an AlGaN/GaN superlattice buffer. AFM images have 0.75 μm × 0.75 μm size.

2.4. *III-nitrides on $LiGaO_2$*

Even though $LiGaO_2$ has a very close lattice-match with GaN, the initial buffer layer still plays a critical role in reducing the dislocation density of III-nitride materials. Figure 7 shows the surface morphology of GaN grown on different buffer layers. A 0.4 μm thick GaN epitaxial layer has been grown on $LiGaO_2$ with (a) no buffer, (b) a low temperature, 600°C, 16 nm thick GaN buffer layer, and (c) 16nm thick 5 period AlGaN/GaN superlattice buffer layers with different Al composition as described below. GaN epitaxial layer grown without a buffer layer shows very grainy features with the surface roughness (RMS) of 6 nm for a 2 μm × 2 μm AFM scan. Using the low temperature GaN buffer layer, step-flow growth has been enhanced, resulting in an improved surface roughness of 1.15 nm. An AlGaN/GaN superlattice buffer layer further enhances lateral growth and results in MOCVD-like step-flow growth, giving an atomic step limited roughness of 0.55 nm. The dislocation density for the 1.0 μm thick GaN films on various buffer layers have been estimated with a Williamson-Hall plot[22,23]. While these types of estimations are not accurate for the film structures presented here, they do offer a numerical means of comparing film quality albeit not a true quantitative method. The results of these estimations are also compared with results from etch pit density measurements as described elsewhere[24] and are listed in Table 2. Without a buffer layer, GaN films on $LiGaO_2$ show a low 10^8 cm^{-2} dislocation density. Using a low temperature GaN buffer layer, the dislocation density was reduced one order lower than that of GaN

Table 2. Dislocation density of 1.0 μm thick GaN with various buffer conditions.

Buffer conditions	*No buffer*	*GaN buffer*	*12%Al SL buffer*	*28% SL buffer*	*44% SL buffer*
$L_{\parallel}$ (μm)	0.687	3.393	3.486	2.069	3.352
N_{screw} (cm^{-2})	5.50×10^7	1.80×10^6	1.72×10^6	4.80×10^6	1.85×10^6
N_{edge} (cm^{-2})	2.55×10^9	9.60×10^7	8.97×10^7	3.16×10^8	1.01×10^8
tilt angle (arcsecond)	160	30	29.2	49	30.3
twist angle (degree)	1.5	0.125	0.12	0.251	0.13
etch pits (cm^{-2})	4×10^8	2.8×10^7	2.2×10^7	9.5×10^7	2.3×10^7

without low temperature GaN buffer layers. Comparing the films grown with different Al compositions in the superlattice, it was found that the film grown with the $Al_{0.12}Ga_{0.88}N$/GaN SL has the lowest dislocation densities (both screw and edge) and longest coherence length. This is due to lower strain energy at the AlGaN/GaN buffer layer growth temperature of 823 K, as indicated in Figure 4. The film grown with the $Al_{0.28}Ga_{0.72}N$/GaN SL has dislocation densities as high as twice that of the other two samples. Therefore, the reduced strain energy of the $Al_{0.12}Ga_{0.88}N$/GaN superlattice buffer layers resulted in enhanced lateral growth as indicated in Figure 7c. Furthermore, both the low temperature GaN and the AlGaN/GaN superlattice proved an effective buffer layer for reducing the dislocation density of GaN epitaxial layers by two order magnitudes compared with GaN films without buffer layers.

2.5. *State of art MSM devices on $LiGaO_2$*

Metal-semiconductor-metal (MSM) photodetectors have been used in modern optical communication systems. MSM devices have ultra-lower intrinsic capacitance compared with other detectors, such as p-n junctions,[25] and p-i-n diodes[26]. Furthermore, the simple planar structure of MSM devices is very attractive due to their fabrication simplicity and suitable for the monolithic integration with regular IC process. Since the

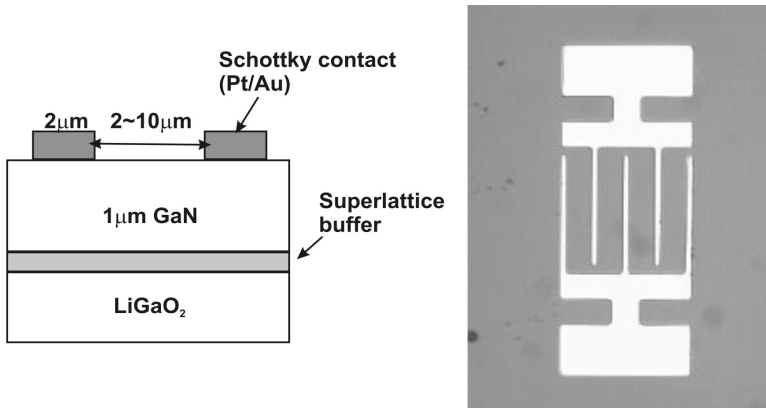

Figure 8. Schematic of GaN MSM device structure on $LiGaO_2$ (left) and fabricated MSM detector (right) (from Seo et al.. [27], reprinted with permission of the American Institute of Physics).

entire $LiGaO_2$ wafer can be easily removed from the III-nitride films in a matter of minutes, the ability to transfer III-nitride devices onto mirrors, heat sinks or complex silicon circuitry, now appears promising and has been demonstrated.[5] Furthermore, GaN based high power transistors can be integrated with GaN MSM detectors for multifunctional integrated systems. Figure 8 shows the structure of a GaN MSM device.[5,27] This typical MSM photodetector consists of interdigitated metal fingers 47 μm long, with 2 μm finger width and 2-10 μm finger spacing, and a detection area of 150×50 μm^2. For Schottky contacts, Pt and Au were used and were deposited for 450 Å and 1500 Å, respectively. Hydrofluoric acid (HF) and ammonium hydroxide (HN_4OH) has been used to remove the surface oxide layer and to improve the Schottky characteristics for 1 and 15 minutes, respectively. Furthermore, the integration process of the GaN MSM on Si is shown in Figure 9. After device fabrication, the devices were mesa etched by ICP. The gas composition and ratio were: 22.5 Cl_2: 2.5 H_2: 4 Ar_2, and the etching rate for GaN was ~1000Å per minute with the RF power of 500W, and pressure was 5 millitorr.

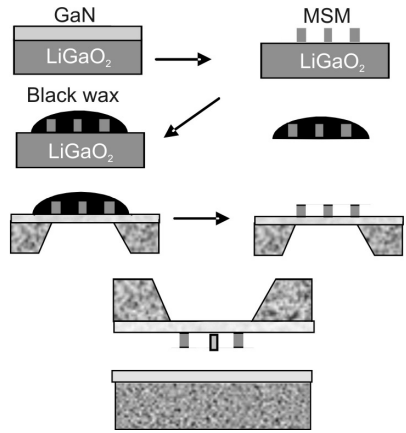

Figure 9. Integration process of GaN MSM on Si. (from Sa et al.. [21], reprinted with permission of author).

Next the surface was protected in black wax, and the substrate was etched off using a solution of HF:H_2O (1:10), which is selective only to the substrate. The etching rate for $LiGaO_2$ of this solution is ~10 μm per minute and for GaN is immeasurable. The devices were then flipped over and bonded on the host substrate, Si. Figure 10 shows the dark and illuminated current–voltage characteristic of a GaN MSM photodiode grown on $LiGaO_2$[5]. The measured dark current at 10 and 60V were 0.8 pA and 20 pA, respectively. The lower dark current can be ascribed to the low density of dislocations in the GaN grown on the closely lattice-matched $LiGaO_2$ substrates. The photoresponse measurement in Figure 10 is also shown using 150W tungsten lamp. The UV light power was 24.8 μW/cm^2 at 308 nm. The measured responsivity was 0.105 A/W and 0.268 A/W at 20 and 60V, respectively[5]. Those values are also comparable to the best reported responsivity value of 0.15 A/W at a 10 V reverse bias condition.[28] Figure 11 shows the average current–voltage characteristics of two MSM devices before and after the devices where removed from the $LiGaO_2$ substrate and transferred to an oxidized silicon wafer. Within the error of the measurements, there is essentially no degradation of the current–voltage characteristics[5]. This example shows

the simplicity of GaN device integration using a LMO substrate and the device performance advantages obtained by using the improved lattice matching.

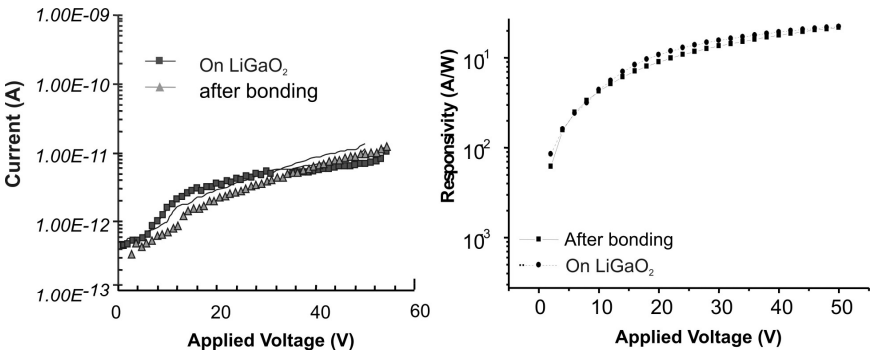

Figure 10. IV characteristics under dark and UV and calculated GaN MSM responsivity as a function of reverse bias (from Seo et al.. [27], reprinted with permission of the American Institute of Physics).

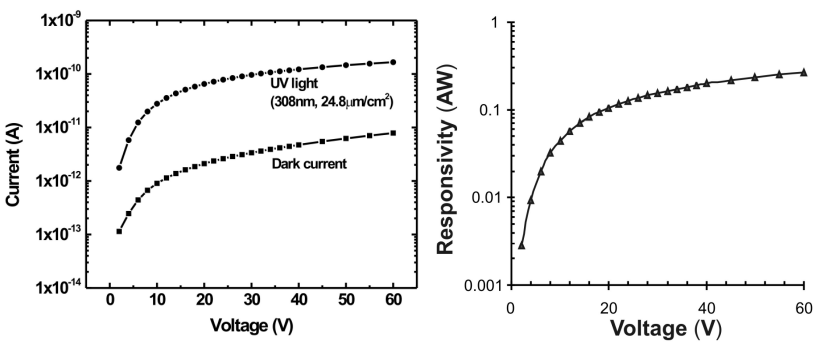

Figure 11. IV characteristics under dark and calculated GaN MSM responsivity as a function of reverse bias before and after removal of the $LiGaO_2$ (from Seo et al.. [5], reprinted with permission of IEEE).

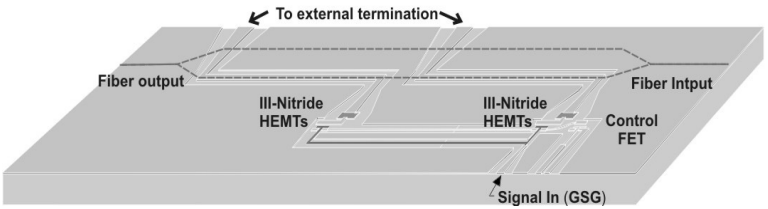

Figure 12. Dual serial drive of $LiNbO_3$ modulator structure. The combined effects of segmenting the electrode structures and the use of larger on chip voltages may permit the electrodes to be treated as lumped elements ((from Madison et al.. [30], reprinted with permission of IEEE).

3. III-Nitride Power Transistor Integration onto Ferroelectric Materials

Next generation ultrahigh capacity networks will rely on advanced packaging/integration strategies to increase functionality, reduce cost and thereby enable cost effective network architectures. The combination of the unique, nonlinear optical properties of $LiNbO_3$ with the wide bandgap properties of III-nitride materials provides great potential for multifunctional electrical and optical applications. An integration solution between III-nitrides and ferroelectric materials via epitaxial growth allows for enhancements in device performance by employing the unique properties of each. For example, an integrated AlGaN/GaN electronic driver on the ferroelectric material $LiNbO_3$ provides the possibility of implementing compact optoelectronic/electronic chips, leading to increased cost savings (among other things).[29,30,31]

3.1. *Integration of III-nitride based amplifiers/drivers on optical modulators*

Current $LiNbO_3$/$LiTaO_3$ modulators require external and discrete driver and amplifier elements that are impedance matched via complex connections. Some level of integration is occurring in various optical components but this is primarily done through packaging techniques and hybrid integration of discrete elements. The III-nitride integration technology on lithium niobate (tantalate) modulator is attractive for a few reasons: 1) The need for impedance matching to external connections is

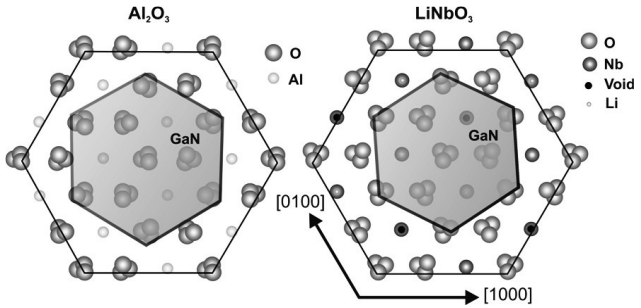

Figure. 13. Schematic diagram showing GaN on (a) the hexagonal unit cell of sapphire and (b) the hexagonal unit cell of $LiNbO_3$. The lattice mismatches of GaN to sapphire and lithium niobate are 15.7% and 6.8%, respectively.

eliminated and thus, the electrical efficiency is improved, (2) package size can shrink due to monolithic design and the availability of high voltage drive, (3) potential cost savings, (4) potential for adding functionality to a component such as on-board temperature compensation. State of the art lithium niobate optical modulators are already capable of supporting 40Gb/s data rates, while the bulk of the market is for 10Gb/s devices. While $LiNbO_3$ modulators dominate the long haul market the short haul market has other competitive modulator solutions like electro-absorption and polymer products. The proposed III-nitride integrated $LiNbO_3$ modulator is shown in Figure 12. Two driver amplifiers along the length of the waveguide compensate for time delay occurring during propagation of the signal along the coplanar waveguide.[30] Importantly, only a single signal input is needed. Group velocity matching is realized by proper choice of the signal path length to the second AlGaN/GaN HEMTs.[30] The combination of significant on chip voltages for the GaN transistors[32] (8-80V range), together with the sequential drive topology, allows for dramatic shortening of the device length and a corresponding increase in device speed.

3.2. *Crystalline relationship between III-nitrides and $LiNbO_3$/$LiTaO_3$*

Figure 13 shows the crystallographic schematic of GaN on Al_2O_3 and $LiNbO_3$ in the (0001) basal plane constructed with Diamond™ version 2.1 crystal modeling software[33] (a crystallographic schematic of $LiTaO_3$

is approximately the same with that of $LiNbO_3$). $LiNbO_3$ ($LiTaO_3$) belongs to the space group *R3c* and their lattice parameters are $\boldsymbol{a}$ = 5.148 Å, $\boldsymbol{c}$ = 13.863 Å and $\boldsymbol{a}$ = 5.154 Å and $\boldsymbol{c}$ = 13.783 Å for $LiNbO_3$ [34,35] and for $LiTaO_3$[34] respectively. While commonly referred to as a rhombohedral or trigonal material[35,36], $LiNbO_3$ does possess hexagonal symmetry with a hexagonal unit cell, as shown in Figure 13. $LiTaO_3$ is nearly identical in lattice constants to $LiNbO_3$ and has an identical surface oxide chemical termination. This hexagonal symmetry within the c-plane is very similar in structure to another commonly used substrate for III-Nitrides, sapphire (Al_2O_3), as show in Figure 13 (a) and (b). The results of extensive crystal modeling[33] show the hexagonal unit cell of Al_2O_3 with a lattice constant of 4.758 Å and also shows the hexagonal unit cell of $LiNbO_3$. Both images are looking down onto the c-plane along the $(000\bar{1})$ direction. While the unit cell lattice mismatch of GaN-Al_2O_3 is ~33%, the commonly quoted lattice mismatch of GaN to Al_2O_3 of ~16% occurs by alignment of the GaN hexagonal base along the oxygen sub-lattice of Al_2O_3[37] as shown in Figure 13. This requires a rotation of the GaN unit cell about the c-axis by 30° and results in a slightly distorted strain. While the crystal structure of $LiNbO_3$ is more complex than that of Al_2O_3 due to the staircase spiraling nature of the oxygen octahedra resulting in a larger dispersion of oxygen atomic positions around the central locations than found in Al_2O_3, the surface structure of $LiNbO_3$ on the c-plane is similar to Al_2O_3. The main difference is that the surface structure has a larger oxygen sub-lattice spacing, resulting in a better average lattice mismatch to III-Nitrides. Even the chemistry of the materials is similar. The sapphire, Al_2O_3, can be thought of as an ABO_3 material with A = B. The lithium niobate, $LiNbO_3$, possess' similar chemical structure, but the lithium niobate does require one oxygen octahedra that possesses a central void instead of a cation in order to maintain proper valence.[35] Lithium tantalate, $LiTaO_3$, is nearly identical in chemical structure (exchanging Ta for Nb) and mechanical structure to $LiNbO_3$ but possesses a smaller, 50 $\mu C/cm^2$ instead of 71 $\mu C/cm^2$, spontaneous polarization[35]. The common oxygen sub-lattice that forms the chemical bridge between III-nitrides and these ABO_3 substrates insures a similar chemical bond configuration whether using lithium niobate or tantalate.

If the oxygen sub-lattice of Al_2O_3 or $LiNbO_3/LiTaO_3$ were geometrically symmetric, this dimension would be the unit cell of these materials instead of the larger a-axis dimensions quoted. In the case of Al_2O_3, the lengths of the triagonal unit cells are 4.750 Å verses 4.762 Å along the [0001] verses the $[01\bar{1}0]$ directions. For $LiNbO_3$, the distortion is less directed with distortions in several directions resulting from the spiraling nature of the oxygen octahedra constructing the crystal. For Al_2O_3 the surface oxygen bond lengths around the hexagon making up the oxygen sub-lattice shown in Figure 13 are two each of length 2.868, 2.872 and 2.513 Å whereas for $LiNbO_3$ ($LiTaO_3$), they are 2.719 (2.722), 3.362 (3.366), and 2.879 (2.882) Å. Thus, the average surface oxygen-oxygen spacing for Al_2O_3 and $LiNbO_3$ ($LiTaO_3$), are 2.751 and 2.981 (2.990) Å, resulting in a lattice mismatch to GaN (3.185 Å) of 15.7% for Al_2O_3 and 6.8% (6.5%) for $LiNbO_3$ ($LiTaO_3$). A similar analysis for the $LiNbO_3$ mismatch to AlN (3.1114 Å) and SiC (4H and 6H with a = 3.0730 and 3.0806 Å) results in lattice mismatches of 4.4%, 3.1% and 3.3% showing the versatility of mixing epitaxial wide bandgap semiconductors on ferroelectrics and vice versa. These lattice mismatches, while better than Al_2O_3, are note very good.

The reciprocal space map of a MBE grown GaN sample grown on $LiNbO_3$ is shown in Figure 14 (a). Clearly, GaN epitaxial layers are epitaxially aligned to the $LiNbO_3$. The dominant reflections present are the symmetric reflections of GaN and $LiNbO_3$, indicating alignment of the (0001) direction of GaN along the (0001) direction of $LiNbO_3$. Figure 14(c)-(d) show x-ray diffraction (XRD) peaks of GaN grown on z-cut $LiNbO_3$ and $LiTaO_3$ compared to as received $LiNbO_3$ shown in Figure 14(b). (0002) GaN XRD peaks are observed on $LiNbO_3/LiTaO_3$ substrates, which indicate that the growth direction of the epitaxial film is GaN [0001] ‖ $LiNbO_3$($LiTaO_3$) [0001]. The distinct difference of GaN growth on $LiNbO_3$, rather than $LiTaO_3$, is the formation of a second phase of $(60\bar{2})$ $LiNb_3O_8$, indicated by a peak on the ω-2θ scan at $2\theta = 38.1°$, in addition to the original $LiNbO_3$ peak. This can be explained by the fact that congruent $LiNbO_3$ (48.39 mole % Li_2O) is metastable and will decompose into the two phases of $LiNb_3O_8$ and Li_2O-rich $LiNbO_3$ at the elevated growth temperature.[38] As-received $LiNbO_3$ samples do not have any of the $LiNb_3O_8$ phase as shown in

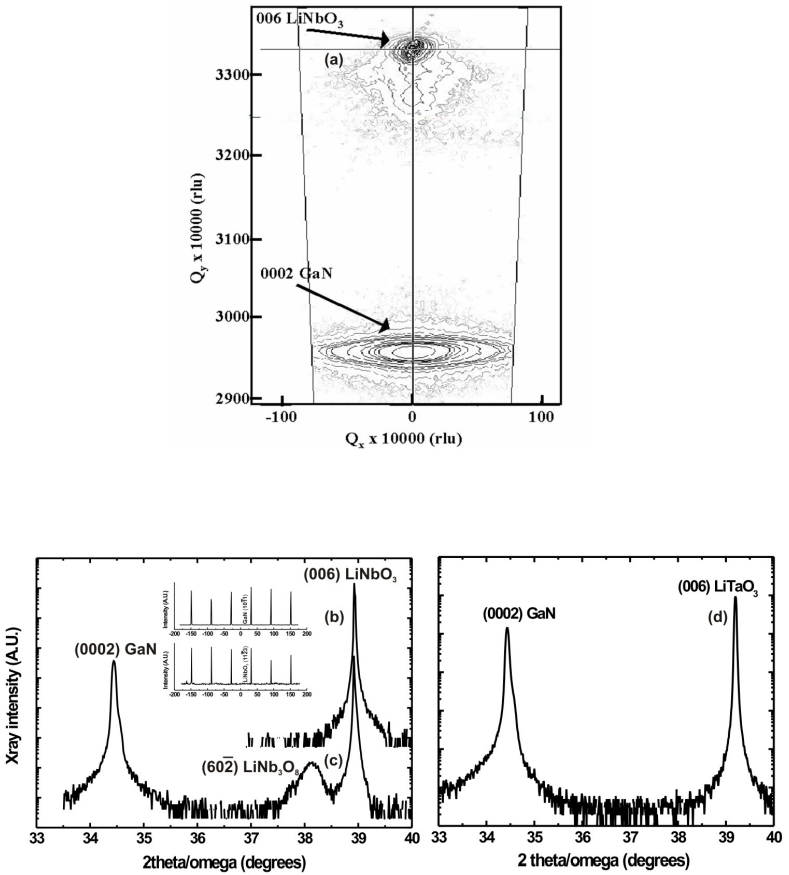

Figure 14. The reciprocal space map for (a) GaN on $LiNbO_3$, 2θ/ω x-ray scan of (b) $LiNbO_3$ and (c) GaN grown on $LiNbO_3$ and (d) GaN on $LiTaO_3$ substrates. Additional $LiNb_3O_8$ peak was observed for GaN on $LiNbO_3$ while as-received $LiNbO_3$ does not show $LiNb_3O_8$.

Figure 14(b), so $LiNb_3O_8$ must form during outgassing of the substrate in the introduction chamber and during the growth. Therefore, the growth conditions of III-nitrides on $LiNbO_3$ must be carefully chosen to avoid formation of the Li-deficient phase interfacial layer, $LiNb_3O_8$, between GaN and $LiNbO_3$.

The in-plane XRD peaks of the GaN epitaxial layer on $LiNbO_3$ ($LiTaO_3$), indicated in the inset of Figure 14, was obtained by a

ø-rotational scan about the c-axis of the $(10\bar{1}1)$ plane of the GaN epitaxial layer and the $(11\bar{2}3)$ plane of the $LiNbO_3$ ($LiTaO_3$) substrate. This shows the in-plane relationship at the interface between GaN and $LiNbO_3$ ($LiTaO_3$). The six respective peaks of GaN $(10\bar{1}1)$ and $(11\bar{2}3)$ planes indicate that the GaN epitaxial layer has hexagonal structure, and is grown on the $LiNbO_3$ ($LiTaO_3$), which also have a hexagonal structure. Furthermore, the ø-scan of GaN $(10\bar{1}0)$ was equivalent to that of $LiNbO_3$ ($LiTaO_3$) $(11\bar{2}0)$, which implies that the hexagonal structure of GaN is rotated 30° relative to the $LiNbO_3$ ($LiTaO_3$) hexagonal structure. Therefore, GaN on $LiNbO_3$/$LiTaO_3$ grows with the crystalline orientation relationship: (0001) GaN ‖ (0001) $LiNbO_3$ ($LiTaO_3$) with [$(10\bar{1}0)$]GaN ‖ [$(11\bar{2}0)$] $LiNbO_3$ ($LiTaO_3$).

3.3. *Surface preparation*

Even with smaller lattice mismatch compared to sapphire substrates, only partial success for GaN epilayers on $LiNbO_3$ has been possible due to delamination of GaN epilayers when thick GaN layers were grown thicker than 0.5 μm, while no delamination was observed on $LiTaO_3$. To overcome this delamination on $LiNbO_3$, the surface of as-received $LiNbO_3$ was examined and improved. As-received $LiNbO_3$ substrates have surface damage such as scratches and corrugations on the nanometer scale range due to mechanical polishing as observed by atomic force microscopy (AFM) and shown in Figure 15 (a). The AFM image in Figure 15(a) shows deep scratches of 2~5 nm depth on the surface. Therefore, high temperature furnace anneals at 1000°C in dry air[39,40] have been performed to produce atomically flat surfaces. After two hours of annealing at 1000°C in air, the AFM image of Figure 15(b) reveals that all surface damage was removed and that there are clear steps and terrace structures present after annealing. A similar high-temperature thermal treatment has been used to obtain atomically flat surface and to remove the surface damage from chemical mechanical polishing (CMP) on many different substrates.[39,40,41, 42]

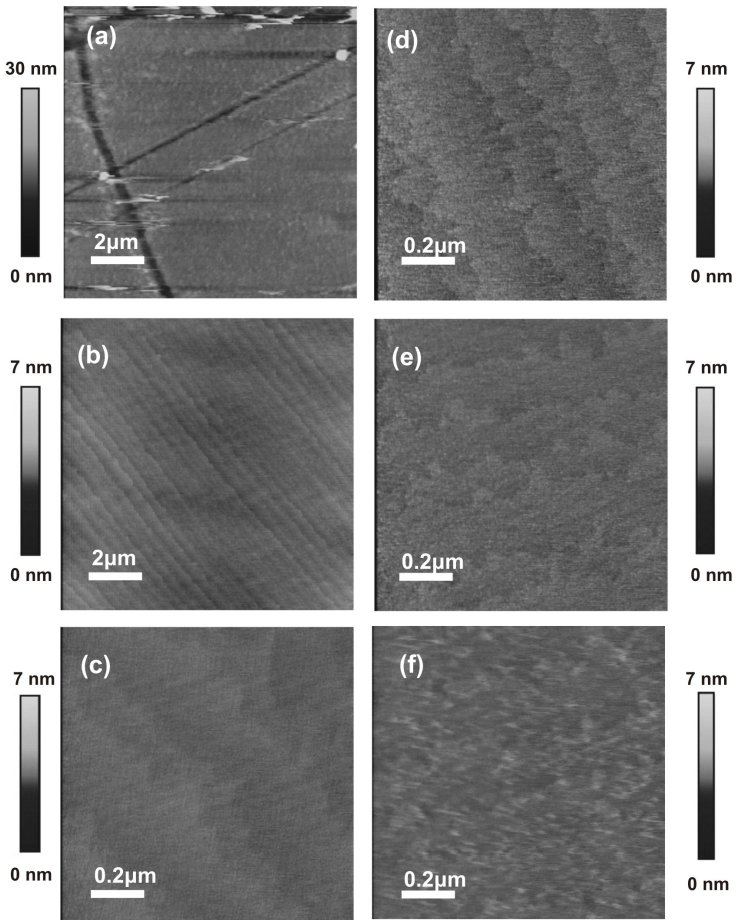

Figure 15. The surface of $LiNbO_3$ by AFM (a) before annealing; (b) after furnace annealing in air at 1000 °C for 2 hours; (c) the same condition with different scale; the surface of $LiNbO_3$ by AFM after (d) furnace annealing in air at 1000°C for 3 hours; (e) 4 hours, and (f) 5 hours (from Lee et al.. [43], reprinted with permission of the American Institute of Physics).

Upon annealing, the topmost surface is thermodynamically unstable and is transformed to the equilibrium crystal surface by the rearrangement of the surface atoms.[44] The surface quality improvement of $LiNbO_3$ has been attributed to diffusion and re-growth processes, when annealed above a high temperature of 900°C, leading to atomic

flatness[39] and removal of scratches from the surface[42]. Further experiments demonstrate that an atomically smooth surface of $LiNbO_3$ shows enhanced adhesion of II-nitrides, resulting in III-Nitride films grown in excess of a few microns. However, longer annealing times produce facet coarsening, resulting in increasing surface roughness. Various annealing time conditions are applied to investigate the change of the width of terraces as shown in Figure 15(d)-(e). After the three hour anneal, congruent $LiNbO_3$ produces atomically flat terraces of ~200 nm width, as shown in Figure 15(d). The surface in Figure 15(e) after a 4 hour anneal is very similar to the three hour annealed sample. But, in Figure 15(f), the 5 hour annealed surface has a slightly porous morphology that increases surface roughness. These observations lead to the conclusion that 2-3 hour anneals give the best surface condition with the largest terrace width.

3.4. *Surface stability of $LiNbO_3$ and $LiTaO_3$*

Stability of the surface is very important for subsequent growth of III-nitride materials. $LiNbO_3$ and $LiTaO_3$ are less stable than SiC or sapphire substrates. Figure 16 shows the phase diagram of $LiTaO_3$ depending on LiO_2 compositions (the phase diagram of $LiNbO_3$ can be found in ref [35]). From these phase diagrams, the relation between the crystal composition and the stable phase can be obtained in the temperature range common for MBE growth temperatures. It is common practice to outgas $LiNbO_3$ and $LiTaO_3$ at 500~600°C and grow the III-nitride epitaxial layer at 600~800 °C. Congruent (~48% mole LiO_2) $LiNbO_3$ exhibits two different phases, $LiNbO_3$ and $LiNb_3O_8$, while congruent $LiTaO_3$ shows only one phase, $LiTaO_3$, indicating $LiTaO_3$ is more stable at the MBE growth temperature of 600~800°C. To minimize the second phase of $LiNb_3O_8$, it is recommended to grow III-nitride epitaxial layers at very high temperatures (900 – 950°C), where the congruent-melting composition in the two-phase field (Li_2O-Nb_2O_5) appears and the $LiNbO_3$ phase is stable.[38] However, the higher temperature growth is very impractical due to the cracking of $LiNbO_3$ due to the larger difference of thermal expansion between $LiNbO_3$ and III-nitride materials. Another, more practical solution is to use stoichiometric

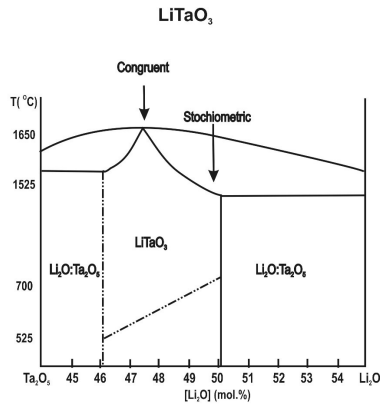

Figure 16. Phase diagram of $LiTaO_3$ (from [45], reprinted with permission of Sawyer Inc.)

$LiNbO_3$ which has around 50% mole LiO_2 composition, which is a stable phase at all increased growth temperatures. Stoichiometric $LiNbO_3$ is much more expensive and difficult to obtain than traditional congruent $LiNbO_3$.

3.5. *Polarity*

To use the unique properties of GaN, the control of polarity is a prerequisite for achieving any benefit from piezoelectric effects. Polarity inversion domains in AlGaN/GaN heterostructures cause significant scattering because of the huge potential fluctuation along the interface, resulting in very low mobility for transistor structures. Since GaN and $LiNbO_3$ ($LiTaO_3$) substrates are polar materials, it is expected that GaN grown on +z-face $LiNbO_3$ ($LiTaO_3$) should show single Ga polarity GaN to minimize the electrostatic charge at the interface between GaN and $LiNbO_3$ ($LiTaO_3$). Gauss's Law[46] states that the divergence in the electric flux density, D, normal to an interface must be equal to the charge density at that boundary. This is,

$$\nabla \bullet D = \rho \quad or \quad \nabla \bullet (\varepsilon E + P) = \rho \tag{7}$$

where ε is the total dielectric constant, E is the electric field, P is the polarization, and ρ is the sheet charge density at the interface. At

the interface between a polar semiconductor and polar substrate, this reduces to

$$(\varepsilon_{semi}E_{semi} + P_{semi}) -- (\varepsilon_{substrate}E_{substrate} + P_{substrate}) = \rho_{sheet} \quad (8)$$

where ρ_{sheet} is the sheet charge at the boundary and the subscripts indicate parameters for the semiconductor (semi) and the substrate (substrate). Clearly from equation 8, having the semiconductor polarity the same as the substrate polarity in sign and, if possible in approximate magnitude, works to reduce the required surface charge at the interface between the semiconductor/substrate and/or internal compensating electric field required. This minimization of the polarization discontinuity is critically important in the first monolayer where, if allowed to exist, the interface charge resulting from polarizations of opposite sign (i.e. – in the semiconductor and + in the substrate or vice versa) would induce a compensating electric field in the semiconductor that could very easily exceed the critical field for breakdown in the semiconductor. Clearly, minimization in the polarization discontinuity is electrostatically preferred and has been experimentally demonstrated, ie, dominant Ga-polarity on +z-face $LiNbO_3$ ($LiTaO_3$) and dominant N-polarity on –z-face $LiNbO_3$ ($LiTaO_3$).

$LiNbO_3$ and $LiTaO_3$ are ferroelectric materials. Wet etching experiments are widely used to discern ferroelectric domains of $LiNbO_3$ and $LiTaO_3$ by the difference in etching rates of the negative and positive ends of the dipoles, where the negative face is etched faster than the positive face[47]. Wet etching experiments were performed on bare $LiNbO_3$ and $LiTaO_3$ and etching pits were not observed on non-annealed $LiNbO_3$ and $LiTaO_3$ substrates, indicating single ferroelectric domains on the surface. On the other hand, we observed random repolarization of domains for $LiNbO_3$ and $LiTaO_3$ after high temperature furnace annealing at 1000°C for two hours. Figure 17 shows the atomic force microscopy (AFM) images of high-temperature treated $LiNbO_3$ and $LiTaO_3$ after etching in $HF+HNO_3$ acids for 30 minutes at 100°C. We observed etch pits on samples, with an etching rate of approximately 2.4 nm per minute, indicating that furnace annealed $LiNbO_3$ and $LiTaO_3$ substrates have ferroelectric multi-domains. Therefore, the high temperature thermal treatment gives a trade-off between adhesion and control of polarity of GaN epitaxial layer on $LiNbO_3$.

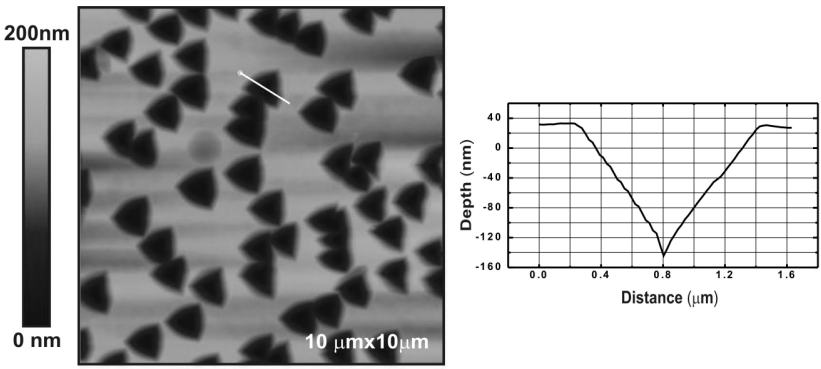

Figure 17. AFM image of etch $LiNbO_3$ and depth profile of etched area.

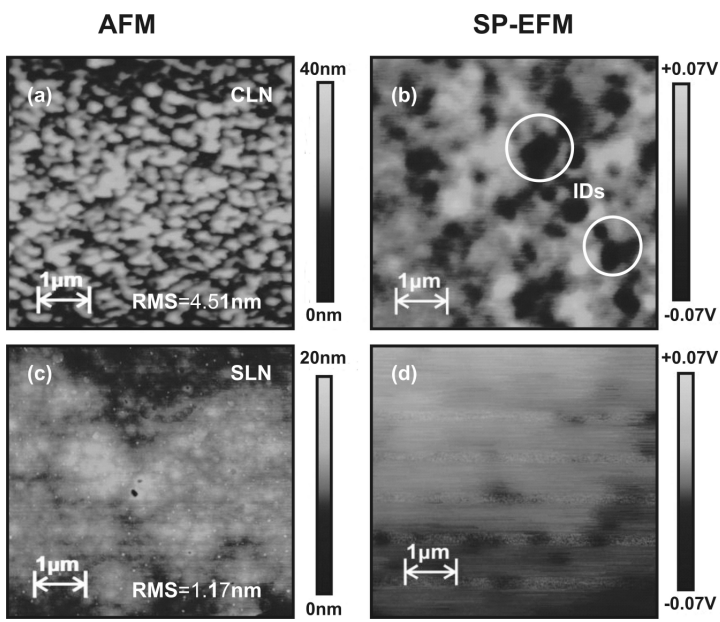

Figure 18. (a) Surface morphology and (b) surface potential measurement of AlGaN/GaN on congruent LN by AFM and surface potential EFM. (c) Surface morphology and (d) surface potential on near stoichiometric LN show smoother surface and no inversion domains (from Lee et al.. [43], reprinted with permission of the American Institute of Physics).

Figure 18 (a) and (b) shows surface morphology and inversion domains for AlGaN/GaN grown on congruent $LiNbO_3$ observed by AFM and surface potential electric-force microscopy (EFM)[48,49] due to the formation of the unintentional ferroelectric inversion domain after high temperature anneals. On the other hand, near stoichiometric (49.9% Li_2O mole) $LiNbO_3$ does not show any inversion domains for AlGaN/GaN, as shown in Figure 18(c) and (d). Furthermore, smoother surface of AlGaN/GaN was observed on near-stoichiometric $LiNbO_3$. It is important to note that we also observed inversion domains on GaN grown on $LiTaO_3$ (not shown here). Previous studies indicate inversion domains can be suppressed by AlN buffer layers, which are widely used on sapphire substrates to produce singular Ga-polar GaN.[48,50] Therefore, $Al_{0.2}Ga_{0.8}N$/GaN HEMT structures were grown using thick 0.1 μm AlN buffer layers, followed by ~1.0 μm thick GaN and 25 nm thick AlGaN layers. Using this approach a two dimensional electron gas (2DEG) can be achieved in the channel layers of AlGaN/GaN heterostructures using thick AlN buffer layers. Contrarily, using GaN buffer layers produces many polarity inversion domains and we cannot achieve 2 DEGs in the channel layer of AlGaN/GaN structures.

3.6. *AlGaN/GaN power transistor integration on $LiNbO_3$*

To integrate high power AlGaN/GaN devices on ferroelectric materials, it is necessary to control the polarity between III-nitrides and ferroelectric materials. Due to unintentional repolarization on the surface, thin AlN buffer layers were grown at low temperatures of 600°C. Then the subsequent GaN epitaxial layer was deposited with a two-step growth approach: 0.5 μm GaN under Ga-rich conditions, followed by 0.3 μm GaN under N-rich conditions. This method is used to reduce dislocation density for GaN layer.[51] The mobility was measured to be 200 and 800 cm^2/Vs, congruent and near-stoichiometric $LiNbO_3$ substrates, respectively. The improved mobility on near-stoichiometric $LiNbO_3$ is attributed to smoother surface and no inversion domains of AlGaN/GaN, as shown in Figure 18. The fabrication of high power III-nitride devices on ferroelectric materials was developed on congruent $LiNbO_3$. The source/drain metal ohmic contact was Ti/Al/Ti/Au

(250 Å /1000 Å / 450 Å /1500 Å) and was annealed for 30 seconds at 600°C. Rapid thermal annealing at 800°C has led to $LiNbO_3$ substrate cracks and peeling nitride layer off on $LiNbO_3$. The anomalous thermal expansion coefficient[35] of $LiNbO_3$ has restricted a rapid thermal annealing process of the ohmic metals.[31] Therefore, a lower temperature 600°C anneal was performed at a slow ramp rate of ~30° per minute. The slow ramp rate and decreased temperature has eliminated the problem of cracking $LiNbO_3$ substrates and peeling epitaxial layers. However, low temperature anneal limits performance of AlGaN/GaN heterostructures and cause the high contact resistance of AlGaN/GaN HEMTs, as described below. The typical DC current-voltage (I-V) device characteristics of the AlGaN/GaN HEMTs on $LiNbO_3$ is presented in Figure 19 for a dual gate device with 200 µm gate width and 2.0 µm gate length. We have evaluated the performance of devices with gate widths ranging between 150 µm and 340 µm. The maximum DC transconductance is ~25 mS/mm. We have observed that the breakdown voltage consistently exceeds 35 V which is sufficient to drive the optical modulators. The electron mobility in the AlGaN/GaN heterojunction is ~210 cm^2/V-s, and is expected to increase with improved epitaxial III-nitride growth on ferroelectric materials.

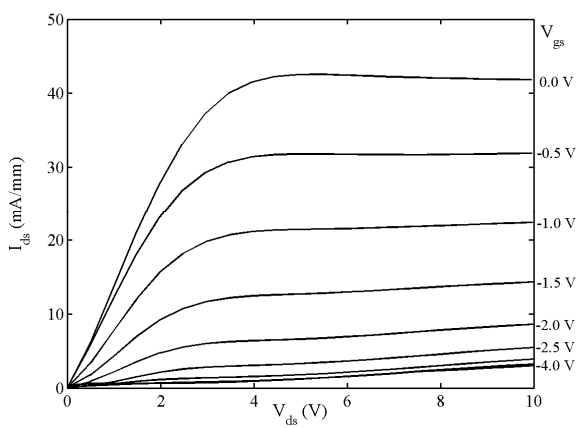

Figure 19. DC I-V characterization of AlGaN/GaN structures.

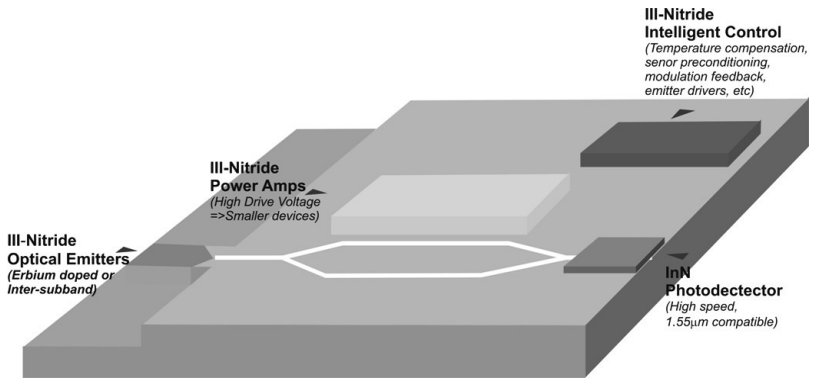

Figure 20. Long term vision for a densely integrated optoelectronics / electronics platform containing, optical emitter, electronic drive and control circuitry, as well as on chip high-speed detectors.

4. Conclusions and Outlook

This article has focused on GaN growth and device application on lithium metal oxide (LMO) substrates, such as $LiGaO_2$, $LiNbO_3$ and $LiTaO_3$. Through advances in the growth of III-nitride materials on $LiGaO_2$, state of the art optoelectronic devices have been demonstrated on $LiGaO_2$. Given its many advantages, for applications where ease of substrate etching is important, $LiGaO_2$ could become the substrate of choice, particularly for MBE growth. Furthermore, future smart integrated III-nitride device on $LiNbO_3$ can be implemented as shown in Figure 20. Electrical signals can be used to modulate the lithium niobate optical modulator, InN sensors can detect the optical pulse power and feedback electronics can adjust and optimize performance, all on the same chip. System cost analysis is highly favorable for at least a ½ reduction of system cost and yield is improved by miniaturization of the modulators made possible by higher drive voltages afforded by the use of GaN. Other advantages include freedom from the electrode design compromises required for "off modulator amplification", allowing higher transistor power added efficiency, higher optical modulation efficiency, and intelligent feedback to control temperature and ionic drift issues.

On-chip 1.55 μm light emitters such as rare earth doped GaN have already been demonstrated by Steckl *et al.*[52] showing little if any temperature quenching effects. Quantum cascade lasers currently under development in several groups could also be used as local light sources providing distributed, multi-wavelength light sources without the need for clumsy off chip solutions. While not widely understood or widely accepted as substrates, the inherent advantages and flexibility of LMO substrates should not be ignored. LMO substrates remain a very promising alternative for advances integrated systems of the near future.

Acknowledgments

This work was supported by basic science grants provided by ONR, monitored by Dr. Colin Wood, and by an NSF Career Award, ECS-0348271, under the direction of Dr. Rajinder Khosla. We would like to thank the many researchers who have aided in the development of GaN devices on LMO substrates including but not limited to April Brown, Nan Jokerst, Sangbeom Kang, Tom Kropenwicki, Paul Kohl, Sangwoo Seo and Kyoung-Keun Lee.

References

1. Stephen E. Ralph and Alan W. Doolittle, I*EEE Lasers & Electro-Optics Society newsletter*, **18**, 9 (2004).
2. M. Marezio, *Acta Crystallogr. A*, **18** 481 (1965).
3. H. Neumann, E. Pirl, and G. Kuhn, *J. Mater. Sci. Lett.* **6** , 495 (1987).
4. T. Kropenwicki, W. A. Doolittle, C. Carter-Common, S. Kang, P. Kohl, A. S. Brown, *J. Electrochem. Soc.* **145**, L88, (1998).
5. S. Seo, K.K. Lee, S.Kang, S. Huang, W.A. Doolittle, N.M. Jokerst, A.S. Brown, M.A. Brooke, *IEEE Photon. Tech. Lett.* **14**, 185 (2002).
6. Y.Tazoh, T.Ishii, S. Miyazawa, *Jpn. J. Appl. Phys.* **36** , L746 (1997).
7. W.A. Doolittle, T. Kropewnicki, C. Carter-Coman, S. Stoke, P. Kohl, N.M. Jokerst, R.A. Metzger, S. Kang, K.K. Lee, G. May, A.S. Brown, *J. Vac. Sci. Technol. B.* **16** ,1300 (1998).
8. E. Klob, R. Laudise, *J. Am. Ceram. Soc*. **48**, 342 (1965).
9. M. Sumiya, and S. Fuke, *MRS Internet J. Nitride Semicond. Res.* **9**, 1(2004).
10. D. Huang, P. Visconti, K. M. Jones, M. A. Reshchikov, F. Yun, A. A. Baski, T. King, and H. Morkoç , *Appl. Phys. Lett.* **78**, 4145 (2001).
11. W. A. Doolittle, S. Kang and A. S. Brown, *Solid-State Electron.* **44**, 229 (2000).

12. S. Strite, and H. Morkoc, *J. Vac. Sci. Technol. B* **10**, 1237 (1992).
13. G.A. Slack, and S.F. Bartram, *J. Appl. Phys.* **46**, 89 (1975).
14. C.J. Rawn, and J. Chhaudhuri, *J. Cryst. Growth* **225**, 214 (2001).
15. S.Nanamatsu, K.Doi, and M. Takahashi, *Jpn. J. Appl. Phys.* **11**, 816 (1972).
16. T. Ishii, Y. Tazoh, and S. Miyazawa, *J. Crst. Growth* **189/190**, 208 (1998).
17. J. Shen, S. Johnston, S. Shang, and T. Anderson, *J. of Cryst. Growth* **240**, 6 (2002).
18. M. Eickhoff , O. Ambacher, G. Krötz and M. Stutzmann, *J. of Appl. Phys.* **90**, 3383 (2001); O. Ambacher, B. Foutz, J. Smart, J. R. Shealy, N. G. Weimann, K. Chu, M. Murphy, A. J. Sierakowski, W. J. Schaff, and L. F. Eastman, R. Dimitrov, A. Mitchell, and M. Stutzmann, *J. of Appl. Phys.* **87**, 334 (2000).
19. A. Polian , M. Grimsditch, and I. Grzegory, *J. of. Appl. Phys.* **79**, 3343 (1996).
20. R. B. Schwarz, K. Khachaturyan, and E. R. Weber, *Appl. Phys. Lett.* **70**, 1122 (1997).
21. S. huang, Doctoral dissertation "GaN-Based and High-Speed Metal -Semiconductor-Metal Photodetector : Growth and Device Structures for Integration", (2003).
22. H. Kang, S. Kandoor, S. Gupta, I. Ferguson, S. P. Guo, and M. Pophristic, *Phys. Stat. Sol. (c)* **2**, 2145 (2005).
23. R. Chierchia1, T. Bottcher, S. Figge, M. Diesselberg, H. Heinke and D. Hommel, *Phys. Stat. Sol. (b)* **228**, 403 (2001).
24. P. Visconti, D. Huang, M. A. Reshchikov, F. Yun, T. King, A. A. Baski, R. Cingolani, C. W. Litton, J. Jasinski, Z. Liliental-Weber, and H. Morkoc¸ *Phys. Stat. Sol. (b)* **228**, 513 (2001).
25. Y. Z. Chiou, Y. K. Su, S. J. Chang, J. Gong, Y. C. Lin, S. H. Liu, and C. S. Chang, *IEEE J. Quantum Electron*. **39**, 681 (2003).
26. G. Y. Xu, A. Salvador, W. Kim, Z. Fan, C. Lu, H. Tang, H. Morkoc, G. Smith, M. Estes, B. Goldenberg, W. Yang, and S. Krishnankutty, *Appl. Phys. Lett*. **71**, 2154 (1997).
27. S.Seo, K.K. Lee, S. Kang, S. Huang, W.A. Doolittle, N.M. Jokerst, A.S. Brown, *Appl. Phys. Lett.* **79**, 1372 (2001).
28. J.C. Carrano, T.Li, P.A. Grudowski, C.J. Eiting, R.D. Dupuis, and J.C. Campbell, *J. Appl. Phys.* **83**, 6148 (1998).
29. S.E Ralph, M. King, G. Namkoong, W.A. Doolittle, *2003 IEEE LEOS Annual Meeting Conference Proceedings* **2**, 652 (2003).
30. S. M. Madison, W. Henderson, G. Namkoong, K. M. Patel, W. A. Doolittle, and S. E. Ralph, *IEEE Lasers and Electro-Optic Soc. (LEOS)*, **1**, 232 (2004).
31. G. Namkoong, K.K. Lee, S. M. Madison, W. Henderson, W. A. Doolittle, and S. E. Ralph, *Appl. Phys. Lett.* **87**, 171107 (2005).
32. W. Saito, Y. Takada, M. Kuraguchi, K. Tsuda, I. Omura, T. Ogura, and H. Ohashi, *IEEE Trans. Electron Devices*, **50**, 2528 (2003).
33. Commercial crystal modeling program, Diamond TM version 2.1e, copyright 1996-2001 Crystal Impact GbR, Author Klaus Brandenburg.
34. R. Hsu, E. N. Maslen, D. du Boulay and N. Ishizawa, *Acta Cryst. B* **53**, 420 (1997).
35. A.M. Prokhorov, and Y.S. Kuzminov, "Physics and Chemistry of Crystalline Lithium Niobate", Institute of Physics Publishing, (1990).

36. R. S. Weis, T. K. Gaylord, *Appl. Phys. A (Solids and Surfaces)*, **37**,191 (1985).
37. R. G. Powell, N.E. Lee, Y.-W. Kim, and J. E. Greene, *J. Appl. Phys*. **73**, 189 (1993).
38. L.O. Svaasand, M. Eriksrud, G. Nakken and A.P. Grande, *J. of Cryst. Growth*, **22**, 230 (1974).
39. A. Saito, H. Matsumoto, S. Ohnisi, M. M. Akai-kasaya, Y. Kuwahara, and M. Aonom, *Jpn. J. of Appl. Phys*. **43**, 2057 (2004).
40. M. Yoshimoto, T. Maeda, T. Ohnishi, H. Koinuma, O. Ishiyama ,M. Shinohara, M. Kubo, R. Miura, and A. Miyamoto, *Appl. Phys. Lett*. **67**, 2615 (1995)
41. X. Gu, M. A. Reshchikov, A. Teke, D. Johnstone, H. Morkoc, B. Nemeth and J. Nause, *Appl. Phys. Lett*. **84**, 2268 (2004).
42. I.E. Kalabin, T.I. Grigorieva, L.D. Pokrovsky, D.V. Sheglov, D.I. Shevtsov, and V.V. Atuchin, *Opt. Comm.* **221**, 359 (2003).
43. Kyoung-Keun Lee, Gon Namkoong, W. Alan Doolittle, Maria Losurdo Giovanni Bruno, and Dieter H. Jundt, *J. of Vacuum Science & Technology B.* **24**, 2093 (2006).
44. G. H. Lee, *Opt. Lett*. **10**, 556 (2002).
45. http://www.sawyerresearch.com/Curie_Temp.htm
46. Simon Ramo, John R. Whinnery, and Theodore Van Duzer, "*Fields and waves in communication electronics*", John Wiley and Sons, New York, (1965).
47. U. Schlarb, S. Klauer, M. Wesselmann, K. Betzler, and M. Wöhlecke, *Appl. Phys. A* **56**, 311 (1993).
48. G. Namkoong, W.A. Doolittle, A.S. Brown, M. Losurdo, P. Capezzuto, and G. Bruno, *J. of Cryst. Growth*, **252**, 159 (2003).
49. K.M. Jones, P. Visconti, F. Yun, A.A. Baski, H. Morkoc, *Appl. Phys. Lett.* **78**, 2497 (2001).
50. X. Q. Shen, T. Ide, S. H. Cho, M. Shimizu, S. Hara, H.Okumura, S. Sonoda, S. Shimizu, *J. Cryst. Growth* **218**, 155 (2000).
51. M. J. Manfra, N. G. Weimann, J. W. P. Hsu, L. N. Pfeiffer, and K. W. West, and S. N. G. Chu, *Appl. Phys. Lett*. **81**, 1456 (2002)
52. A. J. Steckl and J. M. Zavada, *Materials Research Bulletin*, **24**, 33 (1999).

CHAPTER 12

III-NITRIDE LIGHT-EMITTING DEVICES ON PATTERNED SAPPHIRE SUBSTRATES

Dong-Sing Wuu and Wei-Kai Wang

Department of Materials Engineering, National Chung Hsing University
Taichung 40227, Taiwan R.O.C.

Ray-Hua Horng

Institute of Precision Engineering, National Chung Hsing University
Taichung 40227, Taiwan R.O.C.

Characterization of the GaN-based light-emitting diodes (LEDs) grown on patterned sapphire substrates (PSSs) using metalorganic chemical vapor deposition have been explored in this chapter. Dry and wet etching methods were developed to fabricate the PSSs. Conventional and flip-chip device configurations of the PSS-nitride LEDs were discussed. Further improvements in defect density and internal quantum efficiency of ultraviolet emitters can be achieved *via* a combination of epitaxial lateral overgrowth (ELOG) and PSS techniques. These results exhibit that the improved light extraction efficiency by PSS and the reduced dislocation density by ELOG have become the key technology in the high-efficiency solid-state lighting field.

1. Introduction

During the last few years, III-nitride compound semiconductors (e.g. GaN, AlGaN and InGaN) have attracted much attention because of their applications in high-brightness, high-efficiency light-emitting diodes (LEDs) in the green, blue and ultraviolet (UV) wavelength regions [1-3]. These devices have been extensively used in liquid-crystal-display backlight modules, full color displays, flashing lights of digital cameras and conventional traffic lamps [4, 5]. Nevertheless, further progress is

still strongly desired in order for these devices to reach efficiency levels achievable with other III-V material systems. The total external quantum efficiencies of GaN-based LEDs depend on the internal quantum efficiency and extraction efficiency. The improvement in epitaxial technology could lead to the enhanced internal quantum efficiency, while the light extraction efficiency required further optimization in the design of device geometry and packaging [6-8]. Currently, the white LEDs have been in high demand for the solid-state lighting and the most challenging application for white LEDs is as a replacement of conventional fluorescent lamps and light bulbs. The most common method for fabrication of white LEDs is to combine an yttrium aluminum garnet phosphor-coated with InGaN blue LEDs [9]. Such a 'yellow+blue' two emission band white LEDs have also encountered some problems. For example, the electroluminescence (EL) intensity of blue band increases rapidly than the yellow band under higher current injection levels. The EL peak position shift of blue emission also depends on the driven current density. Hence, the high color temperature and low color rendering index occurred in these 'yellow+blue' white LEDs.

To solve the low color-rendering-index problem, UV LEDs can be used as a pumping source for developing the white LEDs. Although the blue/green LEDs have been already commercially available by metalorganic chemical vapor deposition (MOCVD) since 1994, the fabrication of high-efficiency UV LED remains difficult [10-13]. The efficiencies of these UV LEDs are still quite low, especially for the emitting wavelength shorter than 350 nm. Furthermore, the UV LEDs are more sensitive to dislocation than blue GaN-based LEDs, as indicated from previous studies [14-18]. This is due to the fact that the minority carries in UV LEDs are easier trapped at threading dislocations (or non-radiative recombination centers) than the less localization state [19-21]. It is well known that a dislocation density in the order of 10^9-10^{11} cm^{-2} is inherent in the epitaxial GaN films on sapphire substrates due to the large lattice mismatch. High dislocation density will influence the device characteristics, such as device lifetime, electron mobility, and the quantum efficiency of radiative recombination. Therefore, how to further reduce the dislocation density becomes an important issue in fabricating high-performance UV LEDs.

Many different growth approaches have been attempted to alleviate the dislocation density problem. In this chapter, we propose a new approach for growing a high-quality GaN film using a patterned sapphire

substrate (PSS). This technique is expected to reduce the dislocations and increase the light extraction efficiency for the GaN-on-sapphire LEDs. The proposed method can reduce the dislocation density via a single growth process without any interruption and deposition onto the SiO_2 mask. It also eliminates the need for a precise photolithography process to transfer a special pattern axis and prevents the induced contamination. The experiments about the dry and wet etching processes of the PSS fabrication were described. The growth and characterization of near-UV InGaN-based LEDs grown on dry-etched (columnar) and wet-etched (pyramidal) PSSs have been investigated in terms of microstructure, etch pit density, light extraction efficiency, output power,….etc. The device performance of the high-power flip-chip GaN LED (chip size: 1 mm^2) onto PSS was also presented. Particularly, a 400-nm 1mm×1mm micropillar InGaN/Cu LED has been fabricated using a combination of PSS, laser lift-off and copper electroplating processes. Finally, we propose a new approach in the improvement of light efficiency by a combination of PSS and epitaxial lateral overgrowth (ELOG) techniques. The ELOG/SiO_2/GaN/PSS structure can reduce the defect density to a level of 10^5 cm^{-2}. Details of the electrical and optical properties of the ELOG GaN/PSS LED will be described.

2. Experimental Details

2.1. *Fabrication of dry-etched patterned sapphire substrates*

The dry etch of the sapphire substrate was performed in an inductively-coupled-plasma (ICP) etching system, which provides high-density and high ion current plasma at low pressures. Figure 12.1 shows a schematic diagram of the ICP etcher, which consists of a load-locked stainless-steel chamber, a process chamber and a susceptor assembly with backside He cooling. The copper coil linked to a 13.65 MHz RF power supply was wound the center of the ceramic chamber to generate high-density plasma. The dc bias voltage induced by the bottom RF power (13.65 MHz) was capacitively coupled to the substrate electrode to control the ion energy. The dc bias voltage refers to the dc component blocked from the RF generator using the capacitor impedance-matching networks. Various dc bias levels can be adjusted by controlling the applied bias power. The dry-etch PSS used in this study was 2-inch 430-μm-thick (0001) sapphire misoriented 0.2° off toward the (1-100). Prior to the

etching process, a 1-μm-thick nickel (Ni) mask layer was first deposited onto the sapphire substrate using an electron-beam evaporator. The hole dimension (diameter: 3 μm; spacing: 3 μm) was generated by a standard photolithography process. After etching, the patterned Ni mask was then removed to complete the PSS preparation process [22]. The bare PSS sample was prepared for using a periodic hole pattern with etching depths of 1.5 μm and sidewall angle of ~75° examined by field-emission scanning electron microscopy (SEM) as shown in Fig. 12.2.

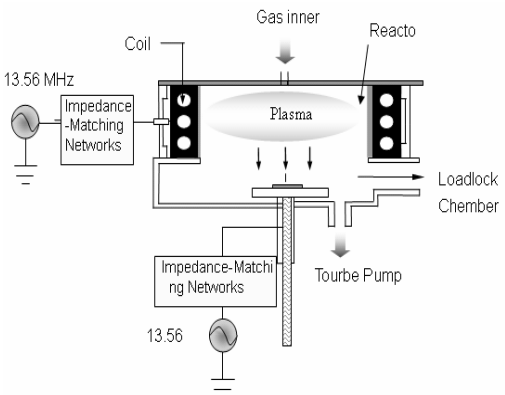

Fig. 12.1 Schematic diagram of the ICP etcher using in this study. The top and bottom RF power supplies (13. 56 MHz) can be adjusted independently.

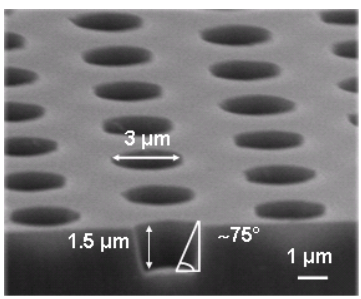

Fig. 12.2 SEM micrograph of bare PSS before MOCVD growth (from Wang et al. [22], reprinted with permission of ©2005 IEEE).

2.2. *Fabrication of wet-etched patterned sapphire substrates*

The wet-etched PSS used in this study was 2-inch 430-μm-thick (0001) sapphire misoriented 0.2° off toward the (1-100). A low-pressure-chemical-vapor-deposited SiO_2 layer was served as the wet etching mask. The pyramidal PSS was prepared using a periodic hole pattern with an etching depth of 1.5 μm. The pyramidal hole array (diameter: 3μm; spacing: 3μm) was generated using standard photolithography process. Two kinds of acid solutions were chosen: 98 wt% H_2SO_4 and 85 wt% H_3PO_4. A mixture of H_2SO_4:H_3PO_4 (3:1) solution was used to etch sapphire substrate at 280℃ [23]. Figure 12.3 shows the etching rate of sapphire at 280℃ as a function of the H_2SO_4:H_3PO_4 mixture ratio. It was found that the etching rate increased linearly when the H_2SO_4 volume

ratio increased from 0 to 75%. Since the etching process starts with the dissolution of the Al_2O_3 molecules into the acids as solvated Al^{+3} ions, the increase of the H_2SO_4 volume ratio will enhance the electrophilic attack of H^+ on the oxygen of Al-O-Al bridging moieties. Furthermore the increase of the H_2SO_4 volume ratio results in the decrease of the etching rate. It is well known that the H_3PO_4 acts as a buffer agent in this mixture; the conjugate phosphate anions are significantly more nucleophilic than the corresponding sulfate ions and both the $Al(H_2PO_4)_3$ and $AlPO_4$ have a high solubility in H_3PO_4. When the H_2SO_4 volume ratio increased above 75%, the insoluble product of the $Al_2(SO_4)_3$ and $Al_2(SO_4)_3 \cdot 17H_2O$ became more dominant, which limited the etching rate of sapphire [24].

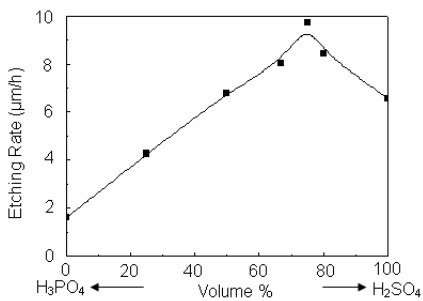

Fig. 12.3 Etching rate of (0001) sapphire at 280℃ as a function of the H_2SO_4:H_3PO_4 mixture ratio (from Wuu et al. [23], reproduced by permission of ECS-The Electrochemical Society).

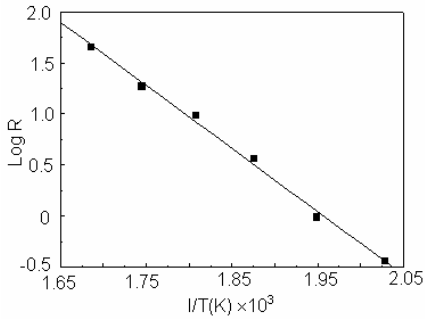

Fig. 12.4 A semi-log plot of *c*-sapphire etch rate as a function of reciprocal temperature using a $3H_2SO_4$:$1H_3PO_4$ mixture solution (from Wuu et al. [23], reproduced by permission of ECS-The Electrochemical Society).

To calculate the activation energy of this reaction, the etching rate of *c*-plane sapphire as a function of reciprocal temperature from 220 to 320℃ using a $3H_2SO_4$:$1H_3PO_4$ mixture solution was investigated and shown in Fig. 12.4. It is found that the etching rate can fit to a linear semi-log plot. The etching rate in micrometers per hole using a $3H_2SO_4$:$1H_3PO_4$ mixture solution can be given by Eq. (1)

$$\log R_{3H_2SO_4:1H_3PO_4} = \frac{-6.17\times10^3}{T} + 12.98 \quad , \tag{1}$$

where T is temperature Kelvin and the R the etching rate. The activation energy of this reaction can be calculated to be 28.2 kcal/mol. A similar result was also obtained by Dwikusuma et al. in their surface treatment report [24]. The evolution of the pyramidal PSS using a $3H_2SO_4$:$1H_3PO_4$ mixture solution at 280℃ under different etching times was examined by FESEM as shown in Fig. 12.5. The (0001) etching facet was first observed onto the sapphire substrate at 5 min [Fig. 12.5(a)]. As the etching depth increased, the (0001) facet decreased [Fig. 12.5(b)]. The sapphire was kept {11-2-k} facets until the pyramid formation [Fig. 12.5(c)]. The corresponding cross-section micrograph of the etched pyramid was shown in Fig. 12.5(d). Finally, the FESEM micrograph of the bare pyramidal PSS before MOCVD growth was shown in Fig. 12.5(e). The formation of the crystallographic pyramidal patterns during the wet etching process can be attributed to the configuration of surface atoms and bond structure [25, 26].

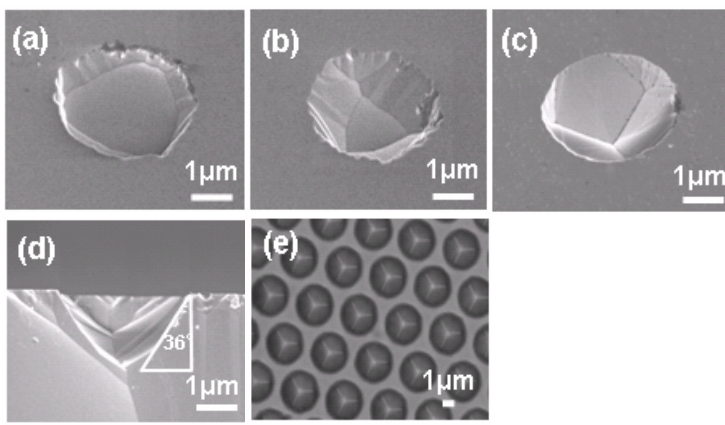

Fig. 12.5 Time-dependent etching evolution of (0001) sapphire substrate using a $3H_2SO_4$:$1H_3PO_4$ mixture solution at 280 ℃: (a) appearance of (0001) etching facet at 5 min, (b) (0001) facet decreased at 15 min, (c) disappearance of (0001) facet until pyramid formation at 25 min, (d) cross-section micrograph of pyramidal hole and (e) pyramidal patterned sapphire substrate with a an etching depth of 1.5 μm before MOCVD growth (from Wuu et al. [23], reproduced by permission of ECS-The Electrochemical Society).

3. Results and Discussion

3.1. *Characterization of nitride based LEDs grown on dry-etched patterned sapphire substrates*

Cross-sectional TEM measurements were performed to investigate the dislocation distribution of the GaN-on-PSS samples with various etching depth of hole (D_h) values. For comparison, the TEM micrograph of the GaN grown on a conventional sapphire substrate is also illustrated in Fig. 12.6(a). It can be seen clearly that a large number of extended threading dislocations (TDs) propagate throughout the GaN film, originating from the GaN/sapphire interface. The generation of these dislocations is caused by the large lattice mismatch between GaN and sapphire. For the sample grown on the PSS with $D_h = 0.5$ μm, the GaN epilayer buried the cavity incompletely and some small voids near the cavity edge were observed as shown in Fig. 12.6(b). These dislocations were generated randomly. For the sample grown on the PSS with $D_h = 1.5$ μm, the GaN epilayer grew laterally from the top of the sapphire substrate and some voids (0.5 μm in size) that formed when two growth front boundaries coalesced were observed on the pattern sidewall. Figure 12.6(c) shows the representative distributions of the 90° bending dislocations in the lateral growth region in the GaN-on-PSS ($D_h = 1.5$ μm) heterostructure. Evidence of dislocation reduction is also obtained from the etch pit density (EPD) measurements. The etching process was carried out in a H_2SO_4 and H_3PO_4 mixture with a 1:3 ratio at 250°C for 10 min. Figure 12.7 presents the EPD data as a function of the PSS D_h value. It was found that the EPD was around 1.1×10^9 cm^{-2} for the sample

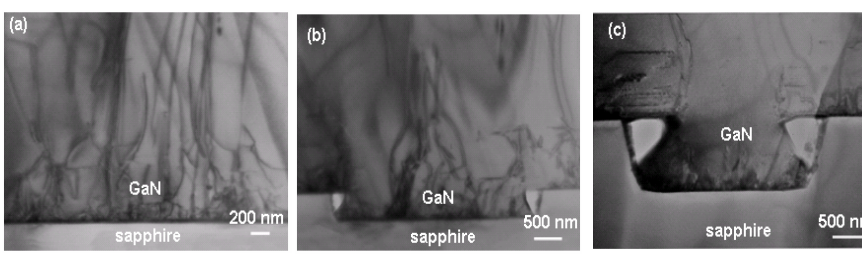

Fig. 12.6 Cross-section TEM image of GaN epilayer grown on (a) conventional sapphire substrate, (b) PSS with $D_h = 0.5$ μm, and (c) PSS with $D_h = 1.5$ μm. (from Wang et al. [22], reprinted with permission of ©2005 IEEE).

with $D_h = 0$ μm (i.e., conventional sapphire substrate) and decreased to 2.8×10^8 cm^{-2} for the sample with $D_h = 1.5$ μm. These results indicated that a reduction in the dislocation density was achieved via the lateral epitaxial overgrowth on the PSS without a SiO_2 mask.

Figure 12.8 shows the crystallinity of the GaN samples examined by double-crystal x-ray diffractometry (DCXRD). The average full-width at half maximum of the (0002) x-ray rocking curves of GaN films grown on PSS and conventional sapphire substrate were found to be 320 and 360 arcsec, respectively. The crystallinity improvement examined by

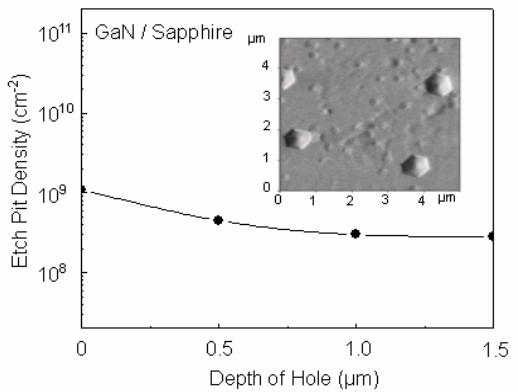

Fig. 12.7 Etching pit density of GaN as a function of PSS-D_h value. The inset shows the corresponding AFM image of the etch pit pattern.

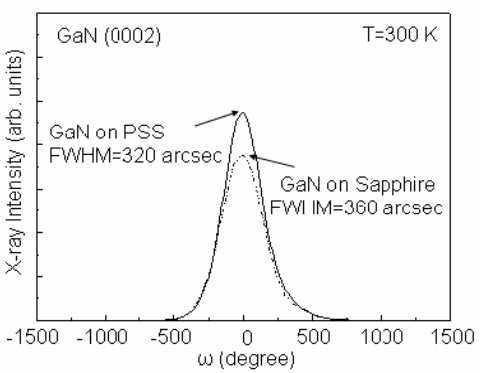

Fig. 12.8 X-ray rocking curves of (0002) reflections for GaN grown on PSS (D_h = 1.5 μm) and conventional sapphire substrate depths (from Wang et al. [22], reprinted with permission of ©2005 IEEE).

x-ray measurements also showed in good agreement with the result revealed by TEM observations.

Figure 12.9 shows the room-temperature photoluminescence (PL) intensity mapping obtained from the near-UV InGaN LED sample grown on a 2-inch sapphire substrate where there exist four zones with various etching depths (i.e., $D_h = 0$, 0.5, 1.0 and 1.5 μm). It was found that the PL peak around 3.07 eV (403 nm) increased remarkably as the D_h increased. At the $D_h = 1.5$ μm zone, the near-band-edge PL intensity is obviously stronger than that of the LED with $D_h = 0$ μm (conventional sapphire substrate). Such a significant enhancement in PL intensity due to the decreases of trap densities and the dislocation-induced nonradiative recombination centers indicates that the PSS can significantly improve the quality of GaN epilayers. It has been reported that the radiative recombination efficiency increases as the EPD decreases from 3×10^8 to 1.2×10^7 cm^{-2} and saturates at less than 1.2×10^7 cm^{-2} [27]. Our experimental results indicated that the EPD of the PSS LED is about 2.8×10^8 cm^{-2}. Hence, the improvement in PL intensity might also be related to the enhancement of the light extraction efficiency through light scattering from the nitride epilayer and the PSS interface. The value of D_h may play a more important role in the enhancement of optical properties of the near-UV InGaN/GaN LEDs.

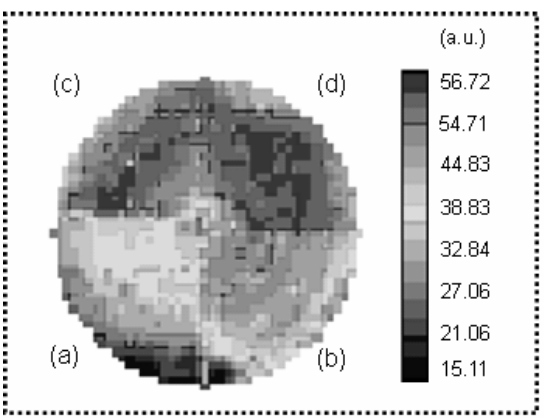

Fig.12.9 Room-temperature photoluminescence intensity mapping of PSS LEDs with various etching depths (from Wang et al. [22], reprinted with permission of ©2005 IEEE).

Figure 12.10 shows a Trace-Pro simulation profile of the ray extraction ratio rate take from the PSS InGaN LED as a function of the D_h value. Here a 1-mW power (50,000 light rays) is assumed to emit randomly from the InGaN/GaN MQW active layer; i.e. the spontaneous emission process. The output power can be calculated by collecting the light rays which hit the observation plane. It was found that there is up to about 70% higher light output at $D_h = 1.5$ μm as compared with that of the unpatterned structure ($D_h = 0$ μm). Moreover, the ray extraction ratio rate increased as the D_h increased and saturated when the D_h reached above 1.0 μm. These results indicate that the D_h has a large effect on the improvement of light extraction efficiency of the PSS LED. Since the PSS LED with $D_h = 1.5$ μm shows the best performance as evidenced by the TEM and PL mapping results, we only focus on the $D_h = 1.5$ μm samples in the following work. Moreover, the forward current-voltage (I-V) characteristics of the near-UV LEDs with and without PSS at room temperature were also investigated. Figure 12.11(a) presents the corresponding forward voltages at 20 mA were 3.83 and 3.84 V, respectively. This indicates that the PSS LED has similar I-V characteristic as compared with that of the conventional LED. Figure 12.11(b) shows the reverse I-V characteristics of both LEDs. The leakage currents of the PSS LED and conventional LED at a reverse voltage of

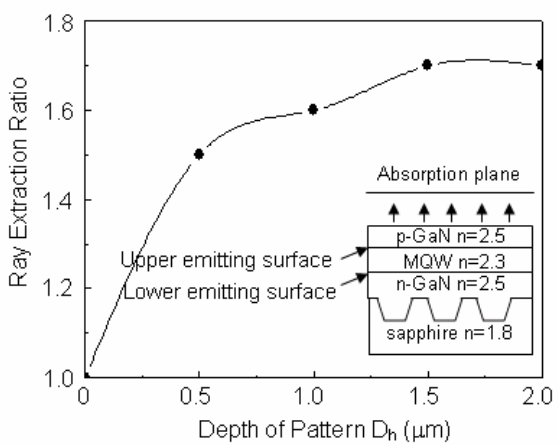

Fig. 12.10 Trace-Pro simulated EL intensity of PSS LED with various D_h values (from Wang et al. [22], reprinted with permission of ©2005 IEEE).

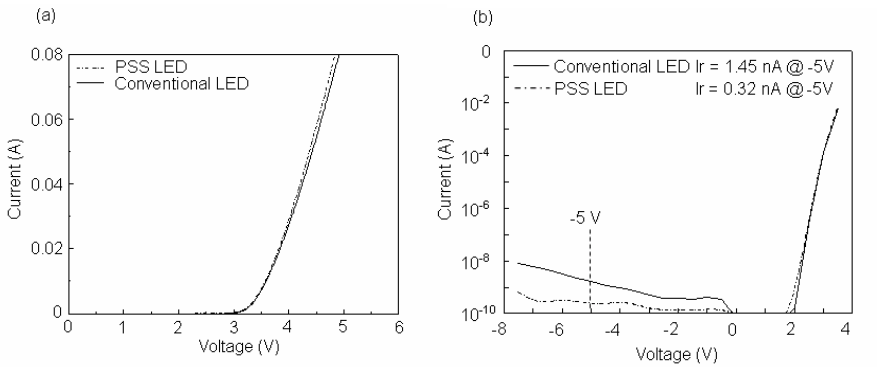

Fig. 12.11 (a) Forward and (b) reverse current-voltage characteristics of the near-UV InGaN LEDs with and without PSS (from Wang et al. [22], reprinted with permission of ©2005 IEEE).

5 V were around 0.32 and 1.45 nA, respectively. The reverse leakage current of the PSS LED was smaller than that of the conventional LED. The decrease in leakage current could be attributed to the elimination of TDs in the GaN film using the PSS.

In order to measure the LED output power, the chips were encapsulated in conventional lamp form (5 mm in diameter). The EL emission was measured from the LED top surface. Figure 12.12(a) shows the light output power of the conventional and PSS LEDs as a function of injection current. The output intensity of both LEDs initially increases linearly with the injection current. With a 20-mA forward injection current, the output power of a lamp-form PSS LED and conventional LED were estimated to be 10.4 and 8.6 mW, respectively. Figure 12.12(b) shows the external quantum efficiency (η_{ext}) of the InGaN LED sample with various forward injection currents up to 100 mA. It was found that the η_{ext} of the PSS LED reached a maximum value of 14.1% (@ 20 mA) and then decreased significantly with a further increase in the forward bias current. Nearly the same trend was also obtained for the conventional LED sample except for a lower peak value of η_{ext} (11.6% @ 20 mA).The degradation in η_{ext} at the higher injection level might be related to carrier saturation and/or the joule heating effect. The η_{ext} can be expressed as

$$\eta_{\text{int}} \times \eta_{lee} = \eta_{ext}, \tag{2}$$

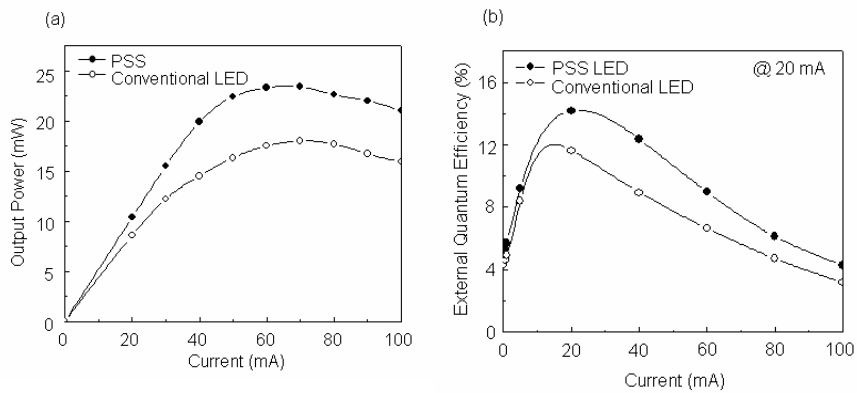

Fig. 12.12 (a) Light output power of the conventional and PSS LEDs as a function of injection current, and (b) External quantum efficiency of conventional and PSS (D_h = 1.5 μm) InGaN LEDs measured at various forward current injections (from Wang et al. [22], reprinted with permission of ©2005 IEEE).

where η_{lee} is the light extraction efficiency and the current injection efficiency is assumed to be 100%. The η_{lee} values of the conventional and PSS LEDs are estimated to be 32 and 37%, respectively. Clearly, the enhancement in η_{lee} plays a more important role in obtaining the higher η_{ext} value of the InGaN PSS LED.

To confirm the point of light extraction effect on PSS, the light output pattern of the PSS LED (@ 20 mA) was measured and shown in Fig. 12.13, where the chip was not encapsulated into epoxy. The light output pattern of the conventional LED is also depicted for comparison. It is clear from the results that the EL intensities obtained from the PSS LED were larger than those from the conventional LED in the near horizontal directions (i.e., small than ± 45°). The improvement in emitted light extraction efficiency is considered as a consequence of the light scattering by the PSS. A prime concern of the PSS LEDs is their reliability revealed by the lifetime test. Figure 12.14 shows the relative EL intensity of the conventional and PSS InGaN LEDs under a forward current of 20 mA at RT during the 1000-hr test. The relative EL intensity to the initial EL intensity is shown as a function of the aging time. It can be seen that the relative EL intensity exhibited the same degradation trend for both LEDs. The PSS LED presents a gradual degradation in the EL intensity with an 8% decrease after 24 h of the test. After 1000 h, the

EL intensity of PSS LED and conventional LED are decayed by 18 and 23%, respectively. The smaller decrease in the intensity of EL was observed in the LED sample having PSS, as compared with the conventional LED. This result suggests indicated that improvement of the EL intensity due to the decreases in trap densities and the TD-induced nonradiative recombination centers via grown on PSS. Even though, the PSS LEDs may still suffer the incomplete step coverage problem at the GaN/PSS interface, there is no evident difference in life time as indicated from our measurement results between the conventional and PSS LED samples.

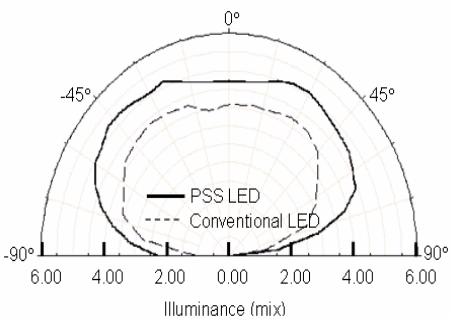

Fig. 12.13 Light output patterns of near-UV InGaN LEDs with and without a PSS. The forward current was driven at 20 mA (from Wang et al. [22], reprinted with permission of ©2005 IEEE).

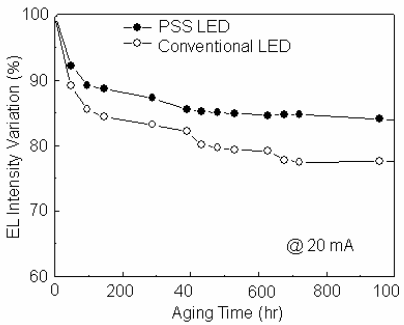

Fig. 12.14 Reliability test of relative EL intensity of conventional and PSS InGaN LEDs (D_h=1.5μm) driven at 20 mA and room temperature (from Wang et al. [22], reprinted with permission of ©2005 IEEE).

3.2. *Characterization of nitride-based LEDs grown on wet-etched patterned sapphire substrates*

A high magnification cross-sectional TEM measurement was performed so as to investigate the dislocation distribution of these samples. Figure 12.15 shows the TEM images of the GaN films on the pyramidal PSS. These dislocations did not subsequently propagate to the surface of the overgrown GaN layer. Hence, free standing laterally grown GaN films were achieved. Evidence of dislocation reduction in the GaN-on-PSS sample was obtained from the EPD measurements where the n-GaN epilayers were chemically etched in a $1H_2SO_4$:$3H_3PO_4$ mixture solution

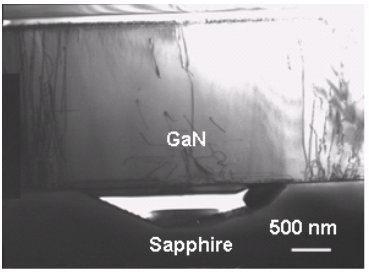

Fig. 12.15 Cross-section TEM image of a GaN layer grown on pyramidal PSS.

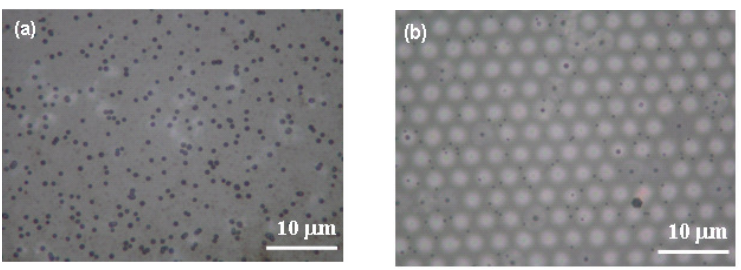

Fig. 12.16 Photographs of the n-GaN etch pits on a (a) conventional sapphire substrate and (b) pyramidal PSS (from Wuu et al. [23], reproduced by permission of ECS-The Electrochemical Society).

at 260°C for 15 min. The EPD was around 1.5×10^9 cm^{-2} for an n-GaN epilayer on a conventional sapphire substrate [Fig. 12.16(a)] and decreased to 2.3×10^8 cm^{-2} for the GaN-on-PSS sample [Fig. 12.16(b)]. This indicates that the dislocation reduction can be achieved via the lateral epitaxial overgrowth on a pyramidal PSS.

Figure 12.17 shows the room-temperature micro-photoluminescence (μ-PL) spectra from two regions designated A (epilayer on pyramidal hole) and B (epilayer on flat sapphire). It was found that the luminescence intensity of the on the A region was about 33% higher than that of the B region. The corresponding PL peak energies were 3.419 and 3.424 eV, respectively. The suspended GaN epilayer on the pyramidal hole is believed to be in smaller compressive strain and lower dislocation density, which resulted in a higher luminescence intensity and lower PL peak energy [28]. The red-shift of the PL in the GaN areas over the holes in the sapphire could be attributed to a relief of compressive stress in the

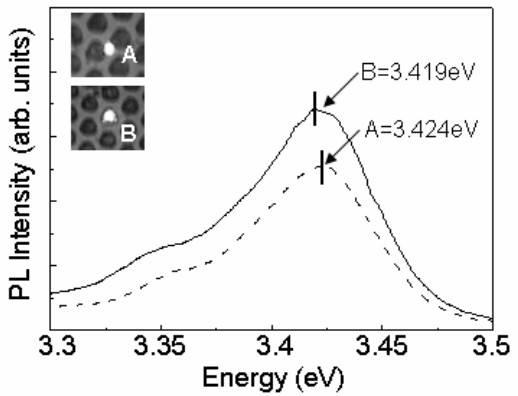

Fig. 12.17 Room-temperature μ-PL spectra of GaN-on-PSS sample from two regions designated A (epilayer on pyramidal hole) and B (epilayer on flat sapphire) (from Wuu et al. [23], reproduced by permission of ECS-The Electrochemical Society).

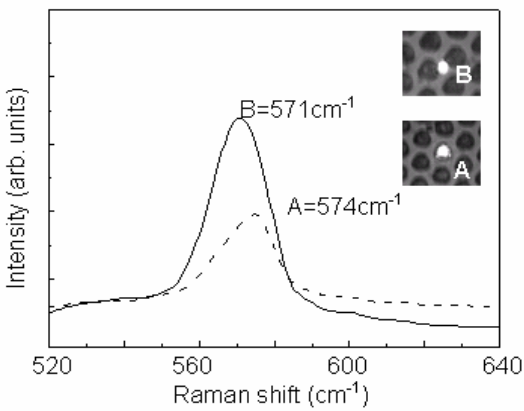

Fig. 12.18 Room-temperature micro Raman spectra of GaN-on-PSS sample from two regions A (epilayer on pyramidal hole) and B (epilayer on flat sapphire) (from Wuu et al. [23], reproduced by permission of ECS-The Electrochemical Society).

GaN. The compressive stress is induced during cooling due to the mismatch in the thermal expansion coefficients between GaN and sapphire. A reduced dislocation density will result in an increase of the total compressive stress at room temperature because dislocations are known to relax stress. The in-grown dislocations directly over substrates can be slightly relaxed stress but will be less relaxed over the hole due to

dislocation-free region. Further evidence from the micro Raman results also supports this point. Figure 12.18 shows the micro Raman spectra from the region A and B, corresponding to 574 and 571 cm^{-1}, respectively. The peak position shifts to lower frequency as a result of the compressive strain relaxation over the holes (region B) in the sapphire [29].

Figure 12.19 shows the light output power of the conventional and pyramidal PSS LEDs as a function of dc injection current. It can be seen that the output power of both LEDs increased linearly with the injection current up to 100 mA. Under a 20-mA forward injection current, the output power of the conventional and pyramidal PSS LEDs (in epoxy lamp form) were 7.45 and 9.35 mW, respectively. A 25% enhancement in output power can be achieved in the pyramidal PSS LED as compared with that of the conventional LED sample. We attributed the enhanced output power to a combination of improved light extraction efficiency and the reduction in dislocation density using a pyramidal PSS. The improved light extraction efficiency can be further supported by the Trace-Pro simulation data as shown in Fig. 12.20. Here a 10-mW power (5000 light rays) is assumed to emit randomly from the MQW active layer and the etching depth of the pyramidal hole in PSS is 1.5 μm. The maximum candelas values in both maps were 1.1 and 1.9 mW/sr for the conventional and pyramidal PSS LEDs, respectively. Although the simulation data did not consider the absorption in the epi-structure and the effect from the silver cup in the epoxy lamp form, the present

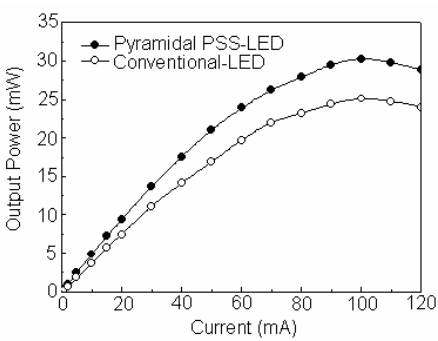

Fig. 12.19 Light output power (λ_D=400 nm) versus injection current for InGaN LEDs grown on conventional sapphire and pyramidal PSS. The insert shows pyramidal PSS-LED structure (from Wuu et al. [23], reproduced by permission of ECS-The Electrochemical Society).

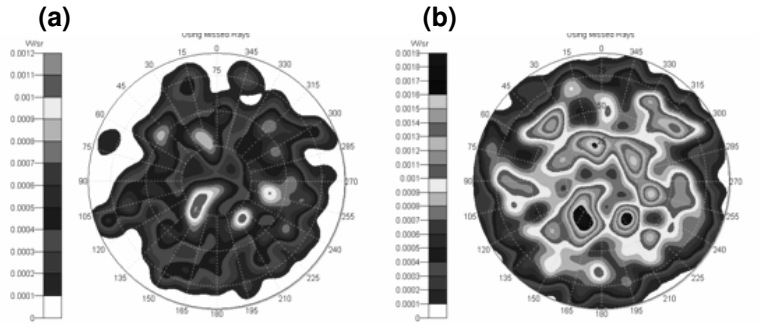

Fig. 12.20 Trace-Pro simulation of candela map taken from InGaN LEDs grown on (a) conventional sapphire substrate and (b) pyramidal PSS (from Wuu et al. [23], reprinted with permission of the Electrochemical Society).

simplified simulation can be used to explain the influence of the optical scattering in the pyramidal PSS. The pyramidal reflector array in the PSS can provide more probability of escaping photons from the GaN/sapphire interface, resulting in an increase in light extracting efficiency. Such a result was also reported by Sun *et al.* [30].

3.3. *Characteristics of flip-chip InGaN-based LEDs on patterned sapphire substrates*

The performance of the InGaN PSS LED (chip size: 1 mm×1 mm) with flip-chip package was discussed in this subsection [31]. The fabrication process of the near-UV PSS LED sample used in this study has been described in subsection 3.1. For the flip-chip structure, an additional 1-μm-thick Al reflective mirror was deposited on the p-contact. The flip-chip processing was ended with a defined Au-based interconnecting metallization on both the p and n contacts. Then the LED chip was soldered to a Si submount via the interconnecting metallization which served to both enhance light extraction from the chip as well as improve heat sinking. A schematic diagram of the PSS flip-chip LED structure is shown in Fig. 12.21. Also illustrated in this figure is an AFM image of the PSS after dry etching. Figure 12.22 presents the typical forward I-V characteristics of flip-chip InGaN LEDs fabricated on the PSS and conventional sapphire substrate at room temperature. It was found that the forward voltages of these LEDs at 20 mA dc current were 3.15 and

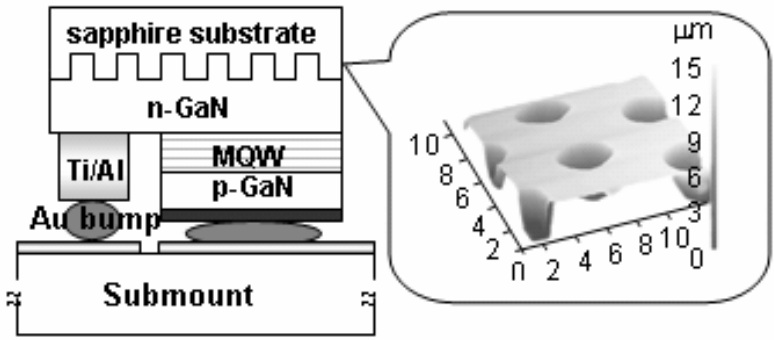

Fig. 12.21 Schematic diagram of near-UV flip-chip InGaN LED structure grown on a PSS. The AFM micrograph shows the PSS after dry etching (from Wang et al. [31], reprinted with permission of the Institute of Pure and Applied Physics).

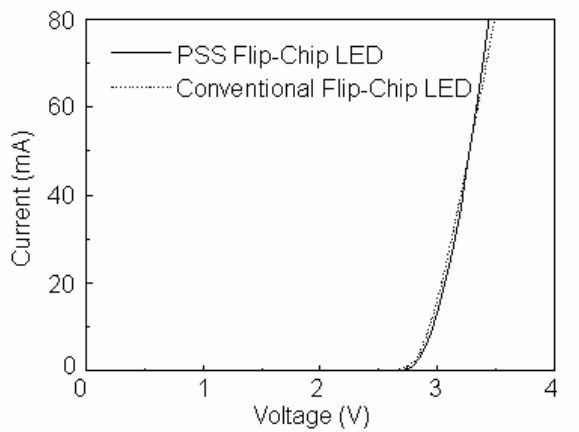

Fig. 12.22 Forward I-V characteristics of near-UV flip-chip InGaN LEDs samples with and without the PSS structure (from Wang et al. [31], reprinted with permission of the Institute of Pure and Applied Physics).

3.11 V, respectively. The corresponding EL spectra of the conventional and PSS flip-chip InGaN LEDs (@100 mA) are shown in Fig. 12.23. Both the EL peak positions were located at 425 nm, since the active layers in both LED samples were deposited under the same growth run. The EL intensity of the PSS flip-chip LED is indicated from a comparison with a conventional flip-chip LED as higher by about 43%.

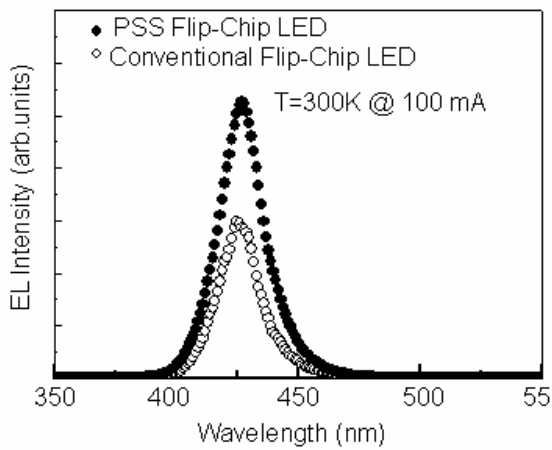

Fig. 12.23 Room-temperature EL spectra for the near-UV flip-chip InGaN LEDs (from Wang et al. [31], reprinted with permission of the Institute of Pure and Applied Physics).

Moreover, the emitted light scattering at the GaN/PSS interface has played a main role in enhancing the light extraction efficiency. However, when the dimple shapes are patterned on the sapphire surface, the propagation emission light can be scattered at the rugged sapphire surface. Notably, due to the output power of flip-chip LED was not measured from the standard flip-chip lamp form so the external quantum efficiency is low.

Figure 12.24 shows the light output power versus injection current curves of the conventional and PSS flip-chip InGaN LEDs as a function of the injection current up to 500 mA. The light output power was greatly increased by 59% for the PSS flip-chip LED (49.58 mW) as compared with that of the conventional flip-chip LED at a forward injection current of 350 mA. The significant enhancement in output power could be mainly attributed to the increase in extraction efficiency by scattering the emission light at the PSS/GaN interface. Figure 12.25 shows a Trace-Pro simulation profile, where the ray extraction ratio is take from the flip-chip InGaN LED with and without the PSS structure. Here a 10 mW power (50,000 light rays) was assumed to emit randomly from the InGaN/GaN MQW active layer; i.e. the spontaneous emission process. The output power can then be calculated by collecting the light rays which hit the observation plane. It was found that there was up to ~94%

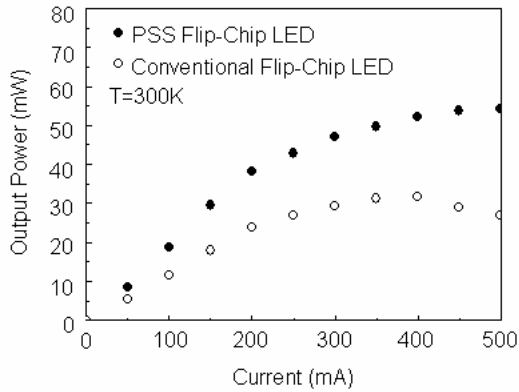

Fig. 12.24 Light output power as a function of injection current for the near- UV flip-chip InGaN LEDs with and without the PSS structure (from Wang et al. [31], reprinted with permission of the Institute of Pure and Applied Physics).

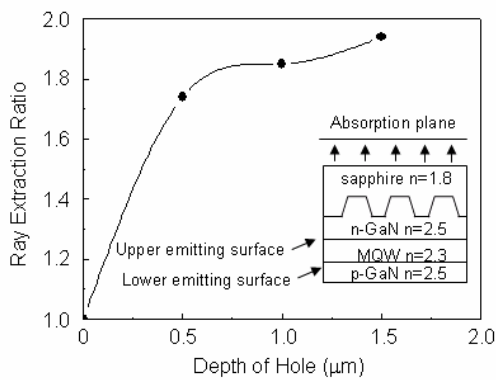

Fig. 12.25 Trace-Pro simulated ray extraction ratio of the flip-chip PSS LED with different etching depths (from Wang et al. [31], reprinted with permission of the Institute of Pure and Applied Physics).

higher light output power at an etching depth of 1.5 μm as compared with that of the conventional flip-chip LED. Moreover, the ray extraction ratio increased as the etching depth increased and saturated when the etching depth reached above 1.5 μm. For this reason, an optimum design of the PSS structure can considerably improve the light output efficiency in the flip-chip LED.

3.4. *Defect reduction and efficiency improvement of near-uv emitters via laterally overgrowth on GaN/patterned sapphire templates*

The great potential of wide-band-gap group III nitrides has been limited in many applications by the very high density of TDs that form when the nitride materials are grown on lattice-mismatched substrates. Particularly, the GaN LEDs operation in the UV region have been attracting more attention due to their practical applications such as flame detection, high-efficiency long-lifetime white lighting, decontamination and sterilization, air cleaner environmental sensor medical equipment, and high-density optical storage. In the past, different growth approaches have been proposed for TD reduction. ELOG is a commonly used technique utilizing MOCVD to reduce the TD density [32], where a GaN epilayer with several μm in thickness is first grown onto a sapphire substrate. Subsequently, a SiN_x or SiO_2 strip type mask is produced, followed by epitaxial growth. A double ELOG technique where a second-layer SiO_2 mask offset over the window regions was utilized to enable a very low defect density ($\leq 10^6$ cm^{-2}) GaN structure. However, this structure needs twice MOCVD regrowth process [33].Here we propose a new approach to improve the defect density and internal quantum efficiency of UV emitters using a combination of PSS and ELOG techniques [34]. Especially, a complementary dot array pattern corresponding to the underlying PSS was used for the ELOG-SiO_2 mask design. This structure needs only single MOCVD regrowth process. Details of the characteristics of the ELOG/SiO_2/GaN/PSS LEDs will be described.

The samples used in this study were all grown over 2 inch (0001) sapphire substrates by MOCVD. A schematic diagram of the near-UV InGaN LED structure is shown in Fig. 12.26(a). The wet-etched PSS was prepared using a periodic hole pattern (diameter: 3 μm; spacing: 3μm) with an etching depth of 1.5 μm. A mixture of H_2SO_4:H_3PO_4 (3:1) solution was used to etch the sapphire substrate at 280 ℃ where the SiO_2 layer was served as the etching mask. Figure 12.26 (b) shows a typical SEM micrograph of the wet-etched pyramidal PSS sample. The MOCVD GaN template with an initial thickness of ~3 μm was then grown on the wet-etched PSS. Following, a dielectric SiO_2 mask (~100 nm thick) was deposited on the GaN/PSS template where a dot array pattern offset over the underlying PSS was developed. Finally, the InGaN LED structure was grown upon the SiO_2/GaN/PSS template via the ELOG process. The LED structure consisted of a 1-μm-thick layer of undoped GaN, a 2-μm-

thick layer of n-type GaN: Si, a n-type $Al_{0.2}Ga_{0.8}N$/GaN layer, an MQW active layer, a p-type $Al_{0.2}Ga_{0.8}N$/GaN superlattice layer, a 0.2-μm-thick p-type GaN: Mg layer and a 3-nm-thick n^{++}-GaN tunneling layer. Finally, the LED wafers were thinned down to 100 μm for laser scribing. The LED sample used in this research had a chip size of 365 μm × 365 μm, fabricated using standard photolithography and dry etch techniques. The transparent indium-tin oxide layer and Ti-Al-Ti-Au were used as the p- and n-contacts, respectively. Note that the active layers in the conventional, PSS and ELOG-PSS LEDs were grown under the same growth run.

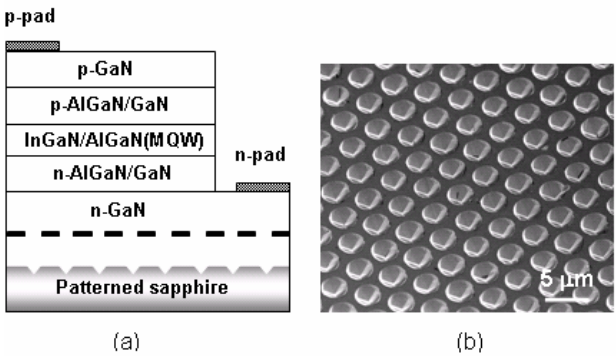

Fig. 12.26 (a) Schematic diagram of near-UV InGaN ELOG-PSS LED, and (b) SEM micrograph of bare wet-etched pyramidal PSS before MOCVD growth (from Wuu et al. [34], reprinted with permission of the American Institute Physics).

Figure 12.27(a) shows cross-sectional TEM micrograph of the InGaN ELOG/SiO_2/GaN/PSS LED structure. The MQW active region of the LED heterostructure is also shown in the inset of Fig. 12.27(b). It was found that the pyramidal pattern was not fully filled with the epilayer, where the GaN coalesced and laterally extended to from cantilever on the top of the pyramidal hole. Hence, free standing laterally grown GaN epilayer was achieved on the pyramidal PSS with small voids. For the GaN-on-PSS sample, above these voids the dislocations do seldom observed. These voids could be associated with the relaxed morphologies of the GaN film side faces and usually led to TD bending in the direction of these voids. Furthermore, it can be seen clearly that a large number of extended TDs propagate throughout the GaN film, originating from the GaN/sapphire interface. The generation of these dislocations is caused by the large lattice mismatch between GaN and sapphire. Fortunately, these

TDs can be terminated by the SiO_2 mask pattern (offset over the underlying PSS). In some active regions, there are almost free of TDs. A schematic diagram of the present TD reduction mechanism can be briefly illustrated in Fig. 12.27(b).

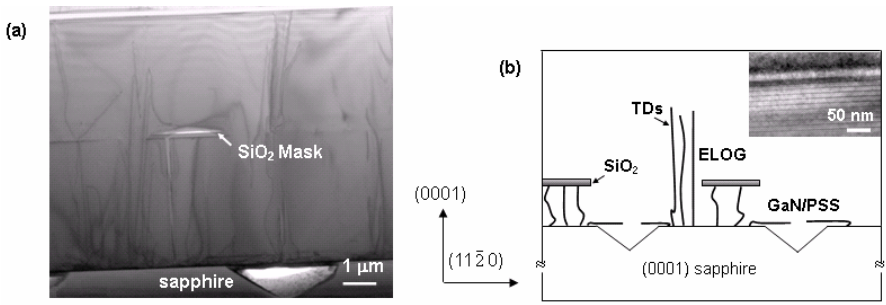

Fig. 12.27 (a) Cross-sectional TEM micrograph of near-UV InGaN ELOG-PSS LED heterostructure, and (b) schematic diagram of the reduction mechanism of threading dislocations in the ELOG-PSS structure. The MQW active region of this LED heterostructure is shown in the inset of this figure (from Wuu et al. [34], reprinted with permission of the American Institute Physics).

A prime concern about the ELOG/SiO_2/GaN/PSS samples is their defect reduction revealed by the EPD measurement. The etching process was carried out in a H_2SO_4 and H_3PO_4 mixture solution with a 1:3 ratio at 250°C for 10 min. Hexagonal shaped pits were observed on the etched GaN surface. The EPD micrographs of the GaN/sapphire and ELOG-PSS samples are shown in Figs. 12.28(a) and 12.28(b), respectively. The total GaN thickness in each sample was kept at 6 μm. Hansen et al. have suggested that the origin of the large size pits were both pure edge and edge-screw mixed dislocations [35]. The small pits were open-core dislocations (or nano-pipes). These etch pits might be produced by the TDs propagating to the top surface of the GaN, which originates from the underlying GaN/sapphire interface. Thus the dislocation density of the ELOG-PSS sample can be estimated to be approximately of 6×10^5 cm^{-2}, which is much less than that of the control sample (2×10^9 cm^{-2}).To clarify the influence of dislocation reduction on the LED quality, we estimated the internal quantum efficiency (η_{int}) of the InGaN LED sample roughly using the temperature dependence of the integrated EL intensity. As shown in Fig. 12.29, the integrated PL intensities of both

the conventional (GaN/sapphire) and ELOG-PSS LEDs were nearly constant below 100 K and declined gradually with a further increase in temperature. At room temperature, the η_{int} value (@ 20 mA) was about 4.3 and 13.8% for the conventional and ELOG-PSS LEDs, respectively. The significant reduction in defect density could contribute the present evident improvements in the η_{int} value.

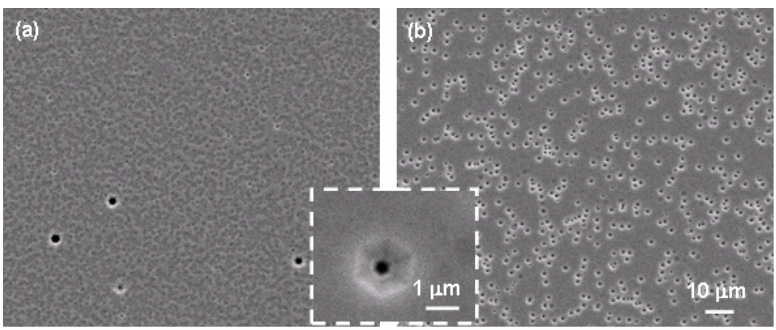

Fig. 12.28 Typical plane-view SEM micrographs of etch pit density in the wet-etched GaN surface for (a) ELOG-PSS and (b) conventional GaN/sapphire sample. The total GaN thickness in both samples was about 6 μm. An enlarged etching pit shape is also illustrated in the inset this figure (from Wuu et al. [34], reprinted with permission of the American Institute Physics).

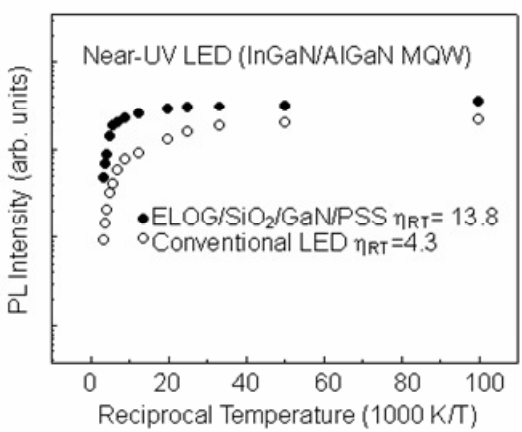

Fig. 12.29 Temperature-dependence of the arrhenius plots for InGaN/AlGaN MQW LEDs grown on ELOG-PSS and conventional sapphire templates. (from Wuu et al. [34], reprinted with permission of the American Institute Physics).

The PL integrated ratios of the near-band-edge emission to the yellow luminescence band (I_{BE}/I_{YL}) and the room-temperature PL FWHM can represent the optical quality of the GaN epilayer. Among the three structures, the ELOG-PSS sample has the strongest I_{BE}/I_{YL} emission ratio and the narrowest PL FWHMs. Figure 12.30 shows the room-temperature EL spectra of the conventional and ELOG-PSS LED samples under an injection current of 20 mA. Both the EL peak positions were located at 388 nm. The EL intensity of the ELOG-PSS LED shows ~30% higher than that of the conventional LED, where the corresponding FWHM was estimated to be approximately 12 and 11 nm, respectively. It is well known that the reduction of dislocation density could benefit the MQW emission efficiency. The improvement in PL intensity might also be related to the enhancement of the light extraction efficiency through light scattering from the nitride epilayer and the PSS interface. The inset of Fig. 12.30 demonstrates the forward I-V characteristics of the conventional and ELOG-PSS LED samples. Both LEDs have the similar I-V characteristics with the corresponding forward voltage (@ 20 mA) of 3.75 and 3.78 V, respectively.Note that the ELOG-PSS LED sample showed a smaller reverse leakage current (3.2 nA@ -5 V) than that of the conventional LED one (35 nA). The result correlates well with lower EPD data as described in Fig. 12.25, i.e. the significant reduction in defect density could contribute the lower leakage current level.

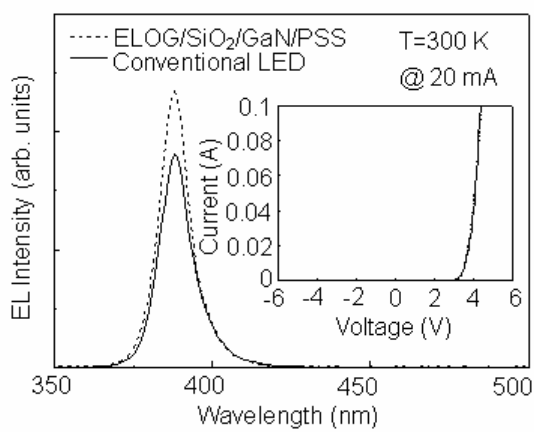

Fig. 12.30 Electroluminescence spectra of InGaN/AlGaN MQW LEDs grown on ELOG-PSS and conventional sapphire templates. The insert presents the I-V characteristics of both LEDs samples(from Wuu et al. [34], reprinted with permission of the American Institute Physics).

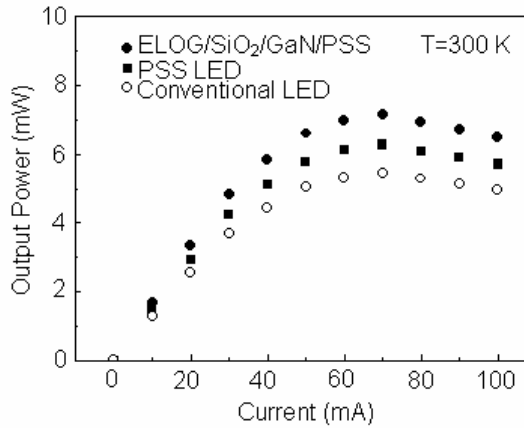

Fig. 12.31 Room-temperature *L-I* characteristics of InGaN/AlGaN MQW LEDs grown on ELOG-PSS, PSS and conventional sapphire templates (from Wuu et al. [34], reprinted with permission of the American Institute Physics).

Figure 12.31 shows the L-I characteristics of these LED samples. Here the LEDs chips were encapsulated in conventional epoxy lamp form (5 mm in diameter). It was found that the output intensity of these LEDs samples were linearly increased with the increase of the injection forward current until 60 mA and then saturated near 70 mA owing to the thermal heating effect. Under a 20-mA forward injection current, the output powers of ELOG-PSS, PSS and conventional LED samples were estimated to be 3.3, 2.9 and 2.54 mW, respectively. A 30% enhancement in output power can be achieved in the ELOG-PSS LED sample as compared with that of the conventional LED one. We attributed the enhanced output power to a combination of improved light extraction efficiency (by PSS) and the reduction in dislocation density (by ELOG). Based on the transmission-electron-microscopy and etch-pit-density results, the ELOG/SiO_2/GaN/PSS structure can reduce the defect density to a level of 10^5 cm^{-2}. Thus, in view of the fact that there only needs single MOCVD regrowth process, the presented ELOG-PSS structure can be used as a suitable growth template for high-quality UV emitters and has high potential for blue/green laser diode applications.

4 Conclusions and Outlook

In this chapter, we have described the characteristics of high-efficiency near-UV InGaN-based LEDs using the PSS technique. The PSS was

prepared using a periodic hole pattern on the (0001) sapphire substrate with different etching depths ranged from 0.5 to 1.5 μm. For the dry-etched PSS LED, the GaN epilayer grew laterally from the top of the sapphire substrate and overhung the trench. From the TEM and EPD studies, the use of dry-etched PSS with an optimum pattern etching depth (1.5 μm) was confirmed to be an efficient way to reduce the TDs in the GaN microstructure. The η_{ext} was estimated to be 21% higher measurement from the LED with dry-etched PSS at RT. We attributed the enhanced output power (21%) to a combination of improved light extraction efficiency and improvement the crystalline quality by the reduction in dislocation density using the dry-etched PSS. We also demonstrate the wet-etched pyramidal PSS to fabricate the near-UV LEDs, which can avoid surface damage induced by the dry etching process. A 25% enhancement in output power was achieved in the wet-etched pyramidal PSS LED as compared with that of the conventional LED sample. A preliminary result of the 425-nm flip-chip InGaN LEDs fabricated onto a PSS was also presented in this chapter. It was found that the output power was greatly increased by 59% for the PSS flip-chip LED sample at a forward injection current of 350 mA.

Moreover, the density of dislocations can be decrease from 2×10^9 to 6×10^5 cm^{-2} via laterally overgrown GaN on a GaN/patterned sapphire template. Experimental results indicated that the ELOG-PSS LED exhibited a 30% enhancement in light output power as compared with that of the conventional GaN/sapphire LED sample. The improvement can be attributed to the reduction of nonradiative recombination centers from a reduced dislocation density (~10^5 cm^{-2}) in the active layer. Based on our experimental results, the PSS technique is suitable for using particularly in the low and/or In-free high-efficiency, high-power UV optical devices.

Recently, the growth of III nitrides-based devices on the GaN substrate (i.e. bulk GaN) has received great attention because of their potential of low defect density epi-structures. However, the GaN substrate technique has encountered a serious problem in that the fabrication process becomes quite complicated, high material cost and the production yields of these devices are decreased. Therefore, the development of a direct epitaxial growth technique of III nitrides on GaN template is eminently required. One can apply the ELOG technique in reducing the TD density in the GaN films upon the GaN/PSS. The GaN film can be grown on PSS and then followed by ELOG of a GaN film on

GaN/PSS. It is conceivable that TD density reduction in the regrown GaN film deposited on GaN/PSS could be even more efficient than that in the case of a traditional ELOG GaN film deposited on a sapphire substrate. Unlike the previous double ELOG approaches, the presented ELOG-PSS structure needs only one regrowth process and will have high potential in future high-quality ultraviolet emitters, even blue/green laser diode applications. Hence, the future work is focused on the subject of ELOG GaN on GaN/PSS in fabrication of high quality UV emitters.

Acknowledgements

The authors would like to thank their co-workers K. S. Wen, S. H. Lin, S. C. Huang, S. Y. Huang, P. R. Lin, and T. E. Yu at NCHU (Taichung, Taiwan) for some of the results used in this chapter. They would also like to thank associate Prof. P. Han and assistant Prof. C. F. Lin at NCHU (Taichung, Taiwan) for their stimulating discussions. Valuable supports from Dr. Y. S. Yu and M. H. Pan at Wafer Works Corp. (Taoyuan, Taiwan) are acknowledged. Special thanks are due to Dr. T. C. Hsu, Donald T.C Hou and M. J. Jou at Epistar Co. (Hsinchu, Taiwan) for their interest and willing cooperation in MOCVD growth of LED samples.

References

1. S. Nakamura and G. Fasol, *The Blue Laser Diode: GaN Based Light Emitters and Lasers* (Springer, Berlin, 1997).
2. A. Zukauskas, M. S. Shur and R. Caska, *Introduction to Solid-State Lighting* (John Wiley & Sons, New York, 2002).
3. E. F. Schubert, *Light-Emitting Diode*, (Cambridge University Press, New York, 2003).
4. R. J. Xie, N. Hirosaki, M. Mitomo, K. Takahashi and K. Sakuma, *Appl. Phys. Lett*, **88**, 101104 (2006).
5. Y. D. Huh, J. H. Shim, Y. Kim, and Y. R. Do, *J. Electrochem. Soc*. **150**, H57 (2003).
6. R. H. Horng, C. C. Yang, J. Y. Wu, S. H. Huang, C. E. Lee and D. S. Wuu, *Appl. Phys. Lett*. **86**, 221101 (2005).
7. H. W. Choi, C. Liu, E. Gu, G. McConnell, J. M. Girkin, I. M. Watson, and M. D. Dawson, *Appl. Phys. Lett*. **84**, 2253 (2004).
8. S. X. Jin, J. Li, J. Y. Lin and H. X. Jiang, *Appl. Phys. Lett*. **77**, 3236 (2000).
9. H. W. Choi, C. W. Jeon, M. D. Dawson, P. R. Edwards and R. W. Martin, *J. Appl. Phys*. **93**, 5978 (2003).

10. J. Han, M. H. Crawford, R. J. Shul, J. J. Figiel, L. Zhang, Y. K. Song, H. Zhou and A. V. Nurmikko, *Appl. Phys. Lett*. **73**, 1688 (1998).
11. H. Hirayama, *J. Appl. Phys*. **97**, 091101 (2005).
12. T. Wang, G. Raviprakash, F. Ranalli, C. N. Harrison, J. Bai, J. P. R. David and P. J. Parbrook, J. P. Ao and Y. Ohno, *J. Appl. Phys*. **97**, 083104 (2005).
13. T. Mukai and S. Nakamura, *Jpn. J. Appl. Phys.* **38**, 5735 (1999).
14. Y. Narukawa, I. Niki, K. Izuno, M. Yamada, Y. Murazaki and T. Mukai, *Jpn. J. Appl. Phys.* **41**, L371 (2002).
15. Y. B. Lee, T. Wang, Y. H. Liu, J. P. Ao, Y. Izumi, Y. Lacroix, H. D. Li, J. Bai, Y. Naoi and S. Sakai, *Jpn. J. Appl. Phys.* **41**, 4450 (2002).
16. X. A. Cao, S. F.LeBoeuf, M. P. D'Evelyn, S. D. Arthur and J. Kretchmer, *Appl. Phys. Lett*. **84**, 4313 (2004).
17. T. Nishida, H. Saito and N. Kobayashi, *Appl. Phys. Lett*. **79**, 711 (2001).
18. D. D. Koleske, A. J. Fischer, A. A. Allerman, C. C. Mitchell, K. C. Cross, S. R. Kurtz, J. J. Figiel, K.W. Fullmer and W. G. Breiland, *Appl. Phys. Lett*. **81**, 1940 (2002).
19. J. Han, M. H. Crawford, R. J. Shul, J. J. Figiel, L. Zhang, Y. K. Song, H. Zhou and A. V. Nurmikko, *Appl. Phys. Lett*. 73, **1688** (2001).
20. S. Nakamura, and T. Mukai *Jpn. J. Appl. Phys.* **31**, Ll457 (1992).
21. S. Nakamura, S. J. Pearton and G. Fasol, *The Blue Laser Diode: The Complete Story, 2nd ed,* Springer, Berlin (2000).
22. W. K. Wang, D. S. Wuu, S. H. Lin, P. Han, R. H. Horng, T. C. Hsu, D. T. C. Huo, and M. J. Jou, Y. H. Yu, and A. Lin, *IEEE J. Quantum Electron.* **41,** 1403 (2005).
23. D. S. Wuu, W. K. Wang, K. S. Wen, S. C. Huang, S. H. Lin, R. H. Horng, Y. S. Yu, and M. H. Pan, *J. Electrochem. Soc.* **183**, G765 (2006).
24. F. Dwikusuma, D. Saulys, *J. Electrochem. Soc.* **149**, G603 (2002).
25. M. Kappelt and D. Bimberg, *J. Electrochem. Soc.* **143**, 3271 (1996).
26. K. C. Chou, K. Hsu, P. C. Teng, C. Hsu, T. Y. Chou, F. H. Kan and J. Y. Chu, *J. Chinese. Ceramic. Soc*. **27**, 727 (1999).
27. T. Hino, S. Tomiya, T. Miyaima, K. Yanashima, S. Hashimoto and M, Ikeda, *Appl. Phys. Lett*. **76**, 3421 (2000).
28. L. Macht, P. R. Hageman, S. Haffouz and P. K. Larsen, *Appl. Phys. Lett*. **87**, 131904 (2005).
29. D. Wang, S. Jia, K. J. Chen, K. M. Lau, Y. Dikme, P. van Gemmern, Y. C. Lin, H. Kalisch, R. H. Jansen, and M. Heuken,P. Puhl, *J. Appl. Phys*. **97**, 056103 (2005).
30. C. C. Sun, C. Y. Lin, T. X. Lee, and T. H. Yang, *Opt. Eng.* **43**, 1700 (2004).
31. W. K. Wang, D. S. Wuu, S. H. Lin, S. Y. Huang, P. Han, and R. H. Horng, *Jpn. J. Appl. Phys.* **45**, 3430 (2006).
32. Z. L. Weber and D. Cherns,Y. Hahn, *J. Appl. Phys*. **89**, 7833 (2001).
33. O. H. Nam, T. S. Zheleva, M. D. Bremser, R. F. Davis, J. Electron. Mater. **27**, 233 (1998).

34. D. S. Wuu, W. K. Wang, S. C. Huang, S.Y. Huang, S. H. Lin, C. F. Lin, and R. H. Horng, *Appl. Phys. Lett*. **89**, 161105 (2006).
35. P. J. Hansen, Y. E. Strausser, A. N. Erickson, E. J. Tarsa, P. Kozodoy, E. G. Brazel, and J. P. Ibbetson, *Appl. Phys. Lett*. **72**, 2247 (1998).

CHAPTER 13

BANDGAP ENGINEERING OF III-NITRIDE DEVICES ON LOW-DEFECT SUBSTRATES

Sergey Yu. Karpov

STR, Inc., P.O. Box 70604, Richmond, VA 23255-0604, USA
Soft-Impact, Ltd., P.O. Box 83, St.Petersburg, 194156, Russia
E-mail: karpov@semitech.us

State-of-the-art low-defect GaN and AlN substrates, including those cut out of bulk single-crystals, are considered in the chapter. They provide a much lower threading dislocation density in the on-grown III-nitride heterostructures than commonly employed sapphire or silicon carbide substrates. The native III-nitride substrates potentially enable an easy choice of the growth surface orientation to control the crystal polarity and, hence, the distribution of polarization charges in a device heterostructure. The impact of these factors on the bandgap engineering of advanced electronic and optoelectronic devices is discussed in the chapter in terms of simulation. The focus is made on light-emitting diodes, laser diodes, and high-electron mobility transistors, as the most important III-nitride devices.

1. Introduction

After first demonstration[1,2] of high-brightness blue light-emitting diodes (LEDs) in early 90th, group-III nitride semiconductors have become very soon the basic materials of visible/ultra-violet (UV) optoelectronics and high-temperature/high-power electronics. The III-nitride heterostructures for optical and electronic devices are conventionally grown on commercial sapphire and SiC substrates for more than a decade. Cheap sapphire substrates are quite suitable for large-scale production of planar low-power blue/green LEDs. In turn, rather expensive SiC substrates are employed in vertical low-power/high-power light emitters[3,4] and high-power

field-effect transistors (FETs) where an extremely high thermal conductivity of SiC is vital for effective thermal management in such devices[5]. As a compromise between the thermal conductivity and cost, silicon substrates have been recently applied to fabricate both optical[6] and electronic[7] devices.

To date, disadvantages of conventional sapphire, silicon, and SiC substrates have become, however, quite evident. First of all, a large mismatch in the lattice constants and thermal expansion coefficients (TECs) between sapphire and III-nitride materials[3,4] (see Table 1) leads to a huge, typically of ~10^9–10^{10} cm^{-2}, threading dislocation density (TDD) in heterostructures grown by various techniques, metalorganic vapor phase epitaxy (MOVPE) and molecular beam epitaxy (MBE). Both 6H-SiC and 4H-SiC have a much smaller lattice constant and TEC mismatch with GaN and AlN. However, a different crystal lattice arrangement and a microscopic roughness of a 6H/4H-SiC surface on the scale of a few atomic bilayers normally produces stacking-mismatch defects at the interface between SiC and III-nitride materials crystallizing in the form of a 2H-polytype[4]. As a result, TDD in III-nitride heterostructures grown on SiC substrates is usually less than in the case of sapphire substrates but still too high. The threading dislocations induce intensive nonradiative carrier recombination in LEDs and laser diodes (LDs), resulting in a low internal quantum efficiency of the devices[8-10], and accelerate

Table 1. Room-temperature physical properties of substrate materials compiled from Refs. 3,4,12-16 and other sources.

Material	In-plane lattice constant (Å)	In-plane TEC $\times 10^{-6}$ (K^{-1})	Thermal conductivity (W/cm·K)	Refractive index at 2.75 eV	Bandgap (eV)	Lattice mismatch with GaN (%)
Sapphire	4.765	5.4	0.25	1.77	> 8.0	–13.9
6H-SiC	3.081	4.3	4.9	2.71	3.00	–3.5
4H-SiC	3.073	4.1	3.7	2.72	3.23	–3.7
Si(111)	3.840[†]	2.6	1.5	3.42	1.12	+17.0
2H-ZnO	3.249	4.6	1.1	2.07	3.37	+1.9
2H-GaN	3.188	4.4	2.0	2.30	3.42	0
2H-AlN	3.112	3.3	3.3	2.15	6.20	–2.4

[†] Interatomic distance in the (111) plane is implied as an equivalent ***a***-lattice constant.

their degradation that is especially pronounced under high-current operation conditions[11]. Second, a remarkable difference in the refractive indices of sapphire (1.77) and III-nitride semiconductors (~2.15-2.90[12-14]) produces waveguiding of light emitted in an LED on sapphire substrate that lowers its light extraction efficiency. The waveguide effect is negligible in LEDs fabricated on SiC substrates due to absence of internal reflection. The substrates are, however, transparent mainly to visible light (see the materials bandgaps in Table 1), so that application of SiC substrates to near- and deep-UV LEDs becomes problematic. In order to overcome the light-extraction and some other problems, special technologies have been developed based on the substrate lift-off after growth of the LED heterostructures and patterning the outer surfaces of the devices[17,18].

In the case of electronic devices, FETs and Schottky diodes, a high TDD inherent in III-nitride materials grown on silicon, sapphire, or SiC substrates negatively affects the breakdown voltage, device reliability, and lifetime, producing additionally a greater noise in the FET structures[19]. It would be very tempting to substitute expensive insulating SiC substrates by fairly cheap silicon ones which are suitable for effective heat sinking from the active region of III-nitride FETs. Unfortunately, a large difference in TECs of GaN and silicon[8] and a still considerable TDD in the heterostructures grown on silicon substrates impedes the application of this substrate material.

A natural solution to the above problems is the use of substrates slightly mismatched with GaN and formed a stable 2H-polytype, i. e. ZnO, GaN, and AlN (see Table 1). Zinc oxide is found, however, to react chemically with gallium and exhibit a poor stability at typical epitaxy temperatures[20]. Thus native GaN, and AlN substrates remain the best choice to grow low-defect heterostructures. These substrate materials are complimentary rather than competitive. Being easily doped with silicon, GaN is quite suitable for fabrication of high-power LEDs and LDs operating in the visible and near-UV regimes[21-23]. In particular, TDD in III-nitride heterostructures on bulk GaN substrates has been demonstrated to be of ~10^4 cm^{-2}, which is sufficiently low to resolve problems related to the non-radiative carrier recombination and rapid device degradation[24]. In the case of deep-UV LEDs, operating at 250-300 nm, AlN substrates

seem to be more promising due to (i) their transparency to emitted light and (ii) a compressive strain in the epilayers grown on the substrates (for comparison, an AlGaN layer on GaN exhibits a tensile strain, frequently resulting in its cracking). Having a thermal conductivity close to that of 6H-SiC, and a high intrinsic resistance, AlN is apparently the best substrate material for high-power FETs. Even first FET heterostructures grown on bulk AlN have demonstrated a low TDD, ~10^5 cm^{-2}, and a considerable reduction in the leakage current of the transistor[19].

Spontaneous electric polarization and a strong piezoeffect are specific features of III-nitride heterostructures normally resulting in huge electric fields built-in in the structures grown in the (0001) direction[25]. The fields are believed to negatively affect the blue/green LED performance because of the radiative life-time reduction due to the quantum-confined Stark effect[26]. To avoid the impact of the polarization fields on device operation, one has suggested to fabricate non-polar or semi-polar LED structures (see, e. g., Refs.[27,28]). However, attempts of growing such heterostructures on alternative planes of sapphire and SiC substrates normally lead to a high density of dislocations (~10^{10} cm^{-2}) and stacking faults (~10^5 cm^{-1})[29,30]. This is likely caused by a combination of a large lattice mismatch between the substrates and III-nitride materials and easy slipping of edge dislocations with a minimum $\frac{1}{3}\langle 11\bar{2}0\rangle$ Burgers vectors in the basal planes of wurtzite semiconductors. With this respect, a proper cutting out of native substrates from the bulk AlN and GaN crystals would enable a defect density reduction and a straightforward control of the growth surface orientation for epitaxy of III-nitride heterostructures.

This study is aimed at a better understanding of a possible impact of low-defect substrates on bandgap engineering of III-nitride devices. The focus of the study is made on two principal problems mentioned above, the dislocation effect on III-nitride device performance and the role of crystal polarity in device operation. Special attention is given to the use of polarization doping in engineering of III-nitride heterostructures, as a tool for effective improvement of the device characteristics. Both polarization doping in heterostructures with abrupt interfaces and in graded-composition materials is considered. Since many aspects of the above

problems are not yet covered by detailed experimental investigations, numerical simulation is involved in the forthcoming analysis.

2. Low-Defect GaN and AlN Substrates

Commercial GaN and AlN substrates are presently unavailable. This is because of lacking growth technologies suitable for industrial production of bulk AlN and GaN crystals. Much progress has been recently made in the development of such growth techniques. In particular, sublimation growth of AlN bulk crystals of 20 mm long and 15 mm in diameter was demonstrated in Ref. 31. AlN wafers cut out of these crystals exhibited a dislocation density less than ~10^3 cm^{-2} and a high crystalline quality confirmed by X-ray difractometry[32]. The substrates were successfully used for the fabrication of UV LEDs[33] and high-electron mobility transistors (HEMTs)[19].

To date, high-pressure crystal growth from solution[34] remains the only reliable technique providing bulk GaN crystals of the size and quality fully acceptable for device fabrication[22,35,36]. In particular, TDD achieved in the bulk GaN grown at high pressure is currently as low as ~10^2 cm^{-2}. This method, however, is not quite suitable for a large-scale production of the true-bulk GaN wafers because of a low growth rate and poorly controlled crystal shape[37].

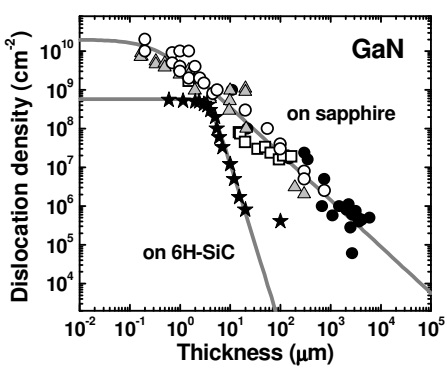

Fig. 1. TDD in a HVPE-grown GaN layer as a function of its thickness. Symbols are experimental data, borrowed from various sources, lines are approximations by Eq.(1).

An alternative approach to fabrication of low-defect III-nitride substrates is based on quasi-bulk materials (boules and thick epitaxial layers with reduced dislocation density) grown by hydride vapor phase epitaxy (HVPE). TDD in the GaN layers grown by this technique is found to depend remarkably on its thickness. Fig. 1 summarizes the data reported in different papers for the quasi-bulk GaN on sapphire[38-40] and 6H-SiC[41]. The data can be accurately approximated by the expression

$$N_d(d) = \frac{N_0}{1+(d/d_0)^\gamma} \ , \qquad (1)$$

where N_d is the threading dislocation density at a thickness d, N_0 is the dislocation density near the GaN/substrate interface, and d_0 is the parameter accounting for the rate of the dislocation density decay with thickness. For GaN grown on sapphire the approximation parameters read: $\gamma = 1.2$, $N_0 = 2.0 \times 10^{10}$ cm^{-2}, and $d_0 = 0.35$ μm. For GaN on 6H-SiC the parameters are estimated as: $\gamma = 4.2$, $N_0 = 5.8 \times 10^8$ cm^{-2}, and $d_0 = 4.0$ μm.

One can see from Fig. 1 that a TDD less than ~10^5 cm^{-2} can be only reached in the GaN layers on sapphire thicker than ~1 cm, i. e. actually in the bulk crystals. In the layers as thick as ~1 mm typically used for the quasi-bulk substrate fabrication the TDD is ~10^6 cm^{-2}. Such a TDD can be also obtained in the quasi-bulk GaN on 6H-SiC at a thickness of ~20 μm (see Fig. 1). However, frequently observed cracking of the material and still expensive initial SiC substrates hinder the development of quasi-bulk GaN on SiC. Recently AlN substrates grown by HVPE with TDD of ~5×10^8 cm^{-2} have been demonsrated[42], expanding the product range of the available quasi-bulk materials.

The fabrication technology of the quasi-bulk GaN substrates with TDD of ~10^6 cm^{-2} is still expensive because of the necessity to grow rather thick epitaxial layers. In order to reduce the cost, a number of companies offer the so-called templates, i. e. relatively thin, ~3-30 μm, GaN and AlN epilayers grown on conventional sapphire and SiC substrates by either MOVPE or HVPE. To reduce TDD in the templates, the epitaxial layers of typically 5-30 μm thick are normally grown by HVPE[42,43], while various epitaxial lateral overgrowth approaches[44,45] are employed in MOVPE, usually operating at noticeably lower growth rates.

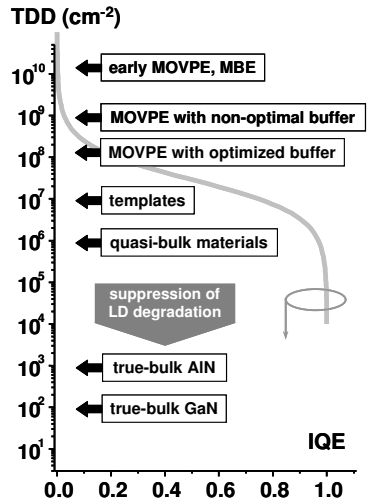

Fig. 2. TDD in III-nitride materials obtained by different approaches. Grey line is IQE of GaN as a function of TDD calculated for the non-equilibrium carrier concentration of 5×10^{17} cm^{-3} (after Ref. 10).

Minimum TDD of ~1-5 × 10^7 cm^{-2} is typically reported for the commercial templates, while the samples of special order have a reduced dislocation density of ~5 × 10^6 cm^{-2}. A wide range of doping variation is available in the templates, from insulating materials necessary for fabrication of electronic devices to heavy-doped semiconductors suitable for the use as spreading layers in LEDs and LDs.

Considerable progress in the quality improvement of III-nitride substrate materials made in recent years has provided a TDD reduction from ~10^{10} cm^{-2} typical of earlier stages of research down to ~10^7 cm^{-2} commonly reported for the commercial templates (see Fig. 2). This resulted, in particular, in an ever rising visible/UV LED efficiency and a lowering of the LD threshold current. The dislocation density reduction down to ~10^6 cm^{-2} by using quasi-bulk materials avoids the dependence of the internal quantum efficiency (IQE) of III-nitride semiconductors on TDD, as shown by grey line in Fig. 2. However, to suppress the degradation of high-power LEDs and LDs, further reducing of TDD is required, at least, an order of magnitude. This is apparently possible by employing substrates sliced from true-bulk GaN and AlN crystals.

3. Light-Emitting Diodes and Laser Diodes

Operation of LEDs and LDs is considered in this section by modeling with the focus on specific elements of heterostructure design and factors largely affecting the IQE of the devices. Simulation of the light emitters has been carried out with the SiLENSe 2.1 package implementing a drift-diffusion model of non-equilibrium carrier transport and a quantum-mechanical model of light emission[46]. The materials parameters used in the simulations have been chosen close to those recommended in Ref. 47.

3.1. *Factors controlling non-radiative carrier recombination in III-nitride heterostructures*

Among variety of factors affecting the IQE of III-nitride LED structures, TDD and operating temperature are found to be most critical. To illustrate this conclusion, let us consider a simple single-quantum-well (SQW) LED heterostructure consisting of an *n*-GaN contact layer ([Si] = 5×10^{18} cm^{-3}), a 3.5 nm *n*-$In_{0.2}Ga_{0.8}N$ SQW ([Si] = 3×10^{17} cm^{-3}), a 100 nm *p*-$Al_{0.2}Ga_{0.8}N$ emitter ([Mg] = 5×10^{19} cm^{-3}), and a *p*-GaN contact layer ([Mg] = 7×10^{19} cm^{-3}) 200 nm thick. The structure is similar to those reported in Refs. 48 and 49.

Figure 3 displays IQE of the SQW LED structure as a function of TDD and operating temperature computed for different values of the

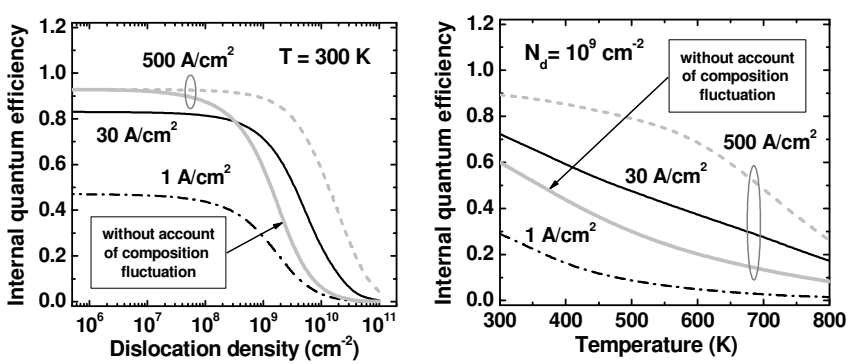

Fig. 3. Computed IQE of blue SQW LED as a function of TDD (left) and operating temperature (right). The Shokley-Read life times of both electrons and holes are assumed to be of 10 ns. See text for other detail.

current density. Both non-radiative carrier recombination on threading dislocations cores and point defects have been considered in the simulation within the model of Ref. 10 and standard Shokley-Read approach. Normally the dislocation-mediated recombination is partly suppressed due to composition fluctuations in InGaN. To account for this effect, the dislocation density in the InGaN SQW has been chosen an order of magnitude lower than in the surrounding layers[50]. At the current density of 500 A/cm^2, however, the compositional fluctuations are expected to be ineffective because of a higher carrier concentration in the SQW and the electron/hole spillover from the local In-rich regions. Thus the IQE computed with neglect of the composition fluctuation effect (also plotted in Fig. 3 by grey solid lines) seems to provide more reliable predictions. In particular, the computed IQE at TDD of 1-2 $\times$ 10^9 cm^{-2} and current density of 500 A/cm^2 is ~1.5-2 times lower than at the current density of 30 A/cm^2, the value typical of low-power LED operation. This result is in line with numerous observations demonstrating degradation of IQE at high currents through the diode.

It is seen from Fig. 3 that IQE of the SQW LED structure starts to decrease at TDD of ~10^7-10^8 cm^{-2}. This value is higher than in the GaN bulk (Fig. 1) due to a higher non-equilibrium carrier concentration typically observed in the InGaN quantum-well (QW). A rise of operation temperature also results in a remarkable IQE reduction. As the LED self-heating and electron/hole spillover from the local potential wells induced by compositional fluctuations become especially pronounced at high current densities, both factors are largely responsible for the observed LED efficiency degradation with current.

3.2. *Indium-free light-emitting diodes with a thick active region*

An active region of a blue/green LED is normally made of InGaN alloys which have a large lattice mismatch with the GaN contact layer. Therefore, it is possible to grow only thin, ~2-5 nm, InGaN epilayers without strain relaxation accompanied by generation of numerous misfit dislocations. In contrast, the use of thick active regions in indium-free LEDs becomes feasible[51,52]. The operation of such LEDs is much less sensitive to the quality of active region interfaces, polarization charges at the inter-

faces, and the current density in the diode. However, the carrier concentration in the thick active region is always lower than in a QW. Thus to get a high IQE, it is necessary to reduce the defect density in the device heterostructure. This has been attained by using either MOVPE growth of LED structures on grooved AlGaN buffer layer[51] or HVPE growth of rather thick GaN buffer[52], as it has been discussed in Sec. 2.

Consider specific operational features of such LEDs with reference to those reported in Ref. 52. The device heterostructure consists of a 6-8 μm *n*-GaN contact layer ([Si] = 7×10^{18} cm^{-3}) and a 0.2 μm *n*-GaN active region ([Si] = 1.5×10^{19} cm^{-3}) placed between 0.2 μm *n*-$Al_{0.22}Ga_{0.78}N$ ([Si] = 1.5×10^{19} cm^{-3}) and *p*-$Al_{0.22}Ga_{0.78}N$ ([Mg] = 1×10^{20} cm^{-3}) emitters. A 0.2 μm *p*-GaN contact layer ([Mg] = 1×10^{20} cm^{-3}) has been deposited on the top of the heterostructure.

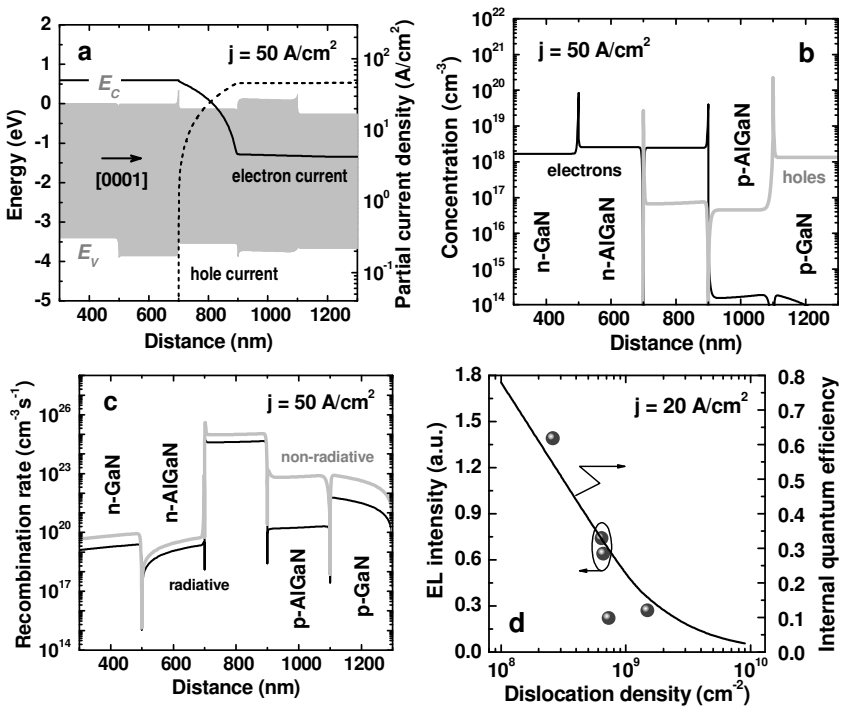

Fig. 4. Band diagram and partial electron/hole current densities (a), carrier concentrations (b), recombination rates (c), and correlation between EL intensity measured at 20 mA and IQE (d) of the indium-free LED with a thick active region reported in Ref. 52.

Figure 4 shows the simulation results obtained for the above LED structure (hereafter referred as the basic structure) operating at the current density of 50 A/cm^2. Under such conditions, the heterostructure provides a rather good carrier confinement in the active region where the light is mainly generated. The majority carrier concentrations in all the layers, including the active one, are controlled by the incorporated donors and acceptors rather than by the superinjection effect typical of QW active regions. Flat bands formed in the thick active region favor the emission spectrum stability.

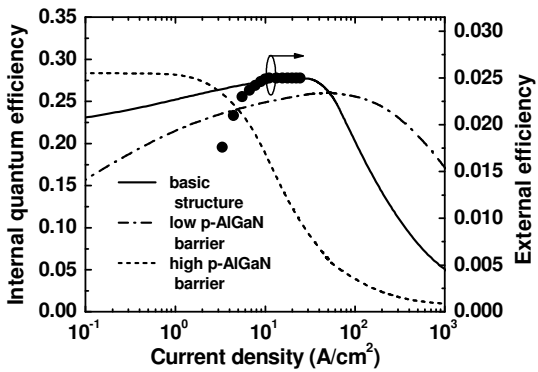

Fig. 5. IQE of the indium-free LED as a function of current density computed for the basic and modified heterostructures. Circles are the external efficiency of the basic structure reported in Ref. 52.

Fig. 4d demonstrates a strong dependence of the electroluminescence (EL) intensity upon TDD in the heterostructure estimated from the X-ray measurements[52]. The data are found to be in close correlation with the computed IQE of the LED structure.

The efficiency of the LED is found experimentally to be independent of the current density in the range of 6-25 A/cm^2. This is in line with the calculated IQE dependence on the current density plotted in Fig. 5 (basic structure). Further increase in the current density is predicted to result in the IQE degradation caused by the electron leakage from the active region (a slight imbalance between the electron and hole partial currents at the current density of 50 A/cm^2 can be already seen in Fig. 4a). A conventional way to suppress the electron leakage is increasing of the AlN

fraction in the *p*-AlGaN emitter aimed at creating a higher confining barrier. To check applicability of the approach to III-nitrides, a similar LED structure but different from the basic one by the *n*-$Al_{0.12}Ga_{0.88}N$ and *p*-$Al_{0.32}Ga_{0.68}N$ emitters has been simulated. It is quite surprising that the modified structure exhibits a higher electronic leakage as compared to the basic structure, resulting in the IQE degradation at much lower current densities (Fig. 5, high *p*-AlGaN barrier). In contrast, an LED structure with the opposite asymmetry, i. e. that implementing *n*-$Al_{0.32}Ga_{0.68}N$ and *p*-$Al_{0.12}Ga_{0.88}N$ emitters, provides effective leakage suppression and, subsequently, an IQE improvement at high current densities (Fig. 5, low *p*-AlGaN barrier).

The latter result shows that the carrier leakage is controlled not only by the conduction/valence band offsets at the active region interfaces, as in the case of conventional III-V compound heterostructures, but also by a particular distribution of the polarization charges in the whole structure. The utilization of this effect is considered below in Sec. 3.4.

3.3. *Effect of crystal polarity on light-emitting diode operation*

Distribution of polarization charges in III-nitride heterostructures is generally controlled by the crystal polarity and growth surface orientation[25]. The LED structures grown by MOVPE on sapphire in the [0001] direction normally exhibit a metal polarity, while the MBE grown materials may be of either metal or nitrogen polarity, depending on a particular procedure of growth initiation[4]. The crystal polarity of the structures on SiC substrates is largely dependent on the initial substrate polarity. Using the non-polar planes of both sapphire and SiC enables growing heterostructures free of the interface polarization charges[27,28]. In this section, operation of LEDs with different polarities is compared, since the polarity control can be easily performed by cutting out the substrates from the bulk GaN and AlN crystals.

We consider here an SQW LED structure different from that described in Sec. 3.1 by a thinner, 30 nm, *p*-AlGaN emitter. The polarity effect is taken into account by the choice of the respective sign of the interface charges or their vanishing in the case of a non-polar heterostructure. We will focus on high-current LED operation, neglecting

the effect of the InGaN composition fluctuations in a manner discussed in Sec. 3.1.

Figure 6 compares the band diagrams of the Ga-polar, N-polar, and non-polar SQW structures at the same current density of 500 A/cm^2. It is seen that both N-polar and non-polar LEDs provide a much better electron/hole confinement near the active region, suppressing the minority carrier leakage. This leads, in particular, to improvement of IQE at the current densities higher than ~4 kA/cm^2 (Fig. 6d). At lower current densities, the IQE of the non-polar structure is predicted to be slightly less than in the case of Ga-polar or N-polar structure.

The comparison of IQE of the heterostructures with different polarities shows that the non-polar structure has no evident advantages over

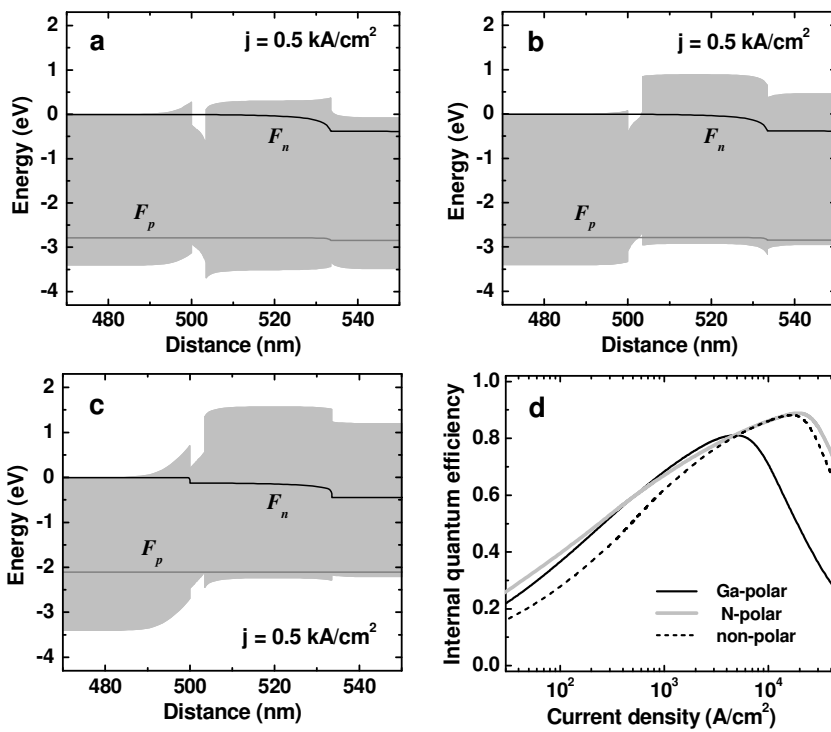

Fig. 6. Band diagrams of Ga-polar (a), N-polar (b), and non-polar (c) InGaN SQW LED structures and their IQEs as a function of current density (d). The electron and hole quasi-Fermi levels are denoted as F_n and F_p, respectively. Bandgap is shown by grey shadow.

the N-polar one from the point of view of carrier confinement and injection efficiency. This conclusion does not, however, take into account the reduction in the radiative recombination efficiency originated from the special separation of the electron and hole wave functions in the QW induced by the built-in polarization field in the N-polar structure. Understanding the role of the latter effect requires more elaborated investigations.

The impact of the crystal polarity on LED emission spectra is shown in Fig. 7. The spectra have been computed without account of the band-

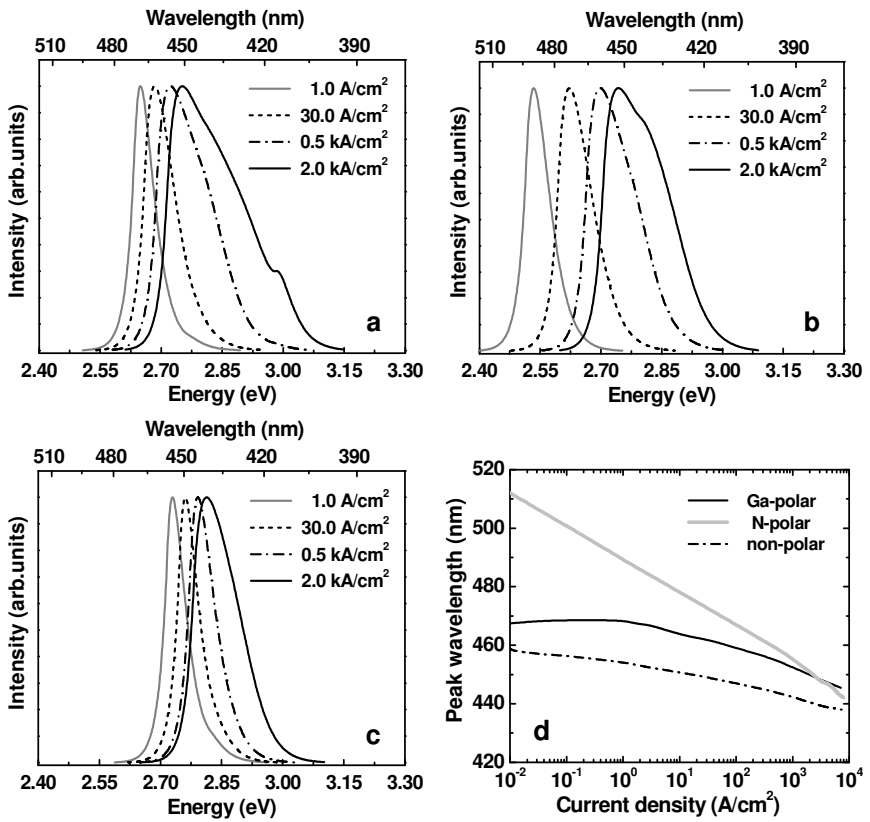

Fig. 7. Emission spectra of Ga-polar (a), N-polar (b), and non-polar (c) InGaN SQW LED structures and the peak wavelength as a function of current density. A uniform spectra broadening of 20 meV, typical of conventional III-V compound is assumed in the computations.

gap narrowing caused by the device self-heating at high operation currents. One can see that the non-polar structure provides a smaller spectrum width at a high current density. In all the heterostructures the spectrum broadening is caused by excitation of the upper hole levels in the quantum wells under high-current operation. In the non-polar structure, however, the ground-state electron wave function turn out to be nearly orthogonal to the upper-state hole wave functions, so that the contribution of the excited hole states to the emission spectrum is insignificant.

Both Ga-polar and non-polar structure provide comparable blue shifts of the emission spectra with current, while the N-polar LED exhibits a much worse wavelength stability. This is due to the fact that the *p-n* junction electric field and the built-in polarization field are co-directed in the N-polar LED, and the quantum-confined Stark effect is especially pronounced in such a structure[53].

A similar analysis carried out for multiple-quantum-well (MQW) LED structures has shown that the polarity effect on IQE manifests itself much weaker than in the case of SQW LEDs. This is due to a lower sensitivity of an MQW LED operation to a particular design of the *p*- and *n*-emitters. The dopant ionization in the MQW barriers and the carrier transport between the individual wells become the factors more critical for the device performance.

3.4. *Carrier confinement in the laser diodes*

The threshold current density in III-nitride LDs varies typically in the range of ~3-10 kA/cm^2. Therefore, carrier confinement in the active region becomes a very important issue for the LD heterostructure engineering. In addition, a reduced defect density is required to lower the threshold current of the LDs, as discussed in Sec. 1. These aspects will be considered in this section with reference to an InGaN LD fabricated on a true-bulk GaN substrate[22,54].

The LD heterostructure consists of an *n*-GaN buffer layer, a 0.66 μm *n*-$Al_{0.08}Ga_{0.92}N$ cladding layer, a 140 nm *n*-GaN waveguide layer, a five undoped 4 nm $In_{0.1}Ga_{0.9}N$ QWs separated by 8 nm *n*-$In_{0.04}Ga_{0.96}N$ barriers, a 10 nm *p*-$Al_{0.3}Ga_{0.7}N$ electron blocking layer (EBL), a 70 nm *p*-GaN waveguide layer, followed by a 0.42 μm *p*-type short-period superlattice

(SPSL) cladding layer with the mean composition close to $Al_{0.08}Ga_{0.92}N$, and a 50 nm *p*-GaN contact layer. The EBL is used in the structure to prevent the electron leakage normally occurring at a high current density in the device (see, for instance, Sec. 3.2 and Sec. 3.3). The donor concentration in the *n*-type layers of 5×10^{18} cm^{-3} and the hole concentration of ~5×10^{18} cm^{-3} measured in a reference $In_{0.01}Ga_{0.99}N$:Mg sample have been reported in Ref. 54.

Figure 8 present the simulation results obtained for the above LD structure. One can see that a distinct electron leakage occurs in the heterostructure despite the inserted EBL. The higher the current density, the

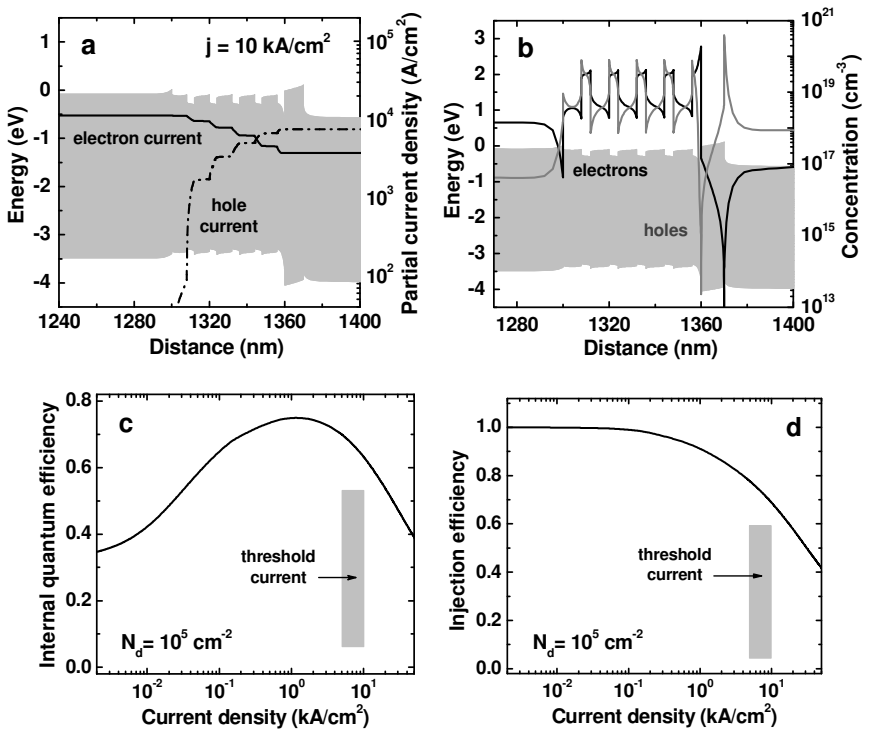

Fig. 8. Band diagram and partial electron/hole current densities (a), carrier concentrations (b), IQE (c), and injection efficiency (d) of the InGaN LD on GaN substrate reported in Refs. 22 and 54. Grey regions in (c) and (d) indicate the range of threshold current density variation. The Shokley-Read electron and hole life times of 10 ns are assumed in the simulations.

more intensive is the leakage, which is clearly seen in Fig. 8d. This effect is responsible for the predicted theoretically ~20-25% IQE degradation at the threshold current (Fig. 8c). In turn, the IQE reduction should lead to an increased LD threshold current.

That a LD heterostructure suffer from insufficient carrier confinement near the active region, is a specific feature of the high-current LD operation. This conclusion is also supported by simulations of a near-UV LD reported in Ref. 55. The LD structure contains in order: a 4 μm *n*-GaN contact layer, a 100 nm *n*-$In_{0.02}Ga_{0.98}N$ compliance layer, a 0.8 μm *n*-type SPSL cladding layer with the average composition equivalent to $Al_{0.12}Ga_{0.88}N$, a 100 nm *n*-$Al_{0.06}Ga_{0.94}N$ waveguide layer, an active region comprised of five 3.5 nm $In_xGa_{1-x}N$ QWs separated by 7 nm $In_{0.01}Al_{0.16}Ga_{0.83}N$ barriers, a 20 nm *p*-$Al_{0.3}Ga_{0.7}N$ EBL, a *p*-$Al_{0.06}Ga_{0.94}N$ waveguide layer 100 nm thick, 0.5 μm *p*-type SPSL cladding layer with the average composition equivalent to $Al_{0.12}Ga_{0.88}N$, and, finally, a 50 nm *p*-GaN contact layer. The InN fraction x in $In_xGa_{1-x}N$ was varied from 0.002 to 0.027, providing the oscillation wavelength from 363 to 375 nm. The LD heterostructure has been grown on sapphire substrate, though it is quite suitable for fabrication on a low-defect GaN substrate. Thus the TDD of 10^9 cm^{-2} is assumed in simulation of the LD. As the doping of the heterostructure has not been reported in Ref. 55, we assume the cladding and waveguide layers of *n*-type to be doped up to the donor concentration of 5×10^{18} cm^{-3} and the respective layers of *p*-type to be doped with the acceptor concentration of 1×10^{19} cm^{-3}.

Figure 9d plots IQE of the LD as a function of current density. The IQE peaks at ~320 A/cm^2 and approaches ~8.5% . This value is about an order of magnitude lower than the IQE of the violet LD considered above. There are two reasons for the low IQE: (i) a considerably higher TDD in the heterostructure grown on sapphire substrate and (ii) a much more pronounced electron leakage over the EBL barrier in the UV LD.

It has been shown in Sec. 3.2 that the carrier leakage in a III-nitride heterostructure is influenced not only by the band offsets at the active region interfaces but also by a particular distribution of the polarization charges in the whole structure. Here, an approach to improvement of the LD performance will be demonstrated based on the use of distributed polarization doping in graded-composition materials. The feasibility of

the approach has been recently justified with reference to III-nitride FETs[56] but, to our knowledge, there is no reported application of the approach to optical devices.

Consider an alternative design of the EBL in the UV LD structure that implies the use of a graded-composition p-$Al_xGa_{1-x}N$ with the AlN molar fraction linearly varied either from 0.1 to 0.5 (graded up structure) or from 0.5 to 0.1 (graded down structure). Such a composition grading keeps the same an integral AlN content in the EBL. Fig. 9a-c compares the band diagrams and the partial electron/hole currents in the initial and modifies LD structures. It is seen that the graded down heterostructure provides a considerable suppression of the electron leakage despite the fact that a pooling built-in field is formed for electrons in the graded-composition EBL. As a result, a more than four-fold improvement in IQE of the graded down heterostructure is predicted. A possible interpre-

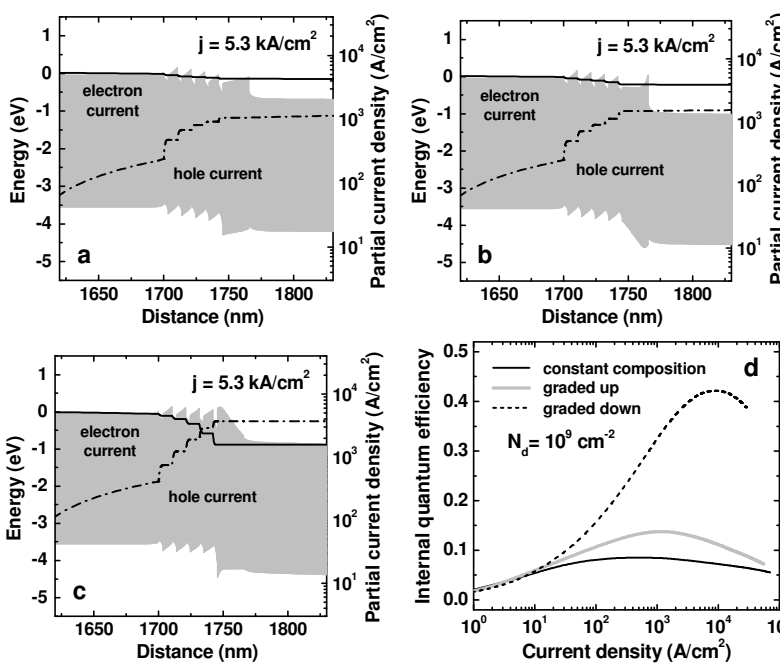

Fig. 9. Band diagrams of the LD reported in Ref. 55 with EBL of constant composition (a), graded up (b), and graded down (c). IQE of the LDs with different EBL designs *versus* current density. Bandgap is shown by grey shadow.

tation of this effect is that a larger conduction band offset between the QW and EBL combined with a negative distributed polarization charge in this layer hinder the electron penetration into the *p*-type region of the heterostructure thus providing improvement of the carrier confinement and IQE.

4. Field-Effect Transistors

In this section, we consider operation of III-nitride HEMTs, the devices coming recently to industrial production. Simulation of the HEMT heterostructures has been carried out by the FETIS 2.0 software combining a coupled solution of the Poisson and Schrödinger equation to find the band diagram of the transistor with the gradual-channel approximation to predict the device characteristics[46]. The same materials properties as in the case of LEDs and LDs have been used in the simulations.

4.1. *Threading dislocation effect on two-dimensional electron mobility*

Effect of threading dislocations on the performance of III-nitride HEMTs is not straightforward. Among variety of mechanisms critical for the carrier transport, the electron scattering on dislocations does not limit its mobility at room temperature. In contrast, the carrier scattering by optical phonons, the alloy scattering in the AlGaN cap layer, and the scattering at the rough AlGaN/GaN interface are the principal mechanisms limiting the mobility of two-dimensional electrons in a conventional HEMT heterostructure consisting of a thick GaN layer followed by a 20-30 nm AlGaN cap[57-59]. On the other part, spiral growth induced by threading dislocations and columnar structure formation are typical of group-III nitride epitaxy on conventional substrates, while a distinct step-flow growth is realized in the epitaxy on true-bulk GaN[60]. The step-flow growth mode manifests itself, first of all, via dramatic reduction of the AlGaN/GaN interface roughness when growing HEMT heterostructures on low-defect substrates. In particular, a record room-temperature two-dimensional electron mobility of ~2000-2500 $cm^2/V{\cdot}s$ corresponding to

the sheet concentration of 2×10^{12}–1×10^{13} cm^{-2}, has been demonstrated in a HEMT fabricated on the native GaN substrate[36,60].

4.2. *Polarization dipoles in transistor heterostructures*

Further mobility improvement can be attained by reducing alloy scattering in the AlGaN cap normally contained in a HEMT heterostructure. For this purpose, an incorporation of a thin, ~1-2 nm, pseudomorphic AlN layer between the GaN layer and the AlGaN cap is quite helpful. First, AlN separates the electron wave functions from the AlGaN alloy,

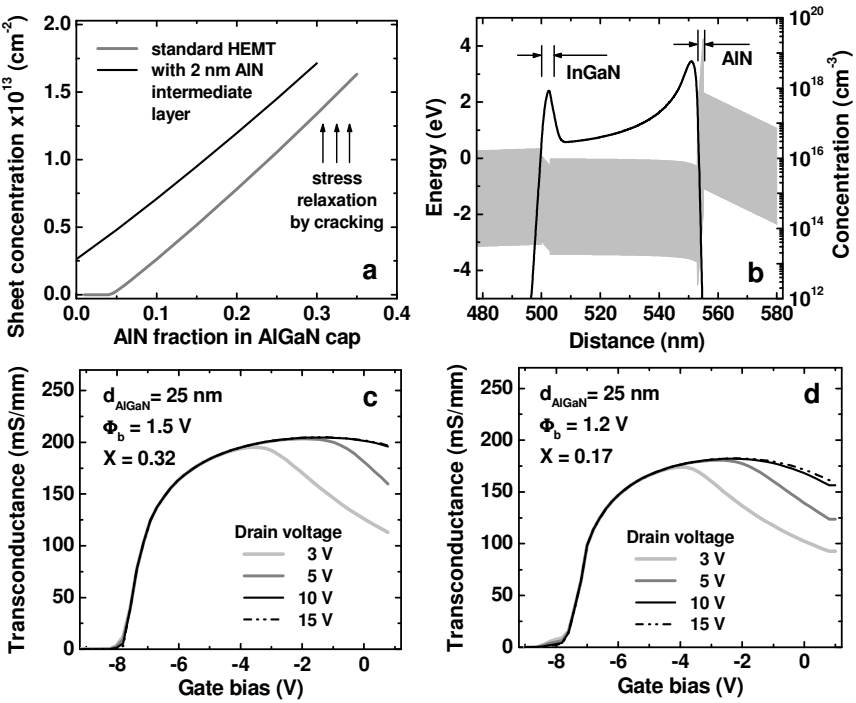

Fig. 10. Sheet electron concentration of standard unintentionally doped HEMT heterostructure with and without AlN intermediate layer (a). Band diagram and electron charge density (effective electron concentration) in GaN/AlN/GaN/InGaN/GaN HEMT structure (b). Transconductance of the standard $Al_xGa_{1-x}N$/GaN structure with $x = 0.32$ (c) and that of the structure with two polarization dipoles ($Al_xGa_{1-x}N$/AlN/GaN/InGaN/GaN, $x = 0.22$) (d).

reducing the alloy scattering and improving the carrier mobility[61]. Second, the AlN layer represents the so called polarization dipole that effectively shifts up the conduction band in the AlGaN cap[62]. Figure 10a compares the computed sheet electron concentration as a function of the alloy composition in a standard 25 nm AlGaN/GaN HEMT heterostructure with and without a 2 nm AlN intermediate layer. One can see that the AlN layer increases the electron concentration in the channel, in addition to the mobility improvement. This allows lowering of the AlGaN cap composition, keeping unchanged the electron sheet concentration, thus avoiding the cap cracking frequently observed at a high AlN fraction in the cap alloy[63].

The polarization dipole, as an element of the heterostructure design, is also used for solution of one more problem related to engineering of III-nitride HEMTs. A polarization charge induced at the AlGaN/GaN interface generally forms a rather shallow potential well confining electrons near the interface. Being heated by electric field in the transistor channel, the electrons become capable of spillover from the well and then capturing by traps in the bulk of the GaN layer. This mechanism is believed to be responsible, at least in part, for the drain current collapse frequently observed under radio-frequency or pulse transistor operation[64]. To prevent the electron spillover, a potential barrier should be created in the channel, hindering the electron penetration in the GaN bulk. This can be done by using two contra-directed polarization dipoles made of InGaN and AlN, respectively, surrounding the GaN channel. Fig. 10b shows the distribution of the effective electron concentration (charge density normalized by the electron charge) in a HEMT heterostructure consisting of a thick GaN buffer and a 50 nm GaN channel sandwiched between a 4 nm $In_{0.1}Ga_{0.9}N$ and a 2 nm AlN polarization dipoles. A 25 nm GaN cap completes this transistor structure. It is seen that electrons are effectively confined in the channel due to the potential barriers formed by the polarization dipoles at both channel interfaces. The sheet electron concentration in such a structure is mainly controlled by the AlN intermediate layer that induces a dominant polarization charge, i. e. the concentration follows the respective curve in Fig. 10a.

The above heterostructure with two polarization dipoles is a natural extension of the transistor design suggested in Ref. 65 where an InGaN

channel has been sandwiched between a GaN buffer and an AlGaN cap. Collapse-free operation of the AlGaN/InGaN/GaN HEMT heterostructure was observed in that study, justifying the applied approach.

4.3. *Transistors on AlN substrate and double-heterostructures*

AlN is a natural substrate material for HEMTs due to its high electrical resistivity and thermal conductivity. Recently a HEMT heterostructure fabricated on true-bulk AlN has been demonstrated[66] that consists of a 100 nm unintentionally doped GaN layer on AlN substrate followed by a 25 nm *n*-$Al_{0.2}Ga_{0.8}N$ cap (it is assumed here that [Si] =3 × 10^{18} cm^{-3}).

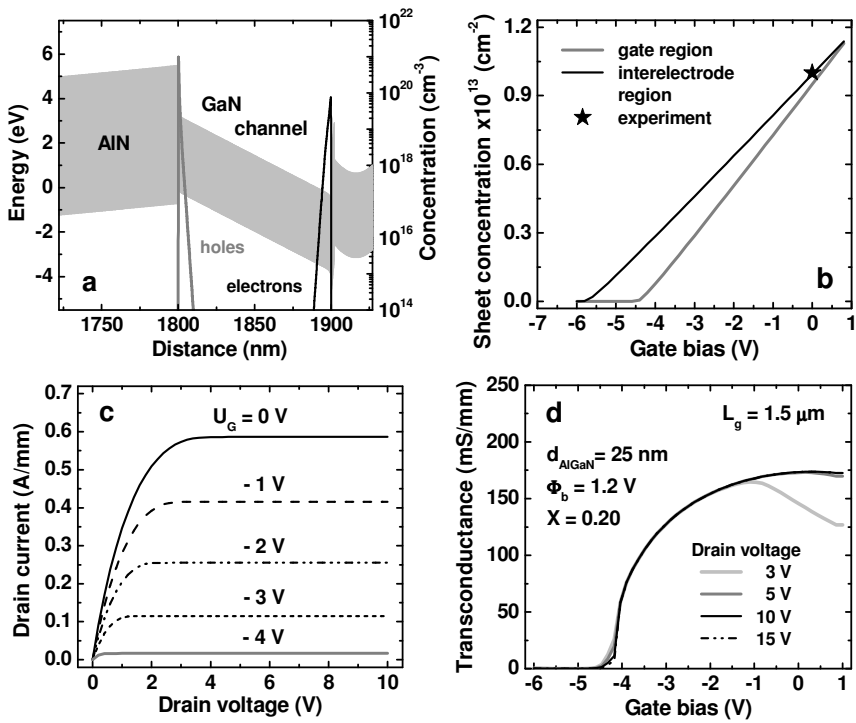

Fig. 11. Equilibrium band diagram and effective carrier concentrations (a), sheet electron concentrations in the gate and interelectrode regions (b), I-V characteristics (c), and transconductance (d) of DHS HEMT on AlN substrate reported in Ref. 66. Bandgap is shown by grey shadow in (a).

A 2 nm AlN polarization dipole has been placed between the GaN channel and the AlGaN cap. The mobility of 1100 $cm^2/V \cdot s$ at the sheet electron concentration of ~10^{13} cm^{-2} has been measured in the structure.

Figure 11 presents the modeling results obtained for the above HEMT double-heterostructure (DHS). Fist of all, one can see that both electron and parasitic hole channels are formed in the DHS because of alternate polarization charges at the GaN layer interfaces (Fig. 11a). The coexistence of electros and holes it typical of any DHS structures made of III-nitride materials. If electron and hole channels are situated close to each other, they may affect negatively the HEMT performance. Indeed, the ohmic source and drain contacts formed in the transistor may overlap both channels. This is expected to result in shunting the electron conductivity by the parasitic holes. In addition, the electrons heated by the electric field in the channel may penetrate into the hole region, leading to carrier losses because of the electron-hole recombination.

To suppress the parasitic hole formation, a number of approaches has been suggested. One is based on the use of an intermediated AlGaN layers inserted between the AlN substrate/buffer layer and GaN channel[67]. Adjusting the composition and thickness of the layer enables one to move the holes far away from the active region of the transistor. Another approach implies compensation of an undesirable polarization charge by doping impurities. It is discussed in detail in Refs. 68 and 69.

Figure 11a demonstrates a specific feature of a DHS, a strong built-in electric field in the GaN channel layer, which is advantageous for suppression of the hot electron spillover from the channel to the structure bulk. The theoretically predicted sheet electron concentration and the maximum drain current of ~0.6 A/mm are in a good agreement with observations of Ref. 66. The simulation shows that the transconductance of ~170 mS/mm can be obtained in the HEMT on AlN substrate at the gate length of 1.5 μm.

4.4. *A prototype of an N-polar transistor on AlN*

In contrast to LEDs, the use of N-polar heterostructures for HEMT fabrication has been examined experimentally in a number of studies[70,71]. These devices were made, however, on conventional substrates and em-

ployed rather non-optimized structures. Therefore, the advantages of the N-polar transistors have not been revealed in full measure. In this section, we will discuss a prototype HEMT heterostructure with superior theoretical performance that utilizes advantages of N-polar heterostructures. The structure consists of a single GaN layer on the top of an AlN substrate/buffer layer. In order to prevent strain relaxation in the GaN layer, it should be made thin enough, i. e. ~5-10 nm. The absence of the AlGaN alloys in the heterostructure avoids the negative influence of the alloys scattering on the electron mobility and improves the thermal management in the device.

Figure 12a presents the equilibrium band diagram and the quantum-mechanical distribution of the effective electron concentration in the

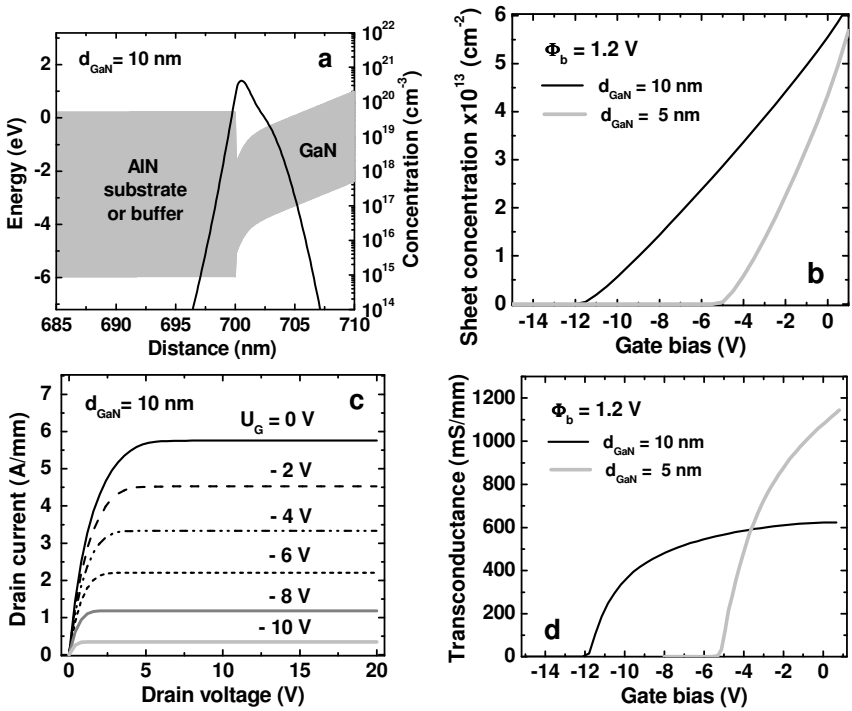

Fig. 12. Equilibrium band diagram and effective carrier concentrations (a), sheet electron concentrations (b), I-V characteristics (c), and transconductances (d) of N-polar HEMTs on AlN substrate. Bandgap is shown by grey shadow in (a).

HEMT heterostructure with a 10 nm top GaN layer. A good carrier confinement is provided in the structure by a positive polarization charge and a high conduction band offset at the GaN/AlN interface. As a result, a sheet electron concentration of ~5-6 × 10^{13} cm^{-2} can be obtained in the structure (Fig. 12b). Maximum drain current estimated for the N-polar heterostructure is of 5.8 A/mm and 3.6 A/mm for the structures with 10 nm and 5 nm GaN layers, respectively. And, a transconductance of 600-1200 mS/mm is predicted for those two types of the device.

The predicted high-performance characteristics of the N-polar HEMT heterostructure are based on the assumption of pseudomorphic GaN growth on the AlN substrate. In practice, strain relaxation may occur in the GaN layer. Even in this case, however, the polarization charge originated from the difference in the spontaneous polarization of GaN and AlN is still high enough to provide the maximum drain current and transconductance much higher than those in the standard HEMT heterostructure (see, e. g., Fig. 10c). Only the mismatch dislocation effect on the electron mobility in the GaN channel is expected to negatively impact the performance of the N-polar transistor with the relaxed strain.

5. Summary

State-of-the-art low-defect substrates for epitaxy of III-nitride semiconductor materials are considered in the chapter. It is shown that various approaches to TDD reduction in GaN grown on sapphire or SiC have resulted in lowering its value down to ~10^6-10^7 cm^{-2}. This is sufficient to provide IQE of light-emitting heterostructures independent of TDD but is still too high to avoid degradation of high-power LEDs and LDs. Further reduction in the TDD can be achieved by using native substrates cut out of the bulk GaN and AlN crystals. The latter enables also an easy choice of the growth surface orientation and, hence, the polarity control in heterostructures grown on the substrates.

Dominant factors controlling IQE of visible LEDs are investigated by modeling. Among them, TDD and operation temperature are found to be most critical. Both delocalization of carriers captured by compositional fluctuations in an InGaN active region and self-heating of the diode at a

high current density are the mechanisms responsible for the commonly observed degradation of LED efficiency with current.

Low-defect substrates allow an alternative concept for engineering of indium-free LEDs, based on the use of a thick active region in the device. The LEDs with thick active regions are easier in fabrication and provide potentially a better stability of the emission spectrum and efficiency upon the current variation. IQE of such an LED is primarily controlled by TDD and carrier leakage from the active layer. In turn, the leakage can be effectively suppressed by a proper design of the emitter layers. For that, however, not only the band offsets at the emitter/active layer interfaces should be accounted for but also the overall electric field redistribution in the heterostructure induced by variation of the polarization charges. The latter factor may lead to non-trivial technical solutions that have no analogies in conventional III-V compound devices.

The carrier leakage becomes especially critical for LDs normally operating at the current densities well exceeding ~2-3 kA/cm^2. The effectiveness of using distributed polarization doping in graded-composition materials to improve the carrier confinement and, hence, to reduce the leakage current is demonstrated with reference to a near-UV LDs.

Playing with polarity of an LED or LD heterostructure is an additional degree of freedom in the bandgap engineering of light-emitting devices. An N-polar SQW LED structure is found to provide a higher injection efficiency than a similar Ga-polar structure. On the other hand, the Ga-polar LED exhibits much better emission wavelength stability upon the current density variation. A non-polar SQW LED structure combines the effective carrier confinement typical of the N-polar structure and the wavelength stability typical of the Ga-polar structure. Therefore, it is quite promising to improve the LED performance. The advantages of the N-polar and non-polar materials are not so pronounced in the case of MQW heterostructures.

The effect of TDD on the HEMT performance is not straightforward as in the case of light-emitting devices. Thus other aspects relevant to the transistor structure engineering become more important. A number of approaches aimed at reducing the alloy scattering in HEMT heterostructures and preventing the electron spillover from the channel to the semiconductor bulk are examined in the chapter. In particular, the use of the

polarization dipoles, i.e. thin epilayers with alternate polarization charges at its interfaces, is found to be beneficial for improvement of the HEMT characteristics.

AlN is a natural substrate material for high-power HEMTs due to inherent high electrical resistivity and thermal conductivity. Actually, all the HEMT heterostructures on AlN form a DHS with co-existing electrons and parasitic holes. The bipolar electric conductivity in such heterostructures may negatively affect the device performance. However, the parasitic hole formation can be suppressed by compensation of the corresponding polarization charge with doped impurities.

A prototype of a high-performance N-polar HEMT on AlN substrate is considered to demonstrate latent capabilities of the polarity engineering in such devices. The N-polar heterostructure is predicted to provide the maximum drain current and transconductance a several times higher than those of standard Ga-polar structures.

It is worth noticing that many approaches to engineering of advanced optical and electronic devices considered in the chapter are valuable not only for the particular case of low-defect wafers but also for heterostructures grown on conventional, sapphire and SiC, substrates. The study reported here enables making a conclusion that capabilities of the bandgap engineering of III-nitride semiconductor devices are not yet exhausted and they may be used for further improvement of the device performance.

Acknowledgments

Simulation of optical and electronic devices presented in this chapter has been made with the software provided by STR, Inc.

I am also pleased to acknowledge helpful discussions with A. Usikov on properties and applications of low-defect substrates and templates and with A. Zhmakin on results of device modeling.

References

1. S. Nakamura, *J. Cryst. Growth* **145**, 911 (1994).
2. S. Nakamura, T. Mukai, M. Senoh, *Appl. Phys. Lett.* **64**, 1687 (1994).
3. O. Ambacher, *J. Phys. D* **31**, 2653 (1998).

4. L. Liu and J. H. Edgar, *Mat. Sci. Engineer.* **R37**, 61 (2002).
5. S. J. Pearton, F. Ren, A. P. Zhang, and K. P. Lee, *Mat. Sci. Engineer.* **R30**, 55 (2000).
6. A. Krost and A. Dadgar, *Mat. Sci. Engineer.* **B93**, 77 (2002).
7. J. W. Johnson, E. L. Piner, A. Vescan, R. Therrien, P. Rajagopal, J. C. Roberts, J. D. Brown, S. Singhal, and K. J. Linthicum, *IEEE Electron. Device Lett.* **25**, 459 (2004).
8. T. Hino, S. Tomiya, T. Miyajima, K. Yanashima, S. Hashimoto, and M. Ikeda, *Appl. Phys. Lett.* **76**, 3421 (2000).
9. M. Iwaya, S. Terao, T. Sano, S. Takanami, T. Ukai, R. Nakamura, S. Kamiyama, H. Amano, and I. Akasaki, *Phys. Status Solidi (a)* **188**, 117 (2001).
10. S. Yu. Karpov and Yu. N. Makarov, *Appl. Phys. Lett.* **81**, 4721 (2002).
11. S. Nakamura, *J. Cryst. Growth* **201/202**, 290 (1999).
12. V. Bougrov, M. Levinstein, S. Rumyantsev, A. Zubrilov, in *Properties of advanced semiconductor materials. GaN, AlN, InN, BN, SiC, SiGe.*, Eds. M. E. Levinshtein, S. L. Rumyantsev, and M. S. Shur, (Wiley-Interscience, New York, 2001), p. 3.
13. Yu. Goldberg, in Ref.12, p. 33.
14. A. Zubrilov, in Ref.12, p. 50.
15. Ü. Özgür, Ya. I. Alivov, C. Liu, A. Teke, M. A. Reshchikov, S. Doğan, V. Avrutin, S.-J. Cho, and H. Morkoç, *J. Appl. Phys.* **98**, 041301 (2005).
16. http://www.crystran.co.uk/products.asp?productid=231
17. T. Fujii, Y. Gao, R. Sharma, E. L. Hu, S. P. DenBaars, and S. Nakamura, *Appl. Phys. Lett.* **84**, 855 (2004).
18. T. Frey and V. Härle, in Abstract Book of the 14th International Conference on Crystal Growth, 431 (2004).
19. X. Hu, J. Deng, N. Pala, R. Gaska, M. S. Shur, C. Q. Chen, J. Yang, G. Simin, M. Asif Khan, J. C. Rojo, and L. J. Schowalter, *J. Cryst. Growth* **82**, 1299 (2003).
20. E. S. Hellman, D. N. E. Buchanan, D. Wiesmann, and I. Brener, *MRS J. Nitride Semicond. Res.* **1**, 16 (1996).
21. T. Mukai, S. Hagahama, T. Yanamoto, and M. Sano, *Phys. Stat. Solidi (a)* **192**, 261 (2002).
22. S. Porowski, I. Grzegory, S. Krukowski, M. Leszczynski, P. Perlin, and T. Suski, Europhysics News 35, 1 (2004).
23. K. Akita, T. Nakamura, and H. Hirayama, *Phys. Stat. Solidi (a)* **201**, 2624 (2004).
24. A. Gassmann, T. Suski, N. Newman, C. Kisielowski, E. Jones, E. R. Weber, Z. Liliental-Weber, M. D. Rubin, H. I. Helava, I. Grzegory, M. Bockowski, J. Jun, and S. Porowski, *J. Appl. Phys.* **80**, 2195 (1996).
25. F. Bernardini, V. Fiorentini, and D. Vanderbilt, *Phys. Rev.* **B63**, 193201 (2001).
26. S. F. Chihibu, A. C. Abare, M. P. Mack, M. S. Minsky, T. Degushi, D. Cohen, P. Kozodoy, S. B. Fleischer, S. Keller, J. S. Speck, J. E. Bowers, E. Hu, U. K. Mishra, L. A. Coldren, S. P. DenBaars, K. Wada, T. Sots, and S. Nakamura, *Mat. Sci. Engeneer.* **B59**, 298 (1999).

27. A. Chitnis, C. Chen, V. Adivarahan, M. Shatalov, E. Kuokstis, V. Mandavilli, J. Yang, and M. Asif Khan, *Appl. Phys. Lett.* **84**, 3663 (2004).
28. R. Sharma, P. M. Pattison, H. Masui, R. M. Farrell, T. J. Baker, B. A. Haskell, F. Wu, S. P. DenBaars, J. S. Speck, and S. Nakamura, *Appl. Phys. Lett.* **87**, 231110 (2005).
29. M. D. Craven, S. H. Lim, F. Wu, J. S. Speck, and S. P. DenBaars, *Appl. Phys. Lett.* **81**, 469 (2002).
30. D. Craven, F. Wu, A. Chakraborty, B. Imer, U. K. Mishra, S. P. DenBaars, and J. S. Speck, *Appl. Phys. Lett.* **84**, 1281 (2003).
31. J. C. Rojo, G. A. Slack, K. Morgan, B. Raghothamachar, M. Dudley, and L. J. Schowalter, *J. Cryst. Growth.* **231**, 317 (2001).
32. B. Raghothamachar, M. Dudley, J. C. Rojo, K. Morgan, and L. J. Schowalter, *J. Cryst. Growth* **250**, 244 (2003).
33. http://www.parc.com/about/pressroom/news/2002-04-10-uvled/default.html
34. S. Porowski, *J. Cryst. Growth* **189/190**, 153 (1998).
35. P. Perlin, T. Suski, M. Leszczyński, P. Prystawko, T. Świetlik, Ł. Marona, P. Wiśniewski, R. Czernecki, G. Nowak, J.L. Weyher, G. Kamler, J. Borysiuk, E. Litwin-Staszewska, L. Dmowski, R. Piotrzkowski, G. Franssen, S. Grzanka, I. Grzegory, and S. Porowski, *J. Crystal Growth* **281**, 107 (2005).
36. C. Skierbiszewski, K. Dybko, W. Knap, M. Siekacz, W. Krupczyński, G. Nowak, M. Boćkowski, J. Łusakowski, Z. R. Wasilewski, D. Maude, T. Suski and S. Porowski, *Appl. Phys. Lett.* **86**, 102106 (2005).
37. I. Grzegory, M. Bockowski, B. Lucznik, S. Krukowski, Z. Romanowski, M. Wroblewski, and S. Porowski, *J. Cryst. Growth* **246**, 177 (2002).
38. R. P. Vaudo, X. Xu, C. Loria, A. D. Salant, J. S. Flynn, and G. R. Brandes, *Phys. Stat. Solidi (a)* **194**, 494 (2002).
39. S. K. Mathisa, A. E. Romanov, L. F. Chena, G. E. Beltzc, W. Pomped, and J. S. Speck, *J. Cryst. Growth* **231**, 371 (2001).
40. A. Usui, *Mat. Res. Symp. Proc.* **482**, 233 (1998).
41. M. Albrecht, I. P. Nikitina, A. E. Nikolaev, Yu. V. Melnik, V. A. Dmitriev, and H. P. Strunk, Phys. Stat. Solidi (a) 176, 453 (1999).
42. Yu. Melnik, V. Soukhoveev, V. Ivantsov, V. Sizov, A. Pechnikov, K. Tsvetkov, O. Kovalenkov, V. Dmitriev, A. Nikolaev, N. Kuznetsov, E. Silveira, and J. Freitas, *Phys. Stat. Solidi (a)* **200**, 22 (2003).
43. V. Dmitriev and A. Usikov, in *III-Nitride Semiconductor Materials*, Ed. Zhe Chuang Feng (Imperial College Press, 2006), Ch.1.
44. B. Beaumont, M. Vaille, G. Nataf, A. Bouillé, J.-C. Guillaume, P. Vénnègues, S. Haffouz, and P Gibart, *MRS J. Nitride Semicond. Res.* **3**, 20 (1998).
45. O.-H. Nam, M. D. Bremser, T. S. Zheleva, R. F. Davis, *Appl.Phys.Lett.* **71**, 2638 (1997).
46. http://www.semitech.us/products
47. I. Vurgaftman, J. R. Meyer, and L. R. Ram-Mohan, *J. Appl. Phys.* **89**, 5815 (2001).

48. S. Nakamura, *Mat. Res. Soc. Symp. Proc.* **395**, 879 (1996).
49. U. Kaufmann, M. Kunzer, K. Köhler, H. Obloh, W. Pletschen, P. Schlotter, J. Wagner, A. Ellens, W. Rossner, and M. Kobusch, *Phys, Stat. Solidi (a)* **192**, 246 (2002).
50. S. Yu. Karpov, K. A. Bulashevich, I. A. Zhmakin, M. O. Nestoklon, V. F. Mymrin, and Yu. N. Makarov, *Phys. Stat. Solidi (b)* **241**, 2668 (2004).
51. M. Iwaya, S. Takanami, A. Miyazaki, Y. Watanabe, S. Kamiyama, H. Amano, and I. Akasaki, *Jpn. J. Appl.Phys.* **42**, 400 (2003).
52. A. S. Usikov, D. V. Tsvetkov, M. A. Mastro, A. I. Pechnikov, V. A. Soukhoveev, Y. V. Shapovalova, O. V. Kovalenkov, G. H. Gainer, S. Yu. Karpov, V. A. Dmitriev, B. O'Meara, S. A. Gurevich, E. M. Arakcheeva, A. L. Zakhgeim, and H. Helava, *Phys. Stat. Solidi (c)* **0**, 2265 (2003).
53. K. A. Bulashevich, S. Yu. Karpov, and R. A. Suris, accepted to publication in *Phys. Stat. Solidi (c)* (2006).
54. C. Skierbiszewski, P. Perlin, I. Grzegory, Z. R. Wasilewski, M. Siekacz, A. Feduniewicz, P. Wisniewski, J. Borysiuk, P. Prystawko, G. Kamler, T. Suski, and S. Porowski, *Semicond. Sci. Technol.* **20**, 809 (2005).
55. M. Kneissl, D. W. Treat, M. Teepe, N. Miyashita, and N. M. Johnson, *Appl. Phys. Lett. 82*, 2386 (2003).
56. D. Jena, S. Heikman, J. S. Speck, U. Mishra, A. Link, and O. Ambacher, *Phys, Stat. Solidi (c)* **0**, 2339 (2003).
57. R. Gaska, J.W. Yang, A. Osinsky, Q. Chen, M.A. Khan, A.O. Orlov, G. L. Snider, M. S. Shur, *Appl.Phys.Lett.* **72**, 707 (1998).
58. L. Hsu, W. Walukiewicz, *J.Appl.Phys.* **89**, 1783 (2001).
59. D. Jena, I. Smorchkova, A.C. Gossard, U.K. Mishra, *Phys.Stat.Solidi (b)* **228**, 617 (2001).
60. C. Skierbiszewski, *Acta Physica Polonica* **A108**, 635 (2005).
61. R. S. Balmer, K. P. Hilton, K. J. Nash, M. J. Uren, D. J. Wallis, D. Lee, A. Wells, M. Missous, and T. Martin, *Semicond. Sci. Technol.* **19**, L65 (2004).
62. S. Keller, S. Heikman, L. Shen, I. P. Smorchkova, S. P. DenBaars, and U. K. Mishra, *Appl. Phys. Lett.* **80**, 4387 (2002).
63. S. Einfeldt, V. Kirchner, H. Heinke, M. Dießelberg, S. Figge, K. Vogeler, and D. Hommel, *J. Appl. Phys.* **88**, 7029 (2000).
64. P. B. Klein and S. C. Binari, *J. Phys.: Condesed Matter* **15**, R1641 (2003).
65. G. Simin, X. Hu, A. Tarakji, J. Zhang, A. Koudymov, S. Saygi, J. Yang, A. Khan, M.S. Shur, and R. Gaska, *Jpn. J. Appl. Phys.* **40**, L1142 (2001).
66. X. Hu, J. Deng, N. Pala, R. Gaska, M. S. Shur, C. Q. Chen, J. Yang, G. Simin, M. A. Khan, J. C. Rojo, and L. J. Schowalter, *Appl. Phys. Lett.* **82**, 1299 (2003).
67. C. Q. Chen, J. P. Zhang, V. Adivarahan, A. Koudymov, H. Fatima, G. Simin, J. Yang, and M. Asif Khan, *Appl. Phys. Lett.* **82**, 4593 (2003).
68. M. Neuburger, I. Daumiller, M. Kunze, T. Zimmermann, B. Jogai, J. van Nostrand, J. Sewell, T. Jenkins, A. Dadgar, A. Krost, and E. Kohn, *Phys. Stat. Solidi (c)* **0**, 86 (2002).

69. V. F. Mymrin, K. A. Bulashevich, N. I. Podolskaya, and S. Yu. Karpov, *J. Cryst. Growth* **281**, 115 (2005).
70. R. Dimitrov, A. Mitchell, L. Wittmer, O. Ambacher, M. Stuztmann, J. Hilsenbeck, and W. Rieger, *Jpn. J. Appl. Phys.* **38**, 4962 (1999).
71. V. G. Mokerov, L. E. Velikovskii, Z. T. Kanametova, V. E. Kaminskii, P. V. Sazonov, J. Graul, O. Semchinova, in *Gallium Arsenide applications symposium,* (Munich 2003), p. 17.

This page intentionally left blank

CHAPTER 14

III-NITRIDE NANOMATERIALS: GROWTH AND PROPERTIES

A. B. Djurišić, X. M. Cai, M. H. Xie

Department of Physics, University of Hong Kong
Pokfulam Road, Hong Kong
E-mail: dalek@hkusua.hku.hk

Nanostructures of semiconducting materials have been attracting great attention due to their exceptional properties over the bulk. Great variety of methods for fabrication of III-nitride nanostructures has been reported up to date. In this chapter, we provide an overview of the fabrication methods and growth mechanisms of different III-nitride nanostructures. First, we discuss chemical synthesis methods for fabrication of nitride nanocrystals. Then, we discuss various vapor deposition methods for fabrication of different 1D nitride nanostructures. Since GaN nanostructures have been most extensively studied, we describe in detail the influence of the fabrication conditions on the obtained GaN nanostructures. In addition to process parameters (substrate temperature, chamber pressure, gas flow rate), the influence of catalysts and source material is also discussed. Then, the fabrication methods of other nitride nanostructures, such as InN and AlN, are presented. Finally, the growth and properties of ternary nitride nanostructures and nanostructured heterojunctions are discussed.

1. Introduction

In recent years, nanostructured semiconductors, especially one-dimensional nanostructures such as nanowires and nanotubes,[1-3] have been attracting increasing attention due to their unique properties different from bulk semiconductors. Semiconductor nanostructures offer the possibility of adjusting the electrical, optical, magnetic, and thermoelectric properties by adjusting the size of the nanostructures.[1] In addition, nanostructures are of great interest for sensing applications.

Their properties are highly dependent on chemical species absorbed on the surface, which can be used for fabrication of sensors for medical, environmental, or security-check purposes.[1] There is a great variety of methods for nanostructure fabrication. They can roughly be divided into solution phase methods and vapor phase methods. Both types of methods can be template directed. For vapor phase methods, the template is usually a patterned or porous substrate with regular channels, while for solution phase template directed synthesis usually involves the use of soft templates to promote nanostructure formation via suitable chemical reaction.[1]

While solution phase methods are often used to fabricate nanocrystals or nanorods (less commonly for nanotubes and nanowires), vapor phase methods are typically used for other, more complex morphologies. While solution methods are inexpensive, the achievement of a desired morphology is often a result of trial-and-error process in selecting capping agents.[1] Furthermore, growth of nanostructures firmly attached to the substrate by solution methods has been achieved for a few materials (for example ZnO), while for others solution methods typically result in free standing nanostructures which are less convenient for direct applications to device fabrication. Thus, vapor phase growth methods such as chemical vapor deposition (CVD), metal organic vapor deposition (MOCVD), molecular beam epitaxy (MBE), laser ablation, sputtering and evaporation, have been extensively studied. Regardless of the method used to produce the gas phase of reactants, three main types of growth mechanisms can be identified: vapor-liquid-solid (VLS), self-catalyzed VLS, and vapor-solid (VS) mechanism. In a VLS mechanism, the nanostructures grow from a liquid alloy of a metal catalyst and target material.[2] The diameters of nanowires grown by a VLS method are usually determined by the size of the catalyst particles.[2] Self-catalytic VLS method has an advantage that possible contamination of nanostructures by metal catalyst is avoided. In this mechanism, the liquid droplets can be formed by decomposition of the target materials. For example, decomposition of GaN will result in formation of liquid Ga nanoparticles, which can form an alloy with nitrogen-rich vapor and result in GaN nanowire growth.[2] On the other hand, VS growth mechanism refers to formation of nanostructures from vapor phase

reactants in absence of metal catalysts and without evidence of self-catalyzed VLS growth.[2] Up to date, different growth mechanisms have been identified for the growth of nitride nanostructures, although VLS mechanism represents the most common one.

In this chapter, we will provide an overview of recent advances in the synthesis and properties of III-nitride nanostructures. III-nitrides are materials of great practical importance for optoelectronic applications, such as high brightness light emitting diodes,[4] laser diodes,[4,5] and various UV optoelectronic devices.[5] Most of these devices are currently based on conventional thin epitaxial films and quantum well structures, but recent progress in synthesis of III-nitride nanostructures is expected to result in their practical applications in near future. We will first provide an overview of achievements in synthesis of individual III-nitride nanostructures, such as BN, GaN, AlN, and InN. Boron nitride and gallium nitride nanostructures have been extensively studied, while there are fewer reports on AlN and InN synthesis and characterization. For each material, all available synthesis methods, both solution and vapor phase, will be discussed. Since GaN is a material of the greatest technological importance and it has been most extensively studied, the growth of GaN nanostructures will be discussed in detail. After reviewing the progress on individual III-nitride materials, the growth of III-nitride ternary alloys and heterostructures will be presented. Finally, summary of achieved results and future outlook is given.

2. Boron Nitride Nanostructures

Boron nitride nanostructures have been widely studied.[6-47] A variety of nanostructures has been fabricated, such as nanotubes,[9,10,12,14,15,17-20,32,33,35-41,44-47] nanocrystals,[22-31] nanowires,[13,14] bamboo-like nanowires,[7] thorn-like nanostructures,[8] nanomesh,[11] nanocages,[15,18] nanorods,[18] and nanohorns.[18] Nanotubes have been most commonly observed and studied in more detail compared to other reported morphologies.

Boron nitride nanocrystals can be synthesized either by chemical or hydrothermal methods,[22-24,27-29] laser-assisted fabrication,[25,26] or plasma enhanced chemical vapor deposition (CVD).[30] Mechanical milling can

also be used to reduce nanocrystal size.[31] BN nanocrystals can be prepared by reaction of Li_3N with BBr_3 at moderate conditions (250°C, 0.3-0.5 MPa).[22] The phase of the nanocrystals can be changed from hexagonal to cubic by adding cubic GaP nanocrystals into the mixture, which served as a structure inducing agent.[22] Cubic BN nanocrystals could also be obtained from benzene solutions of Li_3N and BBr_3 at 480°C without adding any structure inducing agents.[27] The temperature was found to determine the structure of BN nanocrystals obtained from reaction of Li_3N and BBr_3.[28] It was found that, at low temperature the dominant phase was hexagonal.[28,29] With increasing temperature the percentage of cubic phase was increased until it reached the maximum at 480°C, while further increase of temperature resulted in hexagonal phase becoming dominant again.[28] Cubic and orthorhombic BN nanocrystals have been synthesized by a hydrothermal method in aqueous solution.[23,24] The reagents used were boric acid, trimethyl amine and hydrazine hydrate[24] or boric acid, sodium azide, hydrazine hydrate, and ammonium chloride.[23] Pulsed laser induced liquid-solid interfacial reaction was used to prepare BN nanocrystals from hexagonal h-BN wafer.[25,26] Cubic[25,26] and explosion[25] phase BN nanocrystals were obtained by this method.

BN nanowires prepared by a reaction of α-FeB nanoparticles (which served both as a catalyst and a source of boron) and a mixture of N_2 and NH_3.[13] BN nanowires with diameter ~20 nm and length of several tens of μm were obtained at 1100°C.[13] BN nanotubes and nanowires have been prepared by heating boric acid with activated carbon, multiwalled carbon nanotubes, catalytic Fe particles, or mixture of activated carbon and Fe particles in NH_3 gas flow at temperatures 1000°C-1300°C.[14] Morphologies of the obtained products mainly depended on the material mixed with boric acid and synthesis temperature.[14] Orthorhombic BN nanowires with diameters in the range 50-100 nm and lengths of several tens of μm were prepared by a hydrothermal method at 400°C.[7] Thorn-like BN nanostructures were synthesized from a mixture of B and B_2O_3 at 1200°C in NH_3 flow.[8] The BN nanostructures could be grown either on a substrate or on SiC nanowires, which resulted in significant increase of the surface area.[8] High temperature CVD method was used to fabricate a highly regular BN nanomesh.[11] BN nanocages were prepared

by an arc-melting method.[15] Laser ablation method can also be used to fabricate a variety of BN morphologies, such as nanotubes, nanohorns, and nanorods.[18]

While a number of experimental methods have been used to prepare different morphologies of BN nanostructures, majority of the research has been performed on BN nanotubes. BN nanotubes exhibit some very interesting properties. For example, giant Stark Effect has been observed in BN nanotubes prepared by arc-discharge technique.[39] Calculations predict that the specific heat of BN nanotubes is larger than that of carbon nanotubes[42] and experiments have confirmed that the thermal conductivity of multiwalled BN nanotubes is comparable or higher than that of multiwalled carbon nanotubes.[37] Unlike carbon nanotubes, which can be metallic or semiconducting, BN nanotubes are semiconducting and exhibit p-type conductivity.[43] Calculations also predict that carbon doping of BN nanotubes would result in spontaneous magnetization regardless of the species of substituted atom (boron or nitrogen).[38] The band gap of BN nanotubes has been investigated by electron energy loss spectroscopy (EELS)[35] and optical absorption measurements.[40] EELS measurements indicated that the bandgap was ~5.8 eV, regardless of the nanotube geometry. Theoretical studies indicate that different types of BN nanotubes can exhibit small band gap differences.[34] The absorption spectra of BN nanotubes exhibited transitions at ~4.45 eV, 5.5 eV, and 6.15 eV.[40] The lowest transition has been attributed to a Frenkel exciton, and the band gap was found to be 5.5 eV.[40] However, there have been studies which predicted lower bandgap, and experimental cathodoluminescence measurements from BN nanotubes demonstrated strong emission at 3.3 eV.[36] Therefore, while initial studies have confirmed that BN nanotubes have some very interesting properties, further study is needed to fully clarify the relationship between observed properties, nanotube structure, and fabrication method.

Different fabrication methods were proposed for single wall and multiwall BN nanotubes. Ma *et al.*[20] reported fabrication of BN nanotubes with large inner diameters prepared by CVD on α-Al_2O_3 micrometer-sized particles. Large diameter BN nanotubes can also be prepared by a reaction between a mixture of ammonia and N_2 gases with Fe-B catalyst particles.[41] Another method for fabrication of BN

nanotubes is heating the mixture of boron powder, iron oxide and ammonium chloride at 600°C.[32] Multiwall BN nanotubes can also be prepared by transformation of multiwall $B_xC_yN_z$ nanotubes.[44] Growth of BN nanotubes by heating a mixture of boron and silica powders with iron oxide nanoparticles in ammonia gas flow was also reported.[45] Fabrication of BN nanotubes with reduced number of layers was achieved by arc discharge method,[47] while single wall BN nanotubes were fabricated by ion-beam assisted deposition.[46]The use of templates to fabricate BN nanotubes was also reported.[14,33] Multiwalled carbon nanotubes likely served as template for BN nanotube synthesis in a method proposed by Deepak *et al.*[14] BN nanotubes were also synthesized by a CVD method in the channels of mesoporous silica.[33] BN nanotubes themselves can be filled by other nanomaterials.[6,9,10,12,16,17,19,21] Thin BN layers coated on GaN nanowires were reported,[9] as well as BN nanotubes filled with carbon,[16] zirconium oxide,[12] Mg containing compounds,[10] SiC nanowires,[17] and metals.[19] Filling the BN nanotubes with metals is of particular interest to obtain conducting metallic core and insulating BN nanotube sheath.[19,21] Additional interest in such structures originates from theoretical predictions that transition metal filled BN nanotubes would exhibit half-metallic ferromagnetism.[6]

To summarize, there have been many different experimental methods used to fabricate BN nanostructures. While solution methods can result in different allotropic modifications of BN, such as cubic or orthorhombic, most other methods result in hexagonal BN nanostructures. While the studies on the properties of BN nanotubes revealed several interesting results, the properties of other BN nanostructures have not been studied as extensively.

3. Gallium Nitride Nanostructures

GaN nanostructures[48-111] have been studied even more comprehensively than BN nanostructures due to their great potential for a variety of practical applications. GaN nanowire field effect transistors have been reported,[86] and the electrical properties of GaN nanowires have been studied.[51] Lasing from GaN nanowires has also been studied,[53,57] and low lasing thresholds[57] and integration of nanowire cavity with electro-optic

modulator[53] were reported. In addition, transition metal doped GaN nanostructures are expected to exhibit ferromagnetism and thus they are of interest for spintronic applications. Synthesis of Mn doped CdS, ZnS, and GaN has been studied in detail.[50] Room temperature ferromagnetism was reported in Mn doped GaN nanowires[62,71] although other studies reported Curie temperature below room temperature in Mn doped GaN nanowires.[68] Curie temperature was found to depend on ammonia flow rate,[68] which indicates that the obtained results are dependent on fabrication conditions. It should also be noted that theoretical calculations predict that even better results are expected for Cr doped GaN nanowires compared to the Mn doped ones.[56] Magnetic properties of more complex structures, such as ε-Fe_3N-GaN core-shell nanowires have also been studied.[59] Other material combinations have also been reported for GaN based core-shell nanowires, such as GaN-SiO_2 core shell nanowires.[66]

The technological potential of GaN nanostructures has generated lots of interest in developing different fabrication methods for various GaN nanostructures. Similar to BN, GaN nanocrystals fabrication and properties have been studied.[54,102,107-110] Chemical methods[54,102,107-109] or pulsed laser ablation[110] can be used for nanocrystal synthesis. Hexagonal GaN nanocrystals and nanorods were synthesized by a solvothermal method from gallium chloride and sodium azide.[102] Crystallinity of the obtained nanomaterials was poor, but it could be significantly improved by annealing at 750°C.[102] The phase transition in GaN nanocrystals can be induced by high pressure, and it was reported that for 50 nm GaN nanocrystals the change from hexagonal to rock-salt structure would start at 48.8 GPa.[107] Zinc-blende GaN nanocrystals were prepared by heating polymeric gallium imide precursor with trioctylamine.[109] Hexagonal GaN nanocrystals with 5 nm diameter confined in silica xerogels were prepared from $Ga(NO_3)_3$ solutions.[108] GaN nanocrystals with small size are of interest due to possibility to observe quantum confinement, which are expected to be seen in nanocrystals equal or smaller than ~5 nm.[109] Band gap shift due to quantum confinement has been observed in GaN nanocrystals with diameters 4.5 nm,[110] 3 nm,[109] and 2-3 nm.[54]

Different morphologies of GaN have been reported up to date: platelets and nanowires,[82] nanotubes,[90,96,111] nanobelts,[85,93,95,105]

nanorods,[100,101,104] bicrystalline nanorods,[99] nanowires,[49,54,55,58,60,61,63,67,69,70,73,75,77-81,83-85,87-89,91-98,103] zigzag nanorods,[95] beaded nanorods[95] and nanowires,[83] nanorings,[93] porous nanowires,[76] microspindles,[74] branched and hyperbranched nanowire structures,[72] columnar structures with nanowire branches,[65] dendrite like nanowires,[52] and micropyramid/nanowire structures.[48] Unlike BN, where nanotubes represent the most commonly studied morphology, GaN nanowires represent the most frequently observed nanostructures. Different shapes of nanowires and nanorods, such as prism-shaped nanorods[100] and triangular nanorods[101] and nanowires,[67,77] have been reported. The growth direction was found to be catalyst dependent.[77] The growth direction also exhibited temperature dependence.[89] Nanowire morphology was also found to be dependent on the reaction time.[63] Majority of reports in the literature refer to free standing nanowires, although there have been several reports of nanowires synthesized in templates, such as anodic alumina.[88,91,97]

Great variety of different fabrication procedures for the growth of GaN nanorods and nanowires has been reported in the literature. Nanowires and nanorods have been grown using different methods, such as CVD,[75,89,100] MOCVD,[67,69,70,77] MBE,[98] and hydride vapor phase epitaxy.[58,103] Obtained nanowires by vapor phase growth typically have hexagonal crystal structure, but hexagonal-to-cubic phase transformation can be induced by Ga^+ implantation.[75] Low temperature growth can also result in a mixture of hexagonal and cubic phases.[87] Different source materials were used, such as metallic Ga,[55,60,75,84,100] Ga_2O_3,[73,85] GaN,[99,104] Ga/GaN mixture,[101] GaN/Ga_2O_3 mixture,[61] Ga/GaN/B_2O_3 mixture,[78] and organic Ga precursors[54,87] Catalysts such as Au,[54,67,75,77] $HAuCl_4 \cdot 3H_2O$,[101] Ni,[55,67,70,77,80] In,[80] Fe,[67,77,80] $InCl_3$,[84] and $Ni(NO_3)_2$,[60,79,94] have been used, and growth without catalysts has also been reported.[73,85] The use of gold has been somewhat controversial, since both unsuccessful[80] and successful[54,67,75,77] growth have been reported. The wires grown in the presence of metal catalyst grow via VLS mechanism, while it has been shown that those resulting from decomposition of GaN source material grow via self-catalytic VLS mechanism.[81]

Concerning other GaN nanostructure morphologies, GaN microspindles were synthesized by reaction of GaI_3, $NaNH_2$ and NH_4Cl at 500 °C.[74] Micropyramid/nanowire structures were obtained on Au

coated Si substrates by heating gallium oxide powders in a graphite tube reactor.[48] Another method to obtain GaN nanostructures is photoelectrochemical etching, which results in the formation of a central column with nanowire branches.[65] Two-step growth process to obtain dendrite-like GaN nanowires was also reported.[52] In general, branched and hyperbranched nanowire structures can be obtained by multistep nanocluster catalyzed VLS approach.[72] GaN nanotubes have been grown from the mixture of $GaCl_3$ and indium powders at 1100°C in the ammonia flow.[111] The tubes were grown by vapor-liquid-solid mechanism, and indium particle was found at the ends of the tubes.[111] GaN nanotubes and nanowires were also fabricated without any catalysts by a direct reaction of Ga and ammonia gas at 850-900°C.[96] $Ni(NO_3)_2$ has also been used as a catalyst for GaN nanotube fabrication.[90] GaN nanobelts were fabricated by heating the mixture of Ga, GaN, and B_2O_3 in the flow of ammonia gas, while Fe coated alumina served as a substrate.[105] Similar source materials (Ga, Ga_2O_3 and B_2O_3) can result in the formation of porous GaN nanowires. Different GaN nanostructures (nanorods, nanoribbons, curved and beaded nanowires) could be obtained by sublimation of GaN, depending on the substrate used.[95] Substrate dependence of the obtained products (nanobelts vs. nanowires) was also observed for GaN nanostructures prepared from heating Ga_2O_3 powders in ammonia flow.[85] Variation of Ag catalyst nanoparticle size, ammonia flow rate, growth duration, and distance between the substrate and Ga source resulted in formation of different GaN nanostructure morphologies, such as nanorings, nanoribbons, and nanowires.[93] In general, variation of the fabrication conditions was found to significantly affect the obtained morphology of GaN nanostructures.[83]

From all the reported results on different morphologies under relatively similar conditions, we can conclude that the growth of GaN nanostructures from vapor phase is highly sensitive on the temperature, pressure, gas flow rate, type and quantity of the source material, system geometry and the distance from source to the substrate, and the catalyst and substrate used. We have studied the effects of temperature, gas flow rate, and the catalyst on the growth of GaN nanostructures from metallic Ga in the flow of NH_3/Ar gas mixture. It should be noted that, while some conclusions about growth obtained from these data are sufficiently

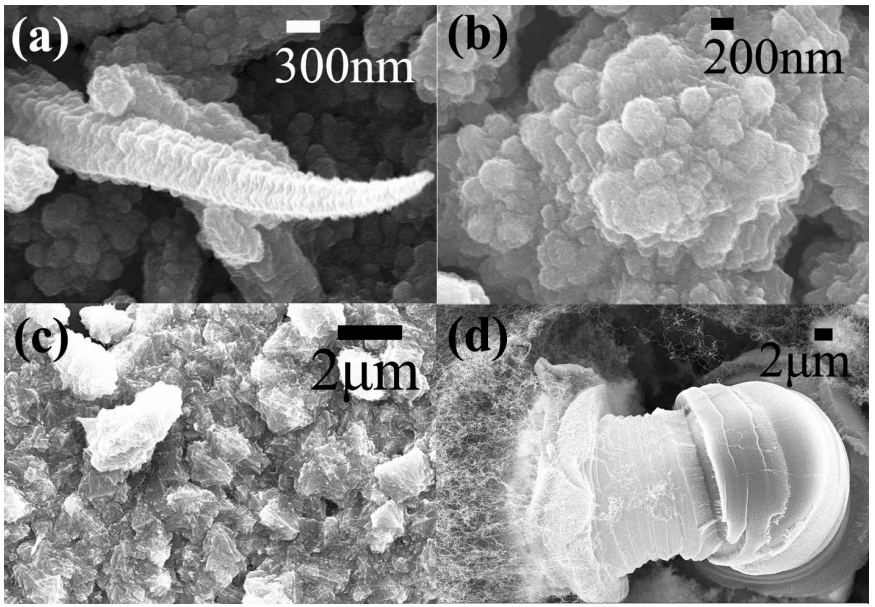

Fig. 1. The influence of substrate temperature (a) 800 °C; (b) 850 °C; (c) 900 °C; (d) 1000 °C.

general (i.e. Ga-rich vs. N-rich conditions), different system geometry would result in different distributions of reactant vapors and thus may result in different morphologies under same temperature and same gas flow. Thus, careful analysis of the nanostructure morphology and properties dependence on the fabrication conditions is necessary.

Effects of temperature and NH_3 flow rate on the growth of GaN nano- and microstructures from metallic Ga in absence of catalysts has been studied.[82,92] It was found that the increase of temperature and increase of NH_3 flow rate led to the growth of larger structures.[82,92] Here we concentrate on the effects of temperature, gas flow rate, and type of catalyst on the growth of GaN nanostructures. Figure 1 shows the influence of substrate temperature. Nanowire growth is obtained only at 950°C. At lower temperatures, microrods and polycrystalline aggregates are obtained, while at higher temperatures SiO_x nanowire bunches are observed. It should be noted that this is a consequence of using a Si substrate. For the growth temperature of 950°C, the influence of different catalysts was studied, as illustrated in Fig. 2. It can be observed that,

when Si is used as a substrate, if large quantity of Ga source is available or oxygen containing catalyst is used, SiO_x nanowire bunches can be obtained in addition to GaN nanowires. It should be noted that SiO_x nanowire bunches obtained when $Ni(NO_3)_2$ is used as a catalyst as a rule have higher oxygen content, indicating that $Ni(NO_3)_2$ acts as an additional source of oxygen for the growth of these structures. Therefore, lower amount of Ga and metallic catalysts such as Ni and Au yield best results in vapor deposition growth with Si as the substrate.

The gas flow rate significantly affects the morphology of the obtained GaN nanostructures. The effects of the gas flow rate are illustrated in Fig. 3. It can be observed that, depending on NH_3 gas flow, smooth-surface or stacked-cone GaN nanowires can be obtained.[55] Stacked cone GaN structures have been observed under different experimental conditions.[55,78,79] The difference in Ga diffusion behavior on polar and non-polar surfaces under Ga-rich and N-rich conditions has been identified as a possible mechanism for morphology difference between

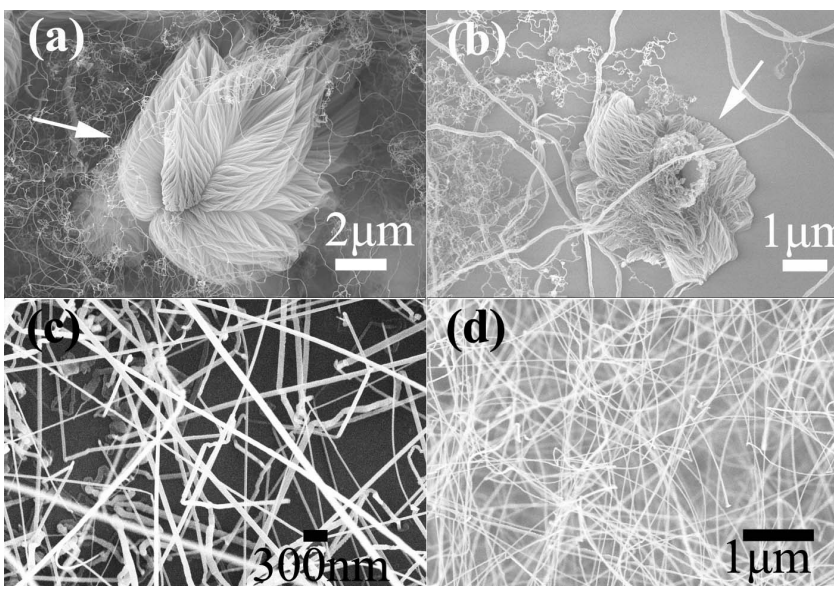

Fig. 2 The influence of catalyst and Ga and N supply (a) $Ni(NO_3)_2$ with Ga = 1045 mg, NH_3=100 sccm, Ar = 50 sccm; (b) Ni with Ga = 1045 mg, NH_3 = 100 sccm, Ar = 50 sccm; (c) Ni with Ga = 100 mg, NH_3 = 50 sccm, Ar = 125 sccm; (d) Au with Ga = 100 mg, NH_3 = 50 sccm, Ar = 125 sccm.

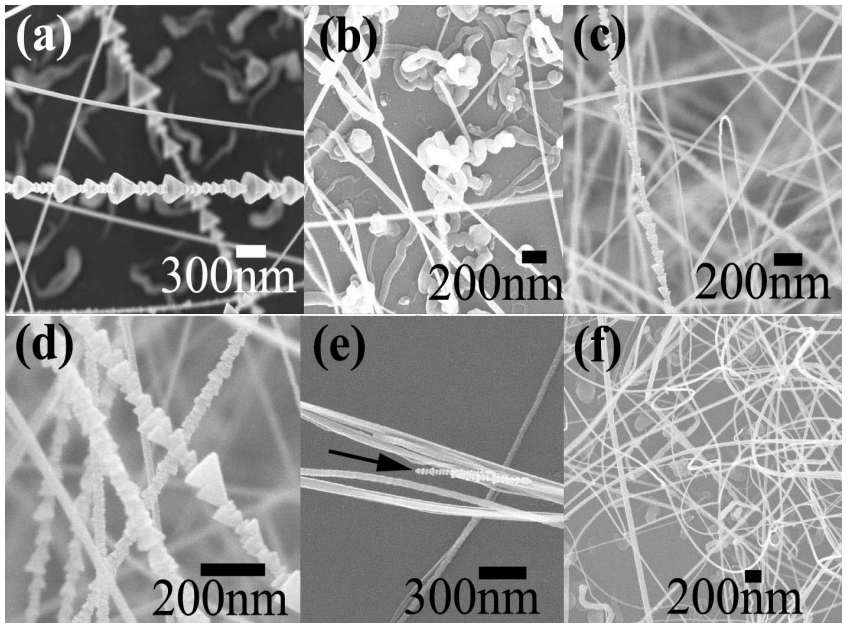

Fig. 3. Influence of the gas flow rate (a) $NH_3 = 25$ sccm, Ar = 50 sccm; (b) $NH_3 = 10$ sccm, Ar = 65 sccm; (c) $NH_3 = 150$ sccm, Ar = 0 sccm; (d) $NH_3 = 125$ sccm, Ar = 25 sccm; (e) $NH_3 = 125$ sccm, Ar = 25 sccm, without any catalysts; (f) $NH_3 = 50$ sccm, Ar = 100 sccm.

smooth and rough surfaces.[73] It should be noted that, at low gas flow rates, some larger structures can be obtained, as illustrated in Fig. 4. The formation mechanism of these large structures is not fully clear. However, it is obvious that gas flow rate represents a significant factor controlling the morphology of obtained GaN. For different growth temperatures, source materials, and system geometry, careful investigation of gas flow rate influence is required to fully understand the growth of the obtained GaN.

Selective growth of GaN nanostructures on patterned Si has been demonstrated.[58] Aligned GaN nanorod growth by hydride vapor phase epitaxy,[103] MOCVD,[69] and MBE[98] has also been demonstrated. CVD growth usually results in random orientation of the nanowires. However, under suitable conditions improvement in the alignment can be achieved,

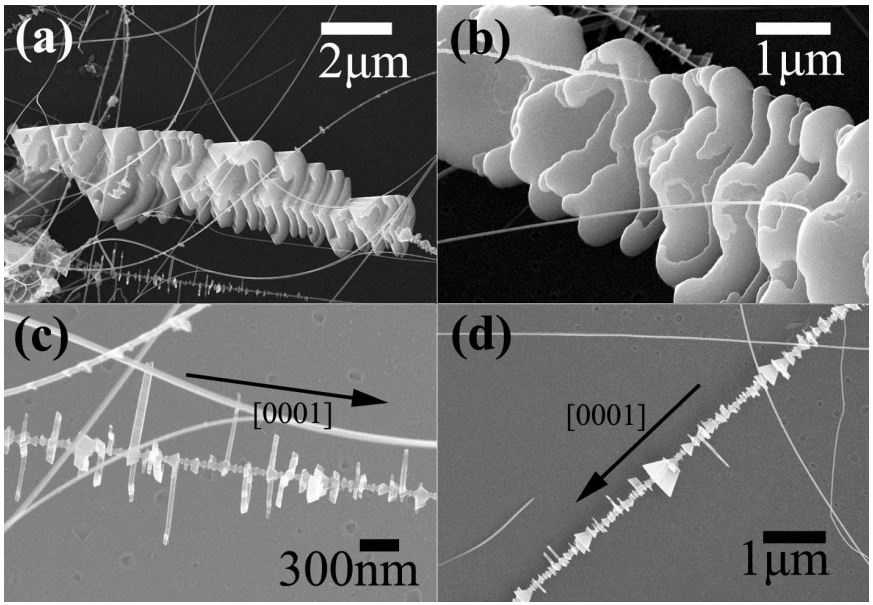

Fig.4 GaN morphologies at low flow rates: NH_3=10 sccm, Ar=25 sccm for (a) to (d). (a) and (b) the microscale GaN morphology; (c) and (d) the lateral growth of GaN nanorods.

so that quasi-aligned[61] and aligned[84] nanorod/nanowire arrays can be achieved.

Concerning the optical properties of GaN nanostructures, typically one broad UV peak is observed in photoluminescence[48,69,76,77,98,101] or cathodoluminescence[70,103] spectra. In the case of micropyramid/nanowire structures, the peak exhibited small red-shift compared to bulk GaN, which was attributed to possible carbon impurities.[48] Red shift was also observed in GaN nanowires grown by hydride vapor phase epitaxy, but the origin of this shift remains unclear.[58] Blue-shifted UV emission, attributed to quantum confinement due to existence of nanowires with very small diameters, and a blue peak at 470 nm attributed to defects or surface states were observed in GaN nanowires.[94] Blue shift of the peak has also been reported for GaN nanotubes, while small peak at 448 nm has been assigned to intrinsic point defects.[111] Blue shift attributed

to quantum confinement was also observed in low temperature photoluminescence spectra of thin GaN nanowires (diameter in the range 10-50 nm, so that some nanowires had smaller diameters than the Bohr radius of 11 nm).[60] On the other hand, very broad photoluminescence with several defect associated lines has been observed from prismatic GaN nanorods.[100] GaN nanowires fabricated in anodized alumina template also showed broad luminescence which could be fitted with three peaks, located at 363 nm, 442 nm, and 544 nm.[91] However, yellow defect band is not commonly observed in GaN nanostructures, although GaN nanowires synthesized at relatively low temperatures may exhibit both blue and yellow defect luminescence.[87]

To summarize, different GaN nanostructures have been grown using a variety of solution and vapor phase methods. A number of different source materials and catalysts has been investigated. The crystal structure of materials obtained by vapor deposition is typically hexagonal, and they exhibit very good optical properties. While in some studies blue defects in addition to UV emission are observed, yellow defect band is only rarely found in GaN nanostructures.

4. Aluminum Nitride Nanostructures

AlN nanostructures[54,112-131] have been studied less comprehensively than BN and GaN nanostructures. AlN nanocrystals[54,112-120] have been prepared by a variety of methods. Similar to other III-nitride nanocrystals, common synthesis method is a solvothermal method.[112-115] AlN nanocrystals have been prepared by a reaction between $AlCl_3$ and Li_3N.[112,115] Other precursors for solvothermal methods include aluminum cupferronate,[113] $AlCl_3$ and Na_3N,[114] and Al:NH_4Cl:NH_4I mixture in ammonia.[120] The obtained nanocrystals, depending on the experimental procedure used can be either a mixture of cubic and hexagonal phases,[112,115] hexagonal[113,120] or cubic[114] phase. Other synthesis methods which resulted in formation of hexagonal AlN nanocrystals include $AlCl_3$ aided CVD route,[116] CVD method,[119] and nitrogen implantation.[117,118]

AlN nanocrystals with either hexagonal or cubic structure can also be fabricated from $Al(H_2NCONH_2)_6)Cl_3$, depending on the experimental conditions.[54] If the same precursor is decomposed over Au islands on Si

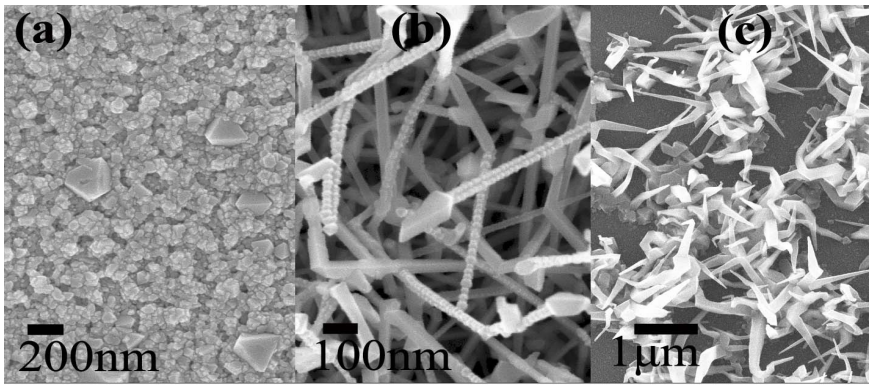

Fig. 5. Influence of the temperature on InN growth. a) 570°C b) 550°C c) 500°C.

substrate in ammonia flow, AlN nanowires are obtained.[54] Other experimental methods for nanowire fabrication have also been proposed.[123-125,127,128,130,131] AlN nanowires were grown by heating Al metal in NH_3 gas flow.[123] No catalysts were used, and obtained AlN nanowires had diameters in the range 5-40 nm, and exhibited blue photoluminescence which was assigned to oxygen impurities.[123] Similar to synthesis of GaN nanowires where either metallic Ga or Ga_2O_3 or GaN or their mixture can serve as a source, AlN nanowires prepared from Al,[124,128,131] Al_2O_3,[124] or their mixture,[124,125] as well as Al and AlN mixture,[130] were reported. When Al_2O_3 or mixture containing Al_2O_3 is used as a source material, carbon nanotubes were added to the source material.[124,125] Carbon nanotubes have dual role as a reducing agent and the template for nanowire fabrication.[124,125] Unlike hexagonal AlN nanowires produced by vapor deposition methods,[124,125] arc-plasma method can be used to fabricate the AlN nanowires and nanoparticles with the mixture of cubic and hexagonal phases, or purely cubic ones, depending on the arc currents.[127] For the fabrication of aligned AlN nanowires, porous alumina template was used.[128] More simple method for fabrication of aligned AlN nanowire array involved heating of Al in ammonia flow, with sapphire substrate placed above the boat with the source material.[131]

Other reported AlN morphologies include AlN nanorings,[121] nanotubes,[122,126] and serrated nanoribbons.[129] AlN nanorings were

fabricated by heating Al:Mn (95:5) alloy in the flow of ammonia gas.[121] For AlN nanotubes, AlN nanotubes were prepared by Dc-arc plasma method[122] as well as by vapor deposition method using carbon nanotubes as templates.[126] Fabrication of serrated AlN nanoribbons by heating $AlCl_3$ in the flow of N_2 and NH_3 gases was also reported.

Comparatively few morphologies reported for AlN are likely due to the fact that AlN has not been as widely studied as GaN and BN. In addition, the studies of optical properties of AlN nanostructures have been scarce. Further work is needed in order to understand the relationship between morphology and other properties of AlN nanostructures and the fabrication conditions.

5. Indium Nitride Nanostructures

Compared to other III-nitride nanostructures, reports on InN nanostructures have been scarce.[132-142] InN thin films are currently receiving lots of attention due to recent discovery of its narrow (0.7-0.8 eV) band gap, but the studies of InN nanostructures have not been common. In addition to its importance in GaN based ternary alloys for optoelectronic applications, there are other promising applications of InN. For example, Pt coated InN nanorods for selective detection of hydrogen were recently reported.[139] Transport in InN nanorods has also been studied.[134]

InN nanorods and nanowires were grown by hydride metalorganic vapor phase epitaxy,[139] electrodeposition,[132] and vapor phase deposition,[134-136,138,140] The commonly used catalyst for InN nanorod/nanowire growth is Au.[134,136,138,140] Growth without catalysts on quartz and polycrystalline AlN can also be achieved.[133] The source material is commonly metallic In.[133,140] Mixture of In and In_2O_3 has also been used to fabricate InN nanowires.[136] Selective growth of InN nanowires on Au patterns on Si substrate was also reported,[138] while ordered InN nanowire arrays were fabricated in anodized alumina templates.[132] In addition to pure InN nanowires, InN/InP core-shell nanowires were also fabricated.[137]

Other morphologies of InN nanostructures include InN nanocrystals,[54,142] and helical nanotubes.[141] Similar to GaN and AlN, InN hexagonal nanowires or nanocrystals with either hexagonal or cubic structure can be fabricated from $In(H_2NCONH_2)_6)Cl_3$, under different experimental conditions.[54] Also similar to GaN nanocrystal synthesis, InN nanocrystals can be synthesized by a solvothermal method from $InCl_3$ and Li_3N.[142] The nanocrystals exhibited mixture of cubic and hexagonal phases,[142] but detailed dependence of the obtained phases as a function of experimental conditions has not been performed. Helical InN nanotubes were prepared by nitridation of In_2O_3 in NH_3 gas flow.[141] The

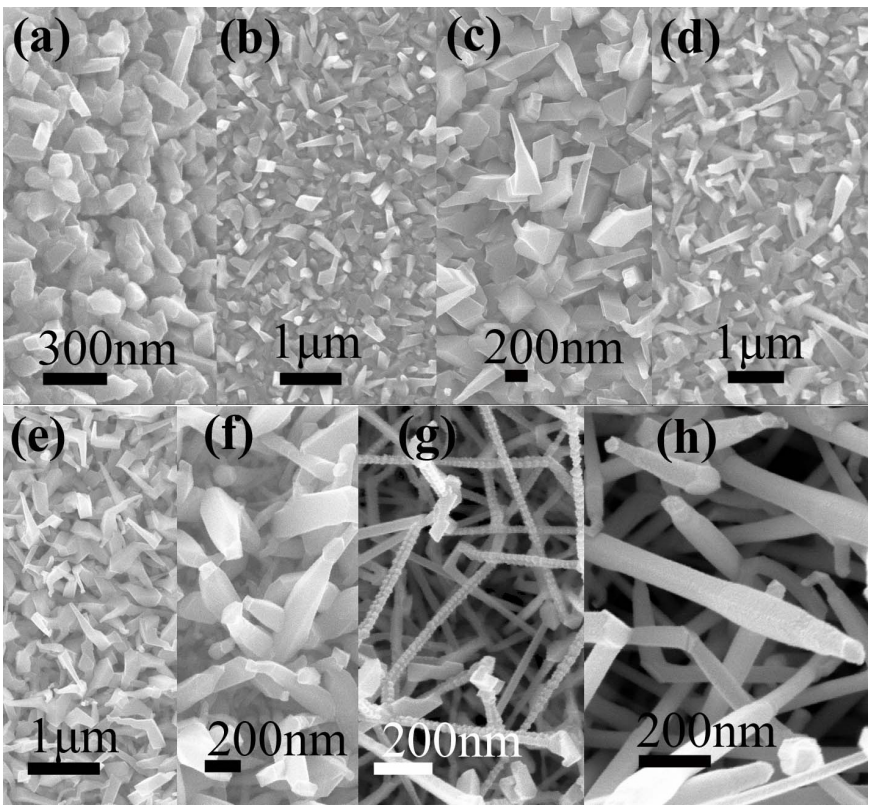

Fig. 6 Influence of the gas flow rate a) NH_3=10 sccm, Ar=25 sccm; (b) NH_3=25 sccm, Ar=25 sccm; (c) NH_3=25 sccm, Ar=50 sccm; (d) NH_3=25 sccm, Ar=75 sccm; (e) NH_3=50 sccm, Ar=50 sccm; (f) NH_3=50 sccm, Ar=100 sccm; (g) NH_3=125 sccm, Ar=25 sccm; (h) NH_3=150 sccm, Ar=0 sccm.

mechanism proposed for the tube formation was spiraling of warped InN nanobelts.[141]

Similar to GaN, InN nanowire/nanorod growth exhibits sensitivity to substrate temperature, as shown in Fig. 5. In this case, metallic In was used as the source, and Au coated Si was used as the substrate. It can be observed that there is a very narrow temperature window in which the growth of InN nanostructures can be obtained. The morphology of obtained products is also sensitive on the gas flow rate, as shown in Fig. 6. It can be observed that longer InN nanorods are obtained at higher gas flow rates, and the rod morphology depends on the ratio of Ar and NH_3 gases. The obtained morphology is also sensitive on the catalyst used. In addition to commonly used gold catalyst, silver can also be used to catalyze the growth of InN nanorods.

While the reports on synthesis of InN have not been as common as for other III-V nitrides, their optical properties have been reported for most fabrication methods. The photoluminescence of InN nanorods exhibited a peak at 0.766 eV assigned to band-edge emission.[134] Similar photoluminescence results (peak at ~0.8 eV) were reported for InN nanowires.[135] It was found that pure InN nanowires exhibited band gap of 0.8 eV, while those with mixed InN and In_2O_3 phases exhibited a peak at ~1.9 eV as well,[133] in agreement with the hypothesis that oxygen impurities cause overestimation of InN bandgap. Mixture of emissions at 0.8 eV and 1.9-2.1 eV, depending on the position on the substrate (center or edge), but no direct evidence of different oxygen content was found.[140] For nanowires grown form In/In_2O_3 mixed source material, only broad luminescence in the range 1.8-2.0 eV is observed.[136] Although the origin of this emission is not discussed, it is reasonable to assume that presence of oxygen in the source material can cause the presence of oxygen impurities in deposition product and consequently different band gap from now commonly accepted value of 0.7-0.8 eV. Hexagonal InN nanotubes which were prepared from In_2O_3 source material also exhibited photoluminescence peak at ~1.77 eV.[141] Thus, it is necessary to minimize the possibility of incorporating oxygen impurities in order to grow high quality InN nanostructures with bandgap in infrared spectral range. Since PL peak at ~1.85 eV was also obtained from InN nanowires prepared from metallic In source,[138] other possible

causes of defects or oxygen impurities besides the presence of oxygen in the source material need to be considered. It should also be noted that InN nanowire arrays in anodized alumina membrane exhibited a broad blue-green luminescence whose origin is not fully clear,[132] so that additional care is needed in interpreting the luminescence results in he presence of a porous template.[132]

To summarize, several methods for fabrication of InN nanostructures were proposed. Their optical properties were highly sensitive to the fabrication conditions. Similar to thin films, growth of good optical quality InN appears to be difficult. Further studies on the issue of observed bandgap in InN nanostructures fabricated under different conditions need to be made to conclusively establish the origin of the bandgap shift and the guidelines for the fabrication of good quality nanostructures. In addition, progress needs to be made in fabrication of ordered and aligned InN nanostructure arrays, which would be of interest for device applications.

6. Ternary Nitride Alloy Nanostructures and III-Nitride Nano-Heterostructures

In addition to simple nanostructures of binary materials, ternary alloys and nanoscale heterojunctions were also studied.[137,143-152] Heterojunctions and quantum wells are of interest to achieve carrier confinement and realize efficient devices. Carrier confinement in AlN nanowires with AlGaN quantum wells has been studied theoretically.[152] AlGaN nanowires growth and spontaneous formation of AlGaN/GaN core-shell nanowires by MOCVD method was reported.[143] Other reported core-shell nanorods or nanowires include GaP/ GaN and GaN/GaP nanowires,[147] GaN/ZnO nanorods,[150] GaN/InGaN/GaN nanowires,[144] and InN/InP nanowires.[137] Concerning the nanoscale junctions, both homojunctions[145,146] and heterojunctions[144,145] have been studied. In addition, nanoscale multiple quantum well structures were also reported.[145,149,151] GaN nanowires with well defined p-n junctions have been studied.[146] In addition to junctions within single wires, other junction geometries have also been studied, such as nanorod growth on nanowires[145] as well as radial heterojunctions.[144] Electroluminescence

has been achieved from n-GaN/InGaN/p-GaN radial heterojunctions.[144] High brightness light emitting diodes based on InGaN/GaN multiquantum well nanorod arrays grown by metalorganic hydride vapor phase epitaxy have also been demonstrated.[151] Multiple quantum well nanorod arrays can also be fabricated by direct etching of a light emitting diode wafer.[145,149]

Although ternary alloy and heterojunction nanostructures represent the least commonly studied form of nitride nanostructures, they are the most relevant ones for the device applications, Some promising results on the growth and applications of these structures have been achieved, but further work is needed to fully understand their properties and optimize them to obtain highly efficient electronic and optoelectronic devices based on these structures.

7. Conclusions and Outlook

This chapter has presented an overview of recent research on the growth and properties of nitride nanostructures. Boron nitride and gallium nitride have been extensively studied, and interesting properties have been demonstrated for common morphologies (nanotubes for BN and nanowires for GaN). In particular, GaN nanowires typically exhibit very good optical properties, and the well-known yellow defect band is only rarely observed. On the other hand, in the case of InN nanostructures, similar to InN epilayers, it is hard to achieve good optical quality of the sample with the band gap in the infrared spectral range. For this reason, it is necessary to minimize the possibility of oxygen contamination and avoid using source materials which contain oxygen. For both InN and AlN, more comprehensive studies of the growth itself and the relationship between the fabrication conditions and obtained properties need to be performed. Finally, even though some promising results on device applications of nanoscale heterojunctions have already been achieved, further studies on more complex nanostructures are needed for their wider practical applications. This also includes the studied on doped nanostructures, which have been scarce.

References

1. Y. Xia, P. Yang, Y. Sun, Y. Wu, B. Mayers, B. Gates, Y. Yin, F. Kim and H Yan, "One-dimensional nanostructures: synthesis, characterization, and applications", *Adv. Mater.* **15**, 353-389 (2003).
2. M. Law, J. Goldberger, P. Yang, "Semiconductor Nanowires and Nanotubes", *Annu. Rev. Mater. Res.* **34**, 83-122 (2004).
3. M. Remškar, "Inorganic nanotubes", *Adv. Mater*. **16**, 1497-1504 (2004).
4. T. Mukai, S. Nagahama, M. Sano, T. Yanamoto, D. Morita, T. Mitani, Y. Narukawa, S. Yamamoto, I. Niki, M. Yamada, S. Sonobe, S. Shioji, K. Deguchi, T. Naitou, H. Tamaki, Y. Murazaki, and M. Kameshima, "Recent progress of nitride-based light emitting devices", *Phys. Stat. Sol. (a)* **200**, 52-57 (2003).
5. M. A. Khan, M. Shatalov, H. P. Maruska, H. M. Wang, E. Koukstis, "III-nitride UV devices", *Jpn. J. Appl. Phys*. **44**, 7191-7206 (2005).
6. H. J. Xiang, J. Yang, J. G. Hou and Q. Zhu, "Half-metallic ferromagnetism in transition-metal encapsulated boron nitride nanotubes," *New J. Phys.* **7**, 39-(1-8) (2005).
7. J. Zhan, X. Hao, S. Wen, M. Jiang, "Research on bamboo-like one dimensional o-BN nanowire," *Physica E* **25**, 409-413 (2005).
8. W. S. Jang, S. Y. Bae, J. Park, J. P. Ahn, "Thorn-like BN nanostructures," *Solid State Commun.* **133**, 139-43 (2005).
9. W. Han, A. Zettl, "GaN nanorods coated with pure BN", *Appl. Phys. Lett.* **81**, 5051-5053 (2002).
10. D. Golberg, Y. Bando, M. Mitome, K. Fushimi, C. Tang, "Boron nitride nanotubes as nanocrucibles for morphology and phase transformations in encapsulated nanowires of the Mg-O system," *Acta Mater.* **52**, 3295-3303 (2004).
11. M. Corso, W. Auwarter, M. Muntwiler, A. Tamai, T. Greber, J. Osterwalder, "Boron nitride nanomesh," *Science* **303**, 217-20, (2004).
12. Z. Q. Shen, L. L. He, E. D. Wu, Y. Y. Fan, J. F. He, H. M. Cheng, D. X. Li, H. Q. Ye, "Boron nitride nanotubes filled with zirconium oxide nanorods," *J. Mater. Res.* **17**, 2761-2764 (2002).
13. K. F. Huo, Z. Hu, F. Chen, J. J. Fu, Y. Chen, B. H. Liu, J. Ding, Z. L. Dong, T. White, "Synthesis of boron nitride nanowires," *Appl. Phys. Lett.* **80**, 3611-3613 (2002).
14. F. L. Deepak, C. P. Vinod, K. Mukhopadhyay, A. Govindaraj, C. N. R. Rao, "Boron nitride nanotubes and nanowires," *Chem. Phys. Lett.* **353**, 345-352 (2002).
15. T. Oku, H. Kitahara, M. Kuno, I. Narita, K. Suganuma, "Synthesis, atomic structures and arrangement of carbon and boron nitride nanocage materials," *Scripta Mater*. **44**, 1557-1560, (2001).
16. A. Loiseau, F. Willaime, "Filled and mixed nanotubes: from TEM studies to the growth mechanism within a phase-diagram approach," *Appl. Surf. Sci.* **164**, 227-240 (2000).

17. W. Han, P. Redlich, F. Ernst, M. Ruhle, "Synthesizing boron nitride nanotubes filled with SiC nanowires by using carbon nanotubes as templates," *Appl. Phys. Lett.* **75**, 1875-1877 (1999).
18. D. Golberg, A. Rode, Y. Bando, M. Mitome, E. Gamaly and B. Luther-Davies, "Boron nitride nanostructures formed by ultra-high-repetition rate laser ablation," *Diamond and Related Materials* **12**, 1269-1274 (2003).
19. D. Golberg, F. F. Xu, Y. Bando, "Filling boron nitride nanotubes with metals," *Appl. Phys. A* **76**, 479-85 (2003).
20. R. Ma, Y. Bando, T. Sato, K. Kurashima, "Thin boron nitride nanotubes with unusual large inner diameters," *Chem. Phys. Lett.* **350**, 434-440 (2001).
21. Y. Bando, K. Ogawa, D. Golberg, "Insulating `nanocables': Invar Fe-Ni alloy nanorods inside BN nanotubes," *Chem. Phys. Lett.* **347**, 349-354 (2001).
22. X. Hao, J. Zhan, W. Fang, D. Cui, X. Xu, M. Jiang and M. Schieber, "Synthesis of cubic boron nitride by structural induction effect," *J. Cryst. Growth* **270**, 192-196 (2004).
23. M. Yu, S. Dong, K. Li, X. Hao, Z. Lai, Q. Wang, D. Cui, M. Jiang, R. S. Feigelson, "Synthesis of BN nanocrystals under hydrothermal conditions," *J. Cryst. Growth* **270**, 85-91 (2004).
24. X. Hao, S. Dong, W. Fang, J. Zhan, L. Li, X. Xu, M. Jiang, "A novel hydrothermal route to synthesize boron nitride nanocrystals," *Inorg. Chem. Commun.* **7**, 592-594 (2004).
25. J. B. Wang, X. L. Zhong, C. Y. Zhang, B. Q. Huang, G. W. Yang, "Explosion phase formation of nanocrystalline boron nitrides upon pulsed-laser-induced liquid/solid interfacial reaction," *J. Mater. Res.***18**, 2774-2778 (2003).
26. J. B. Wang, G. W. Yang, C. Y. Zhang, X. L. Zhong, Z. H. A. Ren, "Cubic-BN nanocrystals synthesis by pulsed laser induced liquid-solid interfacial reaction," *Chem. Phys. Lett.* **367**, 10-14 (2003).
27. X. P. Hao, D. L. Cui, G. X. Shi, Y. Q. Yin, X. G. Xu, J. Y. Wang, M. H. Jiang, X. W. Xu, Y. P. Li, B. Q. Sun, "Synthesis of cubic boron nitride at low-temperature and low-pressure conditions," *Chem. Mater.* **13**, 2457-2459 (2001).
28. X. Hao, M. Yu, D. Cui, X. Xu, Q. Wang, M. Jiang, "The effect of temperature on the synthesis of BN nanocrystals," *J. Cryst. Growth* **241**, 124-128 (2002).
29. X. P. Hao, D. L. Cui, G. X. Shi, Y. Q. Yin, X. G. Xu, M. H. Jiang, X. W. Xu, Y. P. Li, "Low temperature benzene thermal synthesis and characterization of boron nitride nanocrystals," *Mater. Lett.* **51**, 509-513 (2001).
30. V. Ya. Shevchenko and G. S. Yur'ev, "Morphology and structure of BN and B_4C nanocrystals," *Inorg. Mater.* **37**, 935-940 (2001).
31. J. Kawai, S. Tadokoro, Y. Muramatsu, S. Kashiwai, H. Kohzuki, M. Motoyama, H. Kato, H. Adachi, "Detection of dangling bonds in the mechanically milled h-BN nanocrystals by resonance X-ray scattering above threshold," *Physica B* **208-209**, 251-252 (1995).

32. P. Cai, L. Chen, L. Shi, Z. Yang, A. Zhao, Y. Gu, T. Huang, Y. Qian, "One convenient synthesis route to boron nitride nanotube," *Solid State Commun*. **133**, 621-623 (2005).
33. N. Li, X. Li, W. Geng, L. Zhao, G. Zhu, R. Wang, S. Qiu, "Template synthesis of boron nitride nanotubes in mesoporous silica SBA-15," *Mater. Lett*. **59**, 925-928 (2005).
34. H. J. Seung, D. J. Roundy, S. G. Louie, M. L. Cohen, "Formation and electronic properties of double-walled boron nitride nanotubes," *Solid State Commun*. **134**, 397-402 (2005).
35. R. Arenal, O. Stephan, M. Kociak, D. Taverna, A. Loiseau, C. Colliex, "Electron energy loss spectroscopy measurement of the optical gaps on individual boron nitride single-walled and multiwalled nanotubes," *Phys. Rev. Lett.* **95**, 127601-(1-4) (2005).
36. C. Zhi, Y. Bando, C. Tang, D. Golberg, R Xie, T. Sekigushi, "Phonon characteristics and cathodolumininescence of boron nitride nanotubes," *Appl. Phys. Lett.* **86**, 213110-(1-3) (2005).
37. C. W. Chang, W. Q. Han, A. Zettl, "Thermal conductivity of B-C-N and BN nanotubes," *Appl. Phys. Lett*. **86**, 173102-(1-3) (2005).
38. R. Q. Wu, L. Liu, G. W. Peng, Y. P. Feng, "Magnetism in BN nanotubes induced by carbon doping," *Appl. Phys. Lett.* **86**, 122510-(1-3) (2005).
39. M. Ishigami, J. D. Sau, S. Aloni, M. L. Cohen, A. Zettl, "Observation of the giant Stark effect in boron-nitride nanotubes," *Phys. Rev. Lett.* **94**, 056804-(1-4) (2005).
40. J. S. Lauret, R. Arenal, F. Ducastelle, A. Loiseau, M. Cau, B. Attal-Tretout, E. Rosencher, L. Goux-Capes, "Optical transitions in single-wall boron nitride nanotubes," *Phys. Rev. Lett.* **94**, 037405-(1-4) (2005).
41. J. J. Fu, Y. N. Lu, H. Xu, K. F. Huo, X. Z. Wang, L. Li, Z. Hu, Y. Chen, "The synthesis of boron nitride nanotubes by an extended vapour-liquid-solid method," *Nanotech.***15**, 727-730 (2004).
42. Y. Xiao, X. H. Yan, J. Xiang, Y. L. Mao, Y. Zhang, J. X. Cao, J. W. Ding, "Specific heat of single-walled boron nitride nanotubes," *Appl. Phys. Lett.* **84**, 4626-4628 (2004).
43. M. Radosavljevic, J. Appenzeller, V. Derycke, R. Martel, P. Avouris, A. Loiseau, J. L. Cochon, D. Pigache, "Electrical properties and transport in boron nitride nanotubes," *Appl. Phys. Lett.* **82**, 4131-4133 (2003).
44. W. Q. Han, W. Mickelson, J. Cumings, A. Zettl, "Transformation of $B_xC_yN_z$ nanotubes to pure BN nanotubes," *Appl. Phys. Lett.* **81**, 1110-1112 (2002).
45. C. C. Tang, X. X. Ding, X. T. Huang, Z. W. Gan, S. R. Qi, W. Liu, S. S. Fan, "Effective growth of boron nitride nanotubes," *Chem. Phys. Lett.* **356**, 254-258 (2002).
46. E. Bengu, L. D. Marks, "Single-walled BN nanostructures," *Phys. Rev. Lett*. **86**, 2385-2387 (2001).

47. A. Loiseau, F. Willaime, N. Demoncy, G. Hug, H. Pascard, "Boron nitride nanotubes with reduced numbers of layers synthesized by arc discharge," *Phys. Rev. Lett.* **76**, 4737-4740 (1996).
48. X. Xiang, C. Cao, Y. Xu, H. Zhu, "Large-scale synthesis and optical properties of hexagonal GaN micropyramid/nanowire homostructures," *Nanotech*. **17**, 30-34 (2006).
49. V. Srivastava, V. Sureshkumar, P. Puviarasu, K. Thangaraju, R. Thangavel, J. Kumar, "Growth and characterization of gallium nitride nanowire," *J. Cryst. Growth* **275**, e2367-2369 (2005).
50. P. V. Radovanovic, C. J. Barrelet, S. Gradecak, F. Qian, C. M. Lieber, "General synthesis of manganese-doped II-VI and III-V semiconductor nanowires," *Nano Lett.* **5**, 1407-1411 (2005).
51. E. Stern, G. Cheng, E. Cimpoiasu, R. Klie, S. Guthrie, J. Klemic, I. Kretzschmar, E. Steinlauf, D. Turner-Evans, E. Broomfield, J. Hyland, R. Koudelka, T. Boone, M. Young, A. Sanders, R. Munden, T. Lee, D. Routenberg, M. A. Reed, "Electrical characterization of single GaN nanowires," *Nanotech*. **16**, 2941-2953 (2005).
52. R. Ghosh, D. Basak, "Quantum confinement of excitons in dendrite-like GaN nanowires," *J. Appl. Phys.* **98**, 86104-(1-3) (2005).
53. A. B. Greytak, C. J. Barrelet, Y. Li, C. M. Lieber, "Semiconductor nanowire laser and nanowire waveguide electro-optic modulators," *Appl. Phys. Lett*. **87**, 151103-(1-3) (2005).
54. K. Sardar, M. Dan, B. Schwenzer, C. N. R. Rao, "A simple single-source precursor route to the nanostructures of AlN, GaN and InN," *J. Mater. Chem*. **15**, 2175-2177 (2005).
55. X. M. Cai, A. B. Djurišić, M. H. Xie, C. S. Chiu, S. Gwo, "Growth mechanism of stacked-cone and smooth-surface GaN nanowires," *Appl. Phys. Lett.* **87**, 183103-(1-3) (2005).
56. Q. Wang, Q. Sun, P. Jena, Y. Kawazoe, "Ferromagnetic GaN-Cr nanowires," *Nano Lett.* **5**, 1587-1590 (2005).
57. S. Gradecak, F. Qian, Y. Li; H. G. Park, C. M. Lieber, "GaN nanowire lasers with low lasing thresholds," *Appl. Phys. Lett.* **87**, 173111-(1-3) (2005).
58. G. Seryogin, I. Shalish, W. Moberlychan, V. Narayanamurti," Catalytic hydride vapour phase epitaxy growth of GaN nanowires," *Nanotech.* **16**, 2342-2345 (2005).
59. N. S. Gajbhiye, S. Bhattacharyya, "Magnetic properties of epsilon -Fe/sub 3/N-GaN core-shell nanowires," *Nanotech.* **16**, 2012-2019 (2005).
60. B. Ha, S. H. Seo, J. H. Cho, C. S. Yoon, J. Yoo, G. C. Yi, C. Y. Park, C. J. Lee, "Optical and field emission properties of thin single-crystalline GaN nanowires," *J. Phys. Chem. B* **109**, 11095-11099 (2005).
61. B. Liu, Y. Bando, C. Tang, F. Xu, D. Golberg, "Quasi-aligned single-crystalline GaN nanowire arrays," *Appl. Phys. Lett.* **87**, 73106-(1-3) (2005).

62. Y. P. Song, P. W. Wang, H. Q. Lin, G. S. Tian, J. Lu, Z. Wang, Y. Zhang, D. P. Yu, "Physical origin of the ferromagnetic ordering above room temperature in GaMnN nanowires," *J. Phys.: Condens. Matter.* **17**, 5073-5085 (2005).
63. Z. Dong, C. Xue, H. Zhuang, S. Wang, H. Gao, D. Tian, Y. Wu, J. He, Y. Liu, "Synthesis of three kinds of GaN nanowires through Ga_2O_3 films' reaction with ammonia," *Physica E* **27**, 32-37 (2005).
64. L. Yang, X. Zhang, R. Huang, G. Zhang, C. Xue, "Two-step synthesis of one-dimensional single crystalline GaN nanowires," *Physica E* **25**, 582-586 (2005).
65. C. Diaz-Guerra, J. Piqueras, V. Popa, A. Cojocaru, I. M. Tiginyanu, "Spatially resolved cathodoluminescence of GaN nanostructures fabricated by photo-electrochemical etching," *Appl. Phys. Lett*. **86**, 223103-(1-3) (2005).
66. J. Zhang, L. Zhang, F. Jiang, Y. Yang, J. Li, "Fabrication and optical property of silicon oxide layer coated semiconductor gallium nitride nanowires," *J. Phys. Chem. B* **109**, 151-154 (2005).
67. S. K. Lee, H. J. Choi, P. Pauzauskie, P. Yang, N. K. Cho, H. D. Park, E. K. Suh, K. Y. Lim, H. J. Lee, "Gallium nitride nanowires with a metal initiated metal-organic chemical vapor deposition (MOCVD) approach," *Phys. Stat. Sol.(b)* **241**, 2775-2778 (2004).
68. J. M. Baik, J. L. Lee, "Ferromagnetic properties of (Ga,Mn)N nanowires grown by a chemical vapor deposition method," *J. Vac. Sci. Tech. B* **23**, 530-533 (2005).
69. T. Wang, F. Ranalli, P. J. Parbrook, R. Airey, J. Bai, R. Rattlidge, G. Hill, "Fabrication and optical investigation of a high-density GaN nanowire array," *Appl. Phys. Lett.* **86**, 103103-(1-3) (2005).
70. G. Kipshidze, B. Yavich, A. Chandolu, J. Yun, V. Kuryatkov, I. Ahmad, D. Aurongzeb, M. Holtz, H. Temkin, "Controlled growth of GaN nanowires by pulsed metalorganic chemical vapor deposition," *Appl. Phys. Lett.* **86**, 33104-(1-3) (2005).
71. D. S. Han, J. Park, K. W. Rhie, S. Kim, J. Chang, "Ferromagnetic Mn-doped GaN nanowires," *Appl. Phys. Lett.* **86**, 32506-(1-3) (2005).
72. D. Wang, F. Qian, C. Yang, Z. Zhong, C. M. Lieber, "Rational growth of branched and hyperbranched nanowire structures," *Nano Lett.* **4**, 871-874 (2004).
73. C. Y. Nam, D. Tham, J. E. Fischer, "Effect of the polar surface on GaN nanostructure morphology and growth orientation," *Appl. Phys. Lett*. **85**, 5676-5678 (2004).
74. F. Xu, Y. Xie, X. Zhang, S. Zhang, X. Liu, W. Xi, X. Tian, "Single-crystalline gallium nitride microspindles: synthesis, characterization, and thermal stability," *Adv. Funct. Mater.* **14**, a464-470 (2004).
75. S. Dhara, A. Datta, C. T. Wu, Z. H. Lan, K. H. Chen, Y. L. Wang, C. W. Hsu, C. H. Shen, L. C. Chen, C. C. Chen, "Hexagonal-to-cubic phase transformation in GaN nanowires by Ga^+ implantation," *Appl. Phys. Lett.* **84**, 5473-5475 (2004).

76. S. Y. Bae, H. W. Seo, J. Park, H. Yang, B. Kim, "Porous GaN nanowires synthesized using thermal chemical vapor deposition," *Chem. Phys. Lett.* **376**, 445-451 (2003).
77. T. Kuykendall, P. Pauzauskie, S. Lee, Y. Zhang, J. Goldberger, P. Yang, "Metalorganic chemical vapor deposition route to GaN nanowires with triangular cross sections," *Nano Lett.* **3**, 1063-1066 (2003).
78. S. Y. Bae, H. W. Seo, D. S. Han, M. S. Park, W. S. Jang, C. W. Na, J. Park, C. S. Park, "Synthesis of gallium nitride nanowires with uniform [001] growth direction," *J. Cryst. Growth* **258**, 296-301 (2003).
79. K. W. Chang, J. J. Wu, "Temperature-controlled catalytic growth of one-dimensional gallium nitride nanostructures using a gallium organometallic precursor," *Appl. Phys. A* **77**, 769-774 (2003).
80. J. Zhang, L. Zhang, *"Growth of semiconductor gallium nitride nanowires with different catalysts," J. Vac. Sci. Tech. B* **21**, 2415-2419 (2003).
81. E. A. Stach, P. J. Pauzauskie, T. Kuykendall, J. Goldberger, R. He, P. Yang, "Watching GaN nanowires grow," *Nano Lett*. **3**, 867-869 (2003).
82. A. M. S. ElAhl, M. He, P. Zhou, G. L. Harris, L. Salamanca-Riba, F. Felt, H. C. Shaw, A. Sharma, M. Jah, D. Lakins, T. Steiner, S. N. Mohammad, "Systematic study of effects of growth conditions on the (nano-, meso-, micro) size and (one-, two-, three-dimensional) shape of GaN single crystals grown by a direct reaction of Ga with ammonia," *J. Appl. Phys.* **94**, 7749-7756 (2003).
83. Z. J. Li, H. J. Li, K. Z. Li, Q. J. Gong, X. B. Xiong, "Synthesis of the various morphologies GaN one-dimensional nanomaterials," *J. Mater. Sci. Lett.* **22**, 831-833 (2003).
84. J. C. Wang, C. Z. Zhan, F. G. Li, "The synthesis of highly oriented GaN nanowire arrays," *Appl. Phys. A* **76**, 609-611 (2003).
85. J. Jian, X. L. Chen, M. He, W. J. Wang, X. N. Zhang, F. Shen, "Large-scale GaN nanobelts and nanowires grown from milled Ga_2O_3 powders," *Chem. Phys. Lett.* **368**, 416-420 (2003).
86. Y. Huang, X. Duan, Y. Cui, C. M. Lieber, "Gallium nitride nanowire nanodevices," *Nano Lett*. **2**, 101-104 (2002).
87. K. W. Chang, J. J. Wu, "Low-temperature catalytic synthesis of gallium nitride nanowires," *J. Phys. Chem. B* **106**, 7796-7799 (2002).
88. J. Zhang, L. Zhang, "Morphology and Raman scattering spectrum of GaN nanowires embedded in nanochannels of template," *J. Phys. D: Appl. Phys*. **35**, 1481-1485 (2002).
89. H. Y. Peng, N. Wang, X. T. Zhou, Y. F. Zheng, C. S. Lee, S. T. Lee, "Control of growth orientation of GaN nanowires," *Chem. Phys. Lett.* **359**, 241-245 (2002).
90. J. Y. Li, X. L. Chen, Z. Y. Qiao, Y. G. Cao, H. Li, "Synthesis of GaN nanotubes," *J. Mater. Sci. Lett*. **20**, 1987-1988 (2001).

91. J. Zhang, L. D. Zhang, X. F. Wang, C. H. Liang, X. S. Peng, Y. W. Wang, "Fabrication and photoluminescence of ordered GaN nanowire arrays," J. Chem. Phys. **115**, 5714-5717 (2001).
92. M. He, P. Zhou, S. Noor-Mohammad, G. L. Harris, J. B. Halpern, R. Jacobs, W. L. Warney, L. Salamanca-Riba, "Growth of GaN nanowires by direct reaction of Ga with NH_3," *J. Cryst. Growth* **231**, 357-365 (2001).
93. Z. J. Li, X. L. Chen, H. J. Li, Q. Y. Tu, Z. Yang, Y. P. Xu, B. Q. Xu, "Synthesis and Raman scattering of GaN nanorings, nanoribbons and nanowires," *Appl. Phys. A* **72**, 629-632 (2001).
94. X. Chen, J. Li, Y. Cao, Y. Lan, H. Li, M. He, C. Wang, Z. Zhang, Z. Qiao, "Straight and smooth GaN nanowires," *Adv. Mater*. **12**, 1432-1434 (2000).
95. J. Y. Li, Z. Y. Qiao, X. L. Chen, Y. G. Cao, Y. C. Lan, C. Y. Wang, "Morphologies of GaN one-dimensional materials," *Appl. Phys. A* **71**, 587-588 (2000).
96. M. He, I. Minus, P. Zhou; S. Noor-Mohammed, J. B. Halpern, R. Jacobs, W. L. Sarney, L. Salamanca-Riba, R. D. Vispute, "Growth of large-scale GaN nanowires and tubes by direct reaction of Ga with NH_3," *Appl. Phys. Lett*. **77**, 3731-3733 (2000).
97. G. S. Cheng, S. H. Chen, X. G. Zhu, Y. Q. Mao, L. D. Zhang, "Highly ordered nanostructures of single crystalline GaN nanowires in anodic alumina membranes," *Mater. Sci. Eng. A* **286**, 165-168 (2000).
98. Y. H. Kim, J. Y. Lee, S. H. Lee, J. E. Oh, H. S. Lee, "Synthesis of aligned GaN nanorods on Si(111) by molecular beam epitaxy," *Appl. Phys. A* **80**, 1635-1639 (2005).
99. S. M. Zhou, X. H. Zhang, X. M. Meng, X. Fan, K. Zou, S. K. Wu, "The novel bicrystalline GaN nanorods," *Mater. Lett.* **58**, 3578-3581 (2004).
100. J. K. Jian, X. L. Chen, Q. Y. Tu, Y. P. Xu, L. Dai, M. Zhao, "Preparation and optical properties of prism-shaped GaN nanorods," *J. Phys. Chem. B* **108**, 12024-12026 (2004).
101. S. Y. Bae, H. W. Seo, J. Park, H. Yang, H. Kim, S. Kim, "Triangular gallium nitride nanorods," *Appl. Phys. Lett*. **82**, 4564-4566 (2003).
102. L. Grocholl, J. Wang, E. G. Gillan, "Solvothermal azide decomposition route to GaN nanoparticles, nanorods, and faceted crystallites," *Chem. Mater.* **13**, 4290-4296 (2001).
103. H. M. Kim, D. S. Kim, D. Y. Kim, T. W. Kang, Y. H. Cho, K. S. Chung, "Growth and characterization of single-crystal GaN nanorods by hydride vapor phase epitaxy," *Appl. Phys. Lett.* **81**, 2193-2195 (2002).
104. J. Y. Li, X. L. Chen, Z. Y. Qiao, Y. G. Cao, Y. C. Lan, "Formation of GaN nanorods by a sublimation method," *J. Cryst. Growth* **213**, 408-410 (2000).
105. S. Y. Bae, H. W. Seo, J. Park, H. Yang, J. C. Park, S. Y. Lee, "Single-crystalline gallium nitride nanobelts," *Appl. Phys. Lett.* **81**, 126-128 (2002).
106. S. Y. Bae, H. W. Seo, J. Park, H. Yang, S. A. Song, "Synthesis and structure of gallium nitride nanobelts," *Chem. Phys. Lett.* **365**, 525-529 (2002).

107. Q. Cui, Y. Pan, W. Zhang, X. Wang, J. Zhang, T. Cui, Y. Xie, J. Liu, G. Zou, "Pressure-induced phase transition in GaN nanocrystals," *J. Phys.: Condens. Matter.* **14**, 11041-11044 (2002).
108. Y. Yang, C. Tran, V. Leppert, S. H. Risbud, "From $Ga(NO_3)_3$ to nanocrystalline GaN: confined nanocrystal synthesis in silica xerogels," *Mater. Lett.* **43**, 240-243 (2000).
109. O. I. Mićić, S. P. Ahrenkiel, D. Bertram, A. J. Nozik, "Synthesis, structure, and optical properties of colloidal GaN quantum dots," *Appl. Phys. Lett.* **75**, 478-480 (1999).
110. V. J. Leppert, C. J. Zhang, H. W. H. Lee, I. M. Kennedy, S. H. Risbud, "Observation of quantum confined excited states of GaN nanocrystals," *Appl. Phys. Lett*. **72**, 3035-3037 (1998).
111. L. W. Yin, Y. Bando, Y. C. Zhu, D. Golberg, L. W. Yin, M. S. Li, "Indium-assisted synthesis on GaN nanotubes," *Appl. Phys. Lett.* **84**, 3912-3914 (2004).
112. M. Yu, X. Hao, D. Cui, Q. Wang, X. Xu, M. Jiang, "Synthesis of aluminium nitride nanocrystals and their catalytic effect on the polymerization of benzene," *Nanotech*. **14**, 29-32 (2003).
113. K. Sardar, C. N. R. Rao, "AlN nanocrystals by new chemical routes," *Sol. State Sci.* **7**, 217-220 (2005).
114. L. Li, X. Hao, N. Yu, D. Cui, X. Xu, M. Jiang, "Low-temperature solvent thermal synthesis of cubic AlN," *J. Cryst. Growth* **258**, 268-271 (2003).
115. X. P. Hao, M. Y. Yu, D. L. Cui, X. G. Xu, Y. J. Bai, Q. L. Wang, M. H. Jiang, "Synthesize AlN nanocrystals in organic solvent at atmospheric pressure," *J. Cryst. Growth* **242**, 229-232 (2002).
116. T. Xie, X. Y. Yuan, G. S. Wu, Y. Lin, X. X. Xu, G. W. Meng, L. D. Zhang, "Synthesis, characterization and photoluminescence of aluminium nitride nanopowders through an $AlCl_3$ aided CVD route," *J. Phys. Condens. Matter.* **16**, 1639-1644 (2004).
117. T. Reier, J. W. Schultze, W. Oesterle, C. Buchal, "Nucleation and growth of AlN nanocrystallites prepared by N^{2+} implantation," *Surface and Coatings Technology* **103-104**, 415-421 (1998).
118. T. Reier, J. W. Schultze, W. Osterle, C. Buchal, "The growth of aligned AlN-nanocrystals in aluminium after nitrogen-ion implantation at 330 K," *Thin Solid Films* **385**, 29-35 (2001).
119. N. C. Wu, M. S. Tsai, M. C. Wang, H. S. Liu, "The morphology and formation mechanism of aluminum nitride nanocrystals synthesized by chemical vapor deposition," *J. Cryst. Growth* **208**, 189-196 (2000).
120. Y. G. Cao, X. L. Chen, Y. C. Lan, J. Y. Li, Y. P. Xu, T. Xu, Y. Zhang, J. K. Liang, "Synthesis and photoluminescence characteristics of AlN nanocrystalline solids," *Appl. Phys. A* **71**, 351-352 (2000).
121. J. Duan, S. Yang, H. Liu, J. Gong, H. Huang, X. Zhao, J. Tang, R. Zhang, Y. Du, "AlN nanorings", *J. Cryst. Growth* **283**, 291-296 (2005).

122. V. N. Tondare, C. Balasubramanian, S. V. Shende, D. S. Joag, V. P. Godbole, S. V. Bhoraskar, M. Bhadbhade, "Field emission from open ended aluminum nitride nanotubes," *Appl. Phys. Lett.* **80**, 4813-4815 (2002).
123. C. Xu, L. Xue, C. Yin, G. Wang, "Formation and photoluminescence properties of AlN nanowires," *Phys. Stat. Sol. (a)* **198**, 329-335, (2003).
124. Y. Zhang, J. Liu, R. He, Q. Zhang, X. Zhang, J. Zhu, "Synthesis of aluminum nitride nanowires from carbon nanotubes," *Chem. Mater.* **13**, 3899-3905 (2001).
125. J. Liu, X. Zhang, Y. Zhang, R. He, J. Zhu, "Novel synthesis of AlN nanowires with controlled diameters," *J. Mater. Res.* **16**, 3133-3138, 2001.
126. Y. Zhang, J. Liu, R. He, Q. Zhang, X. Zhang, J. Zhu, "Synthesis of alumina nanotubes using carbon nanotubes as templates," *Chem. Phys. Lett.* **360**, 579-584 (2002).
127. C. Balasubramanian, V. P. Godbole, V. K. Rohatgi, A. K. Das, S. V. Bhoraskar, "Synthesis of nanowires and nanoparticles of cubic aluminium nitride," *Nanotech.* **15**, 370-373 (2004).
128. Q. Wu, Z. Hu, X. Wang, Y. Hu, Y. Tian, Y. Chen, "A simple route to aligned AlN nanowires," *Diamond and Related Mater*. **13**, 38-41 (2004).
129. T. Xie, Y. Lin, G. Wu, X. Yuan, Z. Jiang, C. Ye, G. Meng, L. Zhang, "AlN serrated nanoribbons synthesized by chloride assisted vapor-solid route," *Inorg. Chem. Commun.* **7**, 545-547 (2004).
130. H. Cong, H. Ma, X. Sun, "Synthesis of aluminum nitride nanowires," *Physica B* **323**, 354-356 (2002).
131. Q. Zhao, H. Zhang, X. Xu, Z. Wang, J. Xu, D. Yu, G. Li, F. Su, "Optical properties of highly ordered AlN nanowire arrays grown on sapphire substrate," *Appl. Phys. Lett.* **86**, 193101-(1-3) (2005).
132. J. Zhang, B. Xu, F. Jiang, Y. Yang, J. Li, "Fabrication of ordered InN nanowire arrays and their photoluminescence properties," *Phys. Lett. A* **337**, 121-126 (2005).
133. S. Vaddiraju, A. Mohite, A. Chin, M. Meyyappan, G. Sumanasekera, B. W. Alphenaar, M. K Sunkara, "Mechanisms of 1D crystal growth in reactive vapor transport: indium nitride nanowires," *Nano Lett.* **5**, 1625-1631 (2005).
134. C. Y. Chang, G. C. Chi, W. M. Wang, L. C. Chen, K. H. Chen, F. Ren, S. J. Pearton, "Transport properties of InN nanowires," *Appl. Phys. Lett.* **87**, 93112-(1-3) (2005).
135. M. C. Johnson, C. J. Lee, E. D. Bourret-Courchesne, S. L. Konsek, S. Aloni, W. Q. Han, A. Zettl, "Growth and morphology of 0.80 eV photoemitting indium nitride nanowires," *Appl. Phys. Lett.* **85**, 5670-5672 (2004).
136. T. Tang, S. Han, W. Jin; X. Liu, C. Li, D. Zhang, C. Zhou, B. Chen, J. Han, M. Meyyapan, "Synthesis and characterization of single-crystal indium nitride nanowires," *J. Mater. Res*. **19**, 423-426 (2004).
137. L. W. Yin, Y. Bando, Y. C. Zhu, D. Golberg, M. S. Li, "Synthesis of InN/InP core/sheath nanowires," *Appl. Phys. Lett.* **84**, 1546-1548 (2004).

138. C. H. Liang, L. C. Chen, J. S. Hwang, K. H. Chen, Y. T. Hung, Y. F. Chen, "Selective-area growth of indium nitride nanowires on gold-patterned Si(100) substrates," *Appl. Phys. Lett.* **81**, 22-24 (2002).
139. O. Kryliouk, H. J. Park, H. T. Wang, B. S. Kang, T. J. Anderson, F. Ren, S. J. Pearton, "Pt-coated InN nanorods for selective detection of hydrogen at room temperature," *J. Vac. Sci. Tech. B* **23**, 1891-1894 (2005).
140. Z. H. Lan, W. M. Wang, C. L. Sun, S. C. Shi, C. W. Hsu, T. T. Chen, K. H. Chen, C. C. Chen, Y. F. Chen, L. C. Chen, "Growth mechanism, structure and IR photoluminescence studies of indium nitride nanorods," *J. Cryst. Growth* **269**, 87-94 (2004).
141. S. Luo, W. Zhou, W. Wang, Z. Zhang, L. Liu, X. Dou, J. Wang, X. Zhao, D. Liu, Y. Gao, L. Song, Y. Xiang, J. Zhou, S. Xie, "Template-free synthesis of helical hexagonal microtubes of indium nitride," *Appl. Phys. Lett.* **87**, 63109-(1-3) (2005).
142. Y. J. Bai, Z. G. Liu, X. G. Xu, D. L. Cu, X. P. Ha, X. Feng, Q. L. Wang, "Preparation of InN nanocrystals by solvo-thermal method," *J. Cryst. Growth* **241**, 189-192 (2002).
143. J. Su, M. Gherasimova, G. Cui, H. Tsukamoto, J. Han, T. Onuma, M. Kurimoto, S. F. Chichibu, C. Broadbridge, Y. He, A. V. Nurmikko, "Growth of AlGaN nanowires by metalorganic chemical vapor deposition," *Appl. Phys. Lett.* **87**, 183108-(1-3) (2005).
144. F. Qian, Y. Li, S. Gradecak, D. Wang, C. J. Barrelet, C. M. Lieber, "Gallium nitride-based nanowire radial heterostructures for nanophotonics," *Nano Lett.* **4**, 1975-1979 (2004).
145. Z. H. Lan, C. H. Liang, C. W. Hsu, C. T. Wu, H. M. Lin, S. Dhara, K. H.Chen, L. C. Chen, C. C. Chen, "Nanohomojunction (GaN) and nanoheterojunction (InN) nanorods on one-dimensional GaN nanowire substrates," *Adv. Funct. Mater.* **14**, 233-237 (2004).
146. G. Cheng, A. Kolmakov, Y. Zhang, M. Moskovits, R. Munden, M. A. Reed, G. Wang, D. Moses, J. Zhang, "Current rectification in a single GaN nanowire with a well-defined p-n junction," *Appl. Phys. Lett.* **83**, 1578-1580 (2003).
147. H. M. Lin, Y. L. Chen, J. Yang, Y. C. Liu, K. M. Yin, J. J. Kai, F. R. Chen, L. C. Chen, Y. F. Chen, C. C. Chen, "Synthesis and characterization of core-shell GaP@GaN and GaN@GaP nanowires," *Nano Lett.* **3**, 537-541 (2003).
148. T. H. Hsueh, H. W. Huang, C. C. Kao, Y. H. Chang, M. C. Ou-Yang, H. C. Kuo, S. C. Wang, "Characterization of InGaN/GaN multiple quantum well nanorods fabricated by plasma etching with self-assembled nickel metal nanomasks," *Jpn. J. Appl. Phys.* Pt.1, **44**, 2661-2663 (2005).
149. T. H. Hsueh, H. W. Huang, F. I. Lai, J. K. Sheu, Y. H. Chang, H. C. Kuo, S. C. Wang, "Photoluminescence from $In_{0.3}Ga_{0.7}N$/GaN multiple-quantum-well nanorods," *Nanotech.* **16**, 448-450 (2005).

150. S. J. An, W. Il. Park, G. C. Yi, Y. J. Kim, H. B. Kang, M. Kim, "Heteroepitaxial fabrication and structural characterizations of ultrafine GaN/ZnO coaxial nanorod heterostructures," *Appl. Phys. Lett.* **84**, 3612-3614 (2004).
151. H. M. Kim, Y. H. Cho, H. Lee, S. Il. Kim, S. R. Ryu, D. Y. Kim, T. W. Kang, K. S. Chung, "High-brightness light emitting diodes using dislocation-free indium gallium nitride/gallium nitride multiquantum-well nanorod arrays," *Nano Lett.* **4**, 1059-1062 (2004).
152. E. W. S. Caetano, V. N. Freire, G. A. Farias, "Carrier confinement in AlGaN non-abrupt heterostructured nanowires," *Phys. Stat. Sol. (c)* **2**, 2365-2368 (2005).

This page intentionally left blank

CHAPTER 15

RECENT TRENDS IN INDIUM NITRIDE NANOMATERIALS

Abhijit Ganguly[1], Li-Chyong Chen[1], Kuei-Hsien Chen[2],
Surojit Chattopadhyay[3,*]

[1] *Center for Condensed Matter Sciences,*
National Taiwan University, Taipei 106, Taiwan
[2]*Institute of Atomic and Molecular Sciences,*
Academia Sinica, Taipei 106, Taiwan
[3]*Department of Electrical Engineering,*
National Chung Hsing University, Taichung 402, Taiwan
[*]*E-mail: sur@dragon.nchu.edu.tw*

The group III nitrides including gallium nitride, aluminum nitride, and indium nitride (InN) represents a formidable group of semiconductors with a high impact in optoelectronics. This is primarily due to their direct bandgaps that span a wide spectral range with the added flexibility of combining these materials in the ternary form. The momentum for research in nanostructured InN is growing. These materials often serve as semiconductor sensor backbones also. InN, lately, has been at the centre of attraction because of its controversial bandgap and the challenges involved in synthesis and understanding the complexities of the material. This review attempts to present the recent developments in the growth and properties exhibited by the low dimensional InN materials.

1. Introduction

Advances in the group III-Nitride semiconductors were central to the development of the optoelectronics applications. The vast potential for this group of semiconductors is not fully realized in terms of resultant devices apart from the light emitting diodes (LEDs). However, the progress made recently in the nanomaterials section opens up further possibility of broadening the field of application. Gallium nitride (GaN)[1,2] is clearly the most studied material in this class of compounds,

followed by aluminum nitride (AlN). However, the progress was slow. The optical property of GaN[3] was reported twenty years after the report on growth. The progress of understanding the material gathered momentum with the zinc (Zn) doping producing the first blue LED in 1972.[4] Indium nitride (InN) was still unheard of or at best at its infancy then. The first report on optical properties of InN was reported in 1986.[5]

The emergence of nanotechnology promoted the activities in the hexagonal group III-Nitride semiconductors, since the distinctive features of nanodimension lay in optoelectronics, for which the III-Nitrides are the front-runners. Research reports and reviews on GaN are plentiful,[6-9] but there is clearly a lack of report in InN nanomaterials. InN holds a special position in this class of compounds because of several challenges involved with it. They include, the extremely narrow growth window with respect to growth temperature as will be discussed later. Next, there is an ongoing debate on the optical band gap of InN, which was reported between the visible (~2.0 eV) and the infrared (~0.7 eV). These issues notwithstanding, InN made important contributions in the ternary compounds used for the LEDs.

This chapter will give a brief introduction to the growth and characterization methods of InN nanomaterials, in particular the one-dimensional nanostructures. Optical and electrical properties will be discussed in a detail, distinguishing the bulk from the 'nano' wherever possible. Other than the common nanostructures, e.g., nanoparticles (NPs), nanowires (NWs), nanorods (NRs), nanotubes, complex morphologies such as nanotips (NTs) and nanobelts (NBs) will be introduced. The section on application will focus on the sensor applications. In this simple article, readers will be given basic concepts or ideas about InN nanostructures with illustrations as far as practicable.

2. Synthesis of Indium Nitride Nanomaterials

Very informative reviews of the different growth techniques and their successful application to the deposition of group III-nitride epitaxial films and heterostructures have been presented.[10, 11] Systematic efforts at growing the group III-nitrides began in the 1970s by the chemical vapour deposition (CVD) and sputtering processes. At that time, neither metalorganic (MO) precursors containing In or Al with electronic grade purity, plasma sources for nitrogen radicals compatible with molecular beam epitaxy (MBE) systems, nor substrate material with reasonably

good thermal and lattice matches to the nitrides were available. In addition, the InN material had large concentrations of free electrons, presumed to result from oxygen impurities and intrinsic defects, and the structural quality of the films was not good enough for optoelectronic applications. Primarily, the development of MO-CVD and plasma-assisted MBE (PAMBE) over the last few years has led to a number of recent advances and important improvements in the structural properties.

Synthesis of InN is the most challenging work among the group III-nitride compounds. This is mainly because of the difficulties in growing high-quality crystalline InN semiconductors, not only in nanostructure form, but also even in thin film form. Due to the lack of suitable substrates, both the lattice constant and the coefficient of thermal-expansion mismatch induce high defect concentrations during the heteroepitaxial growth of InN. The high equilibrium vapour pressure of N_2 for InN sets a lower limit to the deposition temperature. The low decomposition temperature of InN defines the upper limit of the deposition temperature range. Both the limits constrained the operating temperature-window, which results in high defect densities and, therefore, a poor crystal quality for highly mismatched heterosystems. Recently, due to the development of various growth techniques, several studies on the synthesis of nanostructured InN materials have been reported.

2.1. *Thermal Chemical Vapour Deposition* (*CVD*)

CVD is a chemical process used to produce high-purity, high-performance solid materials. In a typical CVD process, the gas phase reactants (precursor gases, often diluted in carrier gases) are delivered into the reaction chamber at approximately room temperatures. Coming in contact with a heated substrate, the reactants react or decompose forming the desired materials in solid phase, which are deposited onto the substrate. The substrate temperature is a critical parameter and can influence the type of reactions taking place. Volatile by-products are removed by gas flow through the reaction chamber. A number of forms of CVD processes differ in the means by which chemical reactions are initiated or in the process conditions, and are frequently reported. The conventional thermal CVD is a kind of preliminary stage of CVD processes. The basic principle is to heat a foil or powder of the group III metal such as In (metal source) in presence of nitrogen (N_2) or ammonia (NH_3) gas (nitrogen source) at temperatures suitable for the vaporization

of the metal source and the dissociation of the nitriding gas. Thermal CVD, for nanomaterials growth, can be categorized into two general parts, depending on whether the growth is assisted or not by any catalyst.

2.1.1. Catalyst-assisted growth

In the catalyst-assisted growth, the whole deposition process is carried out in the presence of liquid metal clusters, also called catalysts, which acts as the energetically favored site for the absorption of gas-phase reactants. Transition metal and their oxides, along with metals such as gold (Au), were found to be efficient catalyst for the precipitation of the III-nitride materials. During the heating process, catalysts were fed with group-III metal vapour to form a molten state of the catalyst droplet supersaturated with the said metal vapour. Immediately after the introduction of the nitriding gas into the system, the formation of nanostructured III-nitride semiconductors will take place. The size and dispersion of the catalytic particle will determine the lateral dimension and distribution of the target nanomaterial that grows. The length of the nanomaterial, however, depends mostly on the reaction time and reactant flux. However, the choice of catalyst metal (Au, Fe, Ni, Co) remains of utmost importance. Wagner and Ellis[12] first termed the metal catalyst-assisted growth as the vapour-liquid-solid (VLS) growth.

Earlier reports showed the possibility of the formation of InN nanomaterials on silicon (Si) substrates via VLS growth using gold (Au) as a catalyst.[13, 14] Liang *et al.* [13] showed that the locations of these InN NWs could be controlled by depositing Au in desired areas on the substrates [Fig. 1a,b]. Transmission electron microscopy (TEM) studies[13] revealed high quality single crystalline structure of the NWs, having 40 nm diameters. The high-resolution TEM (HRTEM) image [Fig. 1c] clearly exhibited the lattice plane of (100) with 0.308 nm interplanar spacing. The wire axis is along [110] direction. The corresponding selected area electron diffraction (SAED) pattern (inset of the Fig. 1c) has been indexed to the reflections of hexagonal InN crystal along the ⟨001⟩ directions. The individual InN NW/NR was found to be capped with an Au nanoparticle (NP).[13, 14] The presence of Au NPs at the ends of the InN NWs [Fig. 1d] provides the strong evidence for a catalyst-assisted growth or VLS growth mechanism. Moreover, Lan *et al.*[14] reports the effects of reactant flux and temperature gradient along the growth zone. They found variations in the appearance colour: the region

of the substrate in the upstream portion of NH_3 flow produced the optically brown InN NRs (grown near substrate-edge), and black InN NRs grown at the center of the substrate. These two sets of InN NRs also had different optical properties as will be discussed later.

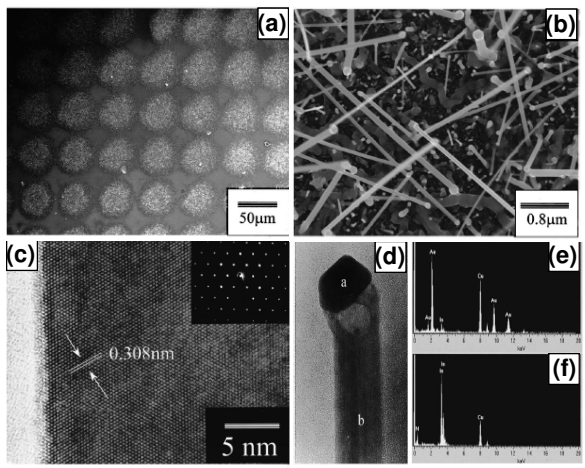

Fig. 1. (a-b) Low and high magnification SEM images of InN NWs grown on the Au patterned (bright circles) silicon substrate. The other areas remain blank. (c) HRTEM image of the InN NW. Inset shows the SAED of the typically wurtzite NW. (d) A TEM image of a single InN NW terminated with a Au NP. Corresponding energy dispersive X-ray spectroscopy (EDS) spectra of the (e) NP and (f) the NW stem, respectively. Cu signals are generated from the microgrid mesh that supports the NWs. [Reprinted with permission from Liang et al., Appl. Phys. Lett. 81, 22 (2002). © 2002, AIP.]

The shape and material-quality of the nanostructure can be affected by the reactant flux and temperature gradient along the growth zone.[15] Single crystalline InN nanobelts (NBs) were synthesized on Au-coated silicon substrates by using a guided stream thermal CVD process at a temperature of 560°C [Fig. 2a, b].[15] The NH_3 gas was delivered to the reaction zone by a separate coaxial quartz tube that opened at the substrate held at the center of the outer quartz tube. This variation of the conventional thermal CVD was responsible for the NB formation[15] without which it produced NWs or NRs.[13, 14] However, the production of the NBs can be explained in terms of the surface energy (γ) and growth kinetics. Unit cells of InN along [001], $[1\bar{1}0]$ and [110] were constructed using the CERIUS2 software package, where the cleaved planes correspond to the structure of the NBs, as shown in Fig. 2c-e. The

number of broken bonds per unit cell along the three directions are 4, 1 and 2, respectively, indicating number of broken bonds per unit area on the crystal plane to be 0.92 nm^{-2} for (001), 1.14 nm^{-2} for (110), and 0.99 nm^{-2} for $(1\bar{1}0)$. This indicates that $\gamma_{(001)} < \gamma_{(1\bar{1}0)} < \gamma_{(110)}$ and that (110) have the highest growth rate followed by $(1\bar{1}0)$ and (001), the latter two forming the width and thickness of the InN nanobelt.

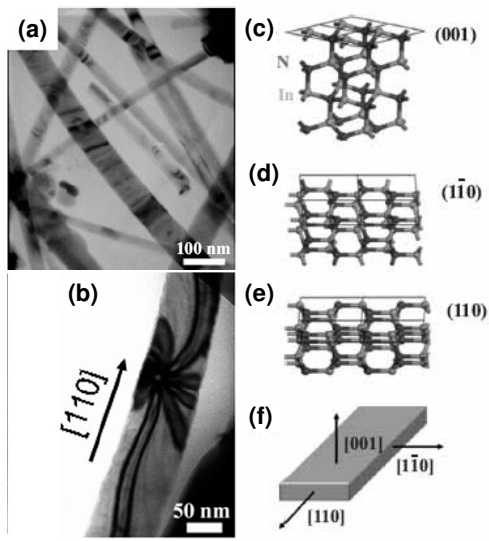

Fig. 2. (a-b) Low magnification TEM images of InN NBs growing along [110]. (c-e) Unit cell model of h-InN constructed using CERIUS2 software: c) (001), d) $(1\bar{1}0)$, and e) (110). f) Schematic diagram of the NB crystallographic directions. [Reprinted with permission from Hu et al., Adv. Funct. Mater. 16, 537 (2006). © 2006, Wiley.]

Another example for modified thermal CVD process is the use of a two-zone CVD technique to assist the vapour generation and the InN NWs growth at different temperatures. The use of single-zone furnace is limited by the inefficiency of NH_3 dissociation at the relatively low synthesis temperatures used and severely hinders the synthesis of InN NWs in bulk-quality. Tang *et al.*[16] used a two-zone furnace [Fig. 3a], having a high-temperature zone (700°C) to break NH_3 molecules and a low-temperature zone to facilitate the NWs growth. The high-quality single-crystalline NWs were produced with a high growth rate (4–10 μm/h) and precisely controlled diameters by using mono-dispersed Au clusters as the catalyst.[16]

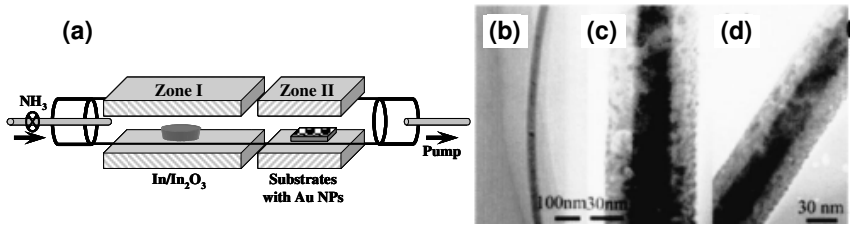

Fig. 3. (a) Schematic diagram of a two-zone CVD system for InN NWs growth. (b) low and (c-d) high magnification TEM images of the InN/InP NWs. [Reprinted with permission from Yin et al., Appl. Phys. Lett. 84, 1546 (2004). © 2004, AIP.]

There are few examples for catalyst-assisted CVD process, which did not follow the conventional VLS route. Yin *et al.*[17] reports a synthesis of InN/InP core/sheath NWs [Fig. 3b-d] through a reaction of a mixture of In_2O_3, In, and InP powders with NH_3 at 1073 K. In order to increase both the fluorescence quantum yield and the stability of the structure, a proven strategy is to grow a shell or sheath of a higher band-gap semiconductor on the core nanocrystal. The liquid In droplets found at the tip could continuously absorb and dissolve the gas phase N and P, and a reaction between In and N, In and P, respectively, continuously takes place. The InN and InP produced under high temperature rapidly condenses into liquid nanoclusters. When the nanoclusters become supersaturated, the existing InN and InP phase precipitate and crystallizes as NWs. The two phases would self-assemble to generate the InN/InP core/sheath composite structure. The uniform core/sheath NWs may result from the fixed solubility of InN and InP into the In liquid droplet, which controlled the rate of the gas absorption, and consequently, controlled the InN and InP growth rate. As the process is assisted by metallic In, in absence of any foreign metal catalyst, it can be called a self-catalytic VLS growth in which the unnecessary contamination (due to the presence of foreign metal) can be avoided.[17-19]

A solution-liquid-solid (SLS) growth route constitutes another type of catalyst-assisted CVD technique. InN nanofibers were grown at 203°C by this process,[20] in which solution-based thermolysis of the azido-indium precursors iPr_2InN_3 and tBu_2InN_3 with the mild reductant of 1,1-dimethylhydrazine, H_2NNMe_2. Apart from its role as a hydrogen donor, H_2NNMe_2, also plays an important role to generate metallic In that were found at the tip of the InN fibers. This observation strongly suggests that the liquid In cluster performed a catalytic role in the fiber

growth. Consequently, SLS technique can grow InN at lower temperature (~203°C)[20] compared to the VLS growth technique.

Thermal CVD technique was employed for the preparation of InGaN NWs, by using Au coated silicon substrates at a temperature of 600°C and pressure of 3.5 Torr.[21] Morphological studies revealed the existence of NWs in either straight or helical shapes [Fig. 4]. The formation of the coiled or helical InGaN NWs with an In-rich core could not be easily explained. One opinion is that it is a result of lateral displacement of the Au catalyst particle with respect to the central axis of the NW during growth. Another thought is the different growth rates for the core and the shell that could probably give the helical shape for the NWs.

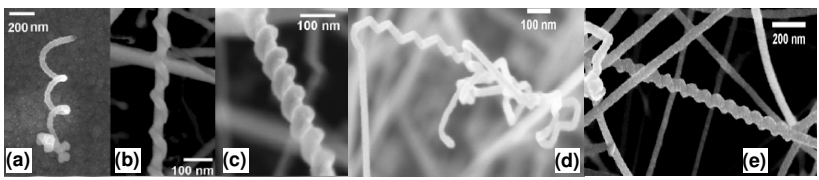

Fig. 4. SEM images of InGaN core–shell NWs (a) coil, (b) and (c) coiled wires growing around straight wire, (d) zigzag NW, (e) straight and coiled NWs. [Reprinted with permission from Cai et al., Nanotechnology 17, 2330 (2006). © 2006, IOP.]

Attempt to grow InGaN NWs via VLS process using In, Ga and NH_3 as precursors and Au as catalyst produced Ga-rich and In-rich InGaN NWs at high and low growth temperatures, respectively.[22] TEM studies revealed that the NWs are either predominantly binary GaN or InN with some ternary self assembled quantum dots (SAQD) embedded in them. The strain in the inhomogeneous structure and the low miscibility of GaN and InN are probable reasons for the formation of SAQDs in NWs. This study also underlines the difficulty in growing defect free and phase pure ternary materials.

2.1.2. Catalyst-free growth

When purity of products is a concern, the template or catalyst-assisted growth is often undesirable since the removal of the catalyst and the template are difficult. The catalyst-free growth is then a viable option. Self-catalytic VLS processes[17-20] can also be considered, since these processes do not contain any foreign catalyst. However, conventional catalyst-free process generally follows the vapour-solid (VS) growth.

The VS growth relies on the vapour phase transport of the precursors to the deposition zone, followed by the adsorption, diffusion, desorption and subsequent deposition giving rise to the growth. The diffusion coefficient and surface migration of the adatoms, instead of the catalyst in VLS process, will control the resultant morphology of the material. The adsorption and ultimate bonding of the adatoms on the growth surface is dependent on the availability of dangling bonds on the surface. Anisotropy in growth is hence a consequence of the density of dangling bonds available at each crystalline face.

Several reports are available for nanocrystalline InN grown by the VS technique.[23-25] Zhang *et al.*[23] demonstrated a large-scale fabrication of InN NWs through a gas phase reaction of In metal and In_2O_3 powders in flowing NH_3 at 700°C. The absence of catalyst particles, observed from TEM image [Fig. 5a], at the end of the NWs confirmed the VS growth mechanism. InN directly condenses on the substrate at a lower temperature region and grows into wire-like nanostructures. The representative X-ray diffraction (XRD) pattern [Fig. 5b] of the NWs revealed a pure hexagonal InN phase with a lattice parameter of a_o ~ 3.52 Å, and c_o ~ 5.71 Å. Simple nitridation of In_2O_3 powders in NH_3 have been employed for the synthesis of InN NWs[26, 27] and NBs[28] [Fig. 6], with a high yield, purity and good reproducibility. Johnson *et al.*[25] used only pure In metal (without In_2O_3) for the nitridation reaction with NH_3 at 700°C to produce InN NWs.

InN/In_2O_3 coaxial nanocables were fabricated via the VS process through a two-stage synthesis.[29] The high melting point (1920°C) In_2O_3

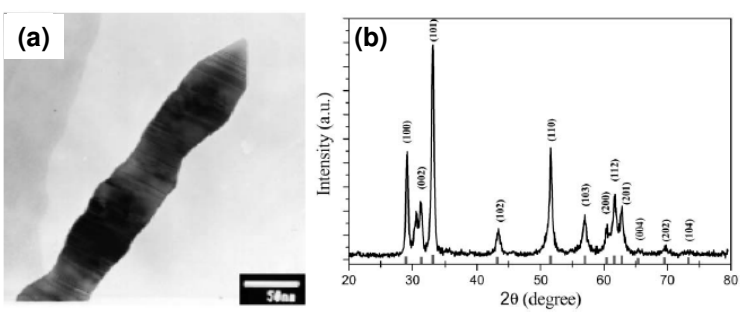

Fig. 5. (a) A typical high magnification TEM image of an InN NW showing no catalyst particle at the tip. (b) XRD pattern taken on InN NWs. The (hkl) values of the wurtzite structure are specified above the peaks. [Reprinted with permission from Zhang et al., J. Mater. Chem. 12, 802 (2002). © 2002, The Royal Society of Chemistry.]

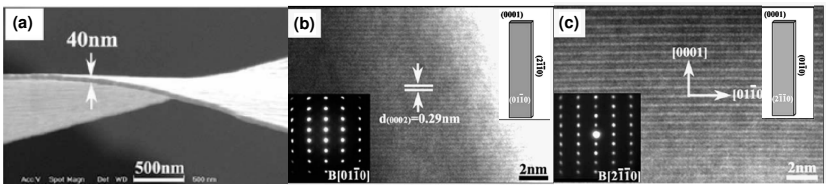

Fig. 6. (a) TEM image of the lateral edge of a single belt. (b-c) HRTEM image and SAED pattern (bottom inset) of a single NB. Inset on the top right of (b) and (c) shows schematic illustrating the surface enclosure of the nanobelt in (b) and (c), respectively. [Reprinted with permission from Luo et al., Chem. Phys. Lett. 411, 361 (2005). © 2005, Elsevier.]

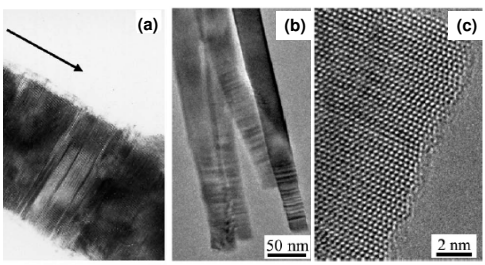

Fig. 7. (a) A typical HRTEM image showing the structures of InN/In_2O_3 nanocable and the growth direction of the nanocable. [Reprinted with permission from Zhang et al., Mater. Lett. 60, 2153 (2006). © Elsevier 2006.] (b) Low- and (c) high-magnification TEM images of MBE-grown InN NWs. [Reprinted with permission from Stoica et al., Nano Lett. 6, 1541 (2006). © 2006, ACS.]

shell act as a chemically inert protecting layer for the core InN. First, InN NWs were prepared through a reaction of In and In_2O_3 powder under a constant NH_3 flow at 700°C for 2 h. Next, the temperature of the system was allowed to cool, with NH_3 turned off and an introduction of Ar/O_2 gases into the quartz tube. After 1~2 min, the Ar/O_2 were turned off and NH_3 was introduced to cool down to room temperature. HRTEM observations demonstrated that the nanocable (NC) consists of wurtzite InN NW core, covered with a layer of In_2O_3 [Fig. 7a].

Besides the techniques mentioned above, there are few other approaches for the synthesis of InN nanostructures. Zhang *et al.* employed the template-based confined chemical reaction to fabricate a uniform assembly of InN NWs within anodic alumina membranes (AAM).[30] Firstly, In NWs were electrodeposited into the nanoholes in AAM by a 3-probe dc method at room temperature. Then the assembly systems (In/AAM) were subjected for direct nitridation of In NWs

under a constant flow of NH_3 at a temperature range 550-700°C. XRD studies revealed that the product synthesized at 700°C showed complete transformation of metallic In into wurtzite InN NWs.

A controlled-carbonitridation thermochemical route has been used to produce NWs and nanotubes. The process used either multiwalled carbon nanotubes (MWCNTs) or high-purity graphite powders as the carbon source for the carbonitridation reaction via VS growth.[31] During the process, In_2O_3 powders, mixed with MWCNTs or graphite powder, are reduced by carbon, and the product In_2O atoms react with N_2 gas to form InN nanostructures. It has been revealed that the hollow InN nanotubes were formed at higher temperature (600-625°C) by a diffusion-limited process, whereas InN NWs were formed by a kinetically limited process at relatively lower temperature (565-590 °C). The InN nanotubes, with wall thickness about 150 nm and pore size ~160 nm, grow along the [010] direction of the tube axis, the NWs (diameters: 150 nm) exhibited the growth along the [110] direction.

2.2. *Molecular Beam Epitaxy (MBE) and plasma-assisted MBE*

MBE is a versatile technique for the growth of thin epitaxial layers of semiconductors, metals or insulators. In principle, a thin epitaxial film will be crystallized via the reactions between molecular or atomic beams of the constituent elements on a substrate surface, maintained at an elevated temperature in ultrahigh vacuum (UHV). For III-nitride growth, the effusion of the metal atoms (Ga, In, Al) from a conventional Knudsen effusion cell has to be combined with a source for N_2 radicals. One of the advantages for MBE technique is the UHV environment and the use of high-purity materials, which minimize contamination. Another important issue is the low growth-temperature especially for the growth of In-based alloy materials with high In contents. At low temperatures, as in InN MBE growth, the thermal desorption of In can be neglected, which consequently provide an easy incorporation of In into the film as well as minimizing the segregation problem. The typical growth rate of 1 monolayer per second (ML s−1) is low enough for surface migration of the impinging species on the substrate surface required for the preferential growth.[10] The growth mechanism is controlled by kinetics of the surface processes occurring when the impinging beams react with the outermost atomic layers of the substrate.

For InN growth, the dissociation of nitrogen to nitrogen radicals is one of the important steps. Nitrogen requires a relatively high amount of energy (946.04 kJ mol-1) to dissociate into reactive atoms.[32] Under the influence of a plasma at reduced pressure, a significant dissociation of the nitrogen molecules was possible. Therefore Group III-nitrides, including InN, can be grown by plasma-assisted (or –induced) MBE (PAMBE), where the plasma-induced nitrogen radicals are combined with the evaporated metal atoms from effusion cells. The decomposition by effusion of nitrogen is a process, which strongly affects the InN growth. This decomposition induces a segregation of In atoms at the free surface.[33] For a sustained MBE growth, the N_2 flux must compensate the incident In-flux, as well as the In accumulation due to this decomposition. MBE with excellent process control have the advantage of enabling both n-type and p-type device fabrication by doping. Jones *et al.* reports the growth of Mg-doped InN films (thickness of ~500 nm) by MBE on c-sapphire substrates with a roughly 200 nm-thick GaN buffer layer.[34]

Although there are numerous successful applications of MBE or PAMBE for the growth of InN epilayers in literature, serious approach for nanostructure growth is relatively new. Successful application of PAMBE was found to produce InN nanocolumns.[35-37] The growth parameters are adjusted to nitrogen-rich conditions to obtain columnar structures (diameter: 50–150 nm, length: few μm), with a relatively good crystalline quality, on Si(111) substrates, at the temperature 440-525°C, using radio-frequency PAMBE. These columns can be easily removed from the original substrate to obtain freestanding nanowires (FSNWs) [Fig. 7b, c], and to construct single wire devices.[32, 37] Shen *et al.*[38] reports the systematic transition of InN films to InN NRs, by adjusting the growth conditions. InN epitaxial film was grown on Si(111) using the epitaxial AlN/β-Si_3N_4 double buffer layer, and adjusting the N/In flux ratio close to the stoichiometric condition, at ~520°C.

On the other hand, vertically aligned InN NR's [Fig. 8] growth proceeded under nitrogen rich conditions, on β- Si_3N_4/Si(111) (without AlN buffer layer). Two different sets of NRs have been grown at low (~330°C, LT-InN) [Fig. 8] and high (~520°C, HT-InN) temperatures, in order to compare the difference between epitaxial films and NRs. Although the size distribution of LT-InN NRs is quite uniform compared to the broad and bimodal distribution of HT-InN NRs; the LT-grown NRs showed a considerable number of structural defects and lower PL efficiency, compared to the HT-InN and the epitaxial film.

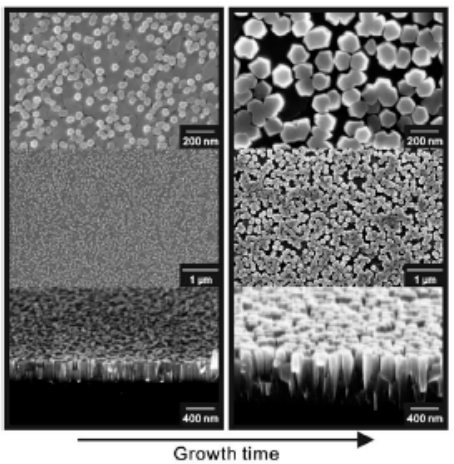

Fig. 8. SEM images of vertically aligned low-temperature (LT) InN nanorods grown on Si(111) substrates by nitrogen-plasma-assisted MBE. [Reprinted with permission from Shen et al., Appl. Phys. Lett. 88, 253104 (2006). © 2006, AIP.]

2.3. *Hydride Vapour Phase Epitaxy* (*HVPE*)

HVPE is a long established epitaxial growth technique often employed to produce III-nitride materials, because of its high growth rates (few tens of μm per hour) and its lack of carbon incorporation into the product material. HVPE has attracted huge interest as a technique to provide lattice-matched growth surfaces and thick, strain-relieved buffer layers. The high growth rate and low defect concentrations offers the possibility of preparing very thick films, which can even be removed from the substrate by polishing or laser-induced thermal decomposition and used as a substrate for homoepitaxy.[10] Carrier gasses commonly used include NH_3, H_2 and various chlorides. However, there are few papers exploring HVPE as a growth method for InN.[39-41] One recent report[42] demonstrated InN layers grown by HVPE on c-plane sapphire substrates and epitaxial GaN, $Al_{0.7}Ga_{0.3}N$, and AlN templates grown on sapphire. InN properties are found to depend on template type with improvement of crystal structure in the template substrate order AlN → AlGaN → GaN. InN layers grown directly on c-plane (0001) sapphire have the micro-columnar structure, with diameters of 200-350 nm and heights from 500 nm to several microns.

Another recent report by Kim *et al*. presented the growth of InGaN NRs on Si (111) utilizing HVPE.[43] The source precursors, synthesized via a reaction of HCl gas with In and Ga metals in N_2-ambient at 750°C, delivered to the substrate region, followed by the growth of InGaN NRs by a reaction with NH_3 at 510°C for 5 hours. The electron microscopic studies revealed that the straight and well-aligned NRs with 50 nm diameter and 10 μm of length, are preferentially oriented in the c-axis direction. The same technique can also produce aligned InGaN NR arrays growing along [0001] on sapphire substrates.[44, 45]

2.4. *Metalorganic Vapour Phase Epitaxy* (*MOVPE*)

MOVPE is a chemical vapour deposition method for epitaxial growth of compound semiconductors, from the surface reaction of organic compounds or metalorganics and metal hydrides. Formation of the epitaxial layer occurs by final pyrolysis of the constituent chemicals at the substrate surface. In contrast to MBE, the growth of crystals is by chemical reaction and not physical deposition. This takes place not in a vacuum, but from the gas phase at moderate pressures. As such, this technique is preferred for the formation of devices incorporating thermodynamically metastable alloys. It has become the dominant process for the manufacture of laser diodes, solar cells, and LEDs.

Growth of InN nanostructures using MOVPE is truly limited. In 2005, Kryliouk *et al.*[46] first reported the successful application of hydride-MOVPE to grow a bed of single crystal InN NRs (Diameter: few nm to 100 nm) on c-Al_2O_3 substrates. In this process, TMIn is first reacted with HCl in the source zone of the hot-wall reactor (temperature was maintained below 300°C to prevent TMIn decomposition) to form chlorinated In species. This stream mixes with NH_3 in the downstream mixing zone and is directed toward the substrate where deposition of InN occurs by reaction of $InCl_x$ with NH_3, at atmospheric pressure in N_2 ambient in the temperature range of 600–650°C at N/In mole ratio of 250 and HCl/TMIn inlet mole ratio of 4 to 5. The authors[46] claim that hydride-MOVPE is more suitable than MOCVD for the growth of InN at low NH_3/TMIn ratio at high growth rate without any In droplet formation.

2.5. *Chemical Beam Epitaxy* (*CBE*)

CBE, a hybrid form of the long established MBE and MOVPE, provides a capability for the epitaxial growth of semiconductors and other advanced materials with control at the atomic level. In CBE, instead of a solid source, a gas source is used. It is also called gas-source MBE. CBE uses room temperature gases as the source materials, thus avoiding significant contamination problems and segregation of dopant atoms. The material is carried into a high vacuum reaction chamber as a gaseous compound, typically in hydride or metalorganic form.

Though CBE is an established growth technique, recent reports showed its suitability for the growth of nanostructures also. Unidirectional InN NRs, with controlled size, have been demonstrated successfully utilizing a homemade CBE system,[47, 48] using TMIn and trimethylaluminum (TMAl) precursors. The precursors were delivered, by direct heating to the source, without a carrier gas over the c-plane sapphire, in presence of the active N_2 radicals supplied by an rf plasma source. At first, a thin amorphous AlN nucleation layer has been grown at 700°C, followed by the growth of InN NRs at ~500°C. The NRs are synthesized along the [001] direction having lengths of 300 nm and diameters around 20-40 nm with the In/N flow ratio from 0.4 to 0.7.

2.6. *Metalorganic Chemical Vapour Deposition* (*MOCVD*)

MOCVD is widely used in semiconductor industry producing material with much better quality than usual chemical methods. Although the fundamental reaction mechanism and the kinetics of MOCVD are not well understood, but there has been a concerted effort to develop it, for the advantages of large-area growth capability, good conformal step coverage and the precise control of epitaxial deposition.

For a typical deposition of epitaxial layer of MN materials (M = Al, Ga, or In) by MOCVD, precursors, like TMIn, TMGa or TMAl (TMM), have been used as a source of metal M to react with NH_3. Recently InN nanotips (NTs) were grown by MOCVD on Au-coated quartz substrates, by the reaction of TMIn and NH_3 (with nitrogen as a carrier gas) at a temperature of 550°C.[49, 50] Analogous to the radius that characterize a wire or tube, the apex angle characterizes a tip [Fig. 9]. For InN NTs a distribution of apex angles (3°-54°), were observed [Fig. 10].[50] Studied by electron microscopy and XRD, the structure of the InN NTs are

observed to grow along [002], via the VLS mechanism, governed by the catalytic effect of Au NPs.

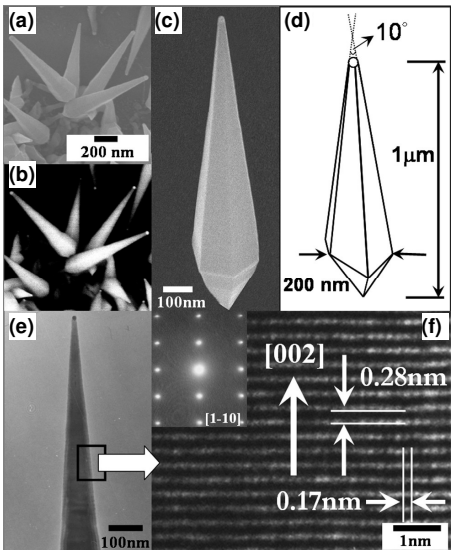

Fig. 9. (a) SEM image and (b) backscattered SEM image of InN nanotips; (c) low magnification SEM image and (d) schematic diagram of a single InN NT; (e) low magnification TEM image of a single NT and (f) HRTEM of the InN NT area marked in (e); inset showing the selected area diffraction pattern of h-InN NTs. [Reprinted with permission from Shi et al., Appl. Phys. Lett. 87, 203103 (2005). © 2005, AIP.]

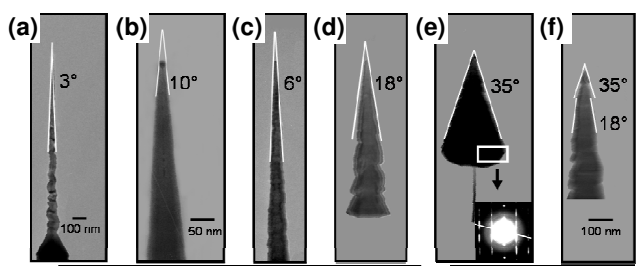

Fig. 10. (a–f) TEM of InN NTs showing different apex angles. Inset in (e) shows the electron diffraction of the marked area in (e); same scale bar for (c–f) shown in (f). [Reprinted with permission from Chattopadhyay et al., Appl. Phys. Lett. 89, 143105 (2006). © 2006, AIP.]

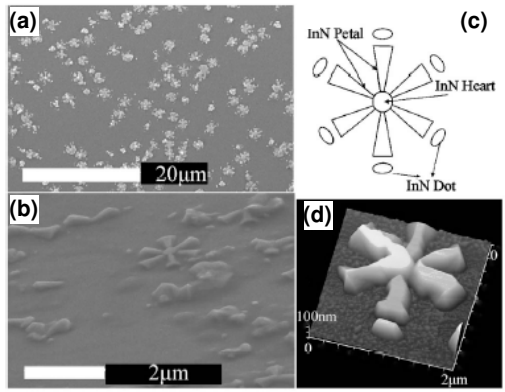

Fig. 11. InN nanoflowers: (a) large-area SEM, (b) SEM stereo view, (c) schematic illustration, and (d) AFM stereo view. [Reprinted with permission from Kang et al., Appl. Phys. Lett. 89, 071113 (2006). © 2006, AIP.]

Another example for MOCVD-grown InN nanostructures is the growth of InN nanoflower [Fig. 11], on c-plane sapphire, at 500°C, using TMIn and NH_3 as precursors.[18] Here H_2 gas was introduced intentionally, to achieve the stable existence of metallic In sustaining the self-catalytic VLS growth of the InN nanostructures.

Earlier report has shown an approach to use a single molecule precursor Azido [bis(3-dimethylamino)-propyl] In, $N_3In[(CH_2)_3NMe_2]_2$ that decomposed with NH_3 gas at low temperature (400–550 °C), producing InN whiskers on bare c-plane sapphire. The results showed the existence of In metal droplet at the tip of the whisker.[51]

MOCVD technique was employed to grow vertical self-organized NTs on InGaN thin films grown on sapphire substrate.[52] A 30 nm thick GaN buffer layer was grown at 500°C, on which a 2 μm thick undoped GaN buffer was grown at 1000°C. Subsequently a 3 nm thick InGaN was grown at relatively lower temperature (730°C). Finally, thermal annealing of the InGaN film at 740°C at atmospheric pressures for 20 minutes in a quartz furnace produced the NTs.

Hierarchial nanostructures are ideal system for the demonstration of homo- and hetero-junctions. Fabrication of such junctions on GaN NWs has been reported.[53] Growing GaN NRs on the surface of GaN NWs, for the fabrication of homo-junctions, and growing InN NRs on GaN NWs, for the fabrication of hetero-junctions. In both cases, starting GaN NWs were coated with Au-film and used as a template for the further

deposition of GaN (or InN) NRs. Brush-like InN NWs were formed on the GaN NWs [Fig. 12a]. Hierarchical structures involving InN NWs on InN NBs can also be formed. The growth strategy is a similar two-stage process. First, the InN NBs were formed by a Au-catalyzed CVD process at 540°C. Next, these InN NBs were coated with Au again for further growth of the InN NW at 540°C. Brush-like structures were formed on the parent InN NBs [Fig. 12b].

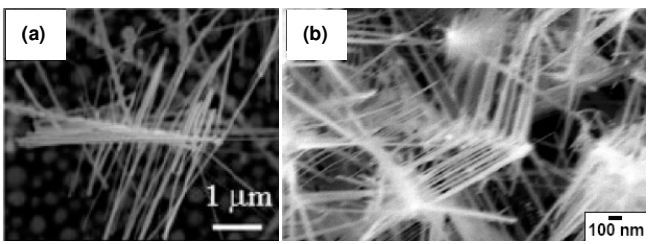

Fig. 12. FESEM images of (a) heterojunction nanobrush, InN NRs on GaNNWs, (b) homojunction nanobrushes, InN NWs on InN NBs, prepared by MOCVD. [Reprinted with permission from Lan et al., Adv. Funct. Mater. 14, 233 (2004). © 2004, Wiley.]

2.7. *Solvothermal methods*

Most of the techniques producing InN nanostructures employ relatively high temperatures that cause its dissociation and gives rise to defects. Requirement of low-temperature reactions have shifted the interest towards the solvothermal processes. In solvothermal method, a solvent (or reactant) is used at an elevated temperature at which the solvent is in its liquid state. The solutes are transported from the solution as metastable molecules and subsequently decompose at a growing surface due to thermodynamic instability.

Synthesis of InN nanocrystals have been reported via the reaction of $InCl_3$ powder and xylene (Li_3N, the solvent) at 250°C in a stainless steel autoclave. XRD and TEM results verified that the product was a mixture of the cubic and hexagonal phases.[54]

Sardar *et al.*[55] has employed the same technique to synthesize the NWs, and nanotubes. By the solvothermal reaction of $In(C_6H_5N_2O_2)_3$ [tris(N-nitroso-phenylhydroxylaminato)indium] and 1,1,1,3,3,3-hexamethyldisilazane (HMDS) in toluene 265°C for 2-4 days, InN nanocrystals with an average diameter of ~15 nm has been obtained. On the other

hand, the reaction of anhydrous $InCl_3$ with HMDS 300°C for 6-96 hr also produced nanocrystals (diameter: 10–15 nm).

A mixture of NWs and nanotubes has been synthesized by the reaction of indium acetate with HMDS in the absence of any solvent.[55] The reaction occurring at 300°C for 48 hr provided yields of 40% and 60% for NWs and nanotubes, respectively. Similar to the nanocrystals, NWs also exhibited wurtzite structure with diameters in the 50-100 nm range and lengths up to ~1 μm.

3. Optical Properties

3.1. *Photoluminescence*

Optical properties of nanomaterials are interesting and rich in information since they carry the quantum mechanical phenomenon of photon confinement with them. Photoluminescence (PL)[56] is a basic characterization tool for the optical properties. The analyses of the PL results are critical since they are sensitive functions of measurement temperature, carrier concentration and defect states in the crystal. In addition, the nanostructure size distribution has significant effect on the broadening of the PL signal. Some of these problems could be avoided in the cathodoluminescence (CL) technique where a narrow electron beam is used which can perform single nano-object spectroscopy and is relatively error-free.

The optical bandgap of InN is being debated with both infrared (IR) and visible energies being reported. Originally InN was thought to be having a bandgap of 1.9 eV.[5] Figure 13 shows the trends of report on the bandgap of InN in the thin film as well as nanostructure form.[5,13-16,19,25-26,28,30-31,33,37-38,42,47-49,55,57-63] The initial report of 1.89 eV was challenged in 2002 by both Russian[58] and US[59] researchers thereafter the IR bandgap started to receive more support [Fig. 13]. A consensus is gradually developing now, that the InN bandgap is in the IR region while the visible bandgap is being attributed to an indium oxide phase in the material,[58] quantum size effect,[64] Burstein-Moss shift,[65] or nitrogen excesses in InN.[66] There is one report that clearly demarcates the bandgaps depending on their sizes. Oxide assisted InN NRs showed a bimodal size distribution with optically black and brown NRs demonstrating diameters of 50-100 nm and 30-50 nm, respectively.[14] The

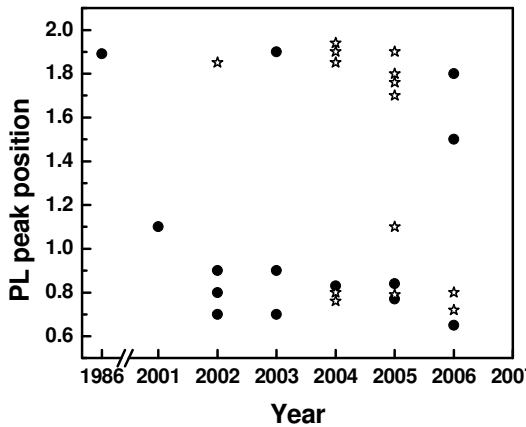

Fig. 13. Trends of the reported values of the bandgap of InN (•) thin film and (☆) nanostructures.

optically black and nearly defect free InN NRs showed a PL emission at 0.76 eV (at 20 K) which blue shifted to 1.9 eV (at 300 K) for the brown InN NRs. This shift of ~1.1 eV was inexplicable based on In_2O_3 formation, Burstein-Moss shift, or quantum size effect alone. For example, the InN crystals should have a size less than 5 nm to have a shift of 1.1 eV according to quantum confinement, whereas the brown InN NRs were 30-50 nm. The Burstein-Moss effect can cause a shift of only 0.5 eV for a carrier concentration increase of over 2 orders in magnitude. Hence, this result indicates a convoluted contribution of quantum confinement, and Burstein-Moss shift towards the blue shift of the PL emission in InN NRs.

Recently a unique nanotip structure of InN has been reported by the resistively heated MOCVD process.[49] PL measurements on these NTs supported the IR band edge emission at 0.77 eV with a small full width at half maxima of 18 meV. A side peak at 0.754 eV was observed and attributed to a 20 meV donor level in InN [Fig. 14a]. However, the striking features in the temperature dependent PL of these InN NTs is the absence of quenching near room temperature [Fig. 14b]. When the measurement temperature was varied from 15K to 300K the emission intensity decreased by only 14%. An Arrhenius plot of the normalized PL intensity with inverse temperature should show two distinct slopes with low and high activation at low and high temperatures, respectively. However, for the InN NTs, the quenching of the PL intensity near room temperature was very weak and hence the high activation region of the

Arrhenius plot was missing altogether. This reduced temperature quenching suggests high internal quantum efficiency, low defect losses, and low thermal escape of carriers in the InN NTs.

Ternary systems involving InN also shows interesting optical emissions. InGaN NRs[43] showed a CL spectrum centred at 428 nm with a full width at half maximum ~30 nm. These NRs have a composition of $In_{0.1}Ga_{0.9}N$. The same $In_xGa_{1-x}N$ NRs show a tunable CL emission from 380 nm (3.26 eV) to 470 nm (2.64 eV) as the In content was varied from x = 0.04-0.2.[45] The low temperature PL spectrum of the InGaN/GaN multiple quantum well (MQW) NR[67] arrays shows a three orders stronger luminescence from the InGaN QWs compared to that of the GaN barrier. The temperature dependent (15-300 K) PL of the MQW NR arrays demonstrate substantially reduced PL quenching of the 477 nm (2.6 eV) peak in the NR arrays as temperature was increased.

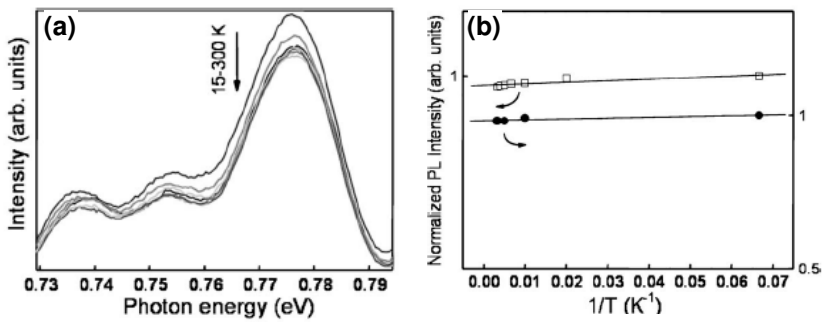

Fig. 14. a) The temperature dependent photoluminescence (PL) spectrum of InN NTs measured with 100 maw incident laser power and 3 mm slit width. b) Two sets of Arrhenius plot of the normalized integrated PL intensity as a function of inverse temperature: (□) 15-300 K with 488 nm laser and 3 mm slit width (•) 15-320 K with 514 nm laser and 0.5 mm slit width. [Reprinted with permission from Shi et al., Appl. Phys. Lett. 87, 203103 (2005). © 2005, AIP.]

3.2. *Raman spectroscopy*

Raman spectroscopy provides a non-intrusive method for the determination of crystalline structure, carrier concentration, stress and quality of the crystal. Evidently, it is one of the best-known tools to characterize InN materials in both the bulk thin film and nanomaterial form. The stable wurtzite InN belongs to the C_{6v}^4 space group and zone

center phonon modes of A_1, B_1, E_1 and E_2 are predicted. The A_1 and E_1 modes can have the field splitted transverse optic (TO) and longitudinal optic (LO) modes. B_1 is silent in Raman scattering. In doped samples however, another mode called LO phonon coupled (LOPC) was observed. Figure 15 shows typical Raman spectra for InN nanostructures.

Figure 16a shows different Raman modes, and their respective positions (y-axis), as observed in thin film or bulk InN samples.[57,68-75] Clearly, the position of each mode differed slightly from sample to sample, indicative of their crystalline quality. The shifts in the position of each mode may originate from difference in stress, carrier concentration,

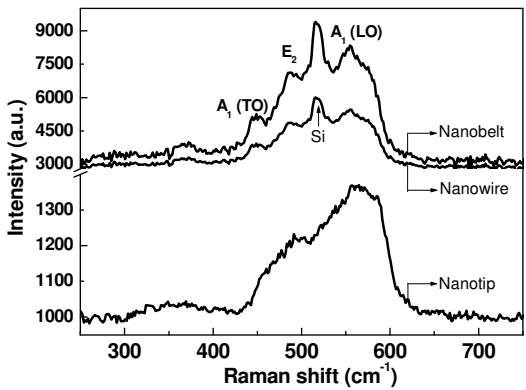

Fig. 15. Representative Raman spectra for InN nanowires, nanobelts and nanotips. The position of the Si Raman line at 520 cm^{-1} is indicated.

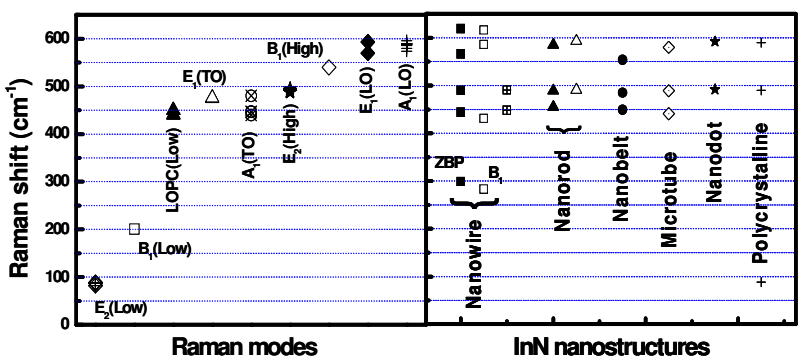

Fig. 16. Different Raman modes and their respective positions (Raman shift) for (a) bulk InN and (b) nanostructured InN. The grid lines in the figure helps in ascertaining the positions of the Raman modes. Abbreviations are described in the text.

grain boundaries, polarization condition and quality of the crystal. The individual effects of the above-mentioned conditions and Raman line shape analysis, however, are beyond the scope of this review.

In comparison to the thin film and bulk, the InN nanomaterial counterpart shows the Raman modes as depicted in figure 16b and detailed in Table 1.[14-16,19,27,47,76-78] Clearly, the close proximity of the different Raman modes may obscure the identity of individual modes. The scatter in the position of these modes in InN nanomaterial speaks of the variable crystalline quality in the nanoscale. Two striking features stand out in the Raman spectroscopic data of the InN nanomaterials. First, the silent or forbidden B1 mode was observed,[16] and second a zone boundary phonon (ZBP)[27] was also found in InN NWs, which were never identified in bulk or thin films.

Table 1. Different Raman modes and their respective positions (Raman shift, cm^{-1}) as observed in InN nanomaterials.

ZBP (cm^{-1})	B_1 (cm^{-1})	A_1(TO) (cm^{-1})	E_2(Low) (cm^{-1})	E_2(High) (cm^{-1})	A_1(LO) (cm^{-1})	E_1(LO) (cm^{-1})	Type of nanomaterial
299	-	444	-	490	566	619	Nanowire[27]
-	283	431	-	-	586	616	Nanowire[16]
-	-	448	-	491	-	-	Nanowire[19]
-	-	-	-	491	593	-	Nanorod[47]
-	-	455	-	489	569 (Red) 585 (Black)	-	Nanorod[14]
-	-	449	-	485	554	-	Nanobelt[15]
-	-	441	-	489	580	-	Microtube[81]
-	-	-	-	492	592	-	Nanodot[82]
-	-	-	88	490	590	-	Polycryst.[83]

4. Electrical Properties

Doping possibilities in nanomaterials demonstrated, electrical measurements are becoming increasingly important and fundamental. However, making a proper contact to the nanomaterial is a concern and the choice of a contact material often relies on trial and error principles.

InN films are intrinsically n-type with high electron concentrations exceeding 10^{20} cm^{-3} and mobilities around 30-100 cm^2/Vs.[79] Residual O_2 or impurities are probably responsible for its n-type conductivity. Transport properties of InN NWs, with diameters of 35-120 nm and lengths of 7-10 μm, grown by a catalytic (Au) thermal CVD were

measured.[80] Using a shadow mask, Pd/Ti/Pt/Au (5/ 20/ 20/ 100 nm in thickness) was evaporated to make ohmic contacts at the end of the NWs [Fig. 17a]. Current- voltage (I-V) characteristic was measured at 300K [Fig. 17b]. A contact resistivity of 1.09 x 10^{-7} Ω-cm^2 and sheet resistivity of ~4 x 10^{-4} Ω-cm was obtained from the fit of the total resistance as a function of the ratio of length to area of the NWs [Fig. 17d]. The specific contact resistivity was obtained from a transmission line method analysis and its value confirmed with reported values.

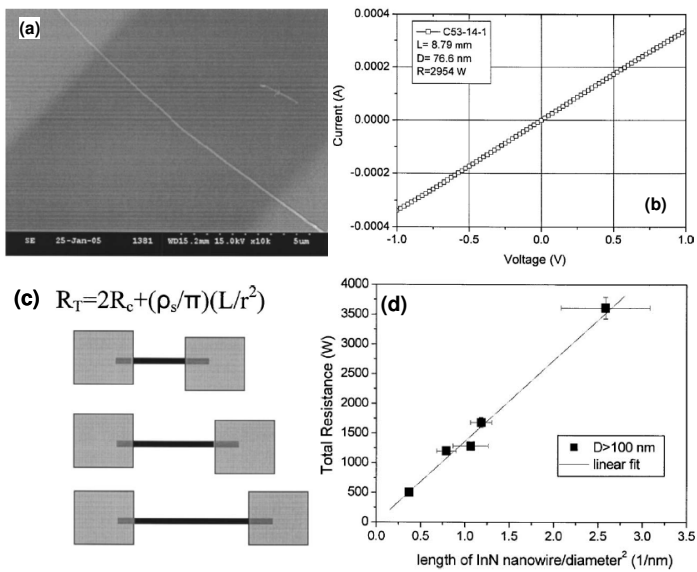

Fig. 17. (a) SEM image of InN NW contacted at both ends; (b) 300 K I-V characteristics. (c) Contact geometry for measuring the NW resistance as a function of length and (d) plot of total resistance vs. length/(radius)^2 for NWs of diameter > 100 nm. [Reprinted with permission from Chang et al., Appl. Phys. Lett. 87, 093112 (2005). © 2005, AIP.]

A comparison of the resistivity values of InN thin film and NWs show that it is around one order less in the NWs although the contact resistivities are similar.[80]A diameter dependent resistivity study of InN NWs was performed[81] in which the total measured resistance of the NW was plotted as a function of the ratio of its length/radius^2. For NW diameters >100 nm, the resistance showed a classical Ohmic behaviour, i.e., the resistance increasing with decreasing diameter of the wire. However, for NWs in the diameter range of <90 nm, a decrease of

resistance was observed as the wire diameter decreased. This is an anomaly, which was later explained by Yin *et al.*[82] In a regime of diffusive transport, if the wire diameter is smaller than the carrier size or scatterer potential, the resistance is not inversely proportional to the square of the radius of the wire, but in fact is proportional to the number of scattering centres. Each scattering centre contributes equally to the resistance as if they are connected in series (neglecting parallel combinations). The electron mean free path (ℓ) is of the order of the impurity-impurity distance and given by

$$\ell \propto (1/n_i)^{1/3} \quad (1)$$

where n_i is the impurity concentration, and for the InN under consideration it was 10^{17}-10^{20} cm^{-3}. Hence, $\ell \approx 2.2$-22 nm is the carrier De-Broglie wavelength or the carrier-carrier distance. For InN NWs with radius <45 nm, the NW dimension $\approx \ell$, and hence the resistance R is given by

$$R = R_C + R_0 n_i AL \quad (2)$$

where R_C is the contact resistance, n_i is the impurity (scatterer) concentration per unit volume (area (A) x length (L)) of the NW, and R_0 is the resistance per scatterer. This expression of resistance, in place of the usual ohmic form, can then explain the anomaly observed by Chang *et al.* for thin InN NWs.[81]

5. Applications

Several applications, most prominently LEDs, of the group III-nitride materials, in general, have been reviewed.[83,84] The role of defects on the properties of these materials and how they can be utilized in devices have also been written.[85,86] Several reviews describes the field effect transistors (FET) using this class of binary or ternary compounds.[87-90] But reviews on applications of one dimensional group III-nitride materials have been scarce.[91,92] This section will discuss primarily on sensing applications and nanoscale LEDs of these materials as addition to what has already been described in other reviews or books.

5.1. *Sensors*

Other than optoelectronic properties, the feature that distinguishes InN from other group III-nitride materials is its unusual surface charge

accumulation. Wurtzite InN has a strong surface charge density of 10^{13} cm^{-2} that is higher than InAs.[93, 94] Most of the lateral conductivity in InN films has its origin in this surface charge concentrated mostly on the top few nanometers.[95] Modulation of this surface charge by external agents could make InN suitable for sensing applications. In addition, the radiation hardness,[96] chemical stability and availability of polar surfaces in InN is advantageous for sensing applications.

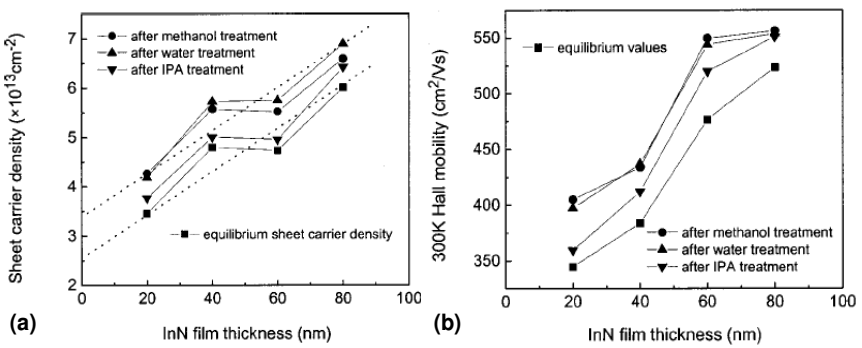

Fig. 18. Room-temperature (a) sheet carrier density and (b) Hall mobility of a series of InN samples with different thickness before and directly after (3 min) methanol, water, and isopropanol (IPA) treatments. [Reprinted with permission from Lu et al., J. Appl. Phys. 96, 3577 (2004). © 2004, AIP.]

MBE grown InN films of thicknesses between 20-80 nm were used for chemical sensing purpose.[97] Standard Hall measurements were done to determine the Hall mobilities, and Van der Pauw geometry was used for the measurements of the sheet carrier densities of the InN film before and after treatment with different solvents. The solvent treatment was done by applying the solvent on the film surface with the help of a cotton swab wetted in the solvent. Residual solvent on the sample surface was intentionally blow-dried and care taken to compensate any loss of temperature due to solvent evaporation. Figure 18 shows a clear change in the sheet carrier density and room temperature Hall mobility of the InN film with different thicknesses before and after the solvent (methanol, water, isopropyl alcohol) treatment. The equilibrium values of the sheet carrier densities and Hall mobilities, which varied nearly linearly with increasing thickness of the film had a parallel shif, after the solvent treatments. IPA had relatively weaker effect whereas water and methanol had similar effect on the carrier density and Hall mobility.

However, the InN NRs coated with 10 nm of Pt showed remarkable change in its resistance. For electrical measurements Al/Ti/Au electrodes with 30 μm separation were deposited on the NRs by using a shadow mask. Figure 19 shows the change in the current and relative change in resistance as a function of time under different flow rates of H_2. The change is reversible, and the current comes back to near initial values after the removal of the H_2. The platinum supposedly catalyzed the dissociation of H_2 to atomic H. Whether the change in resistance is due to the adsorption/desorption of H_2 in the grain boundaries, exchange of charges between adsorbed species and the InN surface, or changes in surface conduction by gas adsorption/desorption, is not clear. The role of a surface charge density cannot be ruled out.

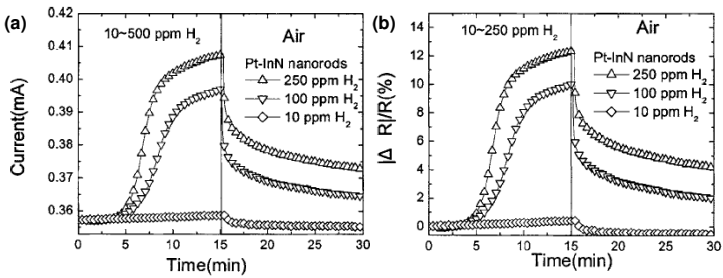

Fig. 19. (a) I-time plot of 10–250 ppm H_2 test by Pt-InN NRs, and (b) |ΔR|/R(%)-time plot of 10–250 ppm H_2 test by Pt-InN NRs. [Reprinted with permission from Kryliouk et al., J. Vac. Sci. Technol. B 23, 1891 (2005). © 2005, AVS The Science and Technology Society.]

6. Concluding Remarks

The growth, structure and optoelectronic properties of indium nitride nanomaterials are outlined. Growth routes including metalorganic chemical vapour deposition, molecular beam epitaxy, thermal chemical vapour deposition, hydride vapour phase epitaxy and solvothermal techniques have been discussed. The structure of the indium nitride nanostructures produced is discussed for these growth modes. Optical properties, including photoluminescence and Raman spectroscopy, have been outlined for one dimensional indium nitride. Electrical resistivity measurements in single InN NW have been discussed and the result critically analyzed. Overall, this chapter intended to give the readers a quick appreciation of the challenges in the growth, observation of

interesting optoelectronic properties, potential for sensing applications, involving nanostructured indium nitride material.

Acknowledgements

This work has been done under the financial assistance from the National Science Council, Ministry Of Education (MOE), and Academia Sinica, Taiwan. One of the authors (S.C) acknowledges support from MOE and the Center of Nanoscience and Nanotechnology, National Chung Hsing University, Taichung.

References

1. W. C. Johnson, J. B. Parsons and M. C. Crew, *J. Phys. Chem.* **234**, 2651 (1932).
2. R. Juza, E. Hahn and Z. Anorg, *Allgem. Chem.* **234**, 282 (1938).
3. H. Grimmeiss and H. Koelmans, *Z. Naturfg* **14a**, 264 (1959).
4. J. I. Pankove, E. A. Miller and J. E. Berkeyheiser, *J. Lumin.* **5**, 84 (1972).
5. T. L. Tansley and C. P. Foley, *J. Appl. Phys.* **59**, 3241 (1986).
6. S. Nakamura, *Mat. Res. Soc. Bull.* **22**, 29 (1997).
7. I. Akasaki and H. Amano, in *GaN*, Vol. 1, Eds. J. I. Pankove and T. D. Moustakas (Academic, New York, 1998), p. 459.
8. S. Nakamura, in *GaN and related Materials*, Ed. S. J. Pearton (Gordon and Breach, New York, 1997), p. 471.
9. H. Morkoc, in *Nitride Semiconductors and Devices* (Springer-Verlag, Berlin Heidelberg, 1999).
10. S. Strite and H. Morkoc, *J. Vac. Sci. Technol. B* **10**, 1237 (1992).
11. O. Ambacher, *J. Appl. Phys. D* **31**, 2653 (1998).
12. R. S. Wagner and W. C. Ellis, *Appl. Phys. Lett.* **4**, 89 (1964).
13. C.H. Liang, L.C. Chen, J.S. Hwang, K.H. Chen, Y.T. Hung and Y.F. Chen, *Appl. Phys. Lett.* **81**, 22 (2002).
14. Z. H. Lan, W. M. Wang, C. L. Sun, S. C. Shi, C. W. Hsu, T. T. Chen, K. H. Chen, C. C. Chen, Y. F. Chen and L. C. Chen, *J. Cryst. Growth* **269**, 87 (2004).
15. M. S. Hu, W. M. Wang, T. T. Chen, L. S. Hong, C. W. Chen, C. C. Chen, Y. F. Chen, K. H. Chen and L. C. Chen, *Adv. Funct. Mater.* **16**, 537 (2006).
16. T. Tang, S. Han, W. Jin, X. Liu, C. Li, D. Zhang, C. Zhou, B. Chen, J. Han and M. Meyyapan, *J. Mater. Res.* **19**, 423 (2004).
17. L. W. Yin, Y. Bando, Y. C. Zhu, D. Golberg and M. S. Li, *Appl. Phys. Lett.* **84**, 1546 (2004).
18. T.T. Kang, X. Liu, R. Q. Zhang, W. G. Hu, G. Cong, F. A. Zhao and Q. Zhu, *Appl. Phys. Lett.* **89**, 071113 (2006).
19. S. Vaddiraju, A. Mohite, A. Chin, M. Meyyappan, G. Sumanasekera, B. W. Alphenaar and M. K. Sunkara, *Nano Lett.* **5**, 1625 (2005).

20. S. D. Dingman, N. P. Rath, P. D. Markowitz, P. C. Gibbons and W. E. Buhro, *Angew. Chem. Int. Ed.* **39**, 1470 (2000).
21. X. M. Cai, Y. H. Leung, K. Y. Cheung, K. H. Tam, A. B. Djurišić, M. H. Xie, H. Y. Chen and S. Gwo, *Nanotechnology* **17**, 2330 (2006).
22. C.W. Hsu, A. Ganguly, C. H. Liang, Y. T. Hung, C. T. Wu, G. M. Hsu, Y. F. Chen, C. C. Chen, K. H. Chen and L. C. Chen, *private commun*..
23. J. Zhang, L. Zhang, X. Peng and X. Wang, *J. Mater. Chem.* **12**, 802 (2002).
24. B. Schwenzer, L. Loeffler, R. Seshardri, S. Keller, F. F. Lange, S. P. DenBaars and U. K. Mishra, *J. Mater. Chem.* **14**, 637 (2004).
25. M.C. Johnson, C.J. Lee, E.D. Bourret-Courchesne, S.L. Konsek, S. Aloni, W.Q. Han and A. Zettl, *Appl. Phys. Lett.* **85**, 5670 (2004).
26. S. Luo, W. Zhou, Z. Zhang, L. Liu, X. Dou, J. Wang, X. Zhao, D. Liu, Y. Gao, L. Song, Y. Xiang, J. Zhou and S. Xie, *Small* **1**, 1004 (2005).
27. G. Cheng, E. Stern, D. Turner-Evans and M. A. Reed, *Appl. Phys. Lett.* **87**, 253103 (2005).
28. S. Luo, W. Zhou, Z. Zhang, X. Dou, L. Liu, X. Zhao, D. Liu, L. Song, Y. Xiang, J. Zhou and S. Xie, *Chem. Phys. Lett.* **411**, 361 (2005).
29. J. Zhang, F. Jiang, Y. Yang, B. Xu, J. Li, X. Wang and S. Wang, *Mater. Lett.* **60**, 2153 (2006).
30. J. Zhang, B. Xu, F. Jiang, Y. Yang and J. Li, *Phys. Lett. A* **337**, 121 (2005).
31. L. W. Yin, Y. Bando, D. Goldberg and M. S. Li, *Adv. Mater.* **16**, 1833 (2004).
32. A. R. Smith, R. M. Feenstra, D. W. Greve, J. Neugebauer and J. E. Northrup, *Phys. Rev. Lett.* **79**, 3934 (1997).
33. T. Stoica, R. Meijers, R. Calarco, T. Richter and H. Lüth, *J. Cryst. Growth* **290**, 241 (2006).
34. R. E. Jones, K. M. Yu, S. X. Li, W. Walukiewicz, J. W. Ager, E. E. Haller, H. Lu and W. J. Schaff, *Phys. Rev. Lett.* **96**, 125505 (2006).
35. E. Dimakis, G. Konstantinidis, K. Tsagaraki, A. Adikimenakis, E. Iliopoulos and A. Georgakilas, *Superlattices Microstruct.* **36**, 497 (2004).
36. J. Grandal, M. A. Sanchez-Garcı´a, F. Calle and E. Calleja, *Phys. Status Solidi C* **2**, 2289 (2005).
37. T. Stoica, R. Meijers, R. Calarco, T. Richter, E. Sutter and H. Lüth, *Nano Lett.* **6**, 1541 (2006).
38. C. H. Shen, H. Y. Chen, H. W. Lin, S. Gwo, A. A. Klochikhin and V. Yu. Davydov, *Appl. Phys. Lett.* **88**, 253104 (2006).
39. L. A. Marasina, I. G. Pichugin and M. Tlaczala, Krist. Tech. **12**, 541 (1977).
40. Y. Sato and S. Sato, *J. Cryst. Growth* **144**, 15 (1994).
41. N. Takahashi, R. Matsumoto, A. Koukitu and H. Seki, *Jpn. J. Appl. Phys.* **36**, L743 (1997).
42. D. Y. Song, V. Kuryatkov, M. Basavaraj, D. Rosenbladt, S. A. Nikishin, M. Holtz, A. L. Syrkin, A. S. Usikov, V. A. Ivantsov and V. A. Dmitriev, *J. Appl. Phys.* **99**, 116103 (2006).
43. H. M. Kim, W. C. Lee, T. W. Kang, K. S. Chung, C. S. Yoon and C. K. Kim, *Chem. Phys. Lett.* **380**, 181 (2003).
44. H. M. Kim, T. W. Kang and K. S. Chung, *J. Ceram. Proc. Res.* **5**, 241 (2004).

45. H. M. Kim, H. Lee, S. I. Kim, S. R. Ryu, T. W. Kang and K. S. Chung, *Phys. Status Solidi B* **241**, 2802 (2004).
46. O. Kryliouk, H.J. Park, H.T. Wang, B.S. Kang, T.J. Anderson, F. Ren and S.J. Pearton, *J. Vac. Sci. Technol. B* **23**, 1891 (2005).
47. C. K. Chao, J. I. Chyi, C. N. Hsiao, C. C. Kei, S. Y. Kuo, H. S. Chang and T. M. Hsu, *Appl. Phys. Lett.* **88**, 233111 (2006).
48. C. K. Chao, H. S. Chang, T. M. Hsu, C. N. Hsiao, C. C. Kei, S. Y. Kuo and J. I. Chyi, *Nanotechnology* **17**, 3930 (2006).
49. S. C. Shi, C. F. Chen, G. M. Hsu, J. S. Hwang, S. Chattopadhyay, Z. H. Lan, K. H. Chen and L. C. Chen, *Appl. Phys. Lett.* **87**, 203103 (2005).
50. S. Chattopadhyay, K. H. Chen, S. C. Shi, C. T. Wu, C. H. Chen and L. C. Chen, *Appl. Phys. Lett.* **89**, 143105 (2006).
51. H. Parala, A. Devi, F. Hipler, E. Maile, A. Birkner, H. W. Becker and R. A. Fischer, *J. Cryst. Growth* **231**, 68 (2001).
52. L. W. Ji, T. H. Fang, S. C. Hung, Y. K. Su, S. J. Chang and R. W. Chuang, *J. Vac. Sci. Technol. B* **23**, 2496 (2005).
53. Z. H. Lan, C. H. Liang, C. W. Hsu, C. T. Wu, H. M. Lin, S. Dhara, K. H. Chen, L. C. Chen and C. C. Chen, *Adv. Funct. Mater.* **14**, 233 (2004).
54. Y. J. Bai, Z. G. Liu, X. G. Xu, D. L. Cui, X. P. Hao, X. Feng and Q. L. Wang, *J. Cryst. Growth* **241**, 189 (2002).
55. K. Sardar, F. L. Deepark, A. Govindaraj, M. M. Seikh and C. N. R. Rao, *Small* **1**, 91 (2005).
56. G. D. Gilliland, *Mater. Sci. Eng. R* **18**, 99 (1997).
57. T. Inushima, V. V. Mamutin, V. A. Vekshin, S. V. Ivanov, T. Sakon, M. Motokawa and S. Ohoya, *J. Cryst. Growth* **227-228**, 481 (2001).
58. V. Y. Davydov, A. A. Klochikhin, R. P. Seisyan, V. V. Emtsev, S. V. Ivanov, F. Bechstedt, J. Furthmuller, H. Harima, A. V. Mudryi, J. Aderhold, O. Semchinova and J. Graul, *Phys. Status Solidi B* **229**, R1 (2002).
59. J. Wu, W. Walukiewicz, K. M. Yu, J. W. Ager III, E. E. Haller, H. Lu, W. J. Schaff, Y. Saito and Y. Nanishi, *Appl. Phys. Lett.* **80**, 3967 (2002).
60. J. C. Ho, P. Specht, Q. Yang, X. Xu, D. Hao and E. R. Weber, *J. Appl. Phys.* **98**, 093712 (2005).
61. X. H. Ji, S. P. Lau, H. Y. Yang and S. F. Yu, *Nanotechnology* **16**, 3069 (2005).
62. S. Luo, W. Zhou, W. Wang, Z. Zhang, L. Liu, X. Dou, J. Wang, X. Zhao, D. Liu, Y. Gao, L. Song, Y. Xiang, J. Zhou and S. Xie, *Appl. Phys. Lett.* **87**, 063109 (2005).
63. H. Y. Chen, C. H. Shen, H. W. Lin, C. H. Chen, C. Y. Yu, S. Gwo, V. Y. Davydov and A. A. Klochikhin, *Thin Solid Films* **515**, 961 (2006).
64. B. R. Nag, *Phys. Status Solidi B* **237**, R2 (2003).
65. J. Wu, W. Walukiewicz, W. Shan, K. M. Yu, J. W. Ager III, E. E. Haller, H. Lu and W. J. Schaff, *Phys. Rev. B* **66**, 201403 (2002).
66. T. V. Shubina, S. V. Ivanov, V. N. Jmerik, M. M. Glazov, A. P. Kalvarskii, M. G. Tkachman, A. Vasson, J. Leymarie, A. Kavokin, H. Amano, I. Akasaki, K. S. A. Butcher, Q. Guo, B. Monemar and P. S. Kop'ev, *Phys. Status Solidi A* **202**, 377 (2005).

67. Y. Sun, Y. H. Cho, H. M. Kim and T. W. Kang, *Appl. Phys. Lett.* **87**, 093115 (2005).
68. T. Matsuoka, H. Okamoto, M. Nakao, H. Harima and E. Kurimoto, *Appl. Phys. Lett.* **81**, 1246 (2002).
69. Y. Saito, H. Harima, E. Kurimoto, T. Yamaguchi, N. Teraguchi, A. Suzuki, T. Araki and Y. Nanishi, *Phys. Status Solidi B* **234**, 796 (2002).
70. J. Aderhold, V. Y. Davydov, F. Fedler, H. Klausing, D. Mistele, T. Rotter, O. Semchinova, J. Stemmer and J. Graul, *J. Cryst. Growth* **222**, 701 (2001).
71. V. V. Mamutin, V. A. Vekshin, V. Yu. Davydov, V. V. Ratnikov, T. V. Shubina, S. V. Ivanov, P. S. Kopev, M. Karlsteen, U. Söderwall and M. Willander, *Phys. Status Solidi A* **176**, 247 (1999).
72. V. Y. Davydov, V. V. Emtsev, I. N. Goncharuk, A. N. Smirnov, V. D. Petrikov, V. V. Mamutin, V. A. Vekshin, S. V. Ivanov, M. B. Smirnov and T. Inushima., *Appl. Phys. Lett.* **75**, 3297 (1999).
73. V. Y. Davydov, A.A. Klochikhin, M.B. Smirnov, V.V. Emtsev, V.D. Petrikov, I.A. Abroyan, A.I. Titov, I.N. Goncharuk, A.N. Smirnov, V.V. Mamutin, S.V. Ivanov and T. Inushima, *Phys. Status Solidi B* **216**, 779 (1999).
74. G. Kaczmarczyk, A. Kaschner, S. Reich, A. Hoffmann, C. Thomsen, D. J. As, A. P. Lima, D. Schikora, K. Lischka, R. Averbeck and H. Riechert, *Appl. Phys. Lett.* **76**, 2122 (2000).
75. E. Kurimoto, H. Harima, A. Hashimoto and A. Yamamoto, *Phys. Status Solidi B* **228**, 1 (2001).
76. S. Luo, W. Zhou, Z. Zhang, J. Shen, L. Liu, W. Ma, X. Zhao, D. Liu, L. Song, Y. Xiang, J. Zhou and S. Xie, *Appl. Phys. Lett.* **89**, 093112 (2006).
77. O. Briot, B. Maleyre, S. Ruffenach, B. Gil, C. Pinquier, F. Demangeot and J. Frandon, *J. Cryst. Growth* **269**, 22 (2004).
78. M. Yoshimoto, H. Yamamoto, W. Huang, H. Harima, J. Saraie, A. Chayahara and Y. Horino, *Appl. Phys. Lett.* **83**, 3480 (2003).
79. C. R. Abernathy, in *GaN and Related Materials*, Ed. S. J. Pearton (Gordon and Breach, New York, 1997), p. 11.
80. C. Y. Chang, G. C. Chi, W. M. Wang, L. C. Chen, K. H. Chen, F. Ren and S. J. Pearton, *Appl. Phys. Lett.* **87**, 093112 (2005).
81. C. Y. Chang, G. C. Chi, W. M. Wang, L. C. Chen, K. H. Chen, F. Ren and S. J. Pearton, *J. Electron. Mater.* **35**, 738 (2006).
82. S. Yin, Z. Z. Sun, J. Lu and X. R. Wang, *Appl. Phys. Lett.* **88**, 233110 (2006).
83. S. Nakamura and G. Fasol, in *The Blue Laser Diodes* (Springer, Heidelberg, 1997).
84. S. Nakamura, in *GaN*, Vol. 1, Eds. J. I. Pankove and T. D. Moustakas (Academic, New York, 1998).
85. S. Nakamura, *Science* **281**, 956 (1998).
86. P. G. Caceres and H. K. Schmid, *J. Am. Ceram. Soc.* **77**, 977 (1994).
87. S. C. Binari and H. C. Dietrich, in *GaN and related Materials*, Ed. S. J. Pearton (Gordon and Breach, New York, 1997), p. 509.
88. M. A. Khan, Q. Chen, J. W. Yang and C. J. Sun, *Inst. Phys. Conf. Ser.* **142**, 985 (1995).
89. M. S. Shur and M. A. Khan, *Mater. Res. Soc. Bull.* **22**, 44 (1997).

90. J. Y. Duboz and M. A. Khan, in *Group III Nitride Semiconductor Compounds*, Ed. B. Gil (Clarendon, Oxford, 1998), p. 343.
91. B. Gil, Ed., *Low dimensional Nitride Semiconductors* (Oxford University Press, New York, 2002).
92. L. C. Chen, K. H. Chen and C. C. Chen, in *Nanowires and Nanobelts: Materials, Properties and Devices: Metal and Semiconductor Nanowires*, Vol. 1, Ed. Z. L. Wang (Kluwer Academic Publishers, 2003), p. 257.
93. H. Lu, W. J. Schaff, L. F. Eastman and C. E. Stutz, *Appl. Phys. Lett.* **82**, 1736 (2003).
94. I. Mahboob, T. D. Veal, C. F. McConville, H. Lu and W. J. Schaff, *Phys. Rev. Lett.* **92**, 036804 (2004).
95. I. Mahboob, T. D. Veal, L. F. J. Piper, C. F. McConville, H. Lu, W. J. Schaff, J. Furthmuller and F. Bechstedt, *Phys. Rev. B* **69**, 201307 (2004).
96. J. Wu, W. Walukiewicz, K. M. Yu, W. Shan, J. W. Ager III, E. E. Haller, Hai Lu, William J. Schaff, W. K. Metzger and Sarah Kurtz, *J. Appl. Phys.* **94**, 6477 (2003).
97. H. Lu, W. J. Schaff and L. F. Eastman, *J. Appl. Phys.* **96**, 3577 (2004).